Gábor Galbács *Editor*

Laser-Induced Breakdown Spectroscopy in Biological, Forensic and Materials Sciences

Springer

Laser-Induced Breakdown Spectroscopy in Biological, Forensic and Materials Sciences

Gábor Galbács
Editor

Laser-Induced Breakdown Spectroscopy in Biological, Forensic and Materials Sciences

Springer

Editor
Gábor Galbács
Department of Inorganic and Analytical Chemistry
University of Szeged
Szeged, Hungary

ISBN 978-3-031-14501-8 ISBN 978-3-031-14502-5 (eBook)
https://doi.org/10.1007/978-3-031-14502-5

This Springer imprint is published by the registered company Springer Nature Switzerland AG
The registered company address is: Gewerbestrasse 11, 6330 Cham, Switzerland

Preface

Laser-induced breakdown spectroscopy (LIBS), which was a curiosity in the 1960s, at the time of its inception, has grown tremendously over the past few decades, and today, it has become a widely known, flexible, and powerful method of analytical spectroscopy. Its popularity is due to its uniquely advantageous set of analytical characteristics, robust instrumentation, and relative ease of use. Analytical chemists, physicists, engineers, chemometrists, biologists, and other scientists are similarly fascinated by the analytical possibilities or complexity of the laser–material interaction processes involved in the laser-induced breakdown of materials.

In the past ca. two decades, LIBS research has apparently greatly intensified, which is easily demonstrated by the fact that nowadays nearly a thousand scientific publications appear in this field every year. LIBS is now one of the dominant, hot methods in atomic spectroscopy, and the range of its analytical applications is rapidly widening. Over the years, the results produced have been compiled and aggregated in several books, book chapters, and dozens of review papers. Most surveys focus on laser–matter and laser–plasma interactions, signal formation, and various calibration methods. In terms of applications, the development was perhaps fastest in the industry (e.g., raw material assessment, process monitoring, and alloy analysis) and in environmental studies, as well as in remote or stand-off measurement scenarios (including space exploration or analysis under extreme conditions). In these fields, many quantitative and qualitative analytical applications explored the potential of LIBS. Consequently, prior summaries focused on these areas.

This book is meant as a contemporary overview of the advances of laser-induced breakdown spectroscopy in some specific application areas, which have only become the subject of research interest most recently. Namely, in the past decade, LIBS has found its way into the field of life sciences (e.g., biology and medical science), as a novel diagnostic tool and a new methodology for studying elemental distributions in biological samples. It has been successfully demonstrated that LIBS has great potential for elemental imaging, even at the cellular level, and the qualitative discrimination of organisms or tissues. Another scientific field which progresses with giant leaps in recent years is materials science. Related sub-fields, like nanotechnology, fabrication of nanoparticles, and composite or layered materials, all require a versatile, fast, sensitive, high spatial resolution measurement technique, which primarily works with inorganic samples and detects elemental composition.

As it turns out, LIBS can fit this bill also well; thus, the development of materials science LIBS applications has also started to grow exponentially. Interdisciplinary areas between life science and materials science can also benefit from the application of LIBS—the studies of the uptake or distribution of nanoparticles (as a form of contamination, or with therapeutic or diagnostic purposes) in organs, tissues, or foodstuff can be mentioned as examples. Forensic investigations also often deal with samples (evidence) of biological or inorganic origin; thus, advancements in the other abovementioned two application fields can also contribute to the solution of forensic problems.

These thoughts led to the conclusion that a book should be dedicated to the comprehensive overview of the results produced by the LIBS community in the fields of biology, materials science, and forensics in recent years. This book is application-oriented and was mainly written for scientists who are interested in solving analytical/diagnostic/material characterization tasks with the application of LIBS. Hence, the emphasis was placed more on the applications and less on basic science. The fundamentals and analytical performance of LIBS are also briefly discussed in a couple of introductory chapters, but the majority of the book deals with the description of contemporary application results in the focus.

It is the hope of the editor that this book will kindle an interest in the readers, who will probably mainly be biologists, chemists, medical doctors, or engineers, toward this technique, and thus can serve as an introduction to the fascinating world of LIBS.

Szeged, Hungary Gábor Galbács
June 2022

Contents

Part I

Fundamentals

Laser-Induced Breakdown Spectroscopy

1

Gábor Galbács

1.1 Principle of Operation

A laser-induced breakdown spectrometer is an atomic emission spectrometer that uses the small plasma generated by a high intensity, focused, and pulsed laser beam as the atom and excitation source. For this reason, the analytical method is sometimes named lased-induced plasma spectroscopy (LIPS), but it is mostly known as laser-induced breakdown spectroscopy (LIBS).

During the LIBS analysis of a solid sample, the laser beam is focused onto the surface of the solid, whereas with fluid samples, the beam is generally focused inside the sample. A high enough laser power density (irradiance) is needed to be used in the process in order to initiate intense laser–matter interaction processes which lead to the formation of the microplasma. In the case of conventional LIBS instruments, the duration of the laser pulse is a few nanoseconds and the pulse energy is typically between 10 and 100 mJ. Focusing the beam down to around a 100 μm diameter spot produces a GW to TW power in a ca. 0.001 mm^3 interaction volume. As soon as the laser pulse reaches the sample, the absorption of the photons will increase the temperature of the material in the focal spot very rapidly. In less than a ns, the temperature reaches the boiling point and the ejection of sample vapor, fragments and particles will start (this process is known as laser ablation). The ablation plume forms so rapidly that it meets the tail of the laser pulse, thus the laser will continue to heat the ablated material, leading to a very high temperature, in excess of 20,000 K. This temperature is high enough to thermally atomize, excite and ionize the plume material, thus within a few nanoseconds, it turns into a plasma (the processes leading to the formation of the microplasma altogether are called the laser-induced optical breakdown, hence the LIBS name). The microplasma will start emitting a strong

G. Galbács (✉)
Department of Inorganic and Analytical Chemistry, University of Szeged, Szeged, Hungary
e-mail: galbx@chem.u-szeged.hu

G. Galbács (ed.), *Laser-Induced Breakdown Spectroscopy in Biological, Forensic and Materials Sciences*, https://doi.org/10.1007/978-3-031-14502-5_1

emission of radiation, which is characteristic of its chemical components; the observation of the emission spectrum allows the process to be used for analytical spectroscopy purposes. As soon as the laser pulse ceases, the plasma will quickly start to cool down as a result of the lack of further energy input. The high-pressure plasma material will continue to expand rapidly into the surrounding medium (typically air), which initiates a pressure wave (shockwave) to form and propagate outwards. This work on the surrounding medium also contributes to the quick decay of the plasma. The typical laser-induced breakdown (LIB) plasma lifetime is between ca. 100 ns and some tens of μs (depending on the experimental conditions). Due to these latter processes, the optical breakdown of the material is accompanied by a snapping sound and a spark-like visual phenomenon. During the cooling and expansion phase of the plume, its material will condense and fall back onto the sample in the form of micro- and nanodroplets/particles, unless the measurement is carried out in vacuum. In the case of a solid sample, the process will leave behind a small crater on the sample surface, with a diameter somewhat larger than the laser spot size and a shallow depth (usually a few μm). These processes are schematically illustrated in Fig. 1.1.

Of course, the above is a largely simplified description of the intense, complex, and highly transient laser–material interaction taking place during the formation of an LIB plasma. The experimental conditions have a tremendous impact on the time scale and balance of the various processes occurring. As the present book and chapter is application- and analysis-oriented, we will not go into the details of the ablation and ionization processes, or associated equilibria. Interested readers are referred to laser and plasma physics books [1, 2] or physics-oriented chapters of some LIBS books which are devoted to the topic (e.g. in [3–5]).

The very short plasma lifetime necessitates the use of a fast, non-scanning spectrometer for the recording of the emission spectrum, the operation of which is tightly synchronized with the laser pulse. The delay and width of the spectrum acquisition time window (also known as gate delay and width, the latter often is also called integration time) must be controlled and optimized with sub-μs accuracy, so that the radiation of the analyte species (atoms, ions, or molecules) can be captured when they are dominant. Early in the plasma lifetime, when its temperature is highest, the dominant emitting species are excited ions and electrons. As the latter emit continuous Bremsstrahlung radiation, the spectrum will consist of ionic lines and a strong continuous background. As the plasma starts to cool down, the ion-electron collisions and recombinations will produce excited atoms which will rule the emission a couple of microseconds after the onset of the plasma and the continuum background emission becomes much less intense. This phase is the typical time window for analytical LIBS measurements, when spectral lines with a good signal-to-noise ratio (S/N) can be observed and elemental analysis can be performed. As usual, the intensity (or peak area) of the emission lines of the analyte will be related to the concentration of the analyte element. In the late phase of the plasma lifetime (after, e.g., 10 μs), the collision and recombination of sample atoms and those of the surrounding medium (e.g., nitrogen and oxygen from air) will generate excited molecules and hence the emission spectrum will be populated mainly by molecular bands. These processes are conceptually depicted in Fig. 1.2.

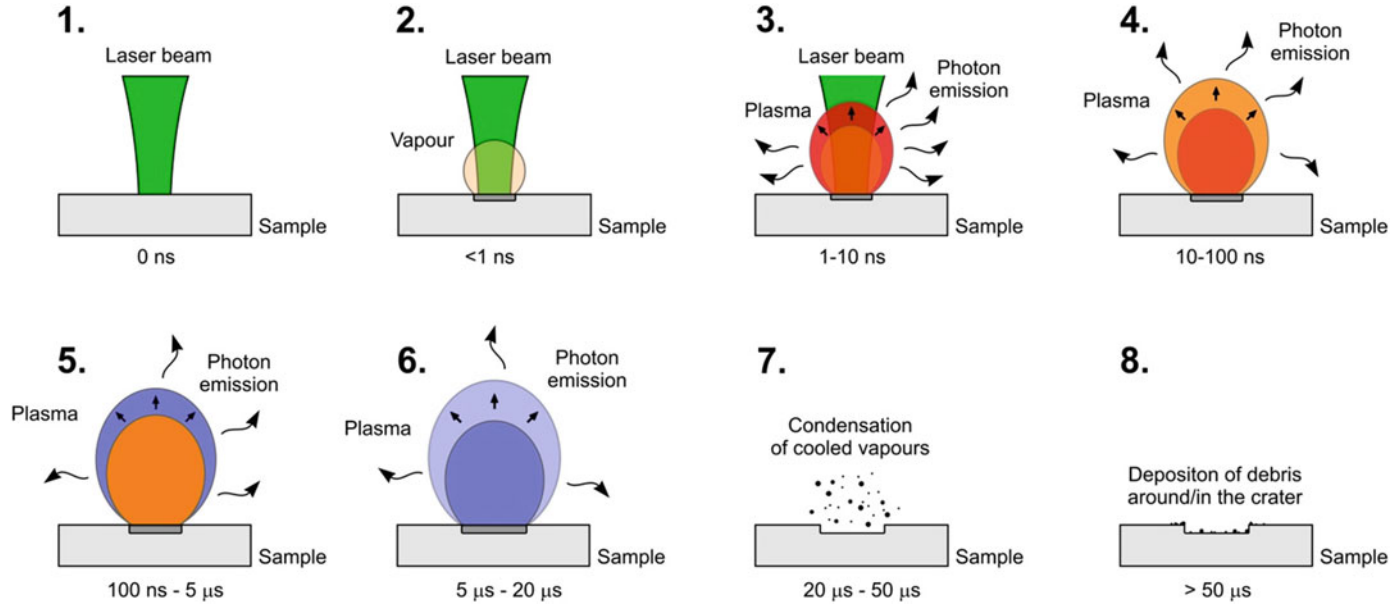

Fig. 1.1 Simplified overview of the time evolution and processes occurring during the laser-induced breakdown of a solid sample under atmospheric conditions and using a 5–10 ns duration laser pulse. Time ranges shown are only meant as indicative values. The trend in the hue of the coloring of the ablation plume is intended to illustrate the course of its temperature. Similarly, the trend in the number of wavy arrows illustrates the changes in the intensity of light emission

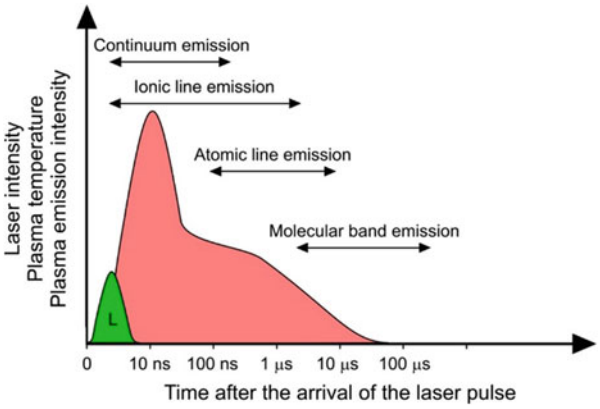

Fig. 1.2 General time evolution of the light emission of a laser-induced breakdown plasma generated with a nanosecond-range duration single laser pulse. *L* designates the laser pulse

Please note that if the laser pulse duration is substantially shorter (e.g., ps or fs) or if the experiment is carried out under vacuum then the time scales are also significantly shorter, as the plasma lifetime decreases [3–8].

In consideration of the above conditions, a typical, conventional laboratory-based LIBS instrument consists of the following essential parts: (1) laser source emitting high intensity, fast laser pulses, preferentially at a wavelength well-absorbed by the sample, (2) focusing optics that focuses the laser beam onto a small spot on or in the sample in order to reach the optical power density required for the laser-induced breakdown, (3) a precision sample stage which holds the sample and allows it to be moved around to select the analytical spot, (4) a light collection optics, (5) a fast-triggerable and sensitive, non-scanning spectrometer capable of recording the UV–Vis-NIR emission spectrum with a minimum of 100 pm spectral resolution and μs-range integration time, (6) fast electronics (e.g., pulse delay generator) which allows the control of the synchronized operation of the spectrometer and the incoming laser pulse with a sub-μs accuracy, (7) a computer with a proper data acquisition and evaluation software. This generalized setup is illustrated in Fig. 1.3. Needless to say that there is a wide variety of LIBS setups in use, which vary in the specifications of the system components and the geometrical layout, as dictated by the optimization for various applications or experiments—the major varieties are discussed in the next section. Portable LIBS instrumentation, which nowadays are more and more popular, tend to be simpler [9, 10].

1.2 Analytical Performance

LIBS is a trace analytical method, with typical detection limits in the ppm (mg/kg) range for metallic/alloy solid samples. For liquids and gases, the detection limits are significantly higher. Most elements in the periodic system can be detected by LIBS with similar detection limits, thus also light elements (a significant advantage over e.g. XRF). If the detection gate delay and width is optimized and other experimental

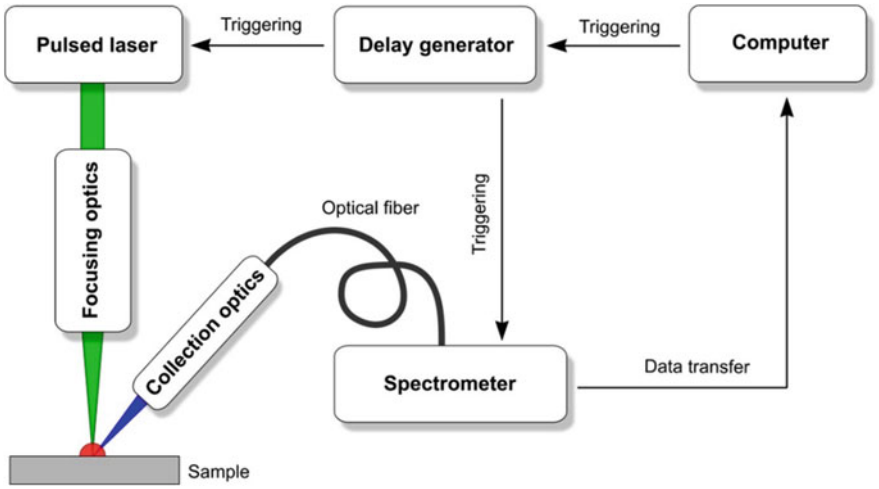

Fig. 1.3 Generalized layout of the essential components of a LIBS experimental setup

conditions also facilitate this, even the isotopic composition of samples can be determined—this is called laser ablation molecular isotope spectroscopy, or LAMIS, a variant of LIBS [11]. The dynamic range is typically around 3 orders of magnitude, thereby allowing LIBS to determine trace and minor components. Above a few % concentration level the calibration plots start to saturate, unless special measurement conditions are used, which may even allow analysis up to 100% concentration. With the application of signal enhancement techniques, the dynamic range can be extended by about two orders of magnitude toward lower detection limits (into the tens of ppb range).

It is a great advantage of LIBS that any phases (solid, gas, liquid) can be analyzed with essentially no (or very little) sample preparation prior to the measurement. In fact, the sample surface of solids can be cleaned by preliminary laser shots (or by discarding spectra recorded for the first couple of laser shots). This also makes LIBS analysis fast. Since (laser) light needs to be directed toward the sample and also light, emitted by the microplasma, is detected during LIBS analysis, therefore a true non-contact measurement is carried out. This not only allows the analysis of hazardous materials, e.g. in a closed sample chamber but also remote or stand-off analysis [12]. LIBS instrumentation is relatively robust, and can be made compact (ultra-portable) and field-deployable. It is becoming increasingly popular in many industrial sectors [13, 14].

A LIBS spectrum consists of hundreds or thousands of narrow spectral lines and molecular bands, thus it has a great information content. A LIBS spectrum can be considered to be a fingerprint-like identifier of the sample, which supports many qualitative discrimination applications (e.g., classification, identification, comparison of samples, diagnostics, monitoring, etc.). These applications require sophisticated multivariate data evaluation techniques, but with the use of the proper

statistical approach, 90+ % accuracy can be achieved. The great information content, the complexity spectrum is advantageous on one hand, but on the other, it also means that quantitative applications have to be very careful with the choice of analytical spectral lines, due to potential interferences (spectral and matrix interferences).

The analytical (or laser) spot size generally is in the 100–300 μm range, but micrometer-range spot sizes can also be achieved relatively easily [6]. These small analytical spots mean that high spatial resolution analysis is possible. If the solid sample and the laser beam is controllably moved with relation to each other (scanning) then elemental mapping is possible of the surface of solid samples along a trajectory or in a rectangular area [15]. Since the laser ablation process ocurring during LIBS analysis is removing only a microscopic amount of matter (e.g. ng to μg), the analysis can be considered to be virtually non-destructive. If the laser beam is directed to the same spot then this ablative feature of LIBS can also be used to "dig" deeper and deeper into the sample material, thus depth-resolved analysis is also possible with micrometer-range depth resolution. This is most useful for the analysis of thin layers/films.

The precision of conventional (single-pulse) LIBS analysis is not very good—10–20% RSD values (or more) for signal repeatability are typical. This is not uncommon for microanalytical methods (e.g., micro Raman, micro X-Ray fluorescence spectroscopy, solid sampling graphite furnace atomic absorption spectroscopy) and it partly stems from e.g. the heterogeneity of solid samples and shot-to-shot laser pulse energy variations. There are however techniques that can greatly improve on this. Some improvement can be achieved statistically, by performing a large number of measurements (e.g., some hundreds) across the sample surface instead of a few. This approach can bring the signal scatter to below ca. 10% RSD. Further, dramatic improvement can be achieved by using collinear multi-pulse delivering techniques (with μs interpulse delays) and integrating the signal across multiple laser shots [16]; with this approach, the signal repeatability can be kept below 5%. To enhance the precision in quantitative applications, the use of robust calibration techniques that rely on most of the spectrum not just on one spectral line, like GLCM (generalized linear correlation method) or PLS (partial least squares), is highly advisable. With the help of the combination of the above techniques, accuracy and precision of around 1% relative have been demonstrated for various alloys under advantageous conditions [17, 18]. All in all, reasonable expectations for accuracy and precision are around a few percents relative with LIBS for solid samples.

Further details about the state-of-the-art analytical performance of LIBS and various calibration approaches can be found in other chapters across this book.

1.3 Instrumentational Details and Variants

In the sections below, an overview is given of the main variants and relations of the major components of LIBS systems. It is not the intention to provide an in-depth description of the technical/optical/electronic details here, but rather to present

information that can help one, e.g., to choose a commercial instrument for a given analytical task and to support considerations toward the optimization of the performance of a specific system. LIBS is generally considered a technically simple analytical method; however, due to the complexity of the laser–material interaction and the joint requirements of the components, it is worth "to look under the hood" of LIBS systems even for those researchers, who only consider themselves users.

1.3.1 Laser Sources

The mass of ablated material and plasma shielding (the absorption of the laser pulse by the laser-induced ablation plume) are both important for efficient LIBS signal generation, and for these reasons ns-duration laser pulses are generally regarded as optimum for LIBS in terms of limits of detection [19]. As laser-ablation reviews reveal (e.g., [3, 20]), the application of ultrashort (femtosecond, fs) laser pulses seems to have distinct analytical advantages, including more stoichiometric sample ablation and thus more accurate analyses, reduced continuum radiation, and cleaner crater rims in solids and thus better spatial resolution [21, 22]. This leads to more and more fs LIBS studies being conducted; however, it is doubtful that bulky and costly fs lasers would soon fully replace the conventional compact, robust, and economical ns laser sources (e.g., Nd:YAG) widely used today.

The effect of the laser wavelength on LIBS performance is a complex one. In the case of ns laser pulses, the laser wavelength should generally be selected so that the light absorption of the sample is large. The achievable minimum laser focal spot size is limited by the diffraction limit, which is a function of the wavelength. These two aspects would lead one to the conclusion that UV lasers should always be preferred. However, plasma shielding, which has a great contribution to plasma heating and thus to the intensity of the emission spectrum, was revealed to scale with λ^3. Thus in this respect, infrared or near-infrared (NIR) wavelengths (in the range of ca. 1.0–1.1 μm) perform better [3]. Frequency upconversion by nonlinear techniques is commonly available to produce visible or UV wavelength radiation from a pulsed, NIR laser emission, but it causes a great reduction in pulse energy. Most LIBS analyses of solids in air are still typically done at around 1.06 μm NIR wavelengths (e.g., fundamental wavelength of a Nd:YAG laser). In portable systems, where eye safety is of primary concern, 1.3–1.5 μm wavelength Er lasers are also used [23]. Following from the above, the choice of the laser wavelength is not a trivial one, but in general only in special cases, when the sample has an exceptionally low absorbance in the NIR region (e.g., glasses or crystals), are Vis or UV laser wavelengths used. Examples include 532 nm (for solids submerged in water), 266 nm or 213 nm wavelengths produced from Nd:YAG lasers or 193 nm pulses from ArF excimer lasers.

As semiconductor laser technology becomes more and more advanced, diode-pumped solid-state (DPSS) lasers are slowly taking over the place from flashlamp-pumped Nd:YAG lasers in LIBS setups, because these lasers have better specifications in most aspects, such as higher repetition rates, better pulse-to-pulse

repeatability, improved beam characteristics, durability, much reduced size, and better energy efficiency. Another promising novel laser type for LIBS is the group of pulsed fiber lasers, which have many attractive features also exploitable in LIBS [24–26], including resistance to vibrations, inherently fiber-coupled output, compactness and extremely high pulse repetition rates (reaching into the MHz range). The top pulse energy of commercial fiber lasers increases every year and now is in excess of 5 mJ, which is sufficient for most LIBS applications, thus it is expected that these sources will find their way into the mainstream of LIBS. DPSS lasers and fiber lasers are also of interest for applications requiring LIBS elemental mapping, as kHz-range pulse repetition rates can result in much faster scanning speeds [27, 28]. The compactness of DPSS and fiber lasers is also an appealing property for portable or industrial applications, the laser being the most bulky component of any LIBS system.

1.3.2 Optics

The optical subsystem of a LIBS setup has two main parts: the laser focusing and light collection optics (together, they are sometimes called beam guiding optics). The purpose of the focusing optics is to guide the laser beam to the sample and focus it to a small spot in order to increase the irradiance to the level needed for the breakdown. In most cases, the laser beam reaches the sample surface at a normal angle. Beam focusing with the use of a single (plano)convex or best-form lens with a long focal length, or a high damage threshold, long-working distance microscope objective are common. The minimum practical lens-to-sample distance is ca. 20–25 mm; however, combustible samples (e.g., plastics or organics) can easily produce "flames" in air higher than this, which necessitates an increase of the distance to avoid damage and the deposition of debris to the focusing optics. Extremely long focal length focusing optics are in use in stand-off LIBS setups [12]. All transmission optical elements in the focusing system need to be coated with an anti-reflection coating in order to maximize the pulse energy available on the sample surface and to minimize back-reflection of laser light into the source. In sophisticated setups, a Faraday isolator can also be incorporated to further eliminate the back-propagation of the laser beam. In principle, beam guiding can be conveniently done by using optical fibers; however, the maximum fluence an optical fiber material can accept without damage (damage threshold) and nonlinear processes, such as Brillouin scattering, is limited, thus the use of free-space focusing optics in LIBS is still far more common (except in some remote LIBS systems).

It is also relevant how the sample surface is brought into focus, especially if the sample has an irregular surface or is moving. Here, the depth of focus also becomes important. The depth of focus, usually characterized by the Rayleigh range, is proportional with the wavelength and the square of the ratio of the focal length to the input beam diameter [5]. If the depth of focus is small (which usually comes together with tight focusing and short focal lengths) then there is a high gradient of beam power density as a function of sample-to-lens distance. This translates into a

high signal scatter if the distance changes, which strongly affects analytical accuracy and precision. The intent to maintain a reasonable depth of focus leads to that most LIBS setups do not employ laser beam focusing to a smaller than around 100 μm diameter spot and tend to use a longer focal length optics ($f \geq 100$ mm). Focusing below the sample surface is typically also considered advantageous, as it produces more stable signals and can prevent air sparks above the sample. It can also be mentioned that, of course, using a collimated laser beam with a properly high laser fluence can eliminate the nuisance associated with focusing; however this is discouraged by the potential damage to the beam delivering optical elements.

Bringing the sample in focus can be done in several ways (in addition to the manual adjustment of the lens-to-sample distance until the signal is highest or the use of a simple mechanical stop which is typical of portable, manual LIBS systems). Often an optical feedback signal is employed that indicates if the sample is in the right distance: this can be done by using, e.g., (1) a beam of an auxiliary diode laser and picking up the reflected beam by a photodiode, (2) a time-of-flight or reversed, short distance laser range finder, (3) an imaging digital camera or (4) autofocus optics. These optical solutions are very practical, but they are slow, which is a hindrance in scanning LIBS experiments and also assume that the sample has a certain level of reflectivity.

The light collection optics, as the name suggests, collects and steers a fraction of the emitted light to the spectrometer. Since the light emission of the plasma is non-directional, therefore the emission has to be collected at a solid angle as large as possible, meaning that relatively large collection lenses or mirrors are typically used. Considering that analytical measurements usually dictate the recording of the spectrum in a broad, at least 400–600 nm wide, spectral window, chromatic aberration of transmission optics can cause a difference in the efficiency of light collection (please note that there are no achromatic lens combinations for wavelengths below ca. 300 nm). This translates into a strong dependence of sensitivity as a function of wavelength (and contributes to the spectrometer instrumental function). This aberration can be avoided if reflective optics (e.g., concave mirrors or reflective telescope arrangements) are used to collect the emitted light. The light collected is often focused into an optical fiber which guides it to the spectrometer; the most efficient way of doing this is to use a two-lens arrangement (Fig. 1.4).

One also has to consider the observation angle of the collection optics. In most, simple LIBS setups, the collection optics is placed at a ca. 45° angle to the surface normal, which arrangement is practical in as much as it offers ample space for the collection optics. However, it has the drawback that if the sample distance or the height of the plasma plume varies during measurements then the collection efficiency will also fluctuate. A more practical approach is to use a collection optics co-axial with the beam guiding optics and separate the two beams by a pierced mirror or a dichroic mirror. A common arrangement uses the same lens for focusing the laser beam to a spot (beam guiding) also for light collection—however, this approach will make the usefulness of an antireflection coating on the focusing lens questionable (consider that these are optimized for a narrow wavelength range and

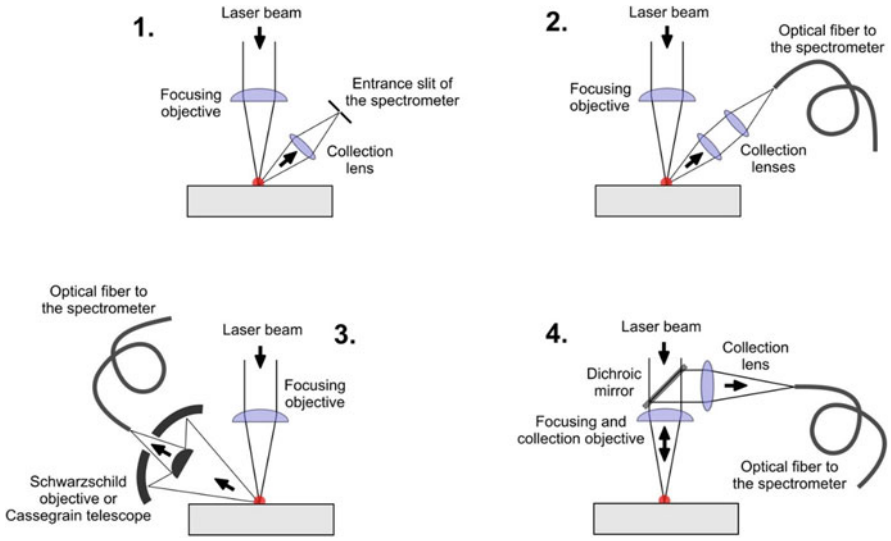

Fig. 1.4 Some typical, meaningful optical setups used in LIBS practice. Setup 2 to 4 is installed in most commercial laboratory systems. Setup 3 and 4 can be best adapted to work in stand-off measurement scenarios. Setup 3 has the advantage that collection efficiency of the broadband (UV to NIR) plasma emission does not suffer from chromatic aberrations that is characteristic of transmission optics

anyway have an influence on the transmitted spectrum). These options are also depicted in Fig. 1.4.

1.3.3 Sample Presentation

Most commonly, solid samples are analyzed by LIBS, thereby exploiting its capability to avoid the usually tedious, lengthy, and trace analytically concernful sample digestion procedures usually required by other atomic spectroscopy methods. Small solid samples are typically simply fixed to a microscope slide using a double-sided adhesive foam tape, and placed on a manual or motorized sample stage. Powdered or fine-grained solid samples are usually either pelletized using a hydraulic press (with or without a binder) or simply directly smeared onto an adhesive tape and then handled analogously to bulk solids. The latter presentation approach, although simple, has the disadvantage that the shockwave generated by the ablation can blow away (rearrange) some of the grains on the adhesive tape. For especially fine powders (e.g., nanoparticles), a novel approach called optical catapulting [29, 30] can also be employed, in which the layer of particles on a rigid substrate are mobilized by the shockwave generated by a pulse from a defocused secondary laser hitting the substrate from the back.

The analysis of bulk liquids by LIBS is challenging for several reasons. For example, the surface and the presence of bubbles or suspended particles within the

liquid will disturb laser beam focusing, and complicates the collection of plasma emission. In addition, a liquid-phase sample has a significantly higher density and stronger cooling effect than a gas, and thus imposes a stronger quenching compared to a plasma created on a solid and expanding into air. As a result of this, plasmas created in liquids have lower temperature, lower emission intensities, and shorter lifetimes and as a consequence, their analytical usefulness is limited. Another sample presentation option is the conversion of the liquid sample to a wet aerosol or liquid jet by a nebulizer [31], which provides better analytical performance, but at the expense of some inconveniences (e.g. smaller sample throughput, greater exposure to a sample mist in an open system, etc.). The liquid can also be converted to a solid by evaporation or freezing, which has the advantage that it requires only a very small droplet (μL or less). However, care has to be exercised to avoid spectral interferences from the co-ablated substrate material (e.g., glass, metal, wood, etc.). In case of evaporation, the coffee-spot effect (uneven lateral distribution of the solid deposits) also has to be minimized, which can be done by the spatial localization of the droplet, by prefabricating small "pits" in the substrate [32].

LIBS gas or solid particle aerosol sample presentation is usually a relatively simple task, which—at least in the laboratory—requires the use of a flow-through sample chamber. This approach requires a large number of repeated measurements for the statistically relevant sampling [33, 34]. In the case of aerosols, the sample presentation can also be done in the way that particles are collected on a filter prior to LIBS analysis. This technique improves sampling statistics, but is also subject to potential spectral interferences from the substrate material [35, 36].

In conventional LIBS analytical measurements, a sample chamber (a closed sample chamber with an optical window on top to allow access for the laser focusing and light collection optics) is traditionally not used, simply because it imposes limitations on the sample size and geometry, and also decreases sample throughput. However, the use of a sample chamber is more and more often considered, especially in commercial instruments. This is mainly due to safety reasons (the exposure of the analyst to hazardous samples or their ablation products is minimized and also allows the installation of an efficient suction system), but it also offers a possibility to control the composition and pressure of the gas environment in the chamber for analytical benefits. In some proprietary LIBS systems (e.g., that of Applied Spectra Inc., USA), which can also be used in the laser ablation sample introduction mode (in tandem LIBS and LA mode), the use of a carrier gas flow and a small volume chamber is a necessity anyway.

Considering the long time (several hours) usually needed for the imaging, the use of a cooling or cryogenic sample holder should be considered in the case of biological samples, as without cooling, the microbiological degradation of the sample can cause analytical errors. To handle such samples, commercial sample holders with thermoelectric cooling, similar to the ones used in microscopy, can be employed.

Most LIBS measurements also require a precision mechanical 3D stage for sample positioning and presentation under the laser beam; if elemental mapping is also planned then this stage must be motorized and software controlled. Please note that imaging LIBS applications, especially for biological samples, have a whole

range of requirements for sample presentation and preparation. For details of these requirements, please see, e.g., [27, 28].

1.3.4 Spectrometer

As it was alluded to above, a non-scanning, high sensitivity, fast-triggerable, high-resolution spectrometer is needed for LIBS spectroscopy, due to that has to be able to record the emission from a highly transient plasma. Major considerations toward the choice of the spectrometer for a LIBS setup have to be directed toward spectral resolution, spectral coverage, and sensitivity. This list is also complemented with the data transfer speed, if high repetition rate measurements are planned (e.g., in industrial monitoring or elemental imaging applications). Thus, as with so many things, a compromise has to be made when selecting a LIBS spectrometer too.

Fiber optics interfaced spectrometers with charge-coupled device (CCD) or complementary metal-oxide semiconductor (CMOS) detectors are most common in LIBS, equipped either with a linear or 2D detector array (intensified with a microchannel plate, or non-intensified). Linear array spectrometers usually have the Czerny–Turner configuration, whereas 2D arrays ("cameras") can be found in Echelle spectrometers. Compact spectrometers incorporating linear array detectors with 2048 or 3684 pixels typically provide a quite good sensitivity, but a combination of spectral resolution (0.05–0.1 nm) and spectral coverage (100–150 nm) they offer is sub-optimal for LIBS spectrum recording, hence are preferred in portable or cost-conscious instruments, in a multi-channel configuration. Echelle spectrometers with 2D detector arrays can provide very good spectral resolution (ca. 0.01–0.03 pm) along with a more or less complete UV–Vis spectral coverage, but have a substantially poorer (as much as 10–100 times lower) sensitivity.

The above types of spectrometers account for well over 95% of the LIBS systems, but two further designs should also be mentioned here. One is the Paschen-Runge spectrometer arrangement with photoelectron multiplier (PMT) detectors set at discrete wavelengths. This arrangement is very bulky though and inflexible thus is in use in some industrial setups only which work with a pre-defined set of analytical lines [13, 19]. The other, more prospectful spectrometer design is the spatial heterodyne (SH) spectrometer, which combines dispersion- and interference-based techniques. It can be built with no moving parts, in a very compact format, either optimized for spectral resolution or for sensitivity. In this spectrometer, an interference pattern (Fizeau fringes) is recorded by an imaging detector array and evaluated. The analytical potential of SHS in LIBS spectroscopy has already been demonstrated in a few scientific studies [37–40] and results therein suggest that SH-LIBS will find more and more applications in the future.

1.3.5 Synchronization

The synchronization of the laser with the spectrometer is an important system aspect. In commercial LIBS instruments, this is already implemented in one way or the

other, but in the case of a lab-built system, some considerations have to be made. In the case of ns laser pulses, 0.1–1 μs time resolution for this synchronization is sufficient, but in the case of ultrashort laser pulses, at least one order of magnitude better timing accuracy is required due to the much shorter plasma lifetime. All electronic/optoelectronic instruments, lasers and spectrometers included, possess an inherent "wake-up" time (the delay experienced between the incoming trigger pulse and the start of the actual action of the device, e.g. output of the laser pulse or start of the recording of the spectrum), and it may be even longer than the allowable gate delay in LIBS experiments (e.g., ≤1–2 μs). Modern lasers almost always have an electronic "laser trigger out" output signal, which indicates the release (onset) of the laser pulse and often also a "laser trigger in" signal, which can initiate the release of the pulse. Similarly, modern CCD or CMOS spectrometers also have a "hardware trigger in" input signal, which can initiate the start of the spectrum recording. Most spectrometers have a built-in, software-controlled delay generator, which can accurately delay the start of the spectrum acquisition with respect to the "hardware trigger in" signal (after the wake-up time, which is the minimum possible delay). If the wake-up delay of the spectrometer is shorter than the required LIBS gate delay, then the laser can be hooked up to the spectrometer so that the laser is fired first and the spectrometer receives its trigger signal from the laser. The gate delay can be then optimized by adjusting the internal delay generator of the spectrometer. If the spectrometer has a too long wake-up delay then the spectrometer has to be pre-triggered, that is it should receive the trigger signal earlier than the release of the laser pulse. Since this can usually not be provided by the laser, therefore an external programmable pulse generator has to be used with two outputs to trigger the start of the laser and spectrometer with a pre-calculated time difference. In these cases, the gate delay has to be controlled by the settings on the external pulse generator. In simple, conventional LIBS experiments, the process can be manually controlled.

Further considerations related to the timing of LIBS experiments are required in some special instrumental situations. For example, if remote/stand-off measurement is to be performed then the propagation time of the laser pulse and the emission signal to and from the target also has to be considered and factored into the triggering scheme—this becomes an issue only if the distance is very long, if the plasma lifetime is very short (e.g., fs pulses) or if long optical fibers are involved. In the case of LIBS elemental mapping applications, the control of the sample translation stage (and the autofocus sub-system), as well as the spectrometer-to-computer data transfer rate also has to be incorporated in the timing scheme and automation is also required.

1.3.6 Data Processing

In most LIBS instruments, the processing of the spectra which were transferred to the computer is done after collecting all measurement data. Data transfer rates between the computer and the spectrometer come into play in applications employing high repetition rate measurements (e.g., LIBS imaging applications or in industrial

monitoring), which produce a huge amount of data, that can definitely not be stored in the onboard buffer memory of the spectrometer. High-speed connectivity options, such as LAN or USB 3 can be considered, but in most cases only direct streaming of the data to the computer, with the help of a fast buffer memory, is feasible. In order to appreciate the amount of data produced in some demanding LIBS applications, one can consider that storing a full UV–Vis-NIR spectrum (e.g., from 200 to 1000 nm) even with the minimum acceptable spectral resolution (0.05–0.1 nm) and only 16-bit intensity resolution requires over ca. 20 kB data. If an area equivalent to the size of a microscope slide is imaged by scanning with just 100 μm lateral resolution in a single layer or if a continuous industrial monitoring is performed for 24 h with a frequency of just 0.5 Hz then already over 3.5 GB data is produced. The problem is of course not the storage of this amount of data, but a timely capture and, later of course, the calculation-intense processing.

Most commercial LIBS instruments today offer some software help with a built-in database for the interpretation and evaluation of the collected spectra. The capabilities and features of the software vary from company to company (e.g., background correction, plotting, calibration, line assignation, chemometric evaluation, etc.), but their operation almost always relies on the use of a built-in spectral atomic line database, which are typically also freely available online. Among the free resources available, the most popular is the NIST Atomic Spectra Database [41], but the Kurucz Atomic Spectral Line Database [42] is also worth mentioning. Recently, an online LIBS spectrum simulation tool is also available to help spectrum modeling and comparison [43]. Periodicals, such as the Journal of Physical and Chemical Reference Data [44], or classic books with compiled lists of identified atomic plasma emission spectral lines can also be considered as primary information sources.

1.4 Trending Applications and Outlook

The LIBS literature is vast: in recent years nearly about a thousand new papers appear in the field per annum and the marching of LIBS has already started about six decades ago… This large scientific output makes LIBS a hot topic in the atomic spectroscopy field, or “a super star” [45]. It is only possible because this spectroscopy has matured to the point that a huge variety of analytical applications are already being developed in addition to fundamental studies. This overwhelming amount of results does not allow one to easily overview all applications briefly.

However, an illustration of the productivity and versatility of LIBS can be provided by the long list of just the review papers that have been published in the past two decades, on tutorial, instrumentational and analytical topics (Table 1.1). Another way to illustrate the unique set of analytical capabilities/features LIBS sports is shown in Table 1.2, which presents some popular application fields and indicates the analytical merits of LIBS that is prominently useful in that particular field. This table also provides a quick survey of the trending applications. The one field in which LIBS can not meaningfully compete with other atomic spectroscopy methods in general is the accuracy and precision of quantitative analysis, which is mainly due to its solid sampling and microanalytical character. At the same time,

Table 1.1 Topical, tutorial, or critical reviews published on LIBS in the past 25 years

Topic/type	Reference
Fundamentals and applications	D.A. Rusak, B.C. Castle, B.W. Smith, et al. *Crit. Rev. Anal. Chem.* 27 (1997) 257–290
Applications	K. Song, Y. I. Lee, J. Sneddon, *Appl. Spectrosc. Rev.* 32 (1997) 183–235
Aerosol analysis	M.Z. Martin, M-D. Cheng, R.C. Martin, *Aerosol Sci. Technol.* 31 (1999) 409–421
Quantitative microanalysis	E. Tognoni, V. Palleschi, M. Corsi, et al. *Spectrochim. Acta B* 57 (2002) 1115–1130
Instrumentational developments	K. Song, Y.I. Lee, J. Sneddon, *Appl. Spectrosc. Rev.* 37 (2002) 89–117
Comparison of analytical performance	J.D. Winefordner, I.B. Gornushkin, T.Correll, et al. *J. Anal. At. Spectrom.* 19 (2004) 1061–1083
Applications	W-B. Lee, J. Wu, Y-I. Lee, et al. *Appl. Spectrosc. Rev.*, 39 (2004) 27–97
Dual-pulse LIBS	J. Scaffidi, S.M. Angel, D.A. Cremers, *Anal. Chem.* 78 (2006) 24–32
Double-pulse LIBS	V.I. Babushok, F.C. De Lucia Jr., J.L. Gottfried, et al. *Spectrochim. Acta B* 61 (2006) 999–1014
Stand-off analysis	B. Sallé, P. Mauchien, S. Maurice, *Spectrochim. Acta B* 62 (2007) 739–768
Overview and applications	C. Pasquini, J. Cortez, L.M.C. Silva, et al. *J. Braz. Chem. Soc.* 18 (2007) 463–512
Diagnostics of LIB plasmas	C. Aragón, J.A. Aguilera, *Spectrochim. Acta B* 63 (2008) 893–916
Explosives analysis	J.L. Gottfried, F.C. De Lucia. Jr., C.A. Munson, et al. *Anal. Bioanal. Chem.* 395 (2009) 283–300
Capabilities, limitations	D.A. Cremers, R.C. Chinni, *Appl. Spectrosc. Rev.* 44 (2009) 457–506
Diagnostics, plasma-particle interactions	D.W. Hahn, N. Omenetto, *Appl. Spectrosc. 64* (2010) 335–366
Environmental, art, and space applications	R. Gaudiuso, M. Dell'Aglio, O. De Pascale, et al. *Sensors* 10 (2010) 7434–7468
Calibration-free LIBS	E. Tognoni, G. Cristoforetti, S. Legnaioli, et al. *Spectrochim. Acta B* 65 (2010) 1–14
Effect of atmospheric conditions	A.J. Effenberger Jr., J.R. Scott, *Sensors*, 10 (2010) 4907–4925
Radiative modeling of LIB	I.B. Gornushkin, U. Panne, *Spectrochim. Acta B* 65 (2010) 345–359
Applications	A.P.M. Michel, *Spectrochim. Acta B* 65 (2010) 185–191
Perspective overview of LIBS	R.E Russo, T.W. Suen, A.A. Bol'shakov, et al. *J. Anal. At. Spectrom.* 26 (2011) 1696–1603
Plant material analysis	D. Santos Jr., L.C. Nunes, G.G.A. de Carvalho, et al. *Spectrochim. Acta B* 71–72 (2012) 3–13
Biomedical applications	S.J. Rehse, H. Salimnia, A.W. Miziolek, *J. Med. Eng. Technol.*, 36 (2012) 77–89
Biological applications	J. Kaiser, K. Novotny, M.Z. Martin, et al. *Surf. Sci. Rep.* 67 (2012) 233–243

(continued)

Table 1.1 (continued)

Topic/type	Reference
Fundamentals, applications, challenges	F. Anabitarte, A. Cobo, J. M. Lopez-Higuera, *ISRN Spectrosc.* (2012) 285240
Spectrochemical analysis by LIBS	A.K. Pathak, R. Kumar, V.K Singh, et al. *Appl. Spectrosc. Rev.* 47 (2012) 14–40
Instrumentation, methodology, applications	D.W.Hahn, N. Omenetto, *Appl.Spectrosc.* 66 (2012) 347–419
Geochemical and environment analysis	R S. Harmon, R.E. Russo, R.R. Hark, *Spectrochim. Acta B* 87 (2013) 11–26
Analytical chemistry by LIBS	F.J. Fortes, J. Moros, P. Lucena, et al. *Anal. Chem.* 85 (2013) 640–669
History of the early years of LIBS	M. Baudelet, B.W. Smith, *J. Anal. At. Spectrom.*, 28 (2013) 624–629
Geological materials analysis	S. Qiai, Y. Ding. D. Tian, et al. *Appl. Spectrosc. Rev.* 50 (2014) 1–26
Chemometric data evaluation practices	J. El Haddad, L. Canioni, B. Bousquet, *Spectrochim. Acta B* 101 (2014) 171–182
Portable instrumentation ad applications	J. Rakovsky. P. Cermák, O. Musset, et al. *Spectrochim. Acta B* 101 (2014) 269–287
Biomedical applications	V.K. Singh, V. Kumar, J. Sharma, et al. *Mater-Focus*, 3 (2014) 169–182
Archeometric applications	V. Spizzichino, R. Fantoni, *Spectrochim. Acta B* 99 (2014) 201–209
Water quality monitoring	X. Yu, Y. Li, X. Gu, et al. *Environ. Monit. Assess.* 186 (2014) 8969–8980
Critical review (DP-LIBS)	E. Tognoni, G. Cristoforetti, *J. Anal. At. Spectrom.* 29 (2014) 1318–1338
Critical review	G. Galbács, *Anal. Bioanal. Chem.* 407 (2015) 7537–7562
Femtosecond LIBS	T.A. Labutin, V.N. Lednev, A.A. Ilyin, et al. *J. Anal. At. Spectrom.*, 31 (2016) 90–118
Nuclear technology applications	C. Li, C.-L. Feng, H.Y. Oderji, et al. *Front. Phys.* 11 (2016) 114214
Sample treatment and preparation	S.C. Jantzi, V. Motto-Ros, F. Trichard, et al. *Spectrochim. Acta B* 115 (2016) 52–63
Soil analysis	G.S. Senesi, N. Senesi, *Anal. Chim. Acta* 938 (2016) 7–17
Molecular isotopic analysis	A.A. Bol'shakov, X. Mao, J.J. González, et al. *J. Anal. At. Spectrom.* 31 (2016) 119–134
Nuclear fusion applications	C. Li, C.L. Feng, H.Y., et al. *Front. Phys.* 11 (2016) 114214
Food analysis	M. Markiewicz-Kecsycka, X. Cama-Moncunill, et al. *Trends Food Sci. Technol.* 65 (2017) 80–93
Novel applications	AJ. Bauer, S.G Buckley, *Appl. Spectrosc.* 71 (2017) 553–566
Comparative review	A. Bengtson, *Spectrochim Acta B* 134 (2017) 123–132
Plant analysis	X.-L. Yu, Y. He, *Appl. Spectrosc. Rev.* 52 (2017) 605–622
Signal enhancement approaches	Y. Li, D. Tian, Y. Ding, et al. *Appl. Spectrosc. Rev.* 53 (2018) 1–35
Chlorine determination in cement	S. Millar, C. Gottlieb, T. Günther, et al. *Spectrochim. Acta B* 147 (2018) 1–8
Analytical performance	J. Laserna, J.M. Vadillo, P. Purohit, *Appl. Spectrosc.* 72 (2018) 35–50

(continued)

Table 1.1 (continued)

Topic/type	Reference
Signal enhancement	Y. Li, D. Tian, Y. Ding, et al. *Appl. Spectrosc. Rev.*, 53 (2018) 1–35
Elemental imaging	B. Busser, S. Moncayo, J.-L. Coll, et al. *Coord. Chem. Rev.* 358 (2018) 70–79
Cultural heritage and archeology	A. Botto, B. Campanella, S. Legnaioli, et al. J. Anal. At. Spectrom., 34 (2019) 81–103
Human and animal health	R. Gaudiuso, M. Noureddine, A.A-S. Zienab, et al. *Spectrochim. Acta B* 152 (2019) 123–148
Calibration strategies	V.C Costa, D.V. Babos, J.P. Castro, et al. *J. Brazilian Chem. Soc.* 31 (2020) 2439–2451
Archeology	F. Ruan, T. Zhang, H. Li, *Appl. Spectrosc. Rev.* 54 (2019) 573–601
Bacterial classification	S.J. Rehse, *Spectrochim. Acta B* 154 (2019) 50–69
Organic compounds	J. Moros, J. Laserna, *Appl. Spectrosc.* 73 (2019) 963–1011
Elemental imaging	L. Jolivet, M. Leprince, S. Moncayo, et al. *Spectrochim. Acta B* 151 (2019) 41–53
Coal analysis	S. Sheta, M.S. Afgan, Z. Hou, et al. *J. Anal. At. Spectrom.*, 34 (2019) 1047–1082
Comprehensive review	S.K.H. Shah, J. Iqbal, P. Ahmad, et al. *Rad. Physics Chem.* 170 (2020) 108666
Agricultural applications	K. Yu, R. Jie, Z. Yanru, *Art. Intell. Agricult.* 4 (2020) 127–139
Self-absorption effects	R. Fatemeh, G. Cristoforetti, E. Tognoni, et al. *Spectrochim. Acta B* 169 (2020) 105878
Soil analysis	P.R. Villas-Boas, M.A. Franco, L. Martin-Neto, et al. *Euro. J. Soil Sci.* 71 (2020) 805–818
Geology	C. Fabre, *Spectrochim. Acta B* 166 (2020) 105799
Soil analysis	G.S. Senesi., *Int. J. Earth. Environ. Sci.* 5 (2020) 172
Bioimaging of plant tissues	P. Modlitbová, P. Pořízka, J. Kaiser, *TrAC Trends Anal. Chem.* 122 (2020) 115729
Portable and handheld instruments	G.S. Senesi, R.S.Harmon, R.R. Hark, *Spectrochim. Acta Part B* 175 (2021) 106013
Human and animal soft tissues	Q. Wang, W. Xiangli, G. Teng, et al. *Appl. Spectrosc. Rev.* 56 (2021) 221–241
Elemental imaging	A. Limbeck, L. Brunnbauer, H. Lohninger, et al. *Anal. Chim. Acta* 1147 (2021) 72–98
Industrial materials	J.D. Pedarnig, S. Trautner, S. Grünberger, et al. *Appl Sci.* 11 (2021) 9274
Hybride LIBS+Raman+LIF	V.S. Dhanada, D.G. Sajan, V.B. Kartha, et al. *Appl. Spectrosc. Rev.* 56 (2021) 463–491
General review	L.-B. Guo, D. Zhang, L.-X. Sun, et al. *Front Phys.* 16 (2021) 1–25
Chemometrics in plastic sorting	E.R.K. Neo, Z. Yeo, J. Low, et al. *Resour. Conserv. Recycl.* 180 (2022) 106217
Cancer diagnosis	M.N. Khan, Q. Wang, B.S. Idrees, et al. *Front. Phys.* 10 (2022) 821057
In situ atmospheric analysis	Q. Zhang, Y. Liu, *At. Spectrosc.* 43 (2022) 174–185
CF-LIBS	Z. Hu, D. Zhang, W. Wang, et al. *TrAC Trends Anal. Chem.* 152 (2022) 116618

Table 1.2 Overview of some popular application fields and related important analytical merits of LIBS. Please note that the selection is only meant as indicative

	Compactness and portability	Robustness	Remote analysis	Trace analytical detection limits	Wide elemental coverage	Wide dynamic range	Potential isotope resolution	Fully fiber optic arrangement	Information rich spectra	Small sample requirement	Minimal sample preparation	Direct solid sampling	High spatial resolution analysis	High analytical throughput
Medical diagnostics and biomedical applications				+				+	+	+	+	+	+	+
Security and forensics (explosives, radioactive materials, etc.)	+	+	+	+			+		+	+	+	+	+	+
Mining, geology, and industrial raw materials	+	+	+	+	+	+				+	+	+		+
Analysis in extreme environments (underwater, space, etc.)	+	+	+					+	+		+	+		
Aerosol and nanoparticle detection			+	+					+		+			+
Archeology and cultural heritage	+		+	+	+				+	+	+	+	+	
Environmental analysis (soil, water, air, etc.)	+	+		+	+	+			+		+	+		
Industrial monitoring (process, quality assessment, etc.)		+	+	+	+	+			+	+	+	+	+	+

LIBS excels in qualitative discrimination, remote/stand-off analysis, or elemental distribution studies.

It can be concluded that LIBS has established itself in the past decades as a versatile and powerful spectroscopy method, which is capable of far more than elemental analysis. New signal enhancement and data evaluation techniques are being continuously developed and novel application fields are explored every year. This is also illustrated by the topic of this very book, which focuses on novel biological, forensic, and materials science applications.

The future also looks bright for LIBS, as its capabilities fit the trend of the need for microanalytical methods that are "industry or field-ready" or can contribute to life science applications. The advancement of photonics and chemometric data evaluation approaches is also clearly up its alley.

Acknowledgments The author kindly acknowledge the financial support received from the National Research, Development and Innovation Office (Hungary) through project No. K 129063.

References

1. Kruer WL. Physics of laser-plasma interactions. Taylor and Francis; 2003.
2. Stafe M, Marcu A, Puscas N. Pulsed laser ablation of solids. Springer; 2013.
3. Musazzi S, Perini U, editors. Laser-induced breakdown spectroscopy: theory and applications, Springer series in optical sciences, vol. 182. Spinger; 2014.
4. Singh J, Thakur S, editors. Laser-induced breakdown spectroscopy. Elsevier; 2020.
5. Cremers LJ, Radziemski DA. Handbook of laser-induced breakdown spectroscopy. Wiley; 2006.
6. Galbács G. A critical review of recent progress in analytical laser-induced breakdown spectroscopy. Anal Bioanal Chem. 2015;407:7537.
7. Miziolek AW, Palleschi V, Schechter I. Laser-induced breakdown spectroscopy: fundamentals and applications. Cambridge University Press; 2006.
8. Andrade DF, Pereira-Filho ER, Amarasiriwardena D. Current trends in laser-induced breakdown spectroscopy: a tutorial review. Appl Spectrosc Rev. 2021;56:98.
9. Senesi GS, Harmon RS, Hark RR. Field-portable and handheld laser-induced breakdown spectroscopy: historical review, current status and future prospects. Spectrochim Acta B. 2021;175:106013.
10. Rakovský J, Čermák P, Musset O, Veis P. A review of the development of portable laser induced breakdown spectroscopy and its applications. Spectrochim Acta B. 2014;101:269.
11. Bol'shakov AA, Mao X, González JJ, Russo RE. Laser ablation molecular isotopic spectrometry (LAMIS): current state of the art. J Anal At Spectrom. 2016;31:119.
12. Li W, Li X, Li X, Hao Z, Lu Y, Zeng X. A review of remote laser-induced breakdown spectroscopy. Appl Spectrosc Rev. 2020;55:1.
13. Noll R. Laser-induced breakdown spectroscopy: fundamentals and applications. Springer; 2012.
14. Noll R, Fricke-Begemann C, Brunk M, Connemann S, Meinhardt C, Scharun M, Sturm V, Makowe J, Gehlen C. Laser-induced breakdown spectroscopy expands into industrial applications. Spectrochim Acta B. 2014;93:41.
15. Limbeck A, Brunnbauer L, Lohninger H, Porízka P, Modlitbova P, Kaiser J, Janovszky P, Kéri A, Galbács G. Methodology and applications of elemental mapping by laser induced breakdown spectroscopy. Anal Chim Acta. 2021;1147:72.

16. Jedlinszki N, Galbács G. An evaluation of the analytical performance of collinear multi-pulse laser induced breakdown spectroscopy. Microchem J. 2011;97:255.
17. Galbács G, Gornushkin IB, Smith BW, Winefordner JD. Semi-quantitative analysis of binary alloys using laser-induced breakdown spectroscopy and a new calibration approach based on linear correlation. Spectrochim Acta B. 2001;56:1159.
18. Galbács G, Jedlinszki N, Cseh G, Galbács Z, Túri L. Accurate quantitative analysis of gold alloys using multi-pulse laser induced breakdown spectroscopy and a correlation-based calibration method. Spectrochim Acta B. 2008;63:591.
19. Hahn DW, Omenetto N. Laser-induced breakdown spectroscopy (LIBS), part II: review of instrumental and methodological approaches to material analysis and applications to different fields. Appl Spectrosc. 2012;66:347.
20. Koch J, Günther D. Review of the state-of-the-art of laser ablation inductively coupled plasma mass spectrometry. Appl Spectrosc. 2011;65:155.
21. Labutin TA, Lednev VN, Ilyin AA, Popov AM. Femtosecond laser-induced breakdown spectroscopy. J Anal At Spectrom. 2016;31:90.
22. Gurevich EL, Hergenröder R. Femtosecond laser-induced breakdown spectroscopy: physics, applications, and perspectives. Appl Spectrosc. 2007;61:233A.
23. Zuclich JA, Lund DJ, Stuck BE. Wavelength dependence of ocular damage thresholds in the near-IR to far-IR transition region: proposed revisions to MPES. Health Phys. 2007;92:15.
24. Baudelet M, Willis CC, Shah L, Richardson M. Laser-induced breakdown spectroscopy of copper with a 2 μm thulium fiber laser. Opt Express. 2010;18:7905.
25. Gravel JFY, Doucet FR, Bouchard P, Sabsabi M. Evaluation of a compact high power pulsed fiber laser source for laser-induced breakdown spectroscopy. J Anal At Spectrom. 2011;26:1354.
26. Jiang Y, Li R, Chen Y. Elemental analysis of copper alloys with laser-ablation spark-induced breakdown spectroscopy based on a fiber laser operated at 30 kHz pulse repetition rate. J Anal At Spectrom. 2019;34:1838.
27. Limbeck A, Brunnbauer L, Lohninger H, Pořízka P, Modlitbová P, Kaiser J, Janovszky P, Kéri A, Galbács G. Methodology and applications of elemental mapping by laser induced breakdown spectroscopy. Anal Chim Acta. 2021;1147:72.
28. Jolivet L, Leprince M, Moncayo S, Sorbier L, Lienemann C-P, Motto-Ros V. Review of the recent advances and applications of LIBS-based imaging. Spectrochim Acta B. 2019;151:41.
29. Fortes FJ, Fernandez-Bravo A, Laserna JJ. Chemical characterization of single micro- and nano-particles by optical catapulting-optical trapping-laser-induced breakdown spectroscopy. Spectrochim Acta B. 2014;100:78.
30. Purohit P, Fortes FJ, Laserna JJ. Subfemtogram simultaneous elemental detection in multicomponent nanomatrices using laser-induced plasma emission spectroscopy within atmospheric pressure optical traps. Anal Chem. 2019;91:7444.
31. Yu X, Li Y, Gu X, Bao J, Yang H, Sun L. Laser-induced breakdown spectroscopy application in environmental monitoring of water quality: a review. Environ Monit Assess. 2014;186:8969.
32. Metzinger A, Kovács-Széles É, Almási I, Galbács G. An assessment of the potential of laser induced breakdown spectrometry for the analysis of cesium in liquid samples of biological origin. Appl Spectrosc. 2014;68:789.
33. Palásti DJ, Villy LP, Kohut A, Ajtai T, Geretovszky ZS, Galbács G. Laser-induced breakdown spectroscopy signal enhancement effect for argon caused by the presence of gold nanoparticles. Spectrochim Acta B. 2022;193:106435.
34. Palásti DJ, Metzinger A, Ajtai T, Bozóki Z, Hopp B, Kovács-Széles É, Galbács G. Qualitative discrimination of coal aerosols by using the statistical evaluation of laser-induced breakdown spectroscopy data. Spectrochim Acta B. 2019;153:34.
35. Ji H, Ding Y, Zhang L, Hu Y, Zhong X. Review of aerosol analysis by laser-induced breakdown spectroscopy. Appl Spectrosc Rev. 2021;56:193.
36. Diwakar PK, Loper KH, Matiaske A-M, Hahn DW. Laser-induced breakdown spectroscopy for analysis of micro and nanoparticles. J Anal At Spectrom. 2012;27:1110–9.

37. Strange Fessler KA, Waldron A, Colon A, Chance Carter J, Michael Angel S. A demonstration of spatial heterodyne spectrometers for remote LIBS, Raman spectroscopy, and 1D imaging. Spectrochim Acta B. 2021;179:106108.
38. Gornushkin IB, Smith BW, Panne U, Omenetto N. Laser-induced breakdown spectroscopy combined with spatial heterodyne spectroscopy. Appl Spectrosc. 2014;68:1076–84.
39. Barnett PD, Lamsal N, Angel SM. Standoff laser-induced breakdown spectroscopy (LIBS) using a miniature wide field of view spatial heterodyne spectrometer with sub-microsteradian collection optics. Appl Spectrosc. 2017;71:583–90.
40. Palásti DJ, Füle M, Veres M, Galbács G. Optical modeling of the characteristics of dual reflective grating spatial heterodyne spectrometers for use in laser-induced breakdown spectroscopy. Spectrochim Acta B. 2021;183:106236.
41. https://www.nist.gov/pml/atomic-spectra-database
42. Kurucz RL, Bell B. Atomic line data Kurucz CD-ROM No. 23. Cambridge, MA: Smithsonian Astrophysical Observatory; 1995.
43. https://physics.nist.gov/PhysRefData/ASD/LIBS/libs-form.html
44. Ralchenko Y. Atomic physics and spectroscopy during the first 50 years of JPCRD. J Phys Chem Ref Data Monogr. 2022;51:013101.
45. Winefordner JD, Gornushkin IB, Correll T, Gibb E, Smith BW, Omenetto N. Comparing several atomic spectrometric methods to the super stars: special emphasis on laser induced breakdown spectrometry, LIBS, a future super star. J Anal At Spectrom. 2004;19:1061–83.

Quantitative Analysis

2

Jeyne Pricylla Castro, Raquel Cardoso Machado, Daniel Fernandes Andrade, Diego Victor de Babos, Edenir Rodrigues Pereira-Filho, José Augusto Garcia, Marco Aurelio Sperança, Raimundo Rafael Gamela, and Vinícius Câmara Costa

2.1 Introduction

Over several decades, analytical chemistry has provided alternatives for the analysis of food, environmental samples, and technological materials, aiming at their elementary characterization [1]. The scientific literature in the area shows applications related to instrumental analytical techniques based on atomic absorption (AA) and emission (AE). Among the most widespread techniques for chemical sample analysis is inductively coupled plasma optical emission spectrometry (ICP-OES) [2]. ICP-OES requires the introduction of the sample typically in the form of a homogeneous liquid solution that must have some favorable characteristics for the

J. P. Castro · D. V. de Babos · E. R. Pereira-Filho (✉)
Group of Applied Instrumental Analysis, Department of Chemistry, Federal University of São Carlos, São Carlos, SP, Brazil
e-mail: erpf@ufscar.br

R. C. Machado
Embrapa Instrumentation, São Carlos, SP, Brazil

D. F. Andrade
Eurofarma, Rod. Presidente Castello Branco, Itapevi, SP, Brazil

J. A. Garcia
SG Soluções Científicas, São Carlos, SP, Brazil

M. A. Sperança
Group of Alternative Analytical Approaches (GAAA), Bioenergy Research Institute (IPBEN), Institute of Chemistry, São Paulo State University (UNESP), Araraquara, SP, Brazil

R. R. Gamela
Departamento de Engenharia de Processamento de Alimentos, Instituto Superior Politécnico de Gaza (ISPG), Gaza, Moçambique

V. C. Costa
Embrapa Instrumentação, São Carlos, SP, Brazil

G. Galbács (ed.), *Laser-Induced Breakdown Spectroscopy in Biological, Forensic and Materials Sciences*, https://doi.org/10.1007/978-3-031-14502-5_2

analysis, such as both low dissolved solids (typically less than 1%) and low acidity (in the order of 10% at most) [3].

The process of transforming a solid sample into a homogeneous aqueous solution is called acid digestion and can be carried out with the aid of concentrated or diluted acid mixtures [4]. The most used reagents are nitric (HNO_3) and hydrochloric (HCl) acids, as well as hydrogen peroxide (H_2O_2) combined with HNO_3. Digestion is complete after subjecting the sample and acid mixture to high temperatures and pressures [5]. The main goal is to make the constituent elements of the sample available in a dilute acid liquid medium, thus allowing their determination largely free from matrix interferences [3]. Furthermore, with the preparation of samples through acid digestion procedures, it becomes possible to carry out external calibration in the practical way of using aqueous solutions.

In several examples that employ solid samples (inorganic or organic), the requirements presented in the previous paragraph are met using simple procedures. Most food samples (meat, vegetables, fruits, flours, among others) and some environmental samples (sediment and soil) are examples of solid samples that can be converted in their entirety into liquid solutions after acid attack. The success of this conversion will depend on some parameters such as the sample mass and acid mixture ratio, time, and type of heating, such as conventional (convective) and assisted by microwave radiation [6]. However, some analytical matrices are extremely complex, recalcitrant or refractory, posing considerable challenges for the dissolution procedure. In many situations, it is necessary to use more oxidizing acids, such as sulfuric acid (H_2SO_4) and more aggressive reagents, such as hydrofluoric acid (HF) in the case of samples with high silicate contents [3]. In addition, sample preparation time can extend from a few minutes to several hours, compromising analytical throughput.

Thus, there is a need to propose analytical procedures that combine accessible techniques, high throughput, lower limits of detection, adequate values for accuracy, precision, and reduced cost *per* analysis. A viable alternative is the direct analysis of solid samples, such as using a laser [7]. This chapter is related to this theme and here we will try to approach the main characteristics related to the direct quantitative analysis of solid samples using laser-induced breakdown spectroscopy (LIBS) [8, 9].

LIBS is an analytical technique that emerged in the 1960s and became widespread from around 2000 onward, which can be applied for the direct analysis of samples of different nature, such as technological (glasses, alloys), radioactive, dangerous (explosives) and those with difficult access, such as soil of the planet Mars and direct analysis of deep waters. Most LIBS applications refer to the analysis of alloys [10], polymeric, agricultural, and geological materials [11]. These aspects will be addressed in the sections of this chapter and more attention was dedicated to solid samples. In the case of liquid and slurry samples, some examples are discussed by encapsulating the sample in a suitable substrate.

2.2 Description of the Main Matrix Effects in LIBS

In the last decades, the technological approaches that allowed direct solid samples analysis improved significantly. Nowadays, LIBS is one of the most used and reported technique in the scientific literature for this purpose [12]. However, besides advantages associated with LIBS technique, the analyst needs to deal with a huge challenge: matrix effects [9]. Actually, matrix effects are an analytical problem mainly associated to several analytical instrumental techniques, not exclusively, but mainly those that employ solid sample analysis. Several authors, such as Cremers and Radziemski [13] and Hahn and Omenetto [14], already discussed these topics. Radiziemski and Cremers [11] for instance, described several aspects that can compromise quantitative analysis: (1) microhomogeneity of the samples, (2) uniformity of the surface, (3) chemical matrix composition, and (4) physical matrix effects.

The chemical composition of the matrix is one of the most critical aspects of LIBS analysis because it influences the emission phenomenon of the analyte. Samples with organic composition (blood, biological tissues, biological microparticles) [15] or inorganic, as forensic samples such as explosive materials and soil fingerprinting, ceramic and nanomaterials [16] may lead to different and harmful matrix effects in the emission signal during the quantitative analysis [17]. The presence of easily ionizable elements (EIEs) in the sample matrix also can lead to chemical matrix effects due to changes in electronic density in the plasma, which shift the ionization equilibrium and compromise the accuracy of the results [18].

The physical properties of the sample are other important aspects that must be considered in LIBS analysis. Differences in these properties, such as humidity, heterogeneous particle size, thermal conductivity, absorption coefficient at the laser wavelength, sample temperature, heat of vaporization, uneven surface, pressure applied to sample to prepare pellets (if required), among others, may influence the amount of ablated mass, plasma formation and affect the vaporization, atomization and ionization processes [17–19].

The analysis of alloys was one of the first LIBS applications rapidly reported in the literature due to the sample characteristics. Sabsabi and Cielo [20] for instance, used LIBS for aluminum alloys quantitative analysis and determined Cu, Mg, Mn, and Si and employed external calibration. Afterward, Santos et al. [21] presented a review about the application of LIBS for macro- and micronutrient determination in leaves, roots, fruits, vegetables, wood, and pollen samples focusing on nutritional purposes. The authors discussed and compared univariate and multivariate calibration approaches. This comparison was also presented by Braga et al. [22] for metal determination in pellets of plants.

Matrix effects are evidence of the challenges in direct solid sample analysis by LIBS, mainly when the technique is used for quantitative analysis. An adjustment in experimental parameters, such as laser defocusing and changing the spectrometer

delay, may contribute to minimizing matrix effects, as was mentioned by Wang et al. [23]. However, some calibration strategies have stood out as a simple and efficient way to minimize or overcome matrix effects even in cases of complex samples [24].

Methods such as matrix-matching calibration (MMC), standard addition (SA), and internal standardization are mostly used when the goal of the analysis is the elemental determination. On the other hand, with intention of exploring other (and new) approaches, using different emission lines (and different sensitivities), reduced number of calibration samples compared to traditional calibration methods and employing physicochemical properties of laser-induced plasma species, novel calibration methods have been developed to minimizing matrix effects. The term calibration sample will be used in this and subsequent sections to describe samples that have known analyte concentration obtained by a reference or confirmatory method. It is important to mention that matrix effects will be never eliminated from an analytical chemistry method, and they are more intense in direct solid sample analysis. In addition, matrix effects can be also responsible for the lack of linearity in several LIBS applications. These methods are called non-traditional calibration strategies and will be discussed in the next sections [25].

Several authors highlight the importance of the matrix-matching approach in the calibration methods. In most cases, to ensure accurate and precise results in LIBS solid samples analysis, the physicochemical properties of the analyzed samples must be similar to samples used to build a calibration model, which is interesting because demonstrate the importance of considering the sample matrix to solve matrix effects [25].

It is a fundamental question in LIBS quantitative analysis, whether it is possible to obtain accurate analytical results without taking into account the differences in the matrix and the physicochemical properties of the calibration samples and the samples with unknown concentrations. A discussion of this question and potential answers are provided in this chapter.

2.3 Traditional Calibration Strategies Applied to LIBS

2.3.1 Matrix-Matching Calibration (MMC)

Calibration is still challenging for direct solid analysis [14, 26]. As discussed before, calibration in LIBS analysis is matrix dependent and limited by matrix effects originated from differences in the physical/chemical properties (i.e., density, porosity, moisture content, light absorption at the laser wavelength, surface roughness, etc.) among standards and samples. These dissimilarities can lead to different ablation behavior, hence resulting in an inadequate calibration that may provide biased results and compromise the accuracy, precision, and sensitivity of the analytical procedure [8, 27].

It is well known that calibration is an indispensable step in any quantitative analytical procedure [28]. Traditionally, calibration is based on recording a series of standards (calibration samples) to determine the correlation between the instrumental response and analyte concentration allowing to obtain the calibration function (usually linear) of which the analyte concentration at unknown samples is obtained [29]. External univariate calibration using matrix-matched standards is the most common approach in LIBS analysis. Ideally, the MMC aims an appropriate chemical and physical match between the calibration samples and the samples with unknown concentrations [25].

Alternatives to obtain appropriate calibration samples are certified reference materials (CRMs) and laboratory-prepared "home-made" standards by mixing samples or synthetic standards based on the main sample matrix component using similar materials (e.g., salts and oxides). The general preparation processes involve milling the sample material, spiking it with suitable elements, mixing to homogenization, diluting, drying if necessary, and pressing it into a pellet. The calibration samples are prepared in an adequate diluent such as cellulose powder [30, 31], salts [31–33], or original samples [34] as well as paraffin wax [35] and polyvinyl alcohol (PVA) [36, 37] for liquid matrices. Other materials have been explored, for example, Silvestre et al. [38] prepared synthetic standard materials by adding increasing concentrations of K and Mg in wood, filter paper, and babassu mesocarp for further plant sample analysis by LIBS. However, it is important to point out that preparing highly matrix-matched standards is a difficult task in practice. Nevertheless, CRMs are expensive, its availability is limited, and do not either cover the different types of matrices or range of concentrations. Despite that, MMC is a traditional calibration approach that works for a variety of samples, especially for simple matrix content. With respect to this, Table 2.1 shows some applications using the MMC procedure for different samples.

For instance, de Carvalho et al. [42] demonstrated the applicability of LIBS for the determination of elemental content in pharmaceutical tablets. Calibration samples were obtained by mixing different samples with known reference values at different ratios, diluting with cellulose powder, and the resulted mixtures were homogenized using a cryogenic mill. The homogenized products were pressed into pellets and analyzed by LIBS. The results obtained for Ca, Cu, Fe, Mg, Mn, P, and Zn by the proposed LIBS method were in concordance with those obtained by the reference method involving microwave-assisted acid digestion and ICP-OES analysis.

Babos et al. [31] developed a quantitative method for the determination of Ca and P in mineral supplements. For calibration purposes, two different strategies were assessed: (1) six reference materials with different concentrations of the elements, and; (2) six solid standards prepared by diluting a reference material of mineral supplement using Na_2CO_3. The proposed methods were compared with other univariate calibration strategies and the results validated using reference values (reference material or ICP-OES data). Promising results (trueness around 90%) were achieved using the MMC, but the matrix effects were even better reduced by combining MMC and internal standardization using a carbon spectral line.

Table 2.1 Studies describing procedures for preparing matrix-matched calibration standards and their analytical application

Research area	Element	Sample	Goal	MMC procedure	Reference
Raw material analysis	B	Synthetic materials prepared from pure reagents	Development of LIBS procedure for direct determination of B content	Synthetic standards prepared by the binary mixture of H_3BO_3 and $C_6H_{12}O_6{\cdot}H_2O$ in powder form	Zhu et al. [39]
Raw material analysis	Cl	Cement	Chorine determination in cement-bound materials used in concrete structures	Original samples of cement with increasing amount of NaCl	Millar et al. [32]
Raw material analysis	Li	Ore mineral	Qualitative and semi-quantitative analysis of mineral samples	CRMs and synthetic glass standards prepared with increasing quantities of Li_2O, Al_2O_3, SiO_2, Rb_2O, and Cs_2O	Sweetapple and Tassios [40]
Food analysis	Ca, K and Mg	Milk and solid dietary supplements	Direct determination of macronutrients in powdered milk and dietary supplements	Original milk samples, and; dilution of dietary supplements with cellulose powder	Augusto et al. [30]
Food analysis	Ca, K, Mg, and Na	Meat	Quantitative determination of nutrients content in bovine and chicken meat	Original samples diluted with cellulose or spiked with increasing amounts of Ca, K, Mg, and Na	Leme et al. [41]
Environmental analysis	Ca, Mg, K, P, Cu, Mn, and Zn	Sugar cane leaves	Determination of macro and micronutrients in plant materials	Original samples diluted using extracted material (i.e., original samples after acid extraction)	Gomes et al. [34]
Food analysis	Ca and P	Mineral supplements for cattle	Calibration strategies for Ca and P determination in mineral supplements for cattle	Reference materials (RMs) or diluted with Na_2CO_3	Babos et al. [31]
Environmental analysis	K and Mg	Plant samples	Direct measurement of K and Mg in plant samples	Synthetic standards prepared by the addition of increasing concentrations of K and Mg in wood, babassu mesocarp, and filter paper	Silvestre et al. [38]
Agricultural inputs analysis	P	Fertilizers	Determination of P in commercial fertilizers	CRMs diluted with combined reagent containing $(NH_2)_2CO$, $CaCO_3$, $CaSO_4$ and KCl	Vieira et al. [33]

Pharmaceutical	Ca, Cu, Fe, Mg, Mn, P and Zn	Pharmaceutical tablets	Determination of macro and micronutrients in multielement tablets	Original samples and mixtures of commercial tablets with cellulose powder at different ratios	de Carvalho et al. [42]
Technological	Al and Pb	Printed circuit boards (PCBs)	Determination of Al and Pb in electronic circuits using different calibration strategies	Original samples	Babos et al. [24]

Millar et al. [32] studied the determination of Cl content in cement-bound materials by LIBS. The calibration curve was prepared using the incremental addition of water and NaCl to Portland cement. For the validation, test samples were obtained by adding different chlorine sources, e.g. NaCl was substituted by KCl, LiCl, or $CaCl_2$. Both calibration samples and test samples were dried at 105 °C, ground to a maximum particle size of 0.09 mm and pressed into pellets prior to LIBS analysis. Good accuracy results were reported for most samples, by comparing LIBS results to those obtained from potentiometric titration after acid digesting the samples. However, chlorine concentrations were systematically overestimated for some samples which were attributed to matrix effects.

The feasibility of using the original samples set for MMC method was demonstrated by Babos et al. [24]. The authors aimed to determine Al and Pb in electronic waste samples comparing different calibrations strategies. For the MMC procedure, the calibration curves ranged from 3.1 to 55 g kg^{-1} for Al and from 0.7 to 11.6 g kg^{-1} for Pb using four waste printed circuit boards (PCBs) as solid standards. These solid samples were previously digested using a mixture of acids in order to obtain reference values using ICP-OES. In addition, the authors obtained more than 400 spectra for sample in order to minimize sample microheterogeneity. The proposed method was validated using reference concentrations (ICP-OES data). Trueness (accuracy) values in the range from 99 to 116%, and relative standard deviation (RSD) values $\leq$4% were obtained.

More recently, a new MMC approach has been proposed based on a data pre-processing method namely adaptive subset matching (ASM) [43]. ASM first establishes a set of calibration models using the similarity of sample matrix properties. Therefore, for an unknown sample, it assigns the most suitable calibration model corresponding to the matrix properties to predict the analyte concentration. This procedure is performed by comparing the errors of each model. The model that presents the lowest error is assigned to the sample. The authors assessed the performance of the method on 90 coal samples, including 41 CRMs and 49 commercial. In order to minimize calibration error, coal powders were air-dried and pressed into pellets before LIBS analysis. Two multivariate regression methods, multiple linear regression (MLR) and partial least squares (PLS) regression, were performed to evaluate the effectiveness of ASM. Both methods were improved in combination with ASM, which efficiently reduced chemical matrix effects and improved LIBS quantification performance.

2.3.2 Internal Standardization

Internal standardization (signal normalization by an internal standard) is widely used in spectroanalysis and in some cases it is considered a calibration strategy. Due to its wide application in LIBS, authors of this chapter provide a discussion about this approach. To enable the possibility of using certain elements as an internal standard (IS) in analytical emission spectroscopy, some requirements need to be fulfilled prior to analysis, such as the element cannot be present in the sample at a considerable

concentration and, the emission line from the element of interest and the IS candidate should be free of self-absorption and spectral interference. Then, the IS needs to be added to the test samples and calibration samples in a proper way. Another practical and useful possibility is to employ an element that is already present in the samples and standards at a high concentration (thus its concentration can be considered more or less constant), such as C (in the case of organics) or Fe (in the case of steel). In addition to this, the physical and chemical characteristics of the internal standard and analyte should also be similar (e.g., excitation or ionization energy) [44].

The main goal of this strategy is to track and minimize instrumental and plasma fluctuations, matrix effects by rationing the analyte signal to that of the IS. Basically, it uses the division of the peak intensity or area of the emission line related to the analyte by the peak intensity or area of a selected emission line related to the IS. The IS has to be added to (or present in) all calibration and unknown samples in the same concentration. The calibration is actually executed in the same way as in external calibration, but the signal ratio is considered to be the analytical signal.

Elements that are expected to be absent or, at least, their concentration would be lower than limits of detection (LOD) and quantification (LOQ) can be added as potential ISs, such as yttrium (Y) [45, 46], scandium (Sc) and bismuth (Bi) [45]. Since the concentration of the IS in the whole set of samples is to be kept at the same level, it is expected that the signal of it only changes due to variations that the analyst desires to minimize or eliminate. Regarding LIBS analysis, selecting an IS is even more difficult, being almost impossible to use any element properly as an IS [47]. Despite that, the use of IS elements is desirable in LIBS analysis because it does help to minimize signal fluctuations caused by matrix or instrumental effects. This type of normalization of the signal using an IS element was applied in several cases in LIBS analysis and in some cases elements that are naturally present in constant concentration in the samples are used as IS (for example, C).

Sperança et al. [45] assessed the possibility of using Y, Sc, and Bi as IS in the determination of Al, Cr, Fe, Mg, Mn, and Ni in Cuban nickeliferous minerals using LIBS. For this, 0.1 g of each element (Y, Sc, and Bi) were accurately weighted in a slurry made with the samples and water and, this mixture was encapsulated in PVA (polyvinyl alcohol), a water-soluble polymer. The authors concluded that Y was the best choice as IS in this study reached a low standard error of validation (SEV) for the elements assessed. In another study, Zn was assessed as IS in the evaluation of soft tissues where the laser-tissue interaction was investigated based on the Zn signal response as the authors optimize the system [48]. Another manner to use internal standardization strategy in LIBS analysis is the use of an inner element, naturally present in the samples [49] or added for another reason, such as C from polymer used for encapsulating the sample and cellulose powder to improve the cohesion in pellets formation [36]. This strategy is feasible when the constituent of the sample that may be used as IS has the same concentration in the whole set of samples, such as C in an organic matrix (e.g., fresh vegetables) [49]. Andrade et al. [36] determined essential and toxic elements in suspended fertilizers using LIBS. For this, the authors encapsulated the samples using PVA and tested C emission signal as

IS, in which a constant mass of PVA was added in each sample. In this study, several normalization modes [50] were assessed for five elements (Cu, K, Mg, Mn, and Zn) and, specifically for Mg and Mn, the normalization mode that had the best results was from the ratio of the peak area normalized by the C emission signal (r of 0.9801 and 0.9834, respectively).

2.3.3 Standard Addition

Solid samples that present a complex matrix can significantly influence the laser pulse-sample interaction and, consequently the analyte emission signal. Thus, it can be difficult to obtain a correlation between the concentration and the emission signal of the analyte in the set of calibration samples and, in the analyzed samples of unknown concentration. In the multiple standard addition (SA) calibration method, a calibration curve is obtained for each unknown sample. As the same sample matrix is present in all calibration samples, the magnitude of matrix effects will be the same [2, 25].

Solid calibration samples in the SA procedure are prepared by adding increasing concentrations of the analyte using a salt, oxide, CRM, or aqueous solutions containing the analyte, to a fixed amount of sample. Five spiked samples are typically prepared *per* sample. When the addition of the analyte to the solid sample is done using a solid standard (a salt, for example), it is necessary to add a blank (which can be a binder) to make the sample mass up to a fixed amount so that the sample dilution will be constant in all samples. Furthermore, an efficient homogenization step of the sample and added analyte is required using an appropriate mill, in order not to compromise the precision of measurements. When the addition of the analyte to the solid sample is made using aqueous solutions, the steps of homogenization and drying of each prepared standard for further analysis are also necessary [51, 52]. Figure 2.1 illustrates an analyte addition procedure in the used calibration samples and the obtained multiple SA calibration curve.

The SA calibration strategy has some limitations. A significant number of additions have to be prepared and analyzed *per* sample. In addition, an efficient sample homogenization step is also necessary, resulting in low analytical throughput and additional costs. This calibration strategy is employed in quantitative analysis using LIBS [25]. An important aspect is to verify that the analyte signal remains in the linear proportionality range (signal saturation is avoided), but the slope of the addition plot is also significant. However, several elemental determinations using the analysis of solid samples with complex matrix by LIBS are described in the literature using SA as a calibration strategy, with acceptable analytical performance parameters.

Soils are a good example of samples with a chemically complex matrix, due to the variability of their composition associated with their geographic distribution [53]. Thus, SA was evaluated for the determination of Pb in soils, with different procedures for addition and homogenization of the analyte being reported in the preparation of solid standards for calibration [51, 53]. Yi et al. [53], prepared soil

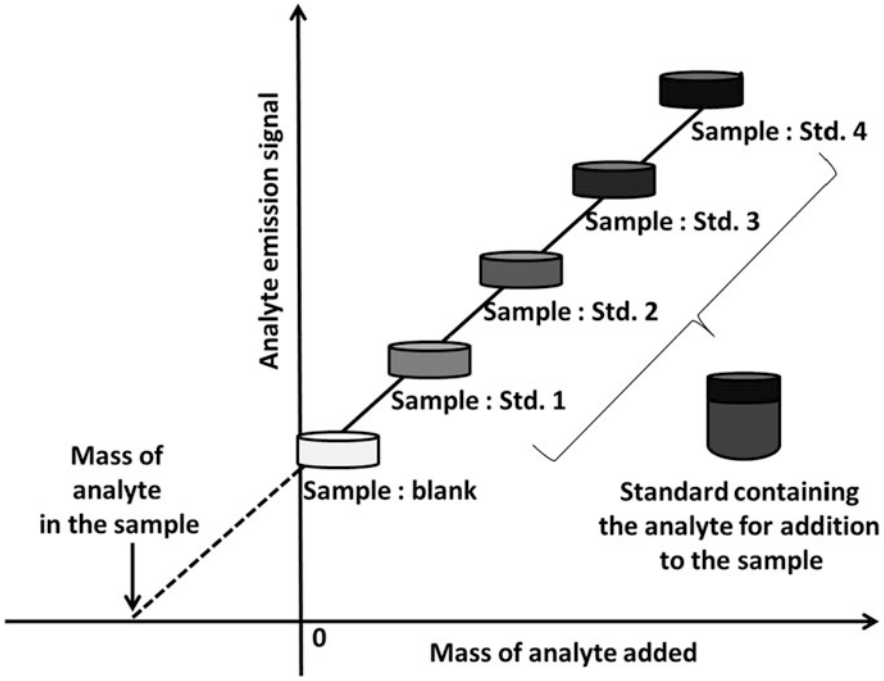

Fig. 2.1 Pictorial description of the SA procedure, which includes adding a standard (Std.) containing the analyte to the sample

suspensions containing aqueous $Pb(NO_3)_2$, which are homogenized using ultrasound, vacuum dried, ground in a mortar, and then pelleted for LIBS analysis. However, Wu et al. [51] added increasing concentrations of Pb using $Pb(NO_3)_2$ to the soil samples and then, diluted with soil samples collected at a depth of 3 m. Subsequently, they added water and homogenized the samples with a magnetic stirrer, dried and pressed them into pellets for further analysis. Note that the addition of the standard containing the analyte to the sample must be done carefully, so that it is homogeneously distributed in the sample and precision is not compromised.

Other analytes were also determined in solid samples by LIBS using SA calibration: (1) determination of Cu and Mn in the medicinal plant glycyrrhiza, using six solid calibration samples and Sr as internal standard [52]; (2) determination of Ca in coral skeleton, where nine calibration samples were used, six Ca I emission lines and, the intensity of a Sr II line were evaluated to normalize the intensity of the Ca I lines [54]; (3) quantitative analysis of *Mentha piperita* L. to determine Ba and Mn, using five calibration samples prepared by adding the analytes from an aqueous solution, and evaluating the precision and accuracy of metal determinations from the calibration curves obtained by the intensities of the emission lines of the analytes without normalization and normalized by the background, and by the lines of the Sr

internal standard, namely Sr I 460.73 nm (for Ba) and Sr II 407.77 nm (for Mn) [55]; among other examples.

Among the examples presented, it appears that several of them use the synergy between the SA and internal standardization calibration strategies to overcome the strong matrix effects and corrections of spectral fluctuations, using an appropriate internal standard [52, 54, 55].

The SA is a traditional calibration strategy that uses the sample itself for calibration adding the analyte to the sample at gradually increasing mass [56, 57]. However, besides of its advantages, this strategy requires a long time to prepare the calibration solid standard for each sample, which compromises the analytical frequency throughput. Therefore, it became not attractive and feasible for routine analysis, considering if an amount of sample needs to be analyzed.

This disadvantage led to the consideration of many other studies as an alternative to SA. One-point gravimetric standard addition (OPGSA) was proposed for matrix-matched standards to improve the LIBS analytical performance. For this strategy, only one calibration point is needed [31].

The linear model is calculated using two mixtures: (S1) sample plus blank (diluent) and, (S2) sample plus standard with known concentration of the analyte, e.g., certified reference material or salt. During the sample preparation, it is necessary that the sample:diluent and sample:standard ratios are the same, and a minor dilution factor can compromise the sensitivity for the determination of the analyte.

The concentration of the analyte in the sample employing this strategy is obtained by extrapolation of the calibration curve, as shown in Fig. 2.2. The x-axis corresponds to the mass of the analyte in the sample: 0 for S1 (sample + blank (diluent)) and, for S2 the mass of the added standard (known). On the y-axis is plotted the intensities of the selected emission line of the analyte for both pellets.

When the linear regression of both points is determined, the respective slope and linear coefficient (intercept) are used in Eq. 2.1 [31].

$$C_{\text{sample}} = \frac{|\ \text{Intercept}\ |}{\text{Slope}} \tag{2.1}$$

As only two calibration points are used, it is necessary to evaluate if the slope of the proposed method is statistically significant at a 95% of confidence level (p-value <0.05). This evaluation is performed comparing two variances: mean of squares of regression (MSR) and mean of squares of residue (MSr). These variances are compared through the F-test. The calculated F value (ratio between the variances described) is compared with the tabulated one, and it is required that the calculated should be at least 10-fold higher than the tabulated value (p value <0.05).

The proposed strategy is an efficient alternative to compensate matrix effects in solid analysis by LIBS and the data treatment is simpler than MEC (Multi-energy calibration, see next section), because only one emission line is used. However, the OPGSA sometimes presents limitations as the choice of an appropriate blank, and requires an efficient homogenization of the standards, which becomes the sample preparation for this strategy laborious [31, 58]. In addition, the linearity of the

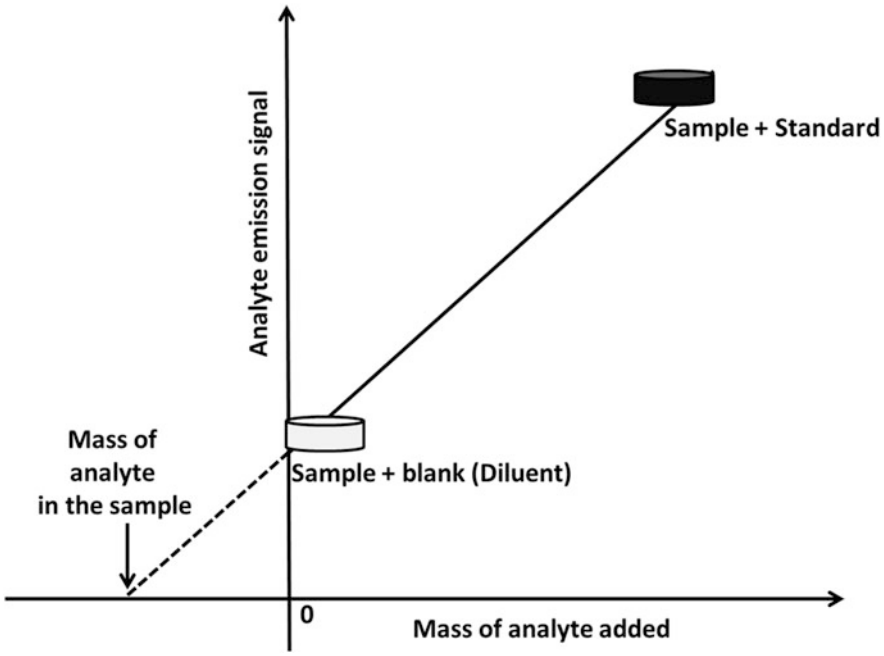

Fig. 2.2 Graphical description of the OP-GSA calibration strategy

proposed method must be checked, then the operator can verify first this condition using at least five calibration samples. This strategy can be useful for routine analysis, where the sample matrix is well known and presents low variability.

This strategy was applied for the determination of Ca and P in mineral supplements [31] and, for the determination of B, Fe, Dy, Gd, Nd, Pr, Sm, and Tb in electronic waste samples employing LIBS [58], showing the efficiency and its applicability to minimize matrix effects in complex samples.

2.4 Nontraditional Calibration Strategies

2.4.1 Multi-Energy Calibration

A LIBS spectrum is rich in information, and it can present several emission lines for a given analyte due to the various electronic transitions that occur between the fundamental and excited levels for a given element. So why not use all these analyte emission lines, with different sensitivities, to propose a calibration model for each analyzed sample? This is exactly what multi-energy calibration (MEC) proposes to obtain the calibration model: simultaneous use of several wavelengths of the analyte and only two calibration samples using the unknown sample itself.

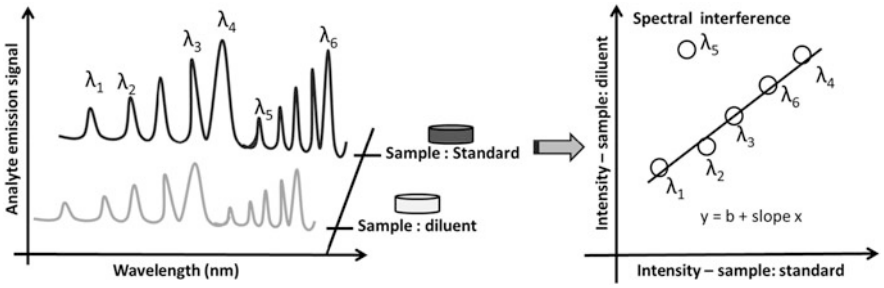

Fig. 2.3 Illustration of the LIBS emission spectra obtained from the analysis of the two calibration samples required *per* unknown sample and a linear MEC model highlighting an emission line (λ_5) with spectral interference

The MEC was initially proposed by Virgilio et al. [59], for elemental determination employing spectroanalytical techniques as ICP-OES, microwave-induced plasma optical emission spectrometry (MIP-OES), and high-resolution continuum source flame atomic absorption spectrometry (HR-CS-FAAS). In 2018, Babos et al. [60] reported the first study using MEC in the quantitative analysis of solid samples by LIBS.

Only two calibration samples *per* unknown sample are required to obtain the calibration model, which are prepared using: (1) one standard containing the analyte added to a given amount of sample and the other (2) a diluent (blank) added to the same amount of sample. The sample:standard and sample:diluent (w /w) ratio should be the same, and normally is 50:50 ratio (w /w). However, this proportion must be evaluated in some situations, so that it does not obtain a large dilution factor of the solid sample and does not compromise the monitoring of low sensitivity analyte emission lines. As the same amount of sample is present in the two calibration samples, a matrix-matching takes place [25, 59, 60].

The standard containing the analyte to be added in preparing the calibration samples can be a salt, oxide, CRM, or a sample with an analyte reference value, among others. The diluent (blank) can be a major constituent of the sample matrix, an appropriate binder or a sample that does not contain detectable analyte contents in its composition. As the addition of the standard and blank are made to solid samples, and in order to obtain precise and accurate measurements and not compromise the analytical parameters of the method, an efficient homogenization procedure must be performed before pelleting the two standards [25, 60].

In addition to obtaining an efficient matrix-matching, another advantage of using MEC is the possibility to identify analyte emission lines with spectral interference. In the MEC model, the interfered emission lines are identified as outliers (nonlinear trend). So it must be evaluated and removed from the linear model so that it does not compromise the accuracy of the analyte determination [25, 60]. Figure 2.3 illustrates the obtaining of the emission spectra of the two required calibration samples, and an MEC model with an emission line with spectral interference (outlier: emission line number 5, λ_5).

To obtain the linear MEC calibration model, the intensity values monitoring the different emission lines of the analyte in the standard prepared by adding a standard to the sample are used as independent variable (*x*-axis), and as dependent variable (*y*-axis) the analytical signal obtained by monitoring different analyte emission lines in the mixture prepared by adding the diluent to the sample. Using least squares regression, a linear model is obtained, where the slope (angular coefficient) of the model can be obtained. Using the slope value obtained and the added (known) analyte concentration in the standard preparation, it is possible to determine the analyte concentration in the analyzed sample [59], as follows (Eq. 2.2):

$$\text{Concentration}_{\text{analyte}} = \frac{\text{slope} \times \text{added standard concentration}}{1 - \text{slope}} \tag{2.2}$$

Several applications are reported in the literature using LIBS for quantitative analysis and employing MEC as a calibration strategy. In food analysis, MEC was evaluated in the determination of Ca, K, and Mg in dietary supplements using microcrystalline cellulose as blank and binder; and performing a study of the influence of different concentrations of analytes added during the preparation of the standard containing sample:standard [61]. In two other studies, MEC-LIBS was evaluated in the analysis of solid mineral supplements for cattle to determine Ca, Cu, Fe, Mn, and Zn, using Na_2CO_3 as blank and 50:50 (w /w) ratio in the preparation of two standards required [60]. In the second study, the authors determined Ca and P using Na_2CO_3 as blank, 80:20 ratio (w /w) in the preparation of calibration mixtures. In addition, identifying an emission line of P I 253.39 nm interfered by the emission of Fe I 253.41 nm [31], both studies obtained satisfactory trueness in the range from 80 to 120%.

MEC was used for the determination of Cr and Ni in nickeliferous ores. Sodium carbonate (Na_2CO_3) was used as blank and diluent, and Cr and Ni nitrates as standards [62]. Carvalho et al. [63] determined Al, Fe, and Ti in high-silicon-content samples. In this study, a CRM containing the analytes was used to prepare the calibration sample, SiO_2 used as blank, and lithium borate flux used in the standards fusion procedure to obtain fused glass discs for LIBS analyses; in addition, B and Li emission lines were evaluated as IS [63].

Electronic waste was analyzed by LIBS to determine strategic, base, and rare earth elements (REE), present in the composition of electronic components and evaluating the advantage of matrix-matching via MEC. In the analysis of liquid crystal display from mobile phones to determine In, the two calibration samples required *per* sample in the MEC were prepared using SiO_2 as a blank and microcrystalline cellulose as a binder in the preparation of the pellets, and one of the five In emission lines monitored presented spectral interference, identified as outlier in the calibration model and removed from the model [64]. In another work, samples of exhausted computer hard disk magnets were analyzed to determine REE (Dy, Gd, Nd, Pr, Sm, and Tb) and base (B and Fe) elements of these components by LIBS. Due to the high Fe concentration (approximately 60% (w /w)) in these samples and

the several Fe emission lines with great potential to interfere with the REE emission lines, the two prepared standards used the ratio 42:58 (w /w) [58].

An iterative multi-energy calibration (IMEC) method was proposed by Li et al. [65] for online Ni-based alloy smelting process monitoring by LIBS. In this study, IMEC used four Al emission lines and an appropriate algorithm to propose the quantitative models. Thus, the potential of this calibration strategy in providing quantitative results with satisfactory analytical parameters in online LIBS applications was demonstrated.

2.4.2 One-Point and Multi-Line Calibration

As it is known from the Boltzmann equation, the emission intensity is proportional to the spectroscopic parameters of a given emission line, experimental constant, plasma temperature, and the concentration of analyte in the sample. In this context, the one-point and multi-line calibration (OPMLC), reported by Hao et al. in [66], proposes a linear calibration model monitoring several analyte emission lines in the sample with unknown concentrations and, only a single calibration sample for analyte determination by LIBS.

Similar to the MEC, in the OPMLC emission lines with different sensitivities are monitored for the proposition of the calibration model. However, in OPMLC only a single calibration sample is required for all samples with unknown concentrations analyzed. This calibration sample must present a matrix similar to all samples that will be analyzed to occur matrix-matching. In addition, the concentration of analytes in the calibration sample cannot be very different from the concentrations that are expected to be determined in the analyzed samples, if the concentration is much higher or lower, the accuracy of the determinations may be compromised [25, 66].

The linear OPMLC calibration model is obtained using least squares regression, with the independent variable (x-axis): intensity values monitoring the different analyte emission lines in the calibration sample, and as dependent variable (y-axis): the intensities values obtained by monitoring different analyte emission lines in the sample with unknown concentration. Figure 2.4 illustrates a linear OPMLC model.

From the slope obtained, and the known analyte concentration value, in the calibration sample, it is possible to determine the analyte concentration in the sample [66], as follows (Eq. 2.3):

$$\text{Concentration}_{\text{analyte}} = \text{slope} \times \text{standard analyte concentration} \tag{2.3}$$

OPMLC is a very interesting univariate calibration strategy to be evaluated in the elemental determination by LIBS in unknown samples that do not show great variability in analyte concentrations (e.g., in certain industrial processes). Furthermore, it is a very promising strategy in the development of analytical methods where

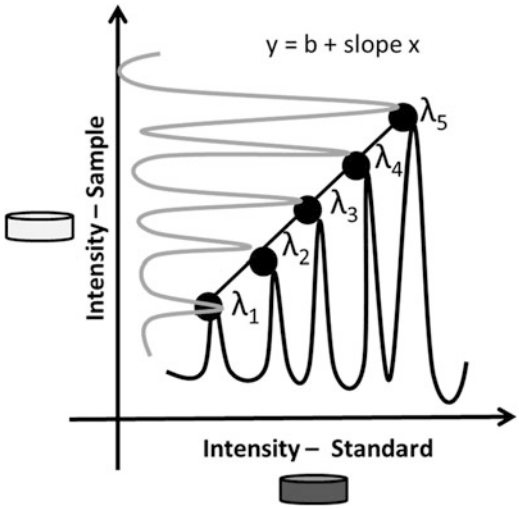

Fig. 2.4 Illustration of a linear OPMLC model monitoring five emission lines (λ) for an analyte in the sample and calibration sample

there are few samples available to be used in the set of calibration samples, as it requires a single calibration sample [25].

Some studies in the scientific literature report the use of OPMLC in the elemental determination by LIBS. In the introductory study of OPMLC [66], the authors determined Cr, Mn, Ni, and Ti in low-alloy steel samples, to minimize instrumental fluctuations in the acquisition of LIBS emission spectra, and they used Fe emission lines as internal standard. Thus, models with an acceptable coefficient of determination values ($R^2 \geq 0.8833$) were obtained for all analytes and, average relative errors for determination in the range from 9 to 36%.

In the direct determination of macronutrients Ca, K and Mg in cocoa seeds by LIBS using OPMLC, RSD values $\leq$26% were obtained for all analytes [67]. In the determination of Al and Pb in six waste printed circuit boards (PCB) samples, OPMLC models were obtained by monitoring four and two analyte emission lines, respectively. Root mean squared error of prediction—RMSEP values of 5.0 g kg^{-1} Al, 0.91 g kg^{-1} Pb and, RSD values $\leq$25% were obtained [24].

Furthermore, in the determination of P in fertilizers and Al in plant tissue, the authors used three P I lines at 213.62, 214.91, and 215.41 nm in the proposition of the OPMLC model [68]. However, for Al determinations, the authors used an interesting strategy to obtain the OPMLC model, using the emission intensities measured at five wavelengths located in the wing of the Al I emission line at 308.22 nm (308.01, 308.07, 308.12, 308.17, and 308.22 nm). This strategy was employed to overcome the limited number of interference-free Al emission lines.

2.5 Single-Sample Calibration

Obtaining a regression model from a previously selected set of calibration samples is the most common practice to further determine the analyte concentration in an unknown sample. However, in the single-sample calibration (SSC) proposed by Yuan et al. [69], a single calibration sample of a similar matrix to other samples is used to provide matrix-matching, which has reference values of the concentration of the analyte and other elements that constitute the standard to be used in the determination of the analyte. The simple correlation (Eq. 2.4) used to calculate the analyte concentration in the analyzed sample ($C_{analyte}$) considers the concentration and emission intensities of the analyte and n other elements monitored in the calibration sample ($C_{\text{standard analyte}}$, $C^n_{\text{standard element}}$, $I_{\text{analyte standard}}$ and $I^n_{\text{element standard}}$), in addition to the emission intensities of the analyte and n others elements monitored in the analyzed sample $\left(I_{\text{analyte sample}} \text{ and } I^n_{\text{element sample}}\right)$ [69]:

$$C_{\text{analyte}} = \frac{\frac{C_{\text{standard analyte}} \times I_{\text{analyte sample}}}{I_{\text{analyte standard}}}}{\sum_{i=1}^{n} \frac{C^n_{\text{standard element}} \times I^n_{\text{element sample}}}{I^n_{\text{element standard}}}} \tag{2.4}$$

Nevertheless, in SSC additional care must be taken to use emission lines free from spectral interference that will be used in the correlation [69].

2.5.1 Slope Ratio Calibration and Two-Point Calibration Transfer

Nunes et al. [70] proposed the slope ratio calibration (SRC) strategy, which is based on a single solid calibration sample. The fundamentals of the method are as follows. The analyte emission intensity (I) is directly proportional to the analyte amount in the ablated mass (m), where $I = k_1 \cdot m$; also being proportional to the number of laser pulses (N_p) in the case of signal accumulation via $m = k_2 . N_p$. Therefore, sample ablation efficiency (k_2) and analyte atomization/thermal excitation/optical efficiency of the system (k_1) can be described by a proportionality factor (K) between I and N_p ($I = K \cdot N_p$). In general, this strategy is related to the increase of the ablated sample mass with the number of accumulated laser pulses.

The single solid calibration sample can be a CRM or a reference sample with known concentration of the element of interest. In addition to that, an unknown sample with the element of interest is also used. Therefore, two linear models are built by plotting the analyte emission intensities (dependent variable) as a function of the number of laser pulses accumulated for both samples (independent variable).

The concentration of the analyte in the test sample (C_{sample}) is calculated according to the ratio between the slopes of standard (b_{std}) and the test sample

(b_{sample}) values and, the known analyte concentration in the standard (C_{std}) using Eq. 2.5:

$$C_{sample} = \frac{b_{sample}}{b_{std}} \times C_{std} \tag{2.5}$$

This strategy was evaluated for the determination of macro- and micronutrients in plant leaves with NIST 1547 as standard, using between 5 and 30 laser pulses *per* site for calibration. The accuracy was assessed from the analysis of CRMs and the comparison with the results by ICP-OES after microwave-assisted acid digestion, with agreement at the 95% confidence level.

Another interesting calibration method similar to SRC was proposed by Castro et al. [58], named as two-point calibration transfer (TPCT). It is derived from the SRC approach with only one difference: the models are calculated using two points (TP) of accumulated laser pulses. In TPCT only two sets of accumulated signals are used for sample with unknown analyte concentration and standards or reference samples (with known analyte concentration). Therefore, two linear models are obtained monitoring two analytical signals from set 1 and set 2.

In LIBS, hundreds of spectra are obtained for a representative analysis, so it is possible to obtain two sets of spectra and sum the spectral information from both. It is important that set 2 must be at least twice as large as set 1. As the model is calculated with two points, an *F*-test is performed to note the variances related to residues and the regression. Therefore, *F*-values are calculated from the MSR and MSr, if the $F_{experimental}/F_{tabulated}$ is ≥ 10 (p value <0.05), the model is considered valid statistically (regression is higher than and different of residue). The concentration of the analyte in the test sample is calculated equal to the SRC using Eq. 2.5.

This strategy was evaluated for the direct analysis of hard disk magnets with determination of REE. The accuracy was calculated using the reference concentrations (ICP-OES results) [58]. TPCT has also been successfully employed by Gamela et al. [67] in the determination of Ca, K, and Mg in cocoa beans, by Costa et al. [71] for the determination of Pb content in recycled polypropylene from car batteries and, by Babos et al. [24] for determination of Al and Pb in waste PCB.

A limitation of both strategies (SRC and TPCT) is the choice of the standard for calibration. The laser-sample interaction depends on the physicochemical characteristics of the sample (sample particle size, porosity, and density of the pressed pellets), the laser properties (wavelength, pulse duration, repetition rate, energy) and optical design (lens-to-sample distance). As the test sample and standard are measured using the same instrumental parameters, the accuracy in the calibration depends on the similarity between both samples (test and standard samples) for a perfect matrix-matching. In general, both strategies minimize the matrix effects, there is a simplicity in the data processing and, for the TPCT the linear model is built with two points being also an advantage over the SRC. Figure 2.5 shows a hypothetical example for both strategies.

Both SRC and TPCT are useful for homogeneous samples as those described in this section. In addition, it is always important to run confirmatory measurements

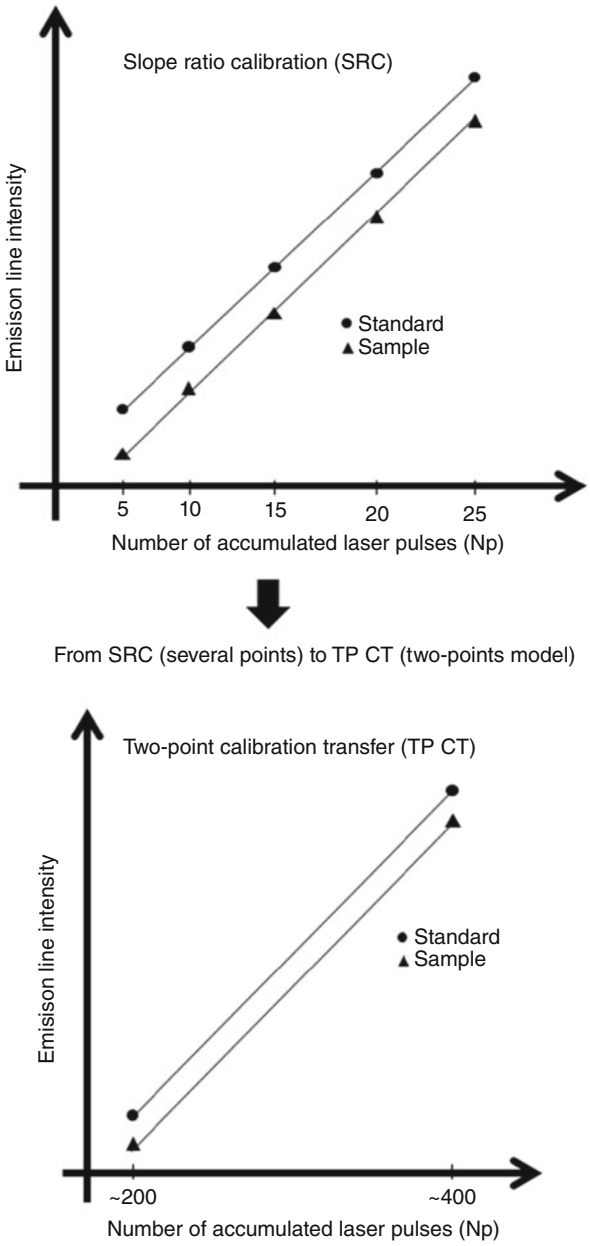

Fig. 2.5 Illustration of the concepts of the slope ratio calibration and two-point calibration transfer methods

using a reference technique as ICP-OES after proper sample preparation. As can be noted, these strategies are useful for routine analysis where the sample matrix only varies slightly.

2.5.2 Inverse Calibration

Generally, univariate calibration models used in LIBS employ simple linear regression to estimate the relationship between an independent and a dependent variable, which usually correspond to the concentration and the analytical signal, respectively [25]. Univariate calibration relates two variables, x and y, through a model to predict one variable based on the other in a second step. The direct model has been widely used to build quantitative models to predict absolute mass or concentration from an instrumental measure that employs spectroscopic techniques such as LIBS. A linear relationship between x and y can be considered from Eq. 2.6 [72]:

$$y_i = b_0 + b_i x_i + \varepsilon_i \tag{2.6}$$

where b_0 and b_i are the coefficients and ε_i, the error.

This model is often used in LIBS and it is called a direct model. The direct model's concentration is the independent variable, and the analytical signal is the dependent variable. In the direct model of y over x, the measures of x are assumed to be error-free. Duponchel et al. [73] evaluated direct and also inverse models for the determination of Ca in soils and Na in glasses. In the inverse model used by the authors, concentration is the dependent variable, and analytical signal is the independent variable. In the inverse linear regression of x on y, measurements of y are assumed to be error-free from Eq. 2.7 [72].

$$x = \beta_0 + y\beta_i + \varepsilon \tag{2.7}$$

When this inversion concerning the dependent and independent variables happens, the values of the intercept and slope of the analytical curve are different. When a test sample is analyzed, the predicted concentrations are different; it shows that the prediction of analyte concentration depends on the chosen model. In this study, the inverse model showed the lowest root mean square error of calibration (RMSEC) and RMSEP. Therefore, comparing direct and inverse models is interesting to find the best strategy for the considered data set. The authors also add that the smaller the signal-to-noise ratio (SNR), the greater the differences. Additionally, researchers are advised to use the inverse models when the number of calibration samples is low.

2.5.3 Fluence Calibration

Different non-traditional calibration strategies were already presented here. It could be observed that among the novel calibration methods, MEC uses several emission lines for the acquisition of analytical signal and OPGSA, SSC, SRC and TPCT use one or two calibration samples to build a calibration curve or linear model [25], but what happens if an instrumental parameter could be used to develop a calibration strategy?

In this sense, fluence calibration (FC) was developed to minimize matrix effects for quantitative LIBS analysis. Laser pulse fluence is an important instrumental parameter in LIBS, because the efficiency of the laser-sample interaction and the vaporization, atomization, ionization process is also dependent on this parameter [74].

Laser (pulse) fluence is the laser energy delivered *per* unit area (J cm^{-2}) and when the fluence value is increased, the plasma temperature also increases, a larger amount of sample is ablated and more analytes are vaporized, atomized, ionized into the plasma [14, 74]. Taking into consideration this relationship between laser pulse fluence and sample mass ablated, FC was developed.

Fluence calibration is based on the use of a single calibration sample (as other aforementioned non-traditional calibration methods) to obtain a linear model at two different laser fluences. Then pellets of this single calibration sample (with the known concentration of the analyte) and of the samples are measured at the same two laser fluences. Authors emphasized that during the application of this FC method, the change of laser fluence has to be obtained via varying the laser pulse energy besides keeping the laser spot size fixed. The linear model is obtained from the emission signals plotted in the *x*-axis (signals obtained for calibration sample, independent variable) and in the *y*-axis (signals obtained for samples with unknown concentrations, dependent variable) and, from Eq. 2.8 it is possible to calculate the analyte concentration:

$$C_{\text{sample}} = \text{slope} \times C_{\text{standard}} \tag{2.8}$$

where C_{sample} is the analyte concentration determined in the sample, slope value is obtained from the linear model and C_{standard} is the known analyte concentration in the calibration sample [75].

In the FC method, both standard and sample are exposed to different laser pulse fluences, i.e., different plasma conditions and this exposition lead to similar plasma conditions for both standard and sample (and of the process that occurs in the plasma as vaporization, atomization, and ionization) which is one of the factors responsible for minimizing matrix effects and ensure accuracy and precision of the results [75].

The first paper reported in the scientific literature combining FC and LIBS (FC-LIBS) by Machado et al. [75]. In this study, the authors evaluated the performance of FC for the determination of Al and Pb in PCB waste and Al, K, Mg, Na, and P in fertilizer samples. The laser fluence values were optimized for each sample matrix and spot size was fixed at 50 μm. The best combinations were achieved using 2546 J cm^{-2} and 4074 J cm^{-2} for PCB samples and 2546 J cm^{-2} and 4584 J cm^{-2} for fertilizers samples. In several LIBS instruments, it is easily possible to prepare laser conditions with different setups in order to obtain distinct fluences. Using these optimized fluences, excellent accuracy and precision results were obtained during the analysis of PCB and fertilizer samples. The selection of the calibration sample was an important aspect to be considered to reach adequate accuracy and precision

using FC-LIBS. Moreover, considering the linear model with two-point, *F*-test was calculated for each model to evaluate its significance (as previously described).

It was observed that depending on matrix complexity, the performance of the calibration method depends on physicochemical properties and the analyte concentration in the calibration sample and samples. The authors also evaluated FC without a matrix-matching approach, using calibration sample prepared mixing salts for PCB and fertilizer samples. Even considering the absence of sample matrix in the calibration sample, good accuracy and precision were obtained for Al in two PCB samples and Al and P in two fertilizer samples. It is completely desirable to have a universal standard for calibration, but for strategies that use only one standard, factors such as different elements, their concentration (in the standard and samples), and sample matrix can influence the obtaining of satisfactory results. Therefore new FC-LIBS applications may bring more knowledge about the influence of these factors in the accuracy of the results. It is important to highlight the FC advantages, such as the capability to overcome matrix effects, simplicity, faster pellet preparation (use of only one calibration sample), fast data acquisition, and data treatment for the direct analysis of complex solid samples.

As a final remark in this section about non-traditional calibration strategies, the LIBS user can first test MEC to verify the presence of spectral interference on the emission lines selected for the determination of the analyte. These lines can be removed if the interference is confirmed. Then, other strategies can be also tested as OPMLC, SRC/TPCT, or FC. Furthermore, it is important to mention that some strategies, such as TPCT, assume a linear relationship between the analyte signal and its concentration. In this case, some confirmatory determinations must be performed using reference techniques such as ICP-OES. Another aspect to be emphasized is the fact that these nontraditional calibration strategies are very useful for routine analysis (in metallurgical applications, for instance) where the sample matrix is stable and well known.

2.6 Multivariate Calibration

Multivariate calibration tools have been widely applied in LIBS to improve the accuracy of quantitative analysis [25, 76]. This type of calibration is used when an element cannot be determined with only one parameter obtained from the spectral data [77]. Multivariate calibration has some advantages such as (1) it can take full use of LIBS spectral information and improve the precision and accuracy of the measures; (2) it is possible to determine the analyte in the sample even in the presence of the interferent, since the interferent is also included in the calibration model [25]. The most popular multivariate calibration methods for LIBS quantitative analysis involve multiple linear regression (MLR), principal component regression (PCR), partial least squares (PLS), and artificial neural networks (ANN) [25]. It is

important to mention that multivariate calibration is unable to solve all analytical problems, but can bring useful applications, as can be noted in the next lines. According to the Web of Science, since 2010, the number of publications on LIBS analysis with multivariate calibration has been increasing significantly, and among the methods mentioned, PLS is the most widely used, as shown in Fig. 2.6.

2.6.1 Multiple Linear Regression

The aim of MLR is to model the linear relationship between a dependent variable (response) and multiple independent variables by regression functions. In MLR, the interferents, impurities, and effects of baseline are treated without problem if they are present in all samples in the calibration dataset. On the other hand, a huge limitation is the number of variables, and this number should be lower than the number of samples to enable the calculation of matrix inversion to obtain the regression vector. Thus, it is necessary to make a variable selection and choose some emission lines for the target element. Moreover, for a good model, besides the limitation of the number of variables, these chosen variables cannot have a huge correlation among them, because this can also cause difficulties in the matrix inversion [78].

In a study by Ayyalasomayajula et al. [79], LIBS and MLR were used to quantify the total carbon concentration in soil. For the variable selection, the authors employed the ratio of C (247.48 nm) with Fe lines (246.51 and 247.48 nm). The results showed that the LIBS and MLR combination can be successfully applied to the quantitative measurement of C in soil with a small error. Wang et al. [80] assessed univariate (MMC and IS) and multivariate (MLR) calibration strategies to determine Pb in tea leaves by LIBS. The MLR presented better quantitative performance than the other two univariate strategies. As mentioned before, the MLR models use more information to predict the concentrations of the element of interest improving the performance of quantitative analysis by LIBS.

Sperança et al. [81] determined Ti in sunscreen using LIBS, where several calibration strategies were applied, being MLR the best option (according to reference values provided by ICP–OES analysis). The authors selected two titanium emission lines: Ti I 498.17 nm and Ti I 499.11 nm. Other applications with good results using MLR and LIBS include the determination of elemental impurities in plastic [82] and determination of P in fertilizer [83].

2.6.2 Principal Component Regression

PCR is a regression based on the same decomposition as PCA. First, PCR decomposes matrix $\mathbf{X}$ with n samples and p pixels or variables (in this case, the number of emission lines recorded in a LIBS spectrum). After this decomposition, the scores and loadings are used to calculate the regression coefficients b for the prediction of a vector $\hat{y}$ with n rows, that is, each row will correspond to a predicted concentration of the element of interest. PCR and PLS have similar mathematics

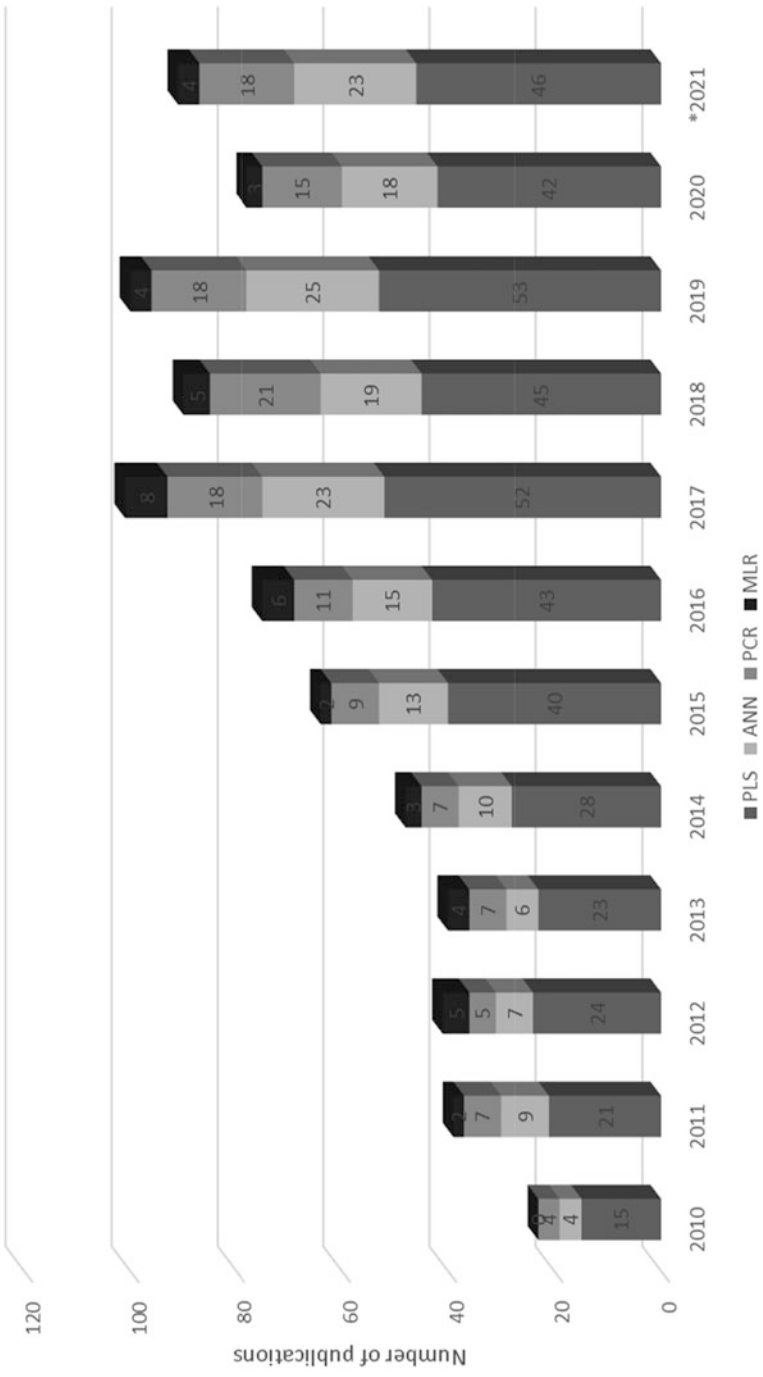

Fig. 2.6 Evolution of the number of LIBS publications using different multivariate calibration strategies (data for the year of 2021 is incomplete)

involved, hence the performance of these tools tends to be also similar. The main difference is that PCR does not relate the scores of matrix **X** with the concentrations, while PLS connects the **T** scores of **X** with the **U** scores of vector *y* [76, 78]. A lowercase letter means vector. Due to similar mathematics of PCR and PLS, the performance of both models is compared in many studies [25, 76].

PCR has already been used in combination with LIBS for the determination of Pb in recycled polypropylene from car batteries [71], to the analysis of Fe in iron ore [84], to the determination of Cr, Mn, Ni, and Si in high-alloyed stainless steels [85], among others [25]. Devangad et al. [86] determined Mn in glass matrices combining PCR. In this study, PCR models reached optimum method LOD and RMSEP of 0.02 and 0.54 w/w%, respectively, in a set of samples with a Mn concentration ranging from 0.77 to 11.61%. Takahashi et al. [87] used PCR to quantify the composition of brass alloys submerged in water using LIBS. The authors determined Cu and Zn, and PCR showed an RMSEP of 2.7 and 2.8%, respectively.

2.6.3 Partial Least Squares

PLS is a regression method that uses a selected number of latent variables to decompose the matrix **X** (independent variables) with *n* samples and *p* variables as well as the vector y (dependent variables) with *n* rows (reference concentration). The parameters of PLS can be obtained using calibration sample set, and there is no matrix inversion involved in the calculation, hence it has only a calculation error, thus high accuracy, fast execution, and a good predictive ability [77].

PLS tool is a powerful chemometric algorithm for multivariate calibration, but several important details must be observed for its correct application. The first, and more general one, is the overfitting when too many latent variables are used, showing a strong capability of predicting the concentrations of the samples used in the calibration, but the poor capability of predicting an unknown sample. In the case of PLS, the number of latent variables is optimized through cross-validation, and this helps to avoid under- or overfitting [77]. Another problem, not much reported but can occur, is present when the regression vector incorrectly correlates emission lines of elements. For instance, the algorithm correlates emission lines from Ca to predict Al concentration. It is, therefore, advisable for the analyst to examine the regression vector and confirm the correctness of the information [25].

In terms of application, PLS is employed to the most diverse types of samples in combination with LIBS including ceramics [88], polymers [71, 89], alloys [50], hard disk magnets [58, 90], medicinal herbs [91], among others [25, 76]. In this sense, Goueguel et al. [92] proposed PLS calibration models along with full LIBS spectra to predict soil texture (clay, silt, and sand percent). The authors reached prediction errors of 10% for sand and 3% for clay using PLS-based calibration models.

In a study published by Costa et al. [93], polycarbonate (PC) and acrylonitrile-butadiene-styrene (ABS) concentrations in blends from waste electrical and electronic equipment (WEEE) were determined. The authors prepared a calibration

curve using 11 calibration solid standards with a varying PC/ABS concentration in 10 w/w% steps. The predictive capability of PC and ABS using PLS models in this application showed standard error of cross-validation to be 5.6%. The prediction of concentrations was confirmed using differential scanning calorimetry (DSC).

Ding et al. [94] determined potential toxic elements (Cu, Zn, Cr, and Ni) in soil employing interval PLS (iPLS). This strategy divides the whole spectrum into n intervals and evaluates each one separately to detect which part is more accurate for the prediction of the concentration of analytes. In this study, the authors divided the full spectrum into 10–90 subintervals, varying from 10 to 100 emission lines. Compared to the PLS model using the full spectrum, the iPLS model showed a higher coefficient of determination values (R^2) and lower prediction error for Cu, Zn, Cr, and Ni.

2.6.4 Artificial Neural Networks

Comprehension, reasoning, perception, communication, and learning are some capabilities of ANN, imitating the structure of a human brain. This method can handle nonlinear, noisy, or imprecise data quite well. It is a nonlinear functional mapping between an input and an output data space. This network operates using a large number of "neurons" (parallel-connected simple arithmetic units), which can be defined as a nonlinear, parameterized, and bound function (examples include sigmoidal and Gaussian functions). The neurons operating on the same input variables are organized in layers, while the weights (combination of the nonlinear functions) are represented as lines, connecting units in different layers. There are three types of layers: input, hidden, and output. The input layer is the data given to the network, the hidden layer is the intermediate computation, and the output layer is the response relative to the input. Therefore, the aim of the neural network is to transform the inputs into meaningful outputs, extracting important features [76, 78, 95].

In the case of LIBS, the inputs are spectra. The ANN models are optimized to obtain the best representation of the output set (concentration of analyte) with a number of known samples (training set). In the training dataset, there is a set of inputs with their respective desired outputs. A function modifies the weights of the network until the resultant error is less than a predefined error, so the network infers a relationship between the inputs and outputs. With this relationship, the ANN can make predictions for an unknown sample [96].

Ferreira et al. [97] determined Cu in soil samples using ANN as calibration strategy for LIBS. The variable selection (for ANN training) was made by simple linear regression and wrapper performance in order to select the wavelengths with the best linear correlation with Cu. ANN used a multilayer perceptron (MLP) and the results presented good accuracy, proving to be an efficient strategy for Cu determination in a heterogeneous set of soil samples. Other studies related to soil analysis and LIBS using ANN as calibration strategy have also been reported in the literature [98–100].

Another application in the literature is with the metallic alloys [101–103]. In this sense, Inakollu et al. [104] performed a comparative study between traditional and ANN calibration for the analysis of different Al alloys by LIBS. The authors used some emission lines for the elements of interest (Cu, Cr, Mg and Mn) and, besides that, they also used the intensity ratio of the spectral lines of these elements compared to an Fe line. In this case, the concentration of the element relative to a reference element (Fe, as an example) can be found. In 75% of the cases, the predicted concentration values using the intensity ratio of the elements by ANN presented better results than the traditional calibration, with values closer to those determined through reference method.

In a recent study with forensic nuclear materials, LIBS and ANN were applied jointly by Bhatt et al. [105]. The authors used LIBS in air at atmospheric pressure for the quantification of trace levels of uranium in cellulose (in order to mimic a typical scenario of illicit nuclear and radiological material) and uranium-bearing mineral ores. The multivariate calibration using ANN (using the back-propagation algorithm) was successfully employed using weak and resonant uranium lines. Other studies dedicated to ANN and LIBS were applied to online measurement for the gross calorific value (GCV) of coal [106], quantitative determination of Ca, K, and Mg in the roots [107], and in the determination of trace elements in geological samples [108].

2.6.5 Calibration Based on Linear Correlation

In 2001, Galbács et al. introduced a new calibration method based on spectrum comparison using the linear correlation formula (linear correlation calibration method, LCM) [109]. This method can be advantageously applied to all multi-component solid samples containing chemical constituents in comparable concentrations (minor and major components). The LCM method produces a calibration plot with the value of the linear correlation coefficient on the *y*-axis calculated by the comparison of the spectrum of one of the components in the sample in the pure form to the spectrum of a series of calibration samples containing the analyte at various relative concentrations (e.g., on the *x*-axis, the mass fraction of the analyte would run from 0 to 100%). It was shown that the calibration curve produced in this way will always be monotonous and monovalent and that it can be very well fitted with a quadratic or cubic polynomial function. The method can be simply extended to multi-component (N) samples, by producing the calibration curves for $N\text{-}1$ components.

The main advantage of the LCM method is that given the complete immunity of the linear regression coefficient to the linear transformation of any of the involved datasets (samples or standards), the calibration curves can be stored and used for a long time, e.g., in portable instruments. It is important to consider that in most cases, an instrumental drift or aging will result in the change of sensitivity or background, hence affecting the data by a near-linear transformation. The analytical precision and accuracy are also largely improved, thanks to the fact that the calibration is based on

the complete spectrum, not, e.g., only the intensity of a single spectral line. It was shown that the repeatability of the data points in the calibration plot is at least ten times better than with univariate calibration.

The LCM method was first developed and demonstrated for LIBS, applied to the accurate analysis of various alloys (e.g., brass, aluminum alloys, gold alloys, etc.) [109, 110]. Later, the same research group extended the applicability of the method to trace analysis of solid and liquid samples by the transformation of the *x*-axis. This extended version of the method was called Generalized Linear Correlation Method (GLCM) and was successfully demonstrated to work not only for LIBS, but also for UV-Vis absorption spectroscopy and ICP-MS [111]. The relative error in concentration determination generally ranged from 0.1% to 5%.

2.6.6 Data Fusion

With the fast development of new chemical analysis procedures, along with modern high-throughput technologies, the data generated has been increasingly larger, complex, and multivariate. The era of big data poses difficulties for extracting value information from a huge volume of data and, according to Meng et al. [112], they are related to "5 V" characteristics: volume, variety, velocity, veracity, and value [112].

In the cases of chemically rich samples, a single measurement method can be unable to extract all the useful information. Combining data from complementary analyses is an alternative way to enhance the extracted knowledge about sample features. In practice, however, increasing availability of multiple data using different acquisition methods brings new challenges to traditional data processing methods that assume independent variables [113]. Indeed, conventional statistical methods are unable to produce reliable, valuable, and accurate information from massive data. On the other hand, besides the information explosion, modern technologies introduce us to several data processing methods to obtain more informative, objective, and accurate information than the original big data [112].

There is always much interest from the scientific community in gathering heterogeneous information systems through a consistent data integration interface. Chemometrics has proven to be a powerful tool in data science for grouping convergent outputs as well as for retrieving hidden chemical information in multivariate data [113, 114]. Data fusion is a method of concatenating multiple blocks of data from different records into a single, consistent, and clean representation [115].

Ways of the successful implementation of data fusion may differ from system to system, due to the various levels of complexity. Three main possibilities are generally explored: low-, mid-, and high-level data fusions [116]. These approaches are similar, differing mainly in the treatment stage of each data source aligned to standardization, preprocessing, and variable selection (if necessary). The choice of the best method to be performed depends on the goal, measurement procedures used, sample matrix, volume, and type of data to combine. The simpler approach is the low-level method that assumes the direct fusion of multiple raw data to obtain a

regression model. Limitations reported for this method include big data sets and predominance of one data over other measure systems. In this case, mid-level data fusion brings the solutions to these limitations, in which it first extracts the relevant features from each data source individually and then these variables are merged into a single matrix. The reduction of the data array and selection of important variables from each data block facilitates the interpretation of the results and the visualization of the contribution from each fused measure source. Finally, the method known as high-level data fusion is accomplished at the decision results obtained from multiple data sets to produce a unique solution [116–118].

Chemometric techniques have been indispensable in the progression of data fusion methods and in the search for quality data. For instance, descriptive models using PCA are carried out for a preliminary exploratory analysis. Classification models include linear discriminant analysis (LDA), k-nearest neighbors (kNN), soft independent modeling of class analogy (SIMCA), partial least squares discriminant analysis (PLS-DA), and supervised learning algorithms such as support vector machine (SVM) and ANN. For the prediction purpose, PLS is the most sought-after method, but other less popular approaches have been investigated, including PCR, MLR, and SVM regression [116].

Data fusion is a relatively novel subject in LIBS analysis, and it has been increasingly applied to the qualitative and quantitative analysis of a variety of matrices. In the concern about food authenticity and classification, LIBS was combined with UV-Vis absorption spectroscopy for the discrimination of 41 Greek olive oils based on their cultivar origin. LDA and gradient boosting algorithms were used to create the prediction models and found to provide excellent classification, resulting in a 96% training accuracy and 94% for external validation [119]. In the same respect of food analysis, Gamela et al. [120] assessed the complementary information of LIBS and wavelength dispersive X-ray fluorescence (WDXRF) for the macronutrients determination in bean seed samples. The data fusion strategy in the low level was proposed using MLR and leave-one-out cross-validation. This method showed a lower standard error of cross-validation (SECV) and better accuracy, precision, and robustness compared to those univariate calibration models for each technique individually [120]. Gamela and coworkers also reported the combination of LIBS and energy dispersive X-ray fluorescence (EDXRF) using PLS chemometric technique for low-level data fusion [121]. The concentrations of K were determined in cocoa beans ranging from 6053 to 8339 mg kg^{-1}, and the proposed model presented good results, as low SECV (0.09%), LOD (0.2%), and acceptable trueness (85–120%).

LIBS and XRF techniques were also combined and used in monitoring the chemical composition of electronic waste samples. Andrade et al. [122] proposed the determination of Cu in 40 fragments of PCB samples, and low-level data fusion was run using PLS regression. The results were compared with the reference concentrations (ranging from 13 to 45% w w^{-1} Cu) obtained after microwave acid extraction and ICP-OES determinations, and the trueness was in the range of 81 to 119% using leave-one-out cross-validation [122]. Other applications including the information from LIBS and XRF techniques were reported for the direct analysis of

human hair samples [123]. A total of 127 samples were evaluated using both analytical techniques, and data fusion was used to build a classification model. The authors proposed the combination of 17 classifiers, that is PLS-DA, kNN, the Mahalanobis distance (MD), sinθ, cosθ, Q-residual (Q res), divergence criterion (DC), the Euclidean distance, determinant, inner product correlation, unconstrained Procrustes analysis (PA), constrained PA (for 2 classifiers), and the extended inverted signal correction difference (EISCD) (for 4 classifiers). The data fusion improved the figures of merit for the classification, confirming that LIBS and XRF spectral features are complementary to each other. The method trueness ranged from 99.2 and 100% in comparison with 94.5–99.2% for WDXRF and 99.2% for LIBS, individually.

Studies have been reported using LIBS combined to other spectroscopy techniques. Of particular interest in environmental analysis, outputs from LIBS and near-infrared spectroscopy -NIRS were combined to produce regression models. In a study published in 2019 de Oliveira et al. [124] assessed the inorganic composition of forage plants, and data fusion models for Ca, Fe, K, Mg, and Mn using PLS showed better figures of merit than any of the two individual techniques [124]. Using the same two techniques coupled with XRF and mid-infrared spectroscopy (MIR), Xu et al. [125] proposed a multi-sensor fusion for monitoring several soil properties such as soil organic matter (SOM), pH, total N, available K, and available P. The prediction capability of data was assessed using different combinations decreased as follows: MIR > NIR > LIBS > XRF [125, 126] assessed the detection of SOM content by LIBS and Fourier transform mid-infrared (FT-IR). This study demonstrated the combination of these complementary techniques using various chemometric algorithms (i.e., PCA, PLS, SVR, and ANN). The quantitative prediction ability of the method was assessed using a low-level and mid-level data fusion. The findings from SVR, ANN models indicate that either calibration strategies are promising for monitoring organic matter in soil samples. Nevertheless, mid-level data fusion of the LIBS and FTIR-ATR spectra based on the latent variables of PLS drastically improved the SOM prediction accuracy [126].

Interestingly, Manrique-Martinez et al. [127] proposed the strategy of data fusion between LIBS and Raman for the investigation of samples in binary mixtures, as a part of simulation in planetary exploration missions. Two different sulfates (epsomite and anhydrous sodium sulfate) and a chloride (hexahydrate magnesium chloride) were used to prepare 27 binary mixture combinations. These samples were analyzed using both techniques and multivariate analysis was performed on Raman, LIBS, and Raman combined with LIBS using low-level fused data sets. As demonstrated in other studies, data fusion method showed better analytical performance and more accurate results when compared with individual sets [127].

2.6.7 Other Multivariate Approaches

The literature also presents other calibration and exploratory analyses using LIBS. For instance, Araújo et al. [128] proposed a method for Ca, K, and Mg determination

in human mineral supplements and Al, Cu, and Fe in PCB using unfolded-PLS with residual bilinearization (U-PLS/RBL). Castro et al. [90] used parallel factor analysis (PARAFAC) for spectral interference identification and removal focusing WEEE [129] precious elements (Ag and Au) determination.

2.7 Hyperspectral Images

The principle of hyperspectral imaging is based on the fact that all materials, due to the difference in their chemical composition and inherent physical structure, reflect, scatter, absorb and emit electromagnetic energy in distinct patterns at specific wavelengths. This feature is called a spectral signature or spectral fingerprint, or simply spectrum. A spectral signature is a unique feature of an object. For a given material, if the percentage of reflectance, absorbance, or transmittance, is plotted against wavelengths, the resulting curve is referred to as the spectral signature of that material. In essence, the spectral signature can be used to characterize, identify and discriminate between classes of any materials in each pixel of the image [130].

According to Wu and Sun [131], the spectral hypercube is composed of voxels (also called vector pixels) containing spectral information (of λ wavelengths) and also bi-dimensional spatial information (of x lines and y columns). Thus, the hyperspectral cube consists of a series of contiguous sub-images one after the other at different wavelengths, so each sub-image provides the spatial distribution of the spectral intensity at a given wavelength. This means that a hyperspectral image described as $I(x,y,\lambda)$ can be seen as a separate spatial image $I(x,y)$ at each individual wavelength or as a spectrum $I(\lambda)$ at each individual pixel (x,y) [139]. Thus, this technology allows, through the generation of concentration maps, the determination of the local composition of the species of interest throughout the spatial structure of the sample. With this local description of chemical information, it is possible to obtain, for example, data on the homogeneity and distributions of constituents and to interpret and monitor processes that may occur on the surfaces of certain samples. Furthermore, the use of spectral images has proved to be an important tool for the acquisition of chemical information in non-homogeneous media and its main advantage is the minimum preparation and handling of samples.

A hyperspectral image can be formed by hundreds of thousands of measurements and one of the main problems with this approach is the requirement to process so much data without a minimal loss of quality and quantity of information. In the case of the LIBS technique, each pixel corresponds to an emission spectrum, and since there are LIBS spectrometers that have the ability to monitor thousand wavelengths, which will generate the same number of emission spectra matrices. The use of data compression techniques such as PCA may satisfactorily solve this problem [132].

The use of hyperspectral images in chemical analysis began in the 1970s, mainly with applications in remote sensing; however, it was only many years after, this tool started to be used in several other different applications such as pharmaceutical research and production, food science, food quality assurance, forensic science, biochemistry and biomedicine, cultural heritage, among others [133]. In the case

of forensic science, hyperspectral imaging can allow investigators to analyze chemical composition and simultaneously visualize the spatial distribution of a given sample at a crime scene. According to Edelman et al. [134], recent technological developments in fast, portable, and high-resolution acquisition systems, such as LIBS, are facilitating the use of hyperspectral images in forensic science, since, in most cases, it is possible to obtain chemical information with little sample manipulation and, in addition, the acquisition of spectra can be performed in the field, minimizing the need to take the sample to a laboratory [134].

Another interesting application of LIBS with hyperspectral imaging was reported by Wu et al. [135]. In this work, the authors developed a fast and efficient way to detect pesticide residues (thiophanate-methyl) in mulberry fruits. PCA and PLS were used to qualitatively and quantitatively analyze the data obtained from fruit samples with different concentrations of thiophanate-methyl. The authors conclude that the use of LIBS technology in combination with hyperspectral images for the detection and identification of residues of the thiophanate-methyl pesticide is feasible, and the best results were provided by the PLS model using optimal pre-processed variables [135].

Therefore, spectral images prove to be a promising, efficient, and reliable technology, which can be used, in conjunction with LIBS [136], to replace other analytical methods, especially in situations where the sample cannot be fully consumed, such as in forensic analysis. By combining spatial and spectral details in one data set, the hyperspectral imaging technique can simultaneously acquire spatial images in many spectrally contiguous bands to form a 3-D hyperspectral cube, and it is considered to have the ability to complement the advantages of spectroscopy and imaging techniques. Predicted values of pixel-level quality or safety attributes can then be used to generate the attribute distribution map, leading to better characterization and better quality and safety assessment results. Currently, there are still many challenges to be tackled, e.g. computing speed, hardware limitations, and high cost before this techniue can be fully exploited. At present, spectral imaging studies often aim at identifying optimal wavelengths for designing a low-cost multispectral imaging system.

2.8 Conclusions and Perspectives

The use of LIBS in the direct quantitative analysis of several types of samples is promising, as the previous steps of sample preparation and handling are considerably simplified. However, the challenges related to the calibration of the obtained signals require special attention from the analyst and strategies aimed at matrix compatibility can be employed, sharply reducing the matrix's contribution. Due to the prevalence of LIBS, several review articles have been published on this topic [137]. A review of calibration strategies used in conjunction with LIBS was published by Costa et al. [25]. An important review was published by Lazic and Jovicevic [138] to present sample preparation strategies for liquid samples designed for quantitative determinations. Jantzi et al. [139] presented a complete review addressing

pretreatments of solid samples aimed at qualitative and quantitative analyses in 2019. In the same year, Costa et al. [140] also published a review on this topic, in which the authors addressed many aspects of LIBS, including history, fundamentals, sample preparation, chemometrics, and the application of LIBS in various fields of science [140].

The circle of LIBS applications is already vast and is still growing fast in the last decade. The outlook for the application of LIBS in industrial processes and product monitoring is very promising. In addition, it is possible to obtain point information from extremely small samples. An important aspect to emphasize is the fact that the information obtained using LIBS has a potential to cooperate with other instrumental techniques. LIBS, for instance is able to detect all elements from light ($Z < 11$) to heavy ones and can be used to analyze practically any type of solid samples (conductive or not) in several challenging conditions (e.g. space or underwater exploration). In addition, as a huge amount of data is collected it is mandatory in several cases to use chemometric tools in order to better exploit the data collected and to identify and eliminate signals from concomitants.

References

1. Nascentes CC, Korn M d GA, Zanoni MVB. Química Analítica No Brasil: Atualidades, Tendências E Desafios. Quim Nova. 2017;40:643.
2. Carter JA, Barros AI, Nóbrega JA, Donati GL. Traditional calibration methods in atomic spectrometry and new calibration strategies for inductively coupled plasma mass spectrometry. Front Chem. 2018;6:504.
3. Krug FJ, Rocha FRP. Métodos de Preparo de Amostras Para Análise Elementar. 2nd ed. São Paulo: EditSBQ; 2019.
4. Rocha DL, Batista AD, Rocha FRP, Donati GL, Nóbrega JA. Greening sample preparation in inorganic analysis. TrAC Trends Anal Chem. 2013;45:79.
5. Meyers RA. Encyclopedia of analytical chemistry: applications, theory and instrumentation, supplementary volumes S1–S3. New York: Wiley-Interscience; 2011.
6. Smith FE, Arsenault EA. Microwave-assisted sample preparation in analytical chemistry. Talanta. 1996;43:1207.
7. Radziemski LJ. From LASER to LIBS, the path of technology development. Spectrochim Acta B. 2002;57:1109.
8. Noll R. Laser-induced breakdown spectroscopy: fundamentals and applications. Springer Science & Business Media; 2012.
9. Pereira FMV, Castilho JPC, Machado RC, de Araújo AS, de Andrade DF, de Babos DV, Beletti DR, Pereira Filho ER, de Mello ML, Hilário FF, Garcia JA, Sperança MA, Gamela RR, Costa VC. Laser-induced breakdown spectroscopy (LIBS): applications and calibration strategies. 1st ed. São Paulo; 2021.
10. Pedarnig JD, Trautner S, Grünberger S, Giannakaris N, Eschlböck-Fuchs S, Hofstadler J. Review of element analysis of industrial materials by in-line laser—induced breakdown spectroscopy (LIBS). Appl Sci. 2021;11:9274.
11. Radziemski L, Cremers D. A brief history of laser-induced breakdown spectroscopy: from the concept of atoms to LIBS 2012. Spectrochim Acta B. 2013;87:3.
12. Machado RC, Andrade DF, Babos DV, Castro JP, Costa VC, Sperança MA, Garcia JA, Gamela RR, Pereira-Filho ER. Solid sampling: advantages and challenges for chemical element determination—a critical review. J Anal At Spectrom. 2020;35:54.
13. Cremers DDA, Radziemski LJ. Handbook of laser-induced breakdown spectroscopy. 2nd ed. Chichester, West Sussex: Wiley; 2013.

14. Hahn DW, Omenetto N. Laser-induced breakdown spectroscopy (LIBS), part II: review of instrumental and methodological approaches to material analysis and applications to different fields. Appl Spectrosc. 2012;66:347.
15. Singh VK, Rai AK. Prospects for laser-induced breakdown spectroscopy for biomedical applications: a review. Lasers Med Sci. 2011;26:673.
16. Galbács G. A critical review of recent progress in analytical laser-induced breakdown spectroscopy. Anal Bioanal Chem. 2015;407:7537.
17. Takahashi T, Thornton B. Quantitative methods for compensation of matrix effects and self-absorption in laser induced breakdown spectroscopy signals of solids. Spectrochim Acta B. 2017;138:31.
18. Popov AM, Zaytsev SM, Seliverstova IV, Zakuskin AS, Labutin TA. Matrix effects on laser-induced plasma parameters for soils and ores. Spectrochim Acta B. 2018;148:205.
19. Lednev VN, Grishin MY, Sdvizhenskii PA, Asyutin RD, Tretyakov RS, Stavertiy AY, Pershin SM. Sample temperature effect on laser ablation and analytical capabilities of laser induced breakdown spectroscopy. J Anal At Spectrom. 2019;34:607.
20. Sabsabi M, Cielo P. Quantitative-analysis of aluminum- alloys by laser-induced breakdown spectroscopy and plasma characterization. Appl Spectrosc. 1995;49:499.
21. Santos D, Nunes LC, Carvalho GGA, Gomes MD, Souza PF, Leme FD, Santos LGC, Krug FJ, L. Laser-induced breakdown spectroscopy for analysis of plant materials: a review. Spectrochim Acta B. 2012;71–72:3.
22. Braga JWB, Trevizan LC, Nunes LC, Rufini IA, Santos D, Krug FJ. Comparison of univariate and multivariate calibration for the determination of micronutrients in pellets of plant materials by laser induced breakdown spectrometry. Spectrochim Acta B. 2010;65:66.
23. Wang W, Sun L, Zhang P, Chen T, Zheng L, Qi L. Study of matrix effects in laser-induced breakdown spectroscopy by laser defocus and temporal resolution. J Anal At Spectrom. 2021;36:1977.
24. Babos DV, Cruz-Conesa A, Pereira-Filho ER, Anzano JM. Direct determination of Al and Pb in waste printed circuit boards (PCB) by laser-induced breakdown spectroscopy (LIBS): evaluation of calibration strategies and economic—environmental questions. J Hazard Mater. 2020;399:122831.
25. Costa VC, Babos DV, Castro JP, Andrade DF, Gamela RR, Machado RC, Sperança MA, Araújo AS, Garcia JA, Pereira-Filho ER. Calibration strategies applied to laser-induced breakdown spectroscopy: a critical review of advances and challenges. J Braz Chem Soc. 2020;31:2439.
26. Andrade DF, Pereira-Filho ER, Amarasiriwardena D. Current trends in laser-induced breakdown spectroscopy: a tutorial review. Appl Spectrosc Rev. 2021;56:98.
27. Musazzi S, Perini U, editors. Laser-induced breakdown spectroscopy: theory and applications, vol. 182. Berlin: Springer; 2014.
28. Mark H. Principles and practice of spectroscopic calibration. 1st ed. New York: Wiley-Interscience; 1991.
29. Donati GL, Amais RS. Fundamentals and new approaches to calibration in atomic spectrometry. J Anal At Spectrom. 2019;34:2353.
30. Augusto AS, Barsanelli PL, Pereira FMV, Pereira-Filho ER. Calibration strategies for the direct determination of Ca, K, and Mg in commercial samples of powdered milk and solid dietary supplements using laser-induced breakdown spectroscopy (LIBS). Food Res Int. 2017;94:72.
31. Babos DV, Barros AI, Nobrega JA, Pereira-Filho ER. Calibration strategies to overcome matrix effects in laser-induced breakdown spectroscopy: direct calcium and phosphorus determination in solid mineral supplements. Spectrochim Acta B. 2019;155:90.
32. Millar S, Gottlieb C, Günther T, Sankat N, Wilsch G, Kruschwitz S. Chlorine determination in cement-bound materials with laser-induced breakdown spectroscopy (LIBS)—a review and validation. Spectrochim Acta B. 2018;147:1.

33. Vieira AL, Silva TV, de Sousa FSI, Senesi GS, Júnior DS, Ferreira EC, Neto JAG. Determinations of phosphorus in fertilizers by spark discharge-assisted laser-induced breakdown spectroscopy. Microchem J. 2018;139:322.
34. Gomes MS, de Carvalho GGA, Santos D, Krug FJ. A novel strategy for preparing calibration standards for the analysis of plant materials by laser-induced breakdown spectroscopy: a case study with pellets of sugar cane leaves. Spectrochim Acta B. 2013;86:137.
35. Papai R, Sato RH, Nunes LC, Krug FJ, Gaubeur I. Melted paraffin wax as an innovative liquid and solid extractant for elemental analysis by laser-induced breakdown spectroscopy. Anal Chem. 2017;89:2807.
36. Andrade DF, Sperança MA, Pereira-Filho ER. Different sample preparation methods for the analysis of suspension fertilizers combining LIBS and liquid-to-solid matrix conversion: determination of essential and toxic elements. Anal Methods. 2017;9:5156.
37. Andrade DF, Guedes WN, Pereira FMV. Detection of chemical elements related to impurities leached from raw sugarcane: use of laser-induced breakdown spectroscopy (LIBS) and chemometrics. Microchem J. 2018;137:443.
38. Silvestre DM, Barbosa FM, Aguiar BT, Leme FO, Nomura CS. Feasibility study of calibration strategy for direct quantitative measurement of K and Mg in plant material by laser-induced breakdown spectrometry. Anal Chem Res. 2015;5:28.
39. Zhu Z, Li J, Guo Y, Cheng X, Tang Y, Guo L, Li X, Lu Y, Zeng X. Accuracy improvement of boron by molecular emission with a genetic algorithm and partial least squares regression model in laser-induced breakdown spectroscopy. J Anal At Spectrom. 2018;33:205.
40. Sweetapple MT, Tassios S. Laser-induced breakdown spectroscopy (LIBS) as a tool for in situ mapping and textural interpretation of lithium in pegmatite minerals. Am Mineral. 2015;100:2141.
41. Leme FO, Silvestre DM, Nascimento AN, Nomura CS. Feasibility of using laser induced breakdown spectroscopy for quantitative measurement of calcium, magnesium, potassium and sodium in meat. J Anal At Spectrom. 2018;33:1322.
42. de Carvalho GGA, Nunes LC, de Souza PF, Krug FJ, Alegre TC, Santos D Jr. Evaluation of laser induced breakdown spectrometry for the determination of macro and micronutrients in pharmaceutical tablets. J Anal At Spectrom. 2010;25:803.
43. Gu W, Song W, Yan G, Ye Q, Li Z, Afgan MS, Liu J, Song Y, Hou Z, Wang Z, Li Z. A data preprocessing method based on matrix matching for coal analysis by laser-induced breakdown spectroscopy. Spectrochim Acta B. 2021;180:106212.
44. Barnett WB, Fassel VA, Kniseley RN. Theoretical principles of internal standardization in analytical emission spectroscopy. Spectrochim Acta B. 1968;23:643.
45. Sperança MA, Pomares-Alfonso MS, Pereira-Filho ER. Analysis of Cuban nickeliferous minerals by laser-induced breakdown spectroscopy (LIBS): non-conventional sample preparation of powder samples. Anal Methods. 2018;10:533.
46. Zachariadis GA, Vogiatzis C. An overview of the use of yttrium for internal standardization in inductively coupled plasma–atomic emission spectrometry. Appl Spectrosc Rev. 2010;45:220.
47. Guezenoc J, Gallet-Budynek A, Bousquet B. Critical review and advices on spectral-based normalization methods for LIBS quantitative analysis. Spectrochim Acta B. 2019;160:105688.
48. Šindelářová A, Pořízka P, Modlitbová P, Vrlíková L, Kiss K, Kaška M, Prochazka D, Vrábel J, Buchtová M, Kaiser J. Methodology for the implementation of internal standard to laser-induced breakdown spectroscopy analysis of soft tissues. Sensors. 2021;21:900.
49. Juvé V, Portelli R, Boueri M, Baudelet M, Yu J. Space-resolved analysis of trace elements in fresh vegetables using ultraviolet nanosecond laser-induced breakdown spectroscopy. Spectrochim Acta B. 2008;63:1047.
50. Castro JP, Pereira-Filho ER. Twelve different types of data normalization for the proposition of classification, univariate and multivariate regression models for the direct analyses of alloys by laser-induced breakdown spectroscopy (LIBS). J Anal At Spectrom. 2016;31:2005.

51. Wu C, Sun DX, Su MG, Yin YP, Han WW, Lu QF, Dong CZ. Quantitative analysis of Pb in soil samples by laser-induced breakdown spectroscopy with a simplified standard addition method. J Anal At Spectrom. 2019;34:1478.
52. Zhu C, Lv J, Liu K, Li Q, Tang Z, Zhou R, Zhang W, Chen J, Liu K, Li X, Zeng X. Fast detection of harmful trace elements in glycyrrhiza using standard addition and internal standard method—laser-induced breakdown spectroscopy (SAIS-LIBS). Microchem J. 2021;168:106408.
53. Yi RX, Guo LB, Zou XH, Li JM, Hao ZQ, Yang XY, Li XY, Zeng XY, Lu YF. Background removal in soil analysis using laser- induced breakdown spectroscopy combined with standard addition method. Opt Express. 2016;24:2607.
54. Haider AFMY, Khan ZH. Determination of Ca content of coral skeleton by analyte additive method using the LIBS technique. Opt Laser Technol. 2012;44:1654.
55. Zivkovic S, Savovic J, Kuzmanovic M, Petrovic J, Momcilovic M. Alternative analytical method for direct determination of Mn and Ba in peppermint tea based on laser induced breakdown spectroscopy. Microchem J. 2018;137:410.
56. Bader MA. Systematic approach to standard addition methods in instrumental analysis. J Chem Educ. 1980;57:703.
57. Bilge G, Boyaci IH, Eseller KE, Tamer U, Cakir S. Analysis of bakery products by laser-induced breakdown spectroscopy. Food Chem. 2015;181:186.
58. Castro JP, Babos DV, Pereira-Filho ER. Calibration strategies for the direct determination of rare earth elements in hard disk magnets using laser-induced breakdown spectroscopy. Talanta. 2020;208:120443.
59. Virgilio A, Gonçalves DA, McSweeney T, Gomes Neto JA, Nóbrega JA, Donati GL. Multi-energy calibration applied to atomic spectrometry. Anal Chim Acta. 2017;982:31.
60. Babos DV, Virgilio A, Costa VC, Donati GL, Pereira-Filho ER. Multi-energy calibration (MEC) applied to laser-induced breakdown spectroscopy (LIBS). J Anal At Spectrom. 2018;33:1753.
61. Augusto AS, Castro JP, Sperança MA, Pereira-Filho EP. Combination of multi-energy calibration (MEC) and laser-induced breakdown spectroscopy (LIBS) for dietary supplements analysis and determination of Ca, Mg and K. J Braz Chem Soc. 2019;30:804.
62. Fortunato FM, Catelani TA, Pomares-Alfonso MS, Pereira-Filho ER. Application of multi-energy calibration for determination of chromium and nickel in nickeliferous ores by laser-induced breakdown spectroscopy. Anal Sci. 2019;35:165.
63. Carvalho AAC, Cozer LA, Luz MS, Nunes LC, Rocha FRP, Nomura CS. Multi-energy calibration and sample fusion as alternatives for quantitative analysis of high silicon content samples by laser-induced breakdown spectrometry. J Anal At Spectrom. 2019;34:1701.
64. Andrade DF, Fortunato FM, Pereira-Filho ER. Calibration strategies for determination of the in content in discarded liquid crystal displays (LCD) from mobile phones using laser-induced breakdown spectroscopy (LIBS). Anal Chim Acta. 2019;1061:42.
65. Li X, Zhao T, Zhong Q, Nie S, Xiao H, Zhao S, Huang W, Fan Z. Iterative multi-energy calibration and its application in online alloy smelting process monitoring using laser-induced breakdown spectroscopy. J Anal At Spectrom. 2020;35:2171.
66. Hao ZQ, Liu L, Zhou R, Ma YW, Li XY, Guo LB, Lu YF, Zeng XY. One-point and multi-line calibration method in laser-induced breakdown spectroscopy. Opt Express. 2018;26:22926.
67. Gamela RR, Costa VC, Babos DV, Araújo AS, Pereira-Filho ER. Direct determination of Ca, K, and Mg in cocoa beans by laser-induced breakdown spectroscopy (LIBS): evaluation of three univariate calibration strategies for matrix matching. Food Anal Methods. 2020;13:1017.
68. Vieira AL, Ferreira EC, Júnior DS, Senesi GS, Neto JAG. Spark discharge-libs: evaluation of one-point and multi-voltage calibration for p and al determination. At Spectrosc. 2021;42:18.
69. Yuan R, Tang Y, Zhu Z, Hao Z, Li J, Yu H, Yu Y, Guo L, Zeng X, Lu Y. Accuracy improvement of quantitative analysis for major elements in laser-induced breakdown spectroscopy using single-sample calibration. Anal Chim Acta. 2019;1064:11.

70. Nunes LC, Rocha FRP, Krug FJ. Slope ratio calibration for analysis of plant leaves by laser-induced breakdown spectroscopy. J Anal At Spectrom. 2019;34:2314.
71. Costa VC, de Mello ML, Babos DV, Castro JP, Pereira-Filho ER. Calibration strategies for determination of Pb content in recycled polypropylene from car batteries using laser-induced breakdown spectroscopy (LIBS). Microchem J. 2020;159:105558.
72. Krutchkoff RG. Classical and inverse regression methods of calibration. Technometrics. 1967;9:425.
73. Duponchel L, Bousquet B, Pelascini F, Motto-Ros V. Should we prefer inverse models in quantitative LIBS analysis? J Anal At Spectrom. 2020;35:794.
74. de Carvalho GGA, Santos D, Nunes LC, Gomes MS, Leme F d O, Krug FJ. Effects of laser focusing and fluence on the analysis of pellets of plant materials by laser-induced breakdown spectroscopy. Spectrochim Acta B. 2012;74–75:162.
75. Machado RC, Babos DV, Andrade DF, Pereira-Filho ER. A novel strategy for direct elemental determination using laser-induced breakdown spectroscopy: fluence calibration. J Anal At Spectrom. 2021;36:2132.
76. Zhang T, Tang H, Li H. Chemometrics in laser-induced breakdown spectroscopy. J Chemometr. 2018;32:1.
77. Geladi P, Kowalski BR. Partial least-squares regression: a tutorial. Anal Chim Acta. 1986;185:1.
78. Brereton RG. Introduction to multivariate calibration in analytical chemistry. Analyst. 2000;125:2125.
79. Ayyalasomayajula KK, Yu-Yueh F, Singh JP, McIntyre DL, Jain J. Application of laser-induced breakdown spectroscopy for total carbon quantification in soil samples. Appl Optics. 2012;51:149.
80. Wang J, Xue S, Zheng P, Chen Y, Peng R. Determination of lead and copper in Ligusticum wallichii by laser-induced breakdown spectroscopy. Anal Lett. 2017;50:2000.
81. Sperança MA, Andrade DF, Castro JP, Pereira-Filho ER. Univariate and multivariate calibration strategies in combination with laser-induced breakdown spectroscopy (LIBS) to determine Ti on sunscreen: a different sample preparation procedure. Opt Laser Technol. 2019;109:648.
82. Ayyalasomayajula KK, McIntyre DL, Jain J, Singh JP, Yu-Yueh F. Determination of elemental impurities in plastic calibration standards using laser-induced breakdown spectroscopy. Appl Optics. 2012;51:B1.
83. Wen S, Jiang-tao L, Cui-ping L, Chun-hou Z. Quantitative analysis of P in compound fertilizer by laser-induced breakdown spectroscopy coupled with linear multivariate calibration. Spectrosc Spect Anal. 2019;39:1958.
84. Yaroshchyk P, Death DL, Spencer SJ. Comparison of principal components regression, partial least squares regression, multi-block partial least squares regression, and serial partial least squares regression algorithms for the analysis of Fe in iron ore using LIBS. J Anal At Spectrom. 2012;27:92.
85. Zaytsev SM, Popov AM, Chernykh EV, Voronina RD, Zorov NB, Labutin TA. Comparison of single- and multivariate calibration for determination of Si, Mn, Cr and Ni in high-alloyed stainless steels by laser-induced breakdown spectrometry. J Anal At Spectrom. 2014;29:1417.
86. Devangad P, Unnikrishnan VK, Tamboli MM, Shameem KMM, Nayak R, Choudhari KS, Santhosh C. Quantification of Mn in glass matrices using laser induced breakdown spectroscopy (LIBS) combined with chemometric approaches. Anal Methods. 2016;8:7177.
87. Takahashi T, Thornton B, Sato T, Ohki T, Ohki K, Sakka T. Temperature based segmentation for spectral data of laser-induced plasmas for quantitative compositional analysis of brass alloys submerged in water. Spectrochim Acta B. 2016;124:87.
88. Hernández-García R, Villanueva-Tagle ME, Calderón-Piñar F, Durruthy-Rodríguez MD, Aquino FWB, Pereira-Filho ER, Pomares-Alfonso MS. Quantitative analysis of lead zirconate titanate (PZT) ceramics by laser-induced breakdown spectroscopy (LIBS) in combination with multivariate calibration. Microchem J. 2017;130:21.

89. Costa VC, Pereira FMV. Laser-induced breakdown spectroscopy applied to the rapid identification of different types of polyethylene used for toy manufacturing. J Chemometr. 2020;34:1.
90. Castro JP, Pereira-Filho ER, Bro R. Laser-induced breakdown spectroscopy (LIBS) spectra interpretation and characterization using parallel factor analysis (PARAFAC): a new procedure for data and spectral interference processing fostering the waste electrical and electronic equipment (WEEE) recycling process. J Anal At Spectrom. 2020;35:1115.
91. Andrade DF, Pereira-Filho ER, Konieczynski P. Comparison of ICP OES and LIBS analysis of medicinal herbs rich in flavonoids from Eastern Europe. J Braz Chem Soc. 2017;28:838.
92. Goueguel CL, Soumare A, Nault C, Nault J. Direct determination of soil texture using laser-induced breakdown spectroscopy and multivariate linear regressions. J Anal At Spectrom. 2019;34:1588.
93. Costa VC, Aquino FWB, Paranhos CM, Pereira-Filho ER. Use of laser-induced breakdown spectroscopy for the determination of polycarbonate (PC) and acrylonitrile-butadiene-styrene (ABS) concentrations in PC/ABS plastics from e-waste. Waste Manag. 2017;70:121.
94. Ding Y, Xia G, Ji H, Xiong X. Accurate quantitative determination of heavy metals in oily soil by laser induced breakdown spectroscopy (LIBS) combined with interval partial least squares (IPLS). Anal Methods. 2019;11:3657.
95. Zhang T-L, Wu S, Tang H-S, Wang K, Duan Y-X, Li H. Progress of chemometrics in laser-induced breakdown spectroscopy analysis. Chin J Anal Chem. 2015;43:939.
96. Li L-N, Liu X-F, Yang F, Xu W-M, Wang J-Y, Shu R. A review of artificial neural network based chemometrics applied in laser-induced breakdown spectroscopy analysis. Spectrochim Acta B. 2021;180:106183.
97. Ferreira EC, Milori DMBP, Ferreira EJ, Da Silva RM, Martin-Neto L. Artificial neural network for Cu quantitative determination in soil using a portable laser induced breakdown spectroscopy system. Spectrochim Acta B. 2008;63:1216.
98. D'Andrea E, Pagnotta S, Grifoni E, Legnaioli S, Lorenzetti G, Palleschi V, Lazzerini B. A hybrid calibration-free/artificial neural networks approach to the quantitative analysis of LIBS spectra. Appl Phys B Lasers Opt. 2015;118:353.
99. El Haddad J, Bruyère D, Ismaël A, Gallou G, Laperche V, Michel K, Canioni L, Bousquet B. Application of a series of artificial neural networks to on-site quantitative analysis of lead into real soil samples by laser induced breakdown spectroscopy. Spectrochim Acta B. 2014;97:57.
100. Lu C, Wang B, Jiang X, Zhang J, Niu K, Yuan Y. Detection of K in soil using time-resolved laser-induced breakdown spectroscopy based on convolutional neural networks. Plasma Sci Technol. 2018;21:034014.
101. D'Andrea E, Pagnotta S, Grifoni E, Lorenzetti G, Legnaioli S, Palleschi V, Lazzerini B. An artificial neural network approach to laser-induced breakdown spectroscopy quantitative analysis. Spectrochim Acta B. 2014;99:52.
102. Li K, Guo L, Li C, Li X, Shen M, Zheng Z, Yu Y, Hao R, Hao Z, Zeng Q, Lu Y, Zeng X. Analytical-performance improvement of laser-induced breakdown spectroscopy for steel using multi-spectral-line calibration with an artificial neural network. J Anal At Spectrom. 2015;30:1623.
103. Lorenzetti G, Legnaioli S, Grifoni E, Pagnotta S, Palleschi V. Laser-based continuous monitoring and resolution of steel grades in sequence casting machines. Spectrochim Acta B. 2015;112:1.
104. Inakollu P, Philip T, Rai AK, Yueh F-Y, Singh JP. A comparative study of laser induced breakdown spectroscopy analysis for element concentrations in aluminum alloy using artificial neural networks and calibration methods. Spectrochim Acta B. 2009;64:99.
105. Bhatt B, Angeyo KH, Dehayem-Kamadjeu A. LIBS development methodology for forensic nuclear materials analysis. Anal Methods. 2018;10:791.
106. Lu Z, Mo J, Yao S, Zhao J, Lu J. Rapid determination of the gross calorific value of coal using laser-induced breakdown spectroscopy coupled with artificial neural networks and genetic algorithm. Energy Fuel. 2017;31:3849.

107. Wang J, Shi M, Zheng P, Xue S, Peng R. Quantitative analysis of Ca, Mg, and K in the roots of Angelica pubescens f. biserrata by laser-induced breakdown spectroscopy combined with artificial neural networks. J Appl Spectrosc. 2018;85:190.
108. Hu Y, Li Z, Lü T. Determination of elemental concentration in geological samples using nanosecond laser-induced breakdown spectroscopy. J Anal At Spectrom. 2017;32:2263.
109. Galbács G, Gornushkin IB, Smith BW, Winefordner JD. Semi-quantitative analysis of binary alloys using laser-induced breakdown spectroscopy and a new calibration approach based on linear correlation. Spectrochim Acta B. 2001;56:1159.
110. Galbács G, Jedlinszki N, Cseh G, Galbács Z, Túri L. Accurate quantitative analysis of gold alloys using multi-pulse laser induced breakdown spectroscopy and a correlation-based calibration method. Spectrochim Acta B. 2008;63:591.
111. Galbács G, Gornushkin IB, Winefordner JD. Generalization of a new calibration method based on linear correlation. Talanta. 2004;63:351.
112. Meng T, Jing X, Yan Z, Pedrycz W. A survey on machine learning for data fusion. Inf Fusion. 2020;57:115.
113. Brereton RG, Jansen J, Lopes J, Marini F, Pomerantsev A, Rodionova O, Roger JM, Walczak B, Tauler R. Chemometrics in analytical chemistry-part I: history, experimental design and data analysis tools. Anal Bioanal Chem. 2017;409:5891.
114. Geladi P. Chemometrics in spectroscopy. Part 1. Classical chemometrics. Spectrochim Acta B. 2003;58:767.
115. Lahat D, Adali T, Jutten C. Multimodal data fusion: an overview of methods, challenges, and prospects. Proc IEEE. 2015;103:1449.
116. Borràs E, Ferré J, Boqué R, Mestres M, Aceña L, Busto O. Data fusion methodologies for food and beverage authentication and quality assessment—a review. Anal Chim Acta. 2015;891:1.
117. Guedes WN, Pereira FMV. Classifying impurity ranges in raw sugarcane using laser-induced breakdown spectroscopy (LIBS) and sum fusion across a tuning parameter window. Microchem J. 2018;143:331.
118. Szymańska E. Modern data science for analytical chemical data—a comprehensive review. Anal Chim Acta. 2018;1028:1.
119. Stefas D, Gyftokostas N, Kourelias P, Nanou E, Kokkinos V, Bouras C, Couris S. Discrimination of olive oils based on the olive cultivar origin by machine learning employing the fusion of emission and absorption spectroscopic data. Food Control. 2021;130:108318.
120. Gamela RR, Costa VC, Sperança MA, Pereira-Filho ER. Laser-induced breakdown spectroscopy (LIBS) and wavelength dispersive X-ray fluorescence (WDXRF) data fusion to predict the concentration of K, Mg and P in bean seed samples. Food Res Int. 2020;132:109037.
121. Gamela RR, Pereira-Filho ER, Pereira FMV. Minimal-invasive analytical method and data fusion: an alternative for determination of Cu, K, Sr, and Zn in cocoa beans. Food Anal Methods. 2021;14:545.
122. Andrade DF, Almeida E, Carvalho HWP, Pereira-Filho ER, Amarasiriwardena D. Chemical inspection and elemental analysis of electronic waste using data fusion—application of complementary spectroanalytical techniques. Talanta. 2021;225:122025.
123. Santos MC, Pereira FMV. Direct analysis of human hair before and after cosmetic modification using a recent data fusion method. J Braz Chem Soc. 2020;31:33.
124. de Oliveira DM, Fontes LM, Pasquini C. Comparing laser induced breakdown spectroscopy, near infrared spectroscopy, and their integration for simultaneous multi-elemental determination of micro- and macronutrients in vegetable samples. Anal Chim Acta. 2019;1062:28.
125. Xu D, Zhao R, Li S, Chen S, Jiang Q, Zhou L, Shi Z. Multi-sensor fusion for the determination of several soil properties in the Yangtze River Delta, China. Eur J Soil Sci. 2019;70:162.
126. Xu X, Du C, Ma F, Shen Y, Wu K, Liang D, Zhou J. Detection of soil organic matter from laser-induced breakdown spectroscopy (LIBS) and mid-infrared spectroscopy (FTIR-ATR) coupled with multivariate techniques. Geoderma. 2019;355:113905.

127. Manrique-Martinez JA, Lopez-Reyes G, Alvarez-Perez A, Bozic T, Veneranda M, Sanz-Arranz A, Saiz J, Medina-Garcia J, Rull-Perez F. Evaluation of multivariate analyses and data fusion between Raman and laser-induced breakdown spectroscopy in binary mixtures and its potential for solar system exploration. J Raman Spectrosc. 2020;51:1.
128. Araújo AS, Castro JP, Sperança MA, Andrade DF, Mello ML, Pereira-Filho ER. Multiway calibration strategies in laser-induced breakdown spectroscopy: a proposal. Anal Chem. 2021;93:6291.
129. Costa VC, Castro JP, Andrade DF, Victor Babos D, Garcia JA, Sperança MA, Catelani TA, Pereira-Filho ER. Laser-induced breakdown spectroscopy (LIBS) applications in the chemical analysis of waste electrical and electronic equipment (WEEE). TrAC Trends Anal Chem. 2018;108:65.
130. Elmasry G, Kamruzzaman M, Sun D-W, Allen P. Principles and applications of hyperspectral imaging in quality evaluation of agro-food products: a review. Crit Rev Food Sci Nutr. 2012;52:999.
131. Wu D, Sun D-W. Advanced applications of hyperspectral imaging technology for food quality and safety analysis and assessment: a review—part I: fundamentals. Innov Food Sci Emerg Technol. 2013;19:1.
132. Gamela RR, Sperança MA, Andrade DF, Pereira-Filho ER. Hyperspectral images: a qualitative approach to evaluate the chemical profile distribution of Ca, K, Mg, Na and P in edible seeds employing laser-induced breakdown spectroscopy. Anal Methods. 2019;11:5543.
133. Amigo JM, Babamoradi H, Elcoroaristizabal S. Hyperspectral image analysis. A tutorial. Anal Chim Acta. 2015;896:34.
134. Edelman GJ, Gaston E, van Leeuwen TG, Cullen PJ, Aalders MCG. Hyperspectral imaging for non-contact analysis of forensic traces. Forensic Sci Int. 2012;223:28.
135. Wu D, Meng L, Yang L, Wang J, Fu X, Du X, Li S, He Y, Huang L. Feasibility of laser-induced breakdown spectroscopy and hyperspectral imaging for rapid detection of thiophanate-methyl residue on mulberry fruit. Int J Mol Sci. 2019;20:1.
136. Garcia JA, da Silva JRA, Pereira-Filho ER. LIBS as an alternative method to control an industrial hydrometallurgical process for the recovery of Cu in waste from electro-electronic equipment (WEEE). Microchem J. 2021;164:106007.
137. Carter S, Clough R, Fisher A, Gibson B, Russell B. Atomic spectrometry update: review of advances in the analysis of metals, chemicals and materials. J Anal At Spectrom. 2021;36:2241.
138. Lazic V, Jovićević S. Laser induced breakdown spectroscopy inside liquids: processes and analytical aspects. Spectrochim Acta B. 2014;101:288.
139. Jantzi SC, Motto-Ros V, Trichard F, Markushin Y, Melikechi N, De Giacomo A. Sample treatment and preparation for laser-induced breakdown spectroscopy. Spectrochim Acta B. 2016;115:52.
140. Costa VC, Augusto AS, Castro JP, Machado RC, Andrade DF, Babos DV, Sperança MA, Gamela RR, Pereira-Filho ER. Laser induced-breakdown spectroscopy (LIBS): histórico, fundamentos, aplicações e potencialidades. Quim Nova. 2019;42:527.

Calibration-Free Quantitative Analysis

3

Igor Gornushkin

Calibration-free methods in laser-induced breakdown spectroscopy, CF LIBS, serve as an alternative to calibration-based LIBS techniques. Their major advantage is the ability for fast chemical analysis in situations where matrix-matched standards are not readily available (as, e.g., in the analysis of biological materials and remote analysis) or amount of samples are limited. Their main applications are in the industry, geology, biology, archeology, and even space exploration. This chapter overviews the principle of operation and performance of CF LIBS techniques.

3.1 Radiative Transfer Equation

Consider a ray of light propagating through a layer of plasma with thickness Δx without scattering [1, 2]. During propagation, the incident intensity I_ν increases due to emission and decreases due to absorption

$$\Delta I_\nu = \varepsilon_\nu \Delta x - \kappa_\nu I_\nu \Delta x \tag{3.1}$$

where ε_ν and κ_ν are the emissivity and absorption coefficients, respectively. Under conditions of local thermodynamic equilibrium (LTE), the emission and absorption coefficients are linked through Kirchhoff's law $\varepsilon_\nu = \kappa_\nu B_\nu$, where B_ν is the blackbody function. For simplicity, the dependence of the variables upon the temperature, frequency, and coordinate is not shown. Note that intensity is a surface characteristic; it is a flux of electromagnetic energy passing through a unit area per unit time and unit frequency interval within a unit solid angle while emissivity is a volumetric characteristic characterized by the electromagnetic energy emitted by a unit volume

I. Gornushkin (✉)
Federal Institute for Materials Research and Testing (BAM), Berlin, Germany
e-mail: igor.gornushkin@bam.de

G. Galbács (ed.), *Laser-Induced Breakdown Spectroscopy in Biological, Forensic and Materials Sciences*, https://doi.org/10.1007/978-3-031-14502-5_3

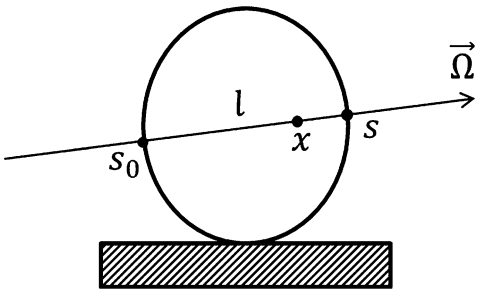

Fig. 3.1 Integration along the line of sight

into unit solid angle per unit time and unit frequency interval. Tending Δx to zero, Eq. (3.1) transforms to

$$dI_\nu/dx + \kappa_\nu I_\nu = \kappa_\nu B_\nu \tag{3.2}$$

or, introducing new variables $y = I_\nu$, $k(x) = \kappa_\nu$, and $P(x) = \kappa_\nu B_\nu$ to

$$dy/dx + k(x)y = P(x)$$

This is an ordinary differential equation of the first order whose solution is found by the multiplication of both parts by $u = e^{\int k(x)dx}$

$$e^{\int k(x)dx}\frac{dy}{dx} + k(x)e^{\int k(x)dx}y = P(x)e^{\int k(x)dx}$$

Noting that the left part is the full differential $d(uy)/dx$, the equation integrates to give $uy = \int P(x)e^{\int k(x')dx'}dx + C$ or

$$y = e^{-\int k(x)dx}\int P(x)e^{\int k(x')dx'}dx + Ce^{-\int k(x)dx} \tag{3.3}$$

To apply this solution to a physical situation, let us integrate Eq. (3.3) from point s_0 to point s located at the outer boundaries of a plasma along direction $\vec{\Omega}$; the integral accounts for the contribution to intensity of all elementary elements dx along path $s_0 \rightarrow s$ (Fig. 3.1).

$$y = e^{-\int_{s_0}^{s} k(x)dx}\int_{s_0}^{s} P(x)e^{\int_{s_0}^{x} k(x')dx'}dx + Ce^{-\int_{s_0}^{s} k(x)dx}$$
$$= \int_{s_0}^{s} P(x)e^{-\int_{x}^{s} k(x')dx'}dx + Ce^{-\int_{s_0}^{s} k(x)dx.}$$

Here the relation $\int_{s_0}^{x} - \int_{s_0}^{s} = -\int_{x}^{s}$ was used. After returning to the original notation, it becomes

$$I_\nu = \int_{s_0}^{s} \kappa_\nu B_\nu e^{-\int_x^s \kappa_\nu(x')dx'} dx + I_{\nu 0} e^{-\int_{s_0}^{s} \kappa_\nu(x)dx}$$

The first term on the right side of this equation describes the radiation which is born and partially absorbed along path $s_0 \rightarrow s$. Second term describes intensity $I_{0\nu}$ from an external light source that enters the plasma at point s_0 and is attenuated along path $s_0 \rightarrow s$. In the absence of sources of external radiation, $I_{0\nu} = 0$ and the final solution of Eq. (3.2) becomes

$$I_\nu = \int_{s_0}^{s} \kappa_\nu B_\nu e^{-\int_x^s \kappa_\nu(x')dx'} dx \tag{3.4}$$

If the plasma is homogeneous, the absorption coefficient κ_ν does not depend on the x-coordinate and can be taken off the integral signs. If, in addition, the plasma is isothermal, the blackbody function can also be taken out of the integral sign. Hence, for a homogeneous isothermal plasma, integration of the remaining terms yields the expression

$$I_\nu = B_\nu\left(1 - e^{-\kappa_\nu l}\right) \tag{3.5}$$

where $l = s - s_0$ is the pathlength through plasma in direction $\vec{\Omega}$.

If, in addition, the plasma is optically thin, meaning the product $\tau_\nu = \kappa_\nu l$, called the optical density, is negligibly small, $\tau_\nu \ll 1$, the exponent in Eq. (3.5) can be expanded into a Taylor series and, retaining only the first term in the series, one obtains

$$I_\nu = \tau_\nu B_\nu \tag{3.6}$$

This expression for a homogeneous, isothermal, and optically thin plasma at local thermodynamic equilibrium (LTE) forms a basis for the so-called "Boltzmann plot method", which is used in spectroscopy for determining plasma temperature and finding plasma composition via calibration-free (CF) analysis.

3.2 CF LIBS by the Boltzmann Plot Method

The Boltzmann plot (BP) method is based on a simplified model of the laser-induced plasma, in which the plasma is assumed to be (1) isothermal, (2) uniform, (3) optically thin at chosen atomic/ionic transitions, and (4) stationary. None of these conditions is fully satisfied in real plasmas; however, the assumption can still be a reasonable approximation if a well-planned measurement routine is adopted. Conditions (1) and (2) can be met by choosing a correct gate time for the detection of LIBS spectra: a start of the gate should be delayed with respect to the laser pulse to

let the plasma thermalize (i.e., equilibrate translational temperatures of electrons and heavy particles), and its duration should not be too short to allow collecting enough light, and yet not too long to assure negligible variation in plasma parameters. Condition (3), of the optical thinness, can be provided by a careful choice of analytical lines, i.e., well-resolved lines with moderate transition probabilities (although, to a certain extent, intensities of optically thick lines can be corrected by combining expressions 3.5 and 3.6). Finally, condition (4), stationarity, is provided, again, by a short gating of plasma emission; such that the plasma parameters (size, temperature, and electron density) are nearly frozen within its duration.

3.2.1 The Boltzmann Plot Equation

Equation (3.6) from the previous section is the working equation for the BP method. It is transformed into a more convenient form by substituting into it the expressions for a line absorption coefficient, κ_ν, and blackbody function, B_ν [2]:

$$\kappa_\nu(\nu, T) = \frac{h\nu}{c}\left(n_i B_{ij} - n_j B_{ji}\right) P_\nu(\nu) \tag{3.7}$$

and

$$B_\nu = \frac{2h\nu^3}{c^2}\frac{1}{e^{h\nu/kT} - 1} \tag{3.8}$$

Here, h and c are the Planck constant and the speed of light, n_i and n_j are the number densities of the lower and upper transition states, correspondingly, B_{ij} and B_{ji} are the Einstein coefficients for absorption and stimulated emission, and $P_\nu(\nu)$ is the unity-normalized line shape function that is assumed to be the same for both absorption and emission. Using the relationships between Einstein coefficients, $g_i B_{ij} = g_j B_{ji}$ and $B_{ij} = \frac{g_j}{g_i}\frac{c^3}{8\pi h\nu^3}A_{ji}$, and the Boltzmann formula for population densities of excited states at LTE, $n_i = n\frac{g_i}{U(T)}e^{-E_i/kT}$, the substitution of (3.7) and (3.8) into (3.2) yields, after simple algebra, the intensity of the optically thin line for a transition $j \to i$

$$I_\nu(\nu) = \frac{h\nu}{4\pi}A_{ji}\mathrm{n}^{(z)}lP_\nu(\nu)\frac{g_j}{U^{(z)}}e^{-E_j/kT} \tag{3.9}$$

where $n^{(z)}$ is the number density of ions in charge state z ($z = 0, 1, 2, \ldots$), g_j and E_j are the degeneracy and energy of the upper excited state j, k is the Boltzmann constant, and $U^{(z)}$ is the ion partition function (the dependence of $U^{(z)}$ upon temperature is omitted). Integrating Eq. (3.9) over a line profile and a full solid angle and noting that $\int_{\text{line}} P_\nu(\nu)d\nu = 1$ and $\nu \approx \nu_0$ across the line profile, where ν_0 is the frequency of the line center, the expression for the line integral intensity, I (W m^{-2}), is obtained

$$I_{ji} = h\nu_0 n^{(z)} l \frac{g_j A_{ji}}{U^{(z)}} e^{-E_j/kT} \tag{3.10}$$

This expression can be linearized as

$$y = mx + d \tag{3.11}$$

by taking the logarithm of both sides of Eq. (3.10), grouping and rearranging terms using $y = \ln\left(\frac{I_{ji}\lambda_0}{g_j A_{ji}}\right)$, $x = E_j$, $m = -\frac{1}{kT}$, and $d = \ln\left(\frac{chl}{U^{(z)}} n^{(z)}\right)$. The relation $\lambda_0 = c/\nu_0$ is used to switch between the frequency and wavelength. Equation (3.11) is the Boltzmann plot equation whose slope m is inversely proportional to the plasma temperature and intercept d is proportional to the logarithm of the number density $n^{(z)}$. This equation is conveniently used for the determination of plasma temperature. For this, a suitable set of spectral lines with upper state energies $x = E_j$ is chosen and the linear regression of y on x yields the line with a negative slope $-1/kT$. For better accuracy, the plot based on Eq. (3.11) should span an as large as possible range of excitation energies.

3.2.2 Number Density of Species

The number density of species $n^{(z)}$ can be found from the value of the intercept d in Eq. (3.11). Indeed, raising the exponent into power d, one obtains $e^d = \frac{chl}{U^{(z)}} n^{(z)}$ or, after rearranging,

$$n^{(z)} = \frac{U^{(z)}}{chl} e^d \tag{3.12}$$

In principle, this equation can be used for determining the physical values of number densities. However, in doing so, all terms in Eq. (3.11) should be expressed in physical units with the special attention to the use of the same consistent system of units for all variables. The latter requirement stems from a non-physical character of transcendent functions, like the logarithm or exponent, when they are applied to dimensioned arguments. Therefore, Eq. (3.12) is rarely used stand-alone mainly because measuring plasma emission in absolute intensity units, i.e., W m^{-2}, is an unwanted and difficult task.

Note that Eq. (3.12) provides the number density of a species in a certain ionization state, i.e., neutral, or singly (doubly, etc.) ionized. To find the total number density, all ionization states must be accounted for. This is done by using the Saha equation

$$\frac{n_e n^{(z)}}{n^{(z-1)}} = \frac{2U^{(z)}}{U^{(z-1)}} \left(\frac{2\pi m_e kT}{h^2}\right)^{3/2} e^{-\frac{\zeta - \Delta\chi}{kT}} \tag{3.13}$$

where $U^{(z)}$ and $U^{(z-1)}$ are the partitions functions of ions in charge states z and $z-1$, m_e and n_e are the mass of an electron and electron number density, and χ and $\Delta\chi$ are the ionization energy and its depreciation due to the Debye shielding. Naming the right part of Eq. (3.13) to $S(T)$ and assuming, for simplicity, only a singly ionized plasma ($z = 1$), the number densities of the complementary neutral and ionized species are found from

$$\begin{aligned} n^0 &= n^+ n_e / S(T) \\ n^+ &= n^0 S(T) / n_e \end{aligned} \tag{3.14}$$

Either equation can be used for finding its counterpart, depending on which species, atoms, or ions are used for the construction of a BP. The total number density is then calculated from $n^{\text{tot}} = n^0 + n^+$. As follows from Eq. (3.14), the prior knowledge of the electron number density n_e is required. Typically, the electron number density is found from widths of suitable spectral lines assuming the dominant pressure broadening is due to the Stark effect. The expression for the Stark broadened FWHM (full width at half maximum) is found in [2, 3]

$$\Delta\lambda_{\text{stark}} = 2\left[1 + 1.75 \cdot 10^{-4} n_e^{1/4} \alpha \left(1 - 0.068 n_e^{1/6} T^{-1/2}\right)\right] \cdot 10^{-16} w n_e \tag{3.15}$$

where w and α are the electron and ion impact broadening parameters and 10^{-16} is the scaling factor for n_e expressed in units (10^{16} cm^{-3}). Considering the dominant role of electrons in line broadening and the weak dependence of $\Delta\lambda_{\text{stark}}$ upon the temperature, Eq. (3.15) is often reduced to

$$\Delta\lambda_{\text{stark}} = 10^{-16} w n_e \tag{3.16}$$

This expression does not imply the knowledge of plasma electron temperature; only electron impact parameter w and measured width $\Delta\lambda_{\text{stark}}$ of the Stark-broadened line profile are required. The Stark broadening parameters for lines of elements from hydrogen through calcium can be found in Griems' tables [3] and for other elements in the periodic literature and reference data sources, e.g., Konjević et al. [4, 5] who consistently, over the years, is extending the database of Stark broadening parameters. Finding the width of the Stark-broadened line may present some difficulty because this profile may be distorted by other broadening mechanisms, e.g., instrumental broadening or thermal (Doppler) broadening. In that case, a deconvolution of the Stark profile from the observed line profile may constitute a substantial difficulty.

3.2.3 CF LIBS by Boltzmann Plot Method

Provided the conditions given in the former chapter are fulfilled, a simplified model of laser-induced plasma can be used, which suggests that atomic/ionic excitations are

distributed according to the Boltzmann statistics and rates of ionization and recombination processes are balanced via the Saha equilibrium in Eq. (3.13). The model yields a semi-logarithmic linear dependence (3.11) of the line integral intensities, factorized by transition characteristics, upon the line excitation energies. The slope of this function is $-1/kT$ while the y-intercept (at zero excitation energy) is proportional to the number density via Eq. (3.12). This dependence is dubbed "the Boltzmann plot" and the plane, defined by its axes, "the Boltzmann plane." To find the concentration of all species, the Boltzmann plot (BP) should be constructed for all of them. The latter implies that each species should be represented by at least one line or a data-point on the Boltzmann plane. To relate the composition of the laser-induced plasma to that of the sample, two assumptions are made: the laser ablation is stoichiometric, and all plasma species are in their pure elemental forms. The latter means that plasma chemistry does not affect the concentrations.

Drawing the line requires at least two points; if only one point is available, the line drawn through this point must be parallel to other lines with slope $-1/kT$. Thus, a one-point BP is "subdued" to many-point BPs and the exact position of that point on the BP-plane is crucial for finding a correct concentration of an element represented by only one point. One can call a one-point BP the "slave BP" and a many-point BP the "master BP." The position of the y-intercept of the one-point BP also crucially depends on how accurately the master BP is drawn. These considerations are correct if all plasma species have the same temperature, i.e., at LTE.

The first algorithm for calibration-free (CF) LIBS was proposed by Ciucci et al. [6] and then numerously reproduced and improved by other authors [7–11]. Reviews of analytical applications of this algorithm can be found in [12–15]. As quantitative analysis operates usually with relative concentrations rather than number densities, Eq. (3.10) must be modified. A factor F is introduced, which accommodates fundamental constants and accounts for a solid angle of light collection, path length, and total (constant) mass of plasma species. Using $\lambda_0 = c/\nu_0$ this equation transforms to

$$I_{ji} = \frac{F c_s^{(z)}}{U_s^{(z)}} \frac{g_j A_{ji}}{\lambda_{ji}} e^{-E_j/kT} \tag{3.17}$$

where I_{ji} is the intensity of radiation at transition $j \to i$, λ_{ji} is the central wavelength of this transition, $c_s^{(z)}$ is the mass concentration of neutral or ionic particles of sort s, and $U_s^{(z)}$ is the partition function of these particles. This equation is further linearized into form (3.11) with the same entries for x, y and m, only the value of the intercept modifies to $d_s = \ln\left(\frac{F c_s^{(z)}}{U_s^{(z)}}\right)$. Typically, BPs for all plasma species are constructed using spectral lines of atoms. Assuming a singly ionized plasma, relative concentrations of atoms, c_s^0, and their complementary ions, c_s^+, are found from values d_s of the BP intercepts and relations (3.14), which are expressed in terms of the concentrations rather than number densities

$$c_s^0 = \frac{U_s^0}{\mathrm{F}} e^{d_s}$$
$$c_s^+ = \frac{U_s^0 S_s(T)}{\mathrm{Fn_e}} e^{d_s} \tag{3.18}$$

Demanding all relative concentrations summing up to unity, $\sum_s \left(c_s^0 + c_s^+\right) = 1$, factor F is easily found from

$$F = \sum_s \left[U_s^0 e^{d_s} \left(1 + \frac{S_s(T)}{n_e} \right) \right] \tag{3.19}$$

and the concentration of species, $c_s = \left(c_s^0 + c_s^+\right)$, are found using (3.18) with the now known factor F. As follows from Eqs. (3.18) and (3.19), the knowledge of electron number density is crucial for the implementation of this method.

3.2.4 CF LIBS by Saha-Boltzmann Plot Method

It is possible to combine separate BPs for neutrals and ions into a single plot that is called a Saha-Boltzmann plot (SBP). This plot spans over a large range of excitation energies that exceeds the ionization energy of an element, for which the plot is constructed. The larger range provides a more accurate measurement of the temperature and intercepts and, hence, more accurate results of CF LIBS analysis. Examples of the use of the Saha–Boltzmann plot for temperature evaluation in LIBS plasmas can be found in the literature [16–20].

It is straightforward to extend the formalism of BP analysis to SBP analysis. To begin with, for a singly ionized plasma, Eq. (3.17) is replicated for atomic, $j \to i$, and ionic, $l \to k$, transition

$$I_{ji} = \frac{F c_s^0}{U_s^0} \frac{g_j A_{ji}}{\lambda_{ji}} e^{-E_j/kT}$$
$$I_{lk} = \frac{F c_s^+}{U_s^+} \frac{g_l A_{lk}}{\lambda_{lk}} e^{-E_l/kT} \tag{3.20}$$

Substituting the second equation of (3.14), into the second equation of Eq. (3.20), $c^+ = \frac{c^0 S(T)}{n_e}$ with $S(T) = \frac{2U^+}{U^0} \left(\frac{2\pi m_e kT}{h^2} \right)^{3/2} e^{-\frac{\chi_s - \Delta\chi}{kT}}$ and taking the logarithm in two parts of Eqs. (3.20), two linear equations with respect to E_j and E_l are obtained

$$\begin{aligned} \ln\left(\frac{I_{ji}^{0}\lambda_{ji}}{g_j A_{ji}}\right) &= \ln\left(\frac{\mathrm{F}c_s^{0}}{U_s^{0}}\right) - \frac{E_j}{kT} \\ \ln\left(\frac{I_{lk}^{+}\lambda_{lk}}{g_l A_{lk}}\right) - \ln\left(\frac{2}{n_e}\left(\frac{2\pi m_e kT}{h^2}\right)^{\frac{3}{2}}\right) &= \ln\left(\frac{\mathrm{F}c_s^{0}}{U_s^{0}}\right) - \frac{\chi_s + E_l - \Delta\chi}{kT} \end{aligned} \tag{3.21}$$

Both equations have form of Eq. (3.11) with

$$\{x, y\} = \left\{E_j, \quad \ln\left(\frac{I_{ji}^{0}\lambda_{ji}}{g_j A_{ji}}\right)\right\}$$

for atomic lines and

$$\{x, y\} = \left\{\chi_s + E_l - \Delta\chi, \quad \ln\left(\frac{I_{lk}^{+}\lambda_{lk}}{g_l A_{lk}}\right) - \ln\left(\frac{2}{n_e}\left(\frac{2\pi m_e kT}{h^2}\right)^{3/2}\right)\right\}$$

for ionic lines and the common intercept $d_s = \ln\left(\frac{\mathrm{F}c_s^{0}}{U_s^{0}}\right)$ at $x = 0$. The rest of the procedure is identical to that in the BP method; the F-factor and concentrations are found from Eqs. (3.18) and (3.19).

It should be emphasized again that the knowledge of n_e is essential for a retrieval of concentrations c_s^0 and c_s^+. The electron density is used in (3.21) for calculating the y-values of the ionic portion of the SBP and in (3.18) for calculating the complimentary concentrations of ions. Also, calculating y's for the ionic SBP requires knowledge of plasma temperature, T. In practice, SBPs are constructed in an iterative manner: a trial value of T is assumed and procedure (3.21) runs until the variation in T between consecutive runs becomes smaller than a predefined epsilon.

3.2.5 Correction for Self-Absorption

Equation (3.6) that creates a foundation for the BP and SBP methods is an approximate solution of the radiative transfer equation under the assumptions of a uniform and *optically thin* plasma. The approximation is accurate up to the second term in the Taylor series $e^{-\tau} \approx 1 - \tau + O(\tau^2)$, $\tau < 1$. An error of this approximation, $100 \times \frac{|e^{-\tau} - (1-\tau)|}{e^{-\tau}}$, is 0.5% for $\tau = 0.1$, 2.3% for $\tau = 0.2$, 18% for $\tau = 0.5$, and 75% for $\tau = 0.9$. If Eq. (3.6) is used with values of τ exceeding $0.1 - 0.2$, it will impose large errors upon the determination of the plasma temperature from slopes of BP or SBP, and, consequently, on values of relative concentrations determined from the BP or SBP intercepts. Therefore, a correction for optical thinness is required for such high values of τ.

Many methods have been proposed for self-absorption (SA) correction [7–11]. A general idea is to replace the intensity of an optically thick spectral line by the equivalent intensity of the same line but under optically thin conditions. This means

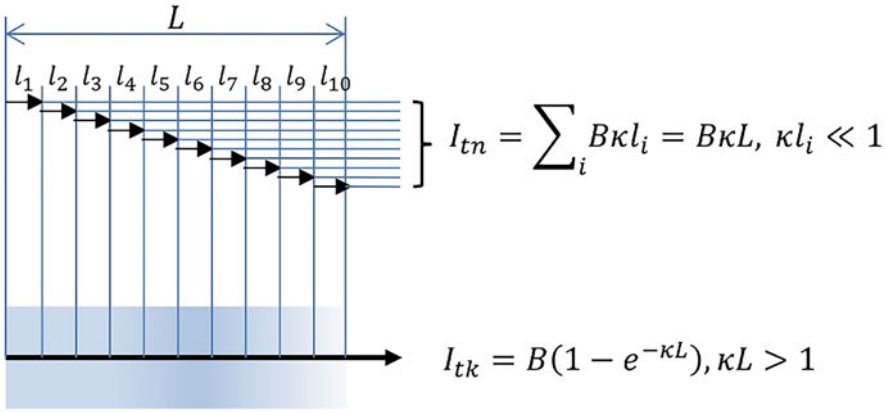

Fig. 3.2 Illustration of the principle of self-absorption correction. Adapted from [10]

that each photon generated along a line of observation and having frequency inside the spectral line profile, passes through the plasma without being absorbed. This situation is illustrated in Fig. 3.2 where pathlength L is split into small intervals l_i such that $\kappa l_i \ll 1$ for each interval. The intensity generated along a full pathlength L equals $B\kappa\sum_i l_i = B\kappa L$ provided each interval emits photons independently of others. Such a situation is non-physical as soon as κL becomes greater than one because in this case, the line intensity exceeds a blackbody limit. This hypothetical procedure of splitting the pathlength into optically thin non-interacting elements serves only for replacing the intensity of the optically thick line I_{obs} with the equivalent intensity of the optically thin line I_{eq} to satisfy the condition of optical thinness needed for the construction of a BP or SBP.

All methods of self-absorption (SA) correction for a uniform, isothermal plasma are based on manipulating with Eqs. (3.5) and (3.6). For example, Praher et al. [11] rewrote the expression

$$I_{\text{obs}}(\lambda) = B\left(1 - e^{-\tau(\lambda)}\right) \tag{3.22}$$

for the observed optically thick line in a form

$$I_{\text{obs}}(\lambda) = \frac{I(\lambda_0)\left(1 - e^{-\tau(\lambda_0)P(\lambda)/P(\lambda_0)}\right)}{\tau(\lambda_0)} \tag{3.23}$$

by using a relation $B = I(\lambda)/\tau(\lambda)$ in Eq. (3.6), factorizing the optical density into a wavelength-independent and a wavelength-dependent terms K and $P(\lambda)$

$$\tau(\lambda) = K \cdot P(\lambda) \tag{3.24}$$

and applying simple relations $K = \tau(\lambda_0)/P(\lambda_0)$ and $I(\lambda)/\tau(\lambda) = I(\lambda_0)/\tau(\lambda_0)$. Here, $P(\lambda)$ is the spectral line profile of the optical transition, and λ_0 is the wavelength of the line

center. Assuming a Lorentzian profile $P(\lambda) = \frac{2\Delta\lambda}{4(\lambda-\lambda_0)^2+\Delta\lambda^2}$ for the Stark broadened transition and using (3.23), a series of profiles $I_{\text{obs}}(\lambda)$ is calculated for different values of $\tau(\lambda_0)$. Then, the ratios of spectral widths

$$R_W[\tau(\lambda_0)] = \Delta\lambda_{\text{obs}}/\Delta\lambda_{\text{eq}} \geq 1 \tag{3.25}$$

and areas

$$R_A[\tau(\lambda_0)] = \int I_{\text{obs}}(\lambda)d\lambda / \int I_{\text{eq}}(\lambda)d\lambda \leq 1 \tag{3.26}$$

of the optically thick and equivalent optically thin profiles are calculated as functions of $\tau(\lambda_0)$ to produce a functional dependence of R_A upon R_W for each value of $\tau(\lambda_0)$, $R_A = f(R_W)$. Further, the width $\Delta\lambda_{\text{obs}}$ and integral intensity $\int I_{\text{obs}}(\lambda)d\lambda$ are measured whereas the width $\Delta\lambda_{\text{eq}}$ of the equivalent optically thin line is determined from an electron density measured via (3.16). Finally, from the known value $R_W = \Delta\lambda_{\text{obs}}/\Delta\lambda_{\text{eq}}$ the corresponding value of R_A is found using $R_A = f(R_W)$ and the sought-for value of the equivalent integral intensity of the optically thin line is obtained from

$$\int I_{\text{eq}}(\lambda)d\lambda = \int I_{\text{obs}}(\lambda)d\lambda / R_A \tag{3.26}$$

This approach has been extended in [10] to using the more general Voigt profile function instead of the Lorentzian.

3.2.6 Factors Affecting the Accuracy of CF LIBS

3.2.6.1 Line Overlap and Deconvolution

CF algorithms require integral intensities of single stand-alone lines whereas finding such lines in dense spectra (e.g., the spectrum of iron) can be problematic due to a limited resolution of optical spectrometers and overlap of emission lines. Thus, the accuracy and reliability of CF analysis critically depends on the ability of data processing software to resolve (deconvolve) overlapping lines. From a mathematical point of view, deconvolution is an ill-posed problem meaning that it does not provide a unique solution within error bounds of experimental data. Over the years, many methods have been developed that helped solving the problem of deconvolution of single lines from the envelope of lines [21, 22].

So, the question is: how stand-alone lines can be decoupled from interfering lines? The solution depends on whether the lines are optically thin or thick. For optically thin overlapping lines, the overall intensity is given by the arithmetic sum of individual line profiles

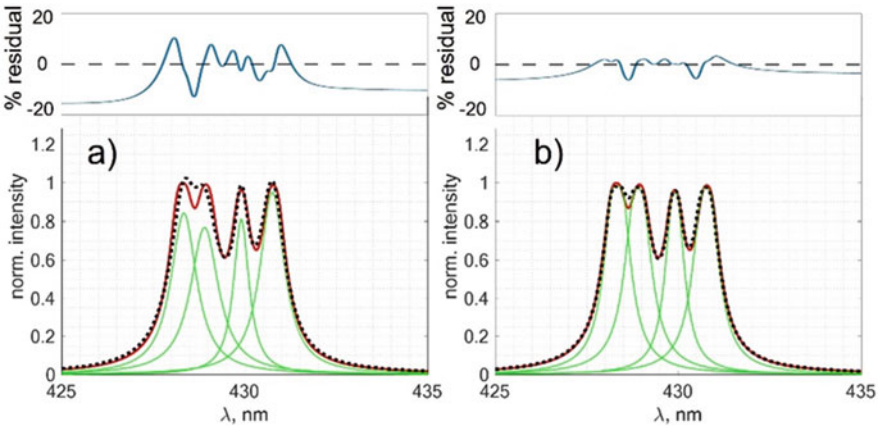

Fig. 3.3 Illustration of different strategies of retrieving stand-alone lines (thin green lines) from the overlapped profile (thick red line). (**a**) decoupling via (3.27); (**b**) decoupling via (3.28). Thick dotted line is the best-fit profile. The insets show the residual errors. Adapted from [10]

$$I_\Sigma(\lambda) = \Sigma_i I_i(\lambda) = B\Sigma_i \tau_i(\lambda) = B\sum\nolimits_i K_i P_i(\lambda,\, \Delta\lambda_i) = \sum\nolimits_i K_i' P_i(\lambda,\, \Delta\lambda_i) \qquad (3.27)$$

where $K_i' = BK_i$ is the amplitude of the line profile with K_i defined in (3.24), $P_i(\lambda, \Delta\lambda_i)$ is the individual profile (e.g., Lorentzian, Gaussian, Voigt), and $\Delta\lambda_i$ is the corresponding line width. Each stand-alone line can be retrieved by a standard decoupling procedure by fitting the envelope consisting of several lines by an arithmetic sum of individual line profiles. For example, N overlapping Lorentzian profiles would require $2 \times N$ fitting parameters.

For optically thick, overlapping lines the situation is different. In this case, the overall intensity is determined by individual contributions which sum up in the power of the exponent

$$I_\Sigma(\lambda) = B\left[1 - e^{-\Sigma_i \tau_i(\lambda)}\right] = B\left[1 - e^{-\sum_i K_i P_i(\lambda,\, \Delta\lambda_i)}\right] \qquad (3.28)$$

and this equation should be used to retrieve stand-alone lines. The number of fitting parameters increases by one (B) neglecting its variation within a fitted spectral interval. Figure 3.3 illustrates two retrieval strategies for four computer-generated overlapping lines that have maximal optical densities in line centers between 2 and 5: (1) fitting the full profile using (3.27), and (2) fitting the full profile using (3.28). It is seen that both methods provide a satisfactory fit with residual errors of about $\pm 10\%$; however, the individual parameters of the retrieved lines are markedly different as is inferred from Table 3.1.

If it is not known in advance whether overlapping lines are optically thin or thick, using Eq. (3.28) is a better option as it works in both optically thin and optically thick situations.

Table 3.1 Relative percent errors of reconstruction for the widths and integrals of spectral lines

	Via (3.27)		Via (3.28)	
Ca I, nm	Width	Integral	Width	Integral
428.30	5.3	8.8	4.2	1.8
428.94	10.9	1.3	13.9	11.5
429.90	20.8	30.1	6.5	6.3
430.77	3.0	2.1	5.0	3.4

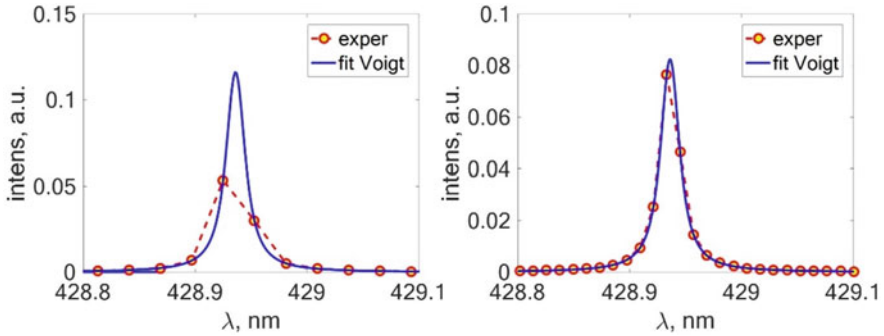

Fig. 3.4 Synthetic line generated on grids with (**a**) 36 pix/mm and (**b**) 84 pix/nm (typical resolution of an echelle spectrometer with ICCD). Adapted from [10]

Table 3.2 Relative % errors of CF SBP analysis with low and high spectral resolutions; numbers below symbols are concentrations of elements in a synthetic sample

	Ca	Al	Mg	Si	Fe	Mn	Ti	Cr
Resolution	27.32	22.01	16.16	8.52	19.03	6.35	0.22	0.40
36 pix/mm	5.1	11.3	1.1	3.4	1.3	12.8	9.1	15.0
84 pix/mm	0.3	0.1	0.6	0.1	1.1	1.1	0.1	2.5

3.2.6.2 Noise

Noise found on experimental spectra obstructs the true positions of line centers and deteriorates the quality of line fitting. If noise is weak and lines are clearly perceptible, no de-noising is needed as this procedure distorts the original spectral signal. However, at high levels of noise, de-noising may provide a more accurate retrieval of widths and integrals of spectral lines. Standard denoising techniques are Savitzky-Golay [23] and Fourier-filtering [24]; more advanced ones are principal component analysis (PCA) [25] or wavelet transform [26].

3.2.6.3 Spectral Resolution and Line Fitting

The accuracy of line fitting and, consequently, retrieval of line widths and integrated intensities crucially depends on the spectrometer resolution and number of detector pixels. This point is illustrated in Fig. 3.4 and Table 3.2, which show the fitted line profiles and result of CF SBP analysis performed with low and high spectral

resolutions. The relative errors are around 1% for the high-resolution spectrum (84 pix/mm) and raise to 15% for the low-resolution spectrum (36 pix/mm).

Obviously, with more pixels per a line, a more accurate fitting of the line profile function can be achieved and, consequently, a better accuracy CF analysis can be obtained. Numerous algorithms exist for the fitting procedure, all requiring a good initial guess for the parameters. Fitting the spectroscopic functions (i.e., Gaussian, Lorentzian, and Voigt) is typically done by non-linear least-squares algorithms such as the trust-region-reflective [27] or Levenberg-Marquardt [28].

3.2.6.4 Electron Density

Accurate evaluation of the electron number density (n_e) is crucial for the accuracy of CF analysis. Table 3.3 shows the relative errors of CF analysis performed with a synthetic spectrum and artificially incremented or decremented values of n_e's. One sees how errors in n_e result in significant errors of quantitative CF analysis. Therefore, careful selection of suitable lines for accurate retrieval of n_e is very important. These lines must be (1) optically thin, (2) free of spectral and instrumental interferences, and (3) having accurate values of Stark broadening parameters.

The electron number density can be most accurately evaluated from hydrogen lines H_α at 656.28 nm and H_β at 486.14 nm [29], which are typically present in LIBS spectra obtained under atmospheric conditions where hydrogen comes from the air moisture even if it is not present in the sample. These lines exhibit a linear Stark effect and are typically much broader than an instrumental slit function that makes deconvolution from the slit function unnecessary. If hydrogen lines are not available, the electron number density can be determined from other lines with trustworthy Stark broadening parameters.

3.2.6.5 Plasma Non-uniformity

Results of a CF method, which assumes a uniform and isothermal plasma, can be compromised by the factual non-uniformity of real plasmas. To estimate this effect, CF SBP analysis was performed on synthetic spectra emitted by the multilayered plasma consisting of N layers with a parabolic temperature profile [10]

Table 3.3 Relative % errors of CF SBP analysis using erroneous electron densities; numbers below chemical symbols show concentrations of elements in synthetic sample. Results with exact n_e are in bold

	Ca	Al	Mg	Si	Fe	Mn	Ti	Cr
$\lvert\Delta n_e/n_e\rvert$ %	27.32	22.01	16.16	8.52	19.03	6.35	0.22	0.40
0	**1**	**0.7**	**0.9**	**0.5**	**1**	**0.7**	**2.7**	**1**
7	0.9	1.8	2.0	1.6	2.8	6.2	3.8	0.9
33	2.8	11.4	7.9	7.3	7.8	26.4	17.2	2.8
67	8.1	30.0	14.3	9.3	18.4	47.6	33.9	8.1

Table 3.4 Relative % errors of CF SBP analysis with no temperature gradient and with parabolic temperature gradients; % concentrations are given below chemical symbols. Results with no temperature gradient are in bold

	Ca	Al	Mg	Si	Fe	Mn	Ti	Cr
T-gradient	27.32	22.01	16.16	8.52	19.03	6.35	0.22	0.40
None	**0.87**	**1.16**	**0.54**	**0.61**	**0.33**	**0.62**	**3.24**	**0.43**
Small	2.33	3.38	0.25	5.53	1.66	2.56	5.67	11.52
Large	6.75	30.62	76.69	42.28	14.66	22.82	5.44	84.66

$$T_N = T_0 + (T_l - T_0)\frac{(x_N - l/2)^2}{(l/2)^2} \tag{3.29}$$

where $x_N \epsilon [0, l]$, l is the pathlength, and T_0 and T_l are the temperatures in plasma center and plasma edge. The plasma density across the plasma was considered uniform and the intensity emitted by each layer was calculated recurrently from

$$I_N = I_{N-1}e^{-\tau(T_N)} + B(T_N)\left(1 - e^{-\tau(T_N)}\right) \tag{3.30}$$

The results for the two temperature gradients: small ($T_l = 9000\ K$, $T_0 = 11000\ K$) and large ($T_l = 5000\ K$, $T_0 = 15000\ K$) are shown in Table 3.4. The small gradient causes still acceptable increase in errors as compared to gradient-free CF analysis whereas the large gradient produces errors up to 80% that make the CF SBP analysis semi-quantitative.

The effect of plasma non-uniformity on results of conventional LIBS analysis was studied by Mercadier et al. [30] on the example of carbon-based materials.

3.2.7 Performance of CF LIBS

The performance of CF LIBS is best demonstrated on synthetic spectra, which can be generated for truly uniform and isothermal plasma (required by the CF model) with precisely known concentrations and spectroscopic parameters of lines. The task is to solve an inverse problem, i.e., to retrieve concentrations of elements using a CF algorithm applied to synthetic spectra. Such a job is performed in [10] on the example of spectra generated for ten slag samples with concentrations of elements corresponding to real samples. To make simulations more realistic, complicating effects were introduced: a finite spectral resolution (84 pix/nm) and Gaussian noise with an amplitude of 0.2% of a maximum spectrum intensity. The result of CF SBP analysis is presented in Fig. 3.5a in the form of a certified-found plot. Even for such an idealistic situation, the points show noticeable scattering around the line of perfect correlation (the 45-degree line). Relative errors for major elements (conc. >1%) range between 0.1% and 10% and for minor elements (conc. <1%) between 1% and 40%. The errors are due to slightly inaccurate line decoupling, insufficient

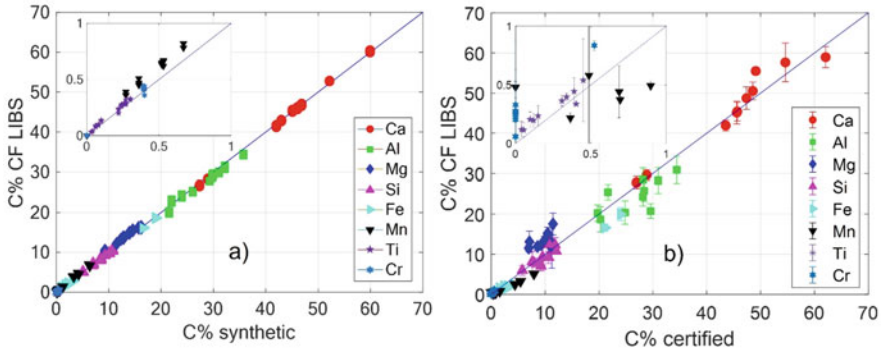

Fig. 3.5 (**a**) Results of CF SBP analysis using synthetic spectra of slag samples; (**b**) Certified-found plot for real slag samples. Inset shows magnified lower parts of the plots. The solid lines in both plots correspond to the ideal correlation between the certified and determined values. [Data in (**b**) is courtesy by S. Eschlböck-Fuchs and J.D. Pedarnig from Johannes Kepler University in Linz, Austria]

compensation of self-absorption, and loss of information due to spectra denoising. Relative standard deviations due to random noise are 1–10%.

The picture becomes less optimistic when the SBP CF algorithm is applied to real slag samples having the same concentrations as the synthetic samples; the result is shown in Fig. 3.5b. The error in concentrations raises to 5–40% for major elements and 40–80% for minor elements; the relative standard deviation increases to 5–20% (in average). The same error margins for CF LIBS analysis of steel slag samples are reported by Kolmhofer et al. [31].

This example demonstrates the typical margins for accuracy and precision of CF analyses. The lower margins correspond to the ideal situation, in which spectra fully correspond to the mathematical model of the CF method. For "real life" margins, complications arise from the mismatch between the object (plasma) and its representation (the model), measurement errors, and imprecise values of parameters taken from spectral databases. The results of CF analysis also strongly depend on the type of a sample, excitation and light collection conditions, and correct choice of analytical lines. Even though remarkably good results are often reported in the literature for SBP or BP CF LIBS, it will not be an exaggeration to say that quantitative analysis by this method is possible mainly for concentrations at a percentage or higher levels. For lower concentrations, the results are mainly semi-quantitative where uncertainties may reach a hundred or hundreds of percent. Several reasons for that are given in the next section.

The overall performance of BP or SBP CF analyses of elements in various samples can be judged from Table 3.5. where the literature data are collected and split into groups depending on concentrations of elements analyzed. One group represents errors in the determination of major elements with concentrations above 1% and the other errors in the determination of minor elements with concentrations below 1%. Errors within each group are determined by

Table 3.5 Percent error of determinations of major and minor elements (bold font) in different samples by CF LIBS. Shown in parentheses are the numbers of elements analyzed within each concentration group

Sample	δ major elements	δ minor elements	Reference
Aluminum alloys	**19** (2)	**8** (5)	[6]
	10 (4)	**25** (3)	[32]
	8 (3)	--	[33]
	4 (7)	**42** (1)	[34]
Bronzes and copper alloys	**7** (9)	**48** (10)	[35]
	26 (17)	**116** (2)	[36]
	12 (4)	--	[37]
Steel, iron-based alloys	**6** (13)	**69** (1)	[9]
Precious alloys	**2** (13)	--	[38]
Soils and rocks	**16** (18)	**14** (14)	[39]
	11 (7)	**61** (4)	[40]
	2 (4)	**2** (6)	[41]
Meteorites	**7** (14)	**18** (6)	[42]
Corals	**1** (1)	**12** (5)	[43]

$$\delta = \frac{100}{N}\sqrt{\sum_{i=1}^{N}\left(\frac{C_i - M_i}{C_i}\right)^2} \tag{3.31}$$

where N is the number of elements in this group and C_i and M_i are the certified and found concentration, correspondingly. One sees that in general, errors are significantly higher for small concentrations than for large ones, sometimes even exceeding 100%.

3.2.7.1 Sources of Errors in BP (SBP) Method

A laser-induced plasma is a dynamic event; both the plasma temperature and electron density decrease nearly exponentially in time. If data are collected with a long- or non-gated detector, the plasma temperature will rapidly change within the observation time and no definite temperature can be assigned to the plasma. Therefore, the temperature retrieved from the slope of the BP or SBP will, in this case, be some "effective temperature" that does not correspond to a physical plasma state. This breaks the condition of stationarity and compromises the validity of the model which requires well-defined values for both T and n_e.

Another potential source of error when using improperly long acquisition gate widths is associated with different behavior of ionic and atomic lines during plasma evolution: when the plasma is hot, ionic lines dominate the spectrum; when it cools down, atomic lines become stronger. This means that atomic and

ionic portions of SBP may have different slopes and, correspondingly, yield different temperatures. This also compromises the validity of the CF model.

Measurement error due to line self-absorption, even though this effect might have been corrected, is another important source of error in CF LIBS [44].

Errors in measurements of the slit and spectral response functions as well as the deconvolution procedure impose errors on results of CF analysis.

Not accounting for light collection geometry may also result in error. It is commonly assumed that the radiation is collected along a single line of sight piercing the plasma. The assumption is not justified for collection of light by a lens or optical fiber from an extended plasma plume [45].

A good quality of a master BP (SBP) is crucial for accuracy of CF analysis because the slopes of slave BPs (SBPs) reproduce the master slope. It is important to construct the master BP (SBP) using lines of that specie, which dictates the plasma properties; the y-intercept of a BP (SBP) built for this specie will determine the overall accuracy of analysis.

In both BP and SBP methods, error comes from a summation of elemental concentrations to 100%; this implies that small relative errors at high concentrations transform into large relative errors at low concentrations.

Other sources of errors that affect results of CF LIBS analysis are considered in [32].

3.3 Monte Carlo LIBS

The MC LIBS method is based on matching synthetic and experimental plasma spectra. The model assumes a uniform, isothermal, and stationary plasma, which, in this case, does not need to be optically thin; which is a difference from the BP (SBP) method. Another important difference is that errors on large and small concentrations are not entangled as in the BP (SBP) method; they are independent. Therefore, low concentrations can be determined with the same accuracy as high concentrations. Besides, the MC approach does not require a deconvolution of overlapped spectral lines or correction for self-absorption; these effects are automatically accounted for at the stage of spectra generation. In the meantime, all limitations due to imperfections of the mathematical model and correctness of spectroscopic data remain the same.

3.3.1 Setting the Problem

As in the BP (SBP) method, the plasma is assumed to be isothermal and uniform at local thermodynamic equilibrium (LTE) and is described by a set of Eqs. (3.1)–(3.10). The goal of this approach is to generate a synthetic spectrum using Eq. (3.5) and match it with an experimental spectrum by varying fitting parameters. The fitting parameters are concentrations of species, plasma size, and plasma temperature. The approach is calibration-free because it retrieves concentrations from spectral data without using standards.

A Monte Carlo (MC) algorithm minimizes a cost function that signifies the difference between synthetic and experimental spectra. During the minimization, physical parameters of the model (T, n_i, n_e) are varied and gradually approach the analogous characteristics of the experimental plasma. After finding the minimum, the sought-for parameters of the experimental plasma are read from the model. Mathematically, the problem is expressed by [46]

$$f(I^{\mathrm{ex}}, I^{\mathrm{syn}}) = \min_D [f(I^{\mathrm{ex}},\ I^{\mathrm{syn}})],\quad D = \left\{ \begin{array}{l} 10^{13} \le n_i\ [\mathrm{cm}^{-3}] \le 10^{19},\quad i = 1..N \\ 5000 \le T\ [K] \le 20000 \\ 0.001 \le R\ [\mathrm{cm}] \le 0.1 \end{array} \right\} \tag{3.32}$$

where $f(I^{\mathrm{ex}}, I^{\mathrm{syn}})$ is the cost function to be minimized; I^{ex} and I^{syn} are the experimental and synthetic spectra (dependency of I^{ex} and I^{syn} upon λ, n_i, T is omitted), and D is the $(N + 2)$-dimensional search domain, where N is the number of chemical elements considered in the model. The absolute value of the cost function is a measure of adequacy of the model for the description of experimental plasma.

3.3.2 Cost Function

A cost function can be any suitable metric that is sensitive to a difference between two sets of data. For example, one can use a correlation coefficient for the construction of the cost function

$$f_C(I^{\mathrm{ex}}, I^{\mathrm{syn}}) = 1 - \frac{\sum \left(I_i^{\mathrm{ex}} - \overline{I^{\mathrm{ex}}}\right)\left(I_i^{\mathrm{syn}} - \overline{I^{\mathrm{syn}}}\right)}{\sqrt{\sum \left(I_i^{\mathrm{ex}} - \overline{I^{\mathrm{ex}}}\right)^2 \sum \left(I_i^{\mathrm{syn}} - \overline{I^{\mathrm{syn}}}\right)^2}} \tag{3.33}$$

Here, I_i^{ex} and I_i^{syn} are the intensities of the experimental and synthetic spectra at wavelengths λ_i and $\overline{I^{\mathrm{ex}}}$ and $\overline{I^{\mathrm{syn}}}$ are their corresponding averages over a wavelength range. Function (3.33) is sensitive to mutual positions and intensities of spectral lines on two compared spectra and depends on the cosine of an angle between two vectors. The vectors represent synthetic and experimental spectra in a multidimensional space $\mathbb{R}^M$ where M is the number of spectral points (λ_i, $i = 1...M$). If the vectors are collinear, the two spectra perfectly match and $f_C(I^{\mathrm{ex}}, I^{\mathrm{syn}}) = 0$. The contribution of an element to the cost function depends on its concentration and number of spectral lines available for this element. To equalize contributions to the cost function from all elements, weights w_k are added in Eq. (3.33)

$$f_{CW}(I^{\mathrm{ex}}, I^{\mathrm{syn}}) = 1 - \frac{\sum_k w_k \sum_{L_k}^{M_k} \left(I_i^{\mathrm{ex}} - \overline{I^{\mathrm{ex}}}\right)\left(I_i^{\mathrm{syn}} - \overline{I^{\mathrm{syn}}}\right)}{\left[\sum_k w_k \sum_{L_k}^{M_k} \left(I_i^{\mathrm{ex}} - \overline{I^{\mathrm{ex}}}\right)^2\right]^{1/2} \left[\sum_k w_k \sum_{L_k}^{M_k} \left(I_i^{\mathrm{syn}} - \overline{I^{\mathrm{syn}}}\right)^2\right]^{1/2}} \tag{3.34}$$

To calculate w_k, equal weights (W) are first assigned to all elements regardless of their concentrations. $W = 1/N$ with N being the number of elements. The contribution of each spectral line of a given element is then calculated based on the integral intensity of this line divided by the sum of integral intensities of all lines belonging to this element: $w_{np_n} = W \cdot (S_{np_n} / \sum_{p_n} S_{np_n}),\ n = 1, \ldots N,\ p_n = 1 \ldots P_n$ where S_{np_n} is the integral intensity of line p_n of element n, and P_n is the number of lines available for this element. The integral intensities of all lines are recovered from the experimental spectrum. A full spectral grid is split into K spectral fragments so that L_k and M_k, $k = 1, \ldots K$ denote the lower and upper boundaries of a particular fragment k. Each fragment may contain one or several lines of the same or different elements. The weight of each fragment is then determined by a simple relation $w_k = \sum_{n,p_n} w_{np_n} S_{np_n} / \sum_{n,p_n} S_{np_n}$.

3.3.3 Monte Carlo Algorithm

The appearance of graphics processing units (GPU) on the market dramatically accelerated the execution of Monte Carlo algorithms by means of massive parallelization of computational codes. One such algorithm is proposed in [46]. Many initial random combinations (configurations), N_C, of plasma parameters (n_i, T, and R) are taken from box D in Eq. (3.32) and used for the generation of N_C synthetic spectra. Each configuration is represented by a point in box D that has a volume V_D in a phase space of plasma parameters. Values of the cost function are calculated for these initial configurations, and a smaller subset N_b of points ($N_b \ll N_C$) is chosen that corresponds to N_b smallest values of $f_{CW}(I^{ex}, I^{syn})$. Boxes of smaller volumes, $V_b^{(1)} < V_D$, are then built around each such point. In the next iteration step, a fraction αN_C of configurations is taken from the original box V_D while another fraction, $(1 - \alpha)N_C$, is taken from the smaller boxes $V_b^{(1)}$, where $0 < \alpha < 1$. After calculating the cost functions for the new set of configurations, new N_b points are chosen for the smallest values of the cost function and new N_b boxes are built around those points such that $V_b^{(2)} < V_b^{(1)} < V_D$, and so on. As a result, a configuration is found that yields the global minimum of the cost function avoiding the danger of being trapped around some local minimum. The adjustable parameters of the optimization are the total number of configurations N_C, number of boxes N_b, rate of reduction of volumes V_b, and fraction of configurations α taken from small, $V_b^{(j)}$, and large, V_D, boxes.

3.3.4 Performance of MC LIBS

As with the BP (SBP) method, the inherent performance of the MC method can best be demonstrated with synthetic spectra. In [47], a synthetic spectrum was generated that contained 74 spectral lines from eight elements of a steel slag sample (their concentrations are given in Table 3.6). Complicating effects imposed on the spectrum were the finite spectral resolution (84 pix/nm) and random Gaussian noise with an amplitude of 0.05% of the maximum spectrum intensity. Treating these spectra as experimental ones, the task is to reconstruct the composition of the sample by the MC method and compare it with true values. The convergence of the MC algorithm is illustrated in Fig. 3.6a. The algorithm scans six orders of magnitude in concentrations, two orders in radii, and 10000 K range in temperatures. Starting 11 times from a random configuration, the cost function consistently converged to a minimum value of 0.051 ± 0.001. Running 50 iterations took ~5 min on the GPU NVIDIA Tesla K40 examining 500000 configurations per iteration. The certified-found correlation plot for the artificial slag sample is shown in Fig. 3.6b and the corresponding accuracy and precision are provided in Table 3.6.

The points in Fig. 3.6b show a little scatter around a 45-degree line and Table 3.6 implies that the relative errors for major and minor elements are below 1% (except for silicon). Relative standard deviations due to random noise and stochasticity of the algorithm are always below 10%. Accuracy and precision are slightly worse for elements represented by a small number of lines (e.g., only one line was used for Si)

Table 3.6 Accuracy and precision of MC analysis of artificial slag sample; % concentrations are given below chemical symbols

	Ca	Al	Mg	Si	Fe	Mn	Ti	Cr
	27.32	22.01	16.16	8.52	19.03	6.35	0.22	0.4
% Rel. Error	0.21	0.07	0.94	3.74	0.28	0.04	0.16	0.73
% RSD	0.73	1.28	2.15	4.0	1.56	1.79	1.72	7.43

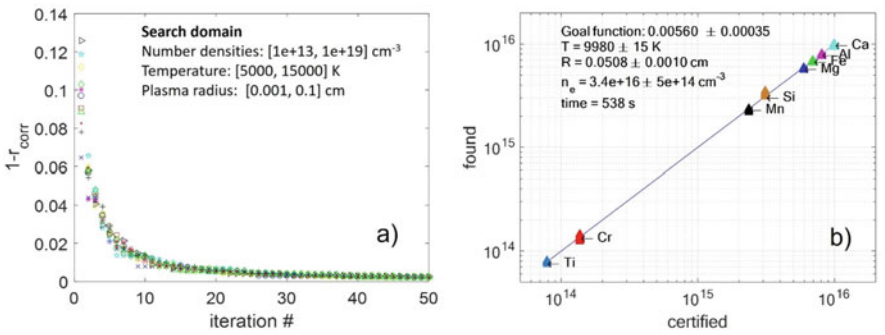

Fig. 3.6 (**a**) Convergence of cost function with number of iterations for 11 runs with random starting point; (**b**) Certified-found correlation plot for slag sample with synthetic spectrum; the x- and y-scales are the number densities in cm^{-3}. Unpublished results [47]

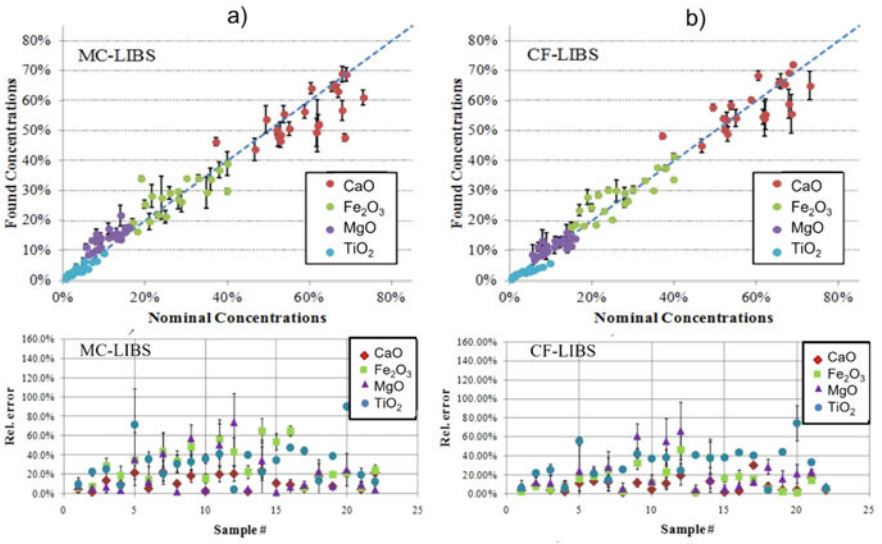

Fig. 3.7 (**a**) Certified-found correlation plot (upper panel) and relative errors (lower panel) of MC-LIBS analysis; (**b**) Certified-found correlation plot (upper panel) and relative errors (lower panel) of SBP CF-LIBS analysis. Adapted from [46]

or weak lines (Cr in this example). Overall, the MC algorithm demonstrates better accuracy and precision than the BP or SBP algorithm when working with synthetic spectra. Also, the MC algorithm allows the determination of low concentrations with the same accuracy and precision as high concentrations, thanks to the independent character of errors.

Analysis of real samples by the MC algorithm does not, however, yield better results than the BP (SBP) algorithm. An example of such an analysis is given in [46]. LIBS spectra were obtained from 22 samples made of metal oxides CaO, Fe_2O_3, MgO, and TiO_2 and simulated steel slags. The comparative results for MC and SBP analyses are given in Fig. 3.7.

This example shows that the accuracy of MC- and CF-LIBS methods is similar for this type of samples. More precisely, the maximum relative errors of MC (as compared to CF) LIBS are 25% (30%) for CaO, 65% (45%) for Fe_2O_3, and 75% (65%) for MgO. For TiO_2, whose concentrations are lower than concentrations of other oxides, the prediction errors increase to 90% (80%). The relative errors of MC and CF LIBS analyses correlate on a sample-to-sample basis. Factors affecting the accuracy and precision of both calibration-free methods are, presumably, the matrix effect and non-stoichiometric ablation, sample inhomogeneity, and shot-to-shot fluctuations of emission signals. Another head-to-head comparison of MC- and CF-LIBS has been done by Herrera et al. [48] on the example of analysis of aluminum samples under vacuum conditions. Based on the relative error of analysis it was concluded that the results from both approaches fall into the semi-quantitative category with 30–200% relative error. This study revealed that under vacuum

conditions the model of uniform isothermal plasma is unsuitable for calibration-free analysis by either BP (SBP) or MC methods.

When comparing the advantages and disadvantages of the BP (SBP) and MC calibration-free approaches, the following can be emphasized. The CF LIBS method cannot be made a fully automated algorithm; it is a highly user-dependent technique, which requires proficiency in identification of suitable spectral lines. It heavily relies on the quality of the master BP (SBP) and ability of the algorithm to reduce the effects of self-absorption and correctly retrieve plasma temperature and electron density. The MC-LIBS approach, on the other hand, although more intricate in the formulation and stochastic, is less user-involved and can be fully automated. On the negative side, the Monte Carlo optimization may take more time to process a spectrum; from several minutes to tens of minutes depending on the type of a CPU or GPU used and number of elemental concentrations to be iterated. Both methods require knowledge of relevant spectroscopic and physical parameters for all species involved in the calculations. In general, performance of both methods is inferior to that of calibration-based analysis, mainly because of the limitations imposed on the underlying plasma models. The methods are best suited for applications, in which standard-based analysis is not feasible and requirements for accuracy and precision are relaxed.

3.4 Other Calibration-Free Methods

Over the years, several modifications of CF LIBS were proposed, all based on the model of a uniform isothermal plasma at local thermodynamic equilibrium (LTE). An algorithm was developed with special attention to plasma uniformity and optical thinness for CF LIBS analysis of steel slags and other industrial materials [11, 49]. The effects of non-uniformity of laser-induced plasma on plasma temperature and concentrations determined by the BP method were analyzed in [50]. An attempt to account for plasma gradients was made in [51] by assuming two-zone plasma, each zone at its own density and temperature. A heuristic two-shell plasma model was developed in [52] to study the influence of plasma non-uniformity on emission spectra and geometric effects. An approach was proposed to find concentrations of analytes by matching experimental and synthetic spectra [53].

3.4.1 Spectrum-Matching Algorithms

An automatic method for standard-less LIBS was developed in [53] that allowed for rapid multi-element analysis without using the Boltzmann plot. The plasma spectrum was represented by a system of simultaneous algebraic equations

$$x_1 I_1(\lambda_k) + x_2 I_2(\lambda_k) + \ldots + x_n I_n(\lambda_k) = e(\lambda_k) \tag{3.35}$$

which formed an overdetermined system

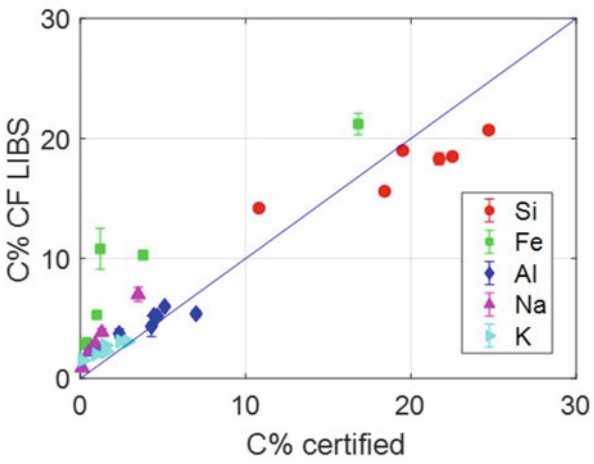

Fig. 3.8 Correlation between certified and found concentrations in mineral samples (andesites, dacites, and scarns). Data from [53]

$$\begin{pmatrix} I_1(\lambda_1)\, I_2(\lambda_1) \ldots I_n(\lambda_1) \\ \cdots \\ I_1(\lambda_p)\, I_2(\lambda_p) \ldots I_n(\lambda_p) \end{pmatrix} \cdot \begin{pmatrix} x_1 \\ \ldots \\ x_n \end{pmatrix} = \begin{pmatrix} e(\lambda_1) \\ \cdots \\ e(\lambda_p) \end{pmatrix} \tag{3.36}$$

where $I_i(\lambda_k)$ is the intensity calculated via Eq. (3.5), n is the number of species, $k = 1 \ldots p$, $p \gg n$ is the number of detector pixels, and $x_1 \ldots x_n$ are the coefficients proportional to number densities of species. This system was solved by a singular value decomposition algorithm and concentrations c_i of the analyzed species were found from the condition of summing all the concentrations to unity

$$(1/F) \cdot \sum\nolimits_i x_i = \sum\nolimits_i c_i = 1 \tag{3.37}$$

where F is the constant parameter that accounts for the optical efficiency of the collection system and plasma density and volume.

This method shows faster convergence than the MC method but, due to condition (3.37), it is still prone to the same problem as the BP (SBP) method: small errors on large concentrations impose large errors on small concentrations. The performance of the method is illustrated by Fig. 3.8 on the example of analysis of minerals [53]. Five elements in six mineral samples were determined at the percentage level of concentrations, with 10–40% errors for high concentrations (>10%) and higher errors of 25–50% (sometimes even >100%), for lower concentrations (0.1–10%).

3.4.2 Single-Standard Calibration Algorithms

With the intention of improving the performance of CF LIBS, some techniques combining CF LIBS and one-point calibration have also been proposed. These techniques, although technically do employ a calibration standard, are still closer

to CF techniques than to conventional calibration techniques because in the end they can provide concentrations for elements without constructing a calibration curve. It is also worth mentioning that providing a single standard with a matrix like other samples is a requirement that can usually be met even in the analytically most challenging cases.

3.4.2.1 Inverse CF LIBS

The single-standard inverse CF LIBS technique was developed in [54], in which a certified sample was used to determine the plasma temperature by iterating its value and minimizing the relative error between the certified c_i^{cert} and calculated c_i concentrations

$$\Delta w_i(T) = \frac{\left|c_i^{\text{cert}} - c_i(T)\right|}{c_i^{\text{cert}}} \tag{3.38}$$

The concentration of element i is calculated by using

$$c_i(T) = n_i M_i / \sum\nolimits_j n_j M_j \tag{3.39}$$

where n_j and M_j are the number densities and atomic masses, correspondingly. The number densities are calculated via Eqs. (3.10) and (3.13) and the mass conservation equation $n_j = n_j^0 + n_j^+$, where n_j^0 and n_j^+ are the number densities of neutral and ionized species, respectively. Hence essentially, the standard is used to train the CF algorithm to give the most accurate estimates of elemental concentrations in the standard and then, assuming the same plasma temperature, CF analysis can be extended to other similar samples and/or elements.

In this method, scaling factor F, which is present in Eq. (3.17), is unnecessary because it cancels out upon taking the ratio in expression (3.39). In contrast to BP (or SBP), this approach allows using a single line per element, provided the line is well chosen. Oppositely, it can be used to preselect lines that yield the most accurate estimate of concentrations in the standard. The method has shown a satisfactory agreement with results of full calibration-based analysis when applied to archeological samples [54]. Its limitation though could be in imposing the temperature determined with the certified sample to other samples with unknown concentrations.

3.4.2.2 One-Point Calibration LIBS

One-point calibration LIBS (OPC-LIBS) was developed in [55]. The idea of this is to correct each point on the BP by an additive factor, which is determined from the BP constructed for a sample with known concentrations. The algorithm is as follows. First, the traditional CF method, Eqs. (3.10)–(3.19), is applied to a standard sample to retrieve approximate concentrations c_s from the BP intercepts at $E_i = 0$; the subscript $s = 1...n$ enumerates elements. Second, a correction

$$y' = y + \Delta y \tag{3.40}$$

is applied to all initial points y on the Boltzmann plane using relations derived based on Eqs. (3.10)–(3.11)

$$\begin{aligned} y_s(\lambda_i) &= \ln\left[\frac{I_s(\lambda_i)}{P_s(\lambda_i)}\right] = \ln\left(\frac{c_s}{U_s}\right) - \frac{E(\lambda_i)}{kT} \\ y'_s(\lambda_i) &= \ln\left[\frac{I_s(\lambda_i)}{P'_s(\lambda_i)}\right] = \ln\left(\frac{c'_s}{U_s}\right) - \frac{E(\lambda_i)}{kT} \end{aligned} \tag{3.41}$$

Here, c'_s are the certified concentrations, $E(\lambda_i)$ is the upper energy of the atomic transition with wavelength λ_i, and $P_s(\lambda_i) = F(\lambda_i)A_i g_i$ and $P'_s(\lambda_i) = F'(\lambda_i)A_i g_i$ are the numeric factors for the original and corrected BPs, correspondingly. Symbols $F(\lambda_i)$, A_i and g_i stand for the numerical factor accounting for the path length and collection efficiency, transition probability, and degeneracy of the upper transition state, respectively. Obviously,

$$\Delta y_s(\lambda_i) = y'_s(\lambda_i) - y_s(\lambda_i) = \ln(c'/c) \tag{3.42}$$

and the numeric factor for the "true" BP, which yields correct concentrations in the certified sample is found from the relation (3.41)

$$P'_s(\lambda_i) = P_s(\lambda_i)e^{-\Delta y_s(\lambda_i)} \tag{3.43}$$

Finally, this factor is applied to correct all points on the Boltzmann plots, which are constructed for unknown samples

$$y''_s(\lambda_i) = \ln\left[\frac{I''_s(\lambda_i)}{P'_s(\lambda_i)}\right] \tag{3.44}$$

where $I''_s(\lambda_i)$ is the integral intensity of the line with central wavelength λ_i of element s from the unknown sample. The application of the OPC-LIBS procedure to the analysis of five bronze samples, four of which were treated as unknowns, yielded a close agreement with the nominal concentrations (Fig. 3.9).

The advantage of this technique is that it disregards possible inaccuracies in transition probabilities thanks to combining factor F and product gA into factor P. This factor is found empirically using the standard sample, which, however, still needs to be compositionally close to analyzed samples to avoid matrix effects as much as possible.

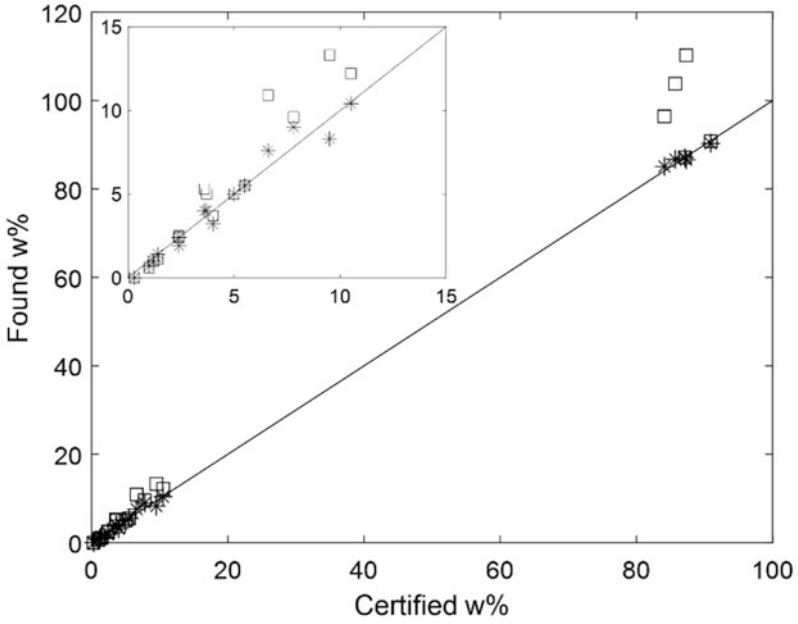

Fig. 3.9 Comparison of the concentrations calculated by OPC-LIBS (stars) and by conventional LIBS (squares) vs. the known concentrations. Inset shows the magnified low concentration range. Data adapted from [55]

3.4.2.3 C-Sigma Technique

The C-Sigma single-point calibration technique by Aragón and Aguilera [56, 57] employs a generalized curve-of-growth approach that embraces lines of various elements at different concentrations. The optical density $\kappa_\lambda l$ in Eq. (3.5), which describes the uniform isothermal plasma at LTE, is factorized into several terms and the whole equation is integrated over the line profile

$$W = B\int_{\text{Line}}\left(1 - e^{-\kappa_\lambda(\lambda)l}\right)d\lambda = B\int_{\text{Line}}\left(1 - e^{-C_s k_s^{(z)} r_s^{(z)}\, NlV_{s,ij}(\lambda)}\right)d\lambda \tag{3.45}$$

Here, B is the blackbody function (3.8) that assumes no λ-dependence across the line profile, C_s is the mole concentration of specie s, N is the total number density of all species in the plasma, l is the pathlength, and $V_s(\lambda)$ is the Voigt profile function for transition $i \rightarrow k$ of element s with a unit integral. Factors $r_s^{(z)}$ relate the total number density of element s to the number densities of its atomic (n_s^0) and ionic (n_s^+) components

$$r_s^0 = \frac{n_s^0}{n_s} = \frac{1}{S+1}$$
$$r_s^+ = \frac{n_s^+}{n_s} = \frac{S}{S+1} \tag{3.46}$$

where $S = \frac{2U_s^+}{n_e U_s^0}\left(\frac{2\pi m_e kT}{h^2}\right)^{3/2} e^{-\frac{\chi_s - \Delta\chi}{kT}}$ is the term in the Saha Eq. (3.13). It follows from (3.46) that $n_s^{(z)} = n_s r_s^{(z)}$. Factors $k_s^{(z)}$ in (3.45) stand for the wavelength- and concentration-independent term in the absorption coefficient, $\kappa_\lambda(\lambda) = k_s^{(z)} n_s^{(z)} V_s(\lambda)$, corrected for stimulated emission

$$k_s^{(z)} = \frac{e^2\lambda_0^2}{4\varepsilon_0 m_e c^2} f_{ik} \frac{g_i e^{-E_i/kT}}{U_s^{(z)}}\left(1 - e^{-\frac{E_k - E_i}{kT}}\right) \tag{3.47}$$

Here, m_e and e are the elementary mass and charge, ε_0 is the permittivity of free space, f_{ik} is the oscillator strength, E_k and E_i are the upper and lower energies of a transition with central wavelength λ_0, and g_i is the degeneracy of the lower transition state. A graph of W/B versus product $C_s k_s^{(z)} r_s^{(z)}$ produces a family of curves for different values of damping parameter, $a = \sqrt{\ln(2)}\Delta\lambda_L/\Delta\lambda_D$, on which the Voigt function depends or, for that matter, for different values of Lorentzian widths $\Delta\lambda_L$ assuming the Doppler width, $\Delta\lambda_D$, to be constant. The authors of [56, 57] noticed that after normalizing both the abscissa and the ordinate of this graph by $\Delta\lambda_L$, the family of curves merges into nearly a single graph.

Furthermore, the absorption coefficient is expressed via the absorption cross-section, $\sigma_{s,i}(\lambda) = \kappa_\lambda(\lambda)/n_{s,i}^{(z)}$, where $n_{s,i}^{(z)}$ is the number density of atoms absorbing at transition $i \to k$, and the quantity $k_s^{(z)} r_s^{(z)}/\Delta\lambda_L$ is interpreted as the line absorption cross section averaged over the line profile. For this to be true, a dubious condition $n_s/n_{s,i}^{(z)} \approx 1$ (i.e., all species of sort s are concentrated at the absorbing level i of ionization state z) must be satisfied:

$$\sigma_l \equiv \overline{\sigma_{s,\ i}^{(z)}} = \frac{1}{\Delta\lambda_L}\int_{\text{Line}} \sigma_{s,i}^{(z)}(\lambda)d\lambda = \frac{1}{\Delta\lambda_L}\int_{\text{Line}} \frac{\kappa_\lambda(\lambda)}{n_{s,i}^{(z)}}d\lambda$$
$$= \frac{n_s k_s^{(z)} r_s^{(z)}}{\Delta\lambda_L n_{s,i}^{(z)}}\int_{\text{Line}} V_s(\lambda)d\lambda = \frac{n_s}{n_{s,i}^{(z)}}\frac{k_s^{(z)} r_s^{(z)}}{\Delta\lambda_L} \approx \frac{k_s^{(z)} r_s^{(z)}}{\Delta\lambda_L} \tag{3.48}$$

Strictly speaking, the expression $\frac{1}{\Delta\lambda_L}\int_{\text{Line}}\sigma_{s,i}^{(z)}(\lambda)d\lambda$ represents the average absorption cross-section only if the integration is taken over the interval $\lambda_0 \pm \Delta\lambda/2$ and not over the whole line profile. Then, in the optically thin limit, $\kappa_\lambda(\lambda)l \ll 1$, Eq. (3.45) normalized by $\Delta\lambda_L$ yields

$$F(C_s\sigma_l) \equiv \frac{W}{B\Delta\lambda_L} = \frac{C_s k_s^{(z)} r_s^{(z)} Nl}{\Delta\lambda_L}\int_{\text{Line}} V_{s,j}(\lambda)d\lambda = C_s\sigma_l\, Nl \tag{3.49}$$

The graph of $W/B\Delta\lambda_L$ vs $C_s\sigma_l$ is dubbed a "C-Sigma" graph and because it is not specific to an element, it can be considered as a multi-element calibration curve,

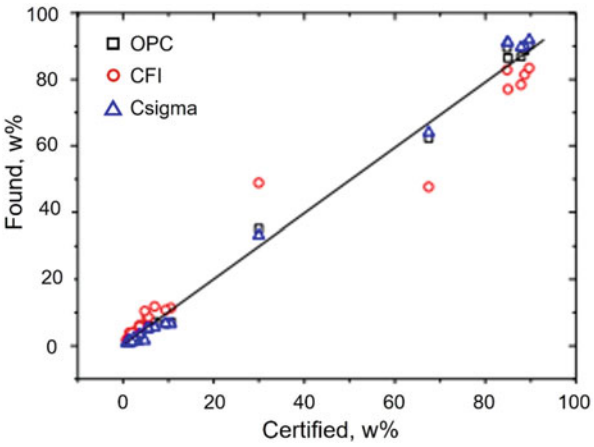

Fig. 3.10 Comparison of the predictions of the one-point calibration (OPC), calibration-free inverse (CFI), and C-Sigma (Cσ) techniques versus the nominal concentration of elements Cu, Zn, and Sn in brass samples. Adapted from [58]

which is valid for different spectral lines of different elements under the assumption of a weak-to-moderate self-absorption. The latter condition puts quite a severe restriction on a choice of spectral lines that may be suitable for a C-Sigma analysis. Unfortunately, the authors of [56, 57] do not provide an explicit form of function $F(C_s\sigma_l)$ for the optically thick case.

The method suggests finding the plasma temperature from the linear part of the C-Sigma graph (as with the conventional Boltzmann plot) and plasma electron density from the Stark broadening of a suitable line via Eq. (3.16). Then, knowing the concentrations, the cross-section σ_l is calculated via Eqs. (3.46–3.48) while the unknown parameter Nl and the other, instrumental parameter (omitted in Eq. (3.45) for simplicity) are calculated in an iterative manner by best fitting the calculated and experimental entries in Eq. (3.49). Having just one standard, the unknown parameters are determined from the $C\sigma$-graph constructed for elements with known concentrations and then, on a second step, the concentrations in unknown samples are determined by adjusting the corresponding $C\sigma$-values such that experimental values of $W/B\Delta\lambda_L$ hit the already known $C\sigma$-graph.

3.4.2.4 Comparison of Single-Standard Techniques

A direct comparison of the three single-standard algorithms was performed in [58] for the case of analysis of brass samples. It was found that the OPC technique performs best with 15% average error against 19% error for the S-Sigma and 53% error for the CF-inverse techniques. These results are graphically shown in Fig. 3.10.

3.5 Summary

Calibration-free algorithms compete with calibration-based ones; however, the latter are usually more reliable and preferred if high accuracy and precision are needed. Such the preference stems from the inherent deficiency of all calibration-free models, which require the transient laser-induced plasma to be stationary, uniform,

isothermal, and not too dense optically. On the other hand, calibration-based models also prescribe a certain type of a behavior to a calibration plot (e.g., linear or a curve-of-growth type) that also may result in errors when interpolating points between calibration grid points. In this respect, multivariate standard-based calibration approaches, either linear or non-linear, can be more robust.

Meanwhile, calibration-free algorithms have a high potential for further development through the improvement of underlying plasma models. Considering the ever-increasing computer power that becomes available every year (e.g., multi-core multi-thread central processing units and powerful graphical processing units), more complex models which describe a dynamic, non-uniform, optically thick plasma, may become feasible to simulate. In this respect, direct stochastic methods, like the Monte Carlo CF LIBS described above, can be very promising; partly because they do not require solving ill-posed problems such as line deconvolution or correction for self-absorption.

Very promising are also the methods with the use of a minimum number of standards, one being the limit. Although not truly calibration-free, calibration with just one standard significantly improves the results of CF LIBS analyses.

References

1. Zel'dovich YB, Raizer YP. Physics of shock waves and high-temperature hydrodynamic phenomena. Dover; 2002. p. 130.
2. Lochte-Holtgreven W. Plasma Diagn. 1968; Ch. 1
3. Griem HR. Plasma spectroscopy. McGraw-Hill; 1964.
4. Konjević N, Dmitrievi ć MS, Wiese WL. Experimental stark widths and shifts for spectral lines of neutral atoms (A critical review of selected data for the period 1976 to 1982). J Phys Chem Ref Data Monogr. 1984;13:619.
5. Konjević N, Lesage A, Fuhr JR, Wiese WL. Experimental stark widths and shifts for spectral lines of neutral and ionized atoms (A critical review of selected data for the period 1989 through 2000). J Phys Chem Ref Data Monogr. 2002;31:819.
6. Ciucci A, Corsi M, Palleschi V, Rastelli S, Salvetti A, Tognoni E. New procedure for quantitative elemental analysis by laser-induced plasma spectroscopy. Appl Spectrosc. 1999;53:960.
7. El Sherbini AM, El Sherbini TM, Hegazy H, Cristoforetti G, Legnaioli S, Palleschi V, Pardini L, Salvetti A, Tognoni E. Evaluation of self-absorption coefficients of aluminum emission lines in laser-induced breakdown spectroscopy measurements. Spectrochim Acta B. 2005;60:1573.
8. Li T, Hou Z, Fu Y, Yu J, Gu W, Wang Z. Correction of self-absorption effect in calibration-free laser-induced breakdown spectroscopy (CF-LIBS) with blackbody radiation reference. Anal Chim Acta. 2019;1058:39.
9. Bulajic D, Corsi M, Cristoforetti G, Legnaioli S, Palleschi V, Salvetti A, Tognoni E. A procedure for correcting self-absorption in calibration free laser induced breakdown spectroscopy. Spectrochim Acta B. 2002;57:339.
10. Gornushkin IB, Völker T, Kazakov AY. Extension and investigation by numerical simulations of algorithm for calibration-free laser induced breakdown spectroscopy. Spectrochim Acta B. 2018;147:149.
11. Praher B, Palleschi V, Viskup R, Heitz J, Pedarnig JD. Calibration free laser-induced breakdown spectroscopy of oxide materials. Spectrochim Acta B. 2010;65:671.

12. Tognoni E, Cristoforetti G, Legnaioli S, Palleschi V. Calibration-free laser-induced breakdown spectroscopy: state of the art. Spectrochim Acta B. 2010;65:1.
13. Hahn DW, Omenetto N. Laser-induced breakdown spectroscopy (LIBS), part II: review of instrumental and methodological approaches to material analysis and applications to different fields. Appl Spectrosc. 2012;66:347.
14. Bauer AJR, Buckley SG. Novel applications of laser-induced breakdown spectroscopy. Appl Spectrosc. 2017;7:553.
15. Hu Z, Zhang D, Wang W, Chen F, Xu Y, Nie J, Chu Y, Guo L. A review of calibration-free laser-induced breakdown spectroscopy. TrAC Trends Anal Chem. 2022;152:116618.
16. Radziemski LJ, Loree TR, Cremers DA, Hoffman NM. Time resolved laser-induced breakdown spectrometry of aerosols. Anal Chem. 1983;55:1246.
17. Simeonsson JB, Miziolek AW. Time-resolved emission studies of ArF laser-produced microplasmas. Appl Optics. 1993;32:939.
18. Aguilera JA, Aragon C. Characterization of a laser-induced plasma by spatially resolved spectroscopy of neutral atom and ion emissions. Comparison of local and spatially integrated measurements. Spectrochim Acta B. 2004;59:1861.
19. Yalçin S, Crosley DR, Smith GP, Faris GW. Influence of ambient conditions on the laser air spark. Appl Phys B Lasers Opt. 1999;68:121.
20. Milan M, Laserna JJ. Diagnostics of silicon plasmas produced by visible nanosecond laser ablation. Spectrochim Acta B. 2001;56:275.
21. J. Dubrovkin, Mathematical processing of spectral data in analytical chemistry: a guide to error analysis, Cambridge scholars; 2018.
22. Morháč M, Matoušek V. Complete positive deconvolution of spectrometric data. Digit Signal Proc. 2009;19:372.
23. Zimmermann B, Kohler A. Optimizing Savitzky-Golay parameters for improving spectral resolution and quantification in infrared spectroscopy. Appl Spectrosc. 2013;67:892.
24. Lasch P. Spectral pre-processing for biomedical vibrational spectroscopy and microspectroscopic imaging. Chemom Intel Lab Syst. 2012;117:100.
25. Chen G, Qian S-E. Denoising and dimensionality reduction of hyperspectral imagery using wavelet packets, neighbor shrinking and principal component analysis. Int J Remote Sens. 2009;30:4889.
26. Zhang B, Sun L, Yu H, Xina Y, Cong Z. Wavelet denoising method for laser-induced breakdown spectroscopy. J Anal At Spectrom. 2013;28:1884.
27. Coleman TF, Li Y. An interior, trust region approach for nonlinear minimization subject to bounds. SIAM J Optim. 1996;6:418.
28. Moré JJ. In: Watson GA, editor. lecture notes in mathematics 630 The Levenberg-Marquardt algorithm: implementation and theory. Numerical analysis. Springer; 1977. p. 105.
29. Surmick DM, Parigger C. Empirical formulae for electron density diagnostics from H_α and H_β line profiles, international review of atomic and molecular. Physics. 2014;5:73.
30. Mercadier L, Hermann J, Grisolia C, Semerok A. Diagnostics of nonuniform plasmas for elemental analysis via laser-induced breakdown spectroscopy: demonstration on carbon-based materials. J Anal At Spectrom. 2013;28:1446.
31. Kolmhofer PJ, Eschlböck-Fuchs S, Huber N, Rössler R, Heitz J, Pedarnig JD. Calibration-free analysis of steel slag by laser-induced breakdown spectroscopy with combined UV and VIS spectra. Spectrochim Acta B. 2015;106:67.
32. Tognoni E, Cristoforetti G, Legnaioli S, Palleschi V, Salvetti A, Mueller M, Panne U, Gornushkin I. A numerical study of expected accuracy and precision in calibration-free laser-induced breakdown spectroscopy in the assumption of ideal analytical plasma. Spectrochim Acta B. 2007;62:1287.
33. Lednev VL, Pershin SM. Plasma stoichiometry correction method in laser-induced breakdown spectroscopy. Laser Phys. 2008;18:1.
34. Sun L, Yu H. Correction of self-absorption effect in calibration-free laser-induced breakdown spectroscopy by an internal reference method. Talanta. 2009;79:388.

35. Herrera K, Tognoni E, Smith BW, Omenetto N, Winefordner JD. Semi-quantitative analysis of metal alloys, brass, and soil samples by calibration-free laser-induced breakdown spectroscopy: recent results and considerations. J Anal At Spectrom. 2009;24:413.
36. Burakov VS, Kiris VV, Naumenkov PA, Raikov SN. Calibration-free laser spectral analysis of glasses and copper alloys. J Appl Spectrosc. 2004;71:740.
37. Fornarini L, Colao F, Fantoni R, Lazic V, Spizzicchino V. Calibration analysis of bronze samples by nanosecond laser induced breakdown spectroscopy: a theoretical and experimental approach. Spectrochim Acta B. 2005;60:1186.
38. Corsi M, Cristoforetti G, Palleschi V, Salvetti A, Tognoni E. A fast and accurate method for the determination of precious alloys caratage by laser induced plasma spectroscopy. Eur Phys J D. 2001;13:373.
39. Colao F, Fantoni R, Lazic V, Paolini A, Fabbri F, Ori GG, Marinangeli L, Baliva A. Investigation of LIBS feasibility for in situ planetary exploration: an analysis on Martian rock analogues. Planet Space Sci. 2004;52:117.
40. Sallé B, Lacour JL, Mauchien P, Fichet P, Maurice S, Manhes G. Comparative study of different methodologies for quantitative rock analysis by laser-induced breakdown spectroscopy in a simulated Martian atmosphere. Spectrochim Acta B. 2006;61:301.
41. Wang L, Zhang C, Feng Y. Controlled calibration method for laser induced breakdown spectroscopy. Chin Opt Lett. 2008;6:5.
42. De Giacomo A, Dell'aglio M, De Pascale O, Longo S, Capitelli M. Laser induced breakdown spectroscopy on meteorites. Spectrochim Acta B. 2007;62:1606.
43. Pandhija S, Rai AK. In situ multielemental monitoring in coral skeleton by CF-LIBS. Appl Phys B Lasers Opt. 2009;94:545.
44. Taleb A, Motto-Ros V, Carru MJ, Axente E, Craciun V, Pelascini F, Hermann J. Measurement error due to self-absorption in calibration-free laser-induced breakdown spectroscopy. Anal Chim Acta. 2021;1185:339070.
45. Shabanov SV, Gornushkin IB. Geometrical effects in data collection and processing for calibration-free laser-induced breakdown spectroscopy. J Quant Spectrosc Rad Tranf. 2014;2018:190.
46. Demidov A, Eschlbck-Fuchs S, Kazakov AY, Gornushkin IB, Kolmhofer PJ, Pedarnig JD, Huber N, Heitz J, Schmid T, Rssler R, Panne U. Monte Carlo standardless approach for laser induced breakdown spectroscopy based on massive parallel graphic processing unit computing. Spectrochim Acta. 2016;125:97.
47. I.B. Gornushkin, A Ya Kazakov, T. Völker, Calibration-free Monte Carlo method for laser induced breakdown spectroscopy, (2022). in preparation
48. Herrera KK, Tognoni E, Gornushkin IB, Omenetto N, Smith BW, Winefordner JD. Comparative study of two standard-free approaches in laser-induced breakdown spectroscopy as applied to the quantitative analysis of aluminum alloy standards under vacuum conditions. J Anal At Spectrom. 2009;24:426.
49. Pedarnig JD, Kolmhofer P, Huber N, Praher B, Heitz J, Rössler R. Element analysis of complex materials by calibration-free laser-induced breakdown spectroscopy. Appl Phys A Matter. 2013;112:105.
50. Gornushkin IB, Shabanov SV, Merk S, Tognoni E, Panne U. Effects of nonuniformity of laser induced plasma on plasma temperature and concentrations determined by the Boltzmann plot method: implications from plasma modeling. J Anal At Spectrom. 2010;25:1643.
51. Hermann J, Gerhard C, Axente E, Dutouquet C. Comparative investigation of laser ablation plumes in air and argon by analysis of spectral line shapes: insights on calibration-free laser-induced breakdown spectroscopy. Spectrochim Acta B. 2014;100:189.
52. Wester R, Noll R. Neuristic modeling of spectral plasma emission for laser induced breakdown spectroscopy. J Appl Phys. 2009;106:123302.
53. Yaroshchyk P, Body D, Morrison RJS, Chadwick BL. A semi-quantitative standardless analysis method for laser-induced breakdown spectroscopy. Spectrochim Acta B. 2006;61:200.

54. Gaudiuso R, Dell'Aglio M, De Pascale O, Santagata A, De Giacomo A. Laser-induced plasma analysis of copper alloys based on local thermodynamic equilibrium: an alternative approach to plasma temperature determination and archeometric applications. Spectrochim Acta B. 2012;74-75:38.
55. Cavalcanti GH, Teixeira DV, Legnaioli S, Lorenzetti G, Pardini L, Palleschi V. One-point calibration for calibration-free laser-induced breakdown spectroscopy quantitative analysis. Spectrochim Acta B. 2013;87:51.
56. Aragón C, Aguilera JA. CSigma graphs: a new approach for plasma characterization in laser-induced breakdown spectroscopy. J Quant Spectrosc Rad Transfer. 2014;149:90.
57. Aragón C, Aguilera JA. Quantitative analysis by laser-induced breakdown spectroscopy based on generalized curves of growth. Spectrochim Acta B. 2015;110:124.
58. Grifoni E, Legnaioli S, Lorenzetti G, Pagnotta S, Poggialini F, Palleschi V. From calibration-free to fundamental parameters analysis: a comparison of three recently proposed approaches. Spectrochim Acta B. 2016;124:40.

State-of-the-Art Analytical Performance

4

Gábor Galbács, Dávid Jenő Palásti, and Patrick Martin Janovszky

Laser-induced breakdown spectroscopy (LIBS) has been around for about six decades. Although in the early years it was more of a curiosity than an analytical method due to some technical complications, but since the 1990s it has evolved and spread slowly but steadily and by today it has become the established versatile and powerful analytical method known by many spectroscopists. LIBS enjoys a strong interest from not only researchers active in fundamental research, but also in many industrial, medical, and other technical applications, some of which are very special. Naturally, over the course of so many years, a lot of effort have been made, not unsuccessfully, to improve the analytical performance of LIBS. This chapter is dedicated to this progress as it attempts to briefly account for the main efforts and current state of the art of LIBS analytical performance.

Needless to say that many of the fields touched upon are interrelated, e.g., signal enhancement also supports achieving a better spatial resolution in elemental imaging or lower limits of detection in quantitative analysis, and some improvements are not specific to LIBS but are the products of an adaptation of technologies and methodologies also employed in other spectroscopies. However, all these improvements are seen as contributions toward the same goal: advancing analytical LIBS spectroscopy and hence will be briefly covered in this chapter. Please note that due to the large variety and abundant literature on related topics, only a description of the general approaches and an outline of achievable best performance will be provided, without attempting to be exhaustive. The focus is on typical LIBS systems that use nanosecond duration laser pulses. The content of the chapter is organized according to the main analytical merits of LIBS. Five of these characteristics are discussed: signal enhancement (limits of detection), dynamic range, signal repeatability and correction, spatial resolution, and measurement distance. The intention of

G. Galbács (✉) · D. J. Palásti · P. M. Janovszky
Department of Inorganic and Analytical Chemistry, University of Szeged, Szeged, Hungary
e-mail: galbx@chem.u-szeged.hu

G. Galbács (ed.), *Laser-Induced Breakdown Spectroscopy in Biological, Forensic and Materials Sciences*, https://doi.org/10.1007/978-3-031-14502-5_4

the authors is to provide tentative information about the methodologies and the overall performance. Readers interested in details are referred to specific reviews.

4.1 Signal Enhancement (Limits of Detection)

Several physical approaches have been described in the literature which aim at the improvement of the sensitivity of LIBS analysis by enhancing the analytical signal. Of course, the final goal of these efforts is to improve the limits of detection, by enhancing the signal-to-noise ratio (S/N). General overviews of these signal enhancement approaches have been recently provided by Li et al. [1] and Fu et al. [2]. A common aspect of all these techniques is that they either employ external conditioning of the LIB plasma by some physical means, or convert the sample into another phase or form that is easier to break down. Please note that simple sample preconcentration approaches that are not LIBS-specific (e.g., enrichment of liquid samples by extraction or partial evaporation) are not covered.

4.1.1 Plasma Conditioning by Means Other than Lasers

4.1.1.1 Ambient Gas

Most LIBS experiments are performed in air at atmospheric pressure for obvious practical reasons, but the effect of the gas environment (ambient gas composition and pressure) on the LIBS analytical signal has long been studied. This research has been fueled by not only fundamental research interest but also by the needs of special applications including, e.g., space exploration or monitoring of industrial equipment.

Results generally indicate that lowering the pressure of the surrounding gas, from 760 to a few Torr, usually increases the LIBS signals, improves the S/N, and increases the resolution of the spectral features (as a result of less pressure and Stark broadening of spectral lines), and less ablation debris is deposited around craters, which can also contribute to a better spatial resolution in elemental imaging. These advantageous effects are caused by the combination of several processes, which can be best exploited by ns laser pulses. Lowering the pressure causes a higher rate of plasma expansion, which in turn gives rise to less plasma shielding, resulting in a significantly increased ablation rate and longer plasma lifetime. In terms of ambient gas quality, mainly the use of nitrogen, oxygen, helium, argon, neon, and carbon dioxide have been tested in the literature. These alternative ambient gases have different thermal conductivity, ionization energy and produce different collision rates, thus strongly affect the ablation and excitation processes and the temporal evolution of plasma. The use of noble gases have the added benefit of providing an inert atmosphere which can help lowering spectral interferences (e.g., produced by absorption of molecular gases forming in the ablation plume [3]). Although there is some dispute in the LIBS literature with respect to what the most beneficial ambient (or buffer) gas is, but generally argon and helium are the two most often proposed

gases. Typically LIBS signals are reported to be generally boosted by a factor of 2–5 in these noble gases; however, most recently a He/Ne/Ar mixture was reported to provide as much as a factor of 9 improvement [4]. The downside of this approach is that it necessitates the use of a gas-controlled ablation chamber, which complicates the setup and its application is usually limited to smaller samples and the laboratory. One workaround to this is the use of synchronized buffer gas jets to just flush the sample surface when and where the laser pulse strikes [5]. A thematic review on the topic was written by Effenberger and Scott [6].

4.1.1.2 Sample Heating

A more or less obvious approach to increase the temperature of the LIB plasma and hence the emission signals is to apply (contact) heating to the solid sample. This increases the ablation rate as it lowers the ablation threshold, thus more laser pulse energy will remain to heat the plasma. This approach can be employed only to non-volatile (refractory) samples without risking a fractionation of elements. The same reason also dictates that typically a maximum of a few hundred of degrees sample temperature elevation can be used, which generally leads to a modest signal enhancement of up to a factor of 5. The effect has been studied for different samples, including but not limited to glasses [7], soils [8], and alloys [9, 10], and was found to vary in magnitude from element to element.

4.1.1.3 Spatial Confinement

The spatial confinement of the LIB plasma is one of the simplest signal enhancement techniques. In this approach, the plasma plume, and the shockwave that accompanies it under ambient conditions, is not allowed to expand freely, but is constrained in a semi-closed cavity with rigid walls. Parallel plates, hemispherical, cylindrical, and rectangular cavity geometries have been tested [11–15], and the hemispherical one was found to be optimal. The cavities can be made of different materials (e.g., quartz, metal, PTFE), often with polished/reflective internal walls in order to facilitate light collection, and typically have a few millimeters internal size. Under these conditions, the expanding shockwave is reflected back from the wall of the cavity and its pressure will perform work on the plasma (compresses it) thereby increasing its temperature, which leads to signal enhancement, up to a factor of about 10. The timing of the signal detection has to be carefully adjusted to match the timescale of the effect, which is determined by the size of the cavity and the rate of propagation of the shockwave. Relative signal enhancements usually can only be realized in the μs integration time regime. On a related note, it is also hypothesized that when multiple laser pulses are delivered to the sample in a regular LIBS experiment, e.g., in depth-resolved measurements, then the ablation crater itself also provides a limited plasma confinement, thereby leading to some signal enhancement for later coming pulses [16, 17]. In general, an easy-to-see nuisance with the confinement signal enhancement approach is the necessity to clean the cavity after each trace analysis.

4.1.1.4 Magnetic Field

The application of an external magnetic field aligned with the surface normal exerts Lorentz force on the movement of electrons and ions, which slows down plasma expansion, causing a reduction of the volume of the plume ("magnetic confinement"). This leads to an increased electron concentration, higher collision frequency, higher plasma temperature, and eventually higher emission intensities. The magnitude of the effect scales with the strength of the magnetic field, thus it is usually done using a field strength of at least 0.5–0.6 T. The easiest way to apply this signal enhancement approach is to use a ring magnet, which is placed on the surface of the solid sample, centered around the analytical spot. This comes with the added benefit of providing both spatial confinement and magnetic field enhancement. The reported overall signal enhancements amount to a factor of max. 6–8 for ionic lines (neutral lines are less intensified) [18, 19], although as it was pointed out, this could, in principle, be further enlarged by employing an even stronger static magnetic field or by using a pulsed field [20, 21]. All in all, this signal enhancement approach is not very practical, due to similar reasons as the ones outlined for spatial confinement, although solenoid-based field application is theoretically possible. Problems with field strength and orientation repeatabilities also do not help its application. It was also reported that with ferroelectric samples, it may even produce decreased signals [22].

4.1.1.5 Microwave Irradiation

The lifetime of the LIB plasma can be significantly increased, and its line emission enhanced, if the plasma is exposed to microwave radiation as it can significantly increase the rate of collisions mediated by electrons. This leads to a strong signal enhancement if time-integrated detection is used and the gate width (integration time) is adjusted accordingly. Studies on various solid samples and several elemental as well as molecular analytes indicate that as much as one or two orders of magnitude signal improvement can be achieved by this approach (e.g., [23–25]). Please note that this, similarly to several other signal enhancement techniques, only translates to a significantly smaller level of improvement in terms of limits of detection, as the background (noise) is also enhanced. Recently it has been also shown that microwave-assisted LIBS can also give rise to a decrease of self-absorption effects thereby extending the dynamic range [26]. Obviously, adding a pulsed, focused kW microwave generator to the LIBS setup largely complicates it, therefore this is one of the less popular, although very effective, signal enhancement techniques. A way to mitigate the associated technical nuisances was provided in a study by Tampo et al. [27], who demonstrated that remote microwave-assisted LIBS analysis is also possible, if a remotely operated, but sample-adjacent wired loop antenna delivers the microwave pulse.

4.1.1.6 Electrical Discharge Assistance

A high voltage electrical discharge (spark) ignited between two electrodes through the laser ablation plume in a LIBS experiment can also be employed to boost the emission signal intensity. In this approach, the spark discharge powered by a high

voltage capacitor re-excites (heats further) the microplasma thereby elongating the plasma lifetime and increasing the emission. For this effect to work, the operation of the spark and laser have to be properly synchronized. As the onset of a spark discharge alone is a random process, thus the practical realization of spark-assisted LIBS requires a so-called laser-triggered spark gap, in which the formation of the LIB plasma itself triggers the ignition of the spark discharge. The presence of charged particles in the plasma significantly lowers the breakdown voltage of the electrode gap, thus as soon as the LIB plasma on the sample is formed, the high voltage discharge strikes [28]. An enhancement of up to two orders of magnitude in the signal-to-noise ratio can be achieved this way. It was found that the signal enhancement is greater for ionized species than for neutrals and the emission signal also increased with the discharge voltage and laser fluences [29]. An effect of a similar magnitude was also demonstrated to work in steady-state and pulsed glow discharges [30], where the reduced pressure also contributes to the improvement of performance.

4.1.1.7 Utilization of Nanoparticles

Applying plasmonic (e.g., Ag or Au) nanoparticles (NPs) deposited on the surface of a solid sample, or preparing a substrate with similar nanoparticles (or nanostructures) and depositing and drying a liquid sample on top of it is another widely researched approach for LIBS signal enhancement. This approach (nanoparticle-enhanced LIBS, NELIBS) has been proposed de Giacomo et al. [31, 32] and his group is also the most active and innovative in its application and in the exploration of the underlying mechanism. It has been established so far that this way, under optimized conditions, up to two orders of magnitude emission signal enhancement is possible for solids (for liquids, the enhancement is smaller). The effect is attributed to electromagnetic field enhancement due to the formation and coupling of surface plasmons on the NPs formed upon the approach of the high-intensity laser pulse, which in turn results in a higher sample ablation rate, higher plasma temperature, and multiple plasma ignition points, which all contribute to the lowering of the detection limit. It was also found that there is a certain optimum surface NP mass concentration and interparticle distance in order to facilitate the coupling of the surface plasmons but to avoid their aggregation/stacking. Furthermore, the laser fluence should also be kept low, so as to keep the NPs in play as long as possible during ablation and to include as many as possible NPs in the process; as a result of this, millimeter range spot sizes are often used in NELIBS.

It follows from the above that the proper NP deposition is a crucial step of the technique, nevertheless, good results are claimed to be obtainable by a simple sample preparation procedure (for solid samples), which involves the creation of a large diameter, shallow crater in the substrate and then depositing a droplet of NP suspension into the crater, followed by drying. The magnitude of the effect also depends on the conductivity of the sample/substrate [33]. It is also worth mentioning that nanostructured substrates (e.g., modified commercial SERS substrates) have also been successfully used for liquid NELIBS analysis [34] and that most recently, strong signal LIBS enhancement was also observed for gas samples which contained

NPs suspended in them [35]. Further information about the NELIBS approach can also be found in Chap. 8 of this book.

4.1.2 Plasma Conditioning by Additional Laser Pulses

4.1.2.1 Double-Pulse and Multi-Pulse LIBS

LIBS analytical signals can also be boosted if not only one but two coaxial laser pulses, with some interpulse time delay between them, are used. According to this concept, if the second pulse arrives within the lifetime of the plasma generated by the first pulse, the second pulse will be efficiently absorbed by the plasma and rekindle it, thereby increasing the emitted, time-integrated analytical intensities. Spectrum acquisition usually starts after the arrival of the second pulse, with some delay. This double-pulse LIBS (DP-LIBS) concept has been actually proposed quite early in the development of LIBS [36, 37], but it could not be routinely realized for several decades due to technical difficulties. Today, owing to the wide availability of reliable, well synchronizable solid-state laser sources, DP-LIBS is a widely accepted and used LIBS technique, which provides substantial (up to 50–60 times) enhancement of signal intensities. This translates into at least an order of magnitude reduction in the limits of detection. Improvements in the linear dynamic range have also been observed.

Detailed studies revealed that the mechanism behind the signal enhancement is usually not purely based on plasma reheating, but also on that (i) the second co-axial laser pulse reaches the sample surface and causes sample ablation, thus contributing with ablated matter to the plasma and (ii) the second laser pulse reaches a preheated sample surface. Without going into much detail here, it is just worth mentioning that laser parameters, especially pulse duration and laser wavelength but also pulse energy ratios, are of paramount importance in DP-LIBS. This is due to the fact that plasma laser heating was found to be proportional with λ^3 and that plasma lifetimes, and thus the required interpulse delays, are also orders of magnitude shorter with, e.g., fs pulses than with the conventional ns pulses (nanoseconds instead of microseconds). Some research even indicates that combining short second pulses with exceptionally long first pulses (e.g., tens of μs or even ms) provides specific advantages [38]. Details of DP-LIBS processes and technicalities can be found in a large number of scientific papers, review papers and book chapters dedicated to this technique (e.g., [39–42]).

DP-LIBS was found to be particularly useful in bulk liquid sample analysis or when solid samples submerged in water are analyzed. The reason for this is that in a liquid environment (mainly water), the formation of plasma with a single laser pulse is largely hindered by the much lower compressibility and far better heat conductivity of a liquid than those of a surrounding gas atmosphere (e.g. air). This results in substantially increased breakdown thresholds, shorter plasma lifetime, and lower plasma temperature, not to mention the fluctuations in focusing and light collection efficiencies of the setup caused by the liquid body. As a consequence of these effects, the performance of conventional (single pulse) LIBS is largely hampered; which

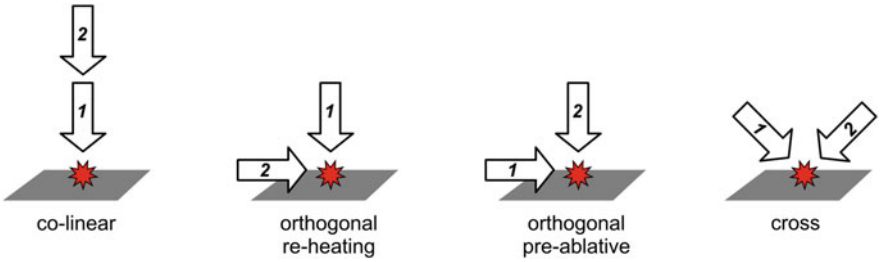

Fig. 4.1 Common double-pulse LIBS (DP-LIBS) beam configurations. Numbers indicate the order in which the pulses reach the sample

manifests in poor LODs and large signal scatters. In the case of DP-LIBS, conditions can be tuned so that the plasma can expand in the bubble of vapors generated by the first pulse, thus the analytical performance will be significantly improved compared to the single pulse case [43–45].

It is also worth mentioning that although colinear DP-LIBS is the most practical and common, but other variants also exist and are used, mostly in fundamental studies. These include the orthogonal and cross arrangements also seen in Fig. 4.1, which all provide similar signal enhancement, but utilize different laser-sample and laser–plasma interactions. The importance of the orthogonal pulse configuration is that only one of the pulses is ablative. In the pre-heating configuration, the signal enhancement is caused by the sample heating achieved by the first pulse, whereas in the pre-ablative combination, the second pulse heats/breaks down the plume produced by the first pulse. The number of combinations, in terms of beam configurations and laser parameters, is quite large, hence the DP-LIBS scene is diverse.

Last, but not least, the multi-pulse LIBS (MP-LIBS) technique should also be mentioned. This principally works by the same concept as collinear DP-LIBS, but uses more than two pulses (e.g., up to 11) and a time-integrated detection across the bursts of several laser pulses. This approach can achieve over an order of magnitude lower limits of detection and several times better signal repeatability than DP-LIBS, for spectral lines with small and medium excitation energy (<7 eV). The dynamic range is also expanded substantially (the upper concentration level in some cases even reaching 100%) by generating plasma conditions that reduce self-absorption. The MP-LIBS approach was first proposed by Piepmeyer and Malmstadt [36], but was only catching on onward from about 2000, and since then an increasing number of studies have explored it (e.g., [46–49]). The technical appeals of the MP-LIBS include that it has far more permitting synchronization criteria than DP-LIBS: it can be done using an ms integration time CCD spectrometer and a free-running high repetition rate laser (e.g., DPSS or fiber laser) or pulse bursts from a passively Q-switched solid-state laser source.

4.1.2.2 Resonance-Enhanced LIBS

It is also possible to use plasma modification with a secondary pulse from a tunable laser (e.g., dye laser) directed into the plasma plume in a colinear or near colinear configuration. In this, so-called resonance-enhanced LIBS (RE-LIBS), approach, the wavelength of the second pulse is tuned to a resonant atomic transition of one of the large concentration matrix elements (e.g., Fe in a steel matrix, or Al in an aluminum alloy, etc.), thereby generating an efficient plasma heating effect. A higher plasma temperature then leads to an increased emission signal for the analytes. A factor of about five signal enhancement was documented for several sample types. The RE-LIBS approach was explored in detail almost exclusively by Cheung and co-workers (e.g., [50–53]). In spite of its need for a costly and bulky additional tunable laser source, the RE-LIBS has the obvious advantage over to the similar LIBS-LIF (described in the next section) that it has multielement capability; in the same matrix (e.g., range of alloy samples) several elements can be determined without the need for re-tuning the laser.

4.1.2.3 LIBS-LIF

In some sense, the LIBS-laser induced fluorescence (LIBS-LIF) technique has a similar premise to that of RE-LIBS in as much as a second laser pulse is used for further excitation. An important difference is however that here the wavelength of the second pulse is tuned to a transition of the analyte. The experimental setup typically follows an orthogonal arrangement. It is important to see that the ablative first pulse generates a plasma plume, which only provides the cloud of free analyte atoms (e.g., the plume is an atom source), whereas excitation from the second laser pulse generates laser-induced fluorescence. Hence the name, LIBS-LIF. The approach has the flexibility that not only ground state atoms, but also excited ones can be measured. The analytical capabilities of LIBS-LIF have been successfully demonstrated in several configurations, for different sample types and analytes and generally it was capable to produce sub-ppm limits of detection for various metallic elements (e.g., [54–56]), which is at least a two orders of magnitude improvement over SP-LIBS. This means that it is a highly effective signal enhancement approach; however, it requires a bulky additional tunable laser source, and does not provide multielement capability, as the secondary laser needs to be re-tuned for each and every analyte.

4.1.3 Phase Conversion Approaches

Liquid samples are very common in analytical practice. They are easy to manipulate in the laboratory (e.g., to homogenize, mix, dose, enrich, etc.) and are also the result of many sample preparation steps in atomic spectroscopy, therefore their liquid LIBS analysis has always been investigated extensively in the literature. The fact that LIBS utilizes a focused laser beam with a focal spot size in the μm range, also has moved the imagination of researchers, as theoretically offers microanalysis on μL-range (or even nL-range) volume liquid samples. However, LODs in bulk liquid

sample analysis are hampered by conditions much more unfavorable for the formation of a laser-induced breakdown plasma in liquids than on solids, as it was briefly alluded to above in Sect. 4.1.2.1. Consequently, intense research efforts have been going into converting liquid samples to other, easier to analyze phases.

Aerosol and liquid jet generation from liquids can be done by using nebulizers, which are mature constructions widely used in atomic spectroscopy. This conversion can help to boost LIBS liquid analysis, because the plasma can form on the surface of liquid droplets or narrow streams, therefore the plasma formation and its expansion can take place in air, under conditions more or less similar to solid samples. Examples of the use of this approach are present widely in LIBS literature, e.g., in refs. [57–60] or more recently in [61]. Significantly improved analytical performance, compared to direct bulk liquid analysis, was achieved this way, however at the expense of making the experimental setup cumbersome. It can also be mentioned that a direct comparison of LIBS performance and practicality with conventional atomic spectroscopy methods (e.g., ICP-OES, ICP-MS, GFAAS) in this approach is the most difficult to avoid and in spite of all efforts, LIBS hardly ever comes out as the winner from this comparison.

The conversion of liquids to solids is perhaps the most popular of all conversion techniques, due to that it is temptingly simple. Many alternatives of this have been successfully tested, including freezing (e.g., [62]), evaporation to dryness on a solid substrate (e.g., [63–65]), adsorption and drying on a porous substrate like filter paper [66, 67], electrospun fibers [68], wood pellets [69] or nanographite [70], and others, as well as using a reagent to form a precipitate [71]. Along this idea, even seperation or selective enrichment of metal ions via sorption on selective membranes have been shown to be exploitable [72–74]. In all cases, the drying of the prepared substrate is important, as the presence of water in solid samples (moisture) is well known to have a signal suppression effect in LIBS [75–77].

However, these simple approaches have serious pitfalls that are very hard to overcome if quantitative analysis is attempted. For example, a liquid droplet tends to spread across the adsorbent/substrate by wetting or capillarity effects, thereby producing an irregular spot (“coffee spot”) usually much larger in diameter than the laser spot size. This does not promote quantitative sample ablation. To prevent this spreading, the use of machined or laser-ablated small “pockets” (semi-spherical pits with a diameter comparable to the laser spot diameter) in the substrate have been proposed (e.g., [63, 64]) which incidentally may also act as a small cavity that can contribute to the signal enhancement by providing spatial confinement. Another way to mitigate this problem is the application of a hydrofobic coating on the substrate prior to the droplet placement which, along with a gentle heating, can aggregate the dissolved matter into a microscopic spot (e.g., [78, 79]). Spectral interference from the substrate can still be a problem, but if not then it may be that the ablation depth is smaller than the thickness of the deposit, which again stands in the way of quantitation. Please also note that when the dissolved material precipitates upon the action of drying then the compactness of the deposited material can be poorly reproducible and the effect of the matrix on the ablation and signal generation process will be huge. If the liquid to solid conversion is done in a way that, e.g., the substrate is

soaked in the solution sample then some of the above pitfalls can be avoided, but other concerns spring forth instead; for example, whether the distribution of the analyte will be homogenous across the substrate or not, or if the capacity of the sorbent has been exceeded or not.

4.1.4 Combination of Methods: Top Performance

Some of the signal enhancement approaches described above are more efficient than others (e.g., NE-LIBS, DP/MP-LIBS, and LIBS-LIF have the greatest potential, as they can provide an enhancement factor as large as 100 or more; however, the improvement in detection limits is usually significantly lower than this). Although a few of the physical signal enhancement approaches are technically mutually exclusive, but logically their majority is available for a combination, thereby allowing a top performance in terms of limits of detection (LOD). This is an appealing opportunity even though this brings about some loss of practicality—obviously, the instrumental setup gets complicated, sometimes costlier, portability deteriorates and in most of the cases it imposes limitations in terms of sample shape and size (e.g., dictates the use of a chamber or cavity). Needless to say that the use of a noble gas atmosphere and spatial confinement are the technically easiest to combine with other methods, although they provide modest signal benefits alone. A lot of studies have been described in the literature over the years which used the combination of two or more techniques—these enabled bringing the LODs down into the ppb (μg/kg, or μg/L) concentration range or even lower from the 10–100 ppm (mg/kg, mg/L) levels of conventional LIBS, depending on the experimental setup, the analyte element, the sample phase, the emission line detected, etc. Here, we only mention one particularly successful combined approach as an illustration.

In 2017, Dong et al. reported about the ultrasensitive, ppt-level determination of Cu and Cd in aqueous solutions by combining nanoparticle enhancement and magnetic confinement [79]. A microscope slide glass substrate was uniformly coated with superhydrophobic liquid agent mixed with a standard Au nanodispersion in an optimized 10:1 ratio using spray coating. Microliter-volume droplets of liquid samples could then be placed and dried onto this substrate and the coating kept the content of the sample solution aggregated in a very small spot (ca. 200 μm), comparable to the laser spot size, when dried. A ring magnet with a conical cavity was then placed onto the substrate, centered around the sample spot. The ring magnet was kept in place by having a ferrous metal plate underneath the glass slide. The laser beam and light collection were uniaxial, along the surface normal of the substrate. One hundred and fifty millijoule pulse energy from a 1064 nm Nd:YAG laser was applied during the experiments. This approach provided a nearly five orders of magnitude signal enhancement and good quality calibration curves in the range from 20 ppt to 500 ppb. Signal normalization to the Au signal was also employed as it helped to decrease the signal scatter to 7.3% RSD.

Table 4.1 provides an overview of the state-of-the-art LIBS limits of detection in solid samples, the most common sample type. Due to the great differences in

Table 4.1 Overview of the best limit of detection values reported in the literature for different elements in solid samples [24, 80–124]

H *300* [83]						Cu *0.03* [106]	Element symbol Limit of detection (ppm) Reference										He
Li *0.69* [84]	Be *0.1* [85]											B *0.2* [86]	C *1.2* [87]	N *15* [88]	O *8* [89]	F *49* [90]	Ne
Na *0.05* [91]	Mg *0.1* [92]											Al *0.18* [93]	Si *0.14* [92]	P *0.7* [95]	S *1.5* [96]	Cl *50* [97]	Ar
K *2* [98]	Ca *1* [99]	Sc *2* [100]	Ti *3* [101]	V *5* [102]	Cr *0.24* [103]	Mn *0.05* [92]	Fe *0.3* [92]	Co *0.2* [105]	Ni *0.1* [101]	Cu *0.03* [106]	Zn *1* [99]	Ga *34* [107]	Ge	As *0.04* [108]	Se	Br *0.11* [109]	Kr
Rb *0.09* [109]	Sr *17* [110]	Y *0.4* [111]	Zr *3* [112]	Nb *8* [113]	Mo *2* [114]	Tc	Ru	Rh *18* [115]	Pd *5* [24]	Ag *0.4* [116]	Cd *0.13* [117]	In *160* [107]	Sn *2.2* [118]	Sb *0.2* [119]	Te	I	Xe
Cs *0.3* [120]	Ba *0.02* [109]		Hf	Ta *59* [113]	W *10* [121]	Re	Os	Ir	Pt *21* [122]	Au *0.8* [116]	Hg *4.6* [118]	Tl *0.5* [123]	Pb *0.07* [124]	Bi *25* [125]	Po	At	Rn
Fr	Ra		Rf	Db	Sg	Bh	Hs	Mt	Ds	Rg	Cn	Uut	Fl	Uup	Lv	Uus	Uuo

La *4* [111]	Ce *300* [126]	Pr *1* [100]	Nd *470* [127]	Pm	Sm *40* [100]	Eu *0.1* [128]	Gd *10* [129]	Tb *60* [100]	Dy *10* [100]	Ho *10* [100]	Er *30* [100]	Tm *30* [100]	Yb *2* [100]	Lu *20* [100]
Ac	Th *0.72* [130]	Pa	U *0.4* [131]	Np	Pu	Am	Cm	Bk	Cf	Es	Fm	Md	No	Lr

experimental conditions (e.g., setup, signal enhancement techniques, transition, etc.), we have not made any attempts to normalize the data; they are only meant as a compilation of the best-reported LOD values for each element and their references.

As a final comment on signal enhancement approaches, it is worth mentioning that most studies in the literature report enhancement factors and scarcely take the trouble of assessing the LOD value (concentration), especially with solid samples. The problem is that the enhancement factor is a relative figure of merit, therefore the level of actual performance depends strongly on the reference. This makes the comparison or the judgment of the absolute level of performance hard. For example, it is well documented that high-time resolution detection using an Echelle spectrograph with an intensified CCD detector has a poorer signal-to-noise ratio than time integrating detection with a spectrometer using a linear CCD detector. Thus the optimized signal with the former detection scheme may be much lower than the signal recorded with the latter, thus timing critical approaches may behave quite differently depending on the detection scheme. Similarly, signal enhancement is relatively easy to produce for liquid samples, where the conventional LIBS signal reference is so small, but it does not always make the signal enhancement practical. Last, but not least, bringing the LODs into the ultra-trace analytical range (ppb or below) also means that sample preparation and measurement requirements will also be harder due to the risk of sample contamination or analyte losses, which may cause the loss of appeal of LIBS altogether.

4.2 Dynamic Range

The linear dynamic range of conventional LIBS measurements is generally around three to four orders of magnitude, spanning roughly from a few ppm to a couple of % concentations [125]. This already requires an optimization of data acquisition parameters, such as a good choice of the spectral line of the analyte and the detection gate delay and width [126, 127], as the transition from an optically thin to optically thick (self-absorbing) plasma causes the calibration plots to level up. In general, a sensitive analysis that can be characterized by a reasonably linear calibration plot dictates the use of strong, but not resonance lines and short, around 1 μs gate delay and gate width values (for nanosecond LIBS). The linear dynamic range can be extended downwards with the application of a signal enhancement technique, that lowers the limit of detection—see, for example, the most sensitive case with over five orders of magnitude range secribed in Sect. 4.1.3. Upwards extension may also be possible under special circumstances, such as in vacuum or when double- or multi-pulse LIBS is used. Under these conditions, the reduced pressure (in DP-LIBS it is present behind the outwards propagating shockwave generated by the first pulse) suppresses self-absorption and successful linear calibration for certain elements and transitions were demonstrated for up to some tens of % concentration with DP-LIBS. Multi-pulse LIBS, which uses time-integrated signal detection for over several laser pulses released in a burst, creates an even more special measurement condition, which is superior from the point of view of dynamic range. MP-LIBS not only

lowers the limit of detection but also expands the upper linear concentration limit to nearly 100% under favorable conditions. This allows for a dynamic range of at least six orders of magnitude [48, 128, 129].

4.3 Signal Repeatability and Correction

Conventional LIBS signals are known to have a quite high scatter; relative standard deviations, based on five to ten repeated measurements, are two-digit % values in most practical applications. This is due to that the signal formation in LIBS is very sensitive to the fluctuation of laser parameters and to the micro-inhomogeneity of samples. Unfortunately, signal scatter directly influences the achievable LOD values, thereby limiting the detection performance. Some improvements in this figure can, at the cost of practicality, be achieved statistically, e.g., by performing a large number (e.g., several hundreds) of repeated measurements.

Matrix effects, especially for solid samples, also hamper LIBS performance—similarly to other solid sampling analytical methods. Signal suppression caused by the sample matrix (or rather the differences between any calibration standards and samples in this regard) will negatively influence the accuracy of the determination. With the intention of correcting for such signal suppression, various calibration methodologies have also been developed and/or tested for LIBS use (please see, e.g., Chap. 2 of this book). Some classical approaches useful to mitigate matrix effects, which were developed for liquid samples (e.g., multiple standard addition) are unfortunately quite difficult to apply for solid samples, the primary sample type for LIBS.

Due to the above reasons, a lot of effort in the literature went into developing signal normalization approaches, with the intention to improve the repeatability, LODs, and accuracy of analysis, sometimes also characterized by the linearity of the calibration plot (value of linear regression coefficient). Different reference signals were derived for the purpose—here, we give a brief overview of the concept of the most popular approaches. Please note that only those are covered which can be easily implemented, thus variants that require exotic hardware components are not considered. Although the above quantitative issues also influence LIBS performance in qualitative discrimination analysis, which alone employs extensive signal preprocessing (e.g., scaling, data normalization, factorization, deconvolution, etc.), but these are also not covered here as the focus is on those approaches that rely on a reference signal related to a physical or material quantity. Readers interested in the details of LIBS signal normalization are referred to reviews dedicated to the topic [130–132].

4.3.1 Internal Standardization

The analytical signal from a sample component (internal standard), that is added to or is present in all samples studied, is widely used as a reference signal in

spectroscopy. The underlying concept is the assumption that whatever fluctuation affects the analyte signal will also influence the signal of the reference component. This normalization technique was already applied in one of the very first LIBS studies too, as early as in 1964 [133]. The internal standard element and the spectral line chosen theoretically have to conform with several rules (e.g., similar evaporation and ionization energies of elements, similar excitation energies and intensities for the analyte and internal standard spectral line, etc.), which were discussed in detail with respect to LIBS by, e.g., Hahn and Omenetto [125]. The fulfillment of these selection rules is very difficult, and if it is also considered that standard addition is complicated for solid samples which are the most typical samples in LIBS analysis, one can conclude that internal standardization is not an ideal approach to correct for signal fluctuations or matrix effects in LIBS.

In spite of this, many studies reported the successful application of this technique, usually by using an element already present in the sample at a reasonably high concentration, such as Sr for Ca determination in an aqueous sample via the filter paper preconcentration method [66], Fe for Ni and Cr determination in stainless steel [133], C for the analysis of several trace elements in fresh vegetables [134], Ba for U determination in barium-borosilicate samples [135], just to name a few. Spiking the samples with a standard solution is less common, but was also successfully demonstrated to work with, e.g., soft tissues [136] or for liquid samples followed by liquid to solid conversion by freezing [137]. It has to be added though that the researchers using internal standardization often follow a trial-and-error approach for the selection of the standard element and spectral line [135, 138], with either the linear correlation coefficient of the calibration plot or the signal repeatability as the objective function. More recently, automatic algorithms for the selection of internal standard lines have also been suggested [139, 140]. Nevertheless, the consensus is that internal standardization can not be applied as a general strategy, but has to be carefully tested under the specific conditions of the analysis.

4.3.2 Laser Pulse Energy

It is a well-known fact in LIBS that laser fluence (or pulse energy if, as usual, the spot size is constant) directly influences the observed spectral intensities—higher fluence generally means higher ablation rate and also higher spectral intensities up to a certain level [141]. Higher pulse energy generally produces a higher temperature plasma, which in turn generates higher emission intensities. This means that if the laser pulse energy fluctuates in a LIBS experiment then it also affects the scatter of the LIBS signal. The effect is stronger for lines of higher excitation potential (e.g., ionic vs. atomic lines) due to that the excited state population is more sensitive in the former case to the plasma temperature. Pulsed Q-switched lasers usually have a couple of RSD% pulse-to-pulse energy fluctuations. Consequently, the simple approach to monitor the laser pulse energy during the experiments and to use it to normalize the signal for improving on LIBS signal repeatability was suggested in the literature several times. Unfortunately, the relationship between the laser fluence and

spectral intensities is usually not linear, and depends on the concentration of the analyte, the transition (c.f. self-absorption effects), and the fluence. Thus, not surprisingly, pulse energy normalization generates mixed results in terms of repeatability improvement. For example, Yue et al. [142] found a factor of 5 improvement for Mg ionic lines, but a factor of 3 deterioration for Mg atomic lines in aluminum alloys. At the same time, Oh et al. [143] and Huang et al. [144] found no improvement when pulse energy normalization was employed in slurry and alloy samples, respectively. It can be concluded that laser pulse energy normalization is not a reliable method.

4.3.3 Total Emission

The total LIBS emission intensity, integrated over the full spectral window of the spectrometer or recorded by a photodiode, was proposed as a reference for signal correction for the first time by Bolger [145]. Body and Chadwick investigated the approach in detail and found that there is a correlation between total emission and the laser pulse energy [146]. This approach is easy to implement, although it produces unconventionally small normalized analytical signals. In general, this approach was found to be useful during the analysis of several sample types, including martian rocks [147], soils [148] or alloys [149], for the improvement of the linearity of calibration plots or for the correction of pulse-to-pulse signal variations.

4.3.4 Continuum Radiation

Signal normalization to the continuum background radiation, either derived from the average measured intensity next to the analytical line or from the integral intensity for the fitted full-spectrum background, was also proposed in the literature to improve signal repeatability and calibration linearity. The concept was first described by Xu et al. [150] and later adopted by many research groups with mixed results (e.g., [151–154]). Although some studies demonstrated that there is indeed a correlation between the continuum emission and the plasma density, and the amount of emitters in the plasma [155], but fundamentals of the methodology were later criticized and the lack of generalizability was declared from a theoretical point of view [131, 132, 156]. Without going into details here and only considering experimental conditions, it seems to be clear that usually the goal of LIBS signal optimization is to minimize the background (continuum) emission and maximize the analytical signal (improve S/N), thus relying on a signal normalization that employs a very small reference signal is not really feasible. In addition to this, in the case of complex samples and an insufficient spectrometer spectral resolution (in other words: in real-world analytical situations) establishing this reference signal in the pure form is also challenging.

4.3.5 Acoustic Wave

The laser-induced breakdown of a solid in air (at atmospheric conditions) is known to be accompanied by a snapping sound (acoustic wave), which is the result of the ablated vapor causing a compression shock in the surrounding gas while traveling away. At the same time, the recoil pressure caused by the ablation process will also cause a transverse vibration of the solid that propagates along the surface. The detection of this acoustic wave can be done by a microphone either placed in the surrounding gas or by contacting the solid surface. The amplitude of the acoustic waveform has been shown to be proportional to the ablated mass [157–159], therefore was deemed to be useful as a reference signal for LIBS signal normalization, if the experimental setup is sound-proofed properly.

Acoustic signal normalization was demonstrated to improve the linearity of LIBS calibration plots ($r^2 > 0.98$) and signal repeatability (reduced to below 9% RSD) for various solid and liquid samples [160–162]; however, Cheung and Yeung also pointed out that the acoustic signal has a strong laser fluence depedence due to plasma shielding, which leads to the non-linear correlation function at high fluences [160]. Further information on the acoustic waves generated in LIBS experiments can be found in Chap. 11 of this book.

4.3.6 Plasma Parameters

One further possibility for signal normalization is the use of plasma diagnostic parameters, such as the plasma temperature and electron density as reference signals. It is based on the logical connection between plasma parameters and emission characteristics. In studies following this normalization approach, plasma parameters are derived from the LIBS emission spectra, using the classical Boltzmann and Saha equations and assuming local thermodynamic equilibrium (LTE). Normalization with plasma parameters was shown to reduce signal fluctuations and improve the linearity of calibration curves in several studies [153, 163, 164]; however, it also failed in some other cases [165]. Please note that calibration-free LIBS, which has become very popular in certain applications in the past two decades, is directly based on the application of plasma parameters to model plasma composition, therefore can be considered to be a sibling of this normalization technique. With regards to this, please see Chap. 3 of this book.

4.4 Spatial Resolution

Localized analysis of solid samples with high spatial resolution is a strong suit of laser ablation techniques, LA-ICP-MS and LIBS alike. Elemental mapping (imaging) of a solid sample is also strongly related to this topic. The best performance of localized LIBS analysis is a complex issue, which not only relates to the laser and optical setup but also the LOD that the specific application requires. On one hand, as

the analytical spot size is decreased, the laser power density delivered to the sample surface increases (in an idealistic optical focusing system) which increases the plasma temperature which in turn should help to increase the plasma emission, but at the same time the amount of ablated matter (and analyte), which strongly determines the signal, will decrease. In addition to this, as optical focusing systems get more and more complicated in a pursuit of a tighter focal spot (e.g., beam expansion, microscope objectives, etc.), more pulse energy is lost on the optical elements. Below a couple of ten micrometers, the laser beam delivery optics usually incorporate a pinhole, which also strongly contributes to the loss of pulse energy, that further deteriorates the analytical signal. In addition to this, the diffraction limit is also a function of the wavelength, thus the minimum spot size is also related to the laser wavelength. On top of this, if the light collection optics is uniaxial with the laser beam then further complications and signal losses can be expected due to the complex requirements for the setup. If localized analysis is to be achieved in the frameworks of elemental mapping, then further issues, related to the depth of focus, sample positioning and data acquisition speed and more, also emerge. These and other issues related to the spatial resolution of LIBS analysis are detailed in LIBS reviews (e.g., [166, 167]) and some chapters of this and other LIBS books (e.g., Motto-Ros et al. [168]).

At present, the best spatial resolution widely used in LIBS is around 10 μm. It was also demonstrated that the sub-micrometer range is also attainable, but this resolution usually already necessitates the use of some signal enhancement technique. Efforts to improve the lateral resolution currently follow three, distinctly different approaches. Micro-LIBS (μ-LIBS) setups employ nanosecond pulse duration UV lasers with sub-mJ pulse energies and a microscope objective in order to keep the diameter of ablation craters low, around a few micrometers (e.g., [169–171]). Femtosecond LIBS setups can utilize the fast laser-matter interaction and produce cleaner, smaller ablation craters. This comes at the cost of analytical sensitivity due to the short lifetime of fs LIB plasmas and the lack of plasma shielding with ultrashort laser pulses, but it produces craters in the micron or sub-micron range [172]; the smallest analytical spot ever achieved was 450 nm [173]. The third approach is called near-field enhancement (NFE-LIBS), in which a very sharp metal tip (e.g., silver) is brought in close vicinity of the sample surface and illuminated by a laser beam which generates a localized surface plasmon resonance in the tip and strongly enhances the incident electromagnetic field. This results in a great signal enhancement and sub-micrometer ablation craters with analytically useful LIBS signals [174]. The inconvenience of the approach is that it works best in vacuum and the tip material gets contaminated and may contribute to the sample spectrum.

4.5 Measurement Distance

Laser spectroscopy techniques have the unique ability that the samples can be interrogated from a distance, as the laser excitation beam has good directionality and the emitted light can also be easily collected and transferred over a great

distance. LIBS is also part of this family, thus its quantitative and qualitative features can also be utilized remotely, to the benefit of various special applications, including, e.g., mining (prospecting), environmental or industrial monitoring, security, space exploration, underwater archeology and more.

Usually, LIBS measurements over a distance can be executed in one of two ways, based on which these are grouped as remote or stand-off measurements [175]. In remote LIBS analysis, breakdown-inducing laser light and plasma emission is carried by long fiber optic cable(s) and focusing and collection optics are attached to the far end of the fiber(s). Beam handling is easy, the distance can be quite long, environmental effects have very little influence, but the performance is limited by the damage threshold and Brillouin scattering of the fiber material, which restricts the conveyable fluence. In the so-called stand-off analysis mode, both the laser and emission beams are propagating in free space. This approach, which is the only option in certain applications (which require the survey of unknown, distant samples), has the drawback that the sample has to be in the line-of-sight. In addition to this, light collection efficiency (sensitivity) strongly decreases with the distance and environmental conditions (e.g., air turbulences, airborne dust, precipitate, etc.) also have a great influence on the performance. Consequently, the distance in stand-off LIBS is usually relatively modest (rarely more than a few tens of meters) [176, 177]. At the same time, using ultrashort laser pulses (fs) and TW intensities in stand-off LIBS has the benefit of exploiting the so-called filamentation effect, which is the periodic self-focusing refraction and self-attenuating diffraction of a laser beam propagating in a medium [178]. This can expand the operational distance to hundreds of meters, the top value so far being 180 m [179]. In order to increase sensitivity and hence the achievable distance, there also is a possibility to use the double-pulse LIBS methodology with either the fiber optics remote analysis mode (e.g., Fobar et al. [180]) or in the stand-off mode [181]. In the stand-off mode, the use of spatial heterodyne detection [182] can also give a boost. It also has to be mentioned that the challenge (and the sensitivity required) greatly differs in different applications, ranging from the detection of a pure metal to the identification of explosive traces.

In conclusion, the general state-of-the-art in LIBS mesurements over distance is about a couple of hundreds of meters, which compares favorably to the performance of other laser spectroscopies (e.g., Raman scattering or laser-induced fluorescence spectroscopy) [176].

Acknowledgments The authors kindly acknowledge the financial support received from the National Research, Development and Innovation Office (Hungary) through project No. K 129063.

References

1. Li Y, Tian D, Ding Y, Yang G, Liu K, Wang C, Han X. A review of laser-induced breakdown spectroscopy signal enhancement. Appl Spectrosc. 2018;53:1.
2. Fu X, Li G, Dong D. Improving the detection sensitivity for laser induced breakdown spectroscopy: a review. Front Phys. 2020a;8:68.

3. Gornushkin IB, Stevenson CL, Galbács G, Smith BW, Winefordner JD. Measurement and modeling of ozone and nitrogen oxides produced by laser breakdown in oxygen-nitrogen atmospheres. Appl Spectrosc. 2003;57:1442.
4. Jianlong Y, Zongyu H, Yuanyuan M, Tianqi L, Yangting F, Yun W, Zheng L, Zhe W. Improvement of laser induced breakdown spectroscopy signal using gas mixture. Spectrochim Acta B. 2020;174:105992.
5. Joon-Gon S, Yonghoon L, Do-Kyeong K. Signal enhancement of laser-induced breakdown spectroscopy by applying synchronized buffer gas pulses. Appl Phys Express. 2018;11: 102401.
6. Effenberger JA, Scott JR. Effect of atmospheric conditions on LIBS spectra (review). Sensors. 2010;10:4907.
7. Jong-Il Yun Y, Reinhardt K, Jae-Il K. Laser-induced breakdown spectroscopy for the on-line multielement analysis of highly radioactive glass melt. Part I: characterization and evaluation of the method. Appl Spectrosc. 2002;56:437.
8. Zeshan AU, Usman L, Rizwan A, Muhammad AB. Detection of lead in soil implying sample heating and laser-induced breakdown spectroscopy. Appl Opt. 2021;60:452.
9. Kaimin G, Anmin C, Wanpeng X, Dan Z, Mingxing J. Effect of sample temperature on time-resolved laser-induced breakdown spectroscopy. AIP Adv. 2019;9:065214.
10. Tavassoli SH, Gragossian A. Effect of sample temperature on laser-induced breakdown spectroscopy. Opt Laser Technol. 2009;41:481.
11. Gao X, Liu L, Song C, Lin J. The role of spatial confinement on nanosecond YAG laser-induced Cu plasma. J Phys D Appl Phys. 2015;48:175205.
12. Guo L, Li C, Hu W, Zhou Y, Zhang B, Cai Z, Zeng X, Lu Y. Plasma confinement by hemispherical cavity in laser-induced breakdown spectroscopy. Appl Phys Lett. 2011;98: 131501.
13. Li C, Guo L, He X, Hao Z, Li X, Shen M, Zeng X, Lu Y. Element dependence of enhancement in optics emission from laser-induced plasma under spatial confinement. J Anal At Spectrom. 2014;29:638.
14. Popov AM, Colao F, Fantoni R. Spatial confinement of laser-induced plasma to enhance LIBS sensitivity for trace elements determination in soils. J Anal At Spectrom. 2010;25:2491.
15. Yin H, Hou Z, Yuan T, Wang Z, Ni W, Li Z. Application of spatial confinement for gas analysis using laser-induced breakdown spectroscopy to improve signal stability. J Anal At Spectrom. 2015;30:922.
16. Corsi M, Cristoforetti G, Hidalgo M, Iriarte D, Legnaioli S, Palleschi V, Salvetti A, Tognoni E. Effect of laser-induced crater depth in laser-induced breakdown spectroscopy emission features. Appl Spectrosc. 2005;59:853.
17. Li K, Guo L, Li X, Hao Z, Zeng X, Shen M, Qingdong Z, Yongfeng L, Xiaoyan Z. Characteristics of spectral lines with crater development during laser-induced breakdown spectroscopy. Appl Opt. 2016a;55:7422.
18. Cheng L, Xun G, Qi L, Chao S, Jingquan L. Spectral enhancement of laser-induced breakdown spectroscopy in external magnetic field. Plasma Sci Technol. 2015;17:919.
19. Hao Z, Guo L, Li CM, Shen M, Zou X, Li X, Lu Y, Zeng X. Sensitivity improvement in the detection of V and Mn elements in steel using laser-induced breakdown spectroscopy with ring magnet confinement. J Anal At Spectrom. 2014;29:2309.
20. Mason KJ, Goldberg JM. Characterization of a laser plasma in a pulsed magnetic field. Part I: spatially resolved emission studies. Appl Spectrosc. 1991a;45:370.
21. Mason KJ, Goldberg JM. Characterization of a laser plasma in a pulsed magnetic field. Part II: time-resolved emission and absorption studies. Appl Spectrosc. 1991b;45:1444.
22. Shen XK, Lu YF, Gebre T, Ling H, Han YX. Optical emission in magnetically confined laser-induced breakdown spectroscopy. J Appl Phys. 2006;100:3662.
23. Liu Y, Baudelet M, Richardson M. Elemental analysis by microwave-assisted laserinduced breakdown spectroscopy: evaluation on ceramics. J Anal At Spectrom. 2010;25:1316.

24. Al Shuaili AA, Al Hadhrami AM, Wakil MA, Alwahabi ZT. Improvement of palladium limit of detection by microwave-assisted laser induced breakdown spectroscopy. Spectrochim Acta B. 2019;159:105666.
25. Wakila MA, Alwahabi ZT. Microwave-assisted laser induced breakdown molecular spectroscopy: quantitative chlorine detection. J Anal At Spectrom. 2019;34:1892.
26. Viljanen J, Sun Z, Alwahabi ZT. Microwave assisted laser-induced breakdown spectroscopy at ambient conditions. Spectrochim Acta B. 2016;118:29.
27. Tampo M, Miyabe M, Akaoka K, Oba M, Ohba H, Maruyama Y, Ikuo W. Enhancement of intensity in microwave-assisted laser-induced breakdown spectroscopy for remote analysis of nuclear fuel recycling. J Anal At Spectrom. 2014;29:886.
28. Ayed Nassef O, Elsayed-Ali HE. Spark discharge assisted laser induced breakdown spectroscopy. Spectrochim Acta B. 2005;60:1564.
29. Sobral H, Robledo-Martinez A. Signal enhancement in laser-induced breakdown spectroscopy using fast square-pulse discharges. Spectrochim Acta B. 2016;124:67.
30. Tereszchuk KA, Vadillo JM, Laserna JJ. Glow-discharge-assisted laser-induced breakdown spectroscopy: increased sensitivity in solid analysis. Appl Spectrosc. 2008;62:1262.
31. De Giacomo A, Rifai RA, Gardette V, Salajková Z, Dell'Aglio M. Nanoparticle enhanced laser ablation and consequent effects on laser induced plasma optical emission. Spectrochim Acta B. 2020;166:105794.
32. Dell'Aglio M, Rifai RA, De Giacomo A. Nanoparticle enhanced laser induced breakdown spectroscopy (NELIBS), a first review. Spectrochim Acta B. 2018;148:105.
33. Jantzi SC, Motto-Ros V, Trichard F, Markushin Y, Melikechi N, De Giacomo A. Sample treatment and preparation for laser-induced breakdown spectroscopy. Spectrochim Acta B. 2016;115:52.
34. Palásti DJ, Albrycht P, Janovszky P, Paszkowska K, Geretovszky Z, Galbács G. Nanoparticle enhanced laser induced breakdown spectroscopy of liquid samples by using modified surface-enhanced Raman scattering substrates. Spectrochim Acta B. 2020;166:105793.
35. Palásti DJ, Villy LP, Kohut A, Ajtai T, Geretovszky Z, Galbács G. Laser-induced breakdown spectroscopy signal enhancement effect for argon caused by the presence of gold nanoparticles. Spectrochim Acta B. 2022;193:106435.
36. Piepmeier EH, Malmstadt HV. Q-switched laser energy absorption in the plume of an aluminum alloy. Anal Chem. 1969;41:700.
37. Scott RH, Strasheim A. Time-resolved direct-reading spectrochemical analysis using a laser source with medium pulse-repetition rate. Spectrochim Acta. 1971;26B:707.
38. Cui M, Deguchi Y, Wang Z, Fujita Y, Liu R, Shiou F-J, Zhao S. Enhancement and stabilization of plasma using collinear long-short double-pulse laser-induced breakdown spectroscopy. Spectrochim Acta B. 2018;142:14.
39. Legnaioli S, Lorenzetti G, Pardini L, Cavalcanti GH, Palleschi V. Double and multiple pulse LIBS techniques. In: Laser-induced breakdown spectroscopy: theory and applications. Series in optical sciences 182. Springer; 2014.
40. Babushok V, Delucia FC Jr, Gottfried JL, Munson CA, Miziolek AW. Double pulse laser ablation and plasma: laser induced breakdown spectroscopy signal enhancement. Spectrochim Acta B. 2006;61:999.
41. Scaffidi J, Angel SM, Cremers DA. Emission enhancement mechanisms in dual-pulse laser-induced breakdown spectroscopy. Anal Chem. 2006;78:24.
42. Bogaerts A, Chen Z, Autrique D. Double pulse laser ablation and laser induced breakdown spectroscopy: a modeling investigation. Spectrochim Acta B. 2008;63:746.
43. Cristoforetti G, Tiberi M, Simonelli A, Marsili P, Giammanco F. Toward the optimization of double-pulse LIBS underwater: effects of experimental parameters on the reproducibility and dynamics of laser-induced cavitation bubble. Appl Opt. 2012;51:B30.
44. De Giacomo A, Dell'Aglio M, De Pascale O, Capitelli M. From single pulse to double pulse ns-laser induced breakdown spectroscopy under water: elemental analysis of aqueous solutions and submerged solid samples. Spectrochim Acta B. 2007;62:721.

45. Lazic V, Jovicevic S. Laser induced breakdown spectroscopy inside liquids: processes and analytical aspects. Spectrochim Acta B. 2014;101:288.
46. Galbács G, Budavári V, Geretovszky Z. Multi-pulse laser-induced plasma spectroscopy using a single laser source and a compact spectrometer. J Anal At Spectrom. 2005;20:974.
47. Galbács G, Jedlinszki N, Herrera K, Omenetto N, Smith BW, Winefordner JD. A study of ablation, spatial, and temporal characteristics of laser-induced plasmas generated bymultiple collinear pulses. Appl Spectrosc. 2010;64:161.
48. Jedlinszki N, Galbács G. An evaluation of the analytical performance of collinear multipulse laser induced breakdown spectroscopy. Microchem J. 2011;97:255.
49. Prochazka D, Pořízka P, Novotný J, Hrdlička A, Novotný K, Šperka P, Kaiser J. Triple pulse LIBS: laser-induced breakdown spectroscopy signal enhancement by combination of pre-ablation and re-heating laser pulses. J Anal At Spectrom. 2020;35:293.
50. Chan SY, Cheung NH. Analysis of solids by laser ablation and resonance enhanced laserinduced plasma spectroscopy. Anal Chem. 2000;72:2087.
51. Lui S, Cheung NH. Resonance-enhanced laser-induced plasma spectroscopy for sensitive elemental analysis: elucidation of enhancement mechanisms. Appl Phys Lett. 2002;81:5114.
52. Lui SL, Cheung NH. Minimally destructive analysis of aluminum alloys by resonanceenhanced laser-induced plasma spectroscopy. Anal Chem. 2005;77:2617.
53. Goueguel C, Laville S, Vidal F, Chaker M, Sabsabi M. Resonant laser-induced breakdown spectroscopy for analysis of lead traces in copper alloys. J Anal At Spectrom. 2011;26:2452.
54. Li J, Guo L, Zhao N, Yang X, Yi R, Li K, Zeng Q, Li X, Zeng X, Lu Y. Determination of cobalt in low-alloy steels using laser-induced breakdown spectroscopy combined with laser-induced fluorescence. Talanta. 2016b;151:234.
55. Li J, Hao Z, Zhao N, Zhou R, Yi R, Tang S, Guo L, Li X, Zeng X, Lu Y. Spatially selective excitation in laser-induced breakdown spectroscopy combined with laser-induced fluorescence. Opt Express. 2017;25:4945.
56. Loudyi H, Rifai K, Laville S, Vidal F, Chaker M, Sabsabi M. Improving laser-induced breakdown spectroscopy (LIBS) performance for iron and lead determination in aqueoussolutions with laser-induced fluorescence (LIF). J Anal At Spectrom. 2009;24:1421.
57. Akshaya K, Yueh FY, Miller T, Singh JP. Detection of trace elements in liquids by laser-induced breakdown spectroscopy with a Meinhard nebulizer. Appl Opt. 2003;42:6040.
58. Cahoon EM, Almirall JR. Quantitative analysis of liquids from aerosols and microdrops using laser induced breakdown spectroscopy. Anal Chem. 2012;84:2239.
59. Fang X, Rafi Ahmad S. Sample presentation considerations in laser-induced breakdown spectroscopy in aqueous solution. Appl Spectrosc. 2007;61:1021.
60. Nadir A, Semira ÜY, Dilek AA, Şerife Y. Ultrasonic nebulizationsample introduction system for quantitative analysis of liquid samples by laser-induced breakdown spectroscopy. Spectrochim Acta B. 2012;74–75:87.
61. Jiang L, Sui M, Fan Y, Su H, Xue Y, Zhong S. Micro-gas column assisted laser induced breakdown spectroscopy (MGC-LIBS): a metal elements detection method for bulk water in-situ analysis. Spectrochim Acta B. 2021;177:106065.
62. Sobral H, Sanginés R, Trujillo-Vázquez A. Detection of trace elements in ice and water by laser-induced breakdown spectroscopy. Spectrochim Acta B. 2012;78:62.
63. Metzinger A, Kovács-Széles É, Almási I, Galbács G. An assessment of the potential of laser induced breakdown spectroscopy (LIBS) for the analysis of cesium in liquid samples of biological origin. Appl Spectrosc. 2014;68:789.
64. Metzinger A, Nagy A, Gáspár A, Márton Z, Kovács-Széles É, Galbács G. The feasibility of liquid sample microanalysis using polydimethylsiloxane microfluidic chips with in-channel and in-port laser-induced breakdown spectroscopy detection. Spectrochim Acta B. 2016;126:23.
65. Yang X, Hao Z, Shen M, Yi RX, Li J, Yu H, Guo L, Xiangyou L, Xiaoyan Z, Yongfeng L. Simultaneous determination of La, Ce, Pr, and Nd elements in aqueous solution using surfaceenhanced laser-induced breakdown spectroscopy. Talanta. 2017;163:127.

66. Choi D, Gong Y, Nam S-H, Han S-H, Yoo J, Lee Y. Laser-induced breakdown spectroscopy (LIBS) analysis of calcium ions dissolved in water using filter paper substrates: an ideal internal standard for precision improvement. Appl Spectrosc. 2014;68:198.
67. Zhichao Z, Wenbao J, Qing S, Xiaoyan Y, Daqian H, Zi W, Yu W, Yongsheng L. Determination of magnesium and sodium in brine by filter paper adsorption laser-induced breakdown spectroscopy. Anal Lett. 2022;55:1771.
68. Lin Q, Wei Z, Xu M, Wang S, Niu G, Liu K, Duan Y, Yang J. Laser-induced breakdown spectroscopy for solution sample analysis using porous electrospun ultrafine fibers as a solid-phase support. RSC Adv. 2014;4:14392.
69. Guanhong W, Duixiong S, Maogen S, Chenzhong D. LIBS detection of heavy metal elements in liquid solutions by using wood pellet as sample matrix. Plasma Sci Technol. 2014;16:598.
70. Wang X, Shi L, Lin Q, Zhu X, Duan Y. Simultaneous and sensitive analysis of Ag(I), Mn(II), and Cr(III) in aqueous solution by LIBS combined with dispersive solid phase micro-extraction using nano-graphite as an adsorbent. J Anal At Spectrom. 2014;29:1098.
71. Díaz Pace DM, D'Angelo CA, Bertuccelli D, Bertuccelli G. Analysis of heavy metals in liquids using laser induced breakdown spectroscopy by liquid-to-solid matrix conversion. Spectrochim Acta B. 2006;61:929.
72. Nam S-H, Kwon S-W, Lee Y. Feasibility of separation and quantification of inorganic arsenic species using ion-exchange membranes and laser-induced breakdown spectroscopy. Anal Lett. 2018;51:2835.
73. Schmidt NE, Goode SR. Analysis of aqueous solutions by laser-induced breakdown spectroscopy of ion exchange membranes. Appl Spectrosc. 2002;56:370.
74. Wang X, Wei Y, Lin Q, Zhang J, Duan Y. Simple, fast matrix conversion and membrane separation method for ultrasensitive metal detection in aqueous samples by laser induced breakdown spectroscopy. Anal Chem. 2015;87:5577.
75. Chen M, Yuan T, Hou Z, Wang Z, Wang Y. Effects of moisture content on coal analysis using laser-induced breakdown spectroscopy. Spectrochim Acta B. 2015;112:23.
76. Eseller KE, Tripathi MM, Yueh F-Y, Singh JP. Elemental analysis of slurry samples with laser induced breakdown spectroscopy. Appl Opt. 2010;49:C21.
77. Wisbrun R, Schechter I, Niessner R, Schroder H, Kompa K. Detector for trace elemental analysis of solid environmental samples by laser plasma spectroscopy. Anal Chem. 1994;66:2964.
78. Wu M, Wang X, Niu G, Zhao Z, Zheng R, Liu Z, Zhao Z, Duan Y. Ultrasensitive and simultaneous detection of multielements in aqueous samples based on biomimetic array combined with laser-induced breakdown spectroscopy. Anal Chem. 2021;93:10196.
79. Dong D, Jiao L, Dua X, Zhao C. Ultrasensitive nanoparticle enhanced laser-induced breakdown spectroscopy using a super-hydrophobic substrate coupled with magnetic confinement. Chem Commun. 2017;53:4546.
80. Alvarez-Llamas C, Pisonero J, Bordel N. A novel approach for quantitative LIBS fluorine analysis. J Anal At Spectrom. 2017;32:162.
81. Anzano J, Cajal J, Lasheras R, Escudero M, Canudo J, Laguna M, Anwar J. Determination of lanthanides in fossil samples using laser induced breakdown spectroscopy. J Chem Soc Pak. 2017;39:516.
82. Asimellis G, Michos N, Fasaki I, Kompitsas M. Platinum group metals bulk analysis in automobile catalyst recycling material by laser-induced breakdown spectroscopy. Spectrochim Acta B. 2008;63:1338.
83. Bhatt CR, Yueh FY, Singh JP. Univariate and multivariate analyses of rare earth elements by laser-induced breakdown spectroscopy. Appl Opt. 2017;56:2280.
84. Chinni RC, Cremers DA, Radziemski LJ, Bostian MB, Navarro-Northrup C. Detection of uranium using laser-induced breakdown spectroscopy. Appl Spectrosc. 2009;63:1238.
85. Darwiche S, Benrabbah R, Benmansour M, Morvan D. Impurity detection in solid and molten silicon by laser induced breakdown spectroscopy. Spectrochim Acta B. 2012;74–75:115.

86. Davari SA, Taylor PA, Standley RW, Mukherjee D. Detection of interstitial oxygen contents in Czochralski grown silicon crystals using internal calibration in laser-induced breakdown spectroscopy (LIBS). Talanta. 2019;193:192.
87. Díaz D, Hahn DW, Molina A. Quantification of gold and silver in minerals by laser-induced breakdown spectroscopy. Spectrochim Acta B. 2017;136:106.
88. El-Deftar MM, Robertson J, Foster S, Lennard C. Evaluation of elemental profiling methods, including laser-induced breakdown spectroscopy (LIBS), for the differentiation of cannabis plant material grown in different nutrient solutions. Forensic Sci Int. 2015;251:95.
89. Fichet P, Mauchien P, Moulin C. Determination of impurities in uranium and plutonium dioxides by laser-induced breakdown spectroscopy. Appl Spectrosc. 1999;53:1111.
90. Freedman A, Iannarilli FJ, Wormhoudt JC. Aluminum alloy analysis using microchip-laser induced breakdown spectroscopy. Spectrochim Acta B. 2005;60:1076.
91. Fu X, Li G, Tian H, Dong D. Detection of cadmium in soils using laserinduced breakdown spectroscopy combined with spatial confinement and resin enrichment. RSC Adv. 2018;8: 39635.
92. Fu X, Zhao C, Ma S, Tian H, Dong D, Li GL. Determining available potassium in soil by laser-induced breakdown spectroscopy combined with cation exchange membrane adsorption. J Anal At Spectrom. 2020b;35:2697.
93. Gao P, Yang P, Zhou R, Ma S, Zhang W, Hao Z, Tang S, Li X, Zeng X. Determination of antimony in soil using laser-induced breakdown spectroscopy assisted with laser-induced fluorescence. Appl Opt. 2018;57:8942.
94. Gautier C, Fichet P, Menuta D, Lacour JL, Hermite DL, Dubessy J. Study of the double-pulse setup with an orthogonal beam geometry for laser-induced breakdown spectroscopy. Spectrochim Acta B. 2004;59:975.
95. Gondal MA, Hussain T. Determination of poisonous metals in wastewater collected from paint manufacturing plant using laser-induced breakdown spectroscopy. Talanta. 2007;71:73.
96. Gornushkin IB, Kim JE, Smith BW, Baker SA, Winefordner JD. Determination of cobalt in soil, steel, and graphite using excited-state laser fluorescence induced in a laser spark. Appl Spectrosc. 1997a;51:1055.
97. Gornushkin IB, Baker SA, Smith BW, Winefordner JD. Determination of lead in metallic reference materials by laser ablation combined with laser excited atomic fluorescence. Spectroc Acta B. 1997b;52:1653.
98. Hemmerlin M, Meilland R, Falk H, Wintzens P, Pauleri L. Application of vacuum ultraviolet laser-induced breakdown spectrometry for steel analysiscomparison with spark-optical emissions spectrometry figures of merit. Spectrochim Acta B. 2001;56:661.
99. Hilbk-Kortenbruck F, Noll R, Wintjens P, Falk H, Becker C. Analysis of heavy metals in soils using laser-induced breakdown spectrometry combined with laser-induced fluorescence. Spectroc Acta B. 2001;56:933.
100. Idris N, Kurniawan H, Lie TJ. Characteristics of hydrogen emission in laser plasma induced by focusing fundamental Q-sw YAG laser on solid samples. Jpn J Appl Phys. 2004;43:4221.
101. Ishizuka T. Laser emission spectrography of rare earth elements. Anal Chem. 1973;45:538.
102. Jabbar A, Akhtar M, Mehmmod S, Iqbal M, Ahmed R, Baig MA. Quantification of copper remediation in the Allium cepa L. leaves using electric field assisted laser induced breakdown pectroscopy. Spectrochim Acta B. 2019;162:105719.
103. Jensen LC, Langford SC, Dickinson JT, Addleman RS. Mechanistic studies of laser-induced breakdown spectroscopy of model environmental samples. Spectrochim Acta B. 1995;50: 1501.
104. Jiang X, Hayden P, Costello JT, Kennedy ET. Double-pulse laser induced breakdown spectroscopy with ambient gas in the vacuum ultraviolet: optimization of parameters for detection of carbon and sulfur in steel. Spectrochim Acta B. 2014;101:106.
105. Kang J, Jiang Y, Li R, Chen Y. Sensitive elemental analysis with high repetition rate laser-ablation spark-induced breakdown spectroscopy combined with lock-in signal detection. Spectrochim Acta B. 2019;155:50.

106. Khater MA, Costello JT, Kennedy ET. Optimization of the emission characteristics of laser-produced steel plasmas in the vacuum ultraviolet: significant improvements in carbon detection limits. Appl Spectrosc. 2002;56:970.
107. Knight AK, Scherbarth NL, Cremers DA, Ferris MJ. Characterization of laser-induced breakdown spectroscopy (LIBS) for application to space exploration. Appl Spectrosc. 2000;54:331.
108. Labutin TA, Popov AM, Raikov SN, Zaytsev SM, Labutina NA, Zorov NB. Determination of chlorine in concrete by laser-induced breakdown spectroscopy in air. J Appl Spectrosc. 2013;80:315.
109. Labutin TA, Zaytsev SM, Popov AM, Zorov NB. A novel approach to sensitivity evaluation of laser-induced breakdown spectroscopy for rare earth elements determination. J Anal At Spectrom. 2016;31:2223.
110. Liu L, Hao Z. Quantitative determination of tantalum and niobium in tantalum–niobium ore using laser-induced breakdown spectroscopy. Appl Opt. 2019;58:461.
111. Loebe K, Uhl A, Lucht H. Microanalysis of tool steel and glass with laser-induced breakdown spectroscopy. Appl Opt. 2003;42:6166.
112. Mei-Ting H, Yin-Hua J, Yu-Qi C, Run-Hua L. Quantitative analysis of trace elements in bismuth brass with high repetition rate laser-ablation spark-induced breakdown spectrum. Rhhz Test. 2021;70:10.
113. Pearce TJ, Martin J, Bromley B, Zigler A, Dix M (2000) Chemostratigraphy - the elemental solution using LIBS-OES. In: LIBS 2000 book of abstracts. First international conference on laser induced plasma spectroscopy and applications, Tirrenia, p 66.
114. Radziemski LJ, Cremers DA. Laser-induced breakdown spectroscopy: principles, applications and instruments. Proc SPIE. 1990;1318:71.
115. Radziemski LJ, Cremers DA, Benelli K, Khoo C, Harris RD. Use of the vacuum ultraviolet spectral region for LIBS-based Martian geology and exploration. Spectrochim Acta B. 2004;60:237.
116. Ramli M, Khumaeni A, Kurniawan KH, Tjia MO, Kagawa K. Spectrochemical analysis of Cs in water and soil using low pressure laser induced breakdown spectroscopy. Spectrochim Acta B. 2017;132:8.
117. Sarkar A, Alamelu D, Aggarwal SK. Determination of thorium and uranium in solution by laser-induced breakdown spectrometry. Appl Opt. 2008;47:G58.
118. Senesia GS, Harmon RS. Laser-induced breakdown spectroscopy: a unique analytical tool for the geosciences. Spectrosc Eur. 2021;33:15.
119. Shen XK, Wang H, Xie ZQ, Gao Y, Ling H, Lu YF. Detection of trace phosphorus in steel using laser-induced breakdown spectroscopy combined with laser-induced fluorescence. Appl Opt. 2009;48:2551.
120. Singh VK, Rai AK, Rai PK, Jindal PK. Cross-sectional study of kidney stones by laserinduced breakdown spectroscopy. Lasers Med Sci. 2009;24:749.
121. Sun Q, Tran M, Smith BW, Winefordner JD. Direct determination of P, Al, Ca, Cu, Mn, Zn, Mg and Fe in plant materials by laser-induced plasma spectroscopy. Can J Anal Sci Spectrosc. 1999;44:164.
122. Tran M, Sun Q, Smith B, Winefordner JD. Direct determination of trace elements in terephthalic acid by laser induced breakdown spectroscopy. Anal Chim Acta. 2000;419:153.
123. Uhl A, Loebe K, Kreuchwig L. Fast analysis of wood preservers using laser induced breakdown spectroscopy. Spectrochim Acta B. 2001;56:795.
124. Xing P, Dong J, Yu P, Zheng H, Liu X, Hu S, Zhu Z. Uantitative analysis of lithium in brine by laser-induced breakdown spectroscopy based on convolutional neural network. Anal Chim Acta. 2021;1178:338799.
125. Hahn DW, Omenetto N. Laser-induced breakdown spectroscopy (LIBS), part II: review of instrumental and methodological approaches to material analysis and applications to different fields. Appl Spectrosc. 2012;66:347.

126. Gornushkin IB, Anzano JM, King LA, Smith BW, Omenetto N, Winefordner JD. Curve of growth methodology applied to laser-induced plasma emission spectroscopy. Spectrochim Acta B. 1999a;54:491.
127. Tognoni E, Palleschi V, Corsi M, Cristoforetti G, Omenetto N, Gornushkin I, Smith BW, Winefordner JD. From sample to signal in laser-induced breakdown spectroscopy: a complex route to quantitative analysis in laser induced breakdown spectroscopy, fundamentals and applications. Cambridge University Press; 2009.
128. Galbács G, Jedlinszki N, Cseh G, Galbács Z, Túri L. Accurate quantitative analysis of gold alloys using multi-pulse laser induced breakdown spectroscopy and a correlation-based calibration method. Spectrochim Acta B. 2008;63:591.
129. Galbács G. A critical review of recent progress in analytical laser-induced breakdown spectroscopy. Anal Bioanal Chem. 2015;407:7537.
130. Guezenoc J, Gallet-Budynek A, Bousquet B. Critical review and advices on spectral-based normalization methods for LIBS quantitative analysis. Spectrochim Acta B. 2019;160:105688.
131. Tognoni E, Cristoforetti G. Signal and noise in laser induced breakdown spectroscopy: an introductory review. Opt Laser Technol. 2016;79:164.
132. Zorov NB, Gorbatenko AA, Labutin TA, Popov AM. A review of normalization techniques in analytical atomic spectrometry with laser sampling: from single to multivariate correction. Spectrochim Acta B. 2010;65:642.
133. Runge EF, Minck RW, Brian FR. Spectrochemical analysis using a pulsed laser source. Spectrochim Acta B. 1964;20:733.
134. Juvé V, Portelli R, Boueri M, Baudelet M, Yu J. Space-resolved analysis of trace elements in fresh vegetables using ultraviolet nanosecond laser-induced breakdown spectroscopy. Spectrochim Acta B. 2008;63:1047.
135. Sarkar A, Mishra RK, Kaushik CP, Wattal PK, Alamelu D, Aggarwal SK. Analysis of barium borosilicate glass matrix for uranium determination by using ns-IR-LIBS in air and Ar atmosphere. Radiochim Acta. 2014;102:805.
136. Šindelářová A, Pořízka P, Modlitbová P, Vrlíková L, Kiss M, Kaška M, Prochazka D, Vrábel J, Buchtová M, Kaiser J. Methodology for the implementation of internal standard to laser-induced breakdown spectroscopy analysis of soft tissues. Sensors. 2021;21:900.
137. de Oliveira Borges F, Ospina JU, de Holanda Cavalcanti G, Farias EE, Rocha AA, Ferreira PILB, Gomes GC, Mello A. CF-LIBS analysis of frozen aqueous solution samples by using a standard internal reference and correcting the self-absorption effect. J Anal At Spectrom. 2018;33:629.
138. Kwak JH, Lenth C, Salb C, Ko EJ, Kim KW, Park K. Quantitative analysis of arsenic in mine tailing soils using double pulse-laser induced breakdown spectroscopy. Spectrochim Acta B. 2009;64:1105.
139. Yan J, Shi Y, Liu K, Li H, Tang Z, Chen W, Jiang W, Li Q, Tang Y, Li X. The distribution of high-quality internal standard lines and their selection method based on the Q-value in portable laserinduced breakdown spectroscopy. Anal Methods. 2021;13:3829.
140. Yang J, Li X, Xu J, Ma X. A calibration-free laser-induced breakdown spectroscopy (CFLIBS) quantitative analysis method based on the auto-selection of an internal reference line and optimized estimation of plasma temperature. Appl Spectrosc. 2018;72:129.
141. Russo R. Laser ablation. Appl Spectrosc. 1995;49:15A.
142. Yue Z, Sun C, Gao L, Zhang Y, Shabbir S, Xu W, Wu M, Zou L, Tan Y, Chen F, Yu J. Machine learning efficiently corrects LIBS spectrum variation due to change of laser fluence. Opt Express. 2020;28:14345.
143. Oh SY, Yueh FY, Singh JP, Herman CC, Zeigler K. Preliminary evaluation of laser induced breakdown spectroscopy for slurry samples. Spectrochim Acta B. 2009;64:113.
144. Huang F, Tian Y, Li Y, Ye W, Lu Y, Guo J, Zheng R. Normalization of underwater laser-induced breakdown spectroscopy using acoustic signals measured by a hydrophone. Appl Opt. 2021;60:1595.

145. Bolger JA. Semi-quantitative laser-induced breakdown spectroscopy for analysis of mineral drill core. Appl Spectrosc. 2000;54:181.
146. Body D, Chadwick BL. Optimization of the spectral data processing in a LIBS simultaneous elemental analysis system. Spectrochim Acta B. 2001;56:725.
147. Fabre C, Cousin A, Wiens RC, Ollila A, Gasnault O, Maurice S, Sautter V, Forni O, Lasue J, Tokar R, Vaniman D, Melikechi N. In situ calibration using univariate analyses based on the onboard ChemCam targets: first prediction of Martian rock and soil compositions. Spectrochim Acta B. 2014;99:34.
148. Yu KG, Zhao YR, Liu F, He Y. Laser-induced breakdown spectroscopy coupled with multivariate chemometrics for variety discrimination of soil. Sci Rep. 2016;6:27574.
149. Kurniawan H, Suliyanti MM, Lie TJ, Kagawa K, Tjia MO. Application of primary plasma standardization to Nd-YAG laser-induced shock wave plasma spectrometry for quantitative analysis of high concentration Au–Ag–Cu alloy. Spectrochim Acta B. 2001;56:1407.
150. Xu L, Bulatov V, Gridin VV, Schechter I. Absolute analysis of particulate materials by laser-induced breakdown spectroscopy. Anal Chem. 1997;69:2103.
151. Galbács G, Kevei-Bárány I, Szőke E, Jedlinszki N, Gornushkin IB, Galbács MZ. A study of stalagmite samples from Baradla Cave (Hungary) by laser induced plasma spectrometry with automatic signal correction. Microchem J. 2011;99:406.
152. Fortes FJ, Cortés M, Simón MD, Cabalín LM, Laserna JJ. Chronocultural sorting of archaeological bronze objects using laser-induced breakdown spectrometry. Anal Chim Acta. 2005;554:136.
153. Lazic V, Fantoni R, Colao F, Santagata A, Morone A, Spizzichino V. Quantitative laser induced breakdown spectroscopy analysis of ancient marbles and corrections for the variability of plasma parameters and of ablation rate. J Anal At Spectrom. 2004;19:429.
154. Cabalín LM, González A, Ruiz J, Laserna JJ. Assessment of statistical uncertainty in the quantitative analysis of solid samples in motion using laser-induced breakdown spectroscopy. Spectrochim Acta B. 2010;65:680.
155. De Giacomo A, Dell'Aglio M, De Pascale O, Gaudiuso R, Santagata A, Teghil R. Laserinduced breakdown spectroscopy methodology for the analysis of copper based alloys used in ancient artworks. Spectrochim Acta B. 2008;63:585.
156. Gornushkin IB, Smith BW, Potts GE, Omenetto N, Winefordner JD. Some considerations on the correlation between signal and background in laser induced breakdown spectroscopy using single-shot analysis. Anal Chem. 1999b;71:5447.
157. Chaléard C, Mauchien P, Andre N, Übbing J, Lacour JL, Geertsen C. Correction of matrix effects in quantitative elemental analysis with laser ablation optical emission spectrometry. J Anal At Spectrom. 1997;12:183.
158. Chen G, Yeung ES. Acoustic signal as an internal standard for quantitation in lasergenerated plumes. Anal Chem. 1988;60:2258.
159. Palanco S, Laserna J. Spectral analysis of the acoustic emission of laserproduced plasmas. Appl Opt. 2003;42:6078.
160. Cheung NH, Yeung ES. Single-shot elemental analysis of liquids based on laser vaporization at fluences below breakdown. Appl Spectrosc. 1993;47:882.
161. Cheung NH, Ng CW, Ho WF, Yeung ES. Ultra-micro analysis of liquids and suspensions based on laser-induced plasma emissions. Appl Surf Sci. 1998;127:274.
162. Hrdlička A, Zaorálková L, Galiová M, Čtvrtníčková T, Kanický V, Otruba V, Novotný K, Krásenský P, Kaiser J, Malina R, Páleníková K. Correlation of acoustic and optical emission signals produced at 1064 and 532 nm laser-induced breakdown spectroscopy (LIBS) of glazed wall tiles. Spectrochim Acta B. 2009;64:74.
163. Feng J, Wang Z, Li Z, Ni W. Study to reduce laser-induced breakdown spectroscopy measurement uncertainty using plasma characteristic parameters. Spectrochim Acta B. 2010;65:549.

164. Panne U, Haisch C, Clara M, Niessner R. Analysis of glass and glass melts during the vitrification process of fly and bottom ashes by laser-induced plasma spectroscopy. Part I: normalization and plasma diagnostics. Spectrochim Acta B. 1998;53:1957.
165. Rammelkamp K. Investigation of LIBS and Raman data analysis methods in the context of insitu planetary exploration. Humboldt University; 2019.
166. Limbeck A, Brunnbauer L, Lohninger H, Pořízka P, Modlitbova P, Kaiser J, Janovszky P, Kéri A, Galbács G. Methodology and applications of elemental mapping by laser induced breakdown spectroscopy. Anal Chim Acta. 2021;1147:72.
167. Jolivet L, Leprince M, Moncayo S, Sorbier L, Lienemann C-P, Motto-Ros V. Review of the recent advances and applications of LIBS-based imaging. Spectrochim Acta B. 2019;151:41.
168. Motto-Ros V, Moncayo S, Fabre C, Busser B. LIBS imaging applications, laser-induced breakdown spectroscopy. 2nd ed. Elsevier; 2020.
169. Fabre C, Devismes D, Moncayo S, Pelascini F, Trichard F, Lecomte A, Bousquet B, Cauzid J, Motto-Ros V. Elemental imaging by laser-induced breakdown spectroscopy for the geological characterization of minerals. J Anal At Spectrom. 2018;33:1345.
170. Gimenez Y, Busser B, Trichard F, Kulesza A, Laurent JM, Zaun V, Lux F, Benoit JM, Panczer G, Dugourd P, Tillement O, Pelascini F, Sancey L, Motto-Ros V. 3D imaging of nanoparticle distribution in biological tissue by laser-induced breakdown spectroscopy. Sci Rep. 2016;6:29936.
171. Menut D, Fichet P, Lacour JL, Rivoallan A, Mauchien P. Micro-laser-induced breakdown spectroscopy technique: a powerful method for performing quantitative surface mapping on conductive and nonconductive samples. Appl Opt. 2003;42:6063.
172. Zorba V, Mao X, Russo RE. Femtosecond laser induced breakdown spectroscopy of Cu at the micron/sub-micron scale. Spectrochim Acta B. 2015;113:37.
173. Zorba V, Mao X, Russo RE. Ultrafast laser induced breakdown spectroscopy for high spatial resolution chemical analysis. Spectrochim Acta B. 2011;66:189.
174. Wang X, Liang Z, Meng Y, Wang T, Hang W, Huang B. Submicroanalysis of solid samples with near-field enhanced atomic emission spectroscopy. Spectrochim Acta B. 2018;141:1.
175. Li W, Li X, Li X, Hao Z, Lu Y, Zeng X. A review of remote laser-induced breakdown spectroscopy. Appl Spectrosc Rev. 2020;55:1.
176. Narlagiri LM, Bharati MSS, Beeram R, Banerjee D, Soma VR. Recent trends in laser-based standoff detection of hazardous molecules. Trends Anal Chem. 2022;153:116645.
177. Sallé B, Mauchien P, Maurice S. Laser-induced breakdown spectroscopy in open-path configuration for the analysis of distant objects. Spectrochim Acta B. 2007;62:739.
178. Chin SL. Femtosecond laser filamentation. Springer; 2010.
179. Rohwetter PH, Stelmaszczyk K, Wöste L, Ackermann R, Méjean G, Salmon E, Kasparian J, Yu J, Wolf JP. Filament-induced remote surface ablation for long range laser-induced breakdown spectroscopy operation. Spectrochim Acta B. 2005;60:1025.
180. Fobar DG, Xiao X, Burger M, Le S, Berre A, Motta T, Jovanovic I. Robotic delivery of laser-induced breakdown spectroscopy for sensitive chlorine measurement in dry cask storage systems. Prog Nucl Energy. 2018;109:188.
181. Gottfried JL, De Lucia FC, Munson CA, Miziolek AW. Doublepulse standoff laser-induced breakdown spectroscopy for versatile hazardous materials detection. Spectrochim Acta B. 2007;62:1405.
182. Barnett PD, Lamsal N, Angel SM. Standoff laser-induced breakdown spectroscopy (LIBS) using a miniature wide field of view spatial heterodyne spectrometer with sub-microsteradian collection optics. Appl Spectrosc. 2017;71:583.

Part II

Applications

Preclinical Evaluation of Nanoparticle Behavior in Biological Tissues

5

Lucie Sancey, Vincent Motto-Ros, and Benoit Busser

Nanoparticles are used in the clinic as contrast agents [1], drug carriers (as Doxil Caelyx [2], or Abraxane [3]), or theranostic agents gathering imaging and therapy purposes (as AGuIX [4]). They are generally developed to overcome some limitations of available active molecules, including inadequate stability, lack of specific targeting, undesired toxicity, poor water solubility, or inappropriate distribution profile. The administration routes of nanoparticles are varied, including the conventional oral and systemic routes, but local and topical administrations also occur.

Hence, their complete characterization is necessarily performed in animals before reaching the clinic, similarly to any drug or contrast agent. Therefore, data about the administration, distribution, metabolism, and elimination (together also called ADME) are collected during these preclinical studies and all this information relevant to the clinical trial is compiled in a regulatory Investigational Medicinal Product Dossier (IMPD).

The investigation of ADME requires tracking the nanoparticle or its metabolites once administered to an animal. One of the easier ways to track a compound in animal studies could be to couple it with a contrast agent moiety, such as a

L. Sancey (✉)
Université Grenoble Alpes, Institute for Advanced Biosciences, INSERM U1209, CNRS, UMR 5309, Grenoble, France
e-mail: Lucie.sancey@univ-grenoble-alpes.fr

V. Motto-Ros
Institut Lumière Matière, UMR 5306, Univ. Lyon 1, CNRS, Villeurbanne, France

B. Busser
Université Grenoble Alpes, Institute for Advanced Biosciences, INSERM U1209, CNRS, UMR 5309, Grenoble, France

Grenoble Alpes University Hospital, Grenoble, France

Institut Universitaire de France (IUF), Paris, France

G. Galbács (ed.), *Laser-Induced Breakdown Spectroscopy in Biological, Forensic and Materials Sciences*, https://doi.org/10.1007/978-3-031-14502-5_5

fluorescent dye. However, any additional modification of the nanoparticle may alter or change either its size or its charge, with a potential direct impact on the kinetics. Accordingly, the collection of ADME information without chemical modification of the nanoparticle is of major importance. In addition to radio-isotopic studies, elemental imaging can also provide insightful data related to the distribution of the nanoparticles at the organ level, but also about their pharmacokinetics and metabolism. In this chapter, we will present an overview of the possibilities offered by LIBS elemental imaging for such preclinical investigations.

5.1 Experimental Set-up

To investigate biological samples using LIBS, the single shot ablation occurs in general via a focused nanosecond laser pulse which ablates a few nanograms of biological matter and excites it in the plasma plume. The light emitted by the plasma is collected through optical fibers and analyzed by one or more spectrometers (Fig. 5.1). The use of several spectrometers with specific spectral ranges allows

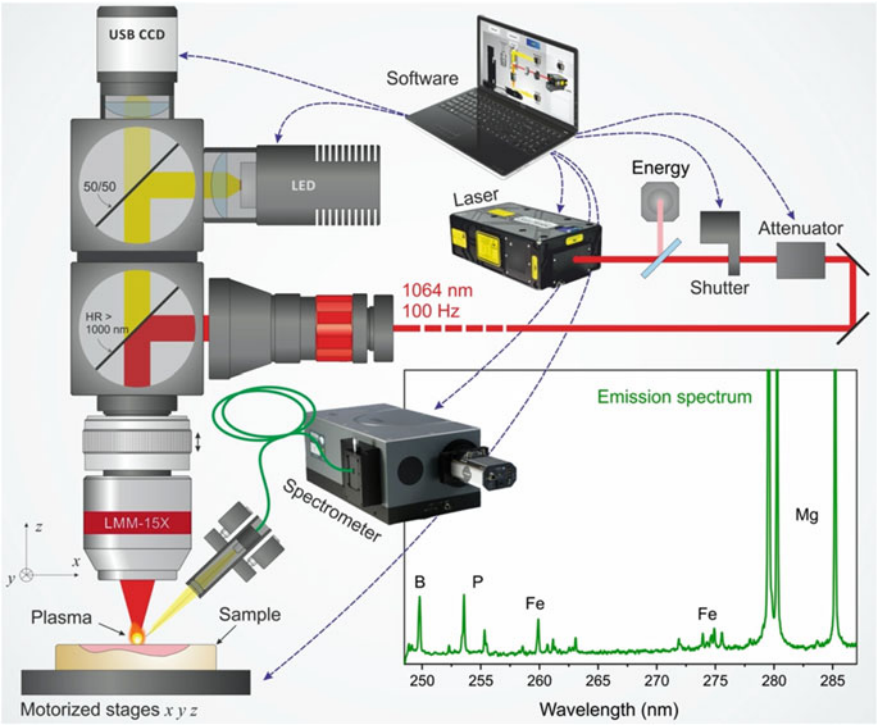

Fig. 5.1 LIBS set-up and representative emission of a sample containing boron. Adapted from Motto-Ros V. et al. [5, 6]

the identification of various elements simultaneously. Complementary details about LIBS instrumental set-up are described in more detail in a recent review [7].

5.2 Sample Preparation and Endogenous Element Detection

Sample preparation is a key step and should be performed with particular attention to ensure the quality of the measurements and the accuracy of the detected signal. The first LIBS elemental imaging experiments on biological tissues were performed on frozen sections with limited spatial resolution [5, 8, 9]. A major improvement has been obtained when samples were embedded in rigid matrices such as epoxy resins [10]. The benefit of this approach is twofold: the hardening of the sample improved the resolution, and the pre-analytical steps of dehydration removed any residual presence of water which improved sensitivity. Elemental images were obtained after performing investigations directly on epoxy blocks [10] or on thin sections [11], and allowed achieving high-spatial resolution ($<$10 μm) and the 3D-reconstruction of entire organs after screening. Epoxy resin embedding is not the gold standard for processing clinical samples, thus we started working on the elemental imaging of paraffin-embedded specimens. As compared to epoxy, paraffin is soft and possesses a very-low melting temperature. These two characteristics significantly alter the achieved lateral resolution of the obtained elemental images; however, paraffin-embedded samples could be very large in size (up to ca. 2 $\times$ 2 cm), and can be analyzed with complementary techniques such as histology [12, 13]. An increase in resolution was considered unachievable; however, a nano-laser probe double-pulse system was used to detect the subcellular distribution of indium phosphide nanoparticles within frozen single cells [14]. The InP nanoparticles were identified by LIBS analysis at the main emission line of indium (In I 410.2 nm) and co-localized with the lysosomal compartment. The analysis of subcellular organelles with a submicrometric resolution (500 nm) with an absolute limit of detection $<$20 fg/pulse is a breakthrough that paves the way for numerous applications in biology. A full organ could be explored in reconstructed 3D analysis with the imaging of consecutive and adjacent sections, or with another strategy consisting of in-depth 3D profiling [11].

In order to clearly identify the biological matter, elements that are homogenously distributed within the tissue could be used to evidence the shape and the main structure of the sample, similarly to conventional histological analysis. Among the endogenous elements used in this perspective, carbon [15], sodium [16, 17], calcium [11], or phosphorus [12, 13, 18] may serve as background elements that will reveal the general histology of the tissue. We consider phosphorous (P) as an ideal candidate for imaging the tissue architecture, since its emission line at 213.61 nm is devoid of interferences from other elements, but also because phosphorous is a ubiquitous element present in the nucleus and in the membrane of every cell. As a consequence, the imaging of phosphorous indirectly reflects the cell density of the tissue. Using specific sample preparation, the main vascular network can also be evidenced with the collection of iron signal that may reflect the iron contained in

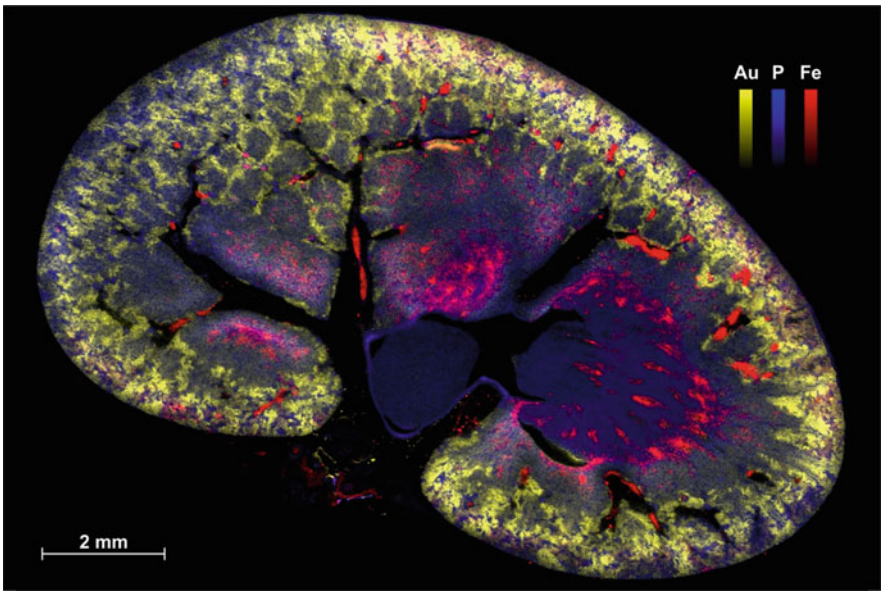

Fig. 5.2 Multi-elemental image of a rat kidney after intravenous injection of Au NPs. Merged image composed of the combination of three false color elemental images for Au (yellow), P (blue), and Fe (red). These animal experiments were approved by the local ethics committee under agreement A21231016EA. Taken from Spectroscopy, Volume 35, Issue 2, Pages: 34–40 with permission from the MJH LIfe Sciences Group

hemoglobin in tissues that have not been cleared before LIBS analysis (Fig. 5.2) [10, 19].

5.3 Nanoparticle Tracking

The identification and the biological localization of metal-based nanoparticles have been described at the organ scale as early as in 2012 [5]. The design of the experiments may allow to observe the kinetics of distribution in a given organ [17], the pharmacokinetic in the blood [20], or the presence of protein corona [21]. In these two last examples, the LIBS analysis is performed directly on blood/serum drops. Such chronologic pharmacokinetic studies are possible when tissue sampling is performed at different time points after the administration of the metal-based nanoparticles.

The analysis of the main organs of elimination, i.e., the liver and the kidneys, is facilitated by the high local accumulation of the compounds (Fig. 5.3). Large nanoparticles are predominantly eliminated by the liver route, while the smallest (< 10 nm) or the degraded nanoparticles are eliminated through the renal route. Chelating nanoparticles, as calcium-responsive contrast nanoparticles, were

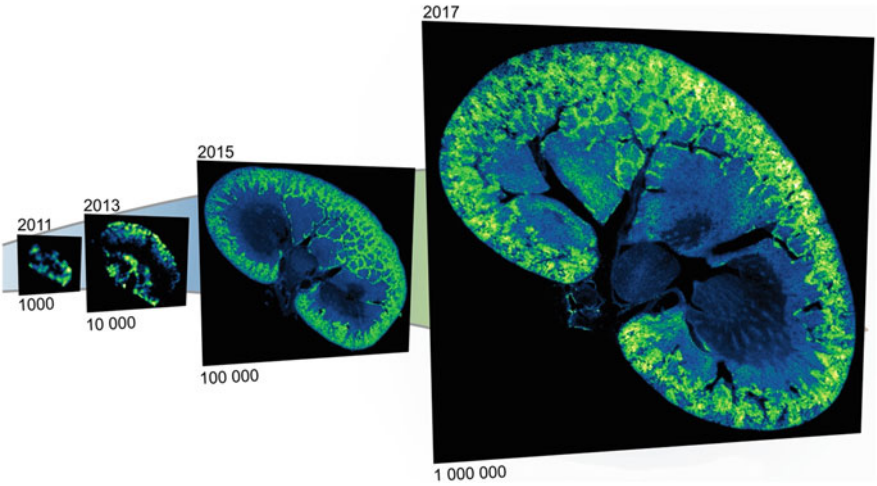

Fig. 5.3 Elemental images of a mouse kidney after intravenous injection of Gd-NPs, represented in false color. The improvement of the image accuracy can be observed over time from 2011 to 2017, together with the increased number of pixels. These animal experiments were approved by the local ethics committee under personal agreements with L. Sancey

evidenced in the cortex of the kidneys due to the transient local accumulation of the nanoparticles in this organ, and this uptake was correlated to the MRI investigations performed after intravenous administration of the nanoparticles [16].

If, in addition to the detection of a single specific element of the nanoparticle, two or more elements could be identified simultaneously, information about the metabolism could also obtained [9, 10] As an example, the absence of metabolism (i.e., absence of degradation) has been evidenced in vivo for Gd/Si nanoparticles using LIBS investigations in mouse kidneys, which has been confirmed by conventional and complementary techniques, such as fluorescence imaging and mass spectroscopy.

For oncology applications, the detection of the nanoparticle at the tumor site could also be necessary for the optimization of the treatment schedule, and for improving the evaluation of the anti-tumor effects of the treatment. In this perspective, the presence of metal nanoparticles has been observed in tumor sections to objectivate the homogeneity of uptake within the tumor, using radiosensitizing nanoparticles made of Gd [22] or Au [23, 24], or to evidence the localization of the nanoparticle at the tumor site versus the healthy surrounding tissues, in the case of LaF_3:Ce nanomaterials [25]. However, not only metal-based nanoparticles can be identified: low-Z metalloid compounds, such as boron (B)-containing nanocomplexes can also be observed within tissues in general and within tumor sections in particular. In the manuscript of Kalot et al., the authors reported the benefits of using innovative boron-rich compounds for a specific type of radiotherapy based on the activation of ^{10}B isotopic activation by neutrons, also known as

boron neutron capture therapy (BNCT). After treatment and neutron exposure, the tumors were collected for analysis, and the tumor sections were studied for the presence of boron using LIBS, several days after the administration of ^{10}B-enriched compounds. LIBS results provided evidence of the long-term retention of boron-rich compounds in tumors.

The identification of nanomaterials could also be achieved in medical samples, in formalin-fixed paraffin-embedded (FFPE) samples [26]. The FFPE embedding procedure is the gold standard procedure for fixing and preserving human tissues collected for diagnostic purposes. It is performed in every hospital for most of the biopsies, and it will advantageously allow the (immuno)-histological observation of the samples. As LIBS investigation requires very low amounts of matter, we believe that LIBS and histopathology analyses are complementary and should be used together to strengthen the diagnosis for specific specimens and clinical cases for which the elemental content could provide useful information to the clinician. Use of this concept has been reported for skin samples. In different skin cancer types, LIBS imaging revealed the heterogenous distribution of various endogenous elements in the tumor itself, but also in its microenvironment [13]. In another study, LIBS analysis of a subcutaneous granuloma revealed a very strong accumulation of Al in the specimen. The medical applications of LIBS imaging are very wide and include the analysis of local cutaneous reactions, pigmented lymph nodes, or biopsies containing exogenous particles [12].

5.4 Conclusions

Elemental imaging is a very powerful tool for the preclinical investigation of nanomaterials. When performed using LIBS, elemental imaging is a fast process that requires moderate sample preparation. LIBS imaging is now operational for working on any kind of tissue, but also on liquid droplets, at room temperature and ambient atmosphere in most of the cases. More complex systems, using nanoparticle enhancement [21, 27], or controlled temperature and atmosphere, may be necessary to track nanoparticles at very low concentrations, especially in biological fluid droplets, or when working with subcellular lateral resolution [14]. All these recent efforts have pushed LIBS imaging technology and procedures to levels that may bridge the gap between physics and biology laboratories, opening avenues for a wider use of LIBS in biological preclinical studies.

Ethical Approval All animal experiments were performed in accordance with national legislation and European guidelines, and with the approval of the institutional and national ("Ministère de l'Enseignement Supérieure et de la Recherche") animal ethics committees (#A21231016EA and APAFIS #00473.01_B691230303).

References

1. Stueber DD, et al. Magnetic nanoparticles in biology and medicine: past, present, and future trends. Pharmaceutics. 2021;13:943.
2. Rivankar S. An overview of doxorubicin formulations in cancer therapy. J Cancer Res Ther. 2014;10:853.
3. Kundranda MN, et al. Albumin-bound paclitaxel in solid tumors: clinical development and future directions. Drug Des Devel Ther. 2015;9:3767.
4. Verry C, et al. Treatment of multiple brain metastases using gadolinium nanoparticles and radiotherapy: NANO-RAD, a phase I study protocol. BMJ Open. 2019;9:e023591.
5. Motto-Ros V, et al. Mapping of native inorganic elements and injected nanoparticles in a biological organ with laser-induced plasma. Appl Phys Lett. 2012;101:223702.
6. Motto-Ros V, et al. Imagerie libs: aux portes de la clinique. Photo-Dermatology. 2020a;103:34.
7. Busser B, et al. Elemental imaging using laser-induced breakdown spectroscopy: a new and promising approach for biological and medical applications. Coord Chem Rev. 2018a;358:70.
8. Motto-Ros V, et al. Mapping nanoparticles injected into a biological tissue using laser-induced breakdown spectroscopy. Spectrochim Acta B. 2013;87:168.
9. Sancey L, et al. Laser-induced breakdown spectroscopy: a new approach for nanoparticle's mapping and quantification in organ tissue. J Vis Exp. 2014;88;e51353.
10. Sancey L, et al. Laser spectrometry for multi-elemental imaging of biological tissues. Sci Rep. 2014;4:6065.
11. Gimenez Y, et al. 3D imaging of nanoparticle distribution in biological tissue by laser-induced breakdown spectroscopy. Sci Rep. 2016;6:29936.
12. Busser B, et al. Characterization of foreign materials in paraffin-embedded pathological specimens using in situ multi-elemental imaging with laser spectroscopy. Mod Pathol. 2018b;31:378.
13. Moncayo S, et al. Multi-elemental imaging of paraffin-embedded human samples by laser-induced breakdown spectroscopy. Spectrochim Acta B. 2017;133:40.
14. Meng Y, et al. Nanoscale laser-induced breakdown spectroscopy imaging reveals chemical distribution with subcellular resolution. Nanoscale Adv. 2020;2:3983.
15. Bonta M, et al. Elemental mapping of biological samples by the combined use of LIBS and LA-ICP-MS. J Anal At Spectrom. 2016;31:252.
16. Moussaron A, et al. Ultrasmall nanoplatforms as calcium-responsive contrast agents for magnetic resonance imaging. Small. 2015;11:4900.
17. Sancey L, et al. Long-term in vivo clearance of gadolinium-based AGuIX nanoparticles and their biocompatibility after systemic injection. ACS Nano. 2015;9:2477.
18. Kunjachan S, et al. Nanoparticle-mediated tumor vascular disruption: a novel strategy in radiation therapy. Nano Lett. 2015;15:7488.
19. Motto-Ros V, et al. LIBS-based imaging: recent advances and future directions. Spectroscopy. 2020b;35:34.
20. Chu Y, et al. Half-life determination of inorganic-organic hybrid nanomaterials in mice using laser-induced breakdown spectroscopy. J Adv Res. 2020;24:353.
21. Dell'Aglio M, et al. Sensing nanoparticle-protein corona using nanoparticle enhanced laser induced breakdown spectroscopy signal enhancement. Talanta. 2021;235:122741.
22. Detappe A, et al. Advanced multimodal nanoparticles delay tumor progression with clinical radiation therapy. J Control Release. 2016;238:103.
23. Kunjachan S, et al. Selective priming of tumor blood vessels by radiation therapy enhances nanodrug delivery. Sci Rep. 2019;9:15844.

24. Le Guevel X, et al. Elemental and optical imaging evaluation of zwitterionic gold nanoclusters in glioblastoma mouse models. Nanoscale. 2018;10:18657.
25. Bulin AL, et al. Radiation dose-enhancement is a potent radiotherapeutic effect of rare-earth composite nanoscintillators in preclinical models of glioblastoma. Adv Sci (Weinh). 2020;7: 2001675.
26. Busser B, et al. LIBS imaging is entering the clinic as a new diagnostic tool. Spectroscopy. 2020;35:17.
27. De Giacomo A, et al. Nanoparticle-enhanced laser-induced breakdown spectroscopy for microdrop analysis at sub-ppm level. Anal Chem. 2016;88:5251.

Imaging of Biological Tissues

6

Pavel Pořízka, Pavlína Modlitbová, and Jozef Kaiser

6.1 Introduction

Investigation of biological samples relies on state-of-the-art instrumentation providing high performance namely in terms of sensitivity and spatial resolution. Optical microscopy is often complemented with other techniques to reach a more complex understanding of investigated phenomena. For those purposes, techniques of analytical chemistry are beneficially used to assess the elemental and molecular composition. The persisting trend in the development of instrumentation and methodology drives away from the direct analysis of sample bulk. However, the bulk chemical analysis through wet chemistry brings the main limitation. The necessity of acid digestion of the sample results in the loss of valuable information about the distribution of elemental/molecular content within the sample.

It has been repeatedly proven that individual diseases manifest themselves also in a significant change in the chemical composition of bodily fluids or tissues [1]. Factual localization of the local singularities in chemical composition and its correlation with changes and degradation of cells is necessary. Providing chemical information with a cell-level resolution is a goal of the spectroscopic community that will have a significant impact on the understanding of disease initiation and proliferation throughout the tissue. Thus, the detection of abundance/deficiency of individual elements/molecules is of paramount interest to biologists. Finally, it must be stressed that in this chapter we restrict our interest to biological tissues, namely soft and hard/calcified tissues. Obviously, imaging the distribution of elements within other biological tissues also found numerous applications that are briefly mentioned and reviewed as well.

Lasers have a broad range of use for therapy and diagnostics of biological tissues [2] with extensions to various medical fields (e.g., dentistry, surgery, dermatology)

P. Pořízka (✉) · P. Modlitbová · J. Kaiser
CEITEC Brno University of Technology, Brno, Czech Republic
e-mail: Pavel.Porizka@ceitec.vutbr.cz

G. Galbács (ed.), *Laser-Induced Breakdown Spectroscopy in Biological, Forensic and Materials Sciences*, https://doi.org/10.1007/978-3-031-14502-5_6

[3]. The laser-tissue interaction is a well-investigated phenomenon in individual applications for which the laser parameters (e.g., laser wavelength, pulse energy, and duration) are optimized [4]. For diagnostic purposes, the laser parameters are varied to the point when they induce desired characteristic response from the investigated tissues. Determination of elemental composition within the laser spot region demands increasing the laser irradiance over the ablation threshold to reach breakdown and plasma formation (GW/cm^2). Laser ablation is, thus, used for material sampling and its characterization is done through the optical emission spectroscopy of laser-induced plasma (LIP) radiation. Pulsed ablation of tissues is well-described in classic literature [5] and will be dissected further in the text.

Laser ablation is typically coupled with optical emission spectroscopy or mass spectrometry while qualitative and quantitative elemental analysis of a sample is obtained. The laser ablation inductively coupled plasma optical emission spectroscopy and mass spectrometry (LA-ICP-OES/MS) is the gold standard in terms of imaging and, thus, the main representative among other techniques of the field in analytical spectroscopy. However, laser-induced breakdown spectroscopy (LIBS) proved to be a suitable alternative due to recent advances in instrumentation and methodology.

LIBS has established its position among other techniques due to its supreme sample throughput and related laser pulse repetition rate. Here we consider the repetition rate as the main benefit of LIBS providing a high number of analyses (spectra) per unit time. Moreover, the LIBS analysis takes a fraction of time also with more robust and less complicated instrumentation when compared to LA-ICP-OES/MS. This makes LIBS a suitable candidate for deployment in various applications with a potential for in-situ analysis of plants and even direct analysis during surgery [6, 7].

The implementation of LIBS to the analysis of various biological samples increasingly attracts attention. Moreover, recent advances have led to promising results in medical and clinical applications which have been a rapidly expanding field since the beginning of this decade (see Sect. 6.4). In general, LIBS provides information about organogenic (e.g., C, O, H, N, P) and macro nutrient elements (e.g., Ca, Mg, K, Na) while lacking considerable sensitivity to reach some biologically relevant minor and trace elements (e.g., Zn, Cu). This analytical performance predetermines LIBS as a complementary technique to LA-ICP-MS which in turn excels in the detection of traces. Their joint utilization has already been studied in the case of bio-tissues, e.g., plants [8], hard tissues (animal teeth) [9], and soft tissues (human tumors) [10]. However, LA-ICP-OES/MS techniques are considered to be a reference to LIBS, which is a contrast to their joint use. Despite that paradox, LA-ICP-related publications provide a vital source of inspiration for further development of LIBS instrumentation and methodology [1, 11–15].

In this chapter, we will focus primarily on the elemental analysis of biological samples (soft and hard/calcified tissues) when the mapping of large-scale areas is involved. Hence, we will refer to the elemental mapping of biological sample surface as the so-called *elemental bioimaging* or just *imaging* in a broader sense. Also, LIBS analysis of other biological tissues (namely plants) is briefly discussed with related

literature. The description of LIBS instrumentation and progress in analytical performance is shown together with concepts of bioimaging (including 3D imaging), and novel approaches to correlative imaging. Remarks on the parameters involved in laser-tissue interaction and sample preparation are also given along with a broader discussion. Then, good practices in data processing are listed in terms of sample discrimination and quantification; basic univariate and advanced multivariate (chemometrics and machine learning) algorithms are mentioned. Finally, imaging of animal and human tissues is dissected with the vision to medical/clinical applications. The chapter is concluded with hints of future perspectives and trends in the development of the field of LIBS bioimaging.

This chapter builds on existing results in current scientific literature. Thus, the reader is referred to respective bioimaging chapters in other LIBS reviews [3, 16–19]. Other literature sources related to the fundamentals of LIBS and its broad applications [20–24], laser-tissue interaction [4, 5], and the use of lasers in medical and clinical applications [2] are also recommended for further reading.

6.2 Laser Ablation of Tissues

6.2.1 Laser Parameters Involved in the Ablation of Tissues

In this chapter, we do not intend to describe the mechanisms of laser-tissue interaction and consequent laser ablation in detail. Presented review was collected from LIBS-related literature and summarizes selected results and conclusions. Moreover, the reader is referred to a more extensive description in other publications [2, 4, 5]. If not stated otherwise, those references were primarily used in this section.

Naturally, the quality of laser-tissue interaction is determined by optical properties of involved soft/hard tissue and the parameters of the laser radiation. First, the composition of soft tissues is dominated by water (50–95%), collagen, hemoglobin, and melanin. Second, hard tissues are composed namely from hydroxyapatite (~96%), and water. From the optical point of view, the wavelength-dependent absorption coefficient of listed building materials is the most important parameter [5] as shown in Fig. 6.1 for the case of soft tissues. Refer to [4] for the absorption coefficient of hydroxyapatite (hard tissues). It is presented as the most critical property to sustain an optimal energy deposition and desired tissue ablation.

The absorption coefficient is of interest to LIBS in three ranges (UV, VIS, and IR) which relate the material properties with the laser source used for ablation. A Nd:YAG laser generating ns laser pulses on fundamental and harmonic wavelengths (1064, 532, and 266 nm) is typically used for this task in LIBS. In general, the absorption of listed tissue compounds is the lowest in IR range and rises in the UV (Fig. 6.1). This includes the case of hydroxyapatite which is not shown in this figure. Water, an important component of soft tissues, has a high increase in the absorption coefficient in the UV and IR ranges, which corresponds to fundamental (1064 nm) and fourth harmonic (266 nm) wavelengths of Nd:YAG. Melanin, dominating chromophore in pigmented tissues (e.g., skin), has a high absorption coefficient in

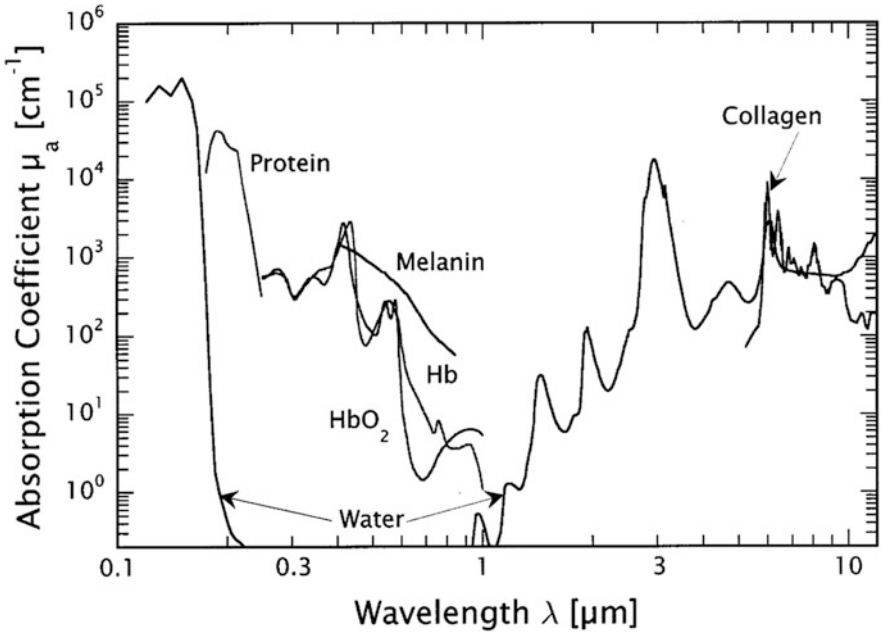

Fig. 6.1 Optical absorption coefficients for selected tissue compounds from 0.1 to 10 μm wavelength range. Hb and HbO_2 correspond to deoxygenated and oxygenated hemoglobin. Obtained from [5] with no permission needed from ACS publications

VIS range where Nd:YAG laser operates on its second harmonic wavelength (532 nm). Thus, the selection of laser wavelength is a crucial step before LIBS analysis.

Harmonics generation is an option to change the wavelength of a pulsed laser, but it is a costly one and it leads to a significant decrease in the peak pulse power. It must be stressed that higher energy is necessary also for the laser ablation with higher harmonics, which is evident when printing relevant irradiances as a function of pulse duration (Fig. 6.2). Selected references with a focus on soft tissues are listed in Table 6.1. Contemporary state-of-the-art LIBS analysis of tissues is dominated by the use of fundamental Nd:YAG wavelength. This is in contrast with the optical absorption coefficients of individual tissue compounds. The fundamental and fourth harmonic wavelengths of an ns-pulsed Nd:YAG laser (1064 vs 266 nm, respectively) were compared in the ablation of murine kidneys [26]. The results of this study pointed toward the advantageous use of 1064 nm for soft tissue ablation as it provided more reproducible ablation and a tighter crater size. The authors suggested that the reason for this was that tissue is transparent to IR radiation, so it is ablated indirectly by the plasma generated on the substrate (150 μm thick cryo sections on a glass slide). Moreover, the increased absorption of the tissue to UV can lead to a broader collateral damage in a broader range. At the same time, the wavelengths of an fs laser (343 and 1030 nm harmonic wavelengths) were selected for the LIBS

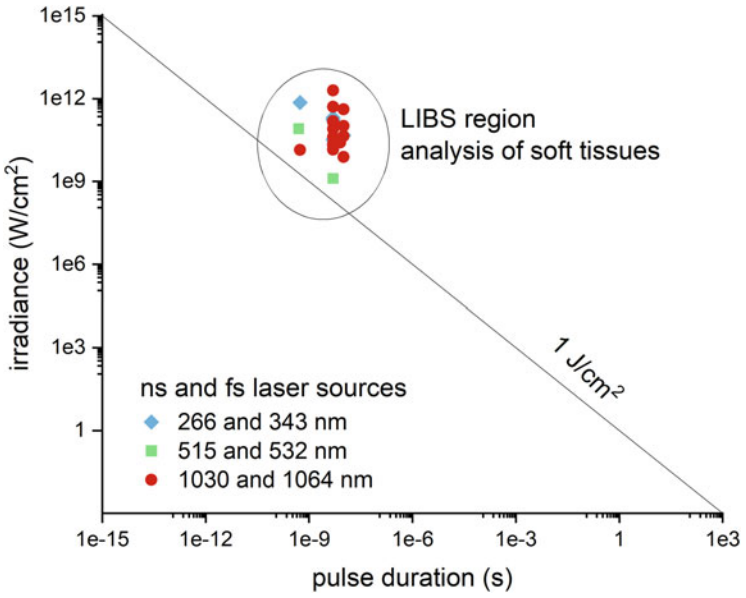

Fig. 6.2 Laser-tissue interaction in terms of pulse duration and irradiance. The circle roughly indicates region of laser-induced plasmas (LIPs) on soft tissues with ns (1064, 532, 266 nm) and fs (1030 and 515 nm) laser sources. Data points were collected from selected literature focused on LIBS analysis of soft tissues. The zoomed region contains references to relevant publications from Table 6.1. Other information on laser-tissue interaction can be found elsewhere [4]

analysis of murine melanoma (40 μm thick sections on a silica substrate) [47]. Their comparison showed similar results as those with the ns-laser ablation—UV wavelength (343 nm) showed higher fluctuations due to inhomogeneity of the tissue and IR wavelength (1030 nm) tended to ablate the tissue indirectly by the ablation of the substrate. The comparison between fs and ns laser pulses is thus appealing for further research while fs lasers are getting more and more affordable and thus are becoming popular in the LIBS community.

Optimization of a LIBS system prior to the analysis is mandatory, however, the optimization of pulse wavelength (UV, VIS, or IR) and pulse duration (fs, ps, and ns) is rare due to complications in the instrumentation. On the other hand, optimization of other experimental parameters (e.g., laser pulse energy, defocus) was discussed in the majority of publications. There is a need for finding the right trade-off between sensitivity and lateral resolution when balancing the amount of ablated material. To achieve the best possible performance, several approaches based on finding the highest signal-to-noise ratio (SNR) were suggested [27, 44]. The optimization in these cases was mostly focusing on the feedback of selected analytes (in the sense of SNR) and the shape and size of the ablation crater. It is advised to implement other optical techniques (e.g., plasma imaging [51] and shadowgraphy [52]) also within the parameter optimization pipeline.

Table 6.1 List of selected publications with focus on the bioimaging of soft tissues or their analysis in the focus. Data assigned with asterix were not directly given in the referred publication and were estimated from existing information or from similar works of the related research group. Selected publications are ordered from oldest to newest

Sample	Pretreatment	Wavelength (nm)	Duration (ns)	Spot size (μm)	Irradiance (GW/cm^2)	Ref.
Murine kidney	Cryo cutting	1064	5	50	152.9	[25]
Murine kidney	Cryo cutting	1064	5	40	79.6	[26]
Murine kidney	Epoxy resin	266	5	25	32.6	[27]
Murine kidney, tumor	Cryo cutting	1064	5	50	40.8	[28]
Human tumor	Cryo cutting	266	10*	40	171.2	[10]
Murine kidney	Epoxy resin	266	5	10	203.8	[29]
Murine kidney	Epoxy resin	1064	5	30	14.2	[30]
Murine tumor	FFPE	1064	5	50	152.9	[31]
Murine tumor	FFPE	1064	5	30*	141.5	[32]
Murine kidney	Epoxy resin	1064	5	5	509.6	[33]
Skin, lungs, lymph nodes	FFPE	1064	5	66	23.4	[34]
Skin	FFPE	1064	5	50	20.4	[35]
Murine tumor	Cryo cutting	266	10	60	46.7	[36]
Murine kidney, spleen, liver, tumor	Epoxy resin	1064	5	5	509.6	[37]
Cutaneous tumor	Cryo cutting	1030	0.55	65	13.7	[38]
Murine tumor	FFPE	1064	10*	100	7.6	[39]
Murine tumor, cell culture	Cryo cutting	1064	8	25*	25.5	[40]
Brain tumor, cell culture	Cryo cutting	1064	8	25	25.5	[41]
Cells	Freeze-dried	515	0.5	0.5	81.5	[42]
Lung tumor	Cryo cutting	1064	10	45*	408.9	[43]
Murine kidney	FFPE	532	5	100	1.3	[44]
Brain	FFPE	1064	10*	45	44.0	[45]
Cutaneous tumor	FFPE	532	5	100	1.3	[46]
Cutaneous tumor	Cryo cutting	343	0.55	15	720.6	[47]
Lung tumor	FFPE	1064	10*	50	101.9	[48]
Leporine lymph nodes and thyroid glands	Tissue smear	1064	5	22*	1997*	[49]
Brain tumor	FFPE	1064	5	22*	1997*	[50]

6.2.2 Sample Preparation

It is a cliché that there is no need for sample preparation prior to the LIBS analysis of biological tissues. Soft and hard tissues have to be prepared following one or the

other ways reviewed elsewhere [53]. The preparation of hard tissues seems straightforward as the most common approach is epoxy embedding, cutting and fine polishing. The preparation of soft tissues is demanding (consider e.g., the handling of the tissue after biopsy) and two most common approaches used (Table 6.1) are (1) freezing at a cryogenic temperature and (2) formaldehyde fixing and paraffin embedding (FFPE). The latter seems to be more feasible and more convenient for manipulation when enabling the LIBS analysis of cross-sections [44] and direct bulk [46]. The FFPE is the standard procedure in pathology and LIBS has a potential to provide relevant information, but it has to be kept in mind that this kind of sample preprocessing might alter the elemental composition of the tissue and the distribution of elements therein [54].

6.2.3 From the Concept to 3D Bioimaging

The concept of imaging, Fig. 6.3, is a simple application of LIBS when the sample material is ablated from its surface at different positions. In each position, a plasma is generated, and its characteristic radiation is collected by means of optical emission spectroscopy. Obtained spectra are then processed, and estimated intensities of selected spectral lines are printed in images showing the distribution of related elements across the sample surface. Bioimaging approaches are boosted by the advantages of LIBS in general, such as multi-elemental capability, minimal need for sample preparation, high-lateral resolution, and sensitivity. However, those benefits seem contradictory to each other when tuning the experimental settings (e.g., spot size, pulse energy, atmosphere) and optimizing the best possible

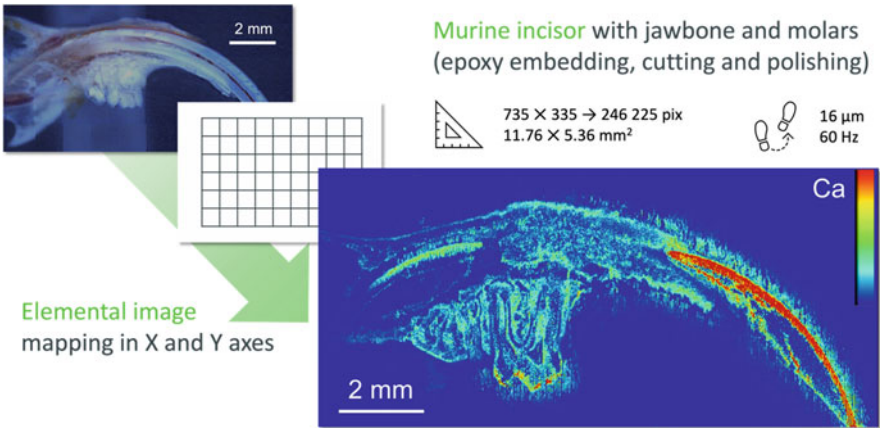

Fig. 6.3 The concept of bioimaging, showing the optical image of epoxy embedded murine incisor (top left), mesh of points in X,Y raster (center), and depicted Ca image (bottom right). The infographics show the total number of pixels and analyzed area, and step size and repetition rate. Authors' unpublished data

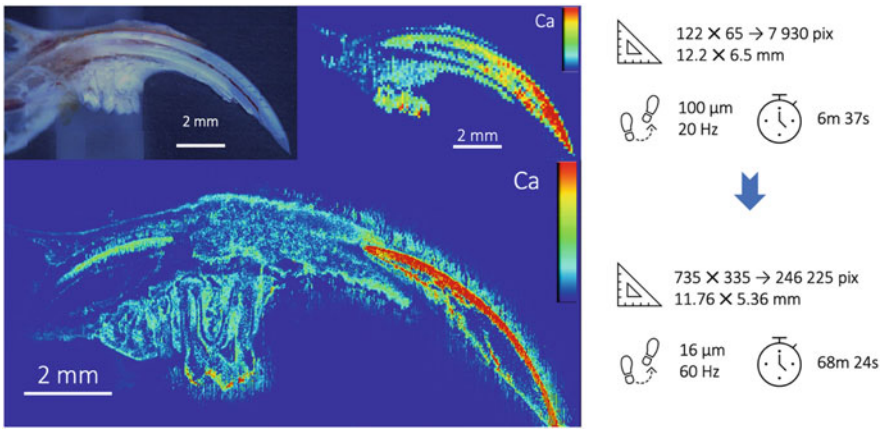

Fig. 6.4 Improvement of the analysis of hard tissues (murine incisor and adjacent jawbone embedded in epoxy resin) in terms of repetition rate and lateral resolution. Authors' unpublished data

performance (e.g., signal to noise ratio, signal to background ratio). Individual issues will be further dissected with respective suggestions.

LIBS imaging is a dynamically evolving field that has recently been driven mainly by the demand from the mining industry [55] and clinical analysis [46]. To give an extreme example of LIBS repetition rate capability, the state-of-the-art instrumentation provides an extreme performance in the analysis of mine drill and cores with 1 kHz repetition rate [56]. Further development of instrumentation for bioimaging will routinely allow elemental imaging with more than 100,000 pixels per sample. For a large-scale sample, the collection of a megapixel image (containing one million spectra) can currently be done within 2 h and 45 min with a 100 Hz laser used. Thanks to this promising performance, LIBS can be used as a fast-prescreening tool in tissue diagnostics before a more precise or sensitive technique is used. However, this tremendous repetition rate yields a high amount of data which requires more intricate data storage and handling (Sect. 6.3.3). The megapixel image will turn into 4.1 GB of data with a simple line CCD detector of a Czerny-Turner (with 2048 pixels per spectrum and 16 bit depth per pixel).

In modern LIBS tissue diagnostics, the desire is the highest possible lateral resolution (~10 µm) which reaches the cell level. This spot size leads to the ablation of a low amount of mass and, thus, a low number of emitting species within the LIP. In turn, a higher lateral resolution is usually reached with the decrease in sensitivity and loss of detection capability in the ppm range. This tradeoff is a matter of system optimization. The ablation spot size in the range of 10–30 µm was found as a reasonable tradeoff when yielding satisfactory results even in the ablation of soft [33, 37] and hard tissues [57]. The improvement in lateral resolution over past years, Fig. 6.4, brings more biologically relevant information with finer details in the heterogeneous structure of tissues. To the best of our knowledge, the highest lateral

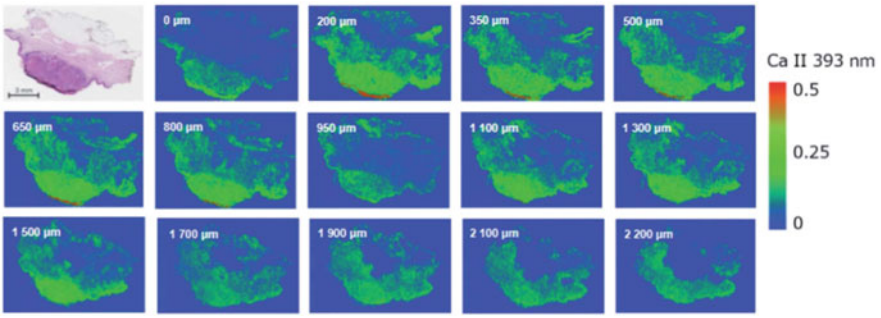

Fig. 6.5 Consequent images of Ca within a bulk of Squamous Cell Carcinoma sample leading to the 3D imaging. The images were obtained by repeated LIBS analysis of consequent sections of paraffine block. The micrometer values refer to the depth from the samples surface (0 µm); the scale shows relative intensity of Ca II 393 nm line. Obtained from [46] while no permission needed from the Royal Society of Chemistry publishing

resolution reached in LIBS bioimaging is on the sub-micron level (~500 nm) [42]. In that study, a combination of fs and ns laser pulses (in the orthogonal double-pulse arrangement) was used to image the distribution of InP nanoparticles (NPs) within a single cell (deposited in wells on quartz wafers).

LIBS enables fast analysis of sample surfaces. Then, the whole sample (e.g., model plant) can be ablated in several layers and signal accumulated along the depth reveals "total" (3D) distribution of elements therein [58]. This feature is often used in the so-called 3D imaging where individual layers of the sample surface are consequently ablated. This approach is an extended use of standard depth profiling and gives further information for the sample investigation. The 3D imaging was already demonstrated on the pesticide penetration into the maize leaf [59]. In past years, 3D imaging was used to analyze layers of murine kidney [33], murine brain [45], and even human cutaneous tumor (squamous cell carcinoma) [46] (Fig. 6.5).

6.3 Data Processing

6.3.1 From Qualitative to Quantitative Imaging

In general, LIBS governs multi-elemental capability and enables the detection of organogenic elements (e.g., C, O, H, N, P), macro nutrient elements (e.g., Ca, Mg, K, Na), and potentially trace elements (e.g., Zn, Cu). The detection of endogenous metals (i.e., macro- and micro-nutrient elements) is indispensable for the so-called metallomics, i.e., the detection of relevant metals as biomarkers within the tissue and estimation of the change in their abundance. It was repeatedly confirmed that any disbalance in the endogenous metal content (deficiency or excess) influences the functioning of tissues and may lead to various diseases, including cancer [3, 16, 18]. Moreover, the detection of exogenous metals (i.e., metals artificially

administered to the tissue) also found its place in biological/medical applications (e.g., indirect biomarkers and labels of selected proteins, toxicology).

Many scientific works in the past focused on the analysis of well-selected spots (line scans or small maps) owing to the limitations in the instrumentation performance (repetition rate and incapability of large-scale mapping). However, proper selection of characteristic regions of the investigated sample led to interesting results that paved the way for further LIBS development in imaging. In the beginning, the ablation of hard tissues was more attractive in the LIBS community owing to its more convenient laser-tissue interaction and consecutive ablation. The body of work by Samek et al. showed the potential of LIBS in human teeth analysis; including the pioneering work on the quantification of trace metals [60], matrix-matched calibration of Al, Pb, and Sr [61], and classification of healthy and carious teeth [62]. Later, the group of Kaiser et al. delivered the line scan of Sr and Ba (Ca served as internal standard for both elements) in prehistoric bear tooth [9], LIBS imaging of Ca and P of snake vertebrae complemented X-Ray Computed Tomography (XCT) scan [63], and small-size mapping of Ca and P as age-related changes in the chameleon teeth [64]. Presented publications can be considered as classical LIBS literature. Moreover, further publications showed other significant benefits of LIBS, e.g., in dentistry [65]. The early detection of caries was proved feasible based on the ratio of Zn and Ca content within the tooth [66].

The LIBS-related research in the case of soft tissues is predominantly focused on the diagnostics of cancer [3]. As LIBS generally lacks the detection capability for trace elements, the interest is mainly in the semiquantitative analysis of abundance of major nutrition elements (e.g., Ca, K, Mg, and Na) with trace elements (e.g., Fe, Cu, and Zn) being seldom presented. The changes in elemental composition were found beneficial in the discrimination of healthy and diseased tissues in many cases, e.g., hemangiosarcoma and normal liver [67], breast and colorectal cancers [68], and breast cancer [69]. A similar approach was then used to differentiate cancerous tissues in large-scale imaging (see further in the text). The next step in the data analysis is the implementation of chemometric algorithms and machine learning (Sect. 6.3.3).

Quantification is a persisting burden of LIBS analyses limiting its extensive use in real-life applications. The main drawback of quantitation in the case of tissues is the absence of matrix-matched standards. Their preparation from real-life samples is limited, while grounding and homogenization of the tissue and spiking it with selected analyte is contradictory to direct imaging of sectioned samples. Production of relevant reference samples is, thus, a subject of many research groups [70].

The case of hard tissues is rather straightforward when matrix-matched standards can be prepared directly from calcium carbonate, calcium oxalate, or hydroxyapatite. First, calcium carbonate was used for production of reference pellets spiked with traces of Al, Pb, and Sr to calibrate the quantitative LIBS analysis of juvenile teeth, adult teeth and bones [61]. Laser pulse energy, electron number density, and electron temperature were monitored during the experiment to ascertain fluctuations in signal feedback and to mitigate potential differences in physical properties between matrices of collected calcified tissues and artificial reference samples. Constructed

calibration curves for individual analytes (Al, Pb, and Sr) were internally standardized to the Ca line intensity and reached detection limits above ppm range (15, 95, and 30 ppm, respectively). Second, calcium oxalate was spiked with Cu, Mg, Sr, and Zn to provide reference standards in the analysis of human kidney stones while reaching tens to hundreds ppm detection level [71]. Third, hydroxyapatite reference samples were spiked with Co, Mn, Ni, Sr, and V prior the quantitative mapping of human teeth [72].

Soft tissues present a more intricate way of matrix-matched standards preparation. Various approaches of soft tissue preparation were utilized (e.g., homogenized pellets, inkjet solution printed on paper, gelatin gel) while the analyte content was administered through spiking [70]. The group of Motto-Ros produced a series of publications in which the quantification of Gd in murine kidneys was subjected. A rather controversial approach was used in their former study where solutions of Gd NPs were simply put on petri dishes and analyzed with the LIBS under the same conditions as soft tissues [26, 28]. More elaborate preparation followed when reference samples from EPON (1:1 mixture of diglycidyl ether and dodecenylsuccinic anhydride, density of 1.22 g/L) were spiked with dispersion containing Gd NPs [27, 29]. This approach provided matrix-matched standards and, in turn, enabled to quantify the content (up to 15 mM per spot) in the series of measurements monitoring the uptake and clearance of Gd NPs through murine kidneys.

The obstruction with matrix-matched standard preparation leads many researchers to utilize calibration-free approaches for quantification of LIBS data (CF-LIBS) [73]. The CF-LIBS demands the knowledge of plasma temperature which has to be accurately estimated for all elements present in the sample. Therefore, it is necessary to detect broader spectral ranges encompassing multiple spectral lines of individual elements to construct Boltzmann plot or even Saha-Boltzmann plot. CF-LIBS was used in the analysis of human hair and nails [74], and gallstones [75]. Most recently, CF-LIBS was used to quantitate Ba, Ca, Mg, and Sr in deer bones with a reasonable fluctuation reaching 10% [76].

6.3.2 Correlative Imaging

Elemental images of sample surfaces obtained through LIBS analysis are suitable for their comparison with other spectroscopic, microscopic, and even tomographic techniques. Such an approach is collectively called *correlative imaging* (also called *hyphenated* or *complementary analysis*) and attracted a great deal of attention in past years. In fact, the joint utilization of various techniques to yield complementary results is well described in several reviews elsewhere [12, 77]. The correlative imaging demands for a parallel processing of large data sets, which creates an increased computation burden. The recent progress is related to the advancement in data mining (including machine learning) providing more convenient ways of data handling and processing [78, 79].

As already stated, the combination of LIBS with LA-ICP-MS extends the performance capacity of both techniques when overshadowing drawbacks of one technique by advantages of another. This combination provides multi-elemental capability in its full sense, enabling the detection of major and macro-elements by LIBS and traces, as well as isotopes, by LA-ICP-MS. This approach was already used more than a decade ago for imaging Mg and Pb in sunflower plants [8], and Sr and Ca in prehistoric bear tooth [9]. It is worth mentioning that in those publications, the performance of LIBS and LA-ICP-MS was rather compared than complemented. A more recent work [10] showed the full potential of joint use of LIBS (C, H, K, O, and N) and LA-ICP-MS (Cu, Fe, P, Pt, and Zn) in an analysis of human tumor. Obtained images complemented the elemental information about the heterogeneity of the tumor and were compared with optical images of the tissues after hematoxylin and eosin (H/E) staining. The tandem use of LIBS and LA-ICP-MS is being optimized; however, their direct combination in one system is still obstructed with differing optimal ablation parameters of each technique. The combination of LIBS with XRF is, thus, more convenient while the non-destructive use of XRF may be used on the sample prior LIBS analysis [80]. It was shown that both techniques can be used in tandem complementing each other as well as cross-reference manner as demonstrated on the quantitation of Ca, Fe, K, Mn, P, and Si in a dried sugar cane leaf [81].

The combination of LIBS and Raman spectroscopy enables to provide complete chemical information (elemental and molecular, respectively). The main drawback is in the low repetition rate of Raman spectroscopy in general. The Raman signal is basically very weak with high fluorescence, thus longer expositions (~1 s) per spot are necessary. Methodological approaches are developed to overcome those limitations and in Raman spectroscopy the mapping and imaging approach must be differentiated [82]. In the point-by-point mapping, whole Raman spectra are detected in each spot showing various Raman shifts with respect to the investigated molecular bonds. On the other hand, Raman imaging provides a direct image of the selected Raman shift from the complete sample surface, but the other spectral information is lost. To the best of our knowledge, the LIBS and Raman techniques have not been used in the manner of correlative large-scale imaging of biological and other samples. However, it has to be mentioned that the joint use of LIBS and Raman was proved feasible and potentially beneficial, e.g., in the discrimination of algae [83] or bacteria [84].

The use of spectroscopic and tomographic techniques is a novel approach potentially providing complete information about the investigated sample. For those purposes, the use of LIBS and X-ray computed tomography (XCT) seems like a vital match. This combination has already been proved feasible in our recent publications [57, 85]. In our recent publication, LIBS and XCT were jointly used for the analysis of murine incisors [57]. Obtained results contributed to the finding of two distinct types of dentins: cementum versus enamel-facing dentin. The elemental analysis (with a focus on Ca and Mg) was extended with chemometrics, and hyperspectral images were processed through principal component analysis (PCA) and characteristic spectra were clustered through *k*-means clustering. XCT

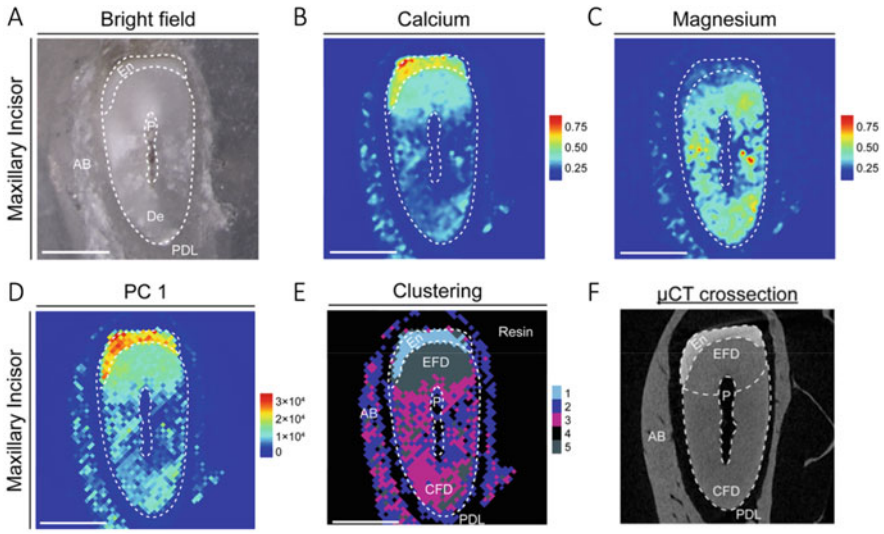

Fig. 6.6 (**a**–**f**) LIBS and XCT analysis of murine incisor. Obtained from [57] with permission and altered. Permission provided from John Wiley and Sons under contract number 5245561066199

volumetric data showed a change in the absorption coefficient in individual matrices/parts of the incisor (i.e., enamel, both dentins, and bone). The XCT image correlated with the LIBS elemental one and cluster images while setting a proof for the existence of two types of dentins (Fig. 6.6).

6.3.3 Multivariate Data Analysis for Imaging Purposes

Collected LIBS data carry characteristic information about investigated sample or relevant position on the sample, the so-called elemental fingerprint. As it was shown above, fine changes in spectral response of selected elemental lines can be related to unique differences between various tissues. However, understanding typical LIBS spectra is tedious namely for their high dimensionality and redundancy [79]. Chemometric and machine learning algorithms are becoming a standard in analytical chemistry [86], incl. LIBS data processing. Those algorithms improve the performance of clustering of characteristic spectra (e.g., related to healthy or diseased tissue) or even classification when the learning process is supervised. Machine learning algorithms were already implemented for the classification of various biological tissues. LIBS and Raman spectra of bacteria were joined together and clustered through Self-Organizing Maps (SOM) classifier after PCA dimensionality reduction [84]. LIBS spectra of deer bones were classified with the use of Artificial Neural Network (ANN) classifier [76]. It is noteworthy that PCA was combined with Linear Discriminant Analysis (LDA) to classify porcine samples (soft and hard tissues) [87].

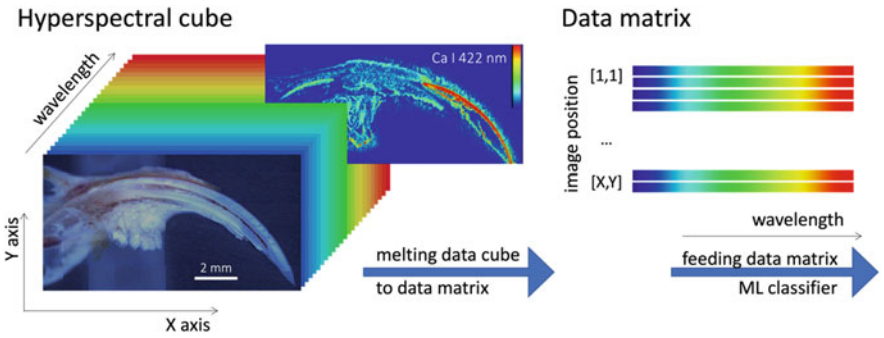

Fig. 6.7 Hyperspectral cube obtained from the analysis of the whole sample. Each [X,Y] position is represented by a related LIBS spectrum. Each layer of high-dimensional data cube provides an elemental image on selected wavelength

The clustering/classification of soft tissue spectra has been repeatedly demonstrated; this is especially appealing in cancer research and other clinical applications. Many feasibility studies were delivered when discriminating healthy and cancerous tissues; e.g., Support Vector Machines (SVM) in the case of lung tumor [43]; LDA, SVM, and ANN were used for the identification of parathyroid gland [49]; SVM and Random Forrest (RF) algorithms were used to cluster brain tumor spectra [50].

The transition from point-by-point analysis to large-scale imaging results in the so-called hyperspectral data cube (Fig. 6.7). The data cube contains high-dimensional data that are organized into a data matrix (spectra as rows, wavelengths as columns) and assigned with metadata (e.g., x, y, and z positions). This simple data handling provides a data structure suitable for further application of machine learning algorithms and consequent clustering or classification of characteristic tissue spectra. The discrimination of melanoma and dermis spectra was proved feasible on mapping (200 × 200 spots with 15 μm steps) of murine skin tumors [47]. The wide spectral range (240–350, 340–450, and 720–800 nm) was downsized with the maximum likelihood technique and selected intensity ratios were then fed to an SVM classifier. Finally, to the best of our knowledge, our group was the first to deliver segmentation of hyperspectral cube (275–290, 380–405, 575–595, and 760–785 nm) obtained from the analysis of human cancer tissues (cutaneous cancers; such as malignant melanoma, basal cell carcinoma, and haemangioma) [46]. The data cube was processed with SOM classifier when showing regions of diseased tissues. Further research and optimization of machine learning (ML) algorithm is necessary in any of the selected publications. There is a clinical need for accurate differentiation of healthy and diseased tissues with highlighted boundary of cancer showing its proliferation throughout the tissue. Thus, this demands a fine-tuning of the ML model prediction and robust thresholding between characteristic spectral responses. However, understanding the performance of ML models is mandatory prior to any further step [78].

Since 2008, the Melikechi group has invested considerable efforts in data processing of LIBS analysis of various blood samples. In their first work [88], they provided a basic visualization of data (mice blood, organic compounds, and proteins) and their distinct separation in PCA space. After the initial success, more sophisticated studies were delivered; e.g., discrimination of healthy and ovarian cancer-prone mice through SVM of LIBS spectra [89]; classification of blood samples from healthy and melanoma-prone mice through LIBS and various classifiers (e.g., LDA, SVM) [90]. Then, Chen et al. analyzed human whole blood samples to guestimate potential occurrence of cancer, lymphoma [91, 92].

6.4 Applications

Broad utilization of LIBS technique led to other bio-applications that are out of scope of this chapter. The investigation of medical samples is also related to the analysis of body fluids and liquids [3]. Considerable attention is also attracted by the potential utilization of LIBS in the detection, classification, and quantification of bacteria and other pathogens [93]. It is also worth mentioning that LIBS provides certain detection power in food analysis [94].

The use of LIBS in biological and medical/clinical applications has already been reviewed [3, 16–19, 65]. Thus, we aim to build on those reviews while offering another perspective to the discussion. Related bioimaging applications are concerned with the detection of elements, mostly metals, that are either naturally present in tissues (i.e., endogenous elements) or administered artificially to tissues (i.e., exogenous elements). In the following paragraphs, selected LIBS research is presented showing its capability to provide valuable information with sufficient sensitivity (reaching ppm level) and lateral resolution (10–100 μm).

6.4.1 Environmental and Plant Tissue Analysis

LIBS is also often used for environmental monitoring and analysis of plants [80, 95, 96]. As in the case of other bio-samples, the detection of macro and micro-nutrients was found to be important. Any change in their abundance within sample bulk (root, stem, leaf) can be correlated with the model-plant growth. There are numerous works that estimate the impact of fertilization and artificially induced stress (e.g., drought, nutrition deficiency, toxicity due to the presence of heavy metals and nanoparticles). Research is generally conducted in terms of qualitative comparison of characteristic spectra collected from various positions in plant organisms. Researchers showed that LIBS could contribute to the analysis of, e.g., wood preservatives [97], the impact of draught stress on gardenia and wheat [98], and Cr(VI) toxicity impact on wheat seedlings [99]. Moreover, quantification of macro-elemental concentration was also provided through chemometrics [100, 101]. The most recent work by Martin et al. [101] manifested the use of partial least squares regression (PLSR) for the determination of major elements (Ca, K, Mg, P, S, and Si) in switchgrass with an accuracy

reaching over 90%. LIBS results were compared to ICP-OES reference data and its capability for high-throughput analysis was recognized. Moreover, the combined use of LIBS and X-ray fluorescence (XRF) spectroscopy was proved beneficial for the determination of macro-elements (Ca, Fe, K, Mn, P, and Si) in dried sugar cane leaves [81]. Thus, LIBS has a clear potential to become a reliable technique for assessing feedstock quality (elemental composition) [96].

The laser ablation of plants shows a lower complexity in laser-plant interaction (due to the relatively hard matrix of plant tissues). Related LIBS experiments are relatively more straightforward in terms of sample preparation (samples grown in soil or in aqueous medium/hydroponic conditions) and handling (from grounding of dried plant to in-vivo analysis). The possibility to grow model samples with a high number of replicates is basically unlimited without any restrictions caused by ethical issues (as opposed to the case of animal and human samples). Despite all the listed advantages, the number of studies involved in large-scale imaging of plants with a high lateral resolution is considerably low [18, 19, 96]. Pioneering papers delivering the first mapping of plant tissues are dated to 2007. Kaiser et al. [102] studied hyperaccumulation of Pb and Cd within sunflower plants by using an fs LIBS. The plants were grown in hydroponic dispersion of various salts, which is typical for toxicology studies. Such an approach enables a fast growth of plants (within several days) with detectable content of toxic metals and a reasonable size of the whole plant (spread across the microscopic slide). In this study, LIBS was supported by X-ray radiography to provide high-resolution imaging of Pb and Cd within the plant leaves.

Since then, LIBS has proved to be an adequate tool for plant elemental imaging when showing the distribution of elements throughout the whole sample. Both in situ and in vitro analysis of plant tissues were demonstrated on maize leaves [59] via extension to 3D imaging. The body of work of Kaiser et al., reviewed among others in [19], significantly contributed to the development of LIBS as a complementary tool to standard plant toxicology. The development of micro-scale LIBS was manifested by Modlitbová et al. [103] when the performance of LIBS with 100 and 25 μm spot sizes was compared. Figure 6.8 illustrates the results used to elucidate the uptake, accumulation, and translocation of Cd-based quantum dots (Cd QDs) and Cd salts as a reference. The samples of white mustard were prepared in the short-term toxicity test (72 h) and were grown in a hydroponic dispersion.

A recent publication by Modlitbová et al. [58] presents LIBS as a straightforward tool for plant biologists which is capable to provide large-scale images. In this work, the typical pipeline of sample preparation and consequent analysis was shown in detail on cabbage. The model plant was grown in the hydroponic dispersion of Y-based upconversion nanoparticles (UCNPs) and Y salts as a toxic reference. Obtained results suggest the UCNPs to be relatively harmless to the model organism in low concentrations with root as the main storage organ and limited translocation to other parts of the plant (stem or leaf).

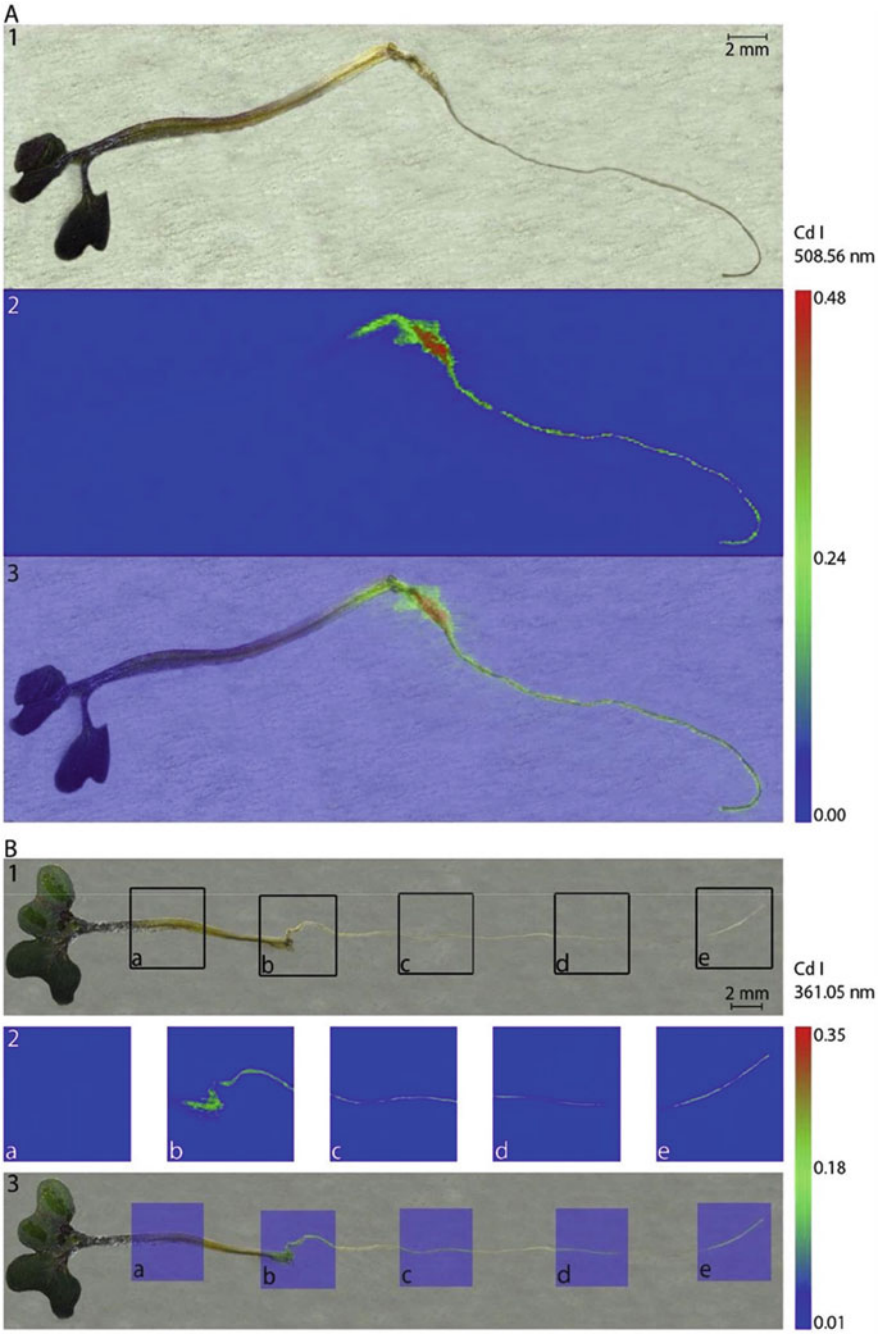

Fig. 6.8 (**a**) (1) Photograph of *S. alba* plant exposed to $CdCl_2$ at the nominal concentration 200 μM Cd before LIBS measurements. (2) LIBS maps constructed for Cd I 508.56 nm (3) Overlap of the original photograph of the plant with LIBS map. (**b**) (1) Photograph of S. alba plant exposed to $CdCl_2$ at the nominal concentration 200 μM Cd before micro-LIBS measurements together with

6.4.2 Bioimaging of Endogenous Elements

The bioimaging of endogenous elements can be considered as the direct detection (label-free) of biomarkers within investigated tissues. It was demonstrated that trace (e.g., Cu, Zn) and even macro elements (Ca, K, Mg, and Na) could be related with biological changes and diseases of tissues as they are manifested through the changes in chemical composition. Their essential presence and approaches to exploit changes in their abundance for the sake of various applications were already presented above.

The development of hard tissues is related to the calcification of soft tissues and formation of hydroxyapatite. The process of calcification is moderate in the presence of Mg. Thus, the presence of Ca, Mg, and P and their abundance is the most significant for any investigation of hard tissues. In our recent study, we have used LIBS for bioimaging of murine teeth (maxillary and mandibular incisors, and molars) [57]. In this work, LIBS was used among other techniques (incl. XCT) to uncover biological phenomena beyond the odontoblast development and led to a discovery of two distinct kinds of dentin tissues induced during the teeth growth of selected mice strains (DSPP-cerulean/DMP1-cherry) and mutants ($Spry2^{+/-}$;$Spry4^{-/-}$). LIBS analysis contributed with fine elemental images (30 μm lateral resolution) of Ca and Mg. The finding of two dentin structures was supported by the use of PCA with *k*-means clustering showing two distinct clusters in the area of enamel and periodontal ligament.

Imaging of cancerous soft tissues revealed the importance of the detection of endogenous metals by LIBS. First, LIBS (C, H, K, Na, and O) was used in tandem with LA-ICP-MS (Cu, Fe, P, Pt, and Zn) to provide complementary bioimaging of human tumor tissues [10]. Second, various cancerous tissues were analyzed by LIBS to show distribution images of selected elements, e.g., Ca, Fe, Mg, Na, P, and Zn in malignant melanoma, Merkel cell carcinoma, and squamous cell carcinoma [35]; C and Mg in murine melanoma [38]; C, Ca, K, Mg lines and CN bands for discrimination of murine melanoma [47]; Al, Ca, Cu, Fe, Mg, Na, and Si for the estimation of lung cancer boundary [48]. Capability of 3D bioimaging was confirmed in the case of Ca, Cu, Mg, Na, and P in murine brain [45], and Ca, K, Mg, and Na in squamous cell carcinoma [46]. Our recent work [46] showed the capability of LIBS to image cutaneous cancer margins through direct imaging of biomarkers (namely Mg) as well as through SOM clustering. The increased content of Mg in the cancer region of malignant melanoma and basal cell carcinoma was in contrast with Mg deficiency in the region of benign hemangioma.

Fig. 6.8 (continued) marked spot analyzed by micro-LIBS (a,b,c,d,e); (2) Micro-LIBS maps constructed for the Cd I 361.05 nm line; (3) Overlap of the original photograph of the plant with micro-LIBS maps. The scale shows the total emissivity of the selected emission lines. Obtained from [103] with permission for reuse from Elsevier publishing under license number 5245750991187

6.4.3 Bioimaging of Exogenous Elements

The bioimaging of exogenous elements can be further divided into two main fields of interest. First, the study of the fate of artificially administered metallic NPs within an organism and the detection of foreign metals present in the organism due to environmental pollution or unhealthy lifestyle (e.g., smoking). Second, the detection of specifically bound nanoparticle labels in the frame of immunochemistry.

NPs are typically used as specific labels, contrasting agents, or drug carriers. Thus, monitoring their fate within the organism, accumulation in organs and natural clearance is of interest also to LIBS bioimaging. Motto-Ros introduced a series of publications with the focus on the detection of Gd-based NPs in murine kidneys [27–29] and with the extension to 3D bioimaging [33]. It was shown that NPs tend to accumulate in the outer part of kidney (cortex). Their clearance was monitored in several mice species over a week period. In another study, the accumulation of Au NPs and renal clearance was investigated through LIBS and synchrotron XCT [37]. The Au-based NPs first targeted the U87MG brain tumor in mice, as visualized in XCT volumetric data. Then, harvested organs (spleen, liver, and kidney) were imaged with LIBS. The use of LIBS for the detection of NPs as enhancers in radiation therapy was also demonstrated. Detappe et al. [32] showed the detection of silica-based gadolinium chelated nanoparticles in murine tumor. In recent studies, LIBS has been used for the detection of ^{10}B atoms in U87MG and U251MG brain tumors [40] and LaF_3:Ce NPs in F98 brain tumor [41]. The aforementioned studies were delivered with a high lateral resolution reaching 10 μm. Further improvement is limited with standard ns laser sources, thus, fs laser was used to obtain the resolution below 1 μm in the imaging of InP NPs within cells [42]. Finally, it is worth mentioning that LIBS was used to detect Al, Cu, Ti, and W in various soft tissues (skin, lymph nodes, and lungs) [34]. The presence of those elements was of foreign origin (e.g., residual debris after surgery) and was relevant to the cases of individual patients.

LIBS essentially struggles with a trade-off between sensitivity and lateral resolution. However, reaching the cell-level resolution with sufficient sensitivity to trace metals is the main analytical challenge [18]. Various techniques are being developed to avoid the performance drawbacks of LIBS, e.g., characteristic labeling of tissues with nanoparticle tags for indirect detection of biomarkers [104]. The so-called Tag-LIBS was originally suggested by the group of Melikechi. They used two NP tags for indirect, yet specific detection of ovarian cancer (CA 125 marker) and leptin hormone in the basic multiplexing scheme [105]. Further works then exploited the advantages of Tag-LIBS; e.g., detection of CdTe quantum dots labeled metallothionein spread on polystyrene surface [106]; detection of streptavidin-coated Ag NPs as labels of human serum albumin [107]; detection of Au NPs as labels of *Escherichia coli* in lateral flow assay (no imaging) [108]. In our recent work, we have compared the performance of upconversion scanner and LIBS in the detection of HER2 biomarker of human breast cancer cells [104]. The Y-based upconversion NPs (UCNPs) showed an excellent specificity as tested on HER2-positive BT-474 cells and HER2-negative MDA-MB-231 cells. In general, LIBS

proved to be an adequate alternative to fluorescence and upconversion scanners for its comparable detection limits, higher dynamic range and no need for crafting of fluorescent-active labels.

6.5 Conclusion and Future Perspectives

As was repeatedly discussed in this chapter and highlighted in many publications, LIBS offers a vital alternative to other analytical techniques in the multi-elemental analysis of biological tissues on a large scale. It is primarily not intended to substitute other analytical techniques but to complement them and in turn to provide a more complete information about the investigated samples, to uncover the biological phenomena in their complexity. Thus, the tandem use of LIBS with LA-ICP-MS, Raman spectroscopy, or even XCT was found beneficial. However, the so-called correlative imaging most commonly relates LIBS elemental images with optical microscopy, e.g., images from histopathology.

A steady improvement of the LIBS instrumentation is aimed at its main benefits, i.e., high-throughput (above 100 Hz to units of kHz) and lateral resolution (below 10 μm). The analytical sensitivity is sacrificed for the sake of said benefits when the best possible detection limit is at the ppm level. Such sensitivity is sufficient for the detection of major and minor elements when also reaches traces for certain experimental parameters. This unique trade-off in analytical performance makes LIBS a potential prescreening tool for fast diagnostics of a higher number of samples.

Further improvement in sensitivity is expected with the constant improvement of utilized instrumentation (e.g., higher throughput of spectrometers, higher quantum efficiency of detectors). However, providing an accurate quantitative analysis is mandatory to strengthen the position of LIBS as a mature technique of analytical chemistry. So far, most of the research works have been concerned with qualitative or semi-quantitative analysis (i.e., showing relative change in the intensity on the sample surface). Production of matrix-matched standards is limiting the quantitation. Usual approaches match the chemical similarity, but not the physical matrix (physical properties, e.g., hardness). Recently, the lack of matrix-matched standards has been mitigated with the use of multivariate regression models and calibration-free algorithms.

LIBS is suitable for bioimaging of endogenous and exogenous elements in various applications, ranging from bioaccumulation of metals to medical/clinical use and immunochemistry. Despite the improvement of LIBS instrumentation, the number of publications presenting large-scale imaging of soft and hard tissues is rather low. The main limiting factors are advanced instrumentation control, tedious sample preparation and optimization of complex, mutually dependent parameters influencing laser-tissue interaction and consecutive laser ablation. Despite these, LIBS presented sufficient detection limits in the case of NPs which were beneficially used for enhancement of tumor radiotherapy and specific marking of selected proteins within tissue. The use of nanometallic labels makes LIBS a promising alternative to standard immunochemistry techniques.

LIBS bioimaging results in a large hyperspectral cube that carries multi-elemental information that can be related to individual spots on the sample surface. The simple projection of elemental maps over the sample surface is substituted with more sophisticated approaches. Advanced statistical algorithms are implemented to discriminate individual matrices of the sample (i.e., healthy and diseased tissues). Thus, future efforts will strive to deliver machine learning pipeline for a robust segmentation of elemental images which will significantly extend current state-of-the-art data processing in various applications (e.g., pathology, developmental biology).

Conclusions presented in reviewed literature sources are usually based on results of feasibility studies where only a small number of samples were analyzed. Such analyses uncover the potential of LIBS in various fields of interest; however, they are not fully convincing in terms of clinical use. It is therefore necessary to focus on analysis of series of samples to confirm causalities between significant chemical changes in tissues and related characteristic spectral response, i.e., cohort studies.

Acknowledgment The authors gratefully acknowledge the financial support of the Czech Science Foundation (GACR Standard, no. 22-27580S). PP and PM gratefully acknowledge the financial support of the Czech Science Foundation (GACR Junior, no. 20-19526Y).

References

1. Sabine Becker J. Imaging of metals in biological tissue by laser ablation inductively coupled plasma mass spectrometry (LA-ICP-MS): state of the art and future developments. J Mass Spectrom. 2013;48:255.
2. Jelínková H. Lasers for medical applications diagnostics, therapy and surgery. Cambridge: Woodhead Publishing; 2013.
3. Gaudiuso R, et al. Laser-induced breakdown spectroscopy for human and animal health: a review. Spectrochim Acta B. 2019;152:123.
4. Niemz MH. Laser-tissue interactions. Berlin: Springer; 2002.
5. Vogel A, Venugopalan V. Mechanisms of pulsed laser ablation of biological tissues. Chem Rev. 2003;103:577.
6. Kanawade R, et al. Qualitative tissue differentiation by analysing the intensity ratios of atomic emission lines using laser induced breakdown spectroscopy (LIBS): prospects for a feedback mechanism for surgical laser systems. J Biophotonics. 2015;8:153.
7. Mehari F, et al. Laser induced breakdown spectroscopy for bone and cartilage differentiation - ex vivo study as a prospect for a laser surgery feedback mechanism. Biomed Opt Express. 2014;5:4013.
8. Kaiser J, et al. Mapping of lead, magnesium and copper accumulation in plant tissues by laser-induced breakdown spectroscopy and laser-ablation inductively coupled plasma mass spectrometry. Spectrochim Acta B. 2009;64:67.
9. Galiová M, et al. Multielemental analysis of prehistoric animal teeth by laser-induced breakdown spectroscopy and laser ablation inductively coupled plasma mass spectrometry. Appl Opt. 2010a;49:C191.
10. Bonta M, Gonzalez JJ, Derrick Quarles C, Russo RE, Hegedus B, Limbeck A. Elemental mapping of biological samples by the combined use of LIBS and LA-ICP-MS. J Anal At Spectrom. 2016;31:252.
11. Becker JS, et al. Bioimaging of metals by laser ablation inductively coupled plasma mass spectrometry (LA-ICP-MS). Mass Spectrom Rev. 2010;29:156.

12. Doble PA, de Vega RG, Bishop DP, Hare DJ, Clases D. Laser ablation–inductively coupled plasma–mass spectrometry imaging in biology. Chem Rev. 2021;121:11769.
13. Francischini DS, Arruda MAZ. When a picture is worth a thousand words: Molecular and elemental imaging applied to environmental analysis – a review. Microchem J. 2021;169:106526.
14. Limbeck A, Galler P, Bonta M, Bauer G, Nischkauer W, Vanhaecke F. Recent advances in quantitative LA-ICP-MS analysis: challenges and solutions in the life sciences and environmental chemistry. Anal Bioanal Chem. 2015;407:6593.
15. Pozebon D, Scheffler GL, Dressler VL, Nunes MAG. Review of the applications of laser ablation inductively coupled plasma mass spectrometry (LA-ICP-MS) to the analysis of biological samples. J Anal At Spectrom. 2014;29:2204.
16. Busser B, Moncayo S, Coll JL, Sancey L, Motto-Ros V. Elemental imaging using laser-induced breakdown spectroscopy: a new and promising approach for biological and medical applications. Coord Chem Rev. 2018a;358:70.
17. Jolivet L, Leprince M, Moncayo S, Sorbier L, Lienemann CP, Motto-Ros V. Review of the recent advances and applications of LIBS-based imaging. Spectrochim Acta B. 2019;151:41.
18. Limbeck A, et al. Methodology and applications of elemental mapping by laser induced breakdown spectroscopy. Anal Chim Acta. 2021;1147:72.
19. Modlitbová P, Pořízka P, Kaiser J. Laser-induced breakdown spectroscopy as a promising tool in the elemental bioimaging of plant tissues. Trends Anal Chem. 2020a;122.
20. Carter S, Clough R, Fisher A, Gibson B, Russell B. Atomic spectrometry update: review of advances in the analysis of metals, chemicals and materials. J Anal At Spectrom. 2021;36:2241.
21. Galbács G. A critical review of recent progress in analytical laser-induced breakdown spectroscopy. Anal Bioanal Chem. 2015;407:7537.
22. Hahn DW, Omenetto N. Laser-induced breakdown spectroscopy (LIBS), part I: review of basic diagnostics and plasmaparticle interactions: still-challenging issues within the analytical plasma community. Appl Spectrosc. 2010;64:335.
23. Hahn DW, Omenetto N. Laser-induced breakdown spectroscopy (LIBS), part II: review of instrumental and methodological approaches to material analysis and applications to different fields. Appl Spectrosc. 2012;66:347.
24. Vanraes P, Bogaerts A. Laser-induced excitation mechanisms and phase transitions in spectrochemical analysis – Review of the fundamentals. Spectrochim Acta B. 2021;179:106091.
25. Motto-Ros V, et al. Mapping of native inorganic elements and injected nanoparticles in a biological organ with laser-induced plasma. Appl Phys Lett. 2012;101:223702.
26. Motto-Ros V, et al. Mapping nanoparticles injected into a biological tissue using laser-induced breakdown spectroscopy. Spectrochim Acta B. 2013;87:168.
27. Sancey L, et al. Laser spectrometry for multi-elemental imaging of biological tissues. Sci Rep. 2014a;4:1.
28. Sancey L, et al. Laser-induced breakdown spectroscopy: a new approach for nanoparticle's mapping and quantification in organ tissue. J Vis Exp. 2014b;88:1.
29. Sancey L, et al. Long-term in vivo clearance of gadolinium-based AGuIX nanoparticles and their biocompatibility after systemic injection. ACS Nano. 2015;9:2477.
30. Moussaron A, et al. Ultrasmall nanoplatforms as calcium-responsive contrast agents for magnetic resonance imaging. Small. 2015;11:4900.
31. Kunjachan S, et al. Nanoparticle mediated tumor vascular disruption: a novel strategy in radiation therapy. Nano Lett. 2015;15:7488.
32. Detappe A, et al. Advanced multimodal nanoparticles delay tumor progression with clinical radiation therapy. J Control Release. 2016;238:103.
33. Gimenez Y, et al. 3D imaging of nanoparticle distribution in biological tissue by laser-induced breakdown spectroscopy. Sci Rep. 2016;6:1.

34. Busser B, et al. Characterization of foreign materials in paraffin-embedded pathological specimens using in situ multi-elemental imaging with laser spectroscopy. Mod Pathol. 2018b;31:378.
35. Moncayo S, et al. Multi-elemental imaging of paraffin-embedded human samples by laser-induced breakdown spectroscopy. Spectrochim Acta B. 2017;133:40.
36. Török S, Limbeck A, Döme B, Bonta M. Tandem LA–LIBS coupled to ICP-MS for comprehensive analysis of tumor samples. Spectroscopy. 2017;32:42.
37. Le Guével X, et al. Elemental and optical imaging evaluation of zwitterionic gold nanoclusters in glioblastoma mouse models. Nanoscale. 2018;10:18657.
38. Moon Y, Han JH, Choi J, Shin S, Kim Y-C, Jeong S. Mapping of cutaneous melanoma by femtosecond laser-induced breakdown spectroscopy. J Biomed Opt. 2018;24:1.
39. Wei H, Zhao Z, Lin Q, Duan Y. Study on the molecular mechanisms against human breast cancer from insight of elemental distribution in tissue based on laser-induced breakdown spectroscopy (LIBS). Biol Trace Elem Res. 2021;199:1686.
40. Kalot G, et al. Aza-BODIPY: a new vector for enhanced theranostic boron neutron capture therapy applications. Cell. 2020;9:1953.
41. Bulin AL, et al. Radiation dose-enhancement is a potent radiotherapeutic effect of rare-earth composite nanoscintillators in preclinical models of glioblastoma. Adv Sci. 2020;7:1.
42. Meng Y, Gao C, Lin Z, Hang W, Huang B. Nanoscale laser-induced breakdown spectroscopy imaging reveals chemical distribution with subcellular resolution. Nanoscale Adv. 2020;2:3983.
43. Lin X, Sun H, Gao X, Xu YT, Wang ZX, Wang Y. Discrimination of lung tumor and boundary tissues based on laser-induced breakdown spectroscopy and machine learning. Spectrochim. Acta Part B At Spectrosc. 2021a;180:106200.
44. Šindelářová A, et al. Methodology for the implementation of internal standard to laser-induced breakdown spectroscopy analysis of soft tissues. Sensors (Switzerland). 2021;21:1.
45. Lin Q, Wang S, Duan Y, Tuchin VV. Ex vivo three-dimensional elemental imaging of mouse brain tissue block by laser-induced breakdown spectroscopy. J Biophotonics. 2021b;14:1.
46. Kiss K, et al. Imaging margins of skin tumors using laser-induced breakdown spectroscopy and machine learning. J Anal At Spectrom. 2021;32:909.
47. Choi JH, Shin S, Moon Y, Han JH, Hwang E, Jeong S. High spatial resolution imaging of melanoma tissue by femtosecond laser-induced breakdown spectroscopy. Spectrochim Acta B. 2021;179:106090.
48. Yin P, Hu B, Li Q, Duan Y, Lin Q. Imaging of tumor boundary based on multielements and molecular fragments heterogeneity in lung cancer. IEEE Trans Instrum Meas. 2021;70:1.
49. Wang Q, et al. Primary study of identification of parathyroid gland based on laser-induced breakdown spectroscopy. Biomed Opt Express. 2021;12:1999.
50. Teng G, et al. Predictive data clustering of laser-induced breakdown spectroscopy for brain tumor analysis. Biomed Opt Express. 2021;12:4438.
51. Buday J, Pořízka P, Kaiser J. Imaging laser-induced plasma under different laser irradiances. Spectrochim Acta B. 2020;168:105874.
52. Buday J, Pořízka P, Buchtová M, Kaiser J. Determination of initial expansion energy with shadowgraphy in laser-induced breakdown spectroscopy. Spectrochim Acta B. 2021;182:106254.
53. Jantzi SC, Motto-Ros V, Trichard F, Markushin Y, Melikechi N, De Giacomo A. Sample treatment and preparation for laser-induced breakdown spectroscopy. Spectrochim Acta B. 2016;115:52.
54. Bonta M, Török S, Hegedus B, Döme B, Limbeck A. A comparison of sample preparation strategies for biological tissues and subsequent trace element analysis using LA-ICP-MS. Anal Bioanal Chem. 2017;409:1805.
55. Moncayo S, et al. Exploration of megapixel hyperspectral LIBS images using principal component analysis. J Anal At Spectrom. 2018;33:210.

56. Mohamed N, et al. Chemical and mineralogical mapping of platinum-group element ore samples using laser-induced breakdown spectroscopy and micro-X-Ray fluorescence. Geostand Geoanalytical Res. 2021;45:539.
57. Lavicky J, et al. The development of dentin microstructure is controlled by the type of adjacent epithelium. J Bone Miner Res. 2022;37:323.
58. Modlitbová P, Střítežská S, Hlaváček A, Prochazka D, Pořízka P, Kaiser J. Laser-induced breakdown spectroscopy as a straightforward bioimaging tool for plant biologists; the case study for assessment of photon-upconversion nanoparticles in *Brassica oleracea* L. plant. Ecotoxicol Environ Saf. 2021;214:112113.
59. Zhao C, Dong D, Du X, Zheng W. In-field, in situ, and in vivo 3-dimensional elemental mapping for plant tissue and soil analysis using laser-induced breakdown spectroscopy. Sensors (Switzerland). 2016;16:1764.
60. Samek O, Beddows DCS, Telle HH, Morris GW, Liska M, Kaiser J. Quantitative analysis of trace metal accumulation in teeth using laser-induced breakdown spectroscopy. Appl Phys A Mater Sci Process. 1999;69:S179.
61. Samek O, et al. Quantitative laser-induced breakdown spectroscopy analysis of calcified tissue samples. Spectrochim Acta B. 2001a;56:865.
62. Samek O, Telle HH, Beddows DCS. Laser-induced breakdown spectroscopy: a tool for real-time, in vitro and in vivo identification of carious teeth. BMC Oral Health. 2001b;9:1–9.
63. Galiová M, et al. Investigation of the osteitis deformans phases in snake vertebrae by double-pulse laser-induced breakdown spectroscopy. Anal Bioanal Chem. 2010b;398:1095.
64. Dosedělová H, et al. Age-related changes in the tooth–bone interface area of acrodont dentition in the chameleon. J Anat. 2016;229:356.
65. Singh VK, Kumar V, Sharma J. Importance of laser-induced breakdown spectroscopy for hard tissues (bone, teeth) and other calcified tissue materials. Lasers Med Sci. 2015;30:1763.
66. Sasazawa S, Kakino S, Matsuura Y. Optical-fiber-based laser-induced breakdown spectroscopy for detection of early caries. J Biomed Opt. 2015;20:065002.
67. Kumar A, Yueh F-Y, Singh JP, Burgess S. Characterization of malignant tissue cells by laser-induced breakdown spectroscopy. Appl Opt. 2004;43:5399.
68. El-Hussein A, Kassem AK, Ismail H, Harith MA. Exploiting LIBS as a spectrochemical analytical technique in diagnosis of some types of human malignancies. Talanta. 2010;82:495.
69. Imam H, Mohamed R, Eldakrouri AA. Primary study of the use of laser-induced plasma spectroscopy for the diagnosis of breast cancer. Opt Photonics J. 2012;02:193.
70. Martinez M, Baudelet M. Calibration strategies for elemental analysis of biological samples by LA-ICP-MS and LIBS – a review. Anal Bioanal Chem. 2020;412:27.
71. Singh VK, Rai AK, Rai PK, Jindal PK. Cross-sectional study of kidney stones by laser-induced breakdown spectroscopy. Lasers Med Sci. 2009;24:749.
72. Martinez M, Bayne C, Aiello D, Julian M, Gaume R, Baudelet M. Multi-elemental matrix-matched calcium hydroxyapatite reference materials for laser ablation: evaluation on teeth by laser-induced breakdown spectroscopy. Spectrochim Acta B. 2019;159:105650.
73. Legnaioli S, Campanella B, Pagnotta S, Poggialini F, Palleschi V. Self-calibrated methods for LIBS quantitative analysis. In: Laser-induced breakdown spectroscopy. Elsevier; 2020. p. 561–80.
74. Zhang S, et al. Quantitative analysis of mineral elements in hair and nails using calibration-free laser-induced breakdown spectroscopy. Optik (Stuttg). 2021;242:167067.
75. Singh VK, Singh V, Rai AK, Thakur SN, Rai PK, Singh JP. Quantitative analysis of gallstones using laser-induced breakdown spectroscopy. Appl Opt. 2008;47:G38.
76. Marín Roldán A, Dwivedi V, de los Terreros JYS, Veis P. Laser-induced breakdown spectroscopy (LIBS) for the analyses of faunal bones: assembling of individuals and elemental quantification. Optik (Stuttg). 2020;218:164992.
77. Kaiser J, et al. Trace elemental analysis by laser-induced breakdown spectroscopy - biological applications. Surf Sci Rep. 2012;67:233.

78. Képeš E, et al. Interpreting support vector machines applied in laser-induced breakdown spectroscopy. Anal Chim Acta. 2021;1192:339352.
79. Pořízka P, Klus J, Képeš E, Prochazka D, Hahn DW, Kaiser J. On the utilization of principal component analysis in laser-induced breakdown spectroscopy data analysis, a review. Spectrochim Acta B. 2018;148:65.
80. Arantes De Carvalho GG, et al. Recent advances in LIBS and XRF for the analysis of plants. J Anal At Spectrom. 2018;33:919.
81. Bueno Guerra MB, et al. Direct analysis of plant leaves by EDXRF and LIBS: microsampling strategies and cross-validation. J Anal At Spectrom. 2015;30:1646.
82. Gierlinger N, Schwanninger M. The potential of Raman microscopy and Raman imaging in plant research. Spectroscopy. 2007;21:69.
83. Pořízka P, et al. Application of laser-induced breakdown spectroscopy to the analysis of algal biomass for industrial biotechnology. Spectrochim Acta B. 2012;74–75:169–76.
84. Prochazka D, et al. Combination of laser-induced breakdown spectroscopy and Raman spectroscopy for multivariate classification of bacteria. Spectrochim Acta B. 2018a;139:6–12.
85. Prochazka D, et al. Joint utilization of double-pulse laser-induced breakdown spectroscopy and X-ray computed tomography for volumetric information of geological samples. J Anal At Spectrom. 2018b;33:1993–9.
86. Ayres LB, Gomez FJV, Linton JR, Silva MF, Garcia CD. Taking the leap between analytical chemistry and artificial intelligence: a tutorial review. Anal Chim Acta. 2021;1161:338403.
87. Rohde M, et al. The differentiation of oral soft- and hard tissues using laser induced breakdown spectroscopy – a prospect for tissue specific laser surgery. J Biophotonics. 2017;10:1250.
88. Melikechi N, Ding H, Rock S, Marcano O. A, Connolly D. Laser-induced breakdown spectroscopy of whole blood and other liquid organic compounds. Opt Diagnostics Sens VIII. 2008;6863:68630O.
89. Melikechi N, Markushin Y, Connolly DC, Lasue J, Ewusi-Annan E, Makrogiannis S. Age-specific discrimination of blood plasma samples of healthy and ovarian cancer prone mice using laser-induced breakdown spectroscopy. Spectrochim Acta B. 2016;123:33.
90. Gaudiuso R, et al. Using LIBS to diagnose melanoma in biomedical fluids deposited on solid substrates: limits of direct spectral analysis and capability of machine learning. Spectrochim Acta B. 2018;146:106.
91. Chen X, Li X, Yang S, Yu X, Liu A. Discrimination of lymphoma using laser-induced breakdown spectroscopy conducted on whole blood samples. Biomed Opt Express. 2018a;9:1057.
92. Chen X, Li X, Yu X, Chen D, Liu A. Diagnosis of human malignancies using laser-induced breakdown spectroscopy in combination with chemometric methods. Spectrochim Acta B. 2018b;139:63.
93. Rehse SJ. A review of the use of laser-induced breakdown spectroscopy for bacterial classification, quantification, and identification. Spectrochim Acta B. 2019;154:50.
94. Sezer B, Bilge G, Boyaci IH. Capabilities and limitations of LIBS in food analysis. Trends Anal Chem. 2017;97:345.
95. Martin MZ, Labbe N, Wagner RJ. Application of high resolution laser-indiced breakdown spectroscopy for environmental and biological samples. Berlin Heidelberg: Springer-Verlag; 2014.
96. Singh VK, et al. Review: application of LIBS to elemental analysis and mapping of plant samples. At Spectrosc. 2021;42:99.
97. Martin MZ, Labbé N, Rials TG, Wullschleger SD. Analysis of preservative-treated wood by multivariate analysis of laser-induced breakdown spectroscopy spectra. Spectrochim Acta B. 2005;60:1179.
98. Kunz JN, Voronine DV, Lee HWH, Sokolov AV, Scully MO. Rapid detection of drought stress in plants using femtosecond laser-induced breakdown spectroscopy. Opt Express. 2017;25:7251.

99. Tripathi DK, Singh VP, Prasad SM, Chauhan DK, Kishore Dubey N, Rai AK. Silicon-mediated alleviation of Cr(VI) toxicity in wheat seedlings as evidenced by chlorophyll florescence, laser induced breakdown spectroscopy and anatomical changes. Ecotoxicol Environ Saf. 2015;113:133.
100. Martin MZ, et al. Correlating laser-induced breakdown spectroscopy with neutron activation analysis to determine the elemental concentration in the ionome of the *Populus trichocarpa* leaf. Spectrochim Acta B. 2017;138:46.
101. Martin M, Brice D, Martin S, André N, Labbé N. Inorganic characterization of switchgrass biomass using laser-induced breakdown spectroscopy. Spectrochim Acta B. 2021;186:106323.
102. Kaiser J, et al. Monitoring of the heavy-metal hyperaccumulation in vegetal tissues by X-ray radiography and by femto-second laser induced breakdown spectroscopy. Microsc Res Tech. 2007;70:147.
103. Modlitbová P, et al. Detail investigation of toxicity, bioaccumulation, and translocation of Cd-based quantum dots and Cd salt in white mustard. Chemosphere. 2020b;251:126174.
104. Pořízka P, et al. Laser-induced breakdown spectroscopy as a readout method for immunocytochemistry with upconversion nanoparticles. Microchim Acta. 2021;188:1.
105. Markushin Y, Melikechi N. Sensitive detection of epithelial ovarian cancer biomarkers using tag-laser induced breakdown spectroscopy. Ovarian Cancer Basic Sci Perspect. 2012; 17:153–70.
106. Konecna M, et al. Identification of quantum dots labeled metallothionein by fast scanning laser-induced breakdown spectroscopy. Spectrochim Acta B. 2014;101:220.
107. Modlitbová P, et al. Laser-induced breakdown spectroscopy as a novel readout method for nanoparticle-based immunoassays. Microchim Acta. 2019;186:1.
108. Gondhalekar C, et al. Detection of *E. coli* labeled with metal-conjugated antibodies using lateral-flow assay and laser-induced breakdown spectroscopy. Anal Bioanal Chem. 2020;412:1291.

Qualitative Classification of Biological Materials

7

Nikolai Sushkov

It is widely known that eye vision gives us the lion's share of the information about the environment, and image is the most efficiently perceived type of information. However, text and numbers, which are easier to create and operate with, have been the basis of science for centuries. They are probably indispensable in many cases, but both the explanatory and predictive capabilities benefit from the use of images in the broad sense of the word. The final result which is often sought is a "qualitative" decision, which is a choice between two or several categories ("yes"/"no", "low"/"medium"/"high", "meat"/"fish" etc.). This gives rise to classification methods, which are designed to convert (numerical) data into categorial variables.

Despite that the LIBS analysis of biological samples became widespread only in the second decade of the current century, the first studies in this direction date back to the early years of LIBS. This also applies to the use of classification and discrimination methodology. Now there is a large demand in such studies in different parts of science and economy.

As it is detailed in other sections of this book, LIBS offers advantages such as the rapidity of measurements, little sample preparation, reduced destructivity, the possibility of stand-off analysis, and relative cheapness and simplicity of experimental setup. Very importantly for the analysis of biological samples, LIBS (unlike XRF) offers good sensitivity towards light elements (H to Na). As in other emission spectroscopic techniques, the lines of alkaline and alkaline earth elements are also easy to observe in laser-induced plasmas. Since these very elements are the main constituents of living tissues, LIBS serves well the analysis of such samples.

The use of LIBS for the qualitative discrimination of biological samples may sound somewhat strange to the reader, because the identity of organisms is primarily defined by their molecular composition (DNA, proteins, etc.). From this point of view, molecular spectroscopic techniques such as Raman spectroscopy would seem

N. Sushkov (✉)
Department of Chemistry, Lomonosov Moscow State University, Moscow, Russia
e-mail: nikolaisushkov@laser.chem.msu.ru

G. Galbács (ed.), *Laser-Induced Breakdown Spectroscopy in Biological, Forensic and Materials Sciences*, https://doi.org/10.1007/978-3-031-14502-5_7

more suitable for the purpose. However, the content of different chemical elements in living tissues varies over a very wide range, which means that LIBS data have a good potential for qualitative analysis, classification, and discrimination purposes, provided that a proper mathematical data treatment is applied. We hope this will be clear from the further parts of this chapter.

7.1 Preliminary Considerations

Despite the versatility of modern LIBS applications [1], one should still admit that LIBS is best suited for the analysis of solid inorganic samples like alloys or rocks. However, its unique technical advantages promoted its use for the examination of biological materials which have intrinsic properties somewhat hampering the obtaining of high-quality data.

It is widely known that biological materials (except the so-called calcified tissues like bones or teeth) contain large quantities of water, often more than 50%. This causes LIBS signal intensities to drop significantly, since the ablation efficiency is usually lower for moist materials compared to dry materials with the same composition [2]. Water requires a considerable energy to be vaporised, so that a 10 μm thick film of water requires ~25 mJ to be evaporated over an area of 1 mm^2. Ablation is also favoured by the formation of moderate quantities of aerosol above the sample surface, but this phaenomenon is suppressed in the presence of water [3]. Biological materials, being very complex structures, are intrinsically inhomogeneous. For this reason, atomic emission signals may vary significantly not only due to the variations of chemical composition across the spatial coordinates but also due to varying ablation conditions. These factors lead to lower signal-to-noise ratios and worse repeatability of spectra compared to those of, say, metal samples. However, this factor should not be overestimated. In one of our experiments with conventional nanosecond lasers, the intensity of the C I 247.856 nm peak in a zooplankton sample had 3.5% relative standard error of mean (RSEM); in a plant sample, it was 2.5%. For the Fe I 330.648 nm line in an iron sample, we obtained RSEM of 1.4%, thus just around two times less. On the other hand, in some applications (like imaging), it is generally not possible to accumulate signals from multiple laser shots, which means that signal uncertainties will be quite large.

Attention should also be paid to the laser wavelength which is used to excite the plasma. It is generally true that the extinction coefficient is reciprocally proportional to λ^4 [4]. Figure 7.1 illustrates this relationship for ovalbumin [5]. The larger the coefficient, the more energy from a laser pulse is going to be absorbed by sample, the more material is going to be ablated, and the stronger the plasma emission is. Although the exact wavelength dependence may be different for short, high-intensity laser pulses, shorter laser wavelengths still appear to be more suitable for analysis than longer ones. For ovalbumin, the extinction coefficient at 270 nm is 20 times larger than at 530 nm and 29 times larger than at 1060 nm. This means that, for Nd:YAG lasers, the fourth harmonic (266 nm) is more suitable than the fundamental one

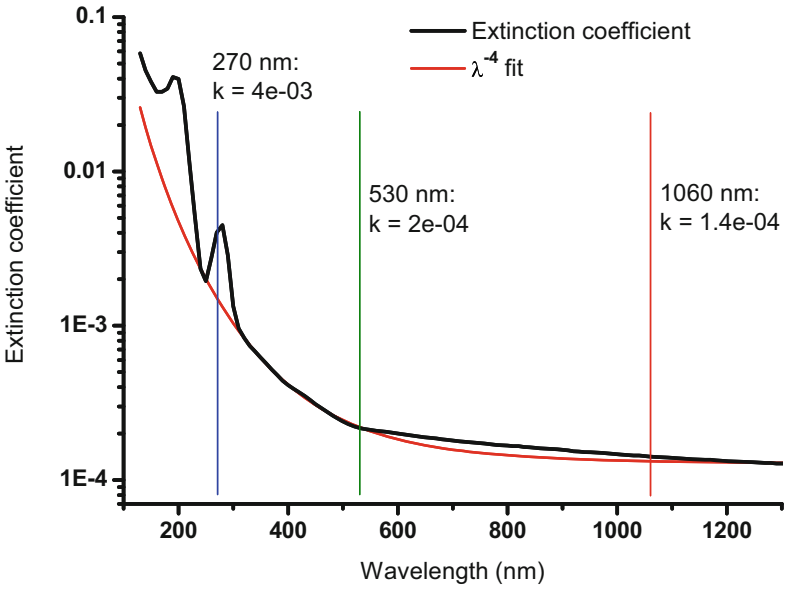

Fig. 7.1 Extinction coefficient for ovalbumin as a function of wavelength [5]

(1064 nm).[1] This increasing emissivity is particularly important for biological samples, which are easily damaged by laser pulses, because less shots will have to be accumulated for a desired signal-to-noise ratio. Increasing the pulse energy is not a good solution, since it aggravates sample destruction. Sample heating is believed to be less pronounced when UV lasers are used [4]. On the other hand, there are indications [7] that UV-induced plasmas can be colder than IR-induced ones and also suffer from incomplete atomization of the ablated samples. This may be explained by relatively more efficient interaction of IR light with the vaporised sample (inverse Bremsstrahlung), resulting in plasma reheating.

In addition, the diffraction limit for the minimum laser spot size is proportional with the wavelength [7], thus a UV laser may provide a smaller irradiation spot which can result in a significantly higher fluence compared to an infrared (IR) laser operating at the same pulse energy. The other consequence is the gain in spatial resolution which is important for imaging applications. Many commercial LIBS instruments are equipped with 266 nm Nd:YAG lasers. However, infrared lasers are nevertheless widely used in LIBS applications, including biology-related studies. For example, imaging is done with infrared lasers in 62% of the studies [8]. This is probably because the use of the fundamental wavelength necessitates the simplest optical setup and also retains more of the pulse energy (frequency upconversion has a substantial loss in pulse energy).

[1] It is interesting to compare the quantum energies (4.67 and 1.17 eV, respectively) with the energies of C–C, C=C, and C–H bonds (3.61, 6.36, and 4.28 eV, respectively) [6].

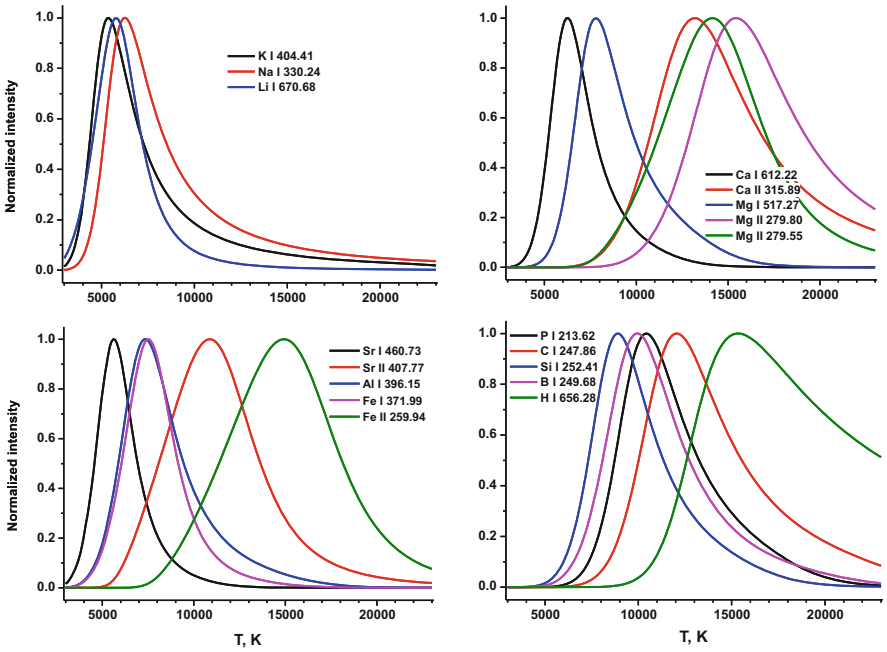

Fig. 7.2 Normalised intensities of atomic and ionic emission lines for principal elements in biological matrices versus temperature in kelvin (computed for $N_e = 5 \times 10^{16}$ cm^{-3})

Here we would like to give the reader an idea about the behaviour of emission line intensities of elements that are most often encountered in the analysis of biological specimens, such as Na, K, Li, Mg, Ca, Sr, Al, Fe, C, P, B, Si, and H. Figure 7.2 shows the dependencies of line intensities as a function of plasma temperature. Although at a given emitter number density, line intensity tends to grow exponentially with temperature, ionisation then causes the number density to drop, so that the resulting function has a maximum which is located around 6000 K for easily ionisable elements, shifting to higher T for less ionisable elements and higher line excitation energies. High temperatures favour the observation of ionic lines. Figure 7.2 makes it clear that the observation of the largest possible number of elemental lines from a biological specimen can only be achieved by choosing compromise experimental conditions. For example, non-metals that make up the matrix are best observed at around 10,000 K when the signals of alkaline metals can be already of relatively modest intensity (transition probabilities are not taken into account here).

An important point is the duration of laser pulse, which can be in the nano-, pico-, or femtosecond range. The principal point is whether the laser pulse has ended by the moment when the surface gets shielded by sample vapour. In the case of nanosecond ablation (laser pulse duration of several nanoseconds or longer), the pulse is sufficiently long to be partially blocked by the emerging plasma, i.e., only a part of the pulse energy is spent to ablate the sample, while the other part reheats the plasma.

Due to relatively low power density of the radiation, the surface is first heated, then it melts and evaporates. The appearance of the resulting craters reflects these processes, featuring molten edges and hemispherical bottom. On the contrary, femtosecond ablation [9], with its typical laser pulse duration on the order of 100 fs, does not cause surface melting. It is believed that electrons are first expelled from the solid material by the laser beam's electromagnetic field, and then the surface "explodes" due to mutual electrostatic repulsion of the resulting positive ions. The resulting craters have a shape that resembles a vertical well without collars on the edges. Other mechanisms are also proposed to describe femtosecond ablation. Interested reader can be referred to a detailed review [10]. Regarding bioanalytical applications, femtosecond ablation is important because of its lower ablation threshold, reduced sample damage, and improved spatial resolution [11]. Since the parameters of femtosecond plasmas are different from those of nanosecond plasmas, different spectral signatures are obtained which is important for classification purposes. On the other hand, the signal-to-noise ratio is usually low [12, 13].

The form in which analysed samples are present and procedures for sample preparation [14] are crucial points not only for scientific studies but also for future practical implementation in clinical or field settings. Sometimes biological samples are suitable for analysis without any preparation (especially leaves or bones). However, care must be taken to ensure that the samples' surface is flat and that there are no surface contaminations (including, e.g., a waxy layer on the surface of leaves). In this regard, it is useful to deliver multiple laser shots to the same spot (if possible) in order to ensure that the bulk matrix is accessed by the laser. Otherwise, pellets are the most widely used sample form in LIBS experiments [15–18]. Loose powders are usually highly disturbed by the plasma shockwave; this is why it is practical to fix them on double-sided sticky tapes. If a material generates dust during ablation, it is good to lower the laser pulse frequency to 1–2 Hz in order to avoid breakdown on the generated aerosol and thus, improve the signal stability [7]. Although pellets require much material and, consequently, much time for sample preparation (e.g., grinding of dried plants or culturing of bacteria in a growth media with subsequent purification and isolation, etc.), they are easy to handle and provide a robust source of high-quality spectra, because they can be quite uniform in composition and normally can withstand many laser pulses necessary for signal accumulation. The reduced moisture content, characteristic of pellets prepared from lyophilised material, helps to obtain a brighter plasma compared to moist samples. However, lyophilisation is an expensive and lengthy procedure. Additionally, too dry samples might yield very brittle and mechanically unstable pellets. In this case, binders [18] like microcrystalline cellulose or polyvinyl alcohol may be used, bearing in mind that this is potential source of sample contamination and the resulting dilution leads to a reduction in signal intensities. Useful advice on pelletising techniques can also be found in handbooks on X-ray fluorescence spectroscopy (XRF) [19].

7.2 Molecular Emission Studies

Apart from atomic and ionic emission lines, laser plasmas of organic matrices also exhibit distinct molecular signals. These are usually diatomic molecules, and the most prominent spectra are observed for CN and C_2. Bands of OH and NH are usually much weaker. For calcium-rich samples, strong bands of CaO, CaCl and possibly CaOH are also often observed.

In principle, two ways of molecule formation are possible: first, they may be fragments of the molecules of the ablated material; and second, they may be formed from single atoms through plasma chemical reactions (simple recombination or more complex processes). Two questions may arise: first, can molecular emission signals be used to discern biosamples from inorganic carbon-containing materials (e.g., activated charcoal)? And second: if yes, then can they be used to discriminate among different biosamples? The answers to these questions are not evident, as we will attempt to demonstrate this below.

One of the first studies in this direction is the 2006 article by M. Baudelet et al. [12]. The authors compared spectra produced by nano- and femtosecond ablation of *Escherichia coli* (*E. coli*), deposited on a Whatman nitrocellulose filter. Discussing the intensity ratios of CN violet, Swan C_2 bands and the C I line at 247.86 nm, they claimed that the higher molecular-to-atomic emission ratios which are obtained in femtosecond LIBS indicate that more native C-C and C-N bonds are retained in the plasma. This conclusion appears to be dubious, because the difference in ratios could rather be explained by the simple fact that the temperatures are lower in the femtosecond plasma, thus the C I line with $E_i = 7.68$ eV should lose much more intensity (compared to nanosecond plasma) than the easily excited CN and C_2 transitions (E_i around 3.2 and 2.5 eV, respectively [20]). However, kinetics of CN emission shows that the radicals can indeed be produced from the ablated specimen's functional groups. This can be detected by performing a time-resolved study of molecular emission (a series of measurements with different acquisition delays with short gates). According to the authors, if the molecules originate directly from the sample (as C_2), the maximum signal is obtained at the earliest delay and decays monotonically with time, following an exponential law (which can be modelled by kinetic equations). Conversely, if they result from plasma chemical reactions (like CN from graphite), there will be an initial intensity growth to a maximum followed by a relatively slow decay. Thus, C-N containing substances (including virtually all biological materials) can be discerned from other carbon-containing chemicals.

An interested reader can obtain further details in [17, 21–24]. However, this approach is quite laborious, while not very informative. Judging from the literature and the author's own experience, molecular emission bands do not open broad horizons for discrimination. Thus, the main strength of LIBS should be used—namely, atomic emission.

7.3 Chemometric Approaches Used for the Discrimination of Biosamples

Modern LIBS setups and instruments yield an enormous amount of spectral information within a short amount of time. Therefore, it is advisable to analyse it with the help of mathematical machinery of chemometrics. If the task is to find distinct classes in a set of samples without any prior information on class memberships ("*unsupervised learning*"), then this is called a *classification* problem. If there is already a set of pre-defined classes, and the task is to decide to which of them a new sample should belong ("*supervised learning*"), then this is a *discrimination* problem. However, in most cases, we will use the both terms interchangeably. Although this topic is detailed in the other relevant sections of this book, here we would like to mention the key points about the major techniques used for the classification and discrimination of biological samples. These are: principal component analysis (PCA); techniques based on the projection on latent structures or "partial least squares" (PLS); discriminant function analysis (DFA); the k-nearest neighbour method (kNN); soft independent modelling of class analogies (SIMCA); support vector machine (SVM); classification tree (CT); random forest (RF) and neural networks (NN).

Data to be analysed are supplied in the form of matrix $\mathbf{X}$ with i rows and j columns ($i \times j$); usually they correspond to i analysed samples and j predictors. In LIBS, the predictors are emission wavelengths (as discrete values corresponding to detector channels); in chromatography, they can be retention times, etc. Thus, many chemometric approaches are formulated as matrix decomposition problems, i.e., the matrix $\mathbf{X}$ needs to be presented as $\mathbf{X} = \mathbf{TP^t} + \mathbf{E}$, where $\mathbf{T}$ ($i \times a$) is the *scores* matrix, whereas $\mathbf{P}$ ($j \times a$) is the *loadings* matrix ($\mathbf{P^t}$ means transposed $\mathbf{P}$), and $\mathbf{E}$ is the residual matrix. Here, a is the number of *latent vectors* (LV) which can be different. Each LV describes a certain (spectral) feature that ideally (but not necessarily) corresponds to a chemical component (spectra of mixtures in $\mathbf{X}$ are converted into spectra of a few individual components in $\mathbf{P}$). Thus, working with the values of a exceeding this number does not make sense, even though the accuracy of description increases with a (as the norm of $\mathbf{E}$ gets smaller). If signals are found in a same LV, then they correlate with each other to some extent. There may also be spurious correlations, especially when there are more predictors than samples. However, this is almost always the case with LIBS spectra (if full spectra are used without selecting a relatively small number of peaks); and it is important to remember that correlation does not necessarily mean a causal relationship. The way in which the LVs are derived and their properties depend on the particular technique.

Before the actual chemometric operations, it is often useful to perform data pre-treatment (this is sometimes included in ready-to-use packages/modules; it is, therefore, advisable to read documentation and/or the source code in order to know exactly what is being done by the software). This includes baseline subtraction (manual or using, e.g., standard normal variate, SNV, or Whittaker algorithm) [25, 26], smoothing (useful with broad spectral profiles, but dangerous when there are just a few data points per peak), removal of outliers (e.g., Grubbs' criterion [27]

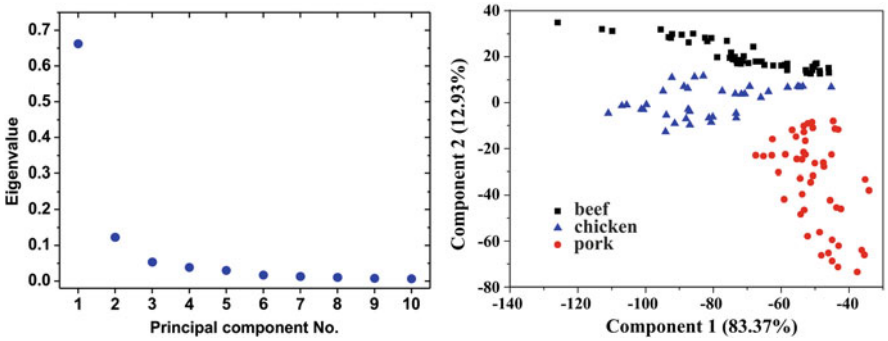

Fig. 7.3 *Left*: an example of scree plot (the author's own work). *Right*: PCA score graph for qualitative discrimination of pure beef, chicken, and pork meat species (adapted from [31] with permission from Elsevier)

and many other algorithms). Data are often centred and normalised. Centring means that the mean of **X** is subtracted from each column (sometimes this operation is done with rows). This is suitable for decompositions which do not imply a constant term. Normalisation implies that each column is multiplied by a weight coefficient, which is often the reciprocal of the standard deviation of that column. This is needed in order to equalise the contributions of data recorded in different scales (e.g., Raman and LIBS spectra if present together). The combination of centring and normalisation is called autoscaling [28].

PCA [28–30] is historically the first (1901), the simplest, and surely the most widely used chemometric technique. The matrix decomposition can be understood as a transformation of coordinates in a multidimensional space. Each sample is represented by a point in the space of predictors, so that all samples make up a cloud of points. The PCA algorithm finds a direction along which this cloud is prolate (the direction of maximum dispersion), and rotates the coordinate system accordingly. The new origin of coordinates is placed at the centre of gravity of the cloud. Then, the second most important direction of scattering is found, and a new coordinate is drawn along this direction. This operation is repeated until there is only a chaotic scattering of points. Anyway, there cannot be more coordinates (i.e., LVs) than samples. LVs are chosen to be orthogonal, so that there are no correlations between them. In PCA, the LVs are called principal components (PCs). In practice, the fullest possible set of PCs is often calculated, and then the decision should be made about how many PCs bear useful information; all the other PCs are then believed to describe noise. The simplest way to make this decision is to study the so-called scree plot of PCA eigenvalues. The eigenvalues correspond to the lengths of respective LVs in the multidimensional space. In Fig. 7.3 (*left*), the data matrix seems to have three PCs.

Studying low-dimensional projections of the principal component space (score plots) is useful for discovering data structure. Similar samples will group together on the plots and form clusters. The larger the distance between points is, the larger is

their chemical difference (Fig. 7.3, *right*). The ideal situation is when the distance between clusters is much larger than their own dimension. The clustering quality can be assessed by different methods. For example, the so-called silhouette metric [32] is defined as

$$\mathrm{Sil} = \sum_k \frac{1}{|C_k|} \sum_{i \in C_k} \frac{b_i - a_i}{\max(a_i, b_i)},$$

where a_i is the mean distance of a given point i from other points within a cluster C_k, and b_i is the mean distance from i to all points outside that cluster. Silhouette values vary from −1 (the worst case, no clusters) through 0 (overlapping clusters) to +1 (distinct compact clusters).

PLS as such is used for multivariate calibration, i.e., there should be two blocks of data: the predictor matrix **X**, and response matrix **Y** (e.g., **X** contains the spectra of samples, and **Y** the concentrations of components therein). The algorithm can be presented as two PCA procedures run on these two blocks. The matrices are decomposed as $\mathbf{X} = \mathbf{TP^t} + \mathbf{E}$, and $\mathbf{Y} = \mathbf{UQ^t} + \mathbf{F}$. These operations are not independent, since the score columns obtained for **Y** ($\mathbf{u_1}$, etc.) are used for the decomposition of **X** ($\mathbf{t_1}$ is replaced by $\mathbf{u_1}$). In the next step, when **Y** is decomposed, $\mathbf{u_1}$ is replaced with $\mathbf{t_1}$. Thus, the data structures of **X** and **Y** influence each other. In this way, a calibration model is built that can predict **Y** values based on **X** data.

PLS discriminant analysis (PLS-DA) is a modification of PLS where **Y** is a column vector filled with categorial values (class designations, e.g., 0 and 1). If there are more than two classes, then the algorithm should be repeated as a yes/no question asked about the membership in each of them. Thus, the classification problem is re-formulated as a regression problem (and the calibration dataset becomes a learning dataset). The performance of classification is best checked using a so-called external validation dataset, i.e., samples which were not used for calibration. The results can be presented as a truth table, which contains the rate of true positives, TP (correct positive assignments of samples to their respective groups); false positives, FP (samples classified to be in a group but in fact belonging to other groups); true negatives, TN (non-member samples excluded from the respective group), and false negatives, FN (samples classified to be outside a group but in fact belonging to it). These four rates are combined to give *sensitivity*, which is TP/(TP + FN), and *specificity*, which is TN/(TN + FP). *Accuracy* is the ratio of the correctly labelled objects to the whole available number of objects, i.e., (TP + TN)/(TP + FP + FN + TN). The overall performance of classification is assessed by calculating weighted averages for these values across groups [33–35].

DFA, also known as linear discriminant analysis (LDA) or normal DA (NDA), is a classification approach. A linear function of the experimental variables (discriminant function, DF) is sought, which maximises the difference between the known classes. For example, if two clusters of points are considered in a bi-dimensional space (x_1, x_2), then this function will define a line that goes between the clusters (considered to be normally distributed) so that the projections of points of the first cluster on that line will be as far as possible from the projections of points of the

second cluster. This projection is called a *score*, given by $D = w_0 + w_1x_1 + w_1x_2$ (a line equation with weights w_0, w_1, w_2). If, for a particular point (object), D is below a certain value, then it belongs to one of the classes, and to the second if otherwise. For standardised data, $w_0 = 0$ and the boundary value of D is zero. For a discrimination between N clusters, N–1 functions are constructed. Ideally, there should be four to five times as many samples as variables [34, 36–38].

In the *kNN* method, the distances between an unknown object and k nearest objects of the training set are compared. The distance measure is usually Euclidean but may be different. The object is classified in a particular group if the majority of those k objects belong to this group. Usually, values of k equal to 3–5 are preferable, but this parameter is subject to optimisation [37].

SIMCA is also used for classification and is based on the consideration of the similarities of objects rather than their particularities. Each class from the learning dataset is modelled independently from the others. If the matrix **X** contains only samples that belong to a certain class, then the task is to decide whether a new sample will join the class or not. PCA is applied to **X**. Depending on the number of PCs chosen, each data point will be described by the sum of two vectors, one laying in the PCs hyperplane, and the other one which is perpendicular to this hyperplane. The lengths of these vectors have a chi-square distribution and can be combined into a statistic that has the same distribution. Thus, the critical value of the statistic can be calculated which determines the class membership. If, for a new point, the critical value is not overrun, then the point is considered as a new member of **X** [37].

The main idea behind *SVM* classification is finding the hyperplane that best separates the data into classes so that the distance between the closest data points of each class and the hyperplane is maximised. These closest data points are called support vectors. This is not always strictly possible, so that some samples are misclassified. To account for that, the cost (penalty) parameter is introduced. Kernel functions can be applied to nonlinearly transform the data and improve the linear separability of classes. Further details can be found in [39, 40].

*CT*s are widely used by LIBS practitioners nowadays. This method implies that the features of studied objects are represented as multidimensional vectors, and the set of available classes is also defined. The aim is to construct a function (called *classifier*) which will translate the space of feature vectors into the space of classes. This function is a set of partitioning (splitting) rules which are often formulated as inequalities and are organised as a decision tree, i.e., they form a branched structure with several levels. A feature vector is first supplied to the root node of the tree, the first splitting rule is evaluated, whereupon the vector goes further along one of several branches depending on the result. For example, a rule may be formulated as: "Is x_2 greater than 5?", and the vector goes either along the "yes"--branch or along the "no"-branch depending on the answer. Further questions give rise to further nods and leaves of the tree. When the vector reaches a leaf (a terminal node), this means that the final class assignment is made.

Defining the rules is the crucial point. To this end, a learning set (a set of feature vectors with known class assignment) must be available. Classification rules are developed so that the largest decrease in diversity of the classification label within

each partition is attained (auxiliary impurity functions are used to define this increase in homogeneity). This can be done manually, but the process can be facilitated by computer programs such as CART (Classification and Regression Trees). The partitioning rules themselves can be directly interpreted in a physical or chemical sense [41, 42].

RF is an extension of the CT method which uses multiple trees instead of one. The most widespread algorithm is the following. For a learning set of N samples with M-dimensional feature vectors, only *m* features out of M are randomly selected. A random subset with replacement (of the size N) is selected from the learning set. Then, a CT is constructed on this subset, taking into account only *m* features. This procedure is repeated and results in a number of trees; each of them gives its own classification result for a given object, and the final result is obtained by taking, e.g., the majority vote. RF often yields higher classification accuracy than CT and is useful when a large number of features and classes are available. On the other hand, the rules become much harder to interpret, and the demand in computational resources is increased [43].

NNs have recently become a very fashionable instrument for data analysis, classification, and prediction. They are loose models of animal brains. Each computational neuron receives a signal (i.e., a number) and applies to it a pre-defined mathematical transformation (usually nonlinear, called an activation function), whereafter the signal is transferred further, to other neurons. The learning process implies the adjustment of the parameters of the activation functions. After learning, an NN can be used for classification, feature recognition, etc. [37].

Of course, the above ones are only the most frequently used algorithms. We would like to draw the readers' attention to less fashionable, but indeed very useful techniques such as independent component analysis (ICA) [44], non-negative matrix factorisation (NMF) [45, 46] and a large family of data fusion techniques such as consensus PCA (CPCA) or common components and specific weights analysis (CCSWA, or ComDim) [47, 48].

In the following, further narration is organised around the major kingdoms and other taxonomic entities and groups of living organisms, namely: microorganisms, including viruses, bacteria, microscopic fungi and protozoa; plants; animal and human tissues.

7.4 Microorganisms

Studies on the discrimination of microorganisms by LIBS have been largely motivated by concerns on biological and bacteriological threats after the events of 11 September 2001 in the United States and subsequent lethal attacks of *Bacillus anthracis* (anthrax agent) transmitted via the U.S. Postal Service. The first publication on LIBS for the detection of bacteria has been released by the workers for the French Ministry of Defence in 2003, followed closely by the U.S. Army in less than two months. Of course, civilian applications can also be imagined, like bacteriological monitoring in medicine or online monitoring in the food industry [15, 49, 50]. A

number of topical reviews exist in the literature, among them are the recent excellent 2019 reviews by S.J. Rehse (on bacterial detection) [13] and R. Gaudiuso et al. (on medical and veterinary applications) [51]. Due to reasons described above, bacteria are currently the most systematically studied organisms in terms of classification by LIBS.

The article by Stéphane Morel et al. "Detection of bacteria by time-resolved laser-induced spectroscopy" [15], appears to be the first study on this topic. The authors point out that, for the determination of hazardous microorganisms, an analytical method is required that would reduce the risks of the contamination of operator or potential sample pollution. It is also required that an early-warning system be available and used to adopt suitable protective measures before triggering more sophisticated, but more time-consuming tools for the accurate identification of microorganisms. LIBS lends itself for this purpose. It has to be noted that the identification of bacteria imposes additional requirements on the analysis, as the determination preferably has to be done from an aerosol, and not from a solid surface, and possibly without preconcentration. However, in this particular study, procedures were carried out with bulk samples for the sake of simplicity. Thus, the radiation of a 1064-nm 100-mJ Nd:YAG laser was focused at the surface of bacterial pellets. The authors tried to use CN molecular emission signals as indicators of the presence of amino acid structures in the analysed material but had to deem this impossible because of CN production from atomic species through plasma chemical reactions. On the other hand, they managed to discriminate different species of bacteria and tree pollen from each other using the phosphorus to carbon ratio (P I and C I lines at 253.560 and 247.856 nm, respectively, were used). This was the simplest approach to classification which did not involve any sophisticated mathematical data treatment. This study was expanded later by developing an aerosol delivery system to demonstrate that time-resolved LIBS can be used to detect biological aerosols [16]. However, no biosamples have been analysed with the aerosol generation unit, as only model experiments were made with natural mineral waters.

Hybl et al. [52] have made the crucial step by examining several common biological agent simulants and interferents (bacterial spores *Bacillus globigii*, growing media, fungal spores such as penicillium or smut, and pollen) with the help of dry aerosol generation units, one based on laser-induced shock wave, the other one based on a loudspeaker. PCA analysis of selected spectral signals made it possible to discriminate the four sample groups in a three-dimensional subspace; the most dispersed class was obtained for tree pollen. The authors pointed out, however, that since the laser ablation volume is very small (around 1 mm^3), a rapid online LIBS monitoring would be a challenging task, since about 20 L of air per minute would have to be probed.

Dixon and Hahn [53] investigated the feasibility of using LIBS for the detection of bacterial spores suspended in water and aerosolised. The detection was based on ionic calcium lines. It was not possible to detect ionic magnesium or neutral sodium lines, and CN molecular emission as well. But since Ca content in a single spore depends on its growth condition, it did not seem to be a valid basis for discrimination

if single-spore, single-shot spectra were considered. The overall conclusion was that although the very detection of spores was feasible, no *rapid* detection of elemental mass loadings appeared consistent with the analytical capabilities of LIBS. Admittedly, it is unclear why the authors have chosen to monitor ionic Ca and Mg lines given the long detection delay they worked with (40 μs); neutral element emission could possibly give better results. The presence of N_2^+ signals instead of CN emission probably indicates that the (decarbonised) air surrounding the spores contributed too much to the spectra (the pulse energy was 275 mJ). This is partially confirmed by the fact that CN bands did appear when CO_2-containing air was ablated.

Boyain-Goitia et al. [54] envisaged single-particle LIBS and Raman analysis of pollen (yellow lily, dark lily, and marguerite). It was shown that bioaerosols can indeed be differentiated from particles of other origin, but large shot-to-shot variations made a unique assignment between an observed spectral pattern and a specific pollen type elusive. The authors suggested that a reference library of experimental spectra be created before reliable detection and identification can be done reliably in real time. Continuing this work, Beddows and Telle [55] tried to address the problem of common aerosol interferences in urban air by comparing LIBS measurements with the data from a mobile single-particle aerosol mass spectrometer (ATOFMS). They also provided a detailed and fruitful discussion of approaches to aerosol analysis available at that moment. Interestingly, self-triggered LIBS mode is described, when the pulse energy is adjusted so that the breakdown occurs only on the airborne particles, and the detection is triggered by a fast PIN photodiode. Ions that lower air breakdown threshold are removed by a pin electrode placed close to the laser focus. The authors expressed their scepticism about the use of LIBS for bioaerosol analysis and suggested that a hyphenated technique, like LIBS-Raman of LIBS-LIF (laser-induced fluorescence), be tried for the application.

The study by Samuels et al. [50], also one of the first in the field, describes a successful PCA-based discrimination of bacterial spores, moulds, pollens, and proteins, deposited on silver porous filters. Their subsequent work dealt with the same biomaterials but also involved phosphorus-containing chemical weapon simulants and landmine casings. Similarly to Morel et al. [15], C/P ratio was employed for discrimination. As an alternative approach, comparison with library spectra by means of linear correlation coefficient was carried out. Later [56], they also proposed the tagging of bacterial spores by exotic metals, such as Sc and Eu, using preferential binding. Munson et al. [57] continued this work, adopting a similar experimental approach, and applied PCA, SIMCA (see above), and linear correlation-based library search to discriminate bacteria and interferents. Not only peak intensities, but also their ratios (like C/P) were used in modelling. A double-pulse standoff LIBS system for the detection of versatile hazardous materials, including explosives and bacilli, was later developed [58]. Kim et al. [59] also attempted to use phosphorus and calcium signals to discriminate between bacteria, including *E. coli*, but it seems that their identification of spectral lines was inaccurate due to biased spectrograph wavelength calibration. Calcium is also important because its concentration is known to be higher in Gram-negative bacteria which

have an additional outer membrane; the cohesion of its proteins is maintained by divalent cations. This idea is highlighted by Baudelet et al. [17], who proposed to combine the intensities of all elemental lines from a spectrum and thus obtain "elemental profiles" for each sample; then each sample will be represented as a point in the multidimensional space with as many axes as available chemical elements, and the points will form separate groups according to their chemical and biological identity. The groups are defined by the direction of corresponding multidimensional vectors. The approach was called "trace element hyperspace classification" (TEHC).

Stand-off LIBS detection of biological and chemical warfare agent surrogates was first attempted in 2008 [60]. The distance was 20 m, and a PLS-DA algorithm was used for the identification. Although the results were generally encouraging, considerable false negative and false positive detection values were reported.

J. Diedrich et al. [61] studied three strains of *Escherichia coli*, one strain of environmental mould, and one strain of *Candida albicans* yeast by nanosecond LIBS. All microorganisms were analysed while still alive and with no sample preparation. DFA (see above) was used to discriminate between the biotypes and *E. coli* strains. The discrimination efficiency was fairly high. The authors stressed the possibility of discrimination between non-pathogenic and pathogenic *E. coli* strains. In the same year, this methodology was applied to several pathogenic and non-pathogenic *E. coli* strains in a separate study [62], which corroborated and expanded the previous results. It was also shown that strains cultured in different media can be identified and efficiently discriminated, being more similar than different strains cultured in identical media. Relatively small laser pulse energy was used to ablate the bacteria which were placed on agar surfaces. Nineteen emission lines of Mg, Ca, P, K, Na, and C were selected and their intensities (areas) were subjected to DFA analysis. The (relative) concentrations of calcium, potassium, and phosphorus were the main drivers of discrimination. In a follow-up article [36], studies were extended to include *Pseudomonas aeruginosa (P. aeruginosa)* strains, which were readily discriminated from *E. coli.* Moreover, it was shown that the classification apparently relies on the composition of cell membranes: bacteria of a same strain grown on different culture media had very similar spectra, but those grown on McConkey agar containing bile salts, known to cause the disruption of cell membranes, formed a separate cluster. Later [63] it was demonstrated that the effect of bile salts is not monotonous: low concentration (0.01%) actually *increased* the calcium content in *P. aeruginosa*, but the Mg content decreased. Higher concentration (0.4%) resulted in a significant drop in Ca content, but for Mg, there was only a slight decrease. The spectra were recorded in an argon atmosphere. This was an indication that LIBS can be used to probe and quantify Gram-negative outer membrane biochemistry. Even in the bile-containing medium, it was still possible to discern between different genera of bacteria (90% accuracy).

In 2009, Rehse and Mohaidat [64] studied the effect of ambient gas on discrimination quality. As a pilot study, brass samples were analysed, and then the approach was tested on *E. coli* (Gram-negative bacterium) and *Staphylococcus mutans* (Gram-positive bacterium). Spectra in argon and helium were acquired sequentially, and the

intensities of pre-selected spectral lines formed a doubled set. There was an enhancement in DFA discrimination based on such sets (increase in the distances between group centroids), compared to calculations using only data for a single ambient gas. Thus, the absolute accuracy of bacteria discrimination was increased from 97 to 100%. This latter method is advantageous when the samples are highly similar to each other.

A further work by the same research group [65] focused on the problem of co-presence of different bacteria. It has been shown that in a mixture of two bacteria (*Mycobacterium smegmatis* and *E. coli*), accurate identification was possible down to an 80:20 mixing ratio; lower mixing proportions lead to stepwise loss of selectivity, but at no time were the spectra classified as anything other than one of the two species comprising the mixture. The authors also studied the effect of dilution of bacterial suspensions on classification and concluded that approximately 2500 bacteria were required for accurate identification.

The further scientific question is whether the identification of bacteria depends on their metabolic state or not. Studies of *E. coli* and *Staphylococcus viridans* [66] suggest that the answer is no. Live, starved, killed and UV-stressed bacteria are still classified correctly. In [67], the authors made a step further and modelled the identification of bacteria in a clinical specimen (urine). In general, the reported truth tables witnessed a good classification accuracy, which was not affected by small amounts of a contaminant strain likely to be present in a clinical specimen. Leave-one-out (LOO) cross-validation was reported to yield artificially high accuracy compared to external validation—a situation which is often described in chemometrics-related studies. Sequential use of two DFA models has been proved to increase accuracy: a "coarse" (e.g., genus-level) model is followed by a "finer" (e.g., species-level) one to eventually obtain an accurate identification at the desired level.

Multari et al. [68] studied the discrimination of lyophilised methicillin-resistant *Staphylococcus aureus* (MRSA) and *E. coli* strains by arranging a blind test with researchers who did not know the identity of samples they dealt with. The researchers managed to successfully differentiate all the provided samples based on their emission spectra. A sequential PLS2-based classification algorithm was used. The importance of Ca and Mg content has been highlighted. A similar approach was successfully tested with bacteria grown on a blood agar [69]. Later on, the same team tested the performance of LIBS in the detection of microbiological contaminants on food surfaces [70]. They focused on *E. coli* and *Salmonella enterica*; the tested substrates were eggshell, milk, bologna, ground beef, chicken, lettuce, metal drain strainer, and cutting board. The authors were making no claim that absolute detection of a biological target has been accomplished; the methods were only claimed to be applicable to the differentiation of samples within a pre-defined sample group. It is reported that the two bacterial species could be discerned from each other and from uncontaminated surfaces. The influence of the metabolic state of bacteria (viable or heat-killed) has been also studied.

Regarding the perspective of identifying bacteria in environmental samples, it is important to assess the effect of trace mineral content and pH of a sample upon the

reliability of classification results. This was the subject of the study by G. Gamble et al. [18], who emphasised the role of pH in gauging the ion-retaining capacity of cell membranes. Bacterial spectra were classified using PCA and Mahalanobis distance analysis (MDA). The authors have found that the classification results depended upon the type of water with which the bacteria were rinsed before freeze-drying and pelletisation: deionised; deionised, nitrogen-purged; reverse osmosis; tap; phosphate buffered saline; and TRIS-buffered water (TRIS = tris (hydroxymethyl)aminomethane). In general, the clusters on PCA score graphs displaced when the water type changed. However, this did not usually lead to confusions in the identification of species. Interestingly, the authors used micro-crystalline cellulose (2.6 times sample weight) to facilitate pelletisation; the resulting pellets were interrogated by a 266-nm laser.

In the study [34] published in 2013, the authors pointed out that there was no consensus among researchers at that moment on whether the use of entire LIBS spectrum or of selected variables (wavelength ranges) provides optimal classification of unknown spectra. It was also not clear which chemometric technique, if any, was best suitable for bacterial identification. The study involved the comparison of PLS-DA with DFA on differently selected datasets. The conclusion was that DFA was more suitable for a genus-level classification of a completely unknown sample, while PLS-DA was able to discriminate more similar spectra at the level of species or strains. The use of complex ratios of elemental line intensities for the training of the models was proved to increase their performance.

A different mounting protocol was tested in 2015 [38]. The bacteria under study were suspended in water and then deposited on standard nitrocellulose filter paper to create flat and uniform bacterial pads. In contrast to the authors' previous studies, a collection system based on two parabolic mirrors was used. This required a more sophisticated laser-based sample height alignment system. The introduction of filter paper (instead of agar, which does not add any substantial contribution to spectra) limited the image intensifier amplification due to a strong carbon emission at 247.86 nm. Despite that, the overall classification performance of the method, with data processing done by DFA and PLS-DA, was better compared to previous studies. The new protocol made it possible to reduce sample preparation by removing the necessity of centrifugation, but also introduced difficulties related to the filter paper as a substrate.

D. Malenfant [35] studied the detection limits for the LIBS determination of bacteria and found it to be no less than 50,000 cells per single laser pulse. Experiments with growing substrates intentionally contaminated with zinc and magnesium have shown that the former is accumulated by *E. coli*; conversely, no accumulation was observed for magnesium. Heat or UV killing of bacteria has been reported not to significantly affect the discrimination between different bacterial species. Importantly, a centrifuge filtration insert has been designed which helped to concentrate all bacteria from a suspension to a particular 150-micron diameter location on a filter paper. This pre-concentration approach can considerably push down the detection limit in the future.

A discrimination of *E. coli* strains was reported in 2020 [71]. The authors found that the Na/K ratio is a highly significant feature for discrimination of the strains with an accuracy of more than 90%.

Somewhat apart from the above-described experiments stands the study by Lewis et al. [72], who investigated the possibilities for the discrimination of bacteria in bauxite soils of Jamaica. In this interesting work, femtosecond LIBS was combined with PCA and PLS to differentiate among bacteria from both un-mined and rehabilitated bauxite soils. Aqueous soil extracts were prepared, and then Luria-Bertani agar was inoculated by a portion of an extract. The resulting colonies were identified by polymerase chain reaction and Gram-staining, i.e., no model microorganisms were used. In the LIBS spectra, the principal peaks were identified, and their integrated intensities served as a basis for chemometric analysis. Different species of bacteria formed distinct clusters on score plots, especially on those obtained by PLS. On the PCA score plots, geographical site-related groups could also be observed. As usual, Ca and Mg emission played a key role in the discrimination.

A related paper [73] deals with the detection of *S. enterica* (more precisely, of its serovar *Typhimurium*) in food. Since this infection prevails in raw meat and dairy products, thus liquid media such as milk, chicken broth (CB), and brain heart infusion (BHI) were studied. The liquids were inoculated with the bacteria and then placed on silicon wafers which were analysed by LIBS after drying. DFA was utilised for the discrimination between pure and inoculated food, as well as between different concentrations of bacteria. It has been found that LIBS could detect bacteria present at 10^5–10^6 CFU/mL concentrations in all the studied media. Although comparative experiments, based on quantitative polymerase chain reaction, demonstrated its ability to detect as little as 10–100 CFU/ml in BHI and CB, respectively, this assay could not detect *Salmonella* from milk (at least with the experimental technique the authors used).

Snyder et al. [74] in 2008 used LIBS to discern between two biological agent surrogates (*Bacillus atrophaeus* and ovalbumin) and potential interferent compounds (mould spores, humic acid, house dust, and Arizona road dust). Mixtures of these were also examined. This study presents one of the first applications of advanced chemometric machinery, namely, neural network (NN) analysis, complemented by multiple linear regression (MLR), to the field. The samples were deposited as solutions into craters on aluminium disks, allowed to dry, and interrogated with laser pulses. Both quantitative and qualitative models were developed. The accuracy of NN classification was assessed based on the percentage of false negative predictions. The authors stated that the detection of 100 CFU (colony forming units) of bacilli was possible. On the other hand, there were significant interferences from humic acid and mould.

Saari et al. [75] applied an interesting experimental approach that involved an electro-dynamic balance to trap aerosol particles, which were generated from an aqueous suspension of fungal and bacterial spores, and subsequently record LIF and LIBS spectra. Calcium, potassium, and sodium were readily measured, and the

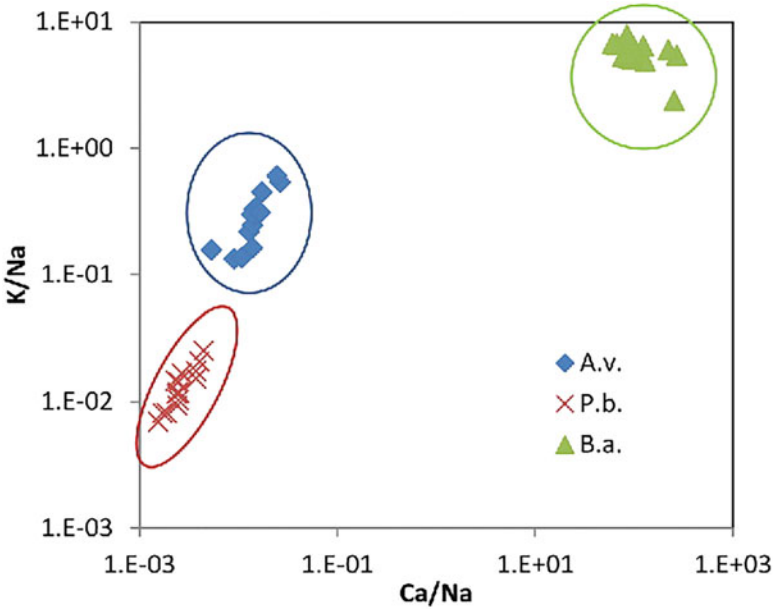

Fig. 7.4 The discrimination of fungal and bacterial spores (*Aspergillus versicolor*, *Penicillium brevicompactum*, and *Bacillus aureus*) using the normalised Ca/Na and K/Na signals [75] Copyright © The American Association for Aerosol Research, https://www.aaar.org//. Reprinted by permission of Taylor & Francis Ltd., http://www.tandfonline.com, on behalf of The American Association for Aerosol Research, https://www.aaar.org/ [75]

species were efficiently discerned using the K/Na vs. Ca/Na graph (Fig. 7.4). Bacteria proved to contain much (≈1000 times) more Ca than moulds.

A research group from Spain [76] used NN to identify and discriminate several bacteria strains (*P. aeruginosa*, *E. coli*, and *Salmonella typhimurium*). To this end, they used a pre-compiled spectral library to train the NN. It has been shown that the growth medium (three types of agars were studied) does not affect the accuracy of identification. Later, the approach was used for 40 bacterial strains causing hospital-acquired infections (HAI), including multi-drug resistant strains [77]. Interestingly, the *E. coli* spectrum shown in this publication is much different from the analogous spectrum in [76], which may be due to a change in detection parameters. In a related work [78], kNN enabled the discrimination between *E. coli* and *S. aureus*.

This methodology was later expanded into a study [79] devoted exclusively to medically relevant *Candida* yeasts, aiming at strain discrimination. Twenty-one strains belonging to seven species of *Candida* were included in the study. Thin layers of suspensions dried in Petri dishes were interrogated by LIBS. The spectra were normalised to the intensity of the H_α line (at 656.28 nm) to decrease intensity variations. Neural network developed in the Matlab environment was used for the classification. The emission spectra present a handful of molecular and atomic

emission signals, most of them, however, belonging to non-metallic species (C_2, CN, N_2, N_2^+, CN, N^+, NH, O^+, and H, together indicative of a quite high plasma temperature), with almost no signs of metal emission lines. Nevertheless, strain classification was impeccable.

Identification of bacteria has also been regarded as an instrument of astrobiology. In connection with this, Sivakumar et al. [80] investigated the discrimination between live and dead *E. coli*. Both nanosecond (10-ns Nd:YAG, 1064 nm, 20 mJ) and femtosecond (150-fs Ti-sapphire, 775 nm, 1.4 mJ) lasers were used, and spectra were acquired in a helium atmosphere. The spectra were analysed by means of PCA and SIMCA. The results show that autoclaving and sonication changed the spectral signatures of bacteria. Especially significant were changes in the fs-LIBS signals of K, P, Na, Ca, and Mg, which dropped strongly after autoclaving. Sonication caused the signals of Na, P, and Ca to drop moderately, whereas K and Mg were barely affected. Considerably different were the results of ns-LIBS, where sonicated samples always gave the most intense signals, followed by live, and then by autoclaved cells. The authors have drawn attention to the fact that the cell damage increased the viscosity of analysed media which led to changes in experimental conditions. It is believed that the use of an internal standard could possibly improve the situation.

Somewhat similar study was published by Farid et al. [81] in 2018 and dealt with the effect of graphene oxide (GO), which is known to cause cell membrane disruption, on *E. coli* and *S. aureus*. They also reported the decrease of P, Mg, Ca, Na, and K signals with addition of GO, while their concentration in the supernatant solution drastically increased.

An interesting study was published by Prochazka et al. [82], who examined five *Staphylococcus* and one *E. coli* strains by LIBS and Raman spectroscopy. Data analysis was done with PCA and Kohonen self-organising maps (SOM, a special variety of NN). LIBS provided better PCA-based classification compared to Raman, but this was vice versa with SOM. Merging the data from both techniques yielded the best classification. Carotenoid and potassium signals seemed to drive the separation of the methicillin-resistant *S. aureus* cluster in PCA score plots (Fig. 7.5).

Cisewski et al. [39] proposed an approach for the classification of sporulating bacteria strains and confusant substances (baking powder and baking soda). The idea was to apply a wavelet transformation to reduce data dimensionality and then

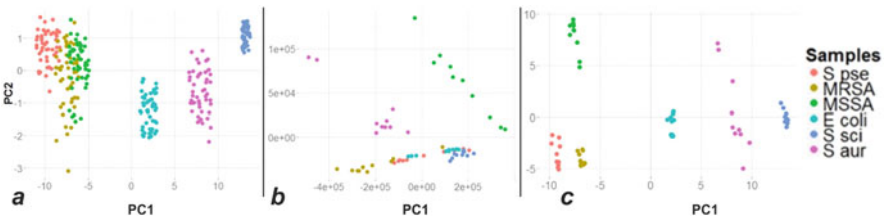

Fig. 7.5 PCA score plots for five Staphylococcus and one E. coli strain, (**a**) LIBS data; (**b**) Raman data; (**c**) merged LIBS + Raman data. Adapted from [82] with permission from Elsevier

classify the spectra using SVM (see above). Thirty percent of the available data was not used in modelling and served as a validation dataset. Misclassification rates were 0.6% for confusant powders and 3.3% for *Bacillus* spore powders. The authors also briefly discussed how the models could be trained for use with multiple different LIBS systems. In [83], LIBS and Raman data were fused to improve the SVM classification of bacteria.

7.5 Viruses

Viruses are the lowest, non-cellular form of life. Studies related to LIBS analysis of viruses are very scarce. This is largely because of the lack of metals in their chemical composition, since viruses are essentially encapsulated nucleic acid molecules. In spite of this, a few studies do exist on the topic.

The first work in this direction is apparently that by J.L. Gottfried, published in 2011 [49]. This scrupulous investigation was aimed at discovering the potential of LIBS to discriminate biological and chemical threat simulators prepared on multiple substrates and in the presence of interferents. Most studied materials were bacteria-related, but there also was MS-2 bacteriophage as a simulant of other viral agents like the *Variola* virus, which is a smallpox agent. The authors investigated the capability of PLS-DA models to discriminate infectious agents on steel, aluminium, and polycarbonate in the presence of interferents such as limestone and ovalbumin. Thin layers of infectious agents were prepared by drying the respective suspensions on the substrate plates, and single-shot spectra were subsequently collected. Although good results were obtained in some cases, but a considerable confusion was provoked by substrates and interferents. Interestingly, the authors mention that their samples differed in transmittance of the incident radiation (1064 nm), so that some of them prevented the formation of substrate spectrum. This certainly has to do with absorbance coefficients, the point which we discussed above. The authors also point out that the analysis would be more robust if a standardised substrate was used—e.g., if swipes were taken from the studied surfaces. On the other hand, in this setting, stand-off analysis would be impossible.

Another group [84] examined four strains of UV-killed *hantavirus* as dilutions on glass slides. The importance of substrate choice was pointed out: glass slides worked better than agar (this may have been due to better laser ablation conditions on glass). The chemometric method used was PLS1 as implemented in the Camo Unscrambler software. In contrast to other pathogens, viruses could not be differentiated by PLS1 alone, so the authors used a predictive flow approach. One of the strains was removed from the analysis, and the three remaining strains were then differentiated. It is, however, unclear what particular spectral features enabled this differentiation (the greatest variances in the model occurred for C, H, N, and O). In a more recent work [85], the same group envisaged the detection and identification of infectious agents in human blood, using the PLS-DA algorithm. Infectious agents, with which the blood was spiked, included bacteria (*Yersinia pseudotuberculosis* and *S. aureus*), *Trypanosoma cruzi* parasite, and the human immunodeficiency (HIV) virus.

Whatman paper/ashless paper filters and glass microfibre filters were used as substrates (see also [86]). The samples were interrogated with a 1064 nm/13 ns Nd:YAG laser. Interestingly, this study compares conventional laser beam focusing with a so-called "long-spark" configuration, when a cylindrical lens was used for focusing. The result of this optical setup is a long, narrow plasma that can be considered uniform in a large portion of its length (in the axial direction) [87, 88] and, importantly, produces much more ablated material than a conventional spheroidal plasma. This helps to increase the sensitivity and the signal-to-noise ratio when spatial resolution is not important, provided the pulse energy is high enough. In this particular study, 1.4 mm^2 of filter surface was ablated with a cylindrical lens, whereas only 0.031 mm^2 with a spherical one. The authors assessed the limits of detection (LOD) and found it to be 10 cells, parasites, or viral copies per 1 mL of blood. Provided that the volume of a bacteria (*S. aureus*) is of the order of 1 μm^3 [89] and hence its mass is around 10^{-12} g, this LOD means that bacterial species were detected at 10^{-5} ppm concentration, and viruses at 10^{-7}–10^{-8} ppm in a chemically very similar medium. Meanwhile, the handbook by Cremers and Radziemski [90] states the LOD for sodium (which has its own highly characteristic and very intense lines) in a 10 M LiCl aqueous solution to be of the order of 10^{-2} ppm. This comparison raises the concern that the chemometric algorithm has been overtrained at some point in the study.

The most recent work of this group [91] is devoted exclusively to viruses, namely, HIV and hepatitis C (HCV) viruses. Using the approach developed in the above-discussed study, the authors have been able to discern the two viruses in clinical blood samples.

7.6 Plants and Related Materials

Studies dedicated to the classification of plant samples are quite numerous [92]. Here we do not mention those of them which are related to the monitoring of environmental pollution or deep-processed food products [93]. Plants are analysed either "as is" (e.g., leaves or wood cuts) or in the form of pellets prepared from ground material [94].

In 2002, a research team from Florida reported the implementation of an online LIBS-based system for the analysis of wood products treated with copper chromated arsenate (CCA) [95]. This wood preservative, though efficient (over 70% of the volume of all treated wood products sold in 1996 were treated with CCA), has been recognised dangerous since 2003 due to the release of arsenic to the environment. The recycling and disposal of CCA-treated wood required a valid means for sorting, and a LIBS-based facility was regarded as a plausible solution for this task [96]. The authors [95] have chosen the chromium line at 424.5 nm as a CCA indicator. Classification was based on the peak-to-base ratio for this line with the threshold value set to 2.2. Accuracy of 100% and 98.9% was reported for the identification of treated and untreated wood, respectively, if 10 laser shots were averaged for each sample. Rotten and soaked wood was difficult to classify due to significant changes

in plasma parameters. This problem could be tackled by increasing the laser pulse energy. An analogous XRF facility could distinguish between CCA-treated wood and wood treated with non-arsenical alternative chemicals [97]. A surprising feature of LIBS was the ability to detect stains that were not visible to the human eye, while XRF tended to "see through" them. An early work on the determination of contaminants in wood by Uhl et al. [98] is also worth mentioning. Wood analysis has also been the focus of the study by Martin et al. [99], who used PCA to classify wood samples according to the preservative with which they were treated. Later [100], they have shown that LIBS spectra of a core obtained from longleaf pine in a scanning manner can reveal the changes in chemical composition due to a fire event. PC analysis was employed to facilitate data interpretation. Importantly, the spectra were intentionally not taken from the fire scar area to ensure that the analysis reveals physiological mechanisms resulting from the fire stress.

In 2007, Xu et al. studied the LIBS spectra of barley, corn, and wheat grain dusts in a remote analytical setting (4.7 m) using a femtosecond laser. While the spectra were quite similar, spectral line intensity ratios (e.g., Mg I (285.17 nm)/Si I (288.16 nm), Na I (588.99 nm)/Ca I (422.67 nm), Mn I (403.31 nm)/CN (388.25 nm) etc.) were different for each of the samples. No advanced chemometric data treatment was attempted [101, 102]. Bossu et al. [103] used fs-LIBS to detect trace elements in sophora leaves and found that their concentration correlates with the level of air pollution in the respective geographical area.

Rai et al. [104] used LIBS to compare the chemical composition of ripe and unripe fruit peel aqueous extracts and found that unripe fruits were relatively rich in Mg but poor in K. Interestingly, the plasma was generated on the surface of bulk liquid samples, and in the liquid jet as well. No elaborate discussion of these technical details has been given. A similar approach was adopted in their subsequent work as well [105]. Zhang et al. [106] compared the concentrations of Ca, Na, K, Fe, Al, and Mg in three kinds of vacuum freeze-dried fruit samples (apple, Chinese gooseberry, and strawberry). It has been found that in apple samples, the relative content of Na was the highest, whereas that of Ca was the lowest. The three plants also differed in the content of K, Fe, Mn, and Mg.

Discrimination of coffee from different manufacturers was shown to be plausible in [107]. This article also contains many other examples of LIBS uses in industrial and security applications.

In 2010, Pereira et al. [108] evaluated the effects of the bacterium *Candidatus* Liberibacter asiaticus (CLas) on inoculated citrus plants. This bacterium is one of the causal agents of citrus greening, also known under the Chinese name "Huanglongbing", which causes serious problems in citrus cultivation all over the world. The authors grafted infected buds to healthy trees of known age and obtained the LIBS spectra of their leaves over the course of 8 months. A logarithmic transformation was applied to the spectra in order to equalise the contributions of weak and strong signals. The data were also mean-centred. PCA and SIMCA were used for the classification between infected trees and healthy trees. The authors were able to carry out this classification with reasonable accuracy (96 and 100% for healthy and inoculated citrus trees, respectively, in the first 3 months of the

experiment, and 74/88% in the eighth month), which was superior to quantitative polymerase chain reaction (qPCR) results. It is important to mention that the infected trees with negative qPCR results were also considered as diseased. The authors emphasised the role of zinc, manganese, and iron in the discrimination. Other authors also found the lines of Fe, Ca, Mg, and K to be important for the detection of various diseases of citrus trees [109, 110]; however, the 22 principal components used for the classification seem to be an overdo in most situations [109].

Huanglongbing is also dealt with in [111], where a collinear double pulse configuration with 700 ns delay between 171 and 180 mJ pulses ($\lambda = 1064$ nm) was used to interrogate the samples of navel oranges. Continuous wavelet transform (CWT) was used to extract emission peaks. Two classification models were compared, both exhibiting good performance. It has, however, remained unclear what spectral features were responsible for the classification. Another study [112] was based on the analysis of tree phloem (sapwood) rather than leaves or fruits. A special ablation regime, effected by 4-ns three laser shots with 10 μs inter-pulse delays, was used to enhance plasma emission. As a simple way to explore spectral differences, subtraction of spectra was considered. The data was coarsened by adding up adjacent points; then, 38 peaks, highlighted by spectra subtraction, were selected, and this small dataset was used for PCA and DFA. In general, high classification accuracy was observed. Discrimination of genetically very close accessions of sweet orange using the so-called classification via regression (CVR) is described in [113].

The authors of the research dealing with tobacco infected with tobacco mosaic virus (TMV) [114] have emphasised the importance of moisture content for the discrimination between healthy and infected plants. Moisture was shown to mask the emission of Fe, Mn, Sc, Sr, Ba, and Li, along with some lines of other elements, in fresh samples as opposed to dry ones, and to increase the RSD of intensity from 5–15 to 30–60%. The clustering quality in PCA changes accordingly (Fig. 7.6).

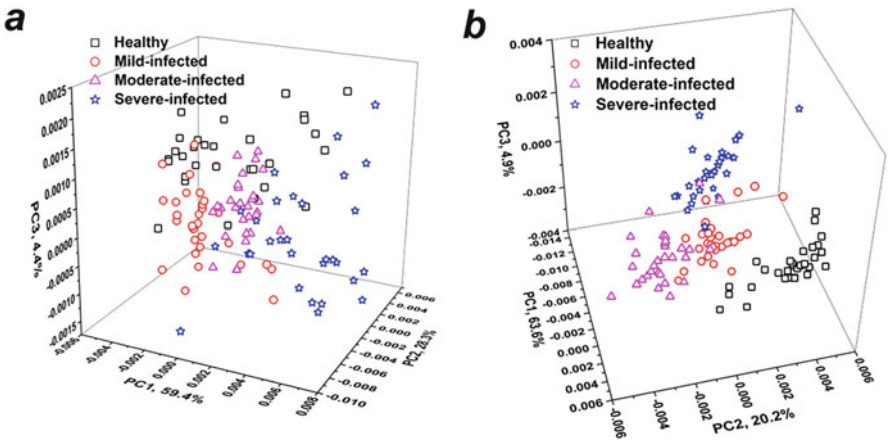

Fig. 7.6 PCA score plots for spectral datasets based on fresh tobacco samples (**a**) and dried samples (**b**). Adapted from [114]

Admittedly, different laser wavelengths were used for fresh and dried samples (532 and 1064 nm, respectively). After variable selection, PLS-DA and SVM models were built with the latter significantly outperforming PLS-DA in accuracy (94 vs. 89% for prediction).

Ranulfi et al. [115] studied the effect of GSFR disease (green stem and foliar retention) on the spectra of soybean. Student's *t*-test was used to identify spectral signals with most differences between healthy and infected plants. CVR and PLS regression were also used. The authors concluded that healthy plants were relatively rich in Ca and Mg and relatively poor in K, and vice versa for the infected soybean. A recent contribution related to soybean seeds can be found in [116].

Martin et al. [117] used LIBS to detect metals such as Mg, Pb, Ca, Zn, and Cd in *Festuca arundinacea* (tall fescue) leaf tissue samples. The implication was that LIBS could serve to control forage quality and to monitor the progress of phytoremediation of contaminated soils. The authors were also interested in whether the presence of a common fungal endophyte such as *Neotyphodium* sp. could affect the concentration of metals in the leaf tissue, but the results were not persuasive due to an insufficient number of samples. A similar study involved scented geranium [118].

In their scrupulous study, Martelli et al. [119] used LIBS with an excimer ArF laser ($\lambda = 193$ nm) to differentiate wheat tissues during the gradual ablation of grain in real time, without any sample preparation. The authors first collected LIBS spectra (230–930 nm) of hand-isolated tissues. The spectra were baseline corrected and normalised to the intensity of the C_2 Swan molecular emission (516.52 nm) to compensate for any experimental fluctuations or laser-matter interactions (plasma temperature, crater depth, and tissue density). A method called *moving-window two-dimensional correlation* (MW2D) was utilised to analyse compositional changes as a function of the number of pulses during the ablation of a grain and to identify the number of pulses necessary to access a particular tissue. Ca II (396.85 nm)/Ca I (422.67 nm) and Mg I (285.22 nm)/Mg II (279.55 nm) emission intensity ratios were used as guides for this procedure. In this fashion, the depth "coordinates" of five tissues, namely: pericarp (PE); seed coat (SC); nucellar epidermis (NE); aleurone (AL), and starchy endosperm (END), were identified. Thus, a subsequent PLS-DA analysis was possible (Fig. 7.7), in which five classes and five latent variables were considered. A high percentage of correct classification was observed for PE, SC, AL, and END. As for NE, this layer was quite thin and was therefore often misclassified. The ablation rate (per laser pulse) for each of the layers could then be calculated and related to the tissue cohesion. Seed coat was found to be the most cohesive material with the lowest ablation rate. This approach was also used in the subsequent work related to the interrelations between the cohesion of wheat grain tissues and their LIBS signatures [120].

Schenk and Almirall [121] investigated the options for classifying unprocessed cotton according to its geographical origin in connection with serious fraud issues. The samples were milled, spiked with a solution of scandium, which served as an internal standard, dried, and pelletised (Sc content in the pellets was 400 ppm, and its ionic line at 361.3 nm was used for the standardisation). A discrete set of element

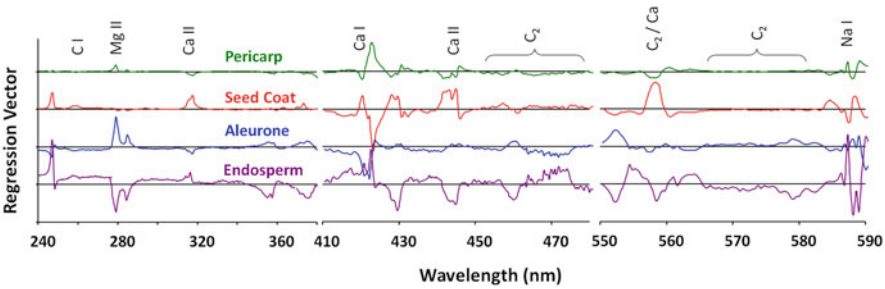

Fig. 7.7 Regression vectors obtained by the PLS-DA to predict wheat tissues: pericarp (PE), seed coat (SC), aleurone layer (AL), and endosperm (END). Reprinted with permission from [119]. Copyright 2010 American Chemical Society

emission lines was considered, namely, nine lines of Al, Ba, Ca, Cr, Cu, Fe, Mg, and Sr. The three-dimensional PCA score plot revealed that the samples formed (somewhat overlapping) clusters according to their provenance. Linear discriminant analysis (LDA, or DFA) yielded more that 97% correct classification rate when classifying by broadly defined regions (south/southwest or south/southeast of the United States), and more than 81% when the state of origin is used as the classification criterion.

Beldjilali et al. [122] found the aluminium and silicon concentrations in potato skin to be much higher than in the flesh. This may have been caused by the close contact of potato skin with soil.

Ferreira et al. [123] used the so-called *random subspace method in principal components space* (RSM-PCS), along with two other related mathematical methods used to construct decision trees, to discriminate Brazilian roasted and ground coffee (RGC) according to its global quality (GQ) indexes. The spectral range around 680 nm was reportedly particularly useful for this sort of discrimination. The three methods allowed a good classification accuracy (around 84%). However, it is not clear which particular spectral feature provides the basis for the discrimination.

In 2012, Kim et al. [124] attempted to distinguish between pesticide-contaminated (10 ppm parathion $C_{10}H_{14}NO_5PS$ or fosetyl-aluminium $C_6H_{18}O_9P_3Al$) from pesticide-free samples of rice and spinach using PLS-DA. Relative intensities of the observed ionic and atomic emission lines stand in accordance with high laser pulse energies used in this study (80–140 mJ). Two-class PLS-DA model provided readily distinguishable clusters when applied both to pesticide-free standard and real samples of rice and spinach. In a similar way, it was possible to detect pesticide contamination, especially in spinach. It should be noted that spinach was spiked with fosetyl-aluminium, whereas rice—with parathion. However, it is not clear which spectral features make the discrimination possible. It could be very sensitive Al lines in the case of fosetyl-Al, but the mechanism of the parathion detection, given its low concentration, is hard to explain.

Tripathi et al. [125] studied the distribution of several elements, including silicon, in wheat plants. They have managed to discern the vegetative organs (leaf, leaf

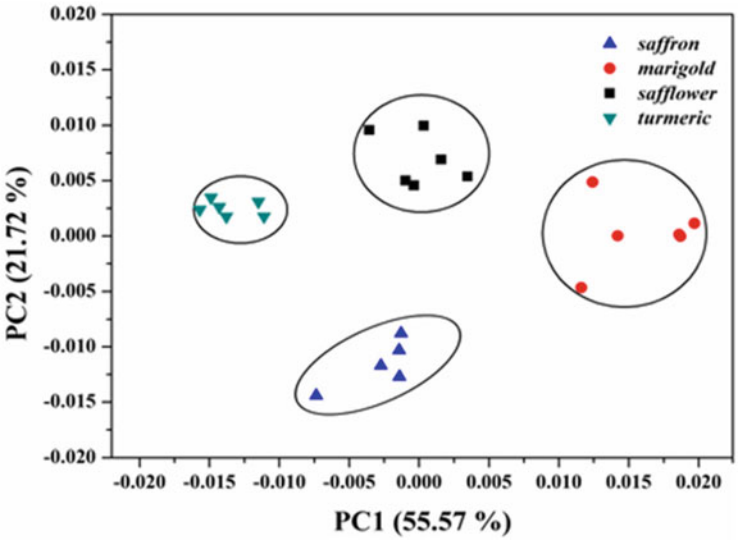

Fig. 7.8 The discrimination of saffron-like adulterants by LIBS using PCA score plots. Copyright by Springer Nature [128]

sheath, and stem) from the fertile organs (awn, lemma, and rachilla) based on a PCA score plot. Similar tasks were faced in [126]. The possibility to detect turmeric adulteration based on the signals of artificial colorants has also been shown [127]. In [128]. it has been demonstrated that saffron, marigold, safflower, and turmeric can be readily classified with the help of LIBS-based PCA score plots (Fig. 7.8). In this regard, LIBS was better than NIR and Raman spectroscopy. This was the basis for the further development of a quantitative PLS method for the determination of adulterants. A similar comparison of spectroscopic techniques has been carried out by Ercioglu et al. [129], who studied the spectra of nine aromatic plants, commonly used in cooking. In this case, NIR was superior to LIBS in terms of PCA classification, which could partially be explained by the fact that five of the herbs belonged to the same family (*Lamiaceae*, or deadnettle family).

Kunz et al. [130] used the Na I (588.99 nm)/K I (404.72 nm) intensity ratio in plants, obtained by fs-LIBS, as a marker of drought stress. Bhatt et al. [131] compared organic and conventionally grown cauliflower and broccoli by using 96 mJ ns-LIBS using both univariate and multivariate (PCA) approaches and found no significant differences between the two growing strategies. Singh et al. [132] managed to discern four species of cucurbit by PCA. It has also been shown possible to detect chlorpyriphos on apples with the help of PCA [133, 134]. Bilge et al. [135] suggested the use of the Ca/K ratio for the discrimination between natural and fortified wheat flour. PLS-DA was utilised to discriminate between pure corn or sorghum flour and their mixtures [136]. Interestingly, the flour (which is known to be difficult for pelletising) was hydrated with deionised water and hot pressed for 4 min at 150 °C to obtain dry sheets.

It is widely known that one of the important aspects of international trade is fraud detection, especially when products of agricultural industries (from raw materials to wines, pharmaceutical substances, etc.) are concerned. In fraud detection, identification of the geographical origin (GO) of a product is often crucial. Luckily, this task can often be more or less easily addressed by the acquisition of the respective trace element profiles which depend on GO due to variations in soil chemistry or fertilisers in use, and also due to differences in subspecies or cultivars of plants that are grown in different regions. Additionally, a cruder forgery such as the addition of foreign materials to a product (adulteration) should be detected. LIBS or vibrational spectroscopy techniques such as Raman spectroscopy or different variants of infrared spectroscopy (e.g., near-infrared, NIR, or mid-infrared, MIR) lend themselves for these purposes. The combination of the data provided by these techniques should give advantages regarding the completeness of sample characterisation, LIBS being responsible for the elemental composition, while vibrational techniques yielding information at the molecular level. This statement, however, should be taken cautiously just because atomic emission spectra usually comprise much more signals than vibrational spectra, the first being composed of single transitions, the second being composed of wide bands which often overlap with each other. Thus, atomic spectra can be no less informative than molecular ones.

The study by Eum et al. [137] is an example of the LIBS+NIR combination. They focused on samples of milk vetch roots, which are widely used in formulations of oriental herbal medicines, and attempted to distinguish Korean domestic products from imported ones. The SVM-based classification using only NIR information resulted in discrimination accuracy of 91.5% (vs. 73.1% for LIBS data). If the data are fused using support vector regression, the accuracy improves to 95.8%. It should be noted that the NIR-based classification is apparently driven by quite subtle differences in the 8400–7700 and 7000–6000 cm^{-1} domains. As for LIBS, 35 selected spectral intensities were utilised, including resonance lines of Na, Ca and K. Magnesium was the main driver of the classification. According to our experience, the results could have been better if the resonance lines were omitted, because they are prone to self-absorption and thus their intensity does not depend linearly on the content of respective elements. SIMCA, kNN, extreme learning machine (ELM), and RF were used by Liu et al. [138] to study the authenticity of kudzu powder (Chinese medicine).

Yang et al. [139] studied the influence of sample preparation method on the classification performance of SVM. The best results of the GO identification of rice were reported for the protocol with no sample pre-treatment (grains were just placed in beaker, and the surface was flattened with a blade). Full spectra were not used; 90 spectral lines were selected instead. In the subsequent work [140], they compared the performance of PCA, decision trees (DT), random forest (RF), PLS-DA, LDA, and SVM for the same task. The following order of classification accuracy has been obtained: SVM > LDA > RF > PLS-DA > DT. In terms of operation time, SVM was, however, the most demanding technique, with the following results: SVM > RF > PLS-DA > DT > LDA. As a result, the authors have proposed LDA (DFA) as the optimal algorithm for rapid, real-time, and in situ measurements.

In [141], the authors used wavelet transform for the noise-reducing pre-treatment of LIBS spectra of coffee powder in the form of pressed pellets. Four varieties of China-grown coffee were studied. Seventy-five percent of the obtained spectra which had the lowest RSD of the signal intensities measured at the C I 247.86 nm were selected for further consideration, while the rest was discarded. The employed chemometric methods included PCA, PLSR, radial basis function neural network (RBFNN), and SVM. PCA was used to select the 20 most important wavelengths. It has been shown that the use of full spectra gives only slightly better classification results than the selected data, a fact that justifies variable selection since it greatly reduces the computational load.

Sezer et al. [142] evaluated the potential of LIBS and chemometrics for the detection of coffee adulteration by roasted chickpea, corn, and wheat. There was a good cluster separation on the PCA score plot (Fig. 7.9a). Judging from the respective loadings (Fig. 7.9b), Ca and probably Na emission seem to be the clustering drivers. The other study by the same group [143] dealt with pistachio adulteration by green pea and spinach. Quantitative PLS-based analysis of artificial binary mixtures has also been carried out. In both studies, laser breakdown was created in the air near the sample surface, which was apparently done to reduce sample destruction. There are also indications [144] that Ca depth profiles in arabica and robusta coffee are different, Ca being surface-concentrated in grains of arabica; its bulk concentration also appears to be higher than in robusta.

Quality control is another major field with a huge demand in analytical instruments and analytical methodology. Silva et al. [145] considered the detection of the so-called BGS (black, green, and sour grain) defects in coffee by LIBS and NIRS, emphasising the role of molecular emission signals.

In 2019, Liu et al. [146] compared the performance of PLS-DA, SIMCA, and extreme learning machine (ELM), which is a kind of a neuron network, for the identification of genetically modified maize. The authors reported an excellent identification rate for all the models, especially for the ELM model based on PCA loadings, which yielded 100% accuracy in both calibration and prediction sets. Variable selection was also attempted, and the results were compared for the models based on selected spectra, on the one hand, and for the models based on full spectra, on the other hand. The latter models yielded somewhat higher identification accuracy, but this gain was not significant (especially bearing in mind the loss in computation speed). The authors claimed that CN emission intensity was the key variable for the identification. However, as the spectra were taken in air, this statement could require an additional consideration.

Porto et al. [147] used PLS-DA to discriminate between sugarcane genotypes (susceptible and resistant to sugarcane borer). Sharma et al. [148] investigated compositional changes in rice grains resulting from false smut infection. A simple comparison of spectral intensities was carried out, revealing that Ca, Mg, Si, Cu, and Fe signals were lower in infected samples. This was corroborated by wavelength-dispersive X-ray spectroscopy (WDXRF). A similar study was dedicated to papaya roots infected by nematodes [149], diseased ber fruits [150] and medicinal herbs [151]. The two latter studies involved PLS-DA on full-length LIBS spectra. Feng

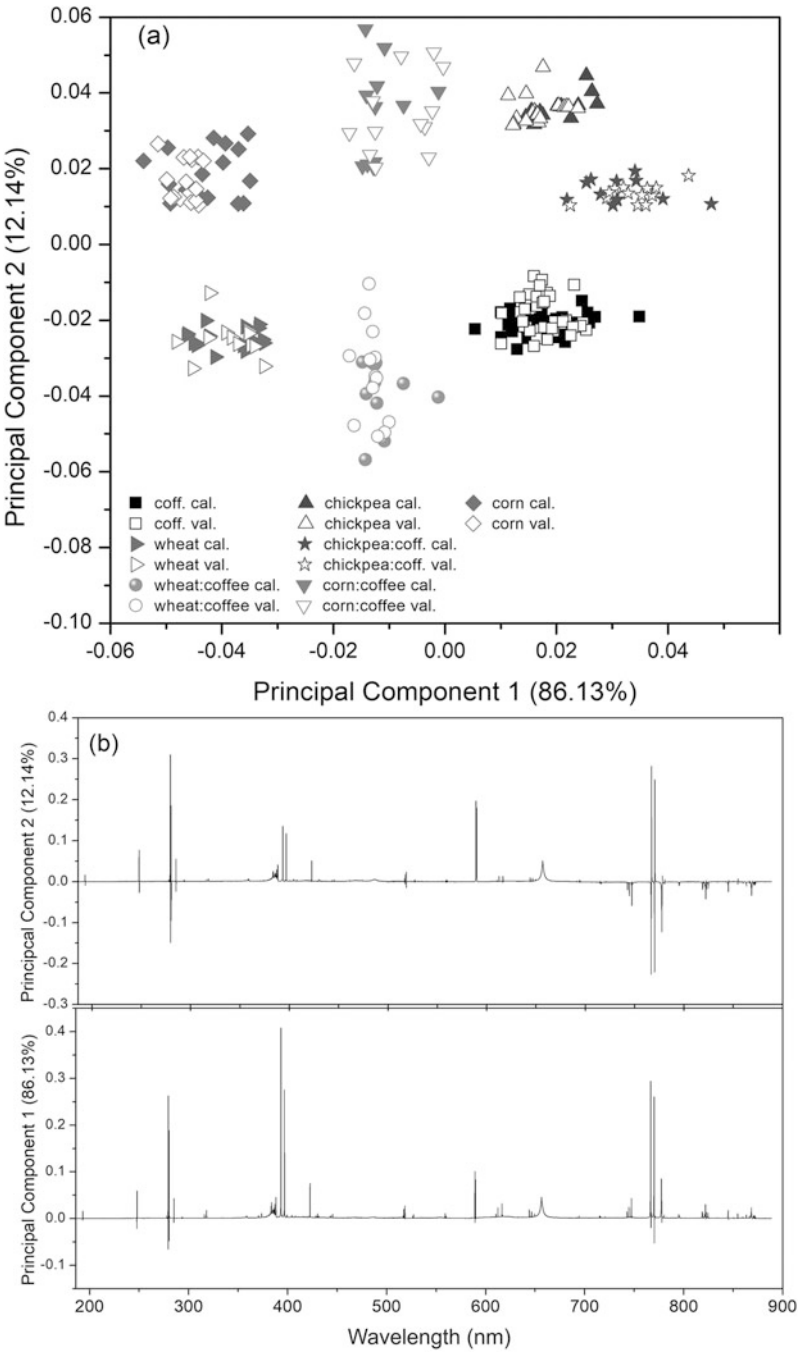

Fig. 7.9 Score plot (**a**) and loadings plot (**b**) of PCA analysis for *Coffee arabica*, chickpea, corn, and wheat samples. Copyright by Elsevier [142]

et al. [152] dealt with the classification of privet, sweet viburnum, and bamboo leaves. PCA-MD (Mahalanobis distance) and PLS-DA were used. The latter method has been reported to be more accurate on the test set, compared to PCA-MD. In a related work [153], they also used LDA (DFA) and SVM, with the latter slightly more efficient than LDA. The interest in the detection of diseases can be further illustrated by [154], where the so-called low-, mid-, and high-level fusion of data from different spectroscopic techniques was considered. This point is so far rarely discussed in the literature on the analysis of biological samples. PCA was used to highlight key features in hyperspectral images, MIR, and LIBS spectra. Autoencoder (AE) has also proved to be efficient in feature extraction and data compression. High-level fusion-based classifiers (SVM, logistic regression (LR), and NN) have been shown to give the best accuracy. As the number of samples was limited (30), NN could not exhibit all its strengths. A summary of analytical and data processing techniques employed for the quality control of natural medicines can be found in [155].

An ingenious sample preparation protocol, based on the conversion of liquid samples into solid polyvinyl alcohol (PVA) matrices, suitable for LIBS analyses, has been used for classifying sugarcane leachates in terms of impurity contents (0–5% or 8–10%) by means of PCA and the fusion of 17 classifiers such as PLS-DA or K-nearest neighbours (KNN) [156, 157]. Recently, Zhao et al. [158] studied the classification between eight varieties of ginseng (four kinds from two geographically close places; two samples were identical except the age). The analytical techniques were represented by hyperspectral imaging and LIBS, and the results were considered both separately and in the fused form. PCA scatter plots showed the best clustering in terms of sample age; the grouping according to GO was less persuasive; the species-based grouping yielded well-defined, but overlapping, clusters. It has been stated that the species discrimination was driven by aluminium signals, whereas GO and age were related to P and Ca, respectively. The identification of tea varieties and their GO using NNs is described in [159].

7.7 Animal and Human Tissues

The analysis of samples of animal and human origin is a vast and quickly developing field to which the world's leading LIBS research groups make their contributions. The main focus obviously lies on the discrimination between healthy and pathological tissues, primarily malignant tumours. Thus, the majority of the publications are related to cancer diagnostics (the first study in this direction dates back to 2004 [160]) and to some other medicine-motivated topics, including the studies of calculi and stones, nails, hair, teeth, bones, monitoring trace elements in tissues and biological fluids, imaging of biological specimens, archaeological and forensic issues, etc. Moreover, there is a recent comprehensive 2019 review of medical and veterinary applications of LIBS by Gaudiuso et al. [51], although a number of new studies have appeared since then, e.g., [161–172]. Therefore, in the following

considerations, we will just highlight selected studies that are not directly related to medicine.

Interestingly, one of the contributions related to the analysis of animal material is at the same time motivated by the above-mentioned Huanglongbing problem [173]. The disease is transmitted by two species of psyllids (sucklings) which host the putative phytopathogen *C*Las (see above). The goal of this study was to find biochemical differences between healthy and infected psyllids. The insects were analysed with the help of a LIBS setup which included a microscope; each 1064-nm, 40-mJ laser shot consisted of a train of three micro-pulses with a 10–25 μs between them. The data processing was similar to the approach adopted in [112]. The authors claimed to have been able to discern the insects using 13 selected spectral signals. Admittedly, the results could have been more persuasive if the quality of the obtained spectra (in terms of, e.g., spectral resolution, which was 0.3 nm) had been higher.

In an early 1998 work, Kim et al. [174] used a 790-nm femtosecond laser and showed that porcine bone and spinal cord can be discerned by using the ratio of emission intensities at 615 and 575 nm which is significantly higher in bone. Given the spectral resolution of their experimental setup, this roughly corresponded to the ratio of the intensity at Ca I 616.217 line to the continuum at 575 nm.

The important study by Yueh et al. [175] dealt with the discrimination of chicken organs (brain, lung, spleen, liver, kidney, and skeletal muscle). The samples were analysed in the frozen form, so the experimental setup was modified accordingly. The laser pulse energy was notably as low as 5 mJ ($\lambda = 532$ nm); though untypical for most studies described in the present chapter, the experimental conditions adopted by the authors ensured a good signal-to-noise ratio. Cluster analysis was carried out by DFA on PCA-compressed data, followed by hierarchical cluster analysis (HCA). PLS-DA and NN were also used. All this was performed on 21 selected analyte lines. The results were reasonably good for the calibration set, i.e., the authors could clearly distinguish the tissue types as visualised by hierarchical dendrograms, but the validation set presented many misidentified cases. Problems were reported concerning the performance of NN.

Li et al. [176] studied pork tissues, or, more precisely, different parts of body (fat, skin, ham, loin, and tenderloin muscle tissues). The samples were randomly obtained from six different animals (thus $5 \times 6 = 30$ samples). PCA, kNN, and SVM results were considered for classification. First, the discrimination was performed between consolidated classes of fat, skin, and muscle tissues with very good results (accuracy 99.8%, sensitivity over 0.995, specificity over 0.998). Then, highly similar ham, loin, and tenderloin were classified. The best results for these "refractory" samples were achieved with SVM (accuracy 76.8%, sensitivity over 0.742, specificity over 0.869). Three-dimensional PCA score plot shows that the three muscle types are almost indistinguishable, but the use of 6 PCs improves the situation. An unusual acquisition delay, as much as 3 μs, was chosen, which could have favoured the recording of the emission of neutral atoms. Another unusual decision is the spectra normalisation by the intensity of sodium resonance line, which is questionable since

this line is usually too much affected by unstable ionisation degree and self-absorption.

Kanawade et al. [177] examined fat, muscle, nerve, and skin taken from pig heads. They used an ArF excimer laser to excite plasma. LDA (DFA) was used for the classification; the leave-one-out approach was utilised for validation. The latter is known to produce artificially high values of classification accuracy, external validation sets being the preferred way for the accuracy assessment; but of course, additional validation samples are not always easy to procure. The quality of classification was assessed by Receiver Operating Characteristic (ROC). Although the obtained data clusters overlapped significantly on PCA score plots, a successful LDA differentiation has been reported. The temporal acquisition parameters are not reported, but the presented spectra reveal a hot and dense plasma. These studies were continued in subsequent works of the same group of researchers, in which line intensity ratios were also used for classification [178, 179].

Abdel-Salam et al. [180] showed the effect of hatching on the elemental composition of avian eggshells. The reported changes in the concentrations of Mg, Na, and Ca were explained by the consumption of these elements by the growing embryo. Further works by the same authors [181, 182] showed that the Mg II (280.26 nm)/Mg I (285.22 nm) and Ca II (373.69 nm)/Ca I (428.9 nm)[2] ratios in calcified tissues (tooth enamel, shell, and eggshell) presented strong positive linear correlation with the hardness. In principle, this could be used for the discrimination of such tissues when the number of materials likely to be encountered is limited (e.g., in dentistry [183, 184]. The approach has also been applied to link the age of a hen to the surface hardness of eggs it laid [185]. This series of works was continued by the study of buffalo bull semen. It has been shown that the content of Ca, Mg, and Fe in seminal plasma (ablated on an ashless filter paper) are season dependent, being higher in winter. These elements are directly related to sperm parameters [186].

The same authors later endeavoured the analysis of milk from different animals (buffalo, camel, goat, and sheep). They found that Ba/Ca and Sr/Ca ratios were different, tending to be higher in buffalos and lower in sheep [187]. Higher sodium content, which was also correlated with somatic cell count (SCC, a mastitis diagnostic marker), was found in the milk of mastitis-infected cows as opposed to healthy animals. Conversely, the calcium signals were lower. LIBS results were also supported by laser-induced fluorescence (LIF) studies [188]. A positive correlation of SCC, CN, and C_2 emission intensities was also reported [189]. In a similar way, it was found that these molecular bands in chicken meat become weaker during its storage [190].

The study by Bilge et al. [31] dealt with meat adulteration and thus involved the classification of pork, chicken, and beef. The samples were minced, dried, Soxhlet de-fatted, ground and pelletised. An extensive pre-processing of spectra involving Whittaker filtration was carried out. PCA score plots proved that the classification is

[2]This choice of Ca lines is good in view of avoiding self-absorption effects.

feasible (*see* Fig. 7.3, *right*). The studies were further extended to the detection of chicken and pork adulteration in beef sausages and salami products [191].

In 2021, Manno et al. studied the effect of cold and hot tea [192] and coffee [193] on the structure and elemental profile of teeth both in vitro and in vivo (in rats). For this purpose, elemental intensity ratios of P, Mg, Zn, Sr, and C to Ca were used. LIBS was also supported by XRF and scanning electron microscopy (SEM). An interesting use of LIBS and NNs was demonstrated in [194], where deer bones from different individuals were discriminated and reassembled. A similar approach was adopted by other researchers, but with archaeological human bones [195], and both human and animal bones from a Palaeolithic site [196].

A study conducted by Sushkov et al. [197–199] was devoted to zooplankton organisms (viz. several taxa of sea crustaceans) which were previously found to accumulate trace elements like lithium, arsenic and uranium [200]. The goal was to investigate correlations between the signal of Li and other elements, on the one hand, and molecules comprising the tissues, on the other hand, in an attempt to shed light on causes and mechanisms underlying the phenomenon. To this end, LIBS and Raman spectra were recorded and compared. Twenty-nine zooplankton samples, representing four animal taxa, were analysed. LIBS spectra of dried and pelletised samples were measured using a commercial instrument (J-200 Tandem LA-LIBS by Applied Spectra, USA; excitation laser: 266 nm Nd:YAG, 20 mJ).

PCA eigenvalues suggested five principal components (PCs) for the dataset. The first PC absolutely prevailed over the others in terms of explained variance (92%). The loadings were dominated by resonance lines (Na I, K I, Ca II) and other intense transitions prone to self-absorption. The authors deemed reasonable to cut out (or "mask") these ranges. After masking, the decomposition yielded six PCs, with the first PC accounting for 71% of variance. Thus, more informative components were obtained, which resulted in an improved clustering in score graphs (Fig. 7.10a, b). Besides visual inspection, the discriminative performance of the models was

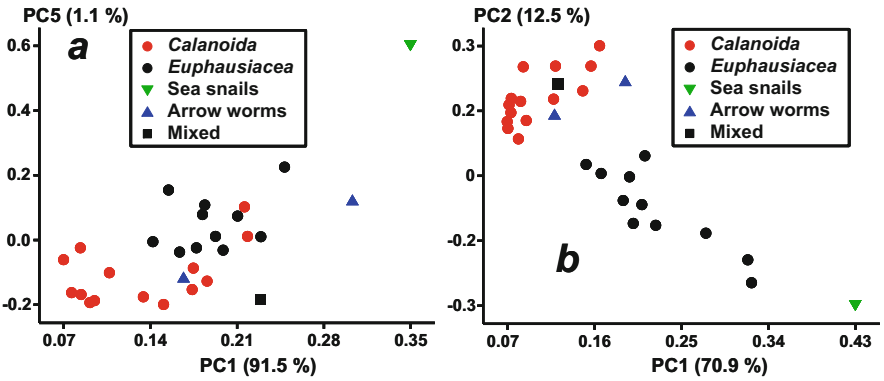

Fig. 7.10 Score plots of PCA decompositions: LIBS spectra before (**a**) and after (**b**) masking of strongest signals [197, 198]

assessed using the silhouette metric (see Sect. 7.3) and was found to improve from 0.34 to 0.62. Arrow worms could not be separated from *Calanoida*, because their main feature is the presence of certain amino acids that could not be detected by LIBS. The only sample of sea snails was always far from the rest of the animals due to its high Ca content. The "best plane" also shifted back from 5–1 to 2–1 due to avoiding excessive influence of resonance lines on the explained variance.

7.8 Conclusion

In this chapter, we attempted to deliver a representative review of the development of LIBS-based qualitative classification and discrimination of biological samples during the last two decades. The first studies, published in 2003, were motivated by biological warfare concerns, but later, the interest of researchers shifted to the field of biochemistry and medicine. Several years after that, the world saw the rapidly emerging number of LIBS applications to cancer research and treatment. Plant discrimination also turned out to be important in view of the needs of industry and trade (adulteration and mislabelling issues, identification of plant diseases). Obvious progress in all these fields has been achieved, which would be impossible without the introduction and popularisation of chemometric algorithms (mainly PCA, PLS, and DFA) as everyday tools of analytical chemists. Now there is no question whether biological samples can at all be discriminated by LIBS, and differences as subtle as inter-strain variations of chemical composition of bacteria have proved to be detectable. Despite that, it should be mentioned that in many cases, the published studies are too much application-oriented, so that LIBS itself is regarded just as an easy-to-use instrumental technique without paying much attention to spectroscopic issues, from the optimisation of experimental parameters (pulse energy, laser wavelength, temporal acquisition parameters, number of surface cleaning pulses) to the identification of spectral lines. We believe this to be a problem that slows down the accumulation of sound and reliable scientific results and gives rise to unrealistic claims. In these studies, an excessive attention is sometimes paid to chemometrics, presumably in a hope that it would compensate for hardware-related drawbacks. Maybe this can be understood (but not tolerated) when a new discipline rapidly develops and brings about inflated expectations because its limitations are not yet clear for everyone. However, LIBS (possibly in combination with other related experimental techniques such as Raman spectroscopy or laser-induced fluorescence), supported by proper chemometric data treatment, has a good potential to get regulatory approval in different parts of economy and become a part of our everyday life.

Acknowledgements This work was funded by the Russian Foundation for Basic Research and the Belarusian Republican Foundation for Fundamental Research, projects Nos. 20–53-04036 and Б21РМ-085, respectively. The author is grateful to colleagues from the Moscow State University—Assoc. Prof. Timur A. Labutin, Dr. Sergey M. Zaytsev, and Ivan N. Krylov—for their valuable advice.

References

1. Singh J, Thakur S, editors. Laser-induced breakdown spectroscopy. 2nd ed. Elsevier; 2020.
2. Popov AM, et al. Spectrochim Acta B. 2018;148:205.
3. Wisbrun R, et al. Anal Chem. 1994;66:2964.
4. von Allmen M. Laser-beam interactions with materials. Berlin: Springer; 1987.
5. Arakawa ET, et al. Biopolymers. 2001;62:122.
6. Pauling L, Die Natur der chemischen Bindung (Verlag Chemie, Weinheim 1968)
7. Tognoni E, et al. Spectrochim Acta B. 2002;57:1115.
8. Jolivet L, et al. Spectrochim Acta B. 2019;151:41.
9. Samek O, et al. Laser Phys Lett. 2006;3:21.
10. Labutin TA, et al. J Anal At Spectrom. 2016;31:90.
11. Assion A, et al. Appl Phys B Lasers Opt. 2003;77:391.
12. Baudelet M, et al. J Appl Phys. 2006;99:84701.
13. Rehse SJ. Spectrochim Acta B. 2019;154:50.
14. Galbács G. Anal Bioanal Chem. 2015;407:7537.
15. Morel S, et al. Appl Optics. 2003;42:6184.
16. Leone N, et al. High Technol Plasma Process. 2004;8:1.
17. Baudelet M, et al. Appl Phys Lett. 2006;89:163903.
18. Gamble GR, et al. Appl Spectrosc. 2016;70:494.
19. Injuk J, et al. In: Beckhoff B, et al., editors. Handbook of practical X-ray fluorescence analysis. Berlin: Springer; 2006. p. 411.
20. Huber KP, Herzberg G. Molecular spectra and molecular structure, vol. 4. Ottawa: Van Nostrand Reinhold Company; 1979.
21. Guyon L, et al. In: Corkum P, et al., editors. Proceedings of the 15th international conference on ultrafast phenomena. Pacific Grove, CA: Optical Society of America; 2006. p. MH10.
22. Baudelet M, et al. Appl Phys Lett. 2006;88:63901.
23. Baudelet M, et al. Spectrochim Acta B. 2007;62:1329.
24. Farooq WA, et al. Plasma Sci Technol. 2014;16:1141.
25. Képeš E, et al. J Anal At Spectrom. 2018;33:2107.
26. Yaroshchyk P, Eberhardt JE. Spectrochim Acta B. 2014;99:138.
27. Grubbs FE, Beck G. Technometrics. 1972;14:847.
28. Wold S, Esbensen K, Geladi P. Chemom Intel Lab Syst. 1987;2:37.
29. Pearson K. London Edinburgh Dublin Philos Mag J Sci. 1901;2:559.
30. Pořízka P, Klus J, Képeš E, Prochazka D, Hahn DW, Kaiser J. On the utilization of principal component analysis in laser-induced breakdown spectroscopy data analysis a review. Spectrochim Acta B At Spectrosc. 2018;148:65.
31. Bilge G, et al. Meat Sci. 2016;119:118.
32. Kaufman L, Rousseeuw PJ. Finding groups in data: an introduction to cluster analysis. Wiley-Interscience; 2008.
33. Vandeginste BGM, et al., editors. Handbook of chemometrics and qualimetrics: part B. Elsevier; 1998. p. 307.
34. Putnam RA, et al. Spectrochim Acta B. 2013;87:161.
35. Malenfant DJ. Master thesis. University of Windsor; 2016.
36. Rehse SJ, Diedrich J, Palchaudhuri S. Spectrochim Acta B. 2007;62:1169.
37. Vandeginste BGM, et al., editors. Handbook of chemometrics and qualimetrics: part B. Elsevier; 1998. p. 207.
38. Malenfant DJ, Gillies DJ, Rehse SJ. Appl Spectrosc. 2016;70:485.
39. Cisewski J, et al. J Chemometr. 2012;26:143.
40. Burges CJC. Data Min Knowl Discov. 1998;2:121.
41. Metzinger A, Rajkó R, Galbács G. Spectrochim Acta B. 2014;94-95:48.
42. Breiman L, et al. Classification and regression trees. Boca Raton: Chapman & Hall/CRC; 1998.

43. Breiman L. Mach Learn. 2001;45:5.
44. Monakhova YB, Rutledge DN. Talanta. 2020;208:120451.
45. Choi S, et al. Neural Inf Process Lett Rev. 2005;6:1.
46. Lee DD, Seung HS. Nature. 1999;401:788.
47. Mishra P, et al. TrAC. 2021;137:116206.
48. Westerhuis JA, Kourti T, MacGregor JF. J Chemometr. 1998;12:301.
49. Gottfried JL. Anal Bioanal Chem. 2011;400:3289.
50. Samuels AC, et al. Appl Optics. 2003;42:6205.
51. Gaudiuso R, et al. Spectrochim Acta B. 2019;152:123.
52. Hybl JD, Lithgow GA, Buckley SG. Appl Spectrosc. 2003;57:1207.
53. Dixon PB, Hahn DW. Anal Chem. 2005;77:631.
54. Boyain-Goitia AR, et al. Appl Optics. 2003;42:6119.
55. Beddows DCS, Telle HH. Spectrochim Acta B. 2005;60:1040.
56. Kiel JL, et al. Proceedings of SPIE volume 5795, chemical and biological sensing VI; 2005. p. 39.
57. Munson CA, et al. Spectrochim Acta B. 2005;60:1217.
58. Gottfried JL, et al. Spectrochim Acta B. 2007;62:1405.
59. Kim T, et al. J Phys Chem B. 2004;108:5477.
60. Gottfried JL, et al. Appl Spectrosc. 2008;62:353.
61. Diedrich J, Rehse SJ, Palchaudhuri S. Appl Phys Lett. 2007;90:163901.
62. Diedrich J, Rehse SJ, Palchaudhuri S. J Appl Phys. 2007;102:14702.
63. Rehse SJ, et al. J Appl Phys. 2009;105:102034.
64. Rehse SJ, Mohaidat QI. Spectrochim Acta B. 2009;64:1020.
65. Rehse SJ, Mohaidat QI, Palchaudhuri S. Appl Optics. 2010;49:C27.
66. Mohaidat Q, Palchaudhuri S, Rehse SJ. Appl Spectrosc. 2011;65:386.
67. Mohaidat QI, et al. Appl Optics. 2012;51:B99.
68. Multari RA, et al. Appl Spectrosc. 2010;64:750.
69. Multari RA, et al. J Pathog. 2013;2013:898106.
70. Multari RA, et al. J Agric Food Chem. 2013;61:8687.
71. Sivakumar V, et al. Proceedings of SPIE volume 11362, clinical biophotonics; 2020. p. 113620A.
72. Lewis DE, et al. Anal Bioanal Chem. 2011;401:2225.
73. Barnett C, et al. Anal Bioanal Chem. 2011;400:3323.
74. Snyder EG, et al. Appl Optics. 2008;47:G80.
75. Saari S, et al. Aerosol Sci Tech. 2016;50:126.
76. Marcos-Martinez D, et al. Talanta. 2011;84:730.
77. Manzoor S, et al. Talanta. 2014;121:65.
78. Rendón Sauz FG, Flores-Reyes T, Ponce-Flores A. Rev Cubana Fis. 2018;35:10.
79. Manzoor S, et al. Talanta. 2016;155:101.
80. Sivakumar P, et al. Astrobiology. 2015;15:144.
81. Farid MU, et al. Nanoscale. 2018;10:4475.
82. Prochazka D, et al. Spectrochim Acta B. 2018;139:6.
83. Teng G, et al. J Raman Spectrosc. 2021;52:805.
84. Multari RA, Cremers DA, Bostian ML. Appl Optics. 2012;51:B57.
85. Multari RA, et al. J Appl Microbiol. 2019;126:1606.
86. Yao M, et al. In: Yu W, editor. Proceedings of the 3rd international conference on biomedical engineering and informatics (BMEI 2010), p. 302.
87. Popov AM, et al. Spectrochim Acta B. 2016;125:43.
88. Popov AM, et al. Mon Not R Astron Soc. 2019;488:5594.
89. Monteiro JM, et al. Nat Commun. 2015;6:8055.
90. Cremers DA, Radziemski LJ. Handbook on laser-induced breakdown spectroscopy. Wiley; 2013.
91. Multari RA, et al. J Appl Microbiol. 2022;132:2431.

92. Santos D, et al. Spectrochim Acta B. 2012;71–72:3.
93. Markiewicz-Keszycka M, et al. Curr Opin Food Sci. 2019;28:96.
94. Gomes M d S, et al. Talanta. 2011;85:1744.
95. Moskal TM, Hahn DW. Appl Spectrosc. 2002;56:1337.
96. Gething BA, Janowiak JJ, Falk RH. For Prod J. 2009;67
97. Solo-Gabriele HM, et al. Waste Manag. 2004;24:413.
98. Uhl A, Loebe K, Kreuchwig L. Spectrochim Acta B. 2001;56:795.
99. Martin MZ, et al. Spectrochim Acta B. 2005;60:1179.
100. Martin MZ, et al. Spectrochim Acta B. 2007;62:1426.
101. Xu HL, et al. Appl Phys B Lasers Opt. 2007;87:151.
102. Chin SL, et al. Appl Phys B Lasers Opt. 2009;95:1.
103. Bossu M, et al. Chin Phys Lett. 2007;24:3466.
104. Rai PK, et al. Instrum Sci Technol. 2007;35:507.
105. Shukla S, et al. Food Biophys. 2012;7:43.
106. Zhang D, et al. Acta Phys Sin. 2008;57:6348.
107. Bol'shakov AA, et al. Appl Optics. 2010;49:C132.
108. Pereira FMV, et al. Talanta. 2010;83:351.
109. Sankaran S, Ehsani R, Morganc KT. Appl Spectrosc. 2015;69:913.
110. Ranulfi AC, et al. Appl Spectrosc. 2017;71:1471.
111. Rao G, et al. Appl Optics. 2018;57:8738.
112. Ponce L, et al. Appl Optics. 2018;57:8841.
113. A.B. Magalhães et al., Molecules 26, (2021)
114. Peng J, et al. Sci Rep. 2017;7:44551.
115. Ranulfi AC, et al. Microchem J. 2018;141:118.
116. Larios GS, et al. Food Anal Methods. 2020;13:1691.
117. Martin MZ, et al. Appl Optics. 2010;49:C161.
118. Hassan M, et al. Spectrochim Acta B. 2008;63:1225.
119. Martelli MR, et al. J Agric Food Chem. 2010;58:7126.
120. Martelli MR, et al. Food Biophys. 2011;6:433.
121. Schenk ER, Almirall JR. Appl Optics. 2010;49:C153.
122. Beldjilali S, et al. Spectrochim Acta B. 2010;65:727.
123. Ferreira EJ, et al. Electron Lett. 2011;47:967.
124. Kim G, et al. J Agric Food Chem. 2012;60:718.
125. Tripathi DK, et al. Agric Res. 2012;1:352.
126. Zhang P, et al. Optik. 2020;218:164979.
127. Tiwari M, et al. Spectrosc Lett. 2013;46:155.
128. Varliklioz Er S, et al. Food Anal Methods. 2017;10:1547.
129. Ercioglu E, Velioglu HM, Boyaci IH. Food Anal Methods. 2018;11:1656.
130. Kunz JN, et al. Opt Express. 2017;25:7251.
131. Bhatt CR, et al. Appl Spectrosc. 2017;71:686.
132. Singh J, et al. Food Chem. 2017;221:1778.
133. Ma F, Dong D. Food Anal Methods. 2014;7:1858.
134. Du X, et al. RSC Adv. 2015;5:79956.
135. Bilge G, et al. Eur Food Res Technol. 2016;242:1685.
136. Akın PA, et al. J Sci Food Agric. 2021;101:1076.
137. Eum C, et al. Spectrochim Acta B. 2018;149:281.
138. Liu F, et al. Sensors. 2019;19:1453.
139. Yang P, et al. J Cereal Sci. 2018;80:111.
140. Yang P, et al. Appl Optics. 2018;57:8297.
141. Zhang C, et al. Sensors. 2018;18:95.
142. Sezer B, et al. Food Chem. 2018;264:142.
143. Sezer B, et al. J Sci Food Agric. 2019;99:2236.

144. Anggraeni K, Nasution A, Suyanto H. In: Hatta AM, Nasution AMT, editors. Proceedings of SPIE 10150, second international seminar on photonics, optics, and its applications (ISPhOA 2016); 2016. p. 1015019.
145. Silva TV, et al. Spectrochim Acta B. 2017;135:29.
146. Liu X, et al. Food Bioproc Tech. 2019;12:347.
147. Porto NA, et al. Spectrochim Acta A. 2019;218:69.
148. Sharma N, et al. Appl Phys B Lasers Opt. 2020;126:122.
149. Sharma N, et al. At Spectrosc. 2020;41:110.
150. Sharma N, et al. Arab J Sci Eng. 2021.
151. Sharma N, et al. At Spectrosc. 2020;41:234.
152. Feng Z, et al. Plasma Sci Technol. 2020;22:74012.
153. Ding J, et al. Spectrosc Spectr Anal. 2021;41:606.
154. Feng L, et al. Front Plant Sci. 2020;11:1664.
155. Wei X-C, et al. Chinas Med. 2020;15:56.
156. Andrade DF, Guedes WN, Pereira FMV. Microchem J. 2018;137:443.
157. Guedes WN, Pereira FMV. Microchem J. 2018;143:331.
158. Zhao S, et al. J Anal At Spectrom. 2021;36:1704.
159. Liu Z, et al. In: Yu J, et al., editors. Proceeding of SPIE 11337, applied optics and photonics China (AOPC2019); 2019. p. 11370K.
160. Kumar A, et al. Appl Optics. 2004;43:5399.
161. Teng G, et al. Spectrochim Acta B. 2020;165:105787.
162. Chu Y, et al. Biomed Opt Express. 2020;11:4191.
163. Idrees BS, et al. Biomed Opt Express. 2022;13:26.
164. Ahmed I, et al. J Pharm Biomed Anal. 2021;194:113805.
165. Gaudiuso R, et al. Appl Spectrosc. 2021;76:887.
166. Abbasi H, et al. Opt Lasers Eng. 2022;148:106765.
167. Yue Z, et al. Biomed Opt Express. 2021;12:2559.
168. Teng G, et al. Biomed Opt Express. 2020;11:4276.
169. Lin X, et al. Spectrochim Acta B. 2021;180:106200.
170. Gaudiuso R, et al. Spectrochim Acta B. 2020;171:105931.
171. Teng G, et al. Biomed Opt Express. 2021;12:4438.
172. Srivastava E, et al. Plasma Sci Technol. 2019;22:15501.
173. Killiny N, et al. Sci Rep. 2019;9:2449.
174. Kim B-M, et al. Appl Surf Sci. 1998;127–129:857.
175. Yueh F-Y, et al. Spectrochim Acta B. 2009;64:1059.
176. Li X, et al. Opt Laser Technol. 2018;102:233.
177. Kanawade R, et al. Spectrochim Acta B. 2013;87:175.
178. Kanawade R, et al. J Biophotonics. 2015;8:153.
179. Rohde M, et al. J Biophotonics. 2017;10:1250.
180. Abdel-Salam ZA, Abdou AM, Harith MA. Int J Poult Sci. 2006;5:35.
181. Abdel-Salam ZA, et al. Spectrochim Acta B. 2007;62:1343.
182. Abdel-Salam ZA, et al. Appl Phys B Lasers Opt. 2009;94:141.
183. Telle HH, Samek O. In: Miziolek AW, Schechter I, Palleschi V, editors. Laser induced breakdown spectroscopy. Cambridge: Cambridge University Press; 2006. p. 282.
184. Niemz MH. Laser-tissue interactions. 4th ed. Springer; 2019. p. 153.
185. Salam ZA, Harith MA. AIP Conf Proc. 2011;1380:107.
186. Abdel-Salam Z, Harith MA. Talanta. 2012;99:140.
187. Aabdel-Salam Z, El-Sayed A. Indian J Anim Sci. 2014;84:1117.
188. Abdel-Salam Z, et al. Dairy Sci Technol. 2015;95:331.
189. Abdel-Salam Z, Abdelghany S, Harith MA. Food Anal Methods. 2017;10:2422.
190. Abdel-Salam Z, Abdel-Salam SAM, Harith MA. Food Anal Methods. 2017;10:2365.
191. Sezer B, et al. Food Chem. 2022;372:131245.
192. Manno SHC, et al. PLoS One. 2021;15:e0244542.

193. Manno SHC, et al. Talanta. 2018;189:550.
194. Marín Roldán A, et al. Optik. 2020;218:164992.
195. Siozos P, et al. J Archaeol Sci Rep. 2021;35:102769.
196. Cáceres JO, Sainz de los Terreros JY. Talanta. 2021;235:122780.
197. Sushkov N, et al. In: Galbács G, Kéri A, editors. International workshop on laser-induced breakdown spectroscopy, Book of abstracts. Szeged; 2020. p. 129.
198. Sushkov NI, et al. The 13th winter symposium on chemometrics. Abstract book, Moscow; 2022. p. 40.
199. Sushkov NI, Galbács G, Fintor K, Lobus NV, Labutin TA. A novel approach for discovering correlations between elemental and molecular composition using laser-based spectroscopic techniques. Analyst. 2022;147:3248.
200. Lobus NV. Oceanology. 2016;56:809.

8 Nanoparticle-Enhanced Laser Induced Breakdown Spectroscopy (NELIBS) on Biological Samples

Alessandro De Giacomo and Marcella Dell'Aglio

8.1 Introduction

The use of plasmonic systems based on metallic nanoparticles (NPs) has been largely used for analytical spectroscopy in the last decades, because it allows extremely high sensitivity and very low limits of detection (LOD). In the case of Laser-Induced Breakdown Spectroscopy (LIBS), the use of NPs deposited on a solid sample surface enables the interaction of the plasmonic system of metallic NPs with the ablated matter during ns-laser pulse irradiation (nanoparticle enhanced laser-induced breakdown spectroscopy, NELIBS) [1] inducing better atomization and excitation of the sample.

The fundamental mechanisms allowing the LIBS signal enhancement are reported in previous papers [1, 2]. Briefly, when metallic NPs are deposited on the sample surface, laser irradiation is more effective as a consequence of the coupling of the electromagnetic field of the laser with the one produced by the plasmonic system. In [1] it has been observed that although the laser irradiance is beyond the breakdown threshold of the sample to form the plasma, the NPs do not vaporize during the laser pulse and allow the electromagnetic field enhancement effect along with the all pulse duration and, in turn, the effective interaction of the plasmonic system with the high density ablated matter in the first stage of expansion. A sketch of the NELIBS working principle is reported in Fig. 8.1.

The observed main characteristics are the following:

A. De Giacomo (✉)
Department of Chemistry, University of Bari, Bari, Italy

Institute of Nanotechnology, CNR-NANOTEC, Bari, Italy
e-mail: alessandro.degiacomo@uniba.it

M. Dell'Aglio
Institute of Nanotechnology, CNR-NANOTEC, Bari, Italy

G. Galbács (ed.), *Laser-Induced Breakdown Spectroscopy in Biological, Forensic and Materials Sciences*, https://doi.org/10.1007/978-3-031-14502-5_8

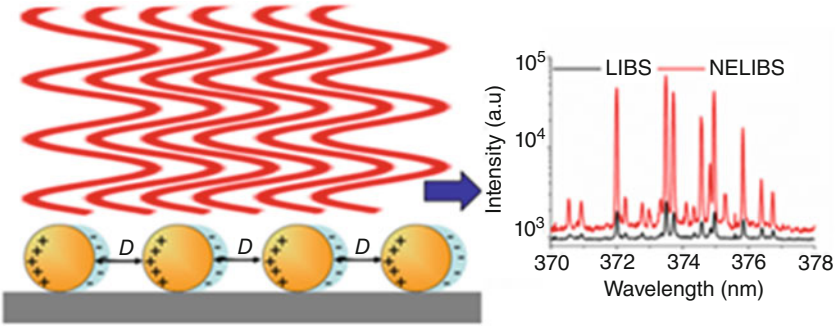

Fig. 8.1 A sketch of the NELIBS working principle

(a) Same amount of removed matter per laser shot as in traditional ablation
(b) Higher atomization yield of the ablated matter
(c) Better laser pulse energy distribution on the sample
(d) Multiple ignition points for plasma induction
(e) Enhancement of the plasma emission signal up to two orders of magnitude
(f) Decrease of the limits of detection

The enhancement of the emission spectra with NELIBS, defined as the ratio between emission line intensity of NELIBS and LIBS (in a single pulse arrangement), is strongly related to the efficiency of the plasmonic coupling between the NPs. This means that 2D deposition with a suitable inter-particle distance is required. According to the plasmon theory, the distance between spherical NPs should be less or comparable to the NP diameter. In the case of NELIBS where high energy pulse is employed, the inter-particle distance should be modulated in order to have the best compromise between the enhancement of the electromagnetic field and the conservation of the NPs system during laser irradiation. The latter means, as an example, that if too high laser irradiance is employed NPs undergo optical breakdown decreasing the enhancement effect on the plasma emission.

Generally, the deposition of NPs is accomplished by depositing and then drying a drop of colloidal solution directly on the sample surface. The concentration of the colloidal solution needs to be optimized in order to achieve a 2D layer of NPs with suitable inter-particle distance [3] as shown in Fig. 8.2.

The deposition of the NP system on the sample surface is the most difficult operation of NP-enhanced laser ablation because during the drying of the droplet, aggregation and stacking of NPs should be avoided in order to maximize the NELIBS effect [2]. Figure 8.2 shows the effect of NPs surface concentration on NELIBS enhancement factor. At very low concentration, the moderate enhancement is probably due to NPs acting like thermally- insulated defects. Once a certain concentration is exceeded, plasmon coupling with the laser field occurs, and the enhancement increases exponentially up to another critical concentration value.

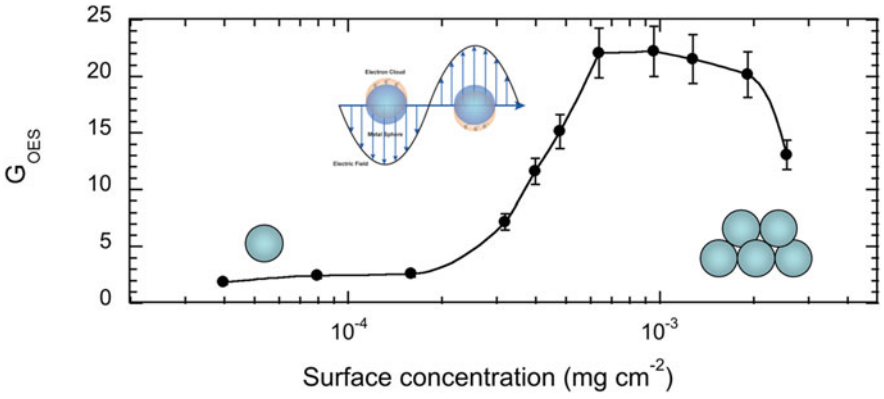

Fig. 8.2 Effect of NP surface concentration on the NELIBS enhancement factor G_{OES}

Beyond this concentration, the enhancement decreases as a consequence of NP aggregation and sample shielding.

NELIBS has been applied in several applications [2, 4, 5] and one of the most interesting uses of such a technique is the elemental analysis of biological samples. As a matter of fact, traditional LIBS does not have a high sensitivity when applied on biological samples because of the high ionization energy of matrix elements (C, N, H) that tends to quench the plasma and therefore spectrum accumulation is needed to reach a suitable signal-to-noise ratio (S/N). Since the latter requires amounts of samples that are not always available in real applications it can hamper the employment of LIBS technique. NELIBS can bypass these inconveniences just employing a single laser shot for the analysis, due to the advantages mentioned above.

In the following sections, a set of examples will clarify the promising advantages of NELIBS with respect to conventional LIBS in the case of biological samples.

8.2 Experimental

The experimental set-up of NELIBS technique is similar to the one of classical LIBS and it consists of a laser source, a spectrograph coupled with an intensified detector and optics for focusing the laser beam and for collecting the emission signal as sketched in Fig. 8.3 and already described in detail in [3–5].

Although the instrumentation of NELIBS is the same as LIBS, the operative protocol should take into account several issues. The laser spot should be as large as possible in order to involve a relevant number of NPs. This means that micro-LIBS is not immediately applicable for obtaining enhancement when NPs are employed. A spot size larger than 200 μm is strongly recommended. For example, in the specific case of NELIBS of liquid samples, for which a drop of solution is deposited on a dried NPs layer and only one laser shot is fired, to obtain the higher removal of the sample as possible, the dimension of laser spot should be comparable to the entire

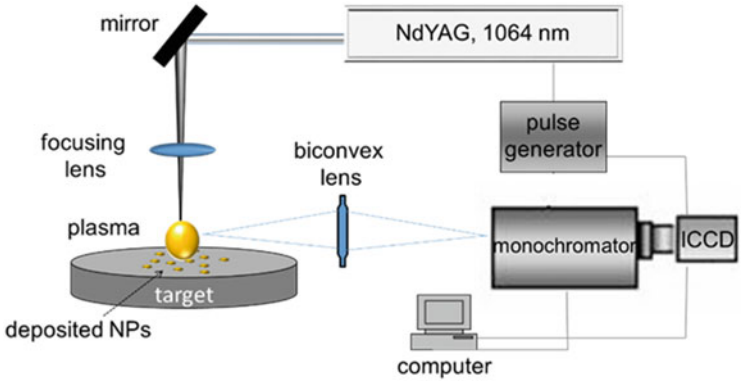

Fig. 8.3 Typical experimental setup for NELIBS

dry sample area in order to vaporize the whole deposited sample. The laser irradiance should be selected so that the breakdown of the NPs can be avoided.

For what concerns the detection, it is important to remember [2] that the laser-induced plasma, when NPs have been deposited on the sample surface, has different dynamics as well as a greater size with respect to the plasma obtained with conventional LIBS as reported in Fig. 8.4.

As a consequence of these differences in the spatial distribution of emitters in the NELIBS and LIBS plasma, the detection optics should be optimized accordingly. For this reason, the use of a large optical field of view for collecting plasma emission allows exploiting the NELIBS advantages better than the use of a small aperture optical fiber.

Beyond these instrumental suggestions the deposition of the colloidal solution drop and the chemical quality of the NPs, as mentioned above, is of great importance for having a reproducible experiment.

NPs must be as pure as possible and this is why NPs produced with Pulsed Laser Ablation in Liquid (PLAL) [7] are strongly recommended. Moreover, the eventual use of capping molecules for stabilizing the NPs or spacers should be evaluated carefully in order to avoid interference with the sample or false detection of trace elements contained as an impurity in the NPs or on the chemicals used in the colloidal solution. The typical NELIBS sample preparation is shown in Fig. 8.5: a set of laser pre-shots is suggested if the substrate/sample is a metal [2, 5]. Then the deposition and drying of the colloidal solution can be performed. Finally, a laser shot can be fired if the sample is the substrate itself or, before firing the laser shot, a liquid sample can be deposited with drop casting on the dried NP layer as will be discussed in the next section.

To improve the quality of colloidal deposition and to obtain an optimal deposition of the plasmonic system on the sample surface, some authors suggested the use of modified SERS (surface-enhanced Raman scattering) substrates for NELIBS on liquid samples [8] or the employment of nanostructured substrate if the substrate itself is the sample to be analyzed with NELIBS [9].

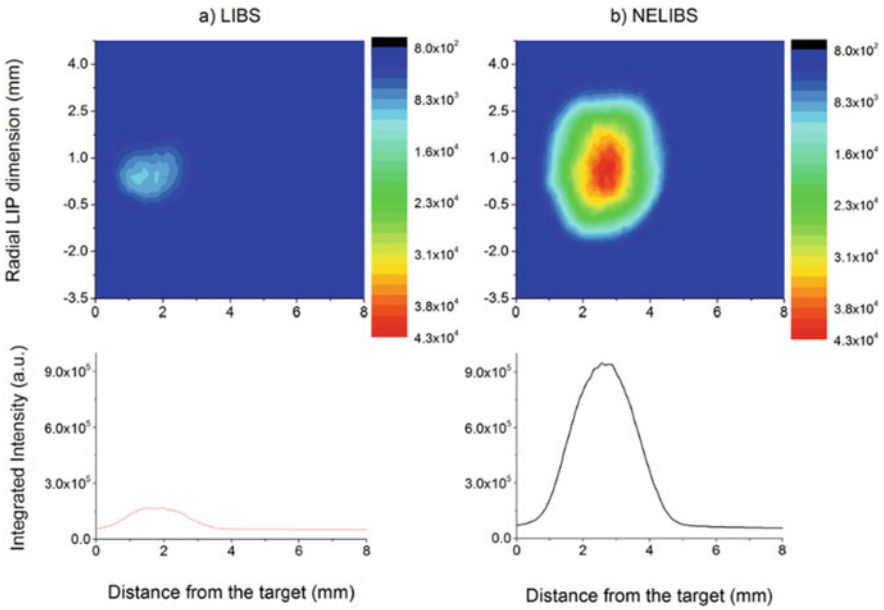

Fig. 8.4 Comparison of laser-induced plasma images and integrated intensities of a sample solution of $PbCl_2$ dried on a glass substrate during (**a**) NELIBS and (**b**) LIBS. (1 μL of $[PbCl_2]$ = 1 ppm; delay time from the laser pulse = 1.3 μs; gate width = 500 ns; laser fluence = 16.3 J cm^{-2}; in the case of NELIBS, 1 μL of AuNPs solution (particle diameter: of 20 nm) 0.04 mg mL^{-1} dried on glass was used). Reprinted with permission from [6]. Copyright 2016 American Chemical Society

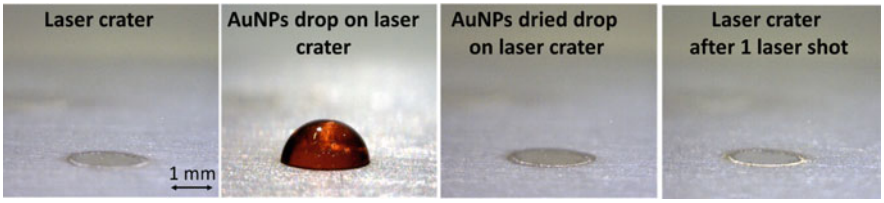

Fig. 8.5 Typical sequence of step during NELIBS sample preparation: laser pre-shots, deposition of 2 μL of colloidal solution, letting the solvent to evaporate, firing of the laser shot

In any case, the plasmonic system in terms of the number of plasmonic elements must be selected with a preliminary experiment for understanding the best experimental surface concentration for having the best inter-particle distance between NPs and therefore the maximum NELIBS enhancement.

8.3 NELIBS on Biological Fluids

Liquid samples are generally analyzed by LIBS followed by converting the liquid matrix into a solid one via several possible approaches [10]. The most common and easiest way is to dry the liquid sample on a suitable substrate. In the case of NELIBS approach, the NPs system is deposited on a substrate (glass or Teflon) with drop casting of a colloidal solution. After that the colloidal drop is suitably dried, the surface of the substrate is covered with a layer of NPs. At this stage, a few microliters of the liquid sample is deposited and dried on the NP bed to make it ready for the LIBS measurement as shown in Fig. 8.6.

A laser spot of diameter comparable to the dried sample spot is recommended in order to turn all samples in the plasma phase. Figure 8.6 shows how all the dried solution was completely ablated after one laser shot. By acquiring the plasma emission and further analyzing the emission spectra, a sub-ppm metal detection and quantification can be obtained with NELIBS on the microdrop. As a general example, Fig. 8.7 shows the calibration curve built with water solutions of $AgNO_3$ and performed with NELIBS by employing ultrapure AuNPs. It is important to underline that at the concentrations reported in Fig. 8.7 the silver signals were not detected with LIBS since those values were far below the LOD.

The importance of transferring this technique to a biological fluid sample is evident. In refs [6, 11], the residual metals on the reaction center of the protein from a bacterium after several cycles of dialysis has been investigated by NELIBS. Because of its multispectral capability, NELIBS allows the simultaneous detection of metals in a few microliters of sample solution [6]. In these experiments, while the dialysis had removed the most of metal under examination, lithium was still detectable and quantifiable also after several cycles of dialysis. Figure 8.8 shows the frame of spectrum corresponding to the Li I line at 670.8 nm obtained with LIBS and NELIBS.

Another important example is the detection of heavy metals in human serum, used to simulate the detection of heavy metals in human blood. In the experiment reported in Fig. 8.9, just 2 μL of human serum (treated with a known concentration of lead) was deposited on the NPs coated substrate. In a so little amount of sample, basically equivalent to a mosquito bite, NELIBS has been able to quantify tens of

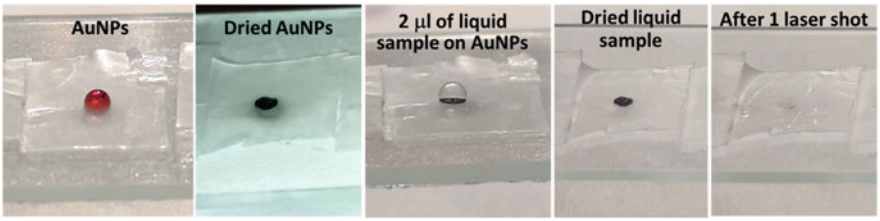

Fig. 8.6 NELIBS for microdrop analysis: images of sample preparation steps before and after the NELIBS measurement (the drop was deposited on parafilm located on glass to avoid glass element interferences in the plasma emission spectra)

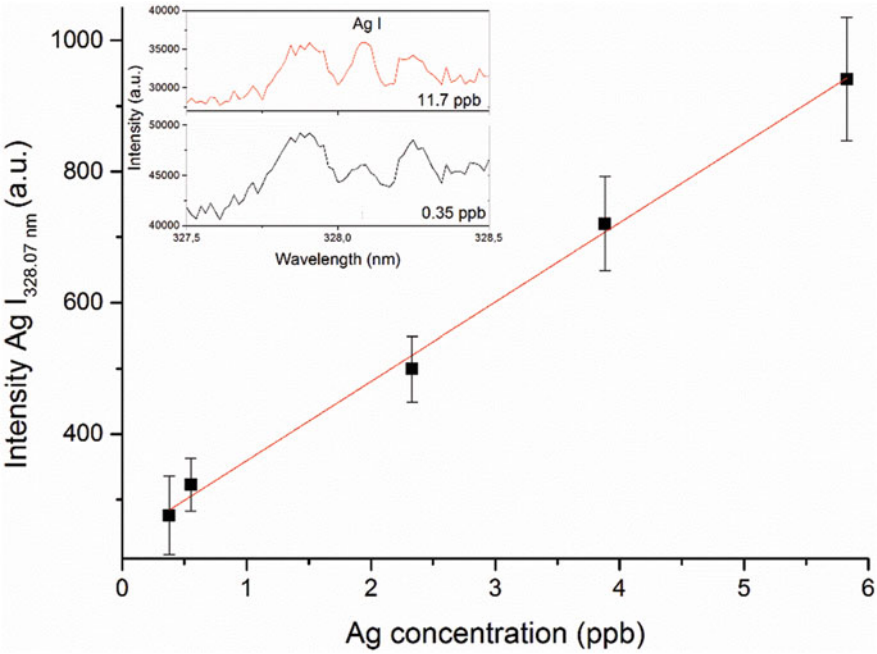

Fig. 8.7 Calibration curve of Ag in the concentration range between 0 and 6 ppb. In the inset, the spectrum around the Ag I 328.07 nm line is shown for 11.7 ppb and 0.35 ppb of Ag concentrations. Experimental conditions: 1 μL of $AgNO_3$ sample solution, laser fluence 12 J cm^{-2}, 1 μL of AuNPs (particle diameter: 20 nm) 0.03 mg mL^{-1}. Reprinted with permission from [6]. Copyright 2016 American Chemical Society

ppb of lead in a single shot experiment. On the contrary, no emission lines corresponding to Pb have been observed with conventional LIBS. This example opens the way to apply NELIBS for fast medical diagnostics related to the detection of metallic pollutants in blood. As a matter of fact, a so little amount of sample can be retrieved just with a sting instead of traditional blood sampling.

In both these examples the advantages of NELIBS are due to a set of synergic advantages [6]:

1. Electromagnetic field enhancement allows a higher local irradiance that in turn allows for a better atomization, avoiding the problems connected to the presence of organic matter.
2. In the case of blood analysis, where heavy metals are mostly present in the ionic state, it may be considered the preferential absorption of ions on the NPs surface when drops of blood are deposited on the NPs layer with a consequent accumulation of ions that will be involved in the plasma phase.
3. Vaporization of the NPs within the sample produces additional electrons that sustain the plasma longer than that produced in the case of classical ablation of a small sample.

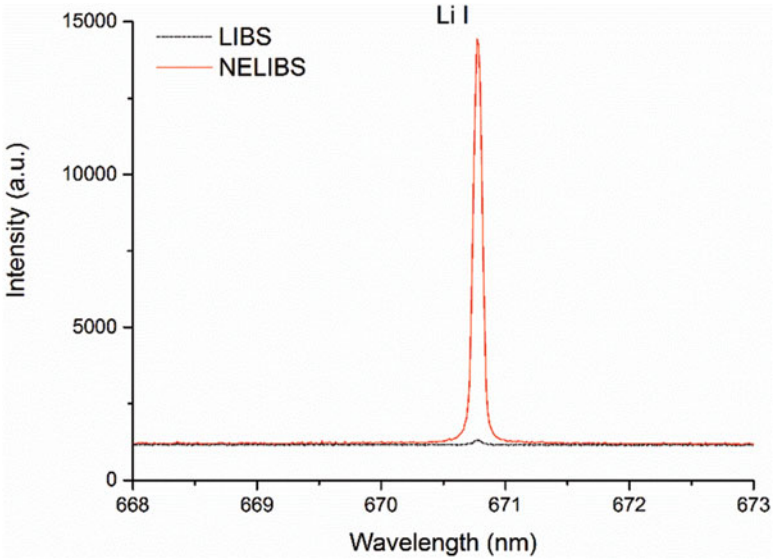

Fig. 8.8 Comparison between NELIBS and LIBS Li signal in 1 μL of solution of the reaction center from the purple bacterium Rhodobacter sphaeroides at a concentration 10^{-5} M. Experimental conditions: laser fluence 20.4 J cm^{-2}, 1 μL of AuNPs (particle diameter: 20 nm) 0.06 mg mL^{-1}] Reprinted with permission from [6]. Copyright 2016 American Chemical Society

In Fig. 8.4, the integrated overall plasma emission for a 2 μL of solution is reported. The figure clearly shows the main differences between the conventional LIBS approach and the NELIBS one, where the plasma appears more intense and larger than the one obtained with LIBS at the same experimental conditions. The large spatial distribution of emitters in the NELIBS plasma also demonstrates the longer duration of the plasma lifetime as a consequence of the higher number of charged particles.

8.4 NELIBS on Plant Tissues

The first time NPs were used for enhancing the LIBS emission signal was for metal detection in leaves [12]. As it is well known, samples containing a substantial amount of water in the matrix strongly decrease the LIBS sensitivity because part of the laser pulse is spent to vaporize the water and mechanical effects. This makes investigators to convert the sample in a different matrix, like pellets produced after the drying of the fresh sample [10]. Instead of this, the use of NPs dried directly on the fresh sample surface allows LIBS measurements without an extensive sample pretreatment, since the NPs strongly improve the conversion of the laser pulse energy in atomization and excitation overcoming the drawbacks of the ablation on a sample with water and organic matter in its matrix. As an example, Fig. 8.10 shows the LIBS and NELIBS spectra obtained with an experiment on a common fresh leave

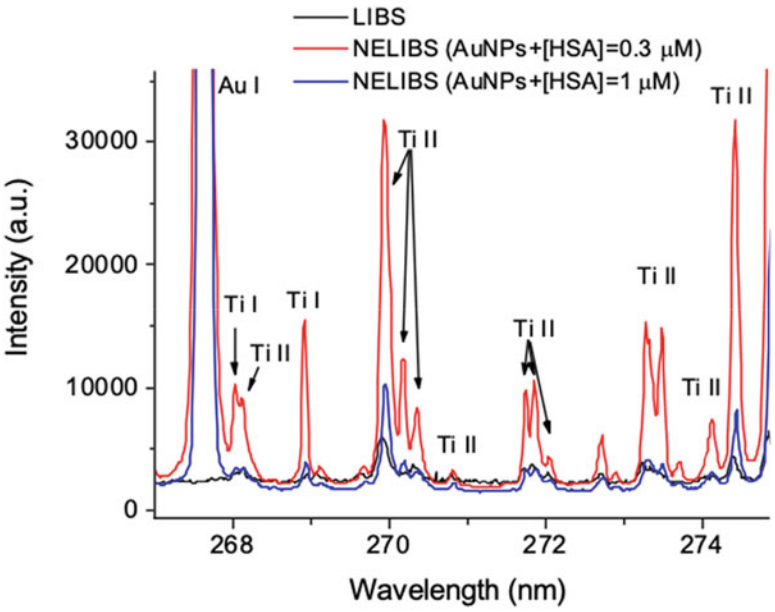

Fig. 8.9 NELIBS of human serum artificially contaminated with $PbCl_2$ at different concentrations: 74 ppb, 740 ppb, and 7400 ppb. Note that the detector gain is different for each measurement in order to optimize the emission signal. Experimental conditions: laser fluence 20.4 J cm^{-2}, 1 μL of Au colloidal solution (NP diameter: 20 nm) with a concentration of 0.08 mg mL^{-1}. Reprinted with permission from [6]. Copyright 2016 American Chemical Society

from a *Brassaia actinophylla*. Figure 8.10 shows the typical LIBS spectrum that, as a consequence of the high content of water in fresh leaves, is characterized mainly by continuum radiation. In contrast to that, the spectrum obtained with NELIBS clearly shows a discrete emission spectrum with typical emission lines relative to the metal included in the leaves, as Mg, Si, and Fe reported in Fig. 8.10.

This example clearly shows the possibility of applying this technique for the direct detection of contaminants in fresh samples for agricultural applications. In [13] the authors succeeded in detecting phosphorous as a tracer of pesticides on the skin of fresh apples at very low concentrations by depositing 80 nm AgNPs directly on the sample (see Fig. 8.11a. In the same paper, the authors also measured the content of Cadmium on fresh lettuce as shown in the spectrum reported in Fig. 8.11b).

8.5 NELIBS of Amyloid Fibrils

NELIBS has been employed for measuring, with very low detection limits, the absorbed metals in a small portion of the amyloid fibrils. For the NELIBS application on the amyloid fibrils system, the NPs are produced by gold thermal reduction

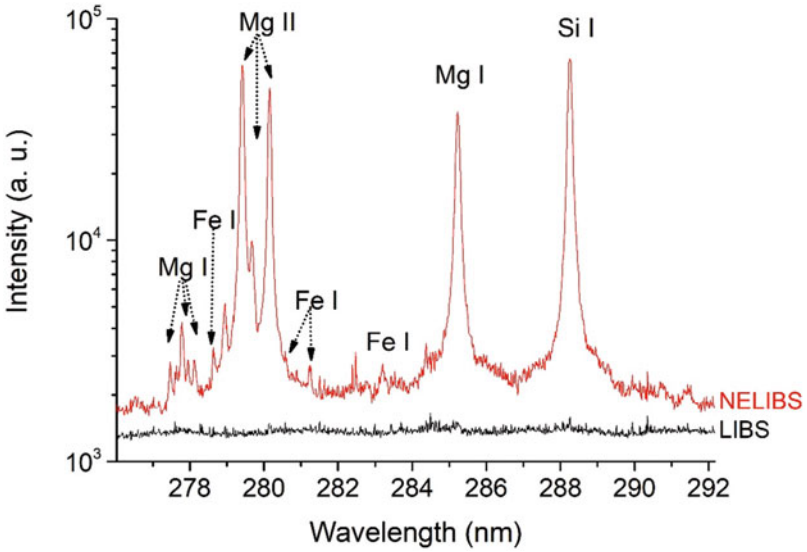

Fig. 8.10 NELIBS and LIBS spectrum on a fresh leave of *Brassaia actinophylla* (New Zealand). Experimental conditions: laser wavelength 532 nm, delay from the laser pulse = 800 ns; gate width = 5 μs, laser fluence 4 J cm^{-2}, 6 μL of AgNPs (particle diameter: 20 nm) 0.02 mg mL^{-1}

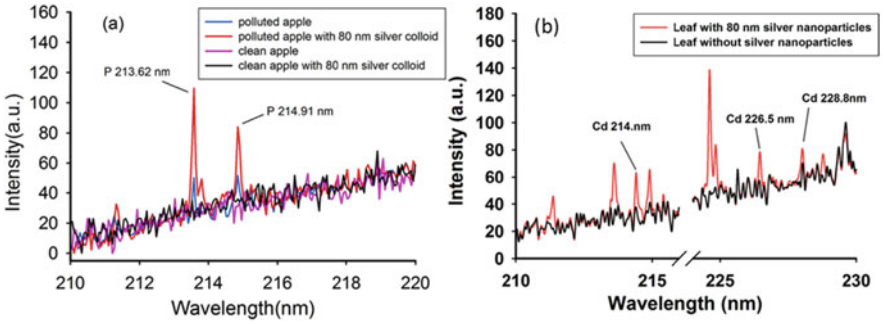

Fig. 8.11 Pollutant elements spectrum with NELIBS and LIBS on fresh sample as reported in [13]. (**a**) Phosphorous on fresh apple and (**b**) Cadmium on fresh lettuce

directly on the fibrils [14, 15]. In this way, reproducible distribution of AuNPs on the sample is obtained, strongly improving the NELIBS reproducibility for the analytical task. The distribution of the NPs on the fibrils is shown in Fig. 8.12.

The interest in AuNP-amyloid fibrils recently is getting the interest of researchers for several applications like water purification, heterogeneous catalysis, materials templating, nutrition applications, etc. Beyond the rapid quantification of metals in the above-mentioned applications, amyloid fibrils also represent a good test for NELIBS for investigating, from a more general point of view, the capability of optimizing laser ablation based techniques on biological systems for trace metal

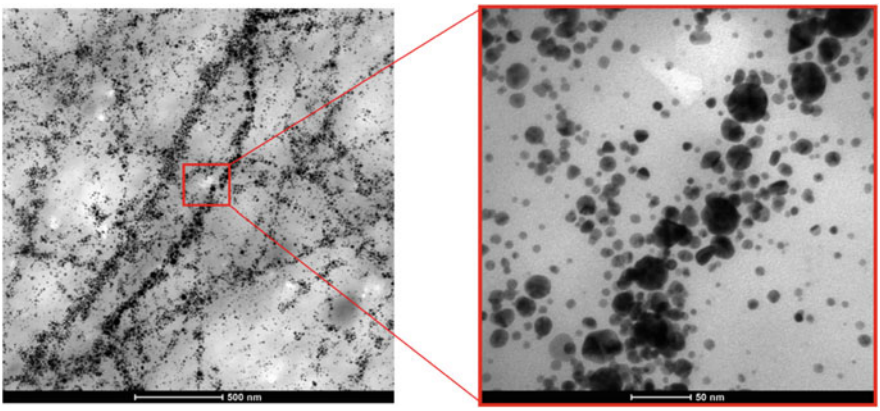

Fig. 8.12 Representative TEM of AuNP-amyloid fibrils deposited on microscopy grids. Reprinted from [16] with permission from Elsevier

element quantification. As an example the formation of amyloid fibrils in neurodegenerative diseases due to the metal binding [17] has important implications in the diagnostics of such diseases and analytical techniques able to detect ppb level of metal in an extremely little amount of sample can be useful in biological and medical applications. The analytical performances of NELIBS on this kind of system can be investigated from a quantitative point of view, taking the advantage that the amyloid fibrils have a strong affinity to metals and so it is possible to tune the concentration of metal in the fibrils by changing the concentration of the solution where the fibrils system is immersed. Therefore the NELIBS experiments were performed to test the limit of detections obtained with AuNPs embedded in the amyloid fibrils. Metal solutions, at different known concentrations, were dried on AuNPs-amyloid fibrils layer, previously deposited on a parafilm substrate located on a glass slide. Figure 8.13 shows the NELIBS and LIBS spectra in the spectral region between 520 and 521 nm from [16]. By the inspection of the spectra, two important peculiarities of the NELIBS can be observed. The first is that, like in the cases of the study examined in the previous sections, NELIBS allows the detection of Cr at a concentration below the LOD of conventional LIBS. The second is that also the molecular band due to the ablation and recombination of the elements constituting the fibrils are strongly enhanced (about one order of magnitude in the reported example). This enhancement on the molecular emission has been already reported in [18] where molecular emission band enhancement was investigated during NELIBS on metallic alloys. Although molecules generally are formed at the late stage of plasma evolution [19], when plasma cooling occurs, this enhancement is probably due to the more efficient ablation when the electromagnetic field of NPs couples with the incoming laser pulse field allowing better atomization of the ejected material.

Figure 8.14 shows the examples of metal detection and the relative calibration curves on AuNPs-treated amyloid fibrils doped with various metals (Cr, Pb, Cd, Tl).

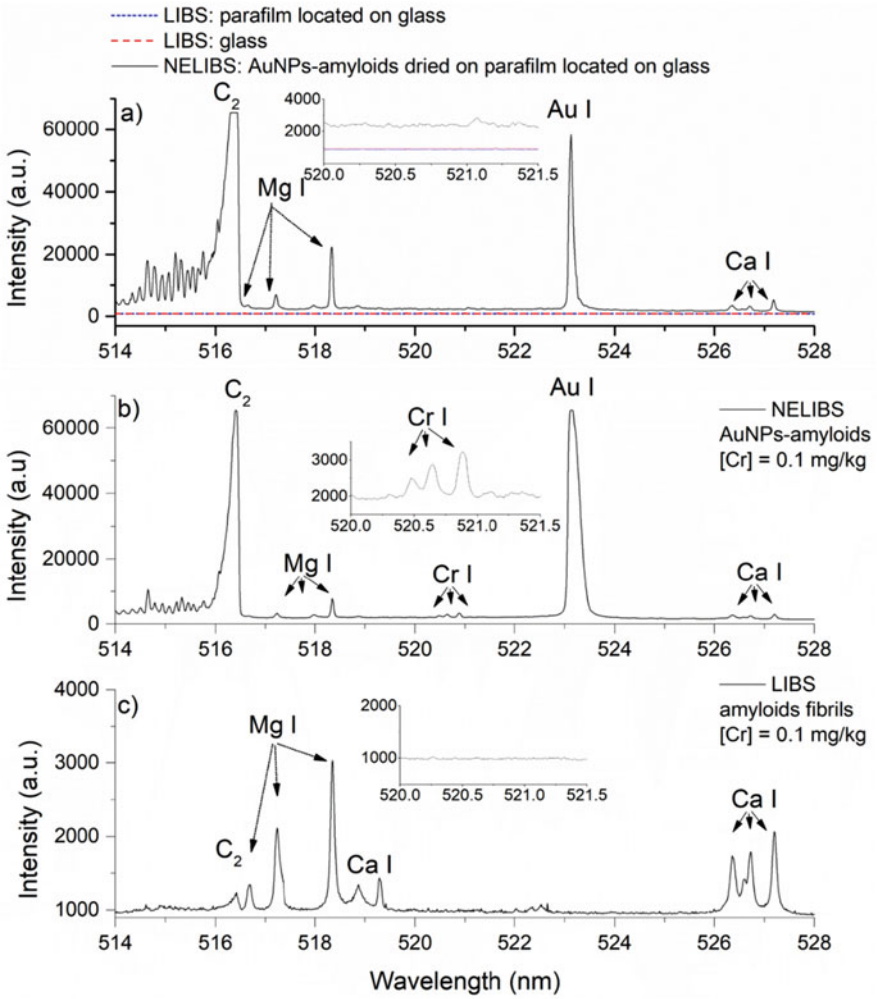

Fig. 8.13 Plasma emission spectra: (**a**) LIBS on parafilm located on glass, LIBS on glass and NELIBS on AuNPs-amyloids dried on parafilm located on glass; (**b**) NELIBS of $Cr(NO_3)_3$ solution on AuNP-amyloids and (**c**) LIBS of $Cr(NO_3)_3$ solution on amyloid fibrils. The Cr concentration was 0.1 ppm and the sample volume was 2 uL. The insets report the enlargement of the spectral region of the emission lines of Cr. (Experimental parameters: laser wavelength = 532 nm, pulse energy of 450 mJ, laser spot size = 2.2 ± 0.2 mm, laser fluence = 11.84 J/cm^2; delay time from the laser shot = 800 ns, gate width = 10 μs.). Reprinted from [16] with permission from Elsevier

It is notable that while NELIBS allows ppb-level detection, the emission signal with LIBS was not detectable.

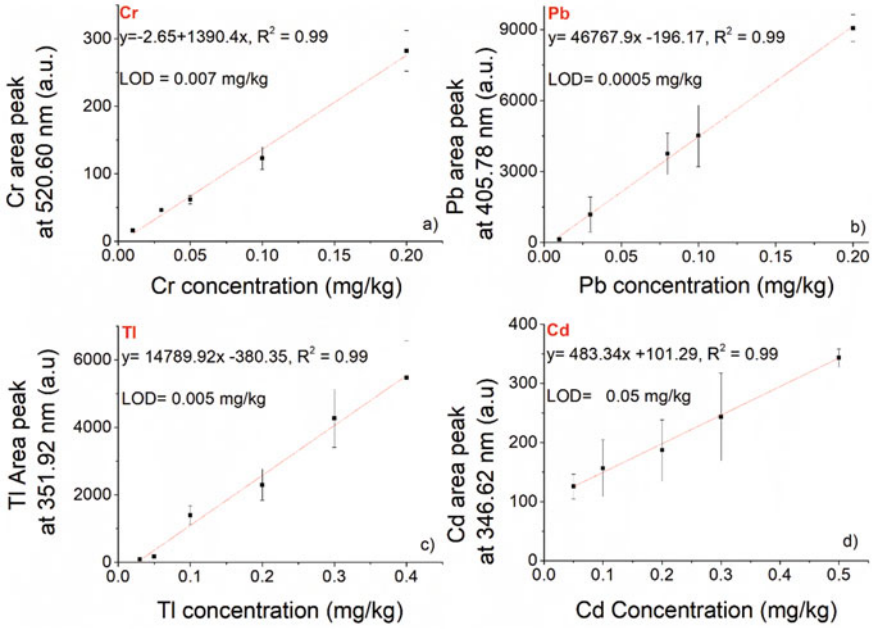

Fig. 8.14 Calibration curves of Cr, Pb, Tl, and Cd. The linear fit with the R-square and the LOD for each element are also reported. (Experimental parameters: laser wavelength = 532 nm, pulse energy of 450 mJ, laser spot size = 2.2 ± 0.2 mm, laser fluence = 11.84 J/cm^2; delay time from the laser shot = 800 ns, gate width = 10 μs.). Reprinted from [16] with permission from Elsevier

8.6 NELIBS for the Sensing of NP-Protein Corona

Beyond the use of NELIBS for trace elements, NELIBS has been recently proposed as a sensor for the investigation of NP–protein structure. The protein corona formation is a dynamic process [20] depending on the binding affinities and rates of absorbed protein on NPs which in turn can be of different types (composition, size, surface charge). Nanoparticle protein corona formation plays an important role in several biological applications. The most common way to detect the protein corona formation is the use of chemical-physical techniques like Dynamic Light Scattering (DLS) and ζ-potential analysis with Laser Doppler Electrophoresis (LDE) for the determination of size and surface charge of protein–NP conjugate, respectively. In [21] the authors have investigated the AuNP–protein conjugates employing two proteins with different molecular mass and therefore different sizes, Human Serum Albumin (HSA) and Cytochrome C (CytC). These two proteins, having both strong affinities for the AuNPs surface due to the bonding between the single free exterior thiol (associated with a cysteine residue) and gold, form stable nanoparticle protein corona. The effect of the concentration of protein on the structure of AuNP–protein conjugate is sketched in Fig. 8.15: increasing the

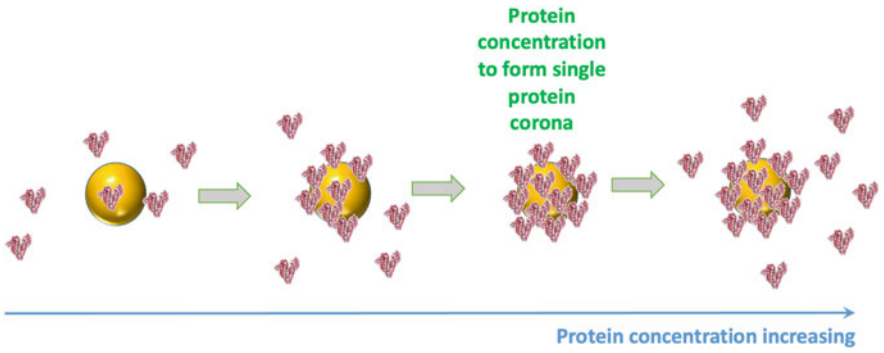

Fig. 8.15 Sketch of AuNP–protein conjugate formation as a function of the protein concentration

protein concentration at fixed AuNPs concentration, the number of proteins covering the AuNP surface increases until it reaches a constant value useful for occupying the whole AuNP surface. Beyond this value, further increase of protein concentration will not vary the number of proteins covering the NP surface.

The technique proposed is based on the fact that the NELIBS enhancement is dependent on the strength of the electromagnetic field induced by the plasmons of the deposited NPs. The electromagnetic field is strongly affected by the surface coverage on the NP since it can affect the interparticle distances between the NPs after the drying on the substrate. For these reasons, NELIBS enhancement on titanium substrate has been measured by using different protein/NP concentration ratios in order to observe the dependence of the signal enhancement on the number of proteins in the colloidal solution of AuNPs. In particular, the dependence of the signal enhancement on protein–NPs interaction is investigated for sensing the structural characteristics of AuNP–protein conjugate in terms of protein content absorbed on the NP surface. This inverse approach to NELIBS demonstrates NP-enhanced laser ablation, although based on high irradiance laser-matter interaction and the breakdown process, it is extremely sensitive to the colloids employed and in turn it opens the way to potentialities beyond elemental analysis.

In the following experiment, the authors prepared a set of solutions while keeping the concentration of AuNPs in the solution constant and adding different concentrations of proteins [21]. It should be noted that all these experiments were performed by using AuNPs produced by PLAL which are stable without any stabilizer since the latter can interfere with the protein absorption on the gold surface. The investigation of the interaction of the protein directly with the naked surface of the NP was therefore possible. For the measurements, a drop of each prepared solution at different protein concentrations was used for the NELIBS experiment on a titanium substrate. The NELIBS spectra at different protein concentrations as well as the LIBS spectra are reported in Fig. 8.16 to show the principle of the measurement. By the inspection of the figure, it is possible to observe the effect of the protein–NP conjugate on the signal enhancement and also the already discussed NELIBS enhancement with respect to LIBS. Different protein concentrations induce

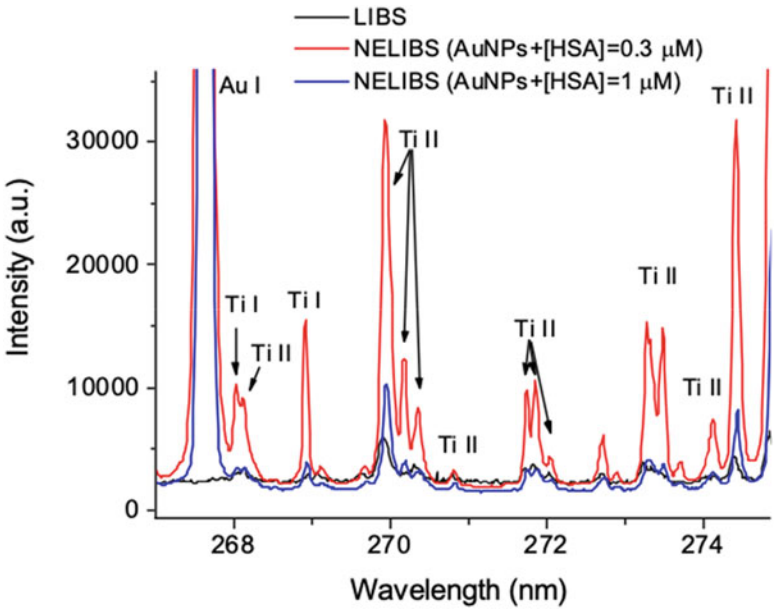

Fig. 8.16 A frame of the emission spectrum of titanium at two different HSA protein concentrations with NELIBS and with LIBS directly on the titanium sample. (Experimental parameters: laser wavelength = 1064 nm, pulse energy of 360 mJ, laser spot size = 1.7 ± 0.2 mm, laser fluence = 15 J/cm^2; delay time from the laser shot = 1 μs, gate width = 5 μs, [AuNPs] = 10.5 nmol L^{-1}, nanoparticle diameter = 13 nm)

different enhancements. Actually, by plotting the enhancement as a function of added protein concentration, it is possible to see a trend strictly linked to the AuNP–protein conjugate structure in terms of the number of proteins covering the AuNP surface. Figure 8.17a shows the NELIBS enhancements as a function of the number of proteins added in the solution. The results regarding the two selected proteins, HSA and CytC, are reported for comparison.

Simultaneously, in Fig. 8.17b and c have reported the diameter of the AuNP–protein conjugate determined with the DLS and the ζ-potential as a function of the number of added protein units. These techniques are the conventional methods for determining the protein corona formation. The size and the surface charge of the NP–protein conjugate change with respect to those of naked NP, until the whole NP surface is completely covered with proteins in dependence on the NP and protein unit size. Once the NP surface is completely covered, size and surface charge of the conjugate will not be considerably affected by further increase of the protein concentration. By the comparison of the reported techniques in Fig. 8.17, it is notable that NELIBS enhancement shows a marked peak in correspondence of the number of protein units needed to form a single corona around NP. This number of proteins can be determined for a fast comparison from the behavior of the size and the ζ-potential or from a geometrical model. More details can be found in [21] where

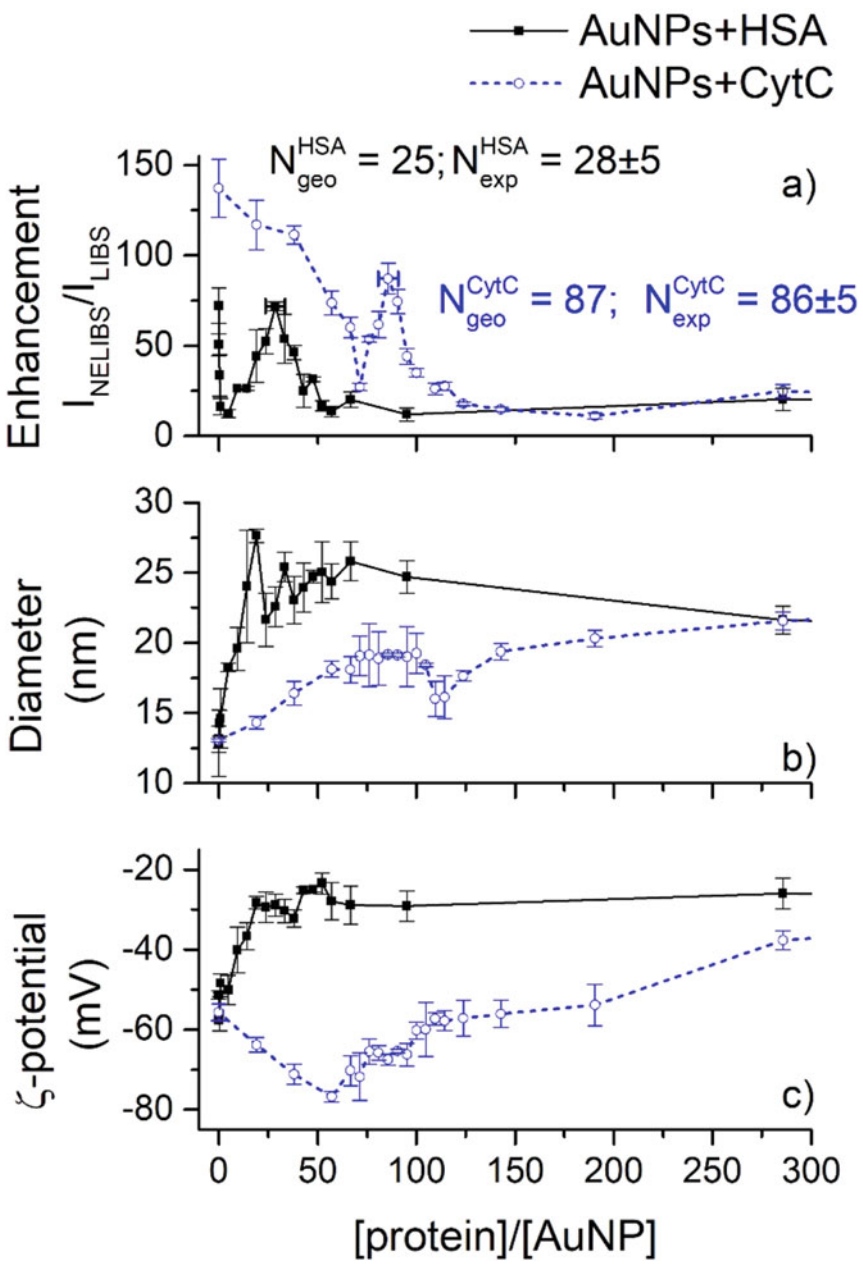

Fig. 8.17 (**a**) NELIBS enhancement, (**b**) hydrodynamic diameter and (**c**) ζ-potential data reported as a function of the number of proteins for two different sets of samples obtained adding HSA or CytC at the solution with fixed concentration of AuNPs (10.5 nmol L^{-1}). . (Experimental parameters: laser wavelength = 1064 nm, pulse energy of 360 mJ, laser spot size = 1.7 ± 0.2 mm, laser fluence = 15 J/cm2; delay time from the laser shot = 1 μs, gate width = 5 μs, AuNPs diameter = 13 nm). Reprinted from [21] with permission from Elsevier

it is also explained how to calculate the number of proteins units needed to form a single corona from the geometrical point of view. Moreover, as previously mentioned, in Fig. 8.7 the trends of the enhancements as well as those of sizes and surface charges of two NP–protein conjugates, AuNP–HSA and AuNP–CytC, are also reported. By the inspection of Fig. 8.17a, it is clear that the concentration at which the corona is formed is peculiar of the specific NP–protein conjugate and consequently the number of CytC (low molecular mass protein, 12 kDa), required for forming protein corona is higher than that required when HSA protein (molecular mass protein, 66.5 kDa) interact with AuNPs. The results experimentally determined with NELIBS are finally in good agreement with the number of proteins taking part to the protein corona as calculated with geometrical models [21] and as determined from DLS and ζ-potential measurements, for both analyzed conjugates.

In conclusion, it has been observed that the Ti-NELIBS enhancement strictly depends on the NP–protein structure and therefore on the plasmonic organization reached after the NP deposition process on the Ti substrate.

8.7 Perspective

The use of nanostructures for enhancing laser ablation-based analytical techniques is a new field and the number of scientific publications on the topic increases year after year. Although several efforts have been made to understand the basic mechanisms leading to emission enhancement, many aspects of nanoparticle-enhanced ablation still need to be elucidated.

The sample preparation also has to be optimized for improving reproducibility and, at the same time, keeping the operation as simple as possible.

Several applications of NELIBS have been reported recently in the literature and among these, the use of NELIBS for biological applications looks particularly promising, especially considering the fast response and low sample requirement.

References

1. De Giacomo A, Rifai RA, Gardette V, Salajková Z, Dell'Aglio M. Nanoparticle enhanced laser ablation and consequent effects on laser induced plasma optical emission. Spectrochim Acta B. 2020;166:105794.
2. Dell'Aglio M, Rifai RA, De Giacomo A. Nanoparticle enhanced laser induced breakdown spectroscopy (NELIBS), a first review. Spectrochim Acta B. 2018;148:105.
3. Salajková Z, Gardette V, Kaiser J, Dell'Aglio M, De Giacomo A. Effect of spherical gold nanoparticles size on nanoparticle enhanced laser induced breakdown spectroscopy. Spectrochim Acta B. 2021;179:106105.
4. Koral C, Dell'Aglio M, Gaudiuso R, Alrifai R, Torelli M, De Giacomo A. Nanoparticle-enhanced laser induced breakdown spectroscopy for the noninvasive analysis of transparent samples and gemstones. Talanta. 2018;182:253.
5. De Giacomo A, Gaudiuso R, Koral C, Dell'Aglio M, De Pascale O. Nanoparticle-enhanced laser-induced breakdown spectroscopy of metallic samples. Anal Chem. 2013;85:10180.

6. De Giacomo A, Koral C, Valenza G, Gaudiuso R, Dellaglio M. Nanoparticle enhanced laser-induced breakdown spectroscopy for microdrop analysis at subppm level. Anal Chem. 2016;88:5251.
7. Kohsakowski S, Santagata A, Dell'Aglio M, De Giacomo A, Barcikowski AS, Wagener P, Gökce B. High productive and continuous nanoparticle fabrication by laser ablation of a wire-target in a liquid jet. Appl Surf Sci. 2017;403:487.
8. Palásti DJ, Albrycht P, Janovszky P, Paszkowska K, Geretovszky Z, Galbács G. Nanoparticle enhanced laser induced breakdown spectroscopy of liquid samples by using modified surface-enhanced Raman scattering substrates. Spectrochim Acta B. 2020;166:105793.
9. Shen J, Wu K, Cao D, Wang J, Hu B. Effect of Ag nanoclusters deposited with magnetron sputtering on laser-induced breakdown spectroscopy enhancement. Spectrochim Acta B. 2019;156:59.
10. Jantzi SC, Motto-Ros V, Trichard F, Markushin Y, Melikechi N, De Giacomo A. Sample treatment and preparation for laser-induced breakdown spectroscopy. Spectrochim Acta B. 2016;115:52.
11. Giustini M, Parente M, Mallardi A, Palazzo G. Effect of ionic strength on intra-protein electron transfer reactions: the case study of charge recombination within the bacterial reaction center. Biochim Biophys Acta Bioenergetics. 2016;1857:1541.
12. Ohta T, Ito M, Kotani T, Hattori T. Emission enhancement of laser-induced, breakdown spectroscopy by localized surface plasmon resonance for analyzing, plant nutrients. Appl Spectrosc. 2009;63:555.
13. Zhao X, Zhao C, Du X, Dong D. Detecting and mapping harmful chemicals in fruit and vegetables using nanoparticle-enhanced laser-induced breakdown spectroscopy. Sci Rep. 2019;9:906.
14. Nyström G, Fernández-Ronco MP, Bolisetty S, Mazzotti M, Mezzenga R. Amyloid templated gold aerogels. Adv Mater. 2015;28:472.
15. Bolisetty S, Mezzenga R. Amyloid–carbon hybrid membranes for universal water purification. Nat Nanotechnol. 2016;11:365.
16. Dell'Aglio M, Salajková Z, Mallardi A, Mezzenga R, Van't Hag L, Cioffi N, Palazzo G, De Giacomo A. Application of gold nanoparticles embedded in the amyloids fibrils as enhancers in the laser induced breakdown spectroscopy for the metal quantification in microdroplets. Spectrochim Acta B. 2019;155:115.
17. Shen Y, Posavec L, Bolisetty S, Hilty FM, Nyström G, Kohlbrecher J, Hilbe M, Rossi A, Baumgartner J, Zimmermann MB, Mezzenga R. Amyloid fibril systems reduce, stabilize and deliver bioavailable nanosized iron. Nat Nanotechnol. 2017;12:642.
18. Koral C, De Giacomo A, Mao X, Zorba V, Russo RE. Nanoparticle enhanced laser induced breakdown spectroscopy for improving the detection of molecular bands. Spectrochim Acta B. 2016;125:11.
19. De Giacomo A, Dell'Aglio M, De Pascale O, Gaudiuso R, Palleschi V, Parigger C, Woods A. Plasma processes and emission spectra in laser induced plasmas: a point of view. Spectrochim Acta B. 2014;100:180.
20. Mahmoudi M, Lynch I, Ejtehadi MR, Monopoli MP, Bombelli FB, Laurent S. Protein–nanoparticle interactions: opportunities and challenges. Chem Rev. 2011;111:5610.
21. Dell'Aglio M, Salajková Z, Mallardi A, Sportelli MC, Kaiser J, Cioffi N, De Giacomo A. Sensing nanoparticle-protein corona using nanoparticle enhanced laser induced breakdown spectroscopy signal enhancement. Talanta. 2021;235:122741.

Analysis of Forensic Trace Evidence

9

Anikó Metzinger and Zsolt Szoldán

9.1 Introduction

Forensic science or criminalistics involves and draws upon a wide variety of scientific disciplines which are applied during the investigation of criminal and civil laws. Forensic science is a tool of the enforcement of laws and regulations, improving public safety and helping to solve cases to policemen. This field covers the document and questioned document examination, engineering, linguistics, pathology, DNA analysis, fingerprinting, electronic/digital media, anthropology, entomology, toxicology, economics, accounting, serology, chemistry, odontology, geology, botany, psychiatry, and behavioral science, physics, biometrics, bloodstain pattern identification, tool mark identification, hair and fiber analysis and firearms identification as well. Because forensic science has the above-mentioned important tasks and has to deal with irreplaceable evidence, forensic scientists use cutting-edge analytical methods and evaluation techniques. Forensic scientists have to collect, preserve and analyze evidence given by policemen and are often challenged in court and have to give an expert witness testimony.

In this chapter, we give an overview of a narrow part of forensic science, which deals with physical trace evidence (the size of the remains in the microscopic range). Actually, anything can be a physical trace evidence, thus it is not possible to list every kind of recovered material. Physical trace evidence categories are listed below:

- Fingerprint
- DNA
- Glass: automobile, buildings windows, beverage glasses, household glasses
- Paint: automobile, tools, wall paints
- Geological materials: soil, rock, stone, minerals

A. Metzinger (✉) · Z. Szoldán
Hungarian Institute for Forensic Sciences, Budapest, Hungary
e-mail: metzingera@nszkk.gov.hu

G. Galbács (ed.), *Laser-Induced Breakdown Spectroscopy in Biological, Forensic and Materials Sciences*, https://doi.org/10.1007/978-3-031-14502-5_9

- Biological samples: wood, insects, pollens
- Human samples: hair, blood, fingernail, organs, saliva, semen, skin
- Banknotes and documents: ink, paper, toner, signature
- Drugs: synthetic precursors, final product, packaging, tools for a drug laboratory
- Fibers: natural and synthetic
- GSR and ammunition
- Plastics, polymers, rubbers
- Impressions: tool marks, shoeprint, tire markings, bite marking
- Explosives and post-blast residues
- Petroleum products

A vital part of the investigation is the proper collection, preservation, and storage of physical trace evidence because of its small size and nature (e.g., biological samples like blood, DNA). It is crucial to avoid any contamination during the search, collection, and of course during the examinations. The sample preparation methods and analysis are also important because the small quantity of the evidence, therefore those analytical methods that need no, or minimal sample preparation are ideal.

In case of the examination of physical trace evidence the aim is the identification (determine the identity of the material) or comparison (determine if the compared samples have a same origin or not) based on results obtained by analytical methods, which requires strict and validated analyzing protocols. During the whole process, from the collection to the analysis, various errors endanger the integrity of information or sample. For instance, there could be a human error committed by the person (CSI policeman, forensic scientist, analyst, etc.) during sample handling, but the applied, comparative methods can also be erroneous. In other instances, the condition of the physical trace evidence generates an error—a trace evidence is often of heterogeneous composition or can be much more contaminated than the "known sample" (material of a known source that presumably was uncontaminated during the commission of the crime; samples with a known composition, identification, type, or source used for comparison), thus their comparison may lead to the conclusion that they are different. The handling error is the one that is the easiest to avoid. If the examiners follow strict rules and standardized methods (e.g., ASTM), these can be minimized. The final results of the formal written report can be different from country to country depending on their law system, technical equipment, and presence or absence of databases. Based on these criteria, the evaluation approach can vary in a wide range. If the law system requires it and the forensic institutes have databases, likelihood ratio and Bayesian approach (e.g., in DNA analysis) can be used.

During the examination of physical trace evidence, typically only microanalytical methods can be used, which can work with very small sample amounts (μg of solids, μL or a droplet of liquids, one fiber, etc.) and have a high spatial resolution. In addition to this, forensic scientists also use common analytical techniques, pattern recognition, and comparison software which were modified or specifically developed for forensic use. Examples include shoeprint, fingerprint comparison and face recognition software. Analytical reference databases are also of great importance,

e.g., for automobile paint: PDQ (Paint Data Query), for ballistics analysis: NIBIN (National Integrated Ballistic Information Network), for DNA tests: CODIS (Combined DNA Index System), for fingerprint analysis: IA-FIS (Integrated Automated Fingerprint Identification System), for handwriting examination: FISH (Forensic Information System for Handwriting), for ink and dye recognition: International Ink Library, for shoeprints pattern recognition: SoleMate, for drugs identification: Ident-A-Drug, etc. The analytical methods most often used in forensic investigations are listed below [1]:

- Scanning electron microscopy (SEM)
- Polarized light microscopy
- Atomic force microscopy (AFM)
- X-ray fluorescence spectroscopy (XRF)
- Scanning electron microscopy-energy dispersive X-ray spectroscopy (SEM-EDX)
- Inductively coupled plasma-mass spectrometry (ICP-MS)
- Laser ablation-inductively coupled plasma-mass spectrometry (LA-ICP-MS)
- Atomic emission spectroscopy (AES)
- Neutron activation analysis (NAA)
- Fourier transform infrared spectroscopy (FTIR)
- Raman spectroscopy
- Ultraviolet/visible spectroscopy (UV/Vis)
- X-ray diffraction (XRD)
- Nuclear magnetic resonance spectroscopy (NMR)
- Fluorescence-spectroscopy
- Mass spectrometry (MS)
- Ion mobility mass spectrometry (IMS)
- Matrix-assisted laser desorption ionization time-of-flight mass spectrometry (MALDI-TOF)
- Capillary electrophoresis (CE)
- Gas chromatography (GC)
- Ion chromatography (IC)
- Liquid chromatography (LC)
- Thin layer chromatography (TLC)
- Differential thermal analysis (DTA)
- Pyrolysis gas chromatography (PGC)
- Thermogravimetric analysis (TGA)

All methods have advantages and disadvantages, thus usually more than one technique is used for the analysis of evidence. In the world of forensic analysis, analytical methods are selected based on the necessary sample preparation time, sample consumption needs (destructiveness), cost per analysis, ease of use and, of course, the analytical figures of merit. When elemental analysis is needed, the methods of SEM-EDX, LA-ICP-MS, and XRF are of primary importance; however, the first two are time-consuming and/or expensive and difficult to use, whereas XRF

cannot analyze light elements. Recently laser-induced breakdown spectroscopy is emerging as a powerful and practical alternative elemental analysis tool.

For the elemental analysis of the physical trace evidence, forensic scientists use a wide variety of methods, for example, ICP-MS, XRF, and SEM-EDX. Beside these well-known and broadly used methods, a relatively new technique, laser-induced breakdown spectroscopy (LIBS) begins to gain ground, which has an advantageous, unique set of analytical characteristics. For example, any samples, regardless of their consistency, can be measured quickly, in situ. The method is microdestructive and requires less than a μg sample mass, with minimal sample preparation. The small dimensions of the LIP plasma allow the execution of spatially resolved measurements. LIBS spectroscopy provides highly characteristic, "fingerprint-like" spectra, which can be used for qualitative analysis efficiently. The examination of light elements is not a problem for the method either, for example, sodium, potassium, calcium, magnesium, chlorine, fluorine, or even hydrogen can be detected with good sensitivity [2, 3]. In-field, real-time measurements are also possible by using compact spectrometers [4–6]. Detection limits of LIBS spectroscopy range from ca. 1 to 100 ppm, depending on the sample, the analyte, the matrix, and the experimental configuration [7, 8]. These detection limit values are suitable for trace analytical applications and even for most solid-sample industrial and environmental applications; however, they do not count as outstanding data in atomic spectroscopy. However, it should be noted that the absolute detection limit values of the method, e.g., the sample consumption, actually fall in the pg-fg range, which is comparable to that of the most sensitive solid sampling atomic spectroscopy methods (e.g., LA-ICP-MS). Detection limits can even be significantly improved by up to two orders of magnitude under special excitation conditions (e.g., two- or multi-pulse LIBS, different gas atmospheres, spatial or magnetic confiments, etc.). The linear dynamic range is limited from above by self-absorption (especially for "strong" spectral lines) to approx. 1–3 wt.% concentration. The linear dynamic range in general LIBS systems is thus 3–4 orders of magnitude wide, which can also be extended by special techniques.

9.2 LIBS Analysis of Various Types of Forensic Evidence

9.2.1 Glass

Glass, defined as "an inorganic product of fusion that has cooled to a rigid condition without crystallization" is frequently and widely used material in everyday life, like windows (e.g., buildings, automobiles), household glass, and beverage containers and it has many different preparation types (e.g., flat, float, toughened, laminated glass) [9, 10]. Because of its widespread use, glass is often the subject of forensic examinations. It has great relevance in cases like hit and run accidents, burglary, vandalism, and car theft, where the fragments can link persons to each other or locations to persons (suspects). The tiny glass fragments, splinters (mm and sub-mm range) can be ejected from the broken glass object in all directions (backward and

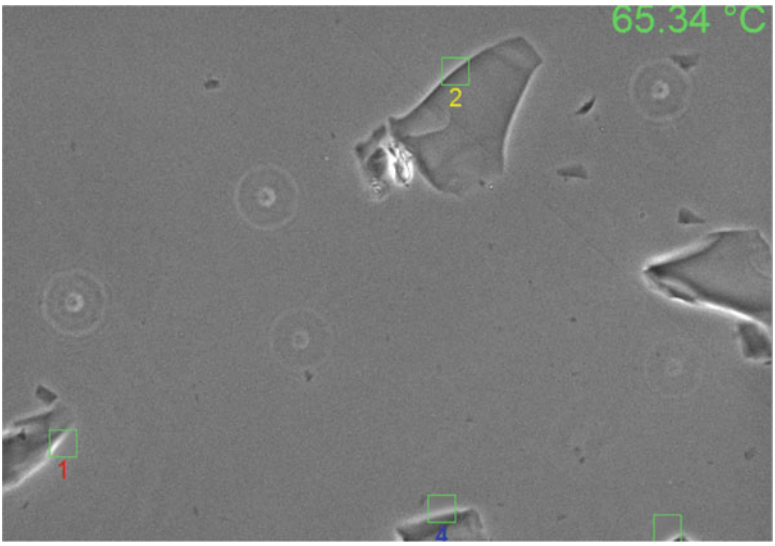

Fig. 9.1 Microscope image of glass microfragments during RI measurements, using the oil immersion/temperature variation technique

toward the direction of the breaking force as well) more than three meters and can be transferred onto anything, like clothing, shoes or hair of a person. The number of transferred glass particles depends on the area of damage, type of the glass, position of the offender to the glass object, nature of the clothing, applying multiple blows or a single blow, etc. The number of recovered glass particles/fragments/shards from clothing, shoes, hair, tools, and other objects depends on the size of the glass object, the weather, the nature of the clothing, length of time that has passed between the time of the arrest and the collection of the clothing, on the lifestyle of the person, or whether the clothing was washed or not, etc. [11].

Historically, forensic glass analysis is based on refractive index (RI), dispersion (it is the change in RI with a change in wavelength of illumination), and density analysis [12]. The first neutron activation analysis of glass took place only in 1991 and this was soon followed by ICP-MS measurements [13, 14]. Nowadays, the most commonly applied methods are refractive index measurements and elemental analysis like micro-XRF and laser ablation inductively coupled plasma mass spectrometry (LA-ICP-MS), as well as SEM-EDX (Fig. 9.1) [15–18]. LIBS provides an essential advantage over SEM-EDX and LA-ICP-MS. It can sensitively detect the elements that are common in glasses, such as the light elements (Li, Na, K) and those which are difficult to measure with other methods (Ca, Fe), too.

El-Deftar et al. determined the elemental composition of 14 laminated and 6 non-laminated architectural window glasses, collected from real crime scenes by LIBS. The experiments were done under argon atmosphere. They found that the repeatability of intensity ratios is far better than that of peak intensities. The discrimination potential of LIBS was also compared to LA-ICP-MS, micro-XRF,

and SEM-EDX. With the three-sigma rule, the achieved discrimination accuracy was 88.6%, which means 68 sample pairs were found to be indistinguishable out of 595. These 68 pairs were then compared with the help of ANOVA followed by Tukey's HSD test which yielded 20 indistinguishable pairs and they got 95% discrimination accuracy with LIBS (96.6%, by LA-ICP-MS: 97.8%, μXRF:96.1%, RI: 81.5%). With the combination of RI and LIBS results, the final accuracy of discrimination was 98.3%. This result was comparable to that of other methods (LA-ICP-MS: 98.5%, μXRF: 98.0%) [19].

A comprehensive study was made by Almirall et al. about different types of glasses that are relevant and often occur as physical trace evidence in forensic analysis. They analyzed automobile glass samples on the float and non-float side, automobile headlamps, brown beverage glasses, and automobile side-mirror samples. Almost in all cases they determined the elemental composition with LIBS (using argon gas atmosphere) and/or LA-ICP-MS and measured the refractive index as well. After the laser–matter interaction, SEM images were also recorded of the ablation craters in order to observe the damage caused by laser. Results showed that LIBS spectra of float glasses were very similar to each other, at least considering the presence of the most intense emission peaks. Because of the high degree of similarity, correlation and multivariate statistical methods were unsuccessful to discriminate the samples. Thus, for comparison, line intensity ratios (single day RSD% varied between 0.8 and 15.0%) were used. In summary, with the combination of RI and LIBS data, a better than 90% discrimination power can be achieved in almost all datasets (at 90% confidence limit). In the case of headlamp glasses, the discrimination efficiency was 100%. These results (a total of 1270 pairwise comparisons) decreased to 79.9% at 99% confidence level. With the combination of LA-ICP-MS and RI, the discrimination results were even better, 99% at 90% confidential level and 97.5% at 99% confidential level [20].

Naes et al. studied the discrimination power of LA-ICP-MS, micro-XRF and LIBS in case of automobile glasses. They used a sample set consisting of 41 fragments (side window, rear window, windshield window) from 14 different vehicles and they only analyzed the non-float surface. For data analysis 22 emission lines, represented in all samples, of 9 elements (Ca, Fe, Al, K, Mg, Na, Si, Sr, and Ti) were chosen. They used peak area instead of peak high or peak intensity, because it gave higher precision. For assessing the discrimination power, all combinations of peak area ratios (231 combinations) were tested using t-test at the 95% confidence level and only 10 were retained. Only five sample pairs were indistinguishable by LIBS, eight by micro-XRF and five by LA-ICP-MS. These samples were coming from the same vehicle and the windows were possibly manufactured in the same plant and time. Based on the results, 99% discrimination power were calculated in case of all methods. In case of LIBS, the applied 266 nm wavelength gave an excellent precision for all elements and ratios. Based on their experience of this study they suggest 10 peak area ratios for LIBS glass discrimination studies, which helped to eliminate false exclusions and reduce false inclusions: 394.4 nm/330.0 nm (Al/Na), 766.5 nm/643.9 nm (K/Ca), 394.4 nm/371.9 nm (Al/Fe), 438.4 nm/766.5 nm (Fe/K), 534.9 nm/766.5 nm (Ca/K), 371.9 nm/396.2 nm (Fe/Al),

766.5 nm/645.0 nm (K/Ca), 394.4 nm/460.7 nm (Al/Sr), 460.7 nm/766.5 nm (Sr/K), and 818.3 nm/766.5 nm (Na/K) [21].

Mcintee et al. also investigated the discrimination power of LIBS for automobile float glasses. Beside LIBS, they also analyzed the samples with LA-ICP-MS and RI and combined the data. The analyzed glass samples were automobile side and rear windows collected from 23 automobiles which resulted in 253 pairwise comparisons. The experiments were performed under argon gas atmosphere and on the float side of the glasses, which contains tin. For the data evaluation, 18 emission lines and 12 emission line ratios were chosen. The discrimination power of LIBS, RI, and LA-ICP-MS data was performed with Tukey honestly significant difference (HSD) test. LIBS was found to achieve 92.9% discrimination power at a 90% confidence level and 82.2% at 99% level of confidence without RI values. With the addition of RI values, these results improved to 98.0 and 95.6%, respectively. In the case of LA-ICP-MS, the discrimination power was 100% both at 90% and 99% confidence level without RI values [22].

In a study by Bridge et al. 27 automobile glass samples, 15 automobile headlamp samples, 15 brown beverages glass samples, and 34 automobile side/mirror samples were analyzed. In order to enhance the emission, argon gas was applied. For the statistical analysis, the Tukey HSD test, emission line ratios, isotope ratios, and RI values were applied. They tested the discrimination power without and with RI values. The aim of the Tukey test was to ensure that the probability of a Type I error is constant. They also used ANOVA for the evaluation of variance in the compared features. In case of the evaluation of LIBS-RI and LA-ICP-MS-RI data combination, they used the Pearson product-moment correlation. In order to get more reliable results, precision was also calculated both by LIBS and LA-ICP-MS. The calculated average RSD% for the peak intensity ratios was 6.5 $\pm$ 1.4%, while in the case of peak ratios determined over 3 days was 24.5 $\pm$ 29.2%. The precision was also determined by LA-ICP-MS and only the between-day value was significantly better than for LIBS. In every case, LIBS combined with RI values gave a better discrimination power than only LIBS. In the case of automobile headlamps and beverage glasses, the discrimination efficiency was almost 100% without the RI, but in the other two cases it was only 74.4% and 56.2%, but the additional use of RI values increased the number of correctly identified samples [23].

In a freshly published article, 17 laboratories decided to collaborate in three interlaboratory exercises. They assessed the discrimination power of RI and elemental analyses (LIBS, XRF) in forensic glass examination. In all cases, the analyzed glass samples were chosen from the collection of Florida International University, which contains laminated windshield glasses. The chosen 31 samples have a very similar elemental composition (22 could not be distinguished by LA-ICP-MS). For LIBS measurements, no ASTM standard method is available, thus the laboratories followed their own protocols, in case of the other methods the ASTM standards were followed. The laboratories examined the glass samples by LIBS, used the three-sigma match criterion based on elemental ratios, but the chosen emission lines (Si, Al, Mg, Ca, Na, K, Sr, Fe, Ti, Ba) were different. The interpretation of the results had significant differences between the laboratories based on their measuring and

evaluation procedures. By every method, there was false inclusion, but the highest rates were given by RI. In case of LIBS and XRF, this rate was lower and only in cases where the model/make/year of the automobiles were the same. Only XRF gave false exclusions in one exercise. This interlaboratory study pointed out that the evaluation of results is different in the countries, there is no standard procedure, which can be caused by differences in the law system, instrumentation, experience, and the presence or lack of a database [24].

Merk et al. applied a combined Raman/LIBS system for the analysis of automobile glasses and used multivariate data analysis for the evaluation. The sample set, which was collected from real cases, contained 16 samples (15 car windows and 1 bus headlight). Amongst the window samples there were laminated and security glasses as well. SEM-EDX and micro-XRF measurements were applied as reference. The authors applied PCA for the evaluation and used only a part of the spectra, in case of Raman the range of 70–3980 cm^{-1} (at 532 nm) and 50–1750 cm^{-1} (at 785 nm), in case of LIBS, the chosen range was 200–630 nm. LIBS emission peaks (Al: 308.215 nm, 394.401 nm, 396.152 nm, Ba: 455.403 nm, 493.408 nm, 614.171 nm, Fe: 238.204 nm, 259.939 nm, 260.708 nm, Mg: 277.983 nm, 285.213 nm, 518.360 nm, Sr: 407.771 nm, 421.552 nm, Ti: 323.452 nm, 336.121 nm, 337.280 nm) were transformed to standard normal distribution and used the center wavelength. For the evaluation of the discrimination, they calculated the decisive Mahalanobis distance for all methods. In case of LIBS, four principal components were needed and achieved a very good discrimination power, only 1 pair out of 120 pairs was indistinguishable. This value was somewhat poorer in the case of Raman (3 pairs were indistinguishable). The combination of the Raman and LIBS data set resulted in the same discrimination power as with pure LIBS data, but the distances between sample clusters were larger. The results of micro-XRF (98 distinguishable pairs) and SEM-EDX (25 distinguishable pairs) were much worse than the results obtained by LIBS and/or Raman [25].

In a freshly published article, Galbács et al. used multivariate chemometric data evaluation methods for LIBS data and combined LIBS and RI data in case of four types of glasses. The 127 tested glass samples belonged to the type of fused silica (optical glass), flint (crystal and optical glass), borosilicate (headlight shield and laboratory glass) and soda-lime (float, container, patterned and security glass) glasses. They applied four well-established multivariate statistical methods for LIBS data (linear discriminant analysis, quadratic discriminant analysis, classification tree and random forest) with and without data compression (principal component analysis). In case of the glass type classification six spectral lines, namely Ca I 422.7 nm, B I 249.7 nm, Pb I 405.8 nm, K I 766.5 nm, Al I 309.2 nm, and Ba II 455.4 nm were chosen. Soda-lime glass is the most common glass type and has a great practical importance thus this group was analyzed further. In case of RI measurements, significant overlaps can be observed between the data. LIBS data showed good repeatability; thus, the evaluation was carried out without normalization or scaling. LIBS spectra were separated into training and validation sets. The achieved cumulative accuracies for the training sets were between 89% and 93% for all four methods, the best results were given by random forest and linear discriminant

analysis methods. In case of the validation data sets, random forest (88.8%) surpassed linear discriminant analysis (85.9%). Lastly, the pairwise comparison was tested as well, where the final results were enhanced with RI pre-screening, this means if the match of the two samples was not unique but involved various database samples, a second step was carried out, which was the chemometric evaluation of LIBS data. The accuracy was around or above 80% for all methods and classification tree and random forest gave the best results, 95.0% and 93.5% [26].

9.2.2 Paint

Paint is an almost as common evidence as glass due to its widespread use. Paint appears in cases like hit-and-run accidents, traffic accidents, burglary, vandalism in the form of chips, smears, drips, splashes, and sprays. It is heterogeneous thus; the analysis of paints is challenging. Forensic scientists, therefore, apply several analytical methods for their examination, like microspectrophotometry (MSP), FTIR, Raman spectroscopy, SEM-EDX, micro-XRF, and LA-ICP-MS, but the first step is always the observation under a microscope, also analyzing the cross section [27–39]. In case of paint chips (a small piece of paint that has broken off of something and usually has a layered structure), indirect and direct physical match, as well as layer order, layer structure, and colors are to be determined.

One of the most analyzed paint samples are automotive paints, which occur in cases of hit-and-run accidents, car accidents, or intentional damages caused by a sharp object (e.g., key). This type of paint contains three main components (binder, pigment, solvent/additives), and the paint chips have at least 3–4 layers (primer, surfacer, basecoat, clearcoat). The binder is usually an organic polymer. Among the pigments, inorganic (black and white) and organic ones can be equally found. There are effect pigments (e.g., absorption pigments, metal effect pigments, pearlescent pigments) as well, which produce special optical effects (Fig. 9.2) [40].

McIntee et al. investigated the discrimination power of LIBS in case of automobile paint samples, which were taken from different manufacturers, models, and production years, and were separated into sets, based on their effect on pigment presence, color, and number of layers. It is important to mention that this study focused on comparison and discrimination of only the samples which had the same color, same number of layers, and similar presence or absence of pigments. For the sample preparation, they removed the paint chip from the substrate and mounted it on poly-isobutylene. Seven different colors, red, black, blue, tan, green, white (most difficult), and silver, were analyzed. They evaluated the $\log_{10}$-scale spectral intensities with nonparametric permutation tests and parametric Wald tests in order to determine the discrimination efficiency and Type I error. The results based on nonparametric permutation test gave an overall 89.83% discrimination power with 4.44% Type I error. The discrimination efficiency in case of inter-sample discrimination was almost 100% in all cases, except with black and white samples. In case of

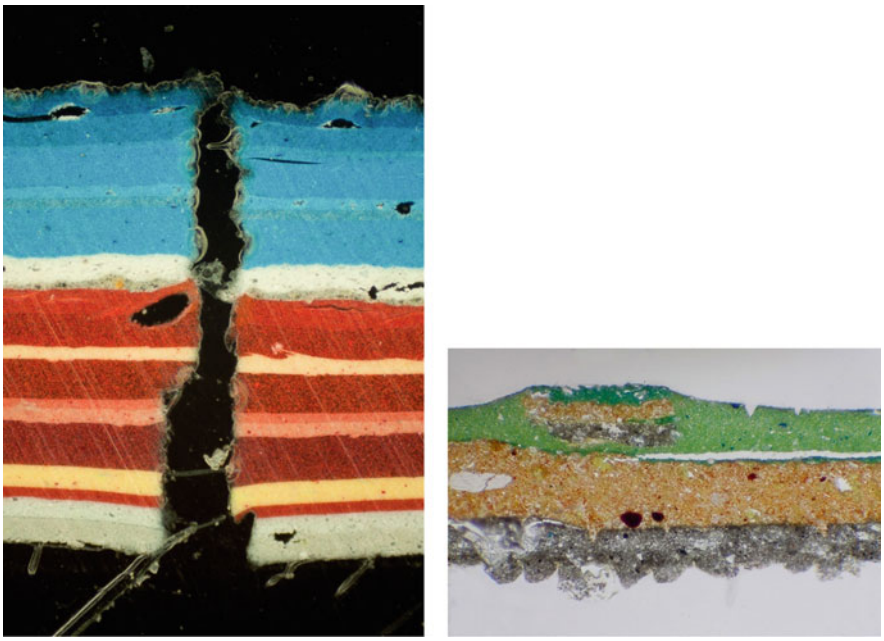

Fig. 9.2 Cross section microscope images of paint chips with a defined layer order. In the image on the left, both the known sample (right side) and recovered sample (left side) can be seen

red, tan, and green color groups, some intra-sample discrimination occurred. Parametric analysis achieved a lower discrimination power [40].

Sigman et al. also investigated the applicability of LIBS to the discrimination analysis of automobile paint samples. The applied methods were XRF, SEM/EDX, LA-ICP-MS, and LIBS. Two sampling approaches were tested but only the one deemed satisfactory and reproducible was later used. They used the "drill-down" procedure as McIntee et al. [40], meaning that they started to ablate the sample perpendicular to the clearcoat surface. The discrimination was performed by hypothesis testing at a 0.05 significance level using parametric and non-parametric statistical methods and Type I error was determined as well. In case of MANOVA (Multivariate Analysis of Variance) data analysis, the spectra were baseline corrected and 14 wavelengths were chosen. They also selected different paint groups based on color (black, blue, green, red, silver, tan, and white), layer number, and pigments. The total number of analyzed samples was 200 but not all of them were analyzed by every analytical method. LIBS had a discrimination accuracy of 90% (10% Type II error) at 5% Type I error rate, but among the white group this value was a little lower, only 86.6%. Comparing the results with the other methods, only LA-ICP-MS (100%) gave better values, XRF and SEM-EDX gave lower, 85%, and 73% discrimination accuracy. For discrimination, they choose 14 emission peaks for MANOVA test and it gave 84.4% discrimination accuracy. When they used the

whole LIBS spectrum and applied the HQI or Z® similarity metric, they achieved 89.8% discrimination accuracy [41].

9.2.3 Paper and Ink

During the course of questionable document analysis, be it printed, copied or handwritten document, forensic scientists examine both the paper and ink (which can be a solid, liquid, pen ink, etc.). In this examination, the subject of study is the dating, paper, document alterations, erasures or obliterations, signature authenticity, examination of typewriting and authenticity. Beside the physical characteristics, the chemical composition of the paper and ink are examined as well. The most important aspect is the identification and discrimination of the chemical composition of inks and paper, to which the applied analytical methods are FTIR, Raman, XRF, LA-ICP-MS, MS, GC-MS, SEM, SEM-EDX, TLC, CE, and HPLC [42–62]. Ink formulations generally contain two main components: the colorant (dyes or pigments) and the carrier (oils, solvents, resins), but many other components like driers, plasticizers, waxes, greases, soaps, and detergents can also occur (Fig. 9.3). The examination of inks is challenging not only due to their complex composition, but also because, e.g., liquid inks penetrate the paper, thus a combined spectrum is recorded.

Elsherbiny and Nassef studied the wavelength dependence (532 and 1064 nm) of LIBS results for questioned document analysis, especially in the case of black gel inks (30 samples from 10 brands were tested). Gel pen inks are the most examined pen types in forensic science. This kind of ink, especially in black color, is difficult to tell apart by conventional methods (e.g., IR and Raman spectroscopies); thus, the aim was to test the discrimination power of LIBS for individual pens and for brand and batch variations. Because the ablation of ink and paper takes place in parallel, therefore the spectrum of the clean paper was always subtracted from the spectrum of

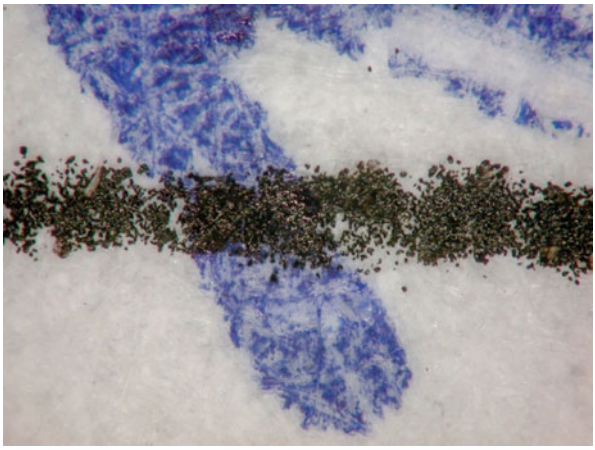

Fig. 9.3 Microscope image showing an intersection of laser printed and ballpoint ink marked lines

inked paper. Relative standard deviation was calculated for three spectral lines, which gave rise to a value of 8.44% for Cu I 327.4 nm, 7.88% for Cr I 359.4 nm, and 8.67% for Mn II 250.6 nm. The discrimination was based on the appearance of Mn, Ni, Cr, Cu, and/or Mg lines and 88% discrimination accuracy was achieved. In case of the NIR wavelength, the same pulse energy was not enough to achieve as good SNR than in the case of 532 nm, it had to be increased. With the higher pulse energy, they could achieve 91% discrimination accuracy. After the LIBS analysis, they recorded SEM images of the ablation craters and found that at 532 nm, the craters are deeper than at 1064 nm. The study concluded that there is no big difference between the discrimination power of the two wavelengths, both can be applied effectively [63].

Cicconi et al. did a detailed study on papers and ink, where four sets of samples were compiled with separate research goals. The first set contained 14 commercial ballpoint inks (8 black, 4 blue, 1 red, and 1 green) which were used only on one type of office paper. They identified Ca, Si and Al in the paper and Cu, Zn, Mn, Ni, Pb, Fe, and Cr in the inks. Not all chosen elements were observable in every inks. Finally, 19 lines were selected for further evaluation, a signal normalization scheme based on carbon was used. Principal component analysis (PCA) and linear discriminant analysis (LDA) were used and they could distinguish all black inks. The second set contained 8 black pens from the first set, but here 10 different paper types were tested (printing papers, notebook papers, envelopes, and recycled papers). The evaluation was more difficult due to the differences in the ablation characteristics of different papers. Using four PCA components, they could completely separate four inks, and with a further PCA component, they could separate one more ink from the others. PCA plots showed greater scatter than in the first case, where only one paper was used. By the use of LDA, four inks could be correctly classified (the same four as with PCA when using four variables). In summary, the overall ink discrimination power decreased from 100% to 89% when they occurred on different papers. The third set contained a former blind test's samples, three ballpoint pens, and one gel pen and two pieces of printing paper. In this set a further aim was to determine the chronological order of deposition of the inks in case of four lines. First, the paper and the three inks were analyzed in a pure spot to get the individual spectra from all samples. With the applied method (ratio of peak intensities), the determination of chronological order was successful in four cases out of six. With the help of PCA, they could not significantly improve the success rate. What makes this analysis difficult is that the ablation depth may be different for different inks (e.g., varying portion of the two layers would co-ablate). The fourth set was also a former blind test, which contained three printed pages with three signatures made with different pens. The aim, in this case, was to verify if all the signatures were coming from the same pen and if the toners were the same or not. It was possible to establish that from two pages out of three were printed using different toners and on the second page the signatures were different from the other two pages [64].

Hilario et al. tested the efficiency of LIBS combined with chemometrics in the field of hand-written documents. The examined sample set contained 6 black and 11 blue ball-point type pens from different manufacturers. The applied paper was a

cheque paper from a bank and the aim was to differentiate between similar colors. ICP-OES was used for reference measurements, after digesting the inks with a single reaction chamber microwave oven. Based on the needs of daily forensic routine, only a small number of pulses were used. For the discrimination of similar colors, PCA was applied on the whole spectrum. This combination did not give a good differentiation, so the average spectra were analyzed first and from those different spectral ranges were chosen for the discrimination (the best were 212–228 and 324–328 nm, where the atomic emission lines of Cu are located). After this comparison, a real situation test was performed. Using a pen, the number "10" was written on the paper and another "0" was added with a different pen of the same color. Based on the difference in their Cu concentration, LIBS was able to distinguish between the pens (their inks) [65].

Oujja et al. used LIBS for the identification of inks and structural characterization of contemporary artistic prints. They used two types of model prints on paper. The first layer of ink was applied on the paper and the second was overlaid onto the first layer. The chosen colors were black and blue based on their prevalence. The elemental composition of prints was obtained from their manufacturer. In the study, first LIB spectra were recorded for the substrate and for the individual inks on the substrate in order to successfully identify when the ablation of a new layer of ink had started. LIBS was able to differentiate between the same colors [66].

Sarkar et al. tested the discrimination efficiency of LIBS for the identification of different types of paper. Their aim was to perform an instant identification of confidential documents based on a LIBS spectral library which contains spectra of papers used for government work. For the study, they used papers of the Department of Atomic Energy (DAE, India). They had a collection from the past 10 years and these 10 papers were the base of the sample set. Because of the same main components, statistical methods were needed for the discrimination. The achieved discrimination accuracy was near 99% with linear correlation and non-parametric rank correlation [67].

Kula et al. examined inks from 34 blue, 30 black, and 21 red writing instruments (ballpoint pens, gel pens, porous pens and rollerball pens) with LIBS. The manufacturers were from different countries (USA, France, Japan, Korea, and Poland) and different kinds of papers (five brands made by three producers) were also tested. During the optimization of the setup was found that the first laser shot already penetrated through the ink and ablated the paper as well, thus it was decided to scan the ink lines and to make an average spectrum. The repeatability of signal intensities was poor and it was attributed to the laser intensity fluctuations and sample heterogeneity. After paper analysis it was determined that there are only quantitative differences between the tested papers, the elemental composition of them is almost the same, thus only one paper was selected for further analysis. Spectral ranges were selected which were relatively free from the paper spectrum (320–420 nm, 505–530 nm, 560–600 nm, 660–715 nm). In case of ink analysis, the researchers started with the examination of intra-ink variation. For these experiments, 8 blue ballpoint pens, 3 black gel pens, and 3 red gel pens were chosen and no significant differences were found between the same brand and manufacturer.

The paper spectrum was subtracted from each sample spectrum, in which they assigned spectral lines to belong to Cr, Ba, Fe, Cu, Li, Mn, Mo, Ni, and W. Based on the elemental composition, 10 groups could be formed from blue samples. In case of black inks, 11 groups could be made. The discrimination power was calculated as the ratio of the number of the discriminated pairs to the number of all possible pairs of inks of a given color. The achieved discrimination power was 83%, 82%, and 61% for blue, black, and red inks. An inter-laboratory test was also performed where they had to analyze three writings, out of which two were made with the same ink. The identification was made possible by the detection of Cu lines, which were only present in the spectrum of two samples [68].

Printing inks were analyzed by Subedi et al. by a tandem LIBS and LA-ICP-MS system. They analyzed the inks of 9 black laser toners, 10 colored inkjet samples, 12 colored offset samples, and 12 intaglio inks from different manufacturers. In case of black inks, numbers and letters were printed, and in case of the colored inks, a test page was printed where all the colors could be found individually. The offset samples were collected from Lincoln visa (printed form) and as a paste and intaglio inks from banknotes. Beside LIBS, LA-ICP-MS and a tandem LIBS/LA-ICP-MS system were also tested. Based on LIBS spectra, they concluded that the inkjet set contains less elements than toners, offset, and intaglio. For example, Li was only detected in inkjets that contained Na and K as well. Toners contained Na, K, Ca, Mn, Fe, Ti, Zr, Nb, Sn, Hf, and Sr. The quantitative analysis was challenging because no standard is available for inks, thus standard solutions were used. LIBS was found to well supplement LA-ICP-MS, because LIBS was able to discriminate samples via the detection of Na, Ca, K, and Si, elements not easily measurable by ICP-MS. The tandem setup increased the discrimination efficiency in all cases [69].

Król et al. studied the elemental composition of polish banknotes by XRF and LIBS. They analyzed banknotes printed before and after 2014 by the National Bank of Poland. All experiments were done without any sample preparation and several areas (microlettering, serial number, Romanesque rosettes, crowned letter, rosette, metallic overcoating) were examined and they found out that no pure paper can be found on the old banknotes. After the optimization of the laser parameters, they tested the repeatability between various sample areas as well, and found it to be between 11.1 and 41.6%. After these results, they decided to average the measurements and in one measuring area they moved the sample only slightly. The spectrum of the banknote paper was richer than the office paper, with assigned lines of Ti, Ca, Na K, Al, and Cr. They investigated the influence of contamination on the LIBS spectra too and found that while the spectra of brand-new banknotes did not differ from each other, but those of used banknotes did. Generally, considering the whole area of banknotes, the following elements were identified: Ca, Fe, Ti, Ba, Co, Cr, Cu, Mn, Ni, Zr, Mg, and V. Only Mn could be found on all of the banknotes. In case of old banknotes, Ba was not detectable, whereas from new banknotes Fe, Cr, Cu, Ni, and V were absent. For some areas, XRF gave a richer spectrum and LIBS for some others. Based on statistical analysis (Kruskal-Wallis one-way analysis of variance by ranks), the black serial number area was determined as the most discriminatory part of the banknotes. After the original banknotes' analysis, a case

study was performed where four different specimens of 10, 20, 50, and 100 złoty notes were examined which were suspected to be counterfeit. In all cases, they could discriminate between counterfeit and authentic ones. Based on the spectra, it was noticeable that the investigated "banknotes" were printed onto an office paper. They could not find Co, Cr, and Ni lines, but found Al which confirmed that the four samples were counterfeit [70].

In a study by Metzinger et al., papers and print types were discriminated based on their LIBS spectra. In this study, 54 samples were analyzed, six different kinds of paper (office paper, color paper, non-bleached paper) and eight printers (color and black inkjet and laser printer). For data evaluation comparative functions like linear correlation coefficient (LCC), overlapping integral (OI), sum of squared deviations (SSD); and advanced statistical methods such as multivariate curve resolution (MCR-ALS), decision tree (CT), and discriminant analysis (DA) were tested. Based on the LIBS results, 2048-element data matrices were used for the evaluation, both for UV and Vis spectral range (channels). The discrimination power was tested using the individual channels and also using the combination of the two. Microscopic images were taken before and after the laser shots. In these images, we observed that compared to inkjet printing, where both the ink and paper were ablated, in case of laser printers the laser beam only had an influence on the toner layer (Fig. 9.4). The ablated spot was much larger than the toner particles or ink droplets, thus the sampling could be considered to be representative. The approach was to first identify the paper type, then the printer. In this case, at least two LIBS spectra are needed, one for the pure paper and one for the printed area. When applying the advanced statistical methods, only one LIBS spectra was used. The statistical evaluation was done without any background correction. In case of comparative functions, masking and data reduction were also applied. With the use of a spectral mask, only the spectral range parts were retained which contained useful information for discrimination, the most varying parts of the whole spectrum. In the case of papers, the comparative functions were only able to discriminate one paper, which had the most homogeneous structure, the others were found to be indistinguishable from each other. Based on these results, the discrimination of prints was performed only at the above-mentioned homogeneous paper. Laser printers could be reliably discriminated from each other and from inkjet printers as well, by using all functions, but SSD gave the best results. LC had the best repeatability values and all functions had a better performance in the UV range. In case of inkjet papers, the discrimination power was poor due to the fact that the ink penetrated into the paper. In the case of DA and CT, prior data compression was performed by the MCR-ALS method. The discrimination power for DA and CT was 96.3% and 83.3% (UV), 88.9% and 60.4% (Vis), and 83.3% and 70.8% (UV-Vis) for papers and print. Results obtained with MCR-ALS-CT were the following: 83.3% and 59.3% (UV), 68.5% and 59.3% (Vis), and 77.8% and 51.9% (UV-Vis) for papers and prints, so the UV range had better discrimination power [71].

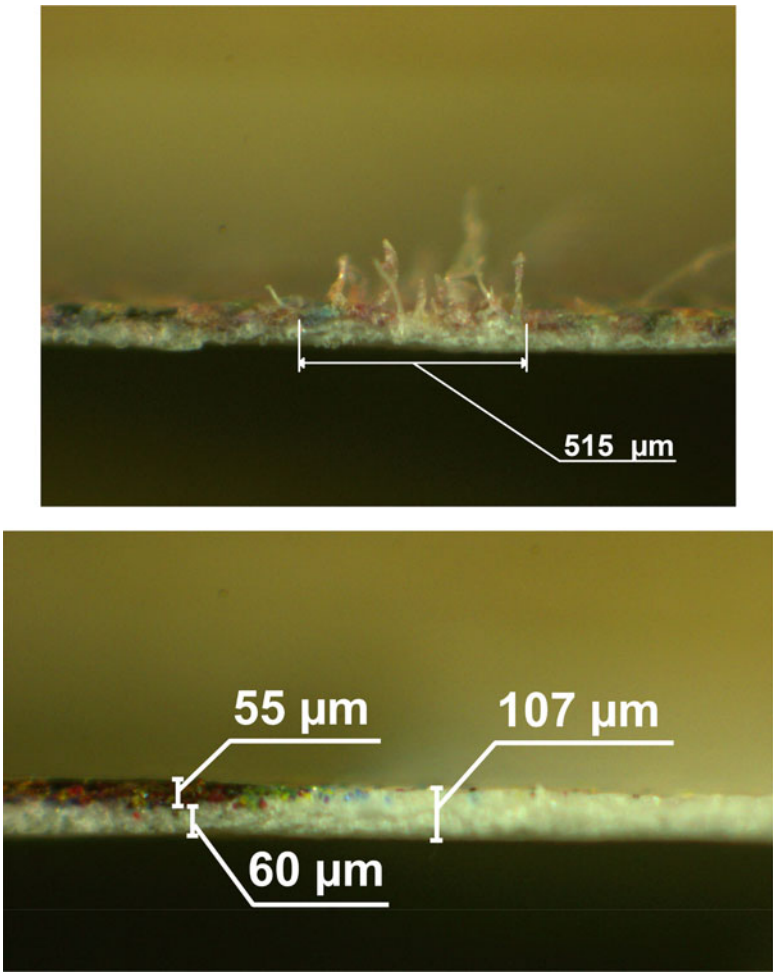

Fig. 9.4 Cross-sectional microscope image of printed papers (above: inkjet printer, below: laser printer) after laser ablation

9.2.4 Adhesive Tapes

Discrimination of different kinds of adhesive tapes is also an important task of forensic investigations. The residue of a wide variety of adhesive tapes can occur in drug cases, kidnapping, rape cases, and explosions. The main components of adhesive tapes are the adhesive layer and the backing layer, which composition depends on the application. In the case of packaging tapes, the backing is usually polypropylene or polyethylene. Duct tapes contain an additional strengthening mesh layer that can be made from cotton, polyester, nylon, rayon, or fiberglass. Adhesive tapes also contain several additives such as colorants, fillers, cross-linkers,

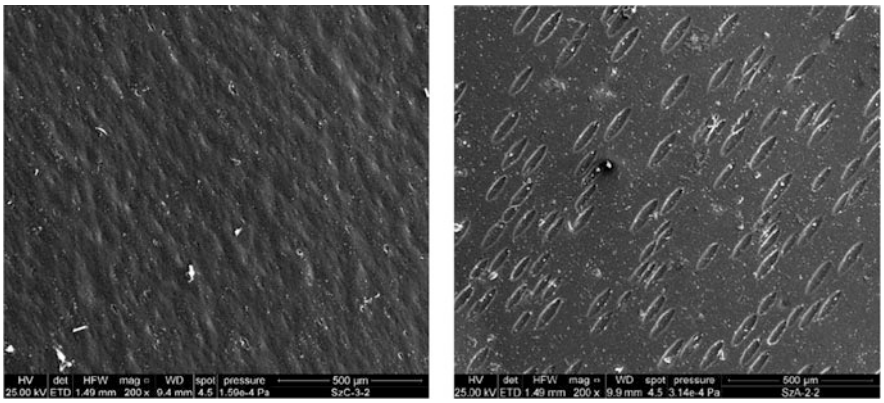

Fig. 9.5 SEM images of electrical tapes from different brands. Differences between the surfaces can be well observed

plasticizers, and stabilizers. Typically, forensic scientists have to compare the adhesive tape residue secured in the crime scene with known samples seized from the suspect. For this purpose, several analytical methods, such as XRF, SEM-EDX, pyrolysis-GC-MS, FTIR, Raman, and LA-ICP-MS, can be used [72–80]. These methods are needed only if no significant difference can be seen between the objects under an optical microscope (Fig. 9.5).

Martinez-Lopez et al. investigated the elemental composition of packaging tapes by LIBS and LA-ICP-MS. The measured sample set contained eight packaging tapes from two countries and six manufacturers. Emission spectral lines were chosen for the study which had no known interferences but could be measured with a good repeatability and large SNR. For the discrimination, three comparison methods were tested: spectral overlay, two-component principal component analysis (PCA) and comparison criteria. For PCA and spectral overlay, the integrated peak areas were used. In the case of PCA the following atomic emission lines were chosen: Ca 422.7 nm, Cr 520.6 nm, K 766.5 nm, Li 670.8 nm, Na 589.0 nm, Ti 334.9 nm, and Zn 481.1 nm. Three different comparison criteria were applied (range overlap, $K_{\text{mean}} \pm 4\sigma$ and $K_{\text{mean}} \pm 5\sigma$). In the case of spectral overlay, first a spectral normalization was applied and the presence or absence of the chosen seven emission lines was observed. Only two samples were indistinguishable from each other. The normalization was found to be very important with regard to the outcome. In case of comparison criteria, the best results were achieved by using the $K_{\text{mean}} \pm 5\sigma$ criterion. Just by using the spectral overlay, with the best comparison criteria the same two samples were undistinguishable after normalization. Before normalization four sample pairs were not distinguished. To compare the results of LA-ICP-MS and LIBS based on PCA, it can be declared that both techniques formed the same groups, contained the same samples and the others were grouped individually. In the case of LA-ICP-MS all the samples could be discriminated from each other based on the presence of Nb, Fe, and Zr, but LIBS found two samples indistinguishable. Overall,

LA-ICP-MS could distinguish all eight samples, while LIBS could only do seven. The RSD was under 10% in both cases [81].

9.2.5 Fingerprints

Fingerprints are among the oldest subjects of forensic examination. The human finger has a series of ridges and furrows whose arrangements have a significant variation and this allows their identification (Fig. 9.6).

Fingerprints are the impressions left on surfaces by the friction ridges on the finger of a human. Fingerprints have three types: visible (print left by an ink-coated finger), plastic (a mechanical impression in wax or another soft material), and latent (impression of oils from the finger on a surface). Traditionally, fingerprint is detected and collected with the application of "fingerprint powder." The dusted fingerprint can be lifted with an adhesive plastic sheet and evaluated by eyes. The forensic scientist marks the ridges, furrows, arches, loops, and whirls and compares the known sample and the fingerprint found on the crime scene by eyes under a small magnification microscope or with a software.

Taschuk et al. tested LIBS for the detection and mapping of latent fingerprints. The test fingerprints were made by one of the authors (right thumb). First, the thumb was brushed against the forehead and then rolled against a previously cleaned Si substrate (wafer). Silicon was selected as a substrate because it has a smooth surface and a strong emission line in the spectral range detected. Sodium was expected to be detected and for each laser pulse. Na I 589.2 nm and Si I 576.2 nm signal-to-noise ratios were calculated. For the 1D analysis, they collected 100 spectra with 50 μm step size along a 5 mm distance. In the case of 2D analysis, a 1 mm by 5 mm region was tested. They demonstrated that latent fingerprints can be detected and mapped by femtosecond micro-LIBS, but this method has many difficulties (damaged fingerprint, re-deposition of ablated materials, detection time, to produce a whole fingerprint, the elemental composition of the substrate) and needs to be investigated further [83].

Fig. 9.6 The six common fingerprint classes [82]

Yang and Yoh used LIBS for the reconstruction of chemical fingerprints that were time-delayed and overlapped. For the sample preparation, fingerprints were collected on aluminum plates from four men. The overlapping fingerprints were made with 10-, 20-, 30- and 40-min time delay. The LIBS analysis followed the sample preparation immediately to avoid any environmental contamination. For validation Raman scattering was used. To detect the latent fingerprint, one LIB spectrum was constructed from the average of 100 spectra taken at individual points of the latent fingerprint. Based on NIST atomic database, CN molecular lines and Mg, K, Na, and Ca atomic and ionic lines were assigned. It was postulated that CN bands are good indicators of time-delayed aging. Because of drying, dehydration, degradation, and migration, the number of double and triple CN bonds increases over time. Based on this statement, only the 384–390 nm spectral range was observed. The assumption was confirmed by LIBS, as the spectra showed a slight increase over time (150% increase after 60 min). Several organic components were detected in the fingerprint by Raman measurements, such as glycine, serine, acetic acid, aspartic acid, pyruvic acid, and lactic acid. Raman measurements confirmed the increase of the number of double and triple CN bonds. After 60 min, the intensity of amino acid, fatty acid, oil and CN band did not change. Two multivariate analysis methods, PCA, SIMCA, and PLS-DA were successfully applied to classify the latent fingerprints in the correct time of imprints (>90% accuracy), when the source was the same. With the help of the aging factor and the multivariate methods, they could successfully reconstruct overlapped fingerprints [84].

9.2.6 Gunshot Residue and Ammunition

Gunshot residues (GSR) is "The total residues resulting from the discharge of a firearm. It includes both gunpowder and primer residues, plus metallic residues from projectiles, fouling, etc." It is a mixture of organic and inorganic materials [85]. The origin of GSR can be the primer, propellant, lubricant, bullet, bullet jacket, cartridge case, or gun barrel. The presence of GSR on a person's hand shows that this person fired a gun. The general aim of GSR analysis is the identification of the potential shooter, the determination of firing distance, and to determine if the case is a homicide, suicide, or an accidental shooting. Because of the complex composition of the gunpowder and the cartridge, organic and inorganic GSR can be found as well [86]. Organic GSR can originate from explosives, gunpowder, and additives, and inorganic GSR can originate from the primer and the combustion of the propulsive charge [87]. At the moment, SEM-EDX combined with a special software is used for the search and analysis of inorganic GSR particles, when forensic scientists looking for particles that are a combination of lead, barium, and antimony with a spherical morphology. For organic GSR the most applied methods are liquid chromatography coupled to a mass analyzer (LC-MS), capillary microextraction of volatiles-gas chromatography-mass spectrometry (CMV-GC-MS) [88], and capillary electrophoresis (CE) [88, 89]. The identification of ammunition is usually done by matching

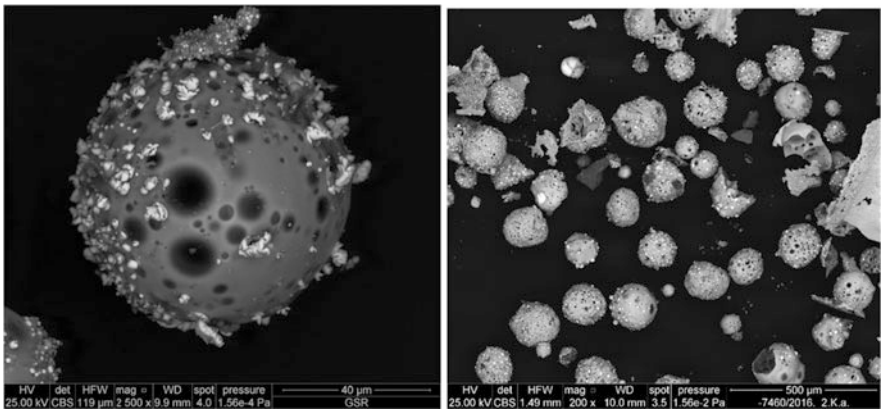

Fig. 9.7 SEM images of gunshot residue particles

striation patterns. An alternative approach can be elemental analysis, because often only fragments are recovered (Fig. 9.7).

Goode et al. applied LIBS for the detection of gunshot residue on the skin of the shooter. For sample collection, they used a double-sided adhesive tape which was pressed to the hand of the shooter and then directly analyzed. Three different situations were evaluated, (*a*) clean hand (blank), (*b*) the shooter's hand (after 1, 3, and 10 shots), and (*c*) from the shooter's hand, but after washing with soap. In case (*a*) only sodium, calcium, and atmospheric lines were identified in the LIBS spectra, whereas in case (*b*) barium and lead emission lines were also found. After washing the hand with soap and water, GSR could be still detected by LIBS, but with a highly decreased intensity [90].

Dona-Fernandez et al. investigated the applicability of LIBS in the real-time detection of GSR particles and they compared the results with SEM-EDX. For the experiments, a newly developed portable LIBS system (iForenLIBS by Indra Systems) was used. The aim of the development of this equipment was to reduce the collection and analysis time of GSR. The advantage of this system is that it is applicable in the field (on the crime scene) to various substrates like stubs, cotton swabs, etc. and that the analysis time can be reduced. Samples were collected from "no shooters," police officers, uniforms of police officers and materials from a scene evidence collection carried out according to international standards. The whole sample set represented many different scenarios (e.g., handling firearm without or after shooting, after making one or more shots, before and after handwash, etc.). The first step was to analyze all the samples with SEM-EDX and divided into groups (number of GSR particles: >100, 100–21, 20–11, 10–4, 3–1, 0), based on the number of GSR particles on the samples. The average percentage of the analyzed sample surface was 41%. The average number of shots to get true positive results (varied between 16 and 98) was inversely proportional to the number of GSR particles containing the sample. Out of 90 samples, LIBS could correctly identify 82. In cases where the stubs contained at least three characteristic GSR particles,

LIBS had a 100% success rate. In the case when the number of GSR particles was between one and three, LIBS gave five false negative results and three false-positive results in the group which contained samples with zero GSR particles. After re-analyzing the 22 samples with SEM-EDX (after LIBS measurements), it was established that all particles under 2 μm diameter were completely ablated by laser-generated plasma. If the particle size was larger than 1 μm, the detection of single GSR particles was stated possible [91].

Rosenberg et al. investigated GSR on the hand of a shooter using LIBS. Their aim was to determine the duration of time after the shot was taken until the GSR is still detectable. For the GSR collection, they used 3M 5490 PTFE extruded film sealing tape and pressed the tape multiple times to the person's hand. A blank library was created with the help of 25 volunteers. Three shooters shot six times and after that only one shooter was chosen for sample collecting. After the shot, shooters were asked not to wash their hands for 1 week, when a sample was taken again. Because the spatial distribution of GSR particles is heterogeneous on the hand and therefore on the tape, LIBS signal averaging across an area will cause a signal dilution and a decrease of the signal-to-noise ratio. For this reason, a protocol had to be introduced, which was based on the net intensity of the Ba 455.403 nm emission line; if it was greater than a certain calculated signal detection limit at any location, then the sample was considered positive. Applying this evaluation protocol to a tape area, it was found that the results become inconsistent after 120 h, but if only one laser pulse was applied, the lifetime (validity) of the GSR extended to 192 h. An exponential decay model was also proposed, and it projected the lifetime to be about 126 h. Naturally, this time depends on the instrumentation, experimental conditions and the life conditions of the shooter [92].

Tarifa and Almirall investigated the possibility of fast detection and characterization of organic and inorganic GSR on the hands of suspects by CMV-GC-MS and LIBS. They collected samples from hands (of shooters, of police officers after shooting, of non-shooters from the campus) with moistened double-sided cotton swabs. ICP-OES was chosen as a reference method for the confirmation of the presence of Ba, Pb, and Sb. In case of LIBS, calibration curves were generated (0.5–300 ppm) for all target elements chosen from literature reports (Al, Ba, Ca, Co, Cr, Cu, Fe, K, Li, Mg, Mn, Na, Ni, P, Pb, S, Sb, Si, Sn, Sr, Ti, Zn, Zr). The obtained absolute LODs were between 0.071 ng and 18 ng, with the exception of P (33 ng). In the blank cotton swabs, the following elements were detected: Al, Ba, Ca, Fe, K, Mg, Mn, Na, and Sr. Samples from the non-shooters contained Al, Ba, Ca, Cr, Cu, Fe, K, Li, Mg, Mn, Na, Ni, P, Pb, S, S, Sr, Ti, Zn, and in two cases also Pb, because these persons worked on a construction site at the time of the sampling. In the samples taken from nine police officers, LIBS detected both Ba and Pb in six cases. The combination of organic and inorganic results gives a more effective discrimination, because the organic analysis can confirm the presence of diphenylamine and nitroglycerin in all cases where Pb and Ba were found. Beside Ba, Pb, and Sb, other elements like Cu, K, P, and Ni were also proposed to be an indicator of GSR, because the quantity of these elements on the shooters' hands was more than double of what was found in samples taken from non-shooters [88].

Silva et al. used a screening analysis method for the detection of GSR by LIBS. With the help of 9 volunteers, they accomplished 51 tests of shots, where the number of shots varied from 1 to 5 and 12 types of ammunition were tested. For the sample collection, an adhesive tape was used by pressing the tape (pressing and removing the same piece 10 times) to the volunteer's hand (dorsal region) after every shot. They also investigated the persistence of the GSR on hands after washing them (after 16 h). For this sample collection, a liquid polymeric resin was used. For the blank sample collection, they asked 15 volunteers, who had never shot a weapon in their life, to help. The false-positive results were also tested by collected samples from three brake mechanic's hand. Five spectral regions, with Ba and Pb lines, were chosen for the evaluation and the spectra were normalized to the maximum intensity. No background correction was employed. Unfortunately, Sb was not detectable in the spectra. In the case of non-shooters, only Ca, Na, and K were detectable. In the spectra of shooters, intense Ba and Pb lines were observed, but Ca and Na were still detectable. After washing the hands, Pb and Ba were still detectable but less intensely. No difference was observed in the efficiency of the two sampling methods (tape and resin), but the applicability of resin is more difficult, time-consuming, and the surface of the resin is more irregular. In case of brake mechanics, intense Ca and Ba lines were observed, but Pb was missing from the spectra. SIMCA classification was successfully implemented. All samples collected from shooters (before and after washing their hands) were correctly classified, without any false negative results. The samples from brake mechanics were also included in the shooter class, but the samples from non-shooters were not classified as shooters. It was concluded that contaminations on the hand in some professional activities can produce a false-positive result, thus the analysis needs to be complemented with SEM imaging [93].

9.2.7 Soils

The soils' physical, mineralogical, biological, and chemical properties differ significantly on different geographical locations, so soil traces are useful and well-known evidence. Unfortunately, the basic physical and chemical properties (color, particle size distribution, carbonate content, etc.) of soils do not have enough discrimination power. The analysis of the mineralogical composition is a relatively long and complex procedure. From a microbiological point of view, soil traces are often contaminated during transfer and can also change during the time that elapses between the sample collection and trial. In contrast to this, the elemental profile of soil is stable over time. Trace, minor, and major elemental components of soil samples from minerals, organic and anthropogenic materials contribute to the characteristic elemental profile of each geographical location.

Jantzi and Almirall performed a discrimination study and concluded that samples removed from different sites can be discriminated on the basis of elemental profiles obtained by both LIBS and LA-ICP-MS using statistical techniques. For quantitative analysis, calibration standards were prepared using clean sand spiked with a wide range of concentrations of elements. The homogenized soil and standard samples

were pelletized, the intensity of emission lines was background-subtracted and normalized to the internal standard line of Sc II 361.4 nm. Precision of the concentrations obtained with LIBS compared well to the precisions observed for LA-ICP-MS. Although LIBS limit of detection values are approximately two to three orders of magnitude those of LA-ICP-MS, the LODs of both methods were well below the certified concentrations in NIST reference soil materials. For discrimination studies, the following emission line ratios chosen were: Sr II 421.6/Ti I 336.1, Ba II 493.4/Mg I 517.3, Ca I 643.9/Mg I 518.4, Fe I 495.8/Mg I 518.4, and Li I 610.4/Mg I 517.3 nm. The LIBS method successfully discriminated samples from two different sites in Dade County, FL. Analysis of variance, Tukey's post hoc test, and Student's *t*-test resulted in 100% discrimination with no Type I or Type II errors. Principal components analysis (PCA) resulted in clear groupings of the two sites and a correct classification rate of 99.4% was obtained with linear discriminant analysis (LDA) as well [94].

Woods et al. investigated the efficiency of different elemental analysis methods for forensic soil examination. They tested three methods, namely LIBS, XRF, and SEM-EDX. The sample set contained surface and sub-surface soil samples from 9 sites around the Canberra area and from 17 samples stored in the CSIRO National Soil Archive (Australia). The soil specimens were oven-dried, lightly crushed and dry sieved. The <38 μm fraction was used for analysis without any other separation procedure. The analysis was performed on compressed soil discs made from 10 mg sample. The discrimination analysis was performed based on using elemental peak ratios proposed by Jantzi and Almirall in [94]). These peak ratios resulted in 31 indistinguishable pairs out of 406 (92.4% accuracy). The majority of pairs indistinguishable by LIBS originated from Canberra (in 30 km diameter) soils (18 indistinguishable pairs out of 66; 72.7% accuracy). The other two tested analytical methods showed slightly higher discrimination power: XRF 98.5% (five indistinguishable pairs), SEM-EDX 99.5% (two indistinguishable pairs) [95].

Jantzi and Almirall introduced a new preparation technique for small amount samples. Soil specimens from Miami–Dade County (FL, USA) were prepared with the pellet and the adhesive tape mounting methods. For this study, a home-built LIBS system was used. During the adhesive tape mounting method, the samples were sieved (150 μm pore size), mixed with spiked calibration standards and reference materials, were affixed with Scotch removable poster tape onto a glass cover slip. All samples were analyzed by both LIBS and LA-ICP-MS. The precision of the tape-mounted specimens analyzed by LA-ICP-MS was better than by LIBS, but the LIBS method provided a sufficient level of precision for forensic comparisons. The main technical problem was the thin layer of soil, which only tolerated only a few laser pulses at the same spot, therefore a line scan was applied instead. During the pellet-mounting procedure, pulverizing by a ball mill or shaking and homogenizing using a vortex touch mixer was tested. The vortex touch mixer seemed to be a better solution, because it was faster and broke up the aggregated soil, so the texture and mineral structure remained unaltered. At last, the precision (RSD %) for non-milled soil was better in many cases, than for the milled soil. The following emission line intensity ratios were used for discrimination: Ca I 643.9/

Fe I 360.9, Cr I 360.5/Sr II 421.6, Fe I 495.8/Li I 670.8, and Ba II 493.4/Fe I 360.9. Using these ratios, the authors got nearly identical results with the different (pellet/tape-mounting) sample preparation methods. The discrimination power was higher than 94% in both cases with multivariate discrimination analysis. The new, speedy, and non-destructive preparation technique consumes only a small portion of the soil in the analyses. In addition, the tape-mounted soils can even be stored and re-analyzed later by other analytical techniques [96].

Xu et al. combined and tested LIBS and FTIR-ATR for forensic soil analysis. The 100 soil samples used for the study were collected from five major regions of China. The sample preparation method was sieving (<2 mm) and pelletization. The atomic and/or ionic emission lines of Si, Mg, Al, Ca, N, O, and K were selected for the statistical analysis. In the case of FTIR-ATR study, the following bands with high FTIR-ATR intensity variations were selected: O–H stretching, O–H/N–H stretching (carboxyl, alcohols and phenols/amine and amide, hydroxyl groups), C=C/C=O stretching (amides, COO−/aromatics/O–H stretching), CO_3^{2-} (carbonates), Si–O stretching (silicates), NH_2 out of plane (primer amin). Based on combining the PCA analysis of raw LIBS and FTIR-ATR spectra the main soil type of China's five major regions could be clearly distinguished from each other. Furthermore, the authors also presented an application of the method to two case studies connected to drownings after falling into a river, which demonstrated that the method can not only be used on soils, but also on recent sediments [97].

9.3 Conclusions

As the publications prove, LIBS is a feasible and practical alternative to LA-ICP-MS, micro-XRF, and SEM-EDX for almost every kind of physical trace evidence. LIBS needs less sample preparation, analysis time, and cost of examination, and it is easier to use. These are very important characteristics in forensic science. The most investigated samples are inks, papers, and glasses and there are a few studies on adhesive tapes, textile fibers, paints, geological and biological samples too. In case of glass analysis, LIBS results can be successfully combined with other techniques like Raman and refractive index measurements. These publications also have shown that more systematical and extensive research is needed. There are no standardized evaluation methods yet, usually the pairwise comparison is applied. The most applied statistical methods used in comparisons are principal component analysis, linear discriminant analysis, and Student's *t*-test. There is no consensus that for the evaluation of the net peak area, net peak intensity or net peak high should be used or the whole spectra. In some publications, scientists are using background correction or masked spectra. Of course, these decisions were made based on the results, but it is not easy to compare the different results because no fixed evaluation method yet.

Another field to be explored is the sample size. In most cases, glass, paint, ammunition, and adhesive tape experiments are done with "macro" sample sizes and not with a sub-mm sample size. In real life, forensic scientists have to examine

the above-mentioned sample types usually in the μm size range. To determine the smallest sample size which is measurable by LIBS, further experiments are needed. The determination of the smallest measurable sample size is crucial also because forensic scientists have to keep the evidence for further analysis. It can also be mentioned that at present there are no ASTM standards available for LIBS as opposed to micro-XRF, SEM-EDX, or LA-ICP-MS analysis. Nevertheless, LIBS definitely has a good potential for becoming an analytical method routinely applicable in forensic science for the examination of physical trace evidence.

References

1. Hark RR, East LJ. In: Musazzi S, Perini U, editors. Laser-induced breakdown spectroscopy. Heidelberg: Springer; 2014. p. 377.
2. Jedlinszki N. Dissertation. University of Szeged; 2011.
3. Galbács G. Dissertation. Hungarian Academy of Sciences; 2012.
4. Rusak DA, Castle BC, Smith BW, Winefordner JD. Recent trends and the future of laser-induced plasma spectroscopy. Trac-Trend Anal Chem. 1998;17:453.
5. Winefordner JD, Gornushkin IB, Correll T, Gibb E, Smith BW, Omenetto N. Comparing several atomic spectrometric methods to the super stars: special emphasis on laser induced breakdown spectrometry, LIBS, a future super star. J Anal Atom Spectrom. 2004;19:1061.
6. Cremers DA, Multari RA, Knight AK. In: Meyers RA, editor. Encyclopedia of analytical chemistry: applications, theory, and instrumentation. John Wiley & Sons; 2010. p. 10245.
7. Song K, Lee Y-I, Sneddon J. Applications of laser-induced breakdown spectrometry. Appl Spectrosc Rev. 1997;32:183.
8. Rusak DA, Castle BC, Smith BW, Winefordner JD. Fundamentals and applications of laser-induced breakdown spectroscopy. Crit Rev Anal Chem. 1997;27:257.
9. Buscaglia JA. Elemental analysis of small glass fragments in forensic science. Anal Chim Acta. 1994;288:17.
10. ASTM E2926-17, Standard test method for forensic comparison of glass using micro X-ray fluorescence (μ-XRF) spectrometry.
11. Curran JM, Champod TNH, Buckleton JS, editors. Forensic interpretation of glass evidence. CRC Press LLC; 2000. p. 121.
12. Thornton JI, Crim D. The use of values in the interpretation of glass density and refractive index data. J Forensic Sci. 1989;34:1323.
13. Pitts SJ, Kratochvil BJ. Statistical discrimination of flat glass fragments by instrumental neutron activation analysis methods for forensic science applications. J Forensic Sci. 1991;36:122.
14. Parouchais T, Warner IM, Palmer LT, Kobus H. The analysis of small glass fragments using inductively coupled plasma mass spectrometry. J Forensic Sci. 1996;41:351.
15. Koons RD, Buscaglia J. The forensic significance of glass composition and refractive index measurements. J Forensic Sci. 1999;44:496.
16. Montero S, Hobbs AL, French TA, Almirall JR. Elemental analysis of glass fragments by ICP-MS as evidence of association: analysis of a case. J Forensic Sci. 2003;48:1101.
17. Trejos T, Montero S, Almirall JR. Analysis and comparison of glass fragments by laser ablation inductively coupled plasma mass spectrometry (LA-ICP-MS) and ICP-MS. Anal Bioanal Chem. 2003;376:1255.
18. Trejos T, Almirall JR. Effect of fractionation on the forensic elemental analysis of glass using laser ablation inductively coupled plasma mass spectrometry. Anal Chem. 2004;76:1236.
19. El-Deftar MM, Speers N, Eggins S, Foster S, Robertson J, Lennard C. Assessment and forensic application of laser-induced breakdown spectroscopy (LIBS) for the discrimination of Australian window glass. Forensic Sci Int. 2014;241:46.

20. Sigman ME, Application of laser-induced breakdown spectroscopy to forensic science: analysis of paint and glass samples. https://www.ojp.gov/library/publications/application-laser-induced-breakdown-spectroscopy-forensic-science-analysis. Accessed 15 October 2010.
21. Naes BE, Umpierrez S, Ryland S, Barnett C, Almirall JR. A comparison of laser ablation inductively coupled plasma mass spectrometry, micro X-ray fluorescence spectroscopy, and laser induced breakdown spectroscopy for the discrimination of automotive glass. Spectrochim Acta B. 2008;63:1145.
22. Bridge CM, Powell LTJ, Steele KL, Williams M, Macinnis JM, Sigman ME. Characterization of automobile float glass with laser-induced breakdown spectroscopy and laser ablation inductively coupled plasma mass spectrometry. Appl Spectrosc. 2006;60:1181.
23. Bridge CM, Powell J, Steele KL, Sigman ME. Forensic comparative glass analysis by laser-induced breakdown spectroscopy. Spectrochim Acta B. 2007;62:1419.
24. Corzo R, Hoffman T, Ernst T, Trejos T, Berman T, Coulson S, Weis P, Stryjnik A, Dorn H, Pollock EC, Workman MS, Jones P, Nytes B, Scholz T, Xie H, Igowsky K, Nelson R, Gates K, Gonzalez J, Voss L-M, Almiral JR. An interlaboratory study evaluating the interpretation of forensic glass evidence using refractive index measurements and elemental composition. Forensic Chem. 2021;22:100307.
25. Merk V, Huber D, Pfeifer L, Damaske S, Merk S, Werncke W, Schuster M. Discrimination of automotive glass by conjoint Raman and laser-induced breakdown spectroscopy and multivariate data analysis. Spectrochim Acta B. 2021;180:106198.
26. Palásti DJ, Kopniczky J, Vörös T, Metzinger A, Galbács G. Qualitative analysis of glass microfragments using the combination of laser-induced breakdown spectroscopy and refractive index data. Sensors. 2022;22:3045. https://www.mdpi.com/1424-8220/22/8/3045
27. Stoecklein W. In: Caddy B, editor. Forensic examination of glass and paint: analysis and interpretation. New York: Taylor and Francis, Inc.; 2001. p. 123.
28. Suzuki EM. Infrared spectra of U.S. automobile original topcoats (1974–1989): I. Differentiation and identification based on acrylonitrile and ferrocyanide C≡N stretching absorptions. J Forensic Sci. 1996;41:376.
29. Suzuki EM, Carrabba M. In situ identification and analysis of automotive paint pigments using line segment excitation Raman spectroscopy: I. Inorganic topcoat pigments. J Forensic Sci. 2001;46:1053.
30. Suzuki EM, McDermot MX. Infrared spectra of U.S. automobile original finishes. VII. Extended range FT-IR and XRF analyses of inorganic pigments in situ—Nickel Titanate and Chrome Titanate. J Forensic Sci. 2006;51:532.
31. Challinor JM. In: Caddy B, editor. Forensic examination of glass and paint: analysis and interpretation. New York: Taylor and Francis, Inc.; 2001. p. 171.
32. Burns DT, Doolan KP. A comparison of pyrolysis–gas chromatography–mass spectrometry and fourier transform infrared spectroscopy for the characterisation of automative paint samples. Anal Chim Acta. 2005;539:145.
33. Plage B, Berg A-D, Luhn S. The discrimination of automotive clear coats by pyrolysis-gas chromatography/mass spectrometry and comparison of samples by a chromatogram library software. Forensic Sci Int. 2008;177:146.
34. Beam TL, Willis WV. Analysis protocol for discrimination of automotive paints by SEM-EDXA using beam alignment by current centering. J Forensic Sci. 1990;35:1055.
35. Deconinck I, Latkoczy C, Gunther D, Govaert F, Vanhaecke F. Capabilities of laser ablation-inductively coupled plasma mass spectrometry for (trace) element analysis of car paints for forensic purposes. J Anal At Spectrom. 2006;21:899.
36. Hobbs AL, Almirall JR. Trace elemental analysis of automotive paints by laser ablation–inductively coupled plasma–mass spectrometry (LA–ICP–MS). Anal Bioanal Chem. 2003;376:1265.
37. Debnath NC, Vaidy SA. Application of X-ray diffraction technique for characterisation of pigments and control of paints quality. Prog Org Coat. 2006;56:159.

38. Nel P, Lau D, Hay D, Wright N. Non-destructive micro-X-ray diffraction analysis of painted artefacts: determination of detection limits for the chromium oxide–zinc oxide matrix. Nucl Instr Methods Phys Res, Sect B. 2006;251:489.
39. Kanngießer B, Malzer W, Rodriguez AF, Reiche I. 3D micro-XRF investigations of paint layers with tabletop set-up. Spectrochim Acta B. 2005;60:41.
40. McIntee E, Viglino E, Rinke C, Kumor S, Ni L, Sigman ME. Comparative analysis of automotive paints by laser induced breakdown spectroscopy and nonparametric permutation tests. Spectrochim Acta B. 2010;65:542.
41. Sigman ME, McIntee EM, Bridge C, Application of laser-induced breakdown spectroscopy to forensic science: analysis of paint samples. https://nij.ojp.gov/library/publications/application-laser-induced-breakdown-spectroscopy-forensic-science-analysis-0. Accessed 28 February 2012.
42. Wilson JD, LaPorte GM, Cantu AA. Differentiation of black gel inks using optical and chemical techniques. J Forensic Sci. 2004;49:364.
43. Mazzella WD, Khanmy-Vital A. A study to investigate the evidential value of blue gel pen inks. J Forensic Sci. 2003;48:419.
44. Mazzella WD, Buzzini P. Raman spectroscopy of blue gel pen inks. Forensic Sci Int. 2005;152:241.
45. Zieba-Palus J, Kunicki M. Application of the micro-FTIR spectroscopy, Raman spectroscopy and XRF method examination of inks. Forensic Sci Int. 2006;158:164.
46. Aginsky VN. Forensic examination of "slightly soluble" ink pigments using thin-layer chromatography. J Forensic Sci. 1993;38:1131.
47. LaPorte GM, Arredondo MD, McConnell TS, Stephens JC, Cantu AA, Shaffer DK. An evaluation of matching unknown writing inks with the United States International Ink Library. J Forensic Sci. 2006;51:689.
48. Houlgrave S, LaPorte GL, Stephens JC. The use of filtered light for the evaluation of writing inks analyzed using thin layer chromatography. J Forensic Sci. 2011;56:778.
49. Weyermann C, Marquis R, Mazzella W, Spengler B. Differentiation of blue ballpoint pen inks by laser desorption ionization mass spectrometry and high-performance thin-layer chromatography. J Forensic Sci. 2007;52:216.
50. Neumann C, Ramotowski R, Genessay T. Forensic examination of ink by high-performance thin layer chromatography--the United States Secret Service Digital Ink Library. J Chromatogr A. 2011;1218:2793.
51. Vogt C, Vogt J, Becker A, Rohde E. Separation, comparison and identification of fountain pen inks by capillary electrophoresis with UV-visible and fluorescence detection and by proton-induced X-ray emission. J Chromatogr A. 1997;781:391.
52. Vogt C, Becker A, Vogt J. Investigation of ball point pen inks by capillary electrophoresis (CE) with UV/Vis absorbance and laser induced fluorescence detection and particle induced X-ray emission (PIXE). J Forensic Sci. 1999;44:819.
53. Mania J, Madej K, Kościelniak P. Inks analysis by capillary electrophoresis analytical conditions optimisation. Chem Anal. 2002;47:585.
54. Siegel J, Allison J, Mohr D, Dunn J. The use of laser desorption/ionization mass spectrometry in the analysis of inks in questioned documents. Talanta. 2005;67:425.
55. Williams MR, Moody C, Arceneaux L, Rinke C, White K, Sigman ME. Analysis of black writing ink by electrospray ionization mass spectrometry. Forensic Sci Int. 2009;191:97.
56. Kaur N, Jasuja OP, Singla AK. Thin layer chromatography of computer printer ribbon inks. Forensic Sci Int. 1992;53:51.
57. Zieba-Palus J, Trzcinska BM. Establishing of chemical composition of printing ink. J Forensic Sci. 2011;56:819.
58. Egan WJ, Galipo RC, Kochanowski BK, Morgan SL, Bartick EG, Miller ML, Ward DC, Mothershead RF II. Forensic discrimination of photocopy and printer toners. III. Multivariate statistics applied to scanning electron microscopy and pyrolysis gas chromatography/mass spectrometry. Anal Bioanal Chem. 2003;376:1286.

59. Zięba-Palus J, Kunicki M. Application of the micro-FTIR spectroscopy, Raman spectroscopy and XRF method examination of inks. Forensic Sci Int. 2006;158:164.
60. Vila A, Jawhari T, García JF. A non-destructive characterization of stratigraphies in contemporary prints using micro-Raman spectroscopy. J Raman Spectrosc. 2007;38:1267.
61. Zieba-Palus J, Borusiewicz R, Kunicki M. PRAXIS-combined μ-Raman and μ-XRF spectrometers in the examination of forensic samples. Forensic Sci Int. 2008;175:1.
62. Alamilla F, Calcerrada M, García-Ruiz C, Torre M. Forensic discrimination of blue ballpoint pens on documents by laser ablation inductively coupled plasma mass spectrometry and multivariate analysis. Forensic Sci Int. 2013;228:1.
63. Elsherbiny N, Nassef OA. Wavelength dependence of laser induced breakdown spectroscopy (LIBS) on questioned document investigation. Sci Justice. 2015;55:254.
64. Cicconi F, Lazic V, Palucci A, Assis ACA, Romolo FS. Forensic analysis of commercial inks by laser-induced breakdown spectroscopy (LIBS). Sensors. 2020;20:3744.
65. Hilario FF, de Mello ML, Pereira-Filho ER. Forensic analysis of hand-written documents using laser-induced breakdown spectroscopy (LIBS) and chemometrics. Anal Methods. 2021;13:232.
66. Oujja M, Vila A, Rebollar E, Garcia JF, Castillejo M. Identification of inks and structural characterization of contemporary artistic prints by laser-induced breakdown spectroscopy. Spectrochim Acta B. 2005;60:1140.
67. Sarkar A, Aggarwal SK, Alamelu D. Laser induced breakdown spectroscopy for rapid identification of different types of paper for forensic application. Anal Methods. 2010;2:32.
68. Kula A, Wietecha-Posłuszny R, Pasionek K, Król M, Woźniakiewicz M, Kościelniak P. Application of laser induced breakdown spectroscopy to examination of writing inks for forensic purposes. Sci Justice. 2014;54:118.
69. Subedi K, Trejos T, Almirall JR. Forensic analysis of printing inks using tandem laser induced breakdown spectroscopy and laser ablation inductively coupled plasma mass spectrometry. Spectrochim Acta B. 2015;103–104:76.
70. Król M, Gondko K, Kula A, Własiuk P, del Hoyo-Meléndez JM, Kościelniak P. Characterization of the elemental composition of polish banknotes by X-ray fluorescence and laser-induced breakdown spectroscopy. Spectrochim Acta B. 2020;169:105898.
71. Metzinger A, Rajkó R, Galbács G. Discrimination of paper and print types based on their laser induced breakdown spectra. Spectrochim Acta B. 2014;94–95:48.
72. Smith JM. In: Blackledge RD, editor. Forensic analysis on the cutting edge: new methods for trace evidence analysis. John Wiley & Sons; 2007. p. 291.
73. Sakayanagi M, Konda Y, Watanabe K, Harigaya Y. Identification of pressure-sensitive adhesive polypropylene tape. J Forensic Sci. 2003;48:68.
74. Mehltretter AH, Bradley MJ, Wright DM. Analysis and discrimination of electrical tapes: part II. Backings. J Forensic Sci. 2011;56:1493.
75. Mehltretter AH, Bradley MJ, Wright DM. Analysis and discrimination of electrical tapes: part I. Adhesives. J Forensic Sci. 2011;56:82.
76. Goodpaster JV, Sturdevant AB, Andrews KL, Brun-Conti L. Identification and comparison of electrical tapes using instrumental and statistical techniques: I. Microscopic surface texture and elemental composition. J Forensic Sci. 2007;52:610.
77. Sun Z, Quan Y, Sun Y. Elemental analysis of white electrical tapes by wavelength dispersive X-ray fluorescence spectrometry. Forensic Sci Int. 2013;232:169.
78. Goodpaster JV, Sturdevant AB, Andrews KL, Briley EM, Brun-Conti L. Identification and comparison of electrical tapes using instrumental and statistical techniques: II. Organic composition of the tape backing and adhesive. J Forensic Sci. 2009;54:328.
79. Zieba-Palus J, Nowinska S, Kowalski R. Application of infrared spectroscopy and pyrolysis gas chromatography for characterisation of adhesive tapes. J Mol Struct. 2016;1126:232.
80. Martinez-Lopez C, Trejos T, Mehltretter AH, Almirall JR. Elemental analysis and characterization of electrical tape backings by LA-ICP-MS. Forensic Chem. 2017;4:96.
81. Martinez-Lopez C, Sakayanagi M, Almirall JR. Elemental analysis of packaging tapes by LA-ICP-MS and LIBS. Forensic Chem. 2018;8:40.

82. Bigun J. In: Li SZ, Jain AK, editors. Encyclopedia of biometrics. New York: Springer Science +Business Media; 2009. p. 468.
83. Taschuk MT, Tsui YY, Fedosejevs R. Detection and mapping of latent fingerprints by laser-induced breakdown spectroscopy. Appl Spectrosc. 2006;60:1322.
84. Yang J-H, Yoh JJ. Reconstruction of chemical fingerprints from an individual's time-delayed, overlapped fingerprints via laser-induced breakdown spectrometry (LIBS) and Raman spectroscopy. Microchem J. 2018;139:386.
85. Brenner JC. Forensic science an illustrated dictionary. Boca Raton: CRC Press LLC; 2004. p. 131.
86. Romolo FS, Margot P. Identification of gunshot residue: a critical review. Forensic Sci Int. 2001;119:195.
87. Dalby O, Butler D, Birkett JW. Analysis of gunshot residue and associated materials--a review. J Forensic Sci. 2010;55:924.
88. Tarifa A, Almirall JR. Fast detection and characterization of organic and inorganic gunshot residues on the hands of suspects by CMV-GC-MS and LIBS. Sci Justice. 2015;55:168.
89. Amadasi A, Gibelli D, Mazzarelli D, Porta D, Gaudio D, Salsarola D, Brandone A, Rizzi A, Cattaneo C. Assets and pitfalls of chemical and microscopic analyses of gunshot residues in skeletonized bodies: a report of five cases. Int J Legal Med. 2015;129:819.
90. Goode SR, Dockery CR, Bachmeyer MF, Nieuwland AA, Morgan SL, Detecting gunshot residue by laser induced breakdown spectroscopy. Paper presented at Laser Induced Plasma Spectroscopy and Applications 2002, Orlando, Florida United States, 25 September 2002.
91. Doña-Fernández A, de Andres-Gimeno I, Santiago-Toribio P, Valtuille-Fernández E, Aller-Sanchez F, Heras-González A. Real-time detection of GSR particles from crime scene: a comparative study of SEM/EDX and portable LIBS system. Forensic Sci Int. 2018;292:167.
92. Rosenberg MB, Dockery CR. Determining the lifetime of detectable amounts of gunshot residue on the hands of a shooter using laser-induced breakdown spectroscopy. Appl Spectrosc. 2008;62:1238.
93. Silva MJ, Cortez J, Pasquini C, Honorato RS, Paim APS, Pimentel MF. Gunshot residues: screening analysis by laser-induced breakdown spectroscopy. J Brazil Chem Soc. 2009;20: 1887.
94. Jantzi SC, Almirall JR. Characterization and forensic analysis of soil samples using laser-induced breakdown spectroscopy (LIBS). Anal Bioanal Chem. 2011;400:3341.
95. Woods B, Kirkbidge KP, Lennard C, Robertson J. Soil examination for a forensic trace evidence laboratory – Part 2: elemental analysis. Forensic Sci Int. 2014;245:195.
96. Jantzi SC, Almirall JR. Elemental analysis of soils using laser ablation inductively coupled plasma mass spectrometry (LA-ICP-MS) and laser-induced breakdown spectroscopy (LIBS) with multivariate discrimination: tape mounting as an alternative to pellets for small forensic transfer specimens. Appl Spectrosc. 2014;68:963.
97. Xua X, Dua C, Maa F, Shena Y, Zhoua J. Forensic soil analysis using laser-induced breakdown spectroscopy (LIBS) and Fourier transform infrared total attenuated reflectance spectroscopy (FTIR-ATR): principles and case studies. Forensic Sci Int. 2020;310:110222.

Advanced Polymer Characterization

10

Zuzana Gajarska, Lukas Brunnbauer, Hans Lohninger, and Andreas Limbeck

10.1 Introduction

Since their invention in the early twentieth century, synthetic polymers have become one of the most widely used and universally applicable materials in our modern world [1]. Without this material type, many of the things we use and do naturally on a daily basis would not be possible. The main reason for the prosperous rise of synthetic polymers is their unique physical and chemical properties easily tunable by a simple change of the monomers used for the synthesis or additives applied (e.g., plasticizers, antioxidants, antistatic agents, lubricants, flame retardants, colorants, or inorganic pigments [2]). This flexibility in properties opened applications in many different fields. Nowadays, polymers are applied not only as (one-way) packaging materials for consumer goods, and construction materials [3] but have also found their way into more demanding fields such as the semiconductor [4, 5] and coating industry [6–8], where they are often employed as an encapsulation material or protective layer. In this case, the primary purpose of the polymer is to prolong the material or device lifetime by protecting it from environmental influences such as humidity, UV radiation, or corrosive gases. Besides all the advantages polymers have to offer, the awareness of the ecological problems this material is causing has drastically increased in the last few years. At the end of their life cycle, polymers often end up in landfills, are incinerated, or end up in the environment in the form of microplastics [9]. The efforts to adapt appropriate recycling and waste management strategies for polymers have intensified lately [10, 11].

To ensure the safe application of polymers and enable the development of novel polymer types, a comprehensive characterization and analysis of this material is required. In the last few years, a wide range of different analytical techniques have been applied to characterize polymers, many of them finding their way to routine

Z. Gajarska · L. Brunnbauer · H. Lohninger · A. Limbeck (✉)
TU Wien, Institute of Chemical Technologies and Analytics, Vienna, Austria
e-mail: andreas.limbeck@tuwien.ac.at

G. Galbács (ed.), *Laser-Induced Breakdown Spectroscopy in Biological, Forensic and Materials Sciences*, https://doi.org/10.1007/978-3-031-14502-5_10

analysis in the industry. The most common tasks in polymer characterization include discrimination, classification and identification of different polymer types, and investigation of polymer degradation. Besides the characterization of the polymer network itself, monitoring of additive or unwanted contamination levels present is also of significant interest. Common techniques used for the analysis of polymers include Fourier Transform-Infrared (FT-IR) [12] spectroscopy and Raman spectroscopy, Pyrolysis—Gas Chromatography-Mass Spectrometry (Py-GC-MS) [13], Thermo Gravimetric Analysis/Differential Thermal Analysis (TGA/DTA) [14], and Matrix Assisted Laser Desorption/Ionization-Time of Flight-Mass Spectrometry (MALDI-TOF-MS) [15] each enabling measurement of specific polymer properties. Providing polymer-specific information, FT-IR and Raman spectroscopy are widely applied to classify and discriminate different polymer types [16–18] or investigate the degradation behavior of polymers [16, 17]. Other techniques used to characterize polymer degradation include Py-GC-MS [13] and TGA/DTA [16, 18]. Even though these techniques all provide unique insight into polymer properties, naturally, all analytical techniques also come with certain limitations. TGA/DTA and Py-GC-MS are techniques that only have access to bulk properties of the sample under investigation, whereas FT-IR, Raman spectroscopy, and MALDI-TOF-MS enable laterally resolved analysis of the sample surface. However, information about changing properties related to the depth within the sample is not easily accessible with any of the techniques mentioned above. Additionally, none of these techniques allows the measurement of inorganic additive levels in polymers. Therefore, to satisfy the need for comprehensive characterization of polymer materials, it is necessary to improve existing analytical approaches and techniques. Furthermore, the development and application of novel analytical procedures that are not conventionally used for polymer analysis can be favorable.

In this chapter, we focus on the benefits LIBS offers when it comes to the characterization of polymer samples. LIBS is usually considered an analytical technique used for elemental analysis to detect all elements of the periodic table. Besides elemental information, under certain circumstances, LIBS can also provide molecular information from the sample under investigation, originating either from incomplete atomization or recombination in the laser-induced plasma [19–21]. The molecular information (e.g., C_2, CN, OH, ...) combined with the possibility of directly detecting the main common constituents of polymers C, H, N, and O (Fig. 10.1) proves to be beneficial for specific fields of polymer characterization. Using the information obtained from LIBS spectra combined with the unique capabilities of LIBS (e.g., imaging, depth profiling, online measurements, lack of sample preparation) results in an analytical technique with powerful characteristics for polymer analysis.

In the following chapters, we present topics where a lot of research is focused on developing novel applications of LIBS for polymer analysis, highlighting the benefits of this technique.

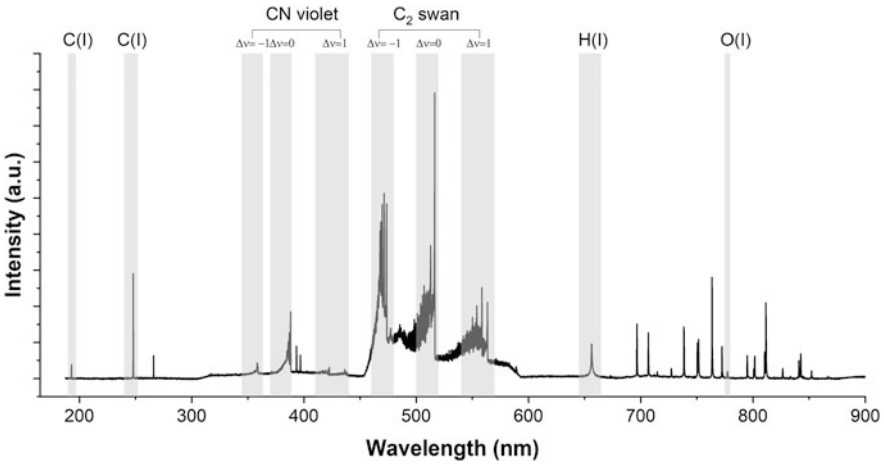

Fig. 10.1 Representative LIBS spectrum of a polymer with typical spectral features marked

10.2 LIBS for Polymer Discrimination/Classification

As mentioned above, LIBS spectra of polymers are mainly dominated by the atomic emission lines of C, H, O, and N. These are often accompanied by the emission bands of molecular fragments, such as C_2 and CN, arising either from the incomplete atomization of the sample or from recombination of the ablated species with other species present in the plasma plume [22]. Moreover, some polymers contain additional elements such as Cl and F, but also S and P. A brief overview of the main atomic and molecular emission signals commonly employed for the LIBS-based analysis of polymers is provided below (Table 10.1 and Fig. 10.2). It should be pointed out, that if analysis is carried out under an ambient atmosphere, O and N signals cannot be attributed to the polymer itself and identification/classification of polymers is restricted to other elements. More details about the evolution of signals in the LIBS plasma of organic molecules can be found in the work of Moros and Laserna [23].

As demonstrated in Fig. 10.3, the similar elemental composition of different polymers results in their almost identical elemental patterns/fingerprints and thus a great similarity of their LIBS spectra, which has long been considered as a major challenge in the LIBS-based discrimination of polymers. Nevertheless, the idea of a rapid, stand-off polymer identification not limited by the polymer thickness or color remained very attractive. Thus, many research groups tried to come up with a chemometric approach that could overcome the limitations of spectral similarity and make the polymer identification by means of LIBS available. Although much work has been done in the field already, certain aspects such as the lack of classifier robustness in real-life scenarios or the influence of polymer additives on classification efficiency have not been fully addressed [26] and shall get more attention in the

Table 10.1 Summary of the emission lines/bands commonly employed for polymer identification [24, 25]

Type of species	Species	Emission lines/bands [nm]
Atomic	C	193.09 247.86 387.64 426.72 723.64
	H	486.13 656.29
	O	777.19 777.42 777.54
	N	744.35 746.83 746.92
	Cl	725.66 741.41 754.7 837.59
	F	685.60
Diatomic/molecular	C_2	473.65 516.42 563.55
	CN	359.04 388.29 421.58

future. Additionally, the recently emerging field of microplastic analysis unlocks new application potentials but also represents a challenge regarding the experimental design (analysis of single particles instead of conventionally performed investigations of compact bulk samples).

All the methods proposed for the LIBS-based identification of polymers utilize the fact that the different polymer types have different elemental ratios, which results in subtle differences in the polymer-specific signal intensities. Thus, the first works in the field tried to differentiate polymers based on the ratios of single emission lines (such as C/H or C_2/C) [27–29] or employ simple statistical methods such as linear and rank correlation to compare the entire LIBS spectra of unknown polymers to a spectral library [30, 31]. Nevertheless, recent advances in instrumentation and computational power have led to an even greater spectral resolution and an increasing availability of high-precision data, which triggered the application of more advanced chemometric techniques. Further, the growing presence of machine learning boosted the achievable results even more. Thus, techniques such as principal component analysis (PCA), support vector machines (SVM), random forest classifiers (RF), or artificial neural networks (ANN) became dominant in the field. As a detailed description of the correlation methods was already presented in the work of Anzano et al. [32], we dedicate this chapter to the most recent chemometric methods employed for the LIBS-based identification of polymers. The following

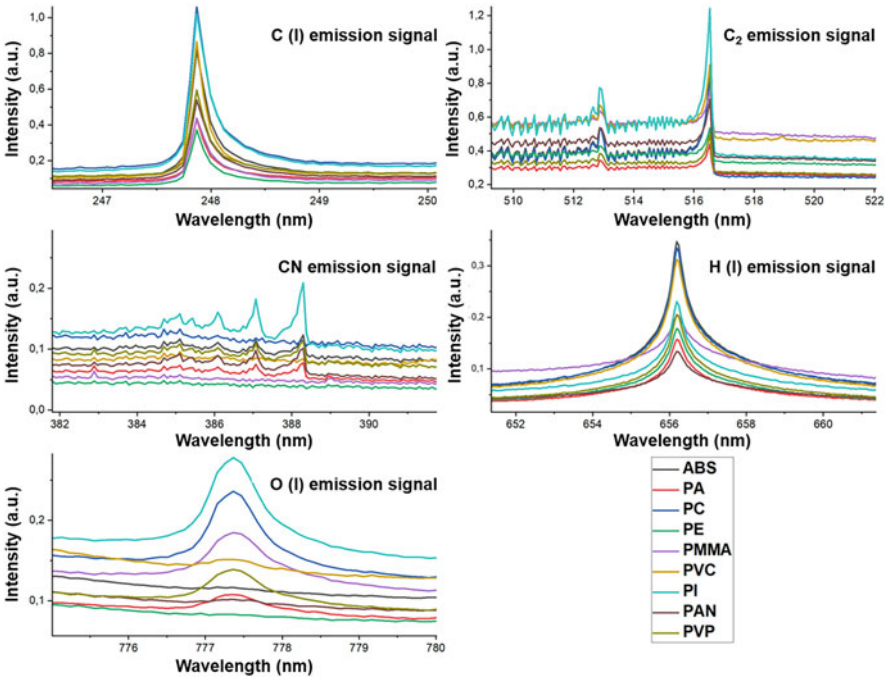

Fig. 10.2 An overview of the spectral features commonly employed for polymer identification. *ABS* acrylonitrile-butadiene-styrene copolymer, *PA* polyamide, *PC* polycarbonate, *PE* polyethylene, *PMMA* poly(methyl methacrylate), *PVC* poly(vinyl chloride), *PI* polyimide, *PAN* polyacrylonitrile, *PVP* polyvinylpyrrolidone

sections aim to provide a short introduction of the multivariate space of LIBS and the most common machine learning algorithms applied in the field.

Considering each detected wavelength as a dimension, each LIBS spectrum can be represented as a point in a multidimensional space, and the mutual distance of the individual points can be used as a measure of spectral similarity. Thus, points representing similar spectra are located closer to each other, whereas points representing spectra with major differences are positioned further apart. Clearly, a discrimination of the different polymer types becomes possible only if the points representing a particular polymer class gather in a constrained region of the space, forming a cluster well-separated from the others (illustrated in Fig. 10.4). Depending on the structure of the polymer clusters, any type of discriminating surface is conceivable, from a linear hyperplane to a complicated nonlinear hypersurface. The complexity of the discriminating (hyper)surface will control the type of utilized classifiers—from a simple partial least square discriminant analysis (PLS-DA) in the case of linear separability to random forest or neural networks in the case of non-linearly separable classes.

As mentioned above, the location of the individual points is determined by the intensities of the individual emission signals, which are, in turn, heavily dependent

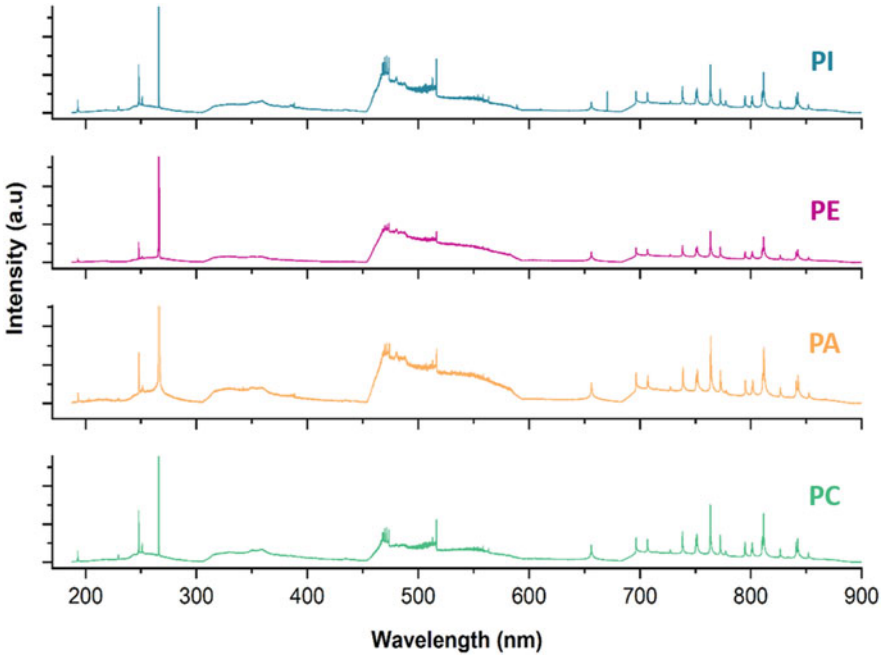

Fig. 10.3 LIBS spectra of four different polymer types demonstrating the identification challenge. *PI* polyimide, *PE* polyethylene, *PA* polyamide, *PC* polycarbonate

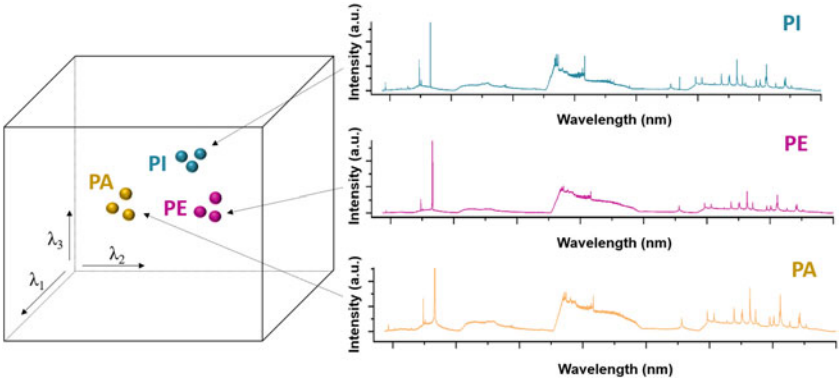

Fig. 10.4 Points representing a single polymer type would ideally gather in one region of the data space well-separated from others. *PI* polyimide, *PE* polyethylene, *PA* polyamide

on the instrumental setup and measurement conditions. This is demonstrated by Fig. 10.5, showing LIBS spectra of the same polymer sample acquired under different combinations of gate delay and atmosphere.

Clearly, such sources of spectral variation complicate the identification of spectra representing a single polymer type. Therefore, the experimental settings shall be kept

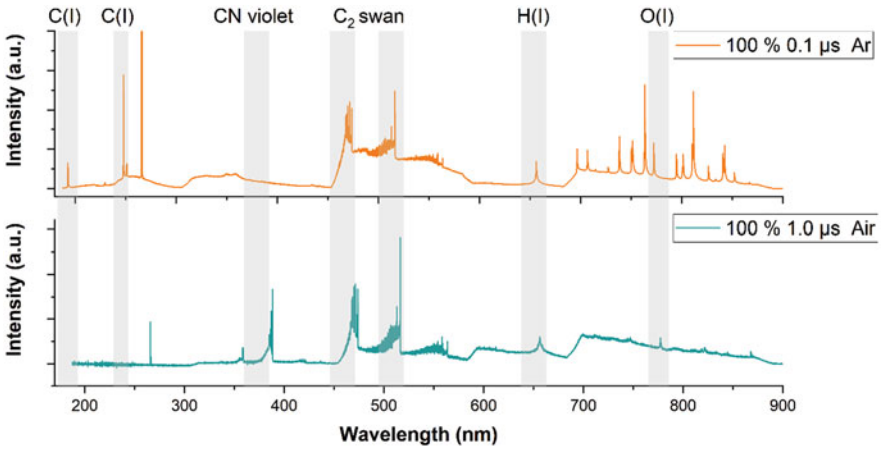

Fig. 10.5 LIBS spectra of polystyrene obtained under different combinations of gate delay and atmosphere. The regions in gray represent polymer-relevant spectral features [33]

constant over the entire analysis. Ideally, they would be optimized to emphasize the emission signals related to the studied polymer types. For a more detailed discussion on the topic, we refer the readers to the recent work of Chamradova et al. describing the effect of different atmospheres on the LIBS spectra of six polymer types [20] and the work of Gajarska et al. [33], providing an insight into a systematic optimization of three experimental conditions (laser energy, gate delay, and atmosphere) with respect to the identification of 20 different polymer types.

However, not even the optimal experimental settings guarantee a constant nature of the signal. The shot-to-shot fluctuations well-known in the LIBS community often distort the representativeness of the spectra belonging to the same polymer type, which might result in poor classifier performance. Therefore, various normalization methods, such as normalization by the total spectral intensity [34] or normalization by C(I) 247.85 nm line [35–38], can be applied. As an improper choice of normalization method can disturb the relationships in the data, it is highly recommended to perform this step with a considerable amount of caution. A more detailed description of the assumptions, advantages, and disadvantages of the different normalization methods can be found in the work of Guezenoc et al. [39].

In addition to the experimental conditions, the efficiency of the classification can be greatly influenced by the variables used to define the multivariate space. If all the variables measured during LIBS analysis are used, the resulting space is high-dimensional, and the great majority of dimensions represent noise or signals irrelevant to the polymer discrimination. This might result in a problem, as in such high-dimensional spaces, data become located in the outer shells of the space, and the distance measures no longer reflect the similarity [40]. Additionally, the increased number of variables often results in a greater number of parameters to be estimated during the training phase, which prolongs the computational times and increases the risk of over-fitting. Therefore, it is often reasonable to select only a

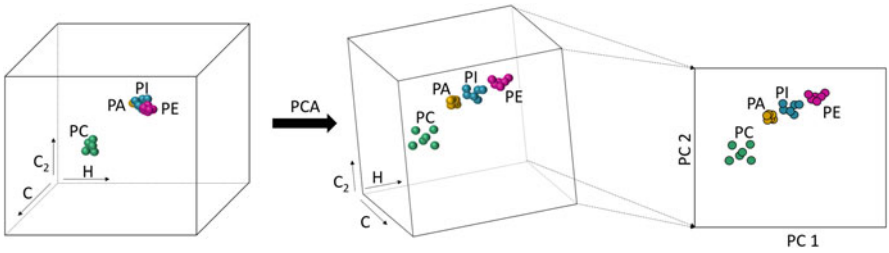

Fig. 10.6 Visualization of high-dimensional data (here: 3D) by their projection onto a 2-dimensional plane spanned by two principal components. *PI* polyimide, *PE* polyethylene, *PA* polyamide, *PC* polycarbonate

subset of variables relevant for the discrimination of the individual classes. As discussed earlier, in the field of polymer analysis, it is common to use emission signals of atoms such as C, H, O, and N (possibly additional ones depending on the elemental composition of the polymer types subjected to the analysis) and of molecular fragments such as C_2 and CN. These can be extracted from the raw spectra in the form of single emission intensities, intensity regions representing peak areas, or other (nonlinear) combinations of the original variables representing characteristic features of the spectra (these are the so-called spectral descriptors) [41]. Alternatively, one can start with variables covering the entire spectral range and apply variable selection methods (e.g., variable selection of random forests) to algorithmically find those which are relevant for the discrimination. Another possibility is to use principal component analysis (PCA) to condense the most important content of the entire spectra in a small number of uncorrelated variables called principal components.

After these steps, one ends up with an observation matrix where each row represents a single observation (LIBS spectrum) and each column a single variable (e.g., single emission intensity or spectral descriptor). Before subjecting the data to further analysis, it is often reasonable to scale the individual variables (columns) to a mean of 0 and standard deviation of 1 to ensure the comparability of their influence (in the case of dimensionality reduction by means of PCA, this step would be performed prior to the PCA).

As the resulting data matrix is quite abstract, exploratory data analysis (EDA) techniques such as PCA are commonly employed to obtain a visual representation (and thus a better understanding) of the data. PCA, for instance, enables for a projection of the high-dimensional data onto a two-dimensional subspace (the computer screen) (Fig. 10.6) in a way to retain the maximum amount of variation/information in data [42]. In the field of polymer identification, this approach has been commonly employed to inspect the separation of the individual classes before the application of a classifier. As an example, Costa et al. performed PCA analysis before using KNN and SIMCA for the classification of 6 polymer types commonly found in e-waste [43]. Stefas et al. used PCA to inspect the separation of ABS samples containing different additives (e.g., fillers, flame retardants, etc.) before applying an LDA classifier [26]. Junjuri et al. employed PCA together with the 2D

scatter plots of H-CN and C_2-CN to examine the separation of five postconsumer plastic types before training an artificial neural network [38]. Furthermore, the works of Unnikrishnan et al. [44], Costa et al. [45], and Shameem et al. [46] employed PCA as the main method to assess the potential of the polymer classification. In addition to PCA, few other unsupervised chemometric methods, such as hierarchical cluster analysis (HCA) [47], k-means clustering [34, 48, 49], or self-organizing maps (SOM) [34], have been used to gain a greater insight into the data and investigate the underlying relationships.

Although PCA provides a very useful representation of the data, the ultimate goal of the analysis is the identification of new/unknown samples, which can only be achieved by using an algorithm ("classifier") trained on a set of polymer LIBS spectra of known polymer types. In the multivariate space analogy, the training of a classifier can be imagined as finding a set of boundaries from the locations of points representing the polymers with a known identity. These boundaries will divide the space into several subspaces where a particular class has the highest probability to occur. Allocation of a new sample in this space will end up in a particular subspace which will decide on its class label.

The fact that different types of classification algorithms have been developed over the years has its reason: each classifier type has advantages and disadvantages and, more importantly, is based on certain assumptions about the data (e.g., linear or nonlinear separability), which pose a limitation on the scenarios to which it can be applied. Thus, there is no such thing as a single algorithm outperforming all other ones in each classification task of the world, which is well-represented by the wide range of classification algorithms covered in the polymer identification literature. The following lines aim to provide a brief introduction to the working principle of the most commonly employed classifier types, along with specific examples of their application in the field of LIBS-based polymer analysis.

10.2.1 Linear Classifiers

Linear classifiers use a line, plane, or hyperplane (depending on the dimensionality of the space) to separate the individual classes. Given the linear separability, there are often many different hyperplanes satisfying this criterion. Clearly, one aims to find the one which would result in the best separation of the classes (and could be applied/generalized well onto the new samples). Here, it is the definition of the "best hyperplane," which is different for different algorithms. For instance, in the case of Fisher's linear discriminant analysis (LDA), the best separating hyperplane is the one that maximizes the ratio of between-class distances to within-class distances. In the case of partial least squares discriminant analysis (PLS-DA), the discriminant function is not based on the spectral variables but rather on their linear combinations to avoid problems with correlation. The linear support vector machine algorithm searches for an optimal hyperplane that is not infinitesimally thin (in contrast to LDA and PLS-DA). Along with their simplicity, linear classifiers offer short training and prediction times and ease of scaling to large datasets. Furthermore, these classifiers

perform well in high-dimensional spaces where nonlinear classifiers tend to overfit. In the field of polymer identification, LDA was successfully employed for the discrimination of ABS (acrylonitrile butadiene styrene) containing carbon black and different types of fillers (e.g., $Mg(OH)_2$, SiO_2, barite) and brominated flame retardants (e.g., decabromodiphenyl ethane (DBDPE), tetrabromobisphenol (TBBPA)). As the authors state, the classification of these compounds is relevant for the recycling of e-waste/WEEE, which is one of the fastest-growing waste streams in the E.U. [50]. Another example of linear classification was presented by Junjuri et al., who employed PLS-DA to discriminate 10 types of postconsumer plastics provided by a local recycling vendor [36]. In this case, the authors compared the performance of two classifiers, one based on the entire spectral range and one only on a few prominent wavelength features (C 244.32–251.07 nm, CN 376.44–388.59 nm, C_2 509.49–517.6 nm, and H 652.41–659.56 nm). Even though the latter one used only 7.3% of the entire spectral information, it could provide competitive classification accuracies. Additionally, Liu et al. used PLS-DA in combination with spectral windows (SW-PLS-DA) to classify plastic bottles made from different polymer types [51]. As the authors stated, the selection of spectral windows based on the continuous wavelet transform (CWT) has the advantage of incorporating more spectral information than conventional methods while reducing the influence of noisy variables, which lowers the risk of over-fitting. The authors reported higher accuracy and shorter classification time of their approach compared to that of the regular PLS-DA, SVM, and RF classifiers.

10.2.2 Kernel Support Vector Machines

In many cases, linear separation of the data is not possible. One of the ways to deal with such situations is the addition of a new (nonlinear) dimension to the existing space such that in the expanded space, the data becomes linearly separable. In the case of SVMs, there is a mathematical trick that allows training a classifier in a non-linearly transformed space without having to construct it explicitly. This approach is commonly called the "kernel trick" and is utilized in kernel SVMs, a version of the linear SVMs allowing to learn more complex nonlinear decision boundaries (Fig. 10.7). On the downside, such more complex approaches often require the tuning of hyperparameters, demand more memory, and exhibit longer run times.

Support vector machines with a radial basis function (RBF) kernel were successfully applied in the work of Yu et al., aiming for the identification of 11 polymer types. The authors based their analysis on 15 emission lines, including C, H, O, N, Mg, Ti, Ca, Al, K, Na, Cl, F, CN, and C_2. In order to increase the influence of the polymer-relevant signals on the outcome, they multiplied the spectral lines of O I 777.41 nm, CN (0, 0), C_2 (0, 0), and N I 746.87 nm by weight factors determined by PCA [35].

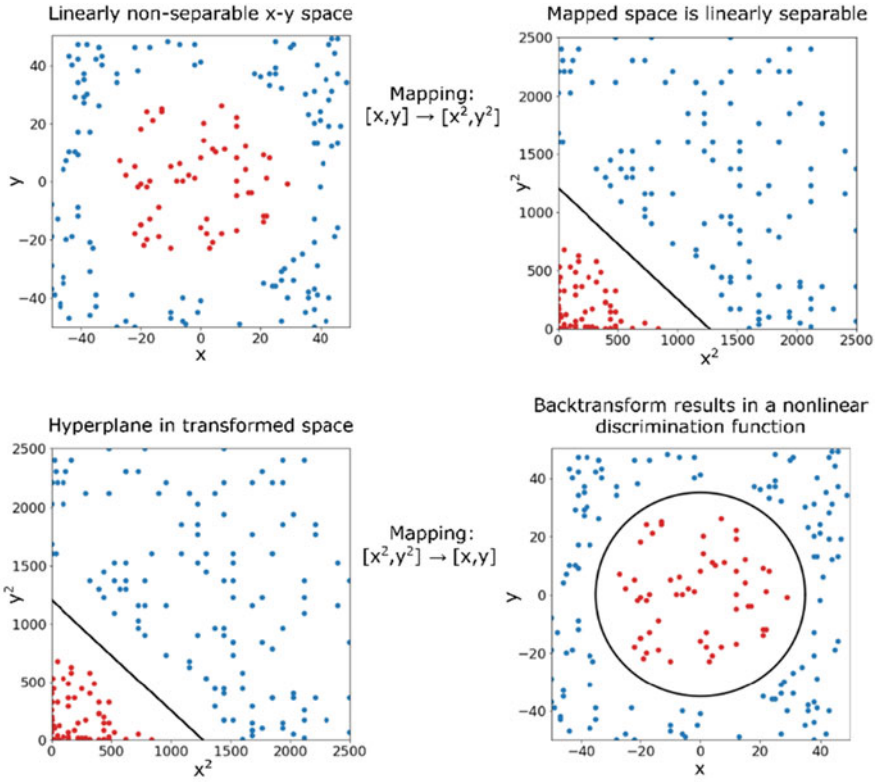

Fig. 10.7 Top left: the two classes (red and blue) cannot be separated by a linear discriminant function. Top right: the space has been transformed by using a simple polynomial function, which leads to a linearly separable dataset. Bottom: back-transforming the hyperplane to the original data space leads to a nonlinear separating function

10.2.3 Artificial Neural Networks

Another type of supervised machine learning algorithm applied in the field of LIBS-based polymer analysis is artificial neural networks (ANNs). From a general perspective, ANNs can be considered as nonlinear mappings of the spectral descriptor space to the space of polymer classes. While there is a considerable amount of different ANN models, the following lines are focused on introducing the most common one, the so-called multi-layer perceptron or back-propagation network. The principal structure of a back-propagation network consists of several layers of processing units (so-called "neurons"), which are fully connected in the sense that each neuron in each layer influences all neurons in the subsequent layer. The signal propagates from the input layer (the values of the spectral descriptors) via one or several hidden layers to the output layer (representing the polymer classes). The individual neurons exhibit nonlinear transfer functions (e.g., a hyperbolic tangent

function). The transfer of a signal from one neuron to another is weighted by multiplicative weights, which are adapted during the training phase in a way that the error in the output layer becomes minimal.

The training of the network begins with random initialization of the weights. Using the input (the variables of a sample in the training set) and the set of initial weights, one can calculate the output. Based on the deviation of the calculated value from the true output value, the weights are adjusted recursively from the output to the input layer. All the training data are presented to the network over many training cycles (epochs), adjusting the weights until the system achieves a stable state, or a maximum number of epochs is reached. This process of adapting the weights is called back-propagation of errors (hence the name "back-propagation networks") [52, 53].

ANNs were used in the work of Boueri et al., who employed a 3-layer perceptron to identify eight polymer types. After initial optimization, the input layer comprised of 13 neurons representing normalized intensities of C, Mg, Ti, CN, Ca, Na, H, F, Cl, N I, Cl, K, and O, the hidden layer (acting as a feature-extraction step) comprised of 12 neurons and the output layer contained eight neurons representing the individual classes/polymer types. The authors conclude that LIBS combined with ANNs has the potential to complement NIR spectroscopy (especially in the case of dark-colored polymers). Nevertheless, the effect of additives on the identification represents a challenge. Additionally, according to the authors, it would be required to train the neural network on a greater dataset containing various materials from industrial environments and daily life [37]. Another example of a three-layered feed-forward-backward propagation ANN was presented in the work of Junjuri et al. [38], who employed femtosecond (fs) LIBS for the identification of five plastic types obtained from a local recycling unit. In this case, the authors investigated five different spectral windows (ranging from entire spectra to only C and H lines) with respect to their effect on the average correct classification rate and the classification time. According to the results, the spectral window comprised only of C and H emissions (2.5% of the total data) could provide comparable performance to the one covering the entire spectral range while taking a considerably lower amount of time. According to the authors stated, this could be possible due to the minimal influence of the ambient atmosphere (the result of fs-LIBS) and the inherent presence of C and H in all of the studied polymer types.

10.2.4 Random Forests

Random forests (RF) have turned out to be a reliable and powerful classification tool. The principal idea behind RFs is the combination of many weak learners (i.e., classifiers, which deliver only poor and unstable results by showing high variance in their answers) into a much stronger ensemble [54]. The individual classifiers ("weak learners") are decorrelated decision trees (typically CARTs—classification and regression trees) which are trained using a randomly selected subspace of the descriptor/variable space. The training set for each individual tree is derived from the

original dataset by a random sampling with replacement (bootstrap), which further enhances the decorrelation of the individual trees. Each of the trees "votes" for the final outcome and combination of votes (usually majority) is employed to determine the classification output. Random forests have been successfully used in the work of Pagnin et al. [55] aimed at the spatially resolved classification of modern art materials.

10.2.5 K-Nearest Neighbors and Soft-Independent Modeling Class Analogy

Two additional supervised classification methods, namely k-nearest neighbors (k-NN) and soft-independent modeling class analogy (SIMCA), were employed in the work of Costa et al. for the identification of 6 polymer types commonly found in e-waste [43]. Whereas in the case of k-NN, the identification of the samples is based on the identity of the k points closest to the unknown point (in the multivariate space) [56, 57]. SIMCA creates a "box model" based on the principal components for each class and calculates the similarity of the unknown point to each class by comparing it to the class box models [58]. While the k-NN model is deterministic and always results in the assignment of a class label, SIMCA is probabilistic and assigns class labels only to samples with a sufficient probability of belonging to one (or multiple) classes.

Finally, Table 10.2 gives an overview of the different multivariate approaches reported in the literature and the investigated polymer types.

10.3 LIBS for Quantitative Metal Analysis in Polymers

There are many different properties of polymers that play an essential role in their application. Most of them are physical and mechanical properties such as strength, toughness, resilience, and lack of both thermal and electrical conductivity. Additionally, chemical properties are of great interest as well. Here, chemical inertness has to be mentioned as a favorable property useful in many applications [64]. The desired properties of a polymer material are often fine-tuned using a wide range of different organic and inorganic additives acting as, e.g., plasticizers, flame retardants, colorants, and UV stabilizers [2]. Therefore, determining additive levels by measuring the metal content is crucial to assure the specifications of a material. Besides the bulk metal content, the spatial distribution of additives is also of interest to ensure the required homogeneity.

Metal content in polymers is not only important in the field of material sciences but is also crucial in environmental and life science. For polymers used as packaging material for food and cosmetics, the content of toxic species (e.g., heavy metals) must be certified and fall below a defined threshold value. When recycling polymers, metal content also plays an important role influencing the applicability of the recyclate [65]. Additionally, the trace metal content of microplastics is also of

Table 10.2 Overview of the approaches employed for the LIBS-based identification of polymers

Polymer types	Nr. of polymer types	Method	Reference
		Statistical methods	
PET, HDPE, PVC, LDPE, PP, PS	6	Linear + rank correlation	[30]
PET, HDPE, PVC, LDPE, PP, PS	6	Linear + rank correlation	[31]
PET, PE, PVC, PP, PS	5	Line ratios	[29]
PET, PE, PP, PS	4	Distance measures, correlation	[59]
HDPE, LDPE, PP, PS, PET, PVC, PTFE, PA, cellulose, rubber	10	Linear + rank correlation, MNC	[60]
		Unsupervised methods	
PE, PP, POM, PVC, PTFE, POE, PA, PBT, ABS, PS, PC, PDMS	12	Line ratios, PCA	[61]
PET, PE, PP, PS	4	PCA	[44]
PET, PE, PP, PS	4	PCA	[46]
LDPE, HDPE, recycled HDPE	3	PCA	[45]
microplastics	–	PCA	[62]
LDPE, HDPE, PP, PS, PET	5	PCA, HCA	[47]
ABS, PLA, PE, PAK, PVC	5	PCA, k-means	[48]
ABS, PVC, PA, PMMA, PC, PE, POM, PP, PS, PTFE, PU	11	k-means	[49]
ABS, PA, PMMA, PVC, PC, PE, POM, PP, PS, PTFE, PU	11	k-means, SOM	[34]
		Linear classification	
HDPE, LDPE, PET, PP, ABS, PC, PS, HIP, PPCP	9	Correlation, PLS-DA	[36]
PVC, PU, PTFE, PS, PP, POM, PMMA, PE, PC, HDPE, ABS	11	VI-PLS-DA	[63]
PET, HDPE, PP	3	SW-PLS-DA	[51]
ABS + additives	–	LDA	[26]
		Nonlinear classification	
PTFE, PU, PS, PC, PVC, ABS, PMMA, PA, PP, PE, POM	11	ASW-SVM	[35]
PP, PVC, PTFE, POM, PE, PA, PC, PMMA	8	ANN	[37]
PET, HDPE, LDPE, PP, PS	5	ANN	[38]
polymer binders	3	RF	[55]

(continued)

Table 10.2 (continued)

Polymer types	Nr. of polymer types	Method	Reference
ABS, PS, PE, PC, PP, PA	6	k-NN + SIMCA	[43]
ABS, PS, EvAc, EvOH, PA, PAN, PBT, PC, PE, PEEK, PET, PI, PMMA, POM, PP, PPSU, PSU, PU, PVC, silicone	20	k-NN + PCA	[33]

Abbreviations: ABS acrylonitrile-butadiene-styrene copolymer, *EVAc* ethylene-vinyl acetate copolymer, *EvOH* ethylene-vinyl alcohol copolymer, *HDPE* high-density polyethylene, *HIP* high impact polystyrene, *LDPE* low-density polyethylene, *PA* polyamide, *PAK* polyester alkyd, *PAN* polyacrylonitrile, *PBT* poly(butylene terephthalate), *PC* polycarbonate, *PDMS* polydimethylsiloxane, *PE* polyethylene, *PEEK* polyetheretherketone, *PET* poly(ethylene terephtalate), *PI* polyimide, *PLA* polylactide, *PMMA* poly(methyl methacrylate), *POE* polyoxyethylene, *POM* polyoxymethylene, *PP* polypropylene, *PPCP* polypropylene co-polymer, *PPSU* poly(phenylene sulfone), *PS* polystyrene, *PSU* polysulfone, *PTFE* polytetrafluoroethylene, *PU* polyurethane, *PVC* poly(vinyl chloride), *PVP* polyvinylpyrrolidone

significant interest. Besides the ecological impact microplastics themselves have on an ecosystem, the uptake or release of heavy metals may increase the harm these particles carry [66].

Conventional approaches for determining the elemental content of polymer samples are usually based on transferring the polymer into a solution with a subsequent liquid inductively coupled plasma mass spectrometry (ICP-MS) or optical emission spectrometry (ICP-OES) analysis. Due to the aforementioned chemical inertness of many polymer types, conversion of the polymer under investigation into a solution is usually challenging and requires complex sample preparation procedures, often including microwave-assisted digestion or combustion [67, 68]. These steps require manual sample handling prone to errors and contamination, and harsh and hazardous chemicals unfavorable both from ecological and economical points of view. Additionally, in modern industries fast monitoring of process parameters is desired which is not compatible with time-consuming sample pretreatment. Therefore, the development of novel approaches for the analysis of metal contents in polymers is required.

Direct solid sampling techniques allow the analyst to circumvent these limitations. For example, techniques such as X-ray fluorescence spectroscopy (XRF) [69, 70] and laser ablation ICP-MS (LA-ICP-MS) [71–73] have already been successfully applied for the quantitative analysis of metals in polymers. However, when employing direct solid sampling techniques for quantitative analysis, other challenges must be addressed to ensure accurate and precise results. For example, these techniques are inherently susceptible to matrix effects meaning a variable absolute signal response based on the bulk composition of the sample. This is especially problematic in the case of polymers, where a large variety of matrix compositions can be encountered.

Even though certified reference materials (CRMs), which can be employed as matrix-matched standards, are available for some commonly used materials and samples encountered in routine analysis, often only a restricted number of elements are included, and the prevailing concentration levels are limited. Therefore, the need for matrix-matched standards poses a severe limitation to the universal applicability of LIBS for quantitative analysis. In the following chapter, the approaches reported in the literature for quantitative assessment of prevailing metal contents in polymers using LIBS will be discussed.

10.3.1 Univariate Approaches

A conventional approach of using matrix-matched standards combined with LIBS analysis to determine Sb in plastics from e-waste is reported by Aquino et al. [74]. Sb can be found in polymers due to Sb_2O_3 being used as a flame retardant. Due to its toxicity, monitoring of Sb levels of polymers is crucial for recycling strategies since heavy metal levels usually must be below a certain threshold in the recycled product. In this work, the authors prepare matrix-matched standards by spiking acrylonitrile–butadiene–styrene (ABS) and polycarbonate (PC) with different levels of Sb. The authors used the carbon signal as an internal standard to provide the best result for the calibration curve. Several different sample types were analyzed and quantified with the prepared calibration curve with reported recoveries in the range of 63–83%. Even though recoveries are not comparable to an analysis consisting of digestion followed by ICP-MS/OES analysis, this work demonstrates the ease of use of LIBS as a direct solid sampling technique providing sufficient sensitivity for the fast analysis of polymer e-waste. Another work dealing with Sb quantification in polymers using LIBS was published by Lazic et al. [75]. The authors investigated a wide range of polymer samples where Sb concentration was determined a priori using XRF. After careful optimization of measurement parameters and normalization to the C signal, a correlation between the Sb signal and Sb content was observed for all investigated polymer samples. Similarly, in the work of Fink et al. [76], the concentration of 8 metals was analyzed in conventional thermoplastic polymers. Reference contents were determined using XRF. Again, the authors demonstrated a correlation between the metal content and the corresponding signal after normalization to the C signal. Besides other reasons, the relatively high uncertainties observed were attributed to matrix effects occurring when analyzing different polymer types, which are not fully compensated by normalization. A similar work was carried out by the same group quantifying Br in thermoplastic polymers [77]. A work where a certified reference material was used to build univariate calibration curves for S and Zn from LIBS data was published by Jasik et al. [78]. The authors prepared standards with contents of the elements of interest by mixing two reference materials in different ratios and pressing the obtained granulate mixtures into pellets. Satisfying quality calibration curves with LODs of 50 μg/g for S and 215 μg/g for Zn were obtained.

Bonta et al. presented a somewhat flexible approach for preparing polymer standards applicable for quantitative LIBS analysis [79]. In this work, standards of 3 different polymer types (PI, PVP, and PMMA) were prepared containing different levels of Co, In, and Pt in the low µg/g range and Na, Sr in the high µg/g range. For this purpose, polymer powders were dissolved in an appropriate solvent, and the obtained solutions were spiked with the elements of interest. Thin films were produced using spiked polymer solutions via spin-coating on high purity Si-Wafer. These in-house prepared standards were thoroughly characterized, and imaging experiments confirmed their homogeneity. This approach of standards preparation is rather flexible and versatile and may easily be extended to other polymer types and analytes of interest.

The need for matrix-matched standards poses a significant limitation when it comes to analyzing polymers. Since polymers come in a wide range of different types with additives highly influencing the material's properties, matrix effects encountered in different polymer samples differ significantly [72]. Therefore, to assure reliable quantitative measurements, matrix-matched standards are required for each polymer type/additive combination [71]. For many analytical questions, information about the exact composition of the polymer under investigation is not available, and therefore, the conventional approach of applying matrix-matched standards for quantification is not feasible. This limitation can be found, e.g., when analyzing metal content in microplastics or dealing with complex high-performance polymers found in different industries. In the case of microplastics, it is evident that the polymer type and additives present in a single particle are usually not known. Additionally, aging of the polymer may also significantly change matrix-effects occurring during analysis, hindering the application of matrix-matched standards. High-performance polymer samples used, e.g., in the semiconductor industry, usually consist of a wide range of different additives required to fulfill the demanding specifications of the industry. In this case, the exact composition of applied polymers is usually considered a trade secret.

In the field of LIBS, several other approaches have been recently investigated to obtain quantitative results without employing matrix-matched standards such as Calibration Free LIBS (CF-LIBS) [80], or multivariate approaches discussed in the following chapter.

10.3.2 Multivariate Approaches

Recently, the LIBS community has experienced a growing interest in using multivariate data evaluation approaches and machine learning for quantitative analysis. In this case, not only the signal from the analyte of interest is used to build a linear calibration model for quantification, but additional information available in the LIBS spectrum is used to obtain more precise and accurate calibration models [81–83]. This approach has also found its way into the field of quantitative metal analysis in polymers using LIBS, significantly improving the performance and enabling the analysis of polymers with an unknown matrix.

The central concept of this multivariate approach is the combination of polymer-specific LIBS signals, which can be used to distinguish between different polymer types, with the signals of the analyte of interest to build a model allowing reliable quantification in different polymer types. Follow-up work by Fink et al. demonstrates the applicability of this approach [84]. The metal content of different thermoplastic polymer samples was first determined using XRF analysis and then analyzed using LIBS. The authors compared different data evaluation strategies applied to their dataset, including a simple correlation of the analyte signal with the metal content and a correlation of the normalized analyte signal with the metal content. Additionally, a PLS model was applied to the dataset, and a test sample set was evaluated to confirm the performance.

Bonta et al. investigated a similar approach, using data of standards of three different polymer types [79]. A tandem LA-ICP-MS/LIBS setup is employed as the sensitivity can be significantly enhanced by ICP-MS detection of certain elements of interest while polymer-specific signals and elements easily detected by LIBS are recorded simultaneously. To investigate the performance of multivariate calibration approaches, conventionally, a dataset is split into a training and a testing dataset requiring a larger number of standards. This was also considered by preparing 15 standards for each polymer type. In the data evaluation procedure, in a first step, the capability of LIBS to distinguish between the three polymer types under investigation using PCA was shown. Next, the LIBS dataset containing information about the polymer type and the analytes of interest detected in LIBS is combined with the ICP-MS data. Using half of the obtained data as a training dataset, a PCR model is built to estimate the analyte concentration of interest in the three different polymer types. Evaluating the second half of the dataset considered a test dataset, the performance of the obtained PCR model can be evaluated. The results show excellent performance with an average deviation of only 4.4% of the nominal concentration within the test data. Therefore, the presented approach enables reliable quantitative analysis within this set of three investigated polymers. In the outlook, the authors suppose that increasing the number of polymer types within this multivariate model may result in a calibration model that is universally appliable for quantitative analysis of polymers in general, eliminating the need for matrix-matched standards.

The outlook of the previously described work was investigated by Brunnbauer et al. [85]. Here, the main goal of the work was to explicitly investigate the capabilities of LIBS for quantitative metal analysis in unknown polymer types or polymer types with an unknown composition where conventional matrix-matched quantification is inherently not possible. Therefore, the authors built a library consisting of standards of 8 different polymer types (Acrylic, PAN, PI, PMMA, PSU, PVA, PVC, and PVP) containing K in the low µg/g range similarly to what was described by Bonta et al. [79]. In a first step, the authors demonstrate that each set of standards of a polymer type can be used to build a conventional univariate calibration model to quantify this specific polymer type. Again, the slopes of the individual calibration functions were quite different, indicating severe differences in the ablation rate and excitation efficiencies of the investigated polymers. A relative error of

7–17% is reported using conventional matrix-matched quantification. The variation of the slopes of the calibration curve of each polymer type cannot easily be compensated by different normalization approaches (e.g., normalization to the C signal, normalization to the ablation rate, or normalization to the C content). Therefore, when performing nonmatrix matched quantification, meaning the metal content of a polymer type is calculated using the calibration function of a different polymer type, may result in relative errors up to 2105% (e.g., when evaluating PVC using PI standards). Nevertheless, for some combinations, reliable quantitative analysis is possible using non-matrix-matched quantification (e.g., evaluating PVA using PMMA standards results in a relative error of 11%). This means, in theory, reliable quantitative analysis of polymers is possible using non-matrix-matched quantification. However, suppose the polymer type or the exact composition of the sample is not known. In that case, the expected error cannot be estimated as the selected calibration function used for non-matrix-matched quantification may be compatible with the sample under investigation or not. To quantify metal content in an unknown polymer sample, the authors proposed using a LIBS-based Partial Least Squares (PLS) model including polymer-specific LIBS signals. Therefore, 8 different PLS models were built, each excluding one of the polymer types which was considered unknown. In a next step, the unknown polymer type is evaluated by the corresponding PLS model. Here, relative errors in the range of 16–90% are obtained when quantifying unknown polymer types providing a universal performance for all investigated polymers. Therefore, the general applicability of this approach for the quantification of metal content in unknown polymer types is concluded. The authors also conclude that the presented approach does not provide the accuracy which could be achieved with matrix-matched quantification, but the PLS model can be employed when dealing with unknown samples where matrix-matched quantification is not feasible. Additionally, highly accurate analysis is often not required, e.g., when determining if the metal content is above a specific threshold value, which is often sufficient for many industrial applications.

10.4 Innovative Characterization of Polymers and Organic Materials

Besides the most common application of LIBS for polymer characterization, such as classification and quantitative metal analysis in polymers, several other innovative applications have been presented in the literature where LIBS is used for the analysis of polymers and other organic materials.

10.4.1 Imaging Applications

LIBS is a promising and upcoming technique for (elemental) imaging and has found its way into many applications ranging from bioimaging, materials science to geology [86, 87]. Conventional elemental imaging is also possible with other

techniques such as LA-ICP-MS or μ-XRF, but LIBS also offers molecular information which has also been applied to polymer samples. Here the unique capability of LIBS enabling discrimination of different polymer types discussed in the previous chapter was used to obtain spatially resolved distributions of different polymer types within a sample.

The work of Brunnbauer et al. [48] presented the feasibility of mapping the distribution of different polymer types within a structured sample using single-shot LIBS spectra for the first time. In the first step, a lateral mapping on a sample consisting of two different polymer types was carried out. Using PCA, obtained LIBS spectra were clustered in two groups enabling the reconstruction of the 2D distribution of the two polymer types within the sample. Besides imaging the polymer distribution, a sample consisting of several layers of three different polymer types was also investigated. Here, a 3D depth profile mapping the sample layer by layer was recorded. Again, the 3D distribution of the three polymer types was reconstructed by clustering the obtained dataset using a multivariate data evaluation approach (k-means clustering). Especially the second application of investigating layered polymer samples shows the advantages of LIBS since this is not easily possible with any other technique.

A second imaging application of LIBS investigating the lateral distribution of polymers was published by Pagnin et al. [55]. This work focused on the classification of modern art materials consisting of mixtures of inorganic pigments and polymeric binder materials. Investigating contemporary art materials is of great interest in cultural heritage science as a tool to adapt adequate restoration measures, authentication studies, and uncover fraud. Enabling simultaneous detection of the inorganic elemental fingerprint from the pigments and polymer-specific signals from the organic binder, LIBS is a promising technique for analyzing these materials. In this work, the authors present a multivariate classification model (RF) trained using data of pigment/binder mixtures based on three different binders and nine inorganic pigments. The obtained RF model allowed identifying both the inorganic pigment and the organic binder of an unknown sample if it is within the training dataset. The developed classification model was also applied to a structured sample of different pigment/binder combinations. Using LIBS imaging combined with the developed classification model, the distribution of the inorganic pigments and organic binder within the sample were reconstructed (Fig. 10.8).

10.4.2 Degradation Studies

During their lifetime, polymers are often exposed to harsh environmental conditions such as high temperatures, UV radiation, or corrosive atmospheres, which may cause degradation altering the materials' properties. Therefore, to assure the functionality of the polymer under these conditions, investigation of degradation behavior is of significant interest both for industrial applications but also for environmental science. Nevertheless, conventional techniques used for this type of characterization are limited to the sample surface or the bulk of the material. Enabling detection of

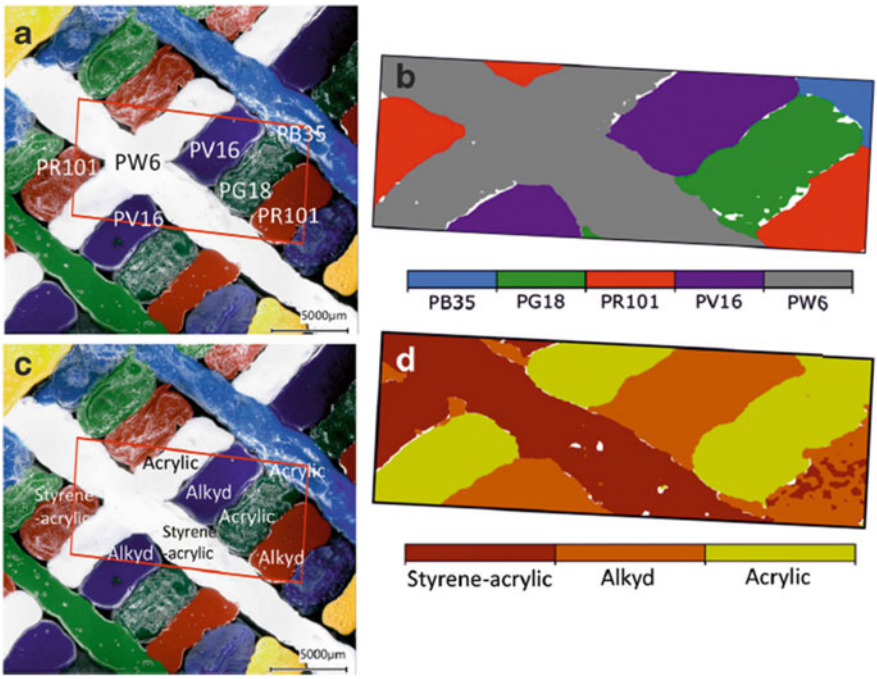

Fig. 10.8 Microscopic image of a sample that consists of different mixtures of inorganic pigments (**a**) and organic binders (**c**) and the results from a laterally resolved LIBS classification of the corresponding pigments (**b**) and binders (**d**) [71]

polymer-specific signals and oxygen (potentially indicating oxidation of the sample) as well as imaging and depth profiling, LIBS is a promising technique for degradation studies of polymers.

One of the first works investigating changes in LIBS signals of organic molecules after chemical aging was published by Farhadian et al. [88]. In this work, the authors observed degradation of composite propellants containing polyurethane as a binder using LIBS after aging times of 60, 120, and 180 days at elevated temperatures. A significant decrease of the CN violet band with increasing aging time was observed in recorded LIBS spectra. Additionally, the C_2/CN, C/H, and O/H ratios showed trends over the aging time. The presented results demonstrated the feasibility of investigating the degradation of organic materials using LIBS.

A work investigating the degradation of polyacrylate exposed to the soil using LIBS was published by Liang et al. [89]. Polyacrylate is commonly used in the agricultural field as controlled-release coated fertilizers and is known to be biodegradable. To investigate the degradation mechanisms of this material, polyacrylate samples were buried in soil for up to 12 months and subsequently analyzed using several analytical techniques, including LIBS. LIBS allows the detection of changes in polymer-specific signals, and the uptake of inorganic species from the surroundings can be measured. In this case, systematic changes in the signal intensities of

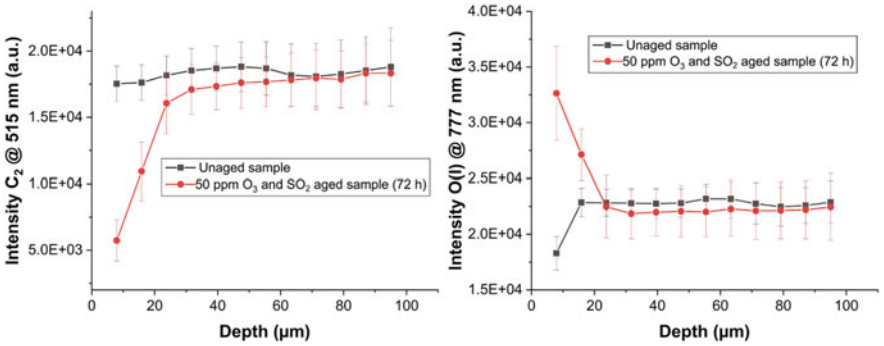

Fig. 10.9 Depth profile measurements of polymer degradation indicated by a change of the C_2 and O signal [23]

nutrient elements (N, P, K), mineral elements (Ca, Mg, Al, Si), and primary constituents of polyacrylate (C, H, O) were observed. Using PCA, a clear distinction of samples aged for different times was possible.

In a work published by Brunnbauer et al. [90], the advantage of LIBS depth profiling was used for the first time to the monitoring of the degradation of polymers. In a first step, LIBS measurements on the surface of a time series of UV-aged polymer samples from the field of cultural heritage science were compared to FT-IR analysis, and the signal of the C_2 swan band was identified as a marker for degradation. In contrast to FT-IR, sample analysis with LIBS is not limited to the surface only but also allows the measurement of depth profiles. Thus, in the mentioned work, the authors analyzed depth profiles to investigate the degree of degradation as a function of depth. Therefore, variations in the intensity of the C_2 Swan band were used as an indicator for degradation. These measurements showed that the sample is degraded on the surface and down to a depth of 20 µm. Additionally, an increase of the oxygen signal was observed in the LIBS spectra indicating oxidation of the polymer sample. In a second application, degradation of a polymer thin film was characterized using a tandem LA-ICP-MS/LIBS system. The polymer film was aged using UV irradiation and subsequently exposed to artificial seawater containing a trace amount of Cd. By the simultaneous recording of LIBS and ICP-MS data, both degradation of the polymer film and changes of the uptake behavior of heavy metals was observed. This work clearly demonstrates the unique advantages LIBS has to offer for the characterization of polymer degradation (Fig. 10.9).

10.4.3 Investigating the Molecular Structure of Organic Compounds

Besides the classification of polymer samples, which is a topic gaining more and more attention in the LIBS community, several groups have dedicated research to investigate if information about the molecular structure of an organic compound can be deduced from LIBS spectra. To this end, systematic analysis of organic

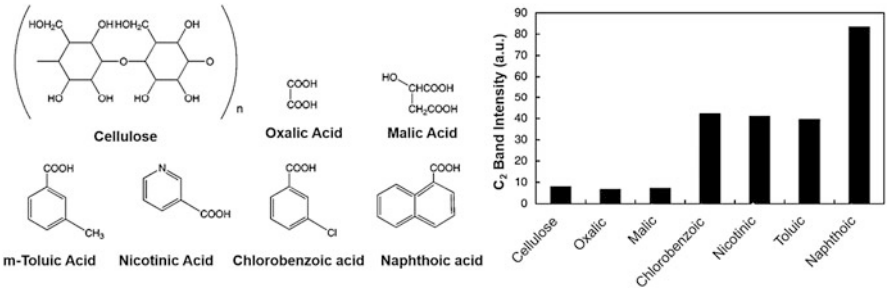

Fig. 10.10 Chemical structures of different analyzed compounds (left) and the corresponding C_2 signal observed in LIBS spectra (right) indicating a correlation to the number of aromatic rings [92]

compounds containing different numbers of aromatic rings, C-C, or C=C bonds can be carried out. Locke et al. [91] published the first work regarding this topic in 1990. In their work, the authors carried out LIBS experiments in combination with gas chromatography, suggesting a "laser microplasma gas chromatography detector (LM-GCD)." Different organic species were investigated, including $CH_3CH_2CH_3$, CH_4, CH_3OH, CO, CO_2, C_6H_6, and various halogenated organic compounds. Analyzing the LIBS spectra of these compounds, the authors found a significant increase in the C_2 signal for C_6H_6 compared to the other molecules, indicating that C=C bonds or aromatic rings in the molecule lead to an intense C_2 signal in the laser-induced plasma. St-Onge et al. [92] carried out a work confirming this finding. Here, the authors investigated seven organic molecules containing different amounts of aromatic rings. The results confirmed an apparent increase of the C_2 emission with the number of aromatic rings present in the sample (Fig. 10.10).

Mousavi et al. [19] increased the number of organic compounds under investigation to 13 in order to systematically investigate the correlation of the C_2 LIBS signal with the number of aromatic rings and the percentage of C-C and C=C bonds present. Again, a clear relationship was found, indicating that fragmentation of the molecule is the primary source of C_2 in the laser-induced plasma.

Besides investigating the influence of the molecular structure of small molecules on LIBS spectra, the works of Grégoire et al. are focused on polymers. Again similar findings compared to small molecules were reported indicating higher C_2 intensities for polymers containing aromatic rings [61]. Besides simply comparing signal intensities with the structural elements of polymers, a more sophisticated approach including plasma imaging was also carried out [93]. Here the spatial distribution of excited species of CN, C_2, and N in the laser-induced plasma of different polymer types was investigated, demonstrating a significant difference.

10.5 Summary and Future Perspectives

In the last decades, the comprehensive chemical characterization of polymers has become mandatory in many research fields and industrial applications. Although several well-established analytical techniques exist for this task, the use of LIBS is continuously gaining more attention. The main features which make this technique so attractive are the ease of use, no need for sample preparation, and speed of analysis. With some constraints, these advantages are also accessible with FT-IR, TGA/DTA, or MALDI-TOF-MS, however, LIBS offers the unique benefit to collect both molecular and elemental information simultaneously.

In the case of polymer identification, usually only molecular emissions (C_2 swan band and CN violet band) and the signals obtained for the elements C, H, and O were used, but LIBS also provides access to elements such as F, Cl, N, S, and P, which could be used to further improve the quality of applied classification procedures. To fully exploit this advantage of LIBS, the measurement of broadband spectra covering the wavelength range necessary for the detection of the most important elements (approximately 200–800 nm) is required. Although much progress has been made in polymer classification in recent years, considering the remarkable developments in the applied chemometric approaches, further improvements could be anticipated in the near future. For example, automatic peak detection combined with multivariate evaluation methods may enable fast and superior data evaluation strategies taking advantage of the information present in broadband LIBS spectra.

Besides polymer classification, the quantitative determination of prevailing additives or contaminations has become essential in the last years. For this task, the multi-element capabilities of LIBS are of utmost importance. Usually, for alkali and earth alkali elements detection limits in the lower μg/g range could be achieved. However, the reduced sensitivity for the measurement of non-metals impedes challenging applications. Common solutions to overcome this limitation are the accumulation of multiple LIBS spectra or the use of more sensitive detectors, as both approaches result in LIBS measurements with significantly improved detection limits.

However, as for most solid sampling techniques, the sample matrix hampers reliable quantification without the use of matrix-matched standards. Since LIBS provides not only information about the main constituents of the polymer but also characteristic molecular features from the organic material under investigation, the polymer-specific signals could be used in combination with statistical methods to circumvent the need for matrix-matched standards. The first pioneering studies demonstrated the applicability of this approach for the analysis of trace elements in bulk polymer samples. In the future, this may give rise to the possibility of analyzing polymers in a matrix-independent manner, enabling fast analysis of additives or contaminations in high-performance polymers as well as the detection of valuable or toxic elements in polymer waste or recycling materials.

In contrast to TGA/DTA, which provide bulk information only, and FT-IR/MALDI-TOF-MS, which are limited to the analysis of the sample surface, LIBS enables laterally resolved investigations as well as the measurement of depth

profiles. Thus, information about the distribution of major, minor, and trace constituents within the polymer sample becomes available, offering the investigation of research tasks not accessible with traditional techniques for polymer analysis. For example, the capabilities of LIBS for polymer classification could be expanded to structured or layered samples. Moreover, the ability to measure depth profiles is a precondition for in-depth studies in polymer corrosion. The effect of UV radiation, humidity, or corrosive environment on the polymer surface could be monitored with several analytical techniques. However, information about changes in the material below the sample surface is only accessible with LIBS. This unique feature of LIBS could be used to support the development of polymers with improved properties but also to monitor the degradation of polymers in the environment.

Although especially the latter application examples must be considered as feasibility studies, the ongoing developments in LIBS instrumentation and the amazingly fast evolution of statistical methods and chemometric approaches will boost work in this research field. Thus, it could be expected that LIBS will become a standard method for polymer analysis, not only for applications where more established techniques fail (e.g., depth profiling) but also for more conventional tasks such as polymer classification or discrimination as well as polymer authentication or adulteration.

References

1. Plastics Europe. Plastics–the facts 2019; 2019.
2. Bart JCJ. Additives in polymers: industrial analysis and applications. New York: Wiley; 2005.
3. Akovali G. Polymers in construction. Shawbury: Rapra Technology; 2005.
4. Kinjo N, Ogata M, Nishi K, Kaneda A, Dušek K. Epoxy molding compounds as encapsulation materials for microelectronic devices. In: Speciality polymers/polymer physics. Berlin: Springer; 1989.
5. Sasajima H, Watanabe I, Takamoto M, Dakede K, Itoh S, Nishitani Y, Tabei J, Mori T. New development trend of epoxy molding compound for encapsulating semiconductor chips. In: Materials for advanced packaging. Cham: Springer; 2017. p. 373.
6. Bellucci F, Nicodemo L, Monetta T, Kloppers MJ, Latanision RM. A study of corrosion initiation on polyimide coatings. Corros Sci. 1992;33:1203.
7. Grundmeier G, Schmidt W, Stratmann M. Corrosion protection by organic coatings: electrochemical mechanism and novel methods of investigation. Electrochim Acta. 2000;45:2515.
8. Sørensen PA, Kiil S, Dam-Johansen K, Weinell CE. Anticorrosive coatings: a review. J Coat Technol Res. 2009;6:135.
9. Cole M, Lindeque P, Halsband C, Galloway TS. Microplastics as contaminants in the marine environment: a review. Mar Pollut Bull. 2011;62:2588.
10. Anuar Sharuddin SD, Abnisa F, Wan Daud WMA, Aroua MK. A review on pyrolysis of plastic wastes. Energ Conver Manage. 2016;115:308.
11. Fink JK. Polymer waste management. New York: Wiley; 2018.
12. Heigl N, Petter CH, Rainer M, Najam-ul-Haq M, Vallant RM, Bakry R, Bonn GK, Huck CW. Near infrared spectroscopy for polymer research, quality control and reaction monitoring. J Infrared Spectrosc. 2007;15:269.
13. Rial-Otero R, Galesio M, Capelo J-L, Simal-Gándara J. A review of synthetic polymer characterization by Pyrolysis–GC–MS. Chromatographia. 2009;70:339.

14. Menczel JD, Prime RB. Thermal analysis of polymers: fundamentals and applications. New York: Wiley; 2009.
15. Li L. MALDI mass spectrometry for synthetic polymer analysis. New York: Wiley; 2009.
16. Wilkie CA. TGA/FTIR: an extremely useful technique for studying polymer degradation. Polym Degrad Stab. 1999;66:301.
17. Celina M, Ottesen DK, Gillen KT, Clough RL. FTIR emission spectroscopy applied to polymer degradation. Polym Degrad Stab. 1997;58:15.
18. Liu X, Yu W. Evaluating the thermal stability of high performance fibers by TGA. J Appl Polym Sci. 2006;99:937.
19. Mousavi SJ, Farsani MH, Darbani SMR, Mousaviazar A, Soltanolkotabi M, Majd AE. CN and C2 vibrational spectra analysis in molecular LIBS of organic materials. Appl Phys B. 2016;122:106.
20. Chamradová I, Pořízka P, Kaiser J. Laser-induced breakdown spectroscopy analysis of polymers in three different atmospheres. Polym Test. 2021;96:107079.
21. Dong M, Mao X, Gonzalez JJ, Lu J, Russo RE. Time-resolved LIBS of atomic and molecular carbon from coal in air, argon and helium. J Anal At Spectrom. 2012;27:2066.
22. Negre E, Motto-Ros V, Pelascini F, Yu J. Classification of plastic materials by imaging laser-induced ablation plumes. Spectrochim Acta B. 2016;122:132.
23. Moros J, Laserna J. Laser-induced breakdown spectroscopy (LIBS) of organic compounds: a review. Appl Spectrosc. 2019;73:963.
24. Mousavi SJ, Farsani MH, Darbani SMR, Asadorian N, Soltanolkotabi M, Majd AE. Identification of atomic lines and molecular bands of benzene and carbon disulfide liquids by using LIBS. Appl Optics. 2015;54:1713.
25. Kramida A, Olsen K, Ralchenko Y. Nist libs database, Natl. Commer: Inst. Stand. Technol. US Dep; 2019.
26. Stefas D, Gyftokostas N, Bellou E, Couris S. Laser-induced breakdown spectroscopy assisted by machine learning for plastics/polymers identification. Atoms. 2019;7:79.
27. Gondal MA, Siddiqui MN. Identification of different kinds of plastics using laser-induced breakdown spectroscopy for waste management. J Environ Sci Health Part A. 2007;42:1989.
28. Couris S, Hatziapostolou A, Anglos D, Mavromanolakis A, Fotakis C. Laser-induced breakdown spectroscopy (LIBS) applications in environmental issues. ALT 96 Int Symp Laser Methods Biomed Appl SPIE. 1996:83–7.
29. Anzano J, Lasheras R-J, Bonilla B, Casas J. Classification of polymers by determining of C1: C2:CN:H:N:O ratios by laser-induced plasma spectroscopy (LIPS). Polym Test. 2008;27:705.
30. Anzano JM, Gornushkin IB, Smith BW, Winefordner JD. Laser-induced plasma spectroscopy for plastic identification. Polym Eng Sci. 2000;40:2423.
31. Anzano J, Casanova M-E, Bermúdez M-S, Lasheras R-J. Rapid characterization of plastics using laser-induced plasma spectroscopy (LIPS). Polym Test. 2006;25:623.
32. Anzano JM, Bello-Gálvez C, Lasheras RJ. Identification of polymers by means of LIBS. In: Musazzi S, Perini U, editors. Laser-induced breakdown spectroscopy: theory and applications. Berlin: Springer; 2014. p. 421.
33. Gajarska Z, Brunnbauer L, Lohninger H, Limbeck A. Identification of 20 polymer types by means of laser-induced breakdown spectroscopy (LIBS) and chemometrics. Anal Bioanal Chem. 2021;413:6581.
34. Tang Y, Guo Y, Sun Q, Tang S, Li J, Guo L, Duan J. Industrial polymers classification using laser-induced breakdown spectroscopy combined with self-organizing maps and K-means algorithm. Optik. 2018;165:179.
35. Yu Y, Guo LB, Hao ZQ, Li XY, Shen M, Zeng QD, Li KH, Zeng XY, Lu YF, Ren Z. Accuracy improvement on polymer identification using laser-induced breakdown spectroscopy with adjusting spectral weightings. Opt Express. 2014;22:3895.
36. Junjuri R, Zhang C, Barman I, Gundawar MK. Identification of post-consumer plastics using laser-induced breakdown spectroscopy. Polym Test. 2019;76:101.

37. Boueri M, Motto-Ros V, Lei W-Q, Ma Q-L, Zheng L, Zeng H-P, Yu J. Identification of polymer materials using laser-induced breakdown spectroscopy combined with artificial neural networks. Appl Spectrosc. 2011;65:307.
38. Junjuri R, Gundawar MK. Femtosecond laser-induced breakdown spectroscopy studies for the identification of plastics. J Anal At Spectrom. 2019;34:1683.
39. Guezenoc J, Gallet-Budynek A, Bousquet B. Critical review and advices on spectral-based normalization methods for LIBS quantitative analysis. Spectrochim Acta B. 2019;160:105688.
40. Bellman R. Dynamic programming. Princeton University Press; 1957.
41. Lohninger H, Ofner J. Multisensor hyperspectral imaging as a versatile tool for image-based chemical structure determination. Spectrosc Eur. 2014;26:6.
42. Bro R, Smilde AK. Principal component analysis. Anal Methods. 2014;6:2812.
43. Costa VC, Aquino FWB, Paranhos CM, Pereira-Filho ER. Identification and classification of polymer e-waste using laser-induced breakdown spectroscopy (LIBS) and chemometric tools. Polym Test. 2017;59:390.
44. Unnikrishnan VK, Choudhari KS, Kulkarni SD, Nayak R, Kartha VB, Santhosh C. Analytical predictive capabilities of laser induced breakdown spectroscopy (LIBS) with principal component analysis (PCA) for plastic classification. RSC Adv. 2013;3:25872.
45. Costa VC, Pereira FMV. Laser-induced breakdown spectroscopy applied to the rapid identification of different types of polyethylene used for toy manufacturing. J Chemometr. 2020;34: e3248.
46. Shameem KMM, Choudhari KS, Bankapur A, Kulkarni SD, Unnikrishnan VK, George SD, Kartha VB, Santhosh C. A hybrid LIBS–Raman system combined with chemometrics: an efficient tool for plastic identification and sorting. Anal Bioanal Chem. 2017;409:3299.
47. Anzano J, Bonilla B, Montull-Ibor B, Casas-González J. Plastic identification and comparison by multivariate techniques with laser-induced breakdown spectroscopy. J Appl Polym Sci. 2011;121:2710.
48. Brunnbauer L, Larisegger S, Lohninger H, Nelhiebel M, Limbeck A. Spatially resolved polymer classification using laser induced breakdown spectroscopy (LIBS) and multivariate statistics. Talanta. 2019:120572.
49. Guo Y, Tang Y, Du Y, Tang S, Guo L, Li X, Lu Y, Zeng X. Cluster analysis of polymers using laser-induced breakdown spectroscopy with K-means. Plasma Sci Technol. 2018;20:065505.
50. Kling M, Zotz F, Huranova D. WEEE compliance promotion exercise Final Report for EC. 2018;2017.
51. Liu K, Tian D, Deng X, Wang H, Yang G. Rapid classification of plastic bottles by laser-induced breakdown spectroscopy (LIBS) coupled with partial least squares discrimination analysis based on spectral windows (SW-PLS-DA). J Anal At Spectrom. 2019;34:1665.
52. Braspenning PJ, Thuijsman F, Weijters AJMM. Artificial neural networks: an introduction to ANN theory and practice. Berlin: Springer Science & Business Media; 1995.
53. Kubat M. Neural networks: a comprehensive foundation by Simon Haykin. Knowl Eng Rev. 1999;13:409.
54. Breiman L. Random forests. Mach Learn. 2001;45:5.
55. Pagnin L, Brunnbauer L, Wiesinger R, Limbeck A, Schreiner M. Multivariate analysis and laser-induced breakdown spectroscopy (LIBS): a new approach for the spatially resolved classification of modern art materials. Anal Bioanal Chem. 2020;13:3187–98.
56. Dasarathy BV. Nearest neighbor (NN) norms: NN pattern classification techniques. IEEE Computer Society Press; 1991.
57. Shakhnarovich G, Darrell T, Indyk P, editors. Nearest-neighbor methods in learning and vision: theory and practice. Cambridge, MA: MIT Press; 2006.
58. Davies AMC, Fearn T. Back to basics: multivariate qualitative analysis. SIMCA. 2008;20:5.
59. Anzano J, Bonilla B, Montull-Ibor B, Lasheras R, Casas-Gonzalez J. Classifications of plastic polymers based on spectral data analysis with leaser induced breakdown spectroscopy. J Polym Eng. 2010;30:177.

60. Lasheras RJ, Bello-Gálvez C, Anzano J. Identification of polymers by libs using methods of correlation and normalized coordinates. Polym Test. 2010;29:1057.
61. Grégoire S, Boudinet M, Pelascini F, Surma F, Detalle V, Holl Y. Laser-induced breakdown spectroscopy for polymer identification. Anal Bioanal Chem. 2011;400:3331.
62. Sommer C, Schneider LM, Nguyen J. Identifying microplastic litter with laser induced breakdown spectroscopy: a first approach. Mar Pollut Bull. 2021;171:112789.
63. Liu K, Tian D, Wang H, Yang G. Rapid classification of plastics by laser-induced breakdown spectroscopy (LIBS) coupled with partial least squares discrimination analysis based on variable importance (VI-PLS-DA). Anal Methods. 2019;11:1174.
64. Brinson HF, Brinson LC. Characteristics, applications and properties of polymers. Polymer engineering science and viscoelasticity: an introduction. Boston, MA: Springer US; 2008. p. 55.
65. Ernst T, Popp R, van Eldik R. Quantification of heavy metals for the recycling of waste plastics from electrotechnical applications. Talanta. 2000;53:347.
66. Derraik JGB. The pollution of the marine environment by plastic debris: a review. Mar Pollut Bull. 2002;44:842.
67. Pereira JSF, Knorr CL, Pereira LSF, Moraes DP, Paniz JNG, Flores EMM, Knapp G. Evaluation of sample preparation methods for polymer digestion and trace elements determination by ICPMS and ICPOES. J Anal At Spectrom. 2011;26:1849.
68. Flores EMM, Muller EI, Duarte FA, Grinberg P, Sturgeon RE. Determination of trace elements in fluoropolymers after microwave-induced combustion. Anal Chem. 2013;85:374.
69. Bichinho KM, Pires GP, Stedile FC, dos Santos JHZ, Wolf CR. Determination of catalyst metal residues in polymers by X-ray fluorescence. Spectrochim Acta B. 2005.
70. Węgrzynek D. Quantitative elemental mapping and characterization of the homogeneity of element distribution in polymer foils by microbeam x-ray fluorescence spectrometry. X-Ray Spectrom. 2001;30:56.
71. Villaseñor Á, Boccongelli M, Luis Todolí J. Quantitative elemental analysis of polymers through laser ablation – inductively coupled plasma by using a dried droplet calibration approach, DDCA. J Anal At Spectrom. 2018;33:1173.
72. Resano M, García-Ruiz E, Vanhaecke F. Laser ablation–inductively coupled plasma–dynamic reaction cell–mass spectrometry for the multi-element analysis of polymers. Spectrochim Acta B. 2005;60:1472.
73. Thieleke JP, Vogt C. A calibration strategy for LA-ICP-MS using isotope dilution for solid reference materials. J Anal At Spectrom. 2016;31:1198.
74. Aquino FWB, Paranhos CM, Pereira-Filho ER. Method for the production of acrylonitrile–butadiene–styrene (ABS) and polycarbonate (PC)/ABS standards for direct Sb determination in plastics from e-waste using laser-induced breakdown spectroscopy. J Anal At Spectrom. 2016;31:1228.
75. Lazic V, Filella M, Turner A. Determination of antimony concentrations in widely used plastic objects by laser induced breakdown spectroscopy (LIBS). J Anal At Spectrom. 2018;33:1917.
76. Fink H, Panne U, Niessner R. Analysis of recycled thermoplasts from consumer electronics by laser-induced plasma spectroscopy. Anal Chim Acta. 2001;440:17.
77. Radivojevic I, Niessner R, Haisch C, Florek S, Becker-Ross H, Panne U. Detection of bromine in thermoplasts from consumer electronics by laser-induced plasma spectroscopy. Spectrochim Acta B. 2004;59:335.
78. Jasik J, Heitz J, Pedarnig JD, Veis P. Vacuum ultraviolet laser-induced breakdown spectroscopy analysis of polymers. Spectrochim Acta B. 2009;64:1128.
79. Bonta M, Limbeck A. Metal analysis in polymers using tandem LA-ICP-MS/LIBS: eliminating matrix effects using multivariate calibration. J Anal At Spectrom. 2018;33:1631.
80. Tognoni E, Cristoforetti G, Legnaioli S, Palleschi V. Calibration-free laser-induced breakdown spectroscopy: state of the art. Spectrochim Acta B. 2010;65:1.
81. Gómez-Nubla L, Aramendia J, Fdez-Ortiz de Vallejuelo S, Madariaga JM. Analytical methodology to elemental quantification of weathered terrestrial analogues to meteorites using a

portable laser-induced breakdown spectroscopy (LIBS) instrument and partial least squares (PLS) as multivariate calibration technique. Microchem J. 2018;137:392.
82. Zaytsev SM, Popov AM, Chernykh EV, Voronina RD, Zorov NB, Labutin TA. Comparison of single- and multivariate calibration for determination of Si, Mn, Cr and Ni in high-alloyed stainless steels by laser-induced breakdown spectrometry. J Anal At Spectrom. 2014;29:1417.
83. Hernández-García R, Villanueva-Tagle ME, Calderón-Piñar F, Durruthy-Rodríguez MD, Aquino FWB, Pereira-Filho ER, Pomares-Alfonso MS. Quantitative analysis of Lead Zirconate Titanate (PZT) ceramics by laser-induced breakdown spectroscopy (LIBS) in combination with multivariate calibration. Microchem J. 2017;130:21.
84. Fink H, Panne U, Niessner R. Process analysis of recycled thermoplasts from consumer electronics by laser-induced plasma spectroscopy. Anal Chem. 2002;74:4334.
85. Brunnbauer L, Gonzalez J, Lohninger H, Bode J, Vogt C, Nelhiebel M, Larisegger S, Limbeck A. Strategies for trace metal quantification in polymer samples with an unknown matrix using laser-induced breakdown spectroscopy. Spectrochim Acta B. 2021;183:106272.
86. Limbeck A, Brunnbauer L, Lohninger H, Pořízka P, Modlitbová P, Kaiser J, Janovszky P, Kéri A, Galbács G. Methodology and applications of elemental mapping by laser induced breakdown spectroscopy. Anal Chim Acta. 2021;1147:72.
87. Jolivet L, Leprince M, Moncayo S, Sorbier L, Lienemann C-P, Motto-Ros V. Review of the recent advances and applications of LIBS-based imaging. Spectrochim Acta B. 2019;151:41.
88. Farhadian AH, Tehrani MK, Keshavarz MH, Karimi M, Darbani SMR, Rezayi AH. A novel approach for investigation of chemical aging in composite propellants through laser-induced breakdown spectroscopy (LIBS). J Therm Anal Calorim. 2016;124:279.
89. Liang D, Du C, Ma F, Shen Y, Wu K, Zhou J. Degradation of polyacrylate in the outdoor agricultural soil measured by FTIR-PAS and LIBS. Polymers. 2018;10:1296.
90. Brunnbauer L, Mayr M, Larisegger S, Nelhiebel M, Pagnin L, Wiesinger R, Schreiner M, Limbeck A. Combined LA-ICP-MS/LIBS: powerful analytical tools for the investigation of polymer alteration after treatment under corrosive conditions. Sci Rep. 2020;10:12513.
91. Locke RJ, Morris JB, Forch BE, Miziolek AW. Spectroscopic studies of laser-generated microplasmas. Appl Optics. 1990;29:4987.
92. St-Onge L, Sing R, Béchard S, Sabsabi M. Carbon emissions following 1.064 μm laser ablation of graphite and organic samples in ambient air. Appl Phys A. 1999;69:S913.
93. Grégoire S, Motto-Ros V, Ma QL, Lei WQ, Wang XC, Pelascini F, Surma F, Detalle V, Yu J. Correlation between native bonds in a polymeric material and molecular emissions from the laser-induced plasma observed with space and time resolved imaging. SpectroChim. Acta B. 2012;74–75:31.

Materials Characterization by Laser-Induced Plasma Acoustics and Spectroscopy

11

Pablo Purohit, César Alvarez-Llamas, Javier Moros, and J. Javier Laserna

Plasma formation by focused high-power, short laser pulses on matter at atmospheric pressure is always accompanied by a characteristic snapping sound. The fraction of incoming energy absorbed by the material contributes to processes like heating and melting that lead to the formation of inertially-confined, high-pressure plasma and vapors. Vibrations propagating into the sample generated by the pressure and inherent recoil reaction of induced stress waves (e.g., shock waves) together with the supersonic expansion of the front edge of the plasma into the ambient gas allow the back-and-forth vibration of close atmospheric particles resulting in sound. Precedents on laser-generated acoustic transients are not numerous in literature specially when compared to other laser-produced phenomena. However, its promising uses make it an interesting area to explore. This chapter reviews the combined use of optical emission and the sound waves generated by laser-induced plasma formation to support the identification of the sample. The first section of the chapter deals with the fundamentals of laser-induced acoustic signals. The next section is devoted to the discussion of how the experimental variables affect acoustics as a source of sample information. Among the discussed variability sources are the excitation parameters, the morphological and the physico-chemical properties of the target as well as the buffer gas under which these optical and acoustic transients develop. A discussion on the synergy of combined optical and acoustic spectroscopies through data fusion strategies toward analytical specificity follows. Finally, the conclusions outline the most relevant achievements so far and future needs focusing mainly on the use of laser-induced acoustics for the in-situ laser-based geochemistry exploration of solar system planets, one of its most interesting applications.

P. Purohit · C. Alvarez-Llamas · J. Moros · J. J. Laserna (✉)
UMA LaserLab, Departamento de Química Analítica, Universidad de Málaga, Málaga, Spain
e-mail: laserna@uma.es

G. Galbács (ed.), *Laser-Induced Breakdown Spectroscopy in Biological, Forensic and Materials Sciences*, https://doi.org/10.1007/978-3-031-14502-5_11

11.1 Laser-Induced Acoustics: Sparking the Interest

Among the most characteristic traits of laser-induced plasmas is the sparking sound that accompanies the optical emission. Interestingly, the produced sound gets louder as the energy of the laser pulse used to generate the plasma increases, thus hinting a correlation between both phenomena at a very primitive level. This fact has, in consequence, drawn the attention of researchers toward pursuing the use of the laser-induced acoustic signal as a pathway to expand the analytical information provided by LIBS. The first references to acoustic recordings associated with laser-induced plasmas date back to the 1960s. Young et al. [1], in 1963, measured the acoustic energy generated by sudden plasma formation (the audible noise noted to resemble that of a cap pistol) and found it to be only 3×10^{-7} J–6×10^{-7} J. Meanwhile, Ujihara et al, in 1969, found that a sonic wave pulse was generated because of the stopped expansion of the emerging laser-produced vapors by the resistance of the surrounding air. In this case, the energy of these sonic waves was estimated to be of the order of 10^{-2} J. The substantially higher values may be explained on the basis of the different excitation conditions used by Ujihara et al. [2] compared to Young et al. [1], 7 MW–100 ns vs. 5 MW–30 ns, and the material originating the sparks, brass and graphite electrodes vs air.

An early example of the integration of laser-induced acoustics detection into an optical spectroscopy setting can be found in the work authored by Chen and Yeung in 1988 [3]. Therein, the magnitude of the acoustic wave was found to be linearly related to the emission intensities of both major and minor elements in the sample of the collected spectra and was, therefore, successfully applied as a mean to correct pulse-to-pulse variations, as will be commented later. The use of acoustics as an internal standard for normalizing the signal from LIBS events is one of the earliest applications suggested and one that still attracts attention nowadays. Sometime later, in 1997, Mesaros et al. used acoustics to identify phase transitions induced by the incoming laser pulsed in metal samples [4]. Upon melting, the acoustic signal produced by the steel targets employed in their experiments exhibited traceable changes when the energy threshold for phase transformations was reached. A piezoelectric transducer connected to a digital oscilloscope was used as the acoustic detector in the described study, with these devices being the most commonly used detectors for laser-induced acoustics second only to microphones. In the same year, Stauter et al. demonstrated that acoustic detectors can be calibrated in order to translate the intensity of the recorded signal in the time domain to control the ablation rate on ceramics [5]. In 2003 and 2004, researchers of the laser lab at the University of Málaga published two papers aiming to extract sample composition-dependent features within the laser-produced acoustic waves as well as to justify the observed particularities on the basis of the plasma evolution in time [6, 7].

These pioneering documents evidenced that the inspection of laser-produced shockwaves recordings in both, the time and the frequency domains, could yield information related to the physical properties of the samples (hardness, density, aggregation phase, porosity, etc.) and guidance on its interaction with the laser pulse. Some results even suggested that information on the sample chemical composition

may also be gathered, as specific frequencies seemed to be tied to particular elements. At the same time, due to the convoluted nature of this signal and how prone it was to being modified by interactions with the environment, unraveling the target-related contribution proved to be a daunting task. Modeling has been used to describe the laser-induced shockwave from a theoretical point of view in order to provide a stronger background capable of supporting conclusions reached from the inspection of plasma acoustic recordings and to open new pathways for their application [8]. Still, the full exploitation of the information carried by the laser-produced acoustic wave is far from being accomplished.

Throughout the present chapter, the fundamentals ruling the phenomenon of laser-induced acoustics will be presented. The most frequently used instrumental configurations for capturing the audios and data processing schemes will be reviewed and recently published bibliography will be referenced to discuss the reasons for the rekindled interest that the topic has experienced during the latter half of the 2010s and its prospective development and future during the 2020s.

11.2 Fundamentals of the Laser-Produced Acoustic Wave

Basic definitions and other aspects related to the physics of laser-induced sound are presented to provide the necessary background about the topics covered in this chapter.

11.2.1 Inception and Evolution of the Wave: From Shockwave to Acoustic Wave

The high energy density of the laser pulse reaching the sample in LIBS studies introduces a strong disturbance in the irradiated area and its close surroundings. In order for the system to respond to the abrupt change in its equilibrium parameters, the energy input is violently shaken off by a number of processes including the formation of a shockwave that precedes the laser-induced plasma expansion in both time and space. In this subsection, we will focus on plasma expansion into a gaseous medium as it is the most common working scenario for both LIBS and laser-induced acoustics experiments.

Supersonic propagation rates along the medium characterize the early lifespan of the shockwave. Therefore, during the initial stages, the shockwave may be treated as a blast wave akin to those mathematically described by the Taylor–Sedov–Von Neuman model where the energy of the pressure wave can be extracted from the dimensionless expression:

$$\zeta = x\left(\frac{\rho_0}{E\,t^2}\right)^{1/5}$$

where x is the distance measured from the place at which the explosion took place, at time t with total energy E and instantly expanded into an undisturbed gas with density ρ_0. The spatial coordinates of the expression are significantly simplified by assuming a spherical wavefront. Moreover, it is suitable for describing a shockwave coming from an event (blast) such as a laser-produced plasma, in which high energy density is released within a short time frame. The energy contained within the wave is the primary entity to be linked to the traits of the inspected sample.

After some time, usually in the nanosecond range, the wavefront loses its supersonic properties and its speed becomes gradually closer to that of the speed of sound ($c = 343\ \mathrm{ms}^{-1}$ in Earth atmosphere, in non-humid air at 293 K, at sea level, static conditions). In consequence, the physical treatment of the wave changes as it no longer expands into an undisturbed medium. Rather, the acoustic wave now relocates in space guided by pressure gradients (Δp) at a speed matching that of the sound in the given medium. Provided that the wavefront can keep inducing at least a small Δp, the wave will keep traveling until its eventual complete absorption (Fig. 11.1). Given the dependency of the expansion on Δp, it is intuitive to relate it to the density and physical traits of the gaseous phase, which plays a key role in the final collected signal. For gases adhering to ideal behavior the speed of sound can be calculated as:

$$c = \sqrt{\frac{\gamma RT}{M}}$$

where γ is the adiabatic index (the specific heat ratio), R is the universal gas constant, T is the temperature of the medium and M is the molecular mass of the medium. As the wave traverses the path separating the target from the receiver in which it is recorded, it interacts with the molecules composing the medium being transmitted through it as a vibration. For example, expansions taking place in low-pressure media are bound to yield signals of reduced intensity owing to energy absorption, which may be biased toward a certain frequency range depending on the medium. Upon reaching the receptor, the acoustic wave induces a response proportional to its remaining energy, thus allowing experimentally measuring E as it is translated at the detector.

11.2.2 Parameters Conditioning the Collected Acoustic Wave

The laser-induced acoustic response of materials can be considered fragile due to the many different sources of uncertainty that may potentially alter the signal reaching the detector. The influence of parameters ranging from laser excitation-related to sample inherent traits and environmental influence is described below based on literature.

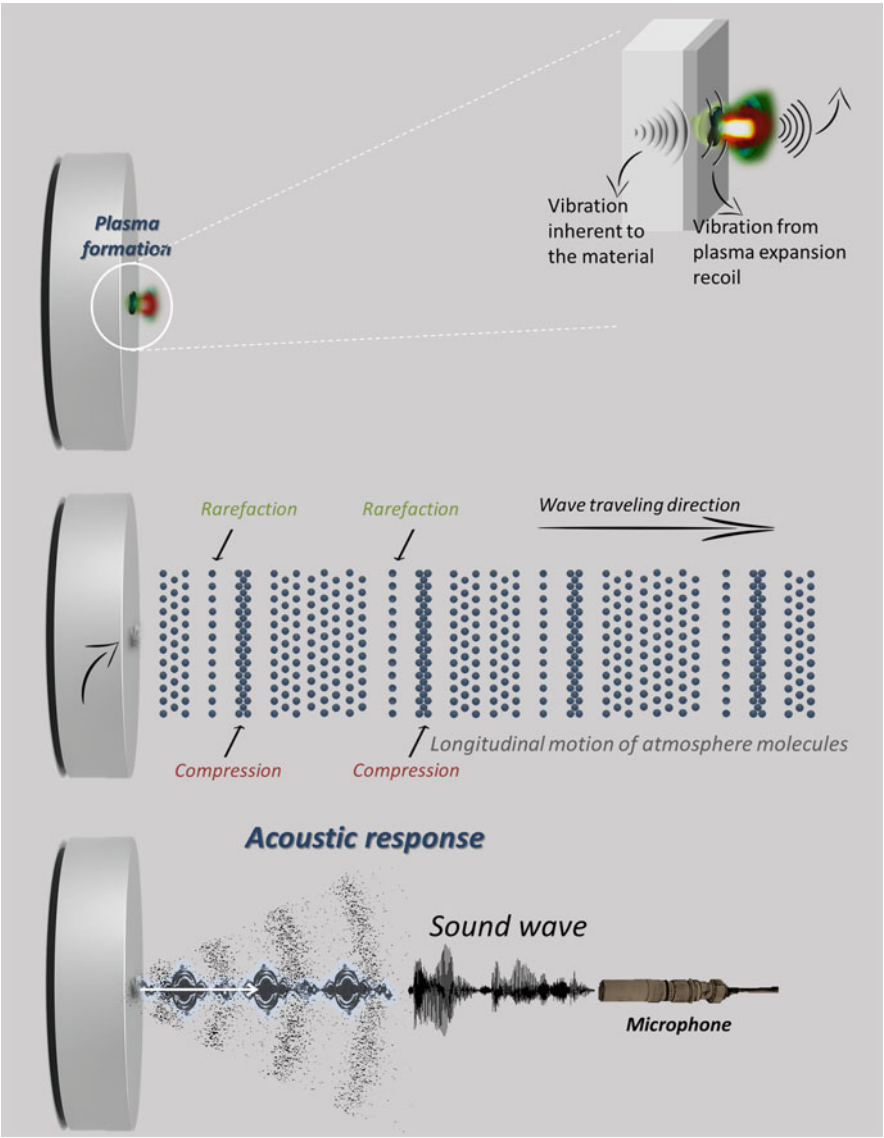

Fig. 11.1 Schematic representation of the generation of a laser-induced plasma acoustic wave

11.2.2.1 Excitation Settings

11.2.2.1.1 Pulse Energy

A straightforward correlation between the pulse energy and, in consequence, the energy density on the sample surface and the collected acoustic signal can be traced. As a rule of thumb, the higher the used irradiance, the louder the recorded sound.

Due to the principles governing the explosive process of plasma formation, the release of the energy excess by the sample leads to a shockwave featuring higher acoustic energy. In the paper by Conesa et al. [7], the direct correlation existing between irradiance and the acoustic energy of the wave was highlighted by the systematic study performed therein. Irradiances from 2.6 GW cm^{-2} up to 12.2 GW cm^{-2} were used to test the response of aluminum samples. The ascending trend featured a change of slope at an irradiance of ca. 4.8 GW cm^{-2} with simultaneously acquired plasma images suggesting that the inflection point was directly linked to a change in the plasma expansion dynamics (Fig. 11.2a). Moreover, the work presented the inference of the excitation energy upon the frequency spectrum, as different components arose at higher energies. In line with the conclusions drawn in the paper, and as will be further discussed below, upon inspection in the time domain, recorded acoustic amplitudes also exhibit increasing values with irradiance. Acoustic amplitudes are a common value used in laser-induced acoustics to quantify the acoustic response of a material to the excitation laser pulse. Amplitudes are measured as the absolute value resulting from the intensities of the first maximum and minimum peaks observed for the acoustic wave as it evolves in time. It is worth noting that, for a same material, no qualitative differences are usually observed in the first maximum-minimum region as a function of pulse energy, yet, after this time window, new components tend to arise. As new interactions occur due to changes in the plasma dynamics with increasing energy, new interferences formed along the acoustic pathway acquire greater relevance along with echoes, while intensities for already existing interferences become enhanced.

11.2.2.1.2 Wavelength

While the acoustic response in the time domain has been reported as a steady signal with little dependence on the wavelength used for sample irradiation [9], in some instances it can greatly modify the amplitude of the emission. For samples featuring

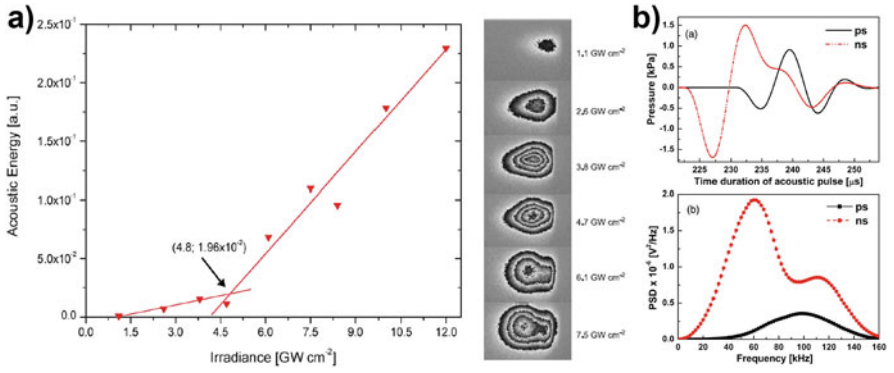

Fig. 11.2 (**a**) (left) Acoustic energy produced by a laser-induced plasma ignited on an Al sample versus laser irradiance at sample surface. (right) Plasma shape evolution as a function of the irradiance value (acquired at a delay of 260 ns from plasma onset). Adapted from [7]. (**b**) Acoustic spectra (in the time and frequency domains) for the ns/ps laser-induced breakdown at 24 mJ laser energy [12]

localized surface plasmon resonance (LSPR), increased acoustic energy was recorded when excitation was performed with λ in resonance with that of the surface plasmon [10]. While these recent results have been only demonstrated to the best of our knowledge, at a theoretical level they are of great relevance to the field of laser-induced acoustic probing as they pave the path toward the use of photoacoustic to measure LSPR values as well as for nanomaterial sizing.

11.2.2.1.3 Pulse Duration

The correlation between the length of the laser pulse used for excitation (τ) and the magnitude of the pressure wave induced was explored by Jansen et al. for tissue phantoms (gels of polyacrylamide (PAA) with various water concentrations to simulate different tissue strengths) covering a Young's modulus range between 0.031×10^6 Nm^{-2} and 0.866×10^6 Nm^{-2} [11]. Samples were tested both in water and in gel phases with pictures of the bubble forming at the tip of the optical fiber delivering the laser pulse being acquired from bubble inception until decay while pressure was registered via a piezoelectric stage coupled to an oscilloscope. A wide τ window from 500 ns to 1100 μs was explored concluding that longer pulses lead to a collapse in the pressure value of the wave. This may be expected as the elongation of the lapse within which the system is perturbed implies that its subsequent release will be performed under circumstances different to those favoring blast wave formation. It is worth mentioning that the work highlighted the extent to which the medium can damp the acoustic signal as pressure was found to decrease severely for samples inspected in 84% gel medium when compared to those examined in water.

A more recent work authored by Manikanta et al. explored the effect of shorter laser pulses (30 ps and 7 ns) in the frequencies collected from the breakdown of air [12]. Reported results indicated that the peak frequencies of both ns and ps acoustic pulses are distinct, indicating the distinct plasma formation mechanisms (Fig. 11.2b). A higher efficiency in the conversion of optical into acoustic energy for ns pulses as frequencies between ca. 10 kHz and 160 kHz were detected in the spectra. Contrarily, ps excitation yielded responses only in the shorter range comprised between 60 kHz and 140 kHz. Moreover, intensity maxima in the frequency domain were shifted toward higher values for ps excitation (34 kHz–68 kHz for ns, 94 kHz–122 kHz for ps). This behavior was attributed to the different mechanisms governing the sparking, expansion and decay of the plasma depending on the excitation regime. In parallel, changes in the acoustic amplitude of the main signal owing to increasing pulse energies were studied. Apart from the expected increase in pressure, the arrival time of the wave at the receptor was found to shorten with higher E values, likely a consequence of the slightly shorter path traversed by the wave as the size of the plasma plume became larger.

11.2.2.1.4 Laser-Matter Interaction

The dependence of the acoustic response on the physical traits of the sample is well-known by now [13]. Among studied variables, sample morphology has been found to yield largely similar results in the time and in the frequency domains for identical

samples, aluminum cylinders of varying diameter and thickness cut from the same alloy rod in the case presented in reference [14]. Differences in the time domain were once again found during later stages of the wave lifespan with reflections and interferences manifesting with a varying relevance degree and slight delays depending on the dimensions of the Al probe. Moreover, results presented therein highlighted the exceptional stability of the acoustic response measured as the first max-to-min amplitude during the ablation of homogeneous samples, further stating the capabilities of the technique to discern layers or phase changes upon laser drilling the sample as will be commented on later.

The value of the linear absorption coefficient (ε) at a given wavelength is one of the main factors determining the efficiency of the laser-matter coupling. As also reported in the work by Bosáková et. al [14], upon adding dyes with different ε to transparent epoxy matrices, the intensity of the recorded acoustic signal changed in agreement with ε at the used excitation wavelength of 1064 nm.

Other quantities directing the sample-matter interaction and the ablation rate, in consequence, are the sample hardness, Young's modulus, the material density and its porosity, as each of them conditions the transmission of the acoustic wave and, therefore, the magnitude of the signal collected as well as minor qualitative components at later times in the recorded wave.

11.2.2.1.5 Sample Surroundings

The objects present in the environment of the sample can substantially modify the final collected signal to the point of totally diluting any possible information regarding the target it may contain. Among often overlooked reported sources of uncertainty one may find the sample support, opto-mechanics or, even, the table on which the experiment is being conducted. Reflections of the acoustic wave upon interaction with external items create interference patterns that may reach the detector and introduce misleading components. Other relevant interactions that need to be addressed to ensure data reliability are concurrent winds during signal acquisition [15], the presence of obstacles scatterers in the acoustic path, and the receiver (microphone) height above ground as well as the emitter-to-receiver (plasma-to-microphone) coordinates [14]. Although in the time domain, these contributions are manifested in the form of very subtle differences, they are more easily identifiable within the frequency domain owing to its higher sensitivity to those interference patterns.

11.3 Capturing Laser-Produced Acoustics

While experiments involving laser-driven acoustics share large similarities to any conventional LIBS set-up as far as the excitation stage is concerned, the nature of the phenomenon to be recorded makes it necessary to complement them with additional capturing infrastructures. Some preliminary attention must be devoted, primarily for those readers familiar exclusively with LIBS, to recording laser-induced acoustics

since certain aspects of the laboratory setting that may be irrelevant to the optical spectroscopy can be of great significance to the acoustic response.

The most critical issue to acoustic detection is the presence of potential interfering artifacts in the path the sound waves travel from the source to the receiver. A simple example of this is the effects from the "ground" or the surface over which sound propagates. In general, surfaces tend to absorb energy from the incident acoustic waves. When the sound propagates over any ground, attenuation may occur due to acoustic energy losses by absorption and reflection mechanisms. For example, for a given geometry represented in Fig. 11.3, the two contributions lead to pressure minima at frequencies where they interfere destructively when the phase difference between them, caused both by path length difference and by the phase change (ϕ) upon reflection on the ground, is an odd number of n radians, that is, $(2n+1)\pi = \frac{2\pi}{\lambda}(r2 - r1) + \phi)$ [15].

These losses depend on several parameters related to the surface, i.e., the geometry of the point sound source and the receiver, distances from the ground and inherent ground properties (smooth/rough, porous, hard/soft ...). Thus, the ground or the mere existence of walls (for cases where laser excitation is performed on a target located inside an ablation chamber) may introduce severe modifications in the waveform owing to the interference patterns (either destructive or constructive) sourcing from the absorbed/reflected waves and merging with the direct soundwave. As a matter of fact, changes in the frequency domain of the acoustic spectra of some targets have been observed simply as a consequence of switching their positions along with the sample holder [16]. In the case of long-range sensing of laser-driven acoustic signals, which is a case in early development stages currently performed with the SuperCam instrument on the Perseverance rover from the M2020 NASA's mission in Mars, the wind speed, the variation of the atmospheric temperature, humidity and pressure as well as thermal gradients from the ground influence the propagation of the acoustic wave in terms of attenuation and sound speed. Therefore, the employed set-up design must account for all these issues, either to fully nullify the negative effects or to minimize them, at least in controllable environments such as laboratory-scale research. An option to do so is the use of absorbing elements (working inside anechoic chambers) or the arrangement of the components in such a

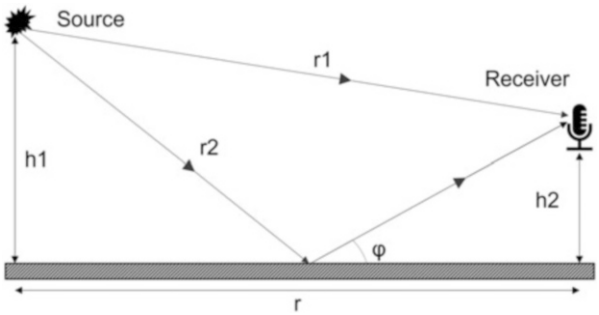

Fig. 11.3 Schematic geometry of a point source and a receiver near to a solid surface

way that the propagation times of echoes and reflections differ significantly from the propagation time of the direct wave.

While the detectors pose the most obvious addition to the layout, we will begin this subsection by describing elements largely absent in the references outlined in the introduction section which have been proven crucial in recent literature [13, 14, 16–20]. Anechoic chambers, in which samples are housed during their inspection, have been proven as valuable assets to minimize the intrusion of reflection arising from the interaction between the acoustic wave and the surroundings of the experiment on the collected signal. Even though the impact of reflections can be greatly damped depending on the processing scheme followed, these interferences hinder the full exploitation of the acquired data as they further convolute the signal to be inspected in the time as well as in the frequency domain. The inner walls of the anechoic chambers are covered with acoustic absorbents, e.g., acoustic foam made from polymers such as polyurethane, which is the main component of the often-used HiLo-N40 foam. Acoustic absorbing panels feature wedges of different dimensions and geometries, with these two parameters requiring ad-hoc optimization for each experiment. The material type, the structure (flat or patterned surface) of the panel as well as the size and shape of the absorbers, for patterned foam tiles, should be carefully selected in order to get the largest ratio of reflected to direct sound [21]. Moreover, the dimensions of the anechoic chamber should also be optimized to provide an environment free of echoing or other radiated signals and reduce the effects of these undesirable signals during the testing. To do so, studying the frequency behavior of the anechoic chamber is mandatory (i.e., the resonances existing in the chamber when excited by an acoustic source). Most of these fundamental resonances are in mid-low frequency range, in one or more of the chamber's dimensions and affect the free field conditions when reflection occurs. Regarding the geometry of the anechoic chamber, the simplest to construct and the easiest for lining of the absorbers is the rectangular-shaped chamber [22]. However, the selection of the optimum geometric proportions of these rectangular chambers is not a trivial matter. Several criteria can be found, such as the ones reported in [23]. Others, just for instance, report that one of the dimension ratios for rectangular enclosures that yield the lowest value of ψ is 1:1.2:1.4, considering the eigenfrequencies of the enclosure up to the Schroeder frequency (a sound frequency zone that ranges from 100 to 200 Hz in which enclosure resonances dominate) and considering a surface averaged sound absorption coefficient (α) of the decided absorber <0.6 [24].

The most commonly reported housings to provide an environment free of echoes and reduce the effects of undesirable signals during the recordings are either full anechoic or hemi-anechoic chambers, depending on the degree up to which their inner walls are covered, with laser incidence being vertical [13] or horizontal [14] to the sample depending on the optical aperture allowed by the design. The sample holder is another important fact to consider in acoustic experiments as it may become the first obstacle in the acoustic pathway yielding interferences as put forward in recent works [13, 14, 19]. Some proposed suitable ways to fix the sample position include resting it on acoustic foam [13] or covering the holder with acoustically insulating materials such as neoprene [14].

As stated above, microphones and piezoelectric stages are the most commonly used devices to translate the pressure wave into an electric signal for further processing. For microphones, omnidirectional polar pattern condenser microphones are the preferred choice. These microphones offer a flat response for frequencies within their working range while being unbiased to the direction from which the sound is coming, thus avoiding the tedious calibration required by directional microphones, which feature anisotropic response. While convenient from the experimental simplicity point of view, omnidirectional detectors are sensitive to the inclusion of many undesired reflections. Cardioid polar pattern microphones may stand in as in-between solutions for the issue as directional calibration is not required while the permeability to backscattered reflections is largely reduced, thus significantly reducing the number of possible interferences entering the detector. The polar pattern of the microphone dictates the degree of flexibility that researchers have for placing the detector, i.e., to set the emitter-to-receiver distance and angle. This is a key point as the acoustic response is direction-dependent in nature. Therefore, the recorded response may substantially vary depending on both parameters. It is also of utmost importance to ensure that the position of the receptor does not allow for wave-receptor interference formation and recording. Microphones are then connected to an audio interface, allowing the control of the sampling rates conditioning the number of points contained in the file, and adequate software such as Audacity for data storage in computers. On the other hand, piezo stages also act as sample holders as direct, intimate contact is required to convert the device vibration into an impulse signal at the oscilloscope to which they are frequently coupled. At the expense of more complicated tracking of the signal origin (e.g., direct sample vibration or a composed interference), piezo stages allow for higher sampling rates and improved resolution of the resulting waveform as well as a larger detectable frequency range, usually up to 200 kHz whereas microphones commonly have an upper limit of ca. 20 kHz. Furthermore, other experimental approaches have been reported to obtain the acoustic signal, such as using the plasma speckle patter via the optical recording of the plasmas and its conversion to acoustic patterns [25].

On a final note, attention should also be directed into minimizing the possible interaction between the sound wave and any element present along the acoustic pathway, especially for experiments involving long sample-to-microphone distances. Isolating the full pathway with absorbers may be of worth for in-lab experiments dealing with fundamental aspects of laser-induced acoustics in order to decrease the vulnerability of the detector to reflected waves that may originate from a number of interactions such as the acoustic wave scattering the surface of an optomechanical component.

Examples of set-ups reported in literature using microphones and piezoelectrics as detectors are provided in Fig. 11.4.

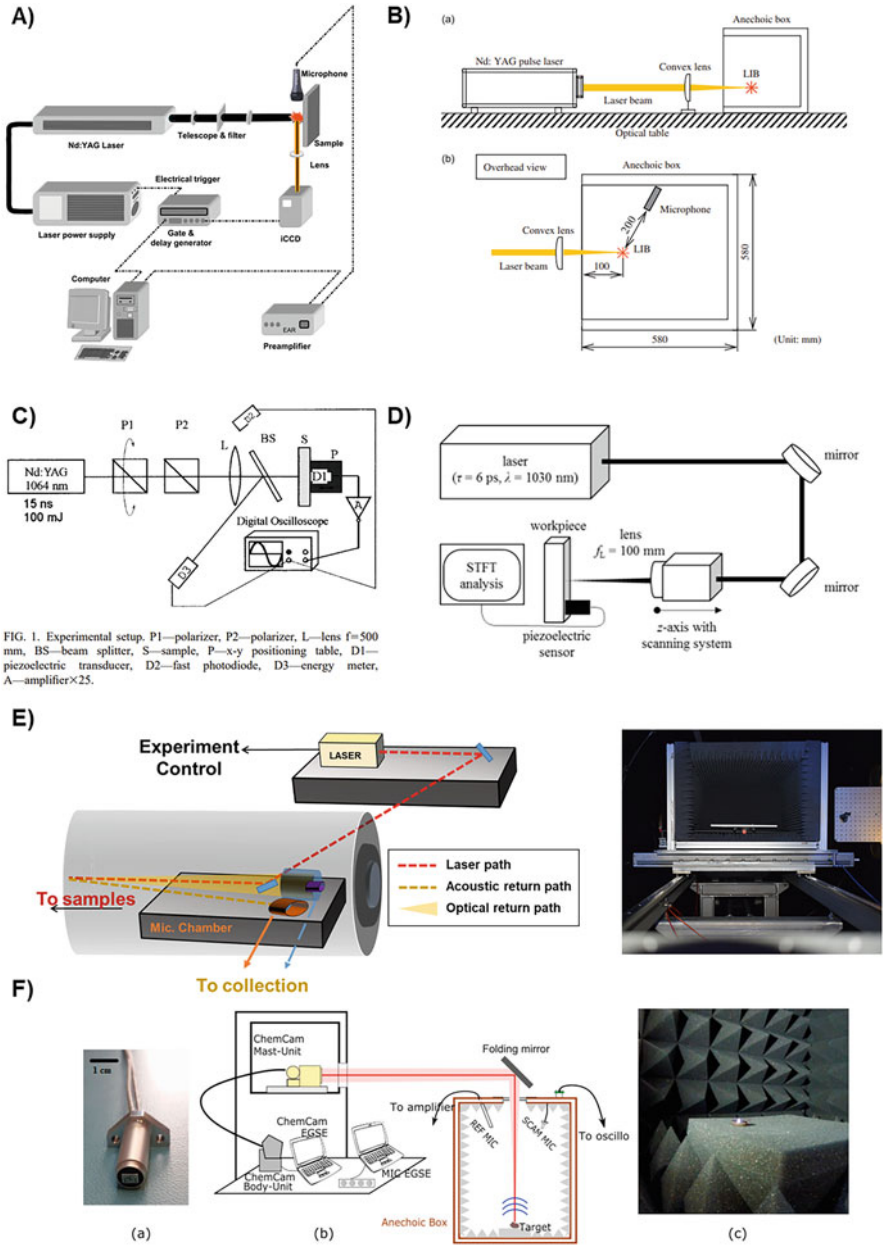

FIG. 1. Experimental setup. P1—polarizer, P2—polarizer, L—lens f=500 mm, BS—beam splitter, S—sample, P—x-y positioning table, D1—piezoelectric transducer, D2—fast photodiode, D3—energy meter, A—amplifier×25.

Fig. 11.4 Example instrumental configurations proposed in literature for capturing laser-induced plasma acoustics on different samples. (**a**) Set-up used by Conesa et al. [7] for simultaneous collection of the optical and acoustic emission of plasmas created on solids. No anechoic chambers were used in the configuration. (**b**) Set-up by Hosoya et al. with both, targets and a closely placed microphone detector located within a hemi-anechoic chamber. The set-up is described in reference [18]. (**c**) Configuration using a piezoelectric transducer, a fast photodiode and a power meter synchronized by an oscilloscope to capture laser-produced plasma acoustics by Mesaros et al. in reference [4]. (**d**)Piezo-based acoustics detection system by Kacaras et al. in reference [36]. (**e**)

11.4 Acoustic Data Processing

The acoustic response recorded corresponds to the wave generated by the pressure variations caused from the pushing of the surrounding atmosphere molecules by the ablated sample fragments. This massless sound source is typically a short-duration impulsive signal that can be represented in both the time and the frequency domains.

For the time-domain, the digitalized recording measures the sound pressure level multiple times per second in measurements often called samples, also defined as sampling rate. A common sampling rate is 96,000 samples per second. Then, the samples can be plot on a graph, with the Y-axis representing the sound pressure level, with positive values representing the sound pressure level being above the ambient atmospheric pressure and negative values representing the sound pressure level being below the ambient atmospheric pressure, and the X-axis being the time. From this signal, some magnitudes such as the shockwave peak-to-peak amplitude, in the case of the typical impulsive response in laser-induced acoustics, the instantaneous power and the energy of the signal can be extracted [26]. The peak-to-peak amplitude of the waveform usually refers to the maximum positive or negative deviation of a waveform from its zero-reference level. The power of the signal, while is referred to an instantaneous value, is normally denoted as its mean square value, calculated by averaging the obtained instantaneous values over a given time, $P(x) = x^2(t)$. However, since power is only significant for stationary or slowly varying signals, for the transient events we focus on, such as vibration shocks or acoustic pulses, the fundamental quantity to be considered is the energy, that is, the accumulation of the power over a time, $E = \int x^2(t)dt$ [26, 27].

For frequencies, the spectral analysis of the audio signal is the process that places it in the mentioned domain to observe how much of the signal lies within each given frequency band over a range of frequencies. The essential connection between the time and frequency domains is a pair of mathematical operators called transforms. Perhaps the most representative operator is the Fourier transform, which converts a time function into a sum or integral of sine waves of different frequencies, each representing a frequency component. "Fourier transform" term refers to the frequency domain representation and the mathematical operation. Fourier transform is a widely applied operator in many techniques and fields, therefore, fully detailing and describing the operator is beyond the scope of this chapter. For this reason, only some concepts that may be of use in processing the data obtained by laser-driven acoustics will be briefly mentioned.

In the frequency domain, the energy of the signal can also be represented in terms of frequency (f), $E = \int x^2(t)dt = \int |X(f)|^2 df$; being thus calculated through either $x(t)$ or $X(f)$, being $X(f)$ the Fourier transform for $x(t)$. The magnitude squared,

Fig. 11.4 (continued) Standoff configuration with samples and microphone encased in a hemi-anechoic chamber with perpendicular laser excitation by Álvarez-Llamas et al. in reference [19]. (**f**) Set-up by Chide et al. in reference [13]. Sample rested on an insulating foam support housed within an anechoic box. Laser incidence was vertical

$|X(f)|^2$, called the energy spectral density (ESD), is always an even, non-negative, real-value function of frequency that represents the distribution of the energy of the signal in the frequency domain. Once defined, the spectral energy density more commonly used is the power spectral density (PSD or simply power spectrum), which refers to the spectral energy distribution found per time unit [26]. The PSD is typically expressed in terms of squared signal units per frequency units (e.g., Pa^2Hz^{-1}) as the power (W) is proportional to the square of the signal.

Resulting from the nature of the acoustic signal, its processing is based on computing the discrete Fourier transform (DFT), that is, to work with information that is discrete and finite in length. However, the fast Fourier transform (FFT) algorithm which enables the speeding up of conversions made by DFT and helps in reducing the complexities of computing replaces it frequently. Furthermore, while DFT is a mere mathematical algorithm that transforms time-domain signals to frequency domain components, FFT algorithm consists of several computation techniques including DFT. Finally, as a result, FFT returns a two-sided spectrum in complex form (real and imaginary parts), which must be treated to get the magnitude and phase.

During the FFT signal processing, some aspects must be considered, like the aliasing of the signal, the use of filters and the application of windows function. Aliasing occurs between frequencies related by an integer multiple of the sampling rate, f_s, the number of points in time-space recorded in 1 s. It is the phenomenon when two distinct continuous signals $x_1(t)$ and $x_2(t)$ produce the same sequence of sample values *x[n]* when sampled at a fixed rate f_s. Thus, to ensure that aliasing effects do not corrupt a signal (or the analysis) sampled at a rate f_s to be fully reconstructed, the signal must only contain frequency components below half that sampling frequency (known as *Nyquist frequency* or maximum frequency f_{max}). Consequently, the *Nyquist rate* ($f_s = 2f_{max}$) is the lowest sampling rate for which a signal can be reconstructed with maximum frequency f_{max}. Filtering is an operation to improve audio signals in many ways, basically separating frequencies associated to the expected signal, from frequencies that are related to uninformative signals, like the sinusoidal oscillations at either 50 Hz or 60 Hz from electrical AC power and their associated high-frequency harmonics and other external signals. This approach helps to further "clean up" the signal in case the performance of an anechoic chamber is not 100%.

Lastly, windowing (application of a windows function) is also a preprocessing step in acoustics to modify the digitized signal before computing the FFT. The Fourier series assumes that the signal is periodic in time t. When the signal is digitized into N samples from 0 to $N - 1$, the Fourier series concludes that the next sample (N) will be the same value as the first (0). Unfortunately, for the vast majority of vibration-originated signals, a discontinuity usually exists between the end of the digitized signal and the beginning of the periodic repetition, thereby causing the FFT algorithm to generate artificial noise. Thus, the windowing adapts the digitized signal by sending it to zero at the beginning and end of the time sample to reduce or eliminate the discontinuity in time and the consequent noise in the FFT. There are different types of window functions that can be applied depending on the

signal and its selection is not a simple task. Each window function has its own characteristics and, therefore, suitability for different applications. Particularly, in the case of impulse signals as those coming from laser-induced plasmas, no window (often called the uniform or rectangular window as there is still a windowing effect) is suggested to be applied.

The recording and processing of the acoustics signal can be carried out via any of the numerous audio editors available, with Audacity being one of the most common since it is free, open-source and cross-platform software. Also, signal processing libraries for acoustic data have been developed for most of the scientific software and languages (e.g., MATLAB, Python).

11.5 Uses of Laser-Produced Acoustic Waves

The fact that short and ultrashort laser pulses of sufficient energy, when focused into a target, no matter the state of the matter, are accompanied by sound and ultrasonic waves has generated interest among various scientific fields (Fig. 11.5) and applications in the last few decades. This section attempts to lay a holistic view of the most actively researched topics in the field of laser-driven acoustics. Doubtlessly, there may be many more references in the scientific literature, but any reader with a deeper interest in any of the presented topics can make use of the cited literature and cross-references therein provided.

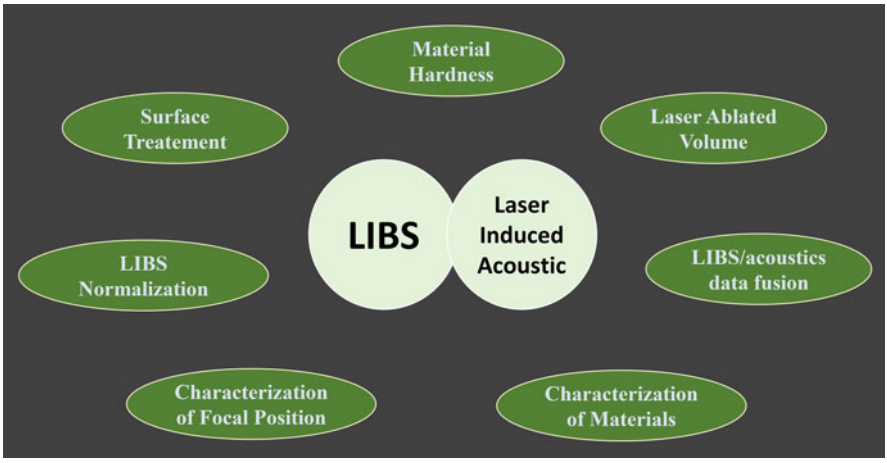

Fig. 11.5 Conceptual map summarizing the prospective main fields of application for laser-induced acoustics in conjunction with LIBS

11.5.1 Optical Emission Signal Normalization

As known, LIBS, as an analytical technique, sometimes has limited applicability, mainly for quantitative purposes. This is due to the inadequate level of analytical figures of merit (particularly accuracy and precision) attainable by the technique compared to other well-established multielemental analytical chemistry tools. While some efforts have been devoted to elucidating the cause-effect relationship of the large pulse-to-pulse optical emission variability, the harsh reality is that LIBS continues to provide unstable signals [28]. In order to alleviate signal fluctuations directly correlated to plasma characteristics and, therefore, to excitation conditions/parameters and physicochemical properties of the sample under evaluation, normalization approaches of raw LIBS data using parameters representative of the actual plasma conditions have been proposed [29]. There are two distinct ways to standardize the recorded lines intensity: (internal) using attributes specific to the LIBS spectrum, such as normalizing to the whole spectrum area, the spectral background or by using the intensity of an internal standard line, or quantities directly derived from them e.g., plasma parameters such as the temperature T_e and electron density n_e; and (external) i.e., monitoring other data in addition to the LIBS spectrum, either simultaneously, like the acoustic signal induced by the shock wave, or after, like the ablated mass.

In particular, regarding normalization with acoustic response, the earliest document in this area dates back to the late 1980s and is attributed to Chen et al. [3]. Using a pulsed excimer laser running at UV 308 nm wavelength, researchers identified that the magnitude of the acoustic wave associated with plume generation is linearly proportional with the emission intensity of both major and minor elements in several pure metallic samples and alloys. Over a wide range of vaporization conditions, including laser power, focusing, and surface pretreatment, and over a limited range of composition, the emission peak area (EMPA) and the acoustic peak height (ACPH) were well correlated with each other, thus advancing the possibility of using the acoustic signal as an internal standard for normalizing analytical signals derived from various types laser-generated plasma plumes [25, 30].

In this context, Hrdlička et al. [9] used the square power of the acoustic signal for the internal standardization of LIBS spectra, in the interval of 290–340 nm, of a glazed wall tile. They successfully compensated for the decrease in the optical emission of some lines of the major elements (Si, Cr, Al, and Ti) monitored during the depth profiling in single-ablation spots with two lasing wavelengths, 1064 nm and 532 nm. Researchers obtained similar results with both lasing wavelengths despite using different irradiance values and demonstrated that the decrease of emission intensity after drilling through the glaze into the substrate as well as the shot-to-shot fluctuations could be successfully compensated for via the acoustic emission.

Anabiarte et al. [25] demonstrated the use of the estimated acoustic energy to normalize atomic LIBS spectra and prevent the results from being affected by unwanted changes in the experimental conditions, such as the laser pulse energy. They did so by means of the speckle pattern perturbation, monitored with a

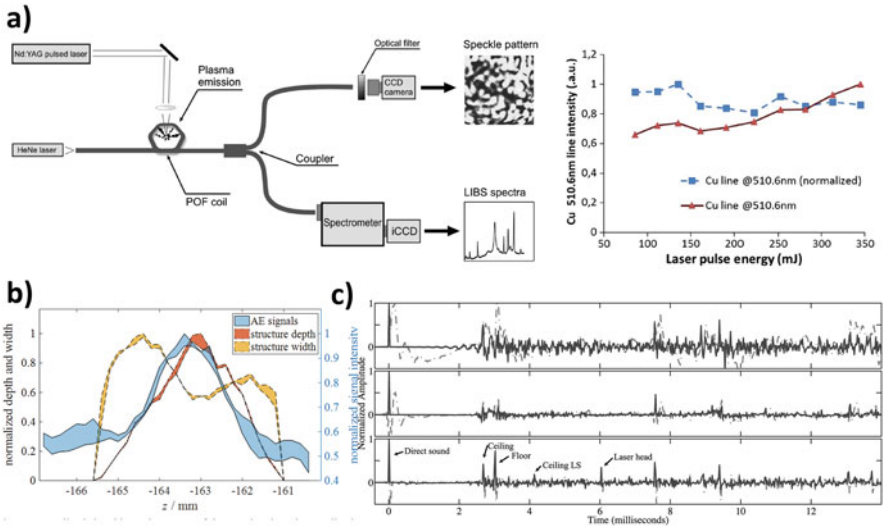

Fig. 11.6 (**a**) Experimental Set-up used in [25] showing the sensing device based on a coiled plastic optical fiber for simultaneously collecting the light emission and the shockwave from the laser-ablation and its acoustic shockwave and the normalization capability for the Cu I emission line at 510.6 nm (Adapted from [25]). (**b**) Normalized signal intensity ranges of the acoustic signals and normalized structure depth and width ranges in dependency on the position of the z-axis [33]. (**c**) Measured (dashed-dotted line) and deconvolved (solid line) room impulse responses for a spherical loudspeaker (upper box), a directional loudspeaker (middle box), and a LIB event (lower box) [36]

conventional CCD camera placed at the end of a coil of plastic optical fiber (POF) and processed with an intra-image contrast ratio method (Fig. 11.6a). This normalization can enable a better estimation of the sample's chemical composition.

Similarly, Lu et al. [31] demonstrated that acoustic normalization can be used to reduce fluctuations in raw LIBS data toward improving the precision and accuracy of coal calorific value measuring. By means of acoustic normalization, the relative standard deviation (*RSD*) of shot-to-shot intensities of spectral lines of C (I) 193.1 nm, C (I) 247.8 nm, H (I) 656.3 nm and N (I) 868.1 nm were significantly reduced from 10.16, 6.53, 3.79 and 5.21% to 7.01, 4.40, 2.81 and 3.54%, respectively. However, they also observed that the compaction pressure of samples affected the correlation between acoustic energy and spectral intensity; a circumstance that shows that normalization is not effective in every analytical scenario.

It should be noted that the approach to acoustic normalization is not limited exclusively to plasmas in air and, therefore, to acoustic waves propagating in this medium. Thus, Huang et al. [32] proposed a spectral normalization method based on the acoustic signals measured by a hydrophone immersed in water. Their results showed clearly that the spectral line intensity had a better linear relationship with the acoustic energy than with the laser energy. Accordingly, acoustic normalization demonstrated better performance in reducing LIBS spectral fluctuation than laser

energy normalization did. Calibration curves for the quantitative analysis of Mn, Sr, and Li were constructed in the work on the basis of the proposed acoustic normalization method with improved analytical performance being observed.

11.5.2 Characterization of Focal Position

Another potential application for which the laser-generated acoustic signals have been used is the accurate establishment of the focal point in experimental setups. Schulze et al. [33, 34] proposed a method capable of automatically positioning the focal spot for ultra-short pulse laser ablation processes by detection of airborne acoustic emissions (Fig. 11.6b). In the field of laser ablation-based manufacturing processes, the correct positioning of the laser focus relative to the work piece and the detection and elimination of geometrical deviations are extremely important to ensure the required precision. Regarding laser ablation fabrication using ultra short pulsed Nd:YAG lasers, problems arise when the focal plane is not on the surface of the work piece. In fabrication schemes using laser ablation, defects sourcing from target mispositioning usually cannot be corrected during the machining process and remain in the final product. To solve this, an acoustical sensor was built to provide a correctly adjusted focal plane at the beginning of the first manufacturing step. The analysis of airborne acoustic emissions during the ablation process yielded specific details about the focal position of the laser beam. Based on this correlation, an acoustic focus positioning model was built up to automatically adjust the focal plane prior to ablation.

In a similar fashion, it was identified that the acoustic environment surrounding a focusing pulsed laser beam can influence the probability of plasma formation from laser-induced breakdown of air at atmospheric pressure [35]. In open air, the location of an air plasma produced by a focused YAG laser pulse was found to be closer to the focal point used to focus the laser beam. In contrast, upon coaxially confining the same beam along the interior of a quartz tube, the position of the air plasma shifted away from the focal point and toward the focusing lens, i.e., to a region of lower laser fluence. Such a circumstance was justified on the basis of the interaction between standing acoustic waves (formed from sound waves produced by previous laser-induced plasmas) and the impinging laser pulse. The standing acoustic waves rarified the medium within the tube, as commented in the fundaments section, producing areas of slight increases and decreases of the atmospheric pressure value. These antinodes had a noticeable effect on the probability of creating an air plasma at given coordinates along the optical path. Rarefaction effects have been shown to be particularly relevant when dealing with sequences of laser pulses and was not observed in single shot experiments. Special consideration of this phenomenon should be given by researchers interested in experiments where the position of a laser-induced plasma is changed without further adjustment of the laser or associated optics (such as raster sampling or *2D*/*3D* mapping).

Lastly, the laser-induced breakdown of air has been proposed as an ideal acoustic point source emitting a repeatable, broadband, and omnidirectional radiation pattern

within the audible bandwidth to provide a more accurate temporal and spatial representation of room reflections than that reported for conventional loudspeakers (Fig. 11.6c) [36].

11.5.3 Surface Treatment

Perhaps, the first report on the use of acoustics to monitor surface ablation can be traced back to the early 1990s [37]. Short duration (<30 ns FWHM), unipolar, acoustic transients corresponding to compressive stress in bulk ceramic YBCO targets 0.5–1 mm thick prepared with plane-parallel faces were monitored for variable fluence ($\leq$ 2 J cm^{-2}) using a KrF laser emitting at a wavelength of 248 nm with pulse of duration ~10 ns full-width at half-maximum (FWHM). The targets were mounted onto a fast time-response piezoelectric transducer formed by a 9 μm thick polyvinylidene fluoride (PVDF) film sandwiched and bonded between the sample and a ~4 mm thick Perspex impedance matching stub. Results demonstrated the usefulness of fast time-response photoacoustic measurements for non-destructive evaluation and characterization of the properties of bulk ceramic superconducting (high-T_c) materials. Acoustics provided information on the magnitude and time evolution of the pressure generated at the material surface by the recoil momentum of the ablating species and by any backscattered products of the interaction with the excimer laser.

From the results on laser-acoustics as a diagnostic tool during the fabrication of layered structures featuring thin films of different elemental composition, other uses of this data produced alongside ablation have also been explored for a variety of purposes. In this line, Lee et al. [38] used acoustic emission to monitor pulsed 532 nm laser-induced damage on aluminum films (of thickness ranging from 13 nm to 50 nm) deposited upon quartz. Results revealed that damage thresholds measured by the acoustic probe (interpreted as evaporative events) were in the 30 mJ·cm^{-2} to 100 mJ·cm^{-2} range, which are about 30% higher than those measured using the optical probe (interpreted as melting events). Furthermore, experimental data were found to be consistent and reproducible and could be satisfactorily simulated by a one-dimensional heat diffusion model with a temperature-dependent absorption. Authors concluded that the ablative acoustic signal seemed to track the vapor pressure pulse released from target surfaces at temperatures well below the boiling point of aluminum. This low threshold temperature was easily reached by small energy increments beyond melting point since the absorptance of liquid aluminum increased upon melting. This explained the unforeseen sensitivity of the acoustic probe relative to the optical one, especially for thicker films.

Gusev et al. [39] studied theoretically and experimentally the influence of melting upon the excitation of surface acoustic wave (SAW) pulses in silicon. According to their prior theoretical background for the optimization of the interface waves generation by lasers in experiments from their analytical solutions for the leaky Rayleigh, Scholte, and lateral waves excited via the laser-induced thermoelastic effect [40]

authors predicted that SAW was predominantly generated in the solid phase due to the absence of shear rigidity of any liquid layer. The characteristic changes in the SAW pulse both the shape and the amplitude, either its saturation or even its decrease, observed above the melting threshold are explained theoretically to be a result of the decrease of the heat flux into the solid phase as well as due to the decrease of the volume of the solid phase caused by melting. Experimentally, for laser pulses of 7 ns duration at 355 nm wavelength, the threshold values of laser fluence for melting $F_m = 0.23 \pm 0.04$ J cm^2 and for ablation $F_a = 1.3 \pm 0.2$ J cm^2 were determined as the situations of characteristic changes in the observed SAW pulses. Furthermore, the influence of reflectivity changes on the SAW pulse was identified negligible in comparison with the effect of melt-front onto the heat flux to the solid phase. Also, Mesaros and collaborators [4] performed real-time detection of Nd:YAG pulsed laser surface melting by analyzing the photoacoustic signals produced on AISI 304 stainless steel samples. Comparison between the amplitudes of the transversal and longitudinal waves allowed them to identify the fluence thresholds for surface melting.

In a similar fashion, Liu and coworkers [41] evaluated excimer laser (at a wavelength of 248 nm and pulse duration of ca. 20 ns) ablation on a chromium thin film (400 nm thick) directly deposited on a glass substrate via DC magnetron sputtering system. No intermediate adhesion layer was present between the film and the substrate. Acoustic emission arising from the ablation process and optical microscope observation of the surface morphology of the patterned areas were used as diagnostic tools. In the experiment, an acoustic emission transducer was coupled to the sample to acquire sound waves sourcing from laser–material interaction and an oscilloscope was used to record the signals. Scores for several characteristics of the acoustic emissions (e.g., average power, RMS, etc.) showed a clear connection with the ablation mechanisms of the thin metal films for variable laser fluences. Furthermore, since those scores discriminated well the damage to the glass substrate, authors considered that the evaluation of acoustic emissions may also be considered as a monitoring strategy for excimer laser micromachining.

Directly related to this topic, acoustic wave generation during excimer laser interaction with copper substrates was also investigated [42]. After finding that audible acoustic waves could be detected during laser surface cleaning processes—the acoustic wave emission disappeared when the surface was completely clean—a numerical model was proposed to study the ablation threshold and morphology change of the substrate material under laser irradiation. This numerical formula, investigating the relationship between the amplitudes of the emitted acoustic waves and some contributing factors as bulk and surface responses from the initial conditions of the substrate, pulse dependence (laser fluence, number of pulses), and morphology change of the substrate surface, was established for real-time monitoring of laser-solid interaction.

The potential of acoustic monitoring was also examined for laser ablation of crust on historical sandstone samples contaminated due to prolonged interaction with the environment and for specimens covered by artificial crust layers [43]. Jankowska et al. studied experimentally the laser cleaning of moistened, thoroughly wet, and dry

historical sandstones covered by a black, porous encrustation and model specimens with artificial coverage using acoustics. An electret microphone was placed either behind of, close to the back surface, or in front of the sample to detect the snapping sound accompanying the interaction of the laser pulse with the sample. Authors confirmed that the detected sound correlated strongly with the progress of the crust ablation process, thereby allowing its reliable monitoring. Dependency of the measured sound intensity on laser interaction parameters, like pulse energy, crust thickness and degree of moistening was identified.

This application continues to prove its usefulness in recent times. The analysis of the spectrum obtained by Fast Fourier Transform of the Photoacoustic Induced by Laser Ablation (PILA) during laser-assisted paint removal process has been described, in order to identify the presence of paint components on a metallic surface, optimize the ablation rate and propose the PILA technique for monitoring the laser ablation of paint layers [44]. Also, a closed-loop control that reflected the status of laser paint removal based on real-time monitoring of the evolution of the amplitude and the local standard deviation of the acoustic signal has been considered to achieve a good clean effect without damaging the substrate. In the work, the frequency range was set in 7 kHz–10 kHz region and signals were found to gradually decrease to a steady value upon removal of the paint as represented in Fig. 11.7a [45].

Recently, a prototype hybrid photoacoustic (PA) and optical system for the on-line monitoring of laser cleaning procedures was presented. The intrinsically generated PA signals combined with high-resolution optical images provided the opportunity to follow the cleaning process accurately in real time [46], Indeed,

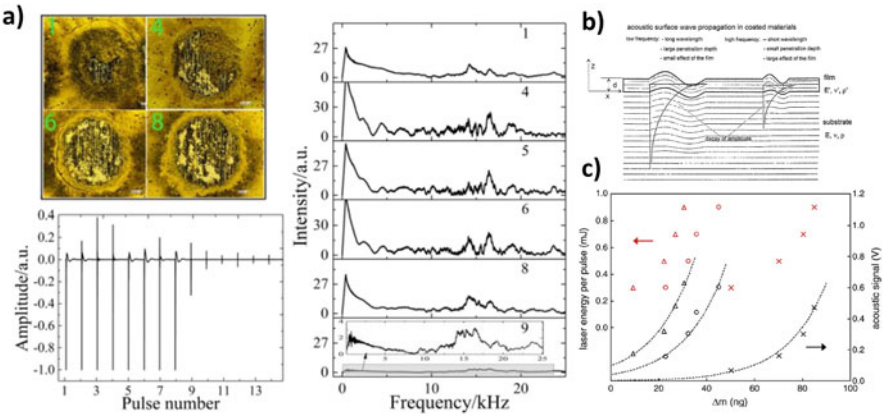

Fig. 11.7 (**a**) Surface morphology of a white paint after irradiation by 1, 4, 6, and 8 laser pulses (45 mJ) together with the time domain acoustic signals (14 pulses) and the frequency domain spectra. Adapted from [45] (**b**) Two surface waves with different frequencies propagating on coated materials[49]. (**c**) Pulsed laser ablation of PVC targets at various focal spot size ϕ (open traingle = 40 μm, open circle = 75 μm, and cross = 100 μm). Plotted are *the laser energy (red) and the acoustic signal (black)* against the mass (Δm) removed per pulse [57]

photoacoustic (PA) imaging technologies have transcended the frontiers of its main niche in contemporary biomedical research studies toward innovative applications in cultural heritage diagnostics and laser cleaning monitoring. As discussed in [47], PA signals offer substantially high detection sensitivity, providing optical absorption contrast at high spatial resolution. This unique combination of features was employed for establishing novel diagnostic methodologies aiming to uncover concealed features and provide structural information in multi-layered objects. Thus, the rich potential of emerging PA technologies, not only in the field of cultural heritage, offer exciting possibilities for its future implementation as a diagnostic and monitoring approach allowing for a safe and well-controlled ablative procedure that will safeguard the original object surface.

11.5.4 Material Hardness

As discussed above, the wideband acoustic impulses generated by short laser pulses and propagating along the surface of the materials are very sensitive to films and surface treatments, since the wave energy is concentrated near the surface. This is particularly true for coated and surface-modified materials the wave velocity depends on frequency. This phenomenon, named dispersion, may be used to elucidate important parameters such as film thickness, density and Young's modulus, which depends on the bonding conditions and the microstructure and is proportional to material's hardness [48]. Multiple uses of acoustic waves for the inspection of surfaces can be found in scientific literature. One of such applications is assessing the thickness of layers. Laser-induced plasma acoustics have been used to evaluate the quality of diamond-like carbon films with thicknesses down to few nanometers [49] (Fig. 11.7b) or to characterize laser-hardened steels up to depths of 1 mm [50, 51]. Further surface traits probed using laser-induced acoustics include the elasticity of plasma-sprayed deposits on multiple substrates [52, 53] or the characterization of nanostructured materials with unusual mechanical properties [54, 55]. Laser acoustics have also helped to evaluate subsurface damage in a non-destructive way [56].

11.5.5 Ablated Volume

One of the observables during pulsed laser ablation is the removed mass. Given the difficulties and the large uncertainties in real-time monitoring of the quantity of ablated sample, in the late 1990s researchers started using acoustical signals to monitor these quantities [5]. Stauter et al. found that, on a specific domain of laser fluence, the ablation rate on ceramics with short laser pulses at different wavelengths could be related to the shock wave energy. Furthermore, results showed that, rather than using the laser beam deflection technique, via a simple calibration procedure, it was possible to replace the laser probe by a microphone.

The photoacoustic signal was also considered as an indirect weighing for measuring mass removed (Δm), especially at sub-ng level [57]. The Δm per pulse in laser ablation at both the *ns* and the *ps* time regimes was shown to correlate with the acoustic signal A and the laser spot size ϕ. Functional forms of $\Delta m(A, \phi)$ were deduced for aluminum and polyvinyl chloride, represented in Fig. 11.7c targets ablated continuously for 2 to 3 h; with the averaged acoustic signal (peak-to-peak) recorded every 15 min, for fluence ranging from 1.5 through 88 J cm^{-2}. Computed Δm agreed with empirical values within the experimental error.

The benefits of this approach have even been extended to field-deployable sampling of solids [58, 59]. In order to track acoustic pressure waves formed for every individual laser ablation event during mass removal by a portable laser ablation (pLA) system, a directional microphone was integrated into the handheld pLA-module. Its performance was investigated for various samples, revealing discrepancies as a function of their ablation thresholds. While samples with high ablation thresholds, such as glasses and minerals, showed a linear relationship between the acoustic signal and the amount of mass removal, for samples with low ablation thresholds, e.g., metals, the acoustic signal was identified to be mainly influenced by the laser fluence at the ablation spot rather than by the amount of mass removal.

Also, in this line, in preparation for the SuperCam/Mars Microphone in-situ scientific tasks, and using a specifically designed LIBS set-up coupled with an acoustic test bench under ambient terrestrial atmosphere, shot-to-shot evolution of the acoustic signal associated with the plasma was studied with regards to the morphology of the laser-induced crater [13]. Results from the experiments revealed that the amplitude of the acoustic signal decreased as a function of the number of shots during a depth profile. Such a decrease in the acoustic energy was well-correlated with the target hardness/density. Furthermore, investigations confirmed that the acoustic energy may be used as a remote tracer of the ablated volume of the target, regardless of its physical properties. Experiments revealed a linear relationship between the normalized acoustic energy and the ablated volume. All this demonstrated that the use of a microphone may add valuable new data to the ablation process associated to the thicknesses of the coatings and the presence of alteration layers; a new information that is independent of the abundances of chemical elements reported from optical emission of LIBS sparks.

11.5.6 Detection and Characterization of Materials

Some research has addressed the nature of acoustic signals as an observable capable of detecting and recognizing a material. In this context, van den Heuvel and collaborators [60] used laser excitation of soils for standoff detection (and classification) of buried landmines including non-metallic mines. An acoustic pulse that propagated along the soil was generated after heating by the delivered pulses, which featured an energy of up to 350 mJ with a 20 Hz repetition rate at 1.064 μm, of a primary small area of the surface of the soil and a secondary volume of air in and

above the soil in few nanoseconds. The acoustic shock wave generated by the laser pulse reflected back from the buried objects into the surface; the echo was then measured with laser a Doppler vibration (LDV) sensor at a range of several meters.

Also framed in the context of security and defense, Moros et al.[61] proposed the acoustic spectroscopy as an approach to detect contents within different packaging. Focused laser pulses (13 ns length) operated at 1 Hz were used to generate sound fields on two-component systems at a distance of 50 cm. Thus, under boundary conditions, the sound fields, directly radiated by the vibrating elastic structure of the outer component but modulated by the inner component that modified the dynamical integrity of the system, excited the surrounding air in contact with it. Consequently, the resulting frequency spectrum was observed to be a useful indicator of the concealed content—gas (air), liquid (water) or solid (sand)—that influenced the acoustic airborne transients originated from the wall of the opaque chemical-resistant polypropylene and stainless-steel containers.

The acoustic responses produced by pulsed laser ablation have also found their use in the field of biomedicine [62]. Already in the early 1990s, Esenaliev et al. [63] investigated the amplitudes and profiles of the acoustical and shock waves generated and propagating in atherosclerotic human aorta tissues and an aqueous $CuCl_2$ solution under pulsed ($\tau = 50$ ns) UV ($\lambda = 308$ nm) laser irradiation (below and above the ablation threshold) to calculate the rise rates, pressure gradients and propagation velocities of shock waves in biotissues. Similarly, Li and collaborators [64] evaluated the thermal effects of the laser-induced surface acoustic waves toward their practical application for measuring the elasticity of normal and diseased tissues in dermatology and other surface epithelia. The challenge of mitigating potential problems owing to heat generation upon direct pulse application to the tissue led them to propose as an alternative the application of a thin agar membrane. The layer would act as a shield to protect the tissue. This approach was verified by measuring the mechanical properties of skin in a Thiel mouse model. Similarly, laser-induced surface acoustic waves were also considered to characterize the elastic properties of different layers of organs such as the urinary bladder, which are essential to ensure its functioning, including the storage and voiding phases of the micturition cycle; in essence, a critical step for understanding various disease processes and improving patient care [65].

In the same fashion, Ghasemi et al. [66] employed laser-induced breakdown spectroscopy and the subsequent acoustic response during microplasma formation to identify cancerous human breast tissue. Higher decibel audio signals emanating from the microplasma and a subsequent audio blueshift were reported for malignant cancerous tissues when compared to those of healthy ones as represented in Fig. 11.8a. Furthermore, authors justified the higher intensities of the acoustic signals (stronger shockwave) in cancerous tissues from the higher abundance of tracer elements (Ca, Na, and Mg) as well as higher plasma temperature and electron density.

Finally, the use of laser-driven acoustic waves has also crossed the Earth borders. One of the latest and most innovative applications of the LIBS+Microphone tandem has been its incorporation in the SuperCam instrument onboard the Perseverance

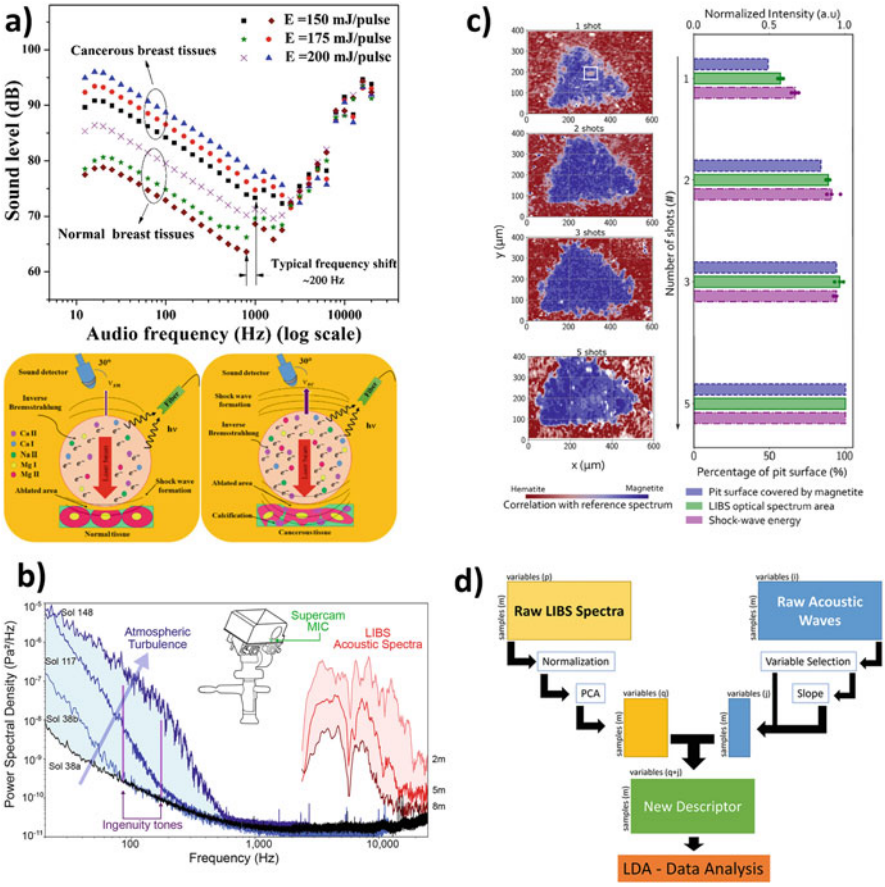

Fig. 11.8 (**a**) (Above) Frequency-domain acoustic signal from cancerous and normal breast tissues after excitation with laser pulses of different energy (150, 175, and 200 mJ·pulse^{-1}); a 200 Hz spectral shift to higher frequency accompanying a sound level elevation for the cancerous tissues with respect to the healthy ones can be observed. (Below) Schematics of plasma formation on the tissues during the laser shot. Adapted from [66]. (**b**) Different sounds recorded by SuperCam. Atmospheric spectra (light blue area) and LIBS acoustic spectra (light red area) are shown [67]. (**c**) Raman mapping of laser-induced craters on hematite resulting from irradiation using 1, 2, 3, and 5 laser shots, showing the change from hematite (red) to magnetite (blue). comparison between the percentage of the crater surface covered by magnetite (blue bars), the LIBS optical spectrum area in the UV range (green) and shockwave energy (purple) [20]. (**d**) Data fusion process scheme combining LIBS and acoustic data for mineral differentiation [19]

rover within the Mars2020 mission. The world's first Mars microphone was fitted into NASA's Mars Polar Lander, yet contact was lost on December 3, 1999, 10 min before landing on Mars. A second microphone was mounted on NASA's Mars Phoenix lander, although it had to be turned off before launch due to last-minute technical difficulties. After these previously unsuccessful attempts, Perseverance

carried out the recording of sounds on Mars successfully for the first time [67]. SuperCam's main mission is the mineralogical study of the Martian surface using, among other analysis techniques, LIBS and sound recordings with a microphone. The SuperCam microphone records sound in the 0.1–10 kHz range, either naturally occurring (atmospheric) or artificially induced (LIBS, Ingenuity helicopter or the rover itself). The microphone can be operated in synchronization with the LIBS laser, recording lapses strictly in the range of the laser pulse and the plasma lifetime, or in a passive way, thus keeping the collection open for larger spans. Figure 11.8b represents the main sounds recorded by SuperCam's microphone and its frequency range.

Previously to its in-situ deployment in Mars, the potential of the Mars microphone was demonstrated for laser ablation under Earth atmosphere in a preliminary study with a small set of samples and fixed experimental conditions [13, 68]. Then, a detailed characterization was performed under Mars environmental conditions [17]. In order to record the sounds of the SuperCam laser hits on rocks under Mars atmosphere, the microphone should be able to record audio signals from 100 Hz to 10 kHz, with a sensitivity sufficient to monitor laser impacts at distances up to 8 m. Thus, tests performed on Martian soil simulants within the Aarhus planetary simulation facility set to controlled Martian conditions, i.e., 6 mbar CO_2 atmosphere, with winds and T at the microphone being -80 °C, confirmed that the SuperCam/Mars Microphone met the requirements satisfactorily. Furthermore, results showed that the variation of the acoustic energy of the shock waves depends on the level of compaction of the target. Additional experiments were also conducted at the *Institut de Recherche en Astrophysique et Planétologi*e (IRAP, Toulouse, France) under Mars atmosphere to explore all the main instrumental, target-dependent, and environmental parameters that likely govern the laser-induced acoustic signal expected to be generated on Mars [69]. Two different types of samples were considered to study the influence of target properties and laser-matter interactions on the acoustic signal and the ablated volume. With these being, five pure metals with tabulated and well-known physical properties and a set of natural homogeneous minerals obtained from the *Collection de Minéraux* at *Sorbonne Université, Paris, France*. As SuperCam observe targets at various distances from the rover, under an atmospheric pressure that follows diurnal and seasonal cycles, the study proposed a sequence of corrections to apply to Mars data in order to compare acoustic signal from targets sampled under different configurations. Results revealed that, for minerals (except graphite) and rocks the growth of the crater was responsible for the shot-to-shot decrease in acoustic energy, thereby confirming that monitoring the acoustic energy during a burst of laser shots could be used to estimate the laser-induced cavity volume. Moreover, since the amount of matter removed by the laser was more relevant when the target was soft, the decreasing rate of the acoustic energy was correlated with the hardness of the material.

Finally, other studies also conducted by Chide et al. [20] have discovered the root cause of the increase in acoustic signal amplitude over some laser shots to the laser ablation of hematite, goethite, and diamond. Subsequent analysis of the craters formed after laser ablation using Raman spectroscopy and scanning electron

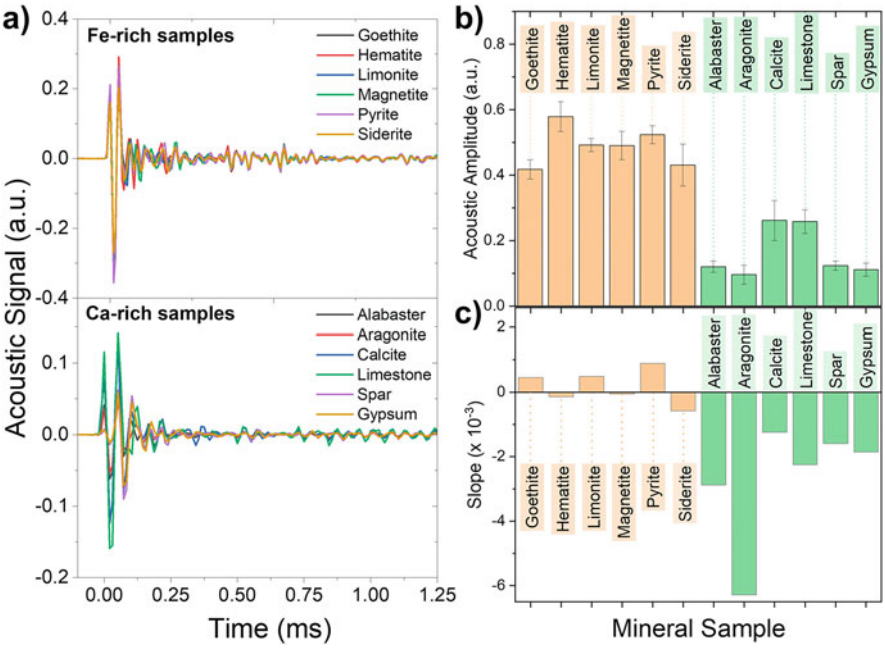

Fig. 11.9 (**a**) Average time domain signals in the 0.1–1.25 ms range. (**b**) Average amplitude in the first maximum of the acoustic wave for each mineral studied. (**c**) Slope value obtained for each mineral. Values closer to 0 indicated stable signal during the laser shot series, while negative values implied decreases in the measured sound intensity. Reproduced faithfully from reference [19]

microscopy revealed that both, hematite, and goethite, had been transformed into magnetite whereas diamond had been transformed into amorphous-like carbon (Fig. 11.8c). These results gave insights into the influence of the target's physical properties over the acoustic signal. Experiments conducted by Alvarez-Llamas et al. [19] have well-corroborated these points. Figure 11.9 shows the variation of both the average amplitude in the first maximum of the acoustic wave (Fig. 11.9b) and the coefficient of intensity variation as the material was drilled by the laser in one sampling position—slope—(Fig. 11.9c), for 6 rich in Fe and 6 rich in Ca geological specimens. As seen, clear differences are detected between the two subgroups. First, the original plasma blast evidence to be more sensitive for Fe-bearing minerals as compared to the Ca-rich ones. Furthermore, the negative slope revealed for the Ca group indicates lower hardness and higher ablation rate per sample.

In summary, all these investigations have revealed a range of complementary information on the physical properties of the ablated targets when listening to the laser-induced acoustic signals that can considerably help to better document the geological material analyzed by SuperCam when associated to the elemental composition of rocks and soils of the Mars surface determined by LIBS. But most importantly, in the context of Mars surface exploration, the extremely specific

behavior of the acoustic response anticipates that the microphone data may help discriminating mineral phases whereas LIBS data can only discern the elements composing the target.

11.5.7 LIBS and Acoustics Data Fusion

Despite the close relationship between laser-induced plasmas and the acoustics derived from them, to date few scientists in the topic have focused their efforts on trying to exploit the synergy of both simultaneous information. As of the writing of this chapter, only the work by Alvarez-Llamas et al. directly addresses the combination of both sources [19]. In that work, LIBS data and simultaneously acquired acoustic recordings from Fe-based and Ca-based minerals laser-probed at a sampling distance of two meters under Earth and Mars-like atmospheres were preprocessed to develop a mid-level data fusion strategy. The scheme was based on the concatenation of scores matrix resulting from LIBS data principal components analysis (PCA) and two different features extracted from the time domain acoustic responses, the wave peak-to-peak amplitude and the variation of this value for a specific sampling position. Figure 11.8d represents the mid-level data fusion scheme used in this work. By doing so, a new global sample descriptor was created allowing for better differentiation of samples with extremely similar LIBS spectra. Results revealed that, under a tightly controlled experimental scenario, acoustic data in the time domain could be merged with LIBS spectra to enhance the discrimination capabilities of the technique owing to differences found in the laser-produced sound wave, thus paving the way toward extracting relevant chemical data from this newly exploited source of information.

This paper constitutes a preliminary attempt at fusing LIBS and acoustics to maximize the information yielded by analysis events. Yet, there is still a long way to go. Mainly for future implementation in the analysis of samples in an open environment. As discussed above, the uncontrollable presence of echoes or interferences at such scenarios can substantially alter the time domain signal and cause an antagonistic effect and may even categorize as similar samples that are significantly different.

Acknowledgments This work was funded by projects UMA18-FEDERJA-272 from the *Junta de Andalucía,* Spain and PID2020-119185GB-I00 from *Ministerio de Ciencia e Innovación*, Spain. P.P. is grateful to the European Union's NextGenerationEU plan and the Spanish Ministerio de Universidades for his Margarita Salas fellowship under the program "Ayudas para la recualificación del Sistema Universitario español."

References

1. Young M, Hercher M, Wu C. Some characteristics of laser-induced air sparks. J. Appl. Phys. 1966;37:4938.
2. Ujihara K, Kamiyama M. Laser-induced sonic waves in air. Proc. IEEE. 1969;57:1664.

3. Chen G, Yeung ES. Acoustic signal as an internal standard for quantitation in laser-generated plumes. Anal. Chem. 1988;60:2258.
4. Mesaros M, Martínez OE, Bilmes GM, Tocho JO. Acoustic detection of laser induced melting of metals. J. Appl. Phys. 1997;81:1014.
5. Stauter C, Gérard P, Fontaine J, Engel T. Laser ablation acoustical monitoring. Appl. Surf. Sci. 1997;109–110:174.
6. Laserna J, Palanco S. Spectral analysis of the acoustic emission of laser-produced plasmas. Laser induced plasma spectroscopy and applications. 2002;42:ThE21.
7. Conesa S, Palanco S, Laserna J. Acoustic and optical emission during laser-induced plasma formation. Spectrochim. Acta B. 2004;59:1395.
8. Chen X, Bian BM, Shen ZH, Lu J, Ni X. Equations of laser-induced plasma shock wave motion in air. Microw. Opt. Technol. Lett. 2003;38:75.
9. Hrdlička A, et al. Correlation of acoustic and optical emission signals produced at 1064 and 532 nm laser-induced breakdown spectroscopy (LIBS) of glazed wall tiles. Spectrochim. Acta B. 2009;64:74.
10. Gandolfi M, Banfi F, Glorieux C. Optical wavelength dependence of photoacoustic signal of gold nanofluid. Photoacoustics. 2020;20:100199.
11. Jansen ED, Asshauer T, Frenz M, Motamedi M, Delacrétaz G, Welch AJ. Effect of pulse duration on bubble formation and laser-induced pressure waves during holmium laser ablation. Lasers Surg. Med. 1996;18:278.
12. Manikanta E, Vinoth Kumar L, Venkateshwarlu P, Leela C, Kiran PP. Effect of pulse duration on the acoustic frequency emissions during the laser-induced breakdown of atmospheric air. Appl. Opt. 2016;55:548.
13. Chide B, et al. Listening to laser sparks: a link between laser-induced breakdown spectroscopy, acoustic measurements and crater morphology. Spectrochim. Acta B. 2018;153:50.
14. Bosáková M, Purohit P, Alvarez-Llamas C, Moros J, Novotný K, Laserna J. A systematic evaluation on the impact of sample-related and environmental factors in the analytical performance of acoustic emission from laser-induced plasmas. Anal. Chim. Acta. 2022;1225:340224.
15. Attenborough K. Review of ground effects on outdoor sound propagation from continuous broadband sources. Appl. Acoust. 1988;24:289.
16. Alvarez-Llamas C, Purohit P, Moros J, Laserna J. Differentiation of closely related mineral phases in a Mars atmosphere using frequency domain laser-induced plasma acoustics. Anal. Chim. Acta. 2022;1226:340261.
17. Murdoch N, et al. Laser-induced breakdown spectroscopy acoustic testing of the Mars 2020 microphone. Planet. Space Sci. 2019;165:260.
18. Hosoya N, Nagata M, Kajiwara I. Acoustic testing in a very small space based on a point sound source generated by laser-induced breakdown: Stabilization of plasma formation. J. Sound Vib. 2013;332:4572.
19. Alvarez-Llamas C, Purohit P, Moros J, Laserna J. LIBS-acoustic mid-level fusion scheme for mineral differentiation under terrestrial and martian atmospheric conditions. Anal. Chem. 2022;94:1840.
20. Chide B, et al. Acoustic monitoring of laser-induced phase transitions in minerals: implication for Mars exploration with SuperCam. Sci. Rep. 2021;11:24019.
21. Beranek LL, Sleeper HP. The design and construction of anechoic sound chambers. J. Acoust. Soc. Am. 1946;18:140.
22. Chung BK, Tunku U, Rahman A, Lumpur K. Handbook of antenna technologies. Handb. Antenna Technol. 2020:1.
23. Bolt RH. Note on normal frequency statistics for rectangular rooms. J. Acoust. Soc. Am. 1946;18:130.
24. Błaszak MA. Acoustic design of small rectangular rooms: normal frequency statistics. Appl. Acoust. 2008;69:1356.

25. Anabitarte F, Rodríguez-Cobo L, López-Higuera J-M, Cobo A. Normalization of laser-induced breakdown spectroscopy spectra using a plastic optical fiber light collector and acoustic sensor device. Appl. Opt. 2012;51:8306.
26. Hartmann W. Acoustic signal processing. In: Springer handbook of acoustics. New York, NY: Springer New York; 2007. p. 503.
27. Havelock D, Kuwano S, Vorländer M. Handbook of signal processing in acoustics. Berlin: Springer; 2008.
28. Castle BC, Talabardon K, Smith BW, Winefordner JD. Variables influencing the precision of laser-induced breakdown spectroscopy measurements. Appl. Spectrosc. 1998;52:649.
29. Zorov NB, Gorbatenko AA, Labutin TA, Popov AM. A review of normalization techniques in analytical atomic spectrometry with laser sampling: from single to multivariate correction. Spectrochim. Acta B. 2010;65:642.
30. Pang HM, Yeung ES. Laser-enhanced ionization as a diagnostic tool in laser-generated plumes. Anal. Chem. 1989;61:2546.
31. Lu P, et al. Determination of calorific value in coal by LIBS coupled with acoustic normalization. Appl. Phys. B Lasers Opt. 2021;127:1.
32. Huang F, et al. Normalization of underwater laser-induced breakdown spectroscopy using acoustic signals measured by a hydrophone. Appl. Opt. 2021;60:1595.
33. Kacaras A, Bächle M, Schwabe M, Zanger F, León FP, Schulze V. Acoustic emission-based characterization of focal position during ultra-short pulse laser ablation. Procedia CIRP. 2019;81:270.
34. Schulze V, Weber P, Ruhs C. Increase of process reliability in the micro-machining processes EDM-milling and laser ablation using on-machine sensors. J. Mater. Process. Technol. 2012;212:625.
35. Craig SM, Brownell K, O'Leary B, Malfitano C, Kelley JA. The effect of standing acoustic waves on the formation of laser-induced air plasmas. Appl. Spectrosc. 2013;67:329.
36. Gómez Bolaños J, Delikaris-Manias S, Pulkki V, Eskelinen J, Hæggström E. Laser-induced acoustic point source for accurate impulse response measurements within the audible bandwidth. J. Acoust. Soc. Am. 2014;135:EL298.
37. Dyer PE, Farrar SR, Key PH. Fast time-response photoacoustic studies and modelling of KrF laser ablated $YBa_2Cu_3O_7$. Appl. Surf. Sci. 1992;54:255.
38. Lee KC, Chan CS, Cheung NH. Pulsed laser-induced damage threshold of thin aluminum films on quartz: experimental and theoretical studies. J. Appl. Phys. 1996;79:3900.
39. Gusev V, Kolomenskii AA, Hess P. Effect of melting on the excitation of surface acoustic wave pulses by UV nanosecond laser pulses in silicon. Appl. Phys. A Mater. Sci. Process. 1995;61:285.
40. Gusev V, Desmet C, Lauriks W, Glorieux C, Thoen J. Theory of Scholte, leaky Rayleigh, and lateral wave excitation via the laser-induced thermoelastic effect. J. Acoust. Soc. Am. 1996;100:1514.
41. Liu G, Toncich DJ, Harvey EC. Evaluation of excimer laser ablation of thin Cr film on glass substrate by analysing acoustic emission. Opt. Lasers Eng. 2004;42:639.
42. Lu YF, Lee YP, Hong MH, Low TS. Acoustic wave monitoring of cleaning and ablation during excimer laser interaction with copper surfaces. Appl. Surf. Sci. 1997;119:137.
43. Jankowska M, Śliwiński G. Acoustic monitoring for the laser cleaning of sandstone. J. Cult. Herit. 2003;4:65.
44. Villarreal-Villela AE, Cabrera LP. Monitoring the laser ablation process of paint layers by PILA technique. Open J. Appl. Sci. 2016;06:626.
45. Chen Y, Deng G, Zhou Q, Feng G. Acoustic signal monitoring in laser paint cleaning. Laser Phys. 2020;30:066001.
46. Papanikolaou A, Tserevelakis GJ, Melessanaki K, Fotakis C, Zacharakis G, Pouli P. Development of a hybrid photoacoustic and optical monitoring system for the study of laser ablation processes upon the removal of encrustation from stonework. Opto-Electronic Adv. 2020;3:19003701.

47. Tserevelakis GJ, Pouli P, Zacharakis G. Listening to laser light interactions with objects of art: a novel photoacoustic approach for diagnosis and monitoring of laser cleaning interventions. Herit. Sci. 2020;8:98.
48. Schneider D. Laser-induced surface acoustic waves for material testing. In: Handbook of advanced non-destructive evaluation. Cham: Springer; 2018. p. 1.
49. Schneider D, Schwarz T, Scheibe H-J, Panzner M. Non-destructive evaluation of diamond and diamond-like carbon films by laser induced surface acoustic waves. Thin Solid Films. 1997;295:107.
50. Schneider D, Hofmann R, Schwarz T, Grosser T, Hensel E. Evaluating surface hardened steels by laser-acoustics. Surf. Coatings Technol. 2012;206:2079.
51. Schneider D, Brenner B, Schwarz T. Characterization of laser hardened steels by laser induced ultrasonic surface waves. J. Nondestruct. Eval. 1995;14:21.
52. Ma XQ, Mizutani Y, Takemoto M. Laser-induced surface acoustic waves for evaluation of elastic stiffness of plasma sprayed materials. J. Mater. Sci. 2001;36:5633.
53. Bescond C, Kruger SE, Lévesque D, Lima RS, Marple BR. In-situ simultaneous measurement of thickness, elastic moduli and density of thermal sprayed wc-co coatings by laser-ultrasonics. J. Therm. Spray Technol. 2007;16:238.
54. F. Vaz, S. Carvalho, L. Rebouta, M. . Silva, A. Paúl, and D. Schneider, "Young's modulus of (Ti,Si)N films by surface acoustic waves and indentation techniques," Thin Solid Films, vol. 408, 1–2, pp. 160, 2002.
55. Yang F, et al. An integrated laser-induced piezoelectric/differential confocal surface acoustic wave system for measurement of thin film young's modulus. Sensors. 2012;12:12208.
56. Podymova NB, Karabutov AA, Cherepetskaya EB. Laser optoacoustic method for quantitative non-destructive evaluation of the subsurface damage depth in ground silicon wafers. Laser Phys. 2014;24:086003.
57. Cai Y, Cheung NH. Photoacoustic monitoring of the mass removed in pulsed laser ablation. Microchem. J. 2011;97:109.
58. Kradolfer S, Heutschi K, Koch J, Günther D. Listening with curiosity–tracking the acoustic response of portable laser ablation. Chimia (Aarau). 2021;75:300.
59. Kradolfer S, Heutschi K, Koch J, Günther D. Tracking mass removal of portable laser ablation sampling by its acoustic response. Spectrochim. Acta B. 2021;179:106118.
60. van den Heuvel JC, Klein V, Lutzmann P, van Putten FJM, Hebel M, Schleijpen HMA. Sound wave and laser excitation for acousto-optical landmine detection. Detect. Remediat. Technol. Mines Minelike Targets VIII. 2003;5089:569.
61. Moros J, Gaona I, Laserna J. Remotely exploring deeper-into-matter by non-contact detection of audible transients excited by laser radiation. Sensors. 2017;17:2960.
62. Cleary SF. Laser pulses and the generation of acoustic transients in biological material. In: Laser applications in medicine and biology. Boston, MA: Springer, US; 1977. p. 175
63. Esenaliev RO, Oraevsky AA, Letokhov VS, Karabutov AA, Malinsky TV. Studies of acoustical and shock waves in the pulsed laser ablation of biotissue. Lasers Surg. Med. 1993;13:470.
64. Li C, Guan G, Zhang F, Nabi G, Wang RK, Huang Z. Laser induced surface acoustic wave combined with phase sensitive optical coherence tomography for superficial tissue characterization: a solution for practical application. Biomed. Opt. Express. 2014;5:1403.
65. Li C, et al. Quantitative elasticity measurement of urinary bladder wall using laser-induced surface acoustic waves. Biomed. Opt. Express. 2014;5:4313.
66. Ghasemi F, Parvin P, Hosseini Motlagh NS, Amjadi A, Abachi S. Laser induced breakdown spectroscopy and acoustic response techniques to discriminate healthy and cancerous breast tissues. Appl. Opt. 2016;55:8227.
67. Maurice S, et al. In situ recording of Mars soundscape. Nature. 2022;605:653.
68. Maurice S, et al. Acoustic recording of LIBS analyses in preparation for Mars 2020. In: 48th Lunar and Planetary Science Conference; 2017. p. 2647.
69. Chide B, et al. Recording laser-induced sparks on Mars with the SuperCam microphone. Spectrochim. Acta B. 2020;174.